NATO Science for Peace and Security Series - B:
Physics and Biophysics

Progress in High Energy Physics and Nuclear Safety

Edited by
Viktor Begun
László L. Jenkovszky
Aleksander Polański

Springer

NATO OTAN

This publication is supported by:

The NATO Science for Peace and Security Programme

Progress in High-Energy Physics
and Nuclear Safety

NATO Science for Peace and Security Series

This Series presents the results of scientific meetings supported under the NATO Programme: Science for Peace and Security (SPS).

The NATO SPS Programme supports meetings in the following Key Priority areas: (1) Defence Against Terrorism; (2) Countering other Threats to Security and (3) NATO, Partner and Mediterranean Dialogue Country Priorities. The types of meeting supported are generally "Advanced Study Institutes" and "Advanced Research Workshops". The NATO SPS Series collects together the results of these meetings. The meetings are co-organized by scientists from NATO countries and scientists from NATO's "Partner" or "Mediterranean Dialogue" countries. The observations and recommendations made at the meetings, as well as the contents of the volumes in the Series, reflect those of participants and contributors only; they should not necessarily be regarded as reflecting NATO views or policy.

Advanced Study Institutes (ASI) are high-level tutorial courses intended to convey the latest developments in a subject to an advanced-level audience

Advanced Research Workshops (ARW) are expert meetings where an intense but informal exchange of views at the frontiers of a subject aims at identifying directions for future action

Following a transformation of the programme in 2006 the Series has been re-named and re-organised. Recent volumes on topics not related to security, which result from meetings supported under the programme earlier, may be found in the NATO Science Series.

The Series is published by IOS Press, Amsterdam, and Springer, Dordrecht, in conjunction with the NATO Public Diplomacy Division.

Sub-Series

A.	Chemistry and Biology	Springer
B.	Physics and Biophysics	Springer
C.	Environmental Security	Springer
D.	Information and Communication Security	IOS Press
E.	Human and Societal Dynamics	IOS Press

http://www.nato.int/science
http://www.springer.com
http://www.iospress.nl

Series B: Physics and Biophysics

Progress in High-Energy Physics and Nuclear Safety

edited by

Viktor Begun
Bogolyubov Institute for Theoretical Physics
National Academy of Sciences of Ukraine
Kiev, Ukraine

László L. Jenkovszky
Bogolyubov Institute for Theoretical Physics
National Academy of Sciences of Ukraine
Kiev, Ukraine

and

Aleksander Polański
The Andrzej Soltan Institute for Nuclear Studies
Otwock-Swierk, Poland

Published in cooperation with NATO Public Diplomacy Division

Proceedings of the NATO Advanced Research Workshop on
Safe Nuclear Energy
Yalta, Crimea, Ukraine
27 September – 2 October 2008

Library of Congress Control Number: applied for

ISBN 978-90-481-2286-8 (PB)
ISBN 978-90-481-2285-1 (HB)
ISBN 978-90-481-2287-5 (e-book)

Published by Springer,
P.O. Box 17, 3300 AA Dordrecht, The Netherlands.

www.springer.com

Printed on acid-free paper

Preface

On September 27 – October 3, 2008 the NATO Advanced Research Workshop (ARW) on progress in high-energy physics and nuclear safety was held in Yalta, Crimea (see: http://crimea.bitp.kiev.ua and http://arw.bitp.kiev.ua). Nearly 50 leading experts in high-energy and nuclear physics from Eastern and Western Europe as well as from North America participated at the Workshop.

The topics of the ARW covered recent results of theoretical and experimental studies in high-energy physics, accelerator, detection and nuclear technologies, as well as problems of nuclear safety in high-energy experimentation and in nuclear industry. The forthcoming experiments at the Large Hadron Collider (LHC) at CERN and cosmic-ray experiments were among the topics of the ARW.

An important aspect of the Workshop was the scientific collaboration between nuclear physicists from East and West, especially in the field of nuclear safety.

The present book contains a selection of invited talks presented at the ARW. The papers are grouped in two parts.

Part I contains original papers on the progress in high-energy physics – theory, phenomenology and experiment. The Part opens with two papers by prominent Russian theorists, members of the Russian Academy of Sciences, L.D. Faddeev and A.A. Slavnov, known for their classical works in quantum field theory and, more generally, in mathematical physics. One of them – Ludwig Faddeev – winner of many prestigious prizes, was also awarded (shared with Vladimir Arnold) by the 2008 Shaw prize for his widespread and influential contributions to mathematical physics.

The subsequent papers of Part I, ordered alphabetically by the author name of presentation, cover most of the current high-energy experiments, thus giving a panorama of the present state of the high-energy particle and nuclear physics. The role of, and the need for the Higgs particle in the standard theory of the micro-world is the frontier of modern physics. Possible explanations of its non-observation are widely presented in the theoretical and experimental papers of Part I. Among other topics is high-energy diffraction – a familiar but still enigmatic phenomenon observed at largest accelerator of particles and nuclei. Recently it was realized that diffraction can produce a glue-rich environment ("glue" comes from "gluon" – an

elementary field in quantum chromo-dynamics), favoring the production and detection of new particles, such as Higgs, magnetic monopoles or super-partners of the known particles.

The chances to create a mini-black hole in an accelerator experiment, e.g. at the LHC and its safety aspects, i.e. its impact on the environment, often exaggerated by the mass media, are also analyzed in the book. On the other hand, the prospects to create a new phase of the hot and dense nuclear matter (quark-gluon plasma, superfluid nuclear matter etc.) in high-energy heavy-ion collisions are more promising. The diagnostic of relevant signals is a key issue in this field.

Part II contains papers on various aspects of nuclear energy safety. This Part opens with a paper by a leading Ukrainian expert, chairman of the nuclear physics department of the Ukrainian National Academy of Sciences, academician I.M. Neklyudov and his collaborators, on the progress in developing new radiation-resistant materials for the present and future nuclear reactors. It is followed by an interesting proposal by S. Taczanowski from Poland to use coal-nuclear symbiotic methods of energy production. In another paper from Ukraine, new and safe nuclear reactor designs, including the so-called slowly-burning (Feoktistov) reactor, are presented, contrasting the background of the Chernobyl disaster and its lessons. More papers deal with recent progress in nuclear safety.

The original color of the figures presented in the book can be recovered in the electronic version of the relevant presentations, by opening http://crimea.bitp.kiev.ua/, then clicking “Presentations”.

We thank the participants of this Workshop for their invaluable contributions. We are grateful to our technical editor Lyuba Shmagailo for her highly professional performance in preparing the camera-ready version of this book. The ARW and the present publication were supported by the NATO SPS Program, grant No 983265.

Viktor Begun
László L. Jenkovszky
Aleksander Polański

Contents

List of Contributors

K. Azizi
Department of Physics, Middle East Technical University, 06531, Ankara, Turkey,
e-mail: e146342@metu.edu.tr

R. Bernabei
Dip. di Fisica, Università di Roma "Tor Vergata" and INFN, sez. Roma "Tor Vergata", I-00133 Rome, Italy, e-mail: rita.bernabei@roma2.infn.it

M.V. Bondarenco
NSC Kharkov Institute of Physics & Technology, Kharkov 61108, Ukraine,
e-mail: bon@kipt.kharkov.ua

F. Bucci
Università di Firenze, via G. Sansone 1, 50019 Sesto Fiorentino, Firenze,
e-mail: francesca.bucci@fi.infn.it

G.W. Buschhorn
Max-Planck-Institute for Physics (Werner-Heisenberg-Institute), Munich, Germany,
e-mail: gwb@mppmu.mpg.de

M.A. Carrettoni
Università degli Studi di Milano-Bicocca, p.zza delle Scienze 3,
e-mail: marco.carrettoni@mib.infn.it

A. Chukanov
Joint Institute for Nuclear Research, Dubna, Russia,
e-mail: chukanov@nusun.jinr.ru

L.D. Faddeev
Mathematical Inst. RAS, St. Petersburg, e-mail: faddeev@pdmi.ras.ru

E. Frlež
Department of Physics, University of Virginia, Charlottesville, VA 22904-4714,
USA, e-mail: frlez@virginia.edu

Ch. Genta
INFN and University of Florence, via Sansone 1 - I50019 Sesto Fiorentino (FI) - Italy, e-mail: genta@fi.infn.it

G. Giacomelli
University of Bologna and INFN Bologna, Italy, e-mail: giacomelli@bo.infn.it

L.L. Jenkovszky
Bogolyubov Institute for Theoretical Physics, National Academy of Sciences of Ukraine, Kiev 143, 03680, Ukraine, e-mail: jenk@bitp.kiev.ua

S. Kilim
Institute of Atomic Energy, 05-400 Otwock-Swierk, Poland

V.P. Konchakovski
Helmholtz Research School, Frankfurt, Germany;
Bogolyubov Institute for Theoretical Physics, Kiev, Ukraine,
e-mail: voka@fias.uni-frankfurt.de

D.O. Krivenkov
Joint Insitute for Nuclear Research, Dubna, Russia, e-mail: krivenkov@lhe.jinr.ru

I. Larin
Alikhanov Institute for Theoretical and Experimental Physics, Moscow, Russia,
e-mail: larin@itep.ru

M. Malberti
INFN Milano-Bicocca, Piazza della Scienza 3, I-20126, Milano, Italy,
e-mail: martina.malberti@mib.infn.it

St. Mersi
CH-1211 Genève 23 Switzerland, e-mail: stefano.mersi@cern.ch

I.M. Neklyudov
National Science Center “Kharkov Institute of Physics and technology”,
1, Akademicheskaya Str., Kharkov 61108

A. Papa
Università degli studi di Pisa and INFN, I-56127 Pisa, Italy

M. Pimenta
LIP/IST, Av. Elias Garcia 14, 1. P-1000-149 Lisboa, Portugal,
e-mail: pimenta@lip.pt

J.L. Pinfold
Centre for Particle Physics Research, Edmonton, Alberta T6G 0V1, Canada,
e-mail: pinfold@phys.ualberta.ca

A. Polański
The A. Soltan Institute for Nuclear Studies, 05-400 Otwock-Swierk, Poland

G. Ruggiero
Scuola Normale Superiore, Pisa, Italy, e-mail: giuseppe.ruggiero@cern.ch

A. Shaykhiev
Institute for Nuclear Research RAS, 60 October Revolution Pr. 7a, 117312 Moscow, Russia, e-mail: shaykhiev@inr.ru

A.A. Slavnov
Steklov Mathematical Institute and Moscow State University, Moscow, Russia

P. Szymański
The Andrzej Soltan Institute for Nuclear Studies, 05-400 Otwock-Swierk, Poland, e-mail: Piotr.Szymanski@ipj.gov.pl

St. Taczanowski
Faculty of Physics and Applied Computer Science, AGH University of Science and Technology, 30 059 Cracow, Poland

V.N. Voyevodin
National Science Center "Kharkov Institute of Physics and technology", 1, Akademicheskaya Str., Kharkov 61108, e-mail: voyev@kipt.kharkov.ua

Chr. Zeitnitz
Bergische Universität Wuppertal, Gaussstrasse 20 D-42119 Wuppertal, e-mail: zeitnitz@uni-wuppertal.de

P. Zhivkov
Institute for Nuclear Research and Nuclear Energy, Bulgarian Academy of Science

Part I
Progress in High-Energy Physics

An Alternative Interpretation of the Weinberg–Salam Model

L.D. Faddeev

Abstract A new interpretation of the Higgs field on the basis of a non-orthodox approach to the Weinberg–Salam (WS) model is suggested. It is argued that the masses of vector mesons can be generated without the use of the Higgs potential.

Keywords: Yang–Mills, Weinberg–Salam, Goldstone, vector meson, scalar field, Abelian transformation, ferromagnetism

Si nous ne trouvons pas des choses agréables,
nous trouverons du moins des choses nouvelles.
Cacambo to Candide before finding Eldorado

My wife and me found this phrase while reading on the Crimean beach during free time Voltaire's ironic description of the Candide's adventures. (What can you do on the beach but collecting pebbles and reading.) We could not help noting, that this sentence reflects feelings of the large part of physical community in wake of the results on LHC. In my talk, based on the joint paper with A. Niemi and M. Chernodub [1], I shall present a nonorthodox approach to WS model, proposing a new interpretation for the Higgs field. In particular I shall argue, that masses of vector bosons could be suplemented without use of the Higgs potential.

The paper [1] was produced by email correspondence and the version of A.N. and M.Ch. was published. Here I shall use my approach, which is fully equivalent to [1] and add some personal remarks.

The new interpretation concerns only bosonic part of WS model, so I shall consider only lagrangian for complex scalar dublet $\Phi = (\phi_1, \phi_2)$, abelian vector field Y_μ and SU(2) Yang–Mills triplet $B^a_\mu, a = 1,2,3$

$$\mathscr{L} = \left(\nabla_\mu \Phi, \nabla_\mu \Phi\right) + \frac{1}{4g^2} B^a_{\mu\nu} B^a_{\mu\nu} + \frac{1}{4g'^2} Y^2_{\mu\nu},$$

L.D. Faddeev
St. Petersburg Department of Steklov Mathematical Institute, Russian Academy of Sciences,
e-mail: faddeev@pdmi.ras.ru

V. Begun et al. (eds.), *Progress in High-Energy Physics and Nuclear Safety*,

where

$$\nabla_\mu \Phi = \partial_\mu \Phi + \frac{i}{2} Y_\mu \Phi + B^a_\mu t^a \Phi$$

$$B^a_{\mu\nu} = \partial_\mu B^a_\nu - \partial_\nu B_\mu + \varepsilon_{abc} B^b_\mu B^c_\nu$$

$$Y_{\mu\nu} = \partial_\mu Y_\nu - \partial_\nu Y_\mu$$

with $t^a = \frac{i}{2}\tau^a$, τ^a — Pauli matrices, $(\cdot,\cdot)$ — hermitian scalar product in $\mathbb{C}^2$, g and g' — coupling constants.

I do not introduce selfinteraction for the scalar field Φ. The interpretation below is exactly based on this omission. In fact all my friends among theoretical physicists hate ϕ^4 interaction, it is not asymptotically free and quite possible dissapears under proper renormalization.

The lagrangian $\mathscr{L}$ has U(2) gauge invariance with parameters: matrix Ω from SU(2) and real function ω:

$$\Phi^\Omega = \Omega\Phi, \quad \Phi^\omega = e^{i\omega}\Phi,$$
$$B^\Omega_\mu = \Omega B_\mu \Omega^{-1} - \partial_\mu \Omega \Omega^{-1}, \quad B^\omega_\mu = B_\mu,$$
$$Y^\Omega_\mu = Y_\mu, \quad Y^\omega_\mu = Y_\mu - 2\partial_\mu \omega.$$

Here $B_\mu = B^a_\mu t^a$. The idea of [1] is to make the change of variables, which leads to the gauge invariant degrees of freedom. Before presenting the explicite formulas I shall give a geometric reason for them. The "target" for the field Φ is $\mathbb{C}^2$ or $\mathbb{R}^4$ if we count real components. In radial coordinates $\mathbb{R}^4$ can be presented as $\mathbb{R}_+ \times \mathbb{S}^3$ and furthermore $\mathbb{S}^3$ is (almost) the same as SU(2). The SU(2) degrees of freedom, realized as matrix g, allow to introduce gauge transformation of the Yang–Mills field, leaving the gauge invariant vector field. In [1] one of realization of this idea was proposed. I am sure, that this comment is not original, a similar considerations were discussed for example long ago in [2]. However, I believe that the interpretation given below is new.

Let us proceed. We should extract the SU(2) degrees of freedom from Φ in most convenient way. Here is my proposal. First write Φ as

$$\Phi = \rho\chi,$$

where ρ is a positive function and χ — normalised as follows

$$(\chi,\chi) = \bar\chi_1\chi_1 + \bar\chi_2\chi_2 = 1.$$

The matrix

$$g = \begin{pmatrix} \chi_1 & -\bar\chi_2 \\ \chi_2 & \bar\chi_1 \end{pmatrix} = |\chi, \sigma\bar\chi|$$

is unimodular and unitary. Here

$$\sigma = \frac{1}{i}\tau_2 = \begin{pmatrix} 0 & -1 \\ 1 & 0 \end{pmatrix}.$$

The doublet $\sigma\bar{\chi}$ transforms under the nonabelian gauge transformation exactly as χ, indeed

$$\left(\sigma\bar{\chi}\right)^{\Omega} = \sigma\bar{\Omega}\bar{\chi} = -\sigma\bar{\Omega}\sigma\sigma\bar{\chi} = \Omega\sigma\bar{\chi},$$

where I use the properties $\sigma^2 = -I$ and $\sigma\bar{\tau}\sigma = \tau$ for all Pauli matrices. Thus the whole matrix g transforms as

$$g^{\Omega} = \Omega g.$$

The abelian transformation is different for χ and $\bar{\chi}$, so that

$$g^{\omega} = g\begin{pmatrix} e^{i\omega} & 0 \\ 0 & e^{-i\omega} \end{pmatrix} = ge^{i\omega\tau_3}.$$

We see, that covariant derivative of g assumes the form

$$\nabla_\mu g = \partial_\mu g + \frac{i}{2}Y_\mu g\tau_3 + B_\mu g$$

and $|\nabla_\mu \Phi|^2$ can be rewritten as

$$|\nabla_\mu \Phi|^2 = \frac{\rho^2}{2}\mathrm{tr}\big((\nabla_\mu g)^*(\nabla_\mu g)\big) + \partial_\mu\rho\partial_\mu\rho.$$

Introduce the new vector field

$$W_\mu = g^* B_\mu g + g^*\partial_\mu g.$$

It is easy to check, that

$$\begin{aligned} W_\mu^{\Omega} &= W_\mu, \\ W_\mu^{\omega} &= e^{-i\omega\tau_3}W_\mu e^{i\omega\tau_3} + i\partial_\mu\omega\tau_3 \end{aligned}$$

and direct calculation shows, that

$$\frac{1}{2}\mathrm{tr}\big((\nabla_\mu g)^*(\nabla_\mu g)\big) = \frac{\rho^2}{4}\mathrm{tr}\big(Z_\mu^2 + [W_\mu, \tau_3]^2\big) = \frac{\rho^2}{4}\big(Z_\mu^2 + W_\mu^+ W_\mu^-\big),$$

where

$$Z_\mu = Y_\mu + W_\mu^3$$

and we introduce the components of field W_μ

$$\begin{aligned} W_\mu &= \frac{i}{2}(W_\mu^1\tau_1 + W_\mu^2\tau_2 + W_\mu^3\tau_3) \\ W_\mu^\pm &= W_\mu^1 \pm W_\mu^2. \end{aligned}$$

In these components

$$(W_\mu^\pm)^\omega = e^{\pm 2i\omega}W_\mu^\pm, \quad (W_\mu^3)^\omega = W_\mu^3 + 2\partial_\mu\omega,$$

so that abelian vector field Z_μ is completely gauge invariant and $W_\mu^\pm$ and W_μ^3 behave under abelian transformation as charged and abelian gauge vector field, correspondingly.

The vector part of the lagrangian can be rewritten as

$$\frac{1}{4g'^2}Y_{\mu\nu}^2+\frac{1}{4g^2}(W_{\mu\nu}^3+H_{\mu\nu})^2+\frac{1}{4g^2}(\nabla_\mu W_\nu^+-\nabla_\nu W_\mu^+)(\nabla_\mu W_\nu^--\nabla_\nu W_\mu^-),$$

where

$$\begin{aligned}W_{\mu\nu}^3=&\partial_\mu W_\nu^3-\partial_\nu W_\mu^3\\ H_{\mu\nu}=&\frac{1}{2i}(W_\mu^+W_\nu^--W_\mu^-W_\nu^-)\end{aligned}$$

and

$$\nabla_\mu W_\nu^\pm=\partial_\mu W_\nu^\pm\pm iW_\mu^3W_\nu^\pm.$$

To express the sum of quadratic forms of $Y_{\mu\nu}$ and $W_{\mu\nu}^3$ via Z_μ it is convenient to introduce the combination

$$A_\mu=\frac{1}{g^2+g'^2}(g'^2W_\mu-g^2Y_\mu)$$

such that

$$\frac{1}{4g'^2}Y_{\mu\nu}^2+\frac{1}{4g^2}(W_{\mu\nu}^3)^2=\frac{1}{4(g^2+g'^2)}Z_{\mu\nu}^2+\frac{g^2+g'^2}{4g^2g'^2}A_{\mu\nu}^2$$

with as usual

$$Z_{\mu\nu}=\partial_\mu Z_\nu-\partial_\nu Z_\mu,\quad A_{\mu\nu}=\partial_\mu A_\nu-\partial_\nu A_\mu.$$

The abelian vector field A_μ transforms in the same way as W_μ^3

$$A_\mu^\omega=A_\mu-2\partial_\mu\omega$$

and enters into lagrangian via $\frac{1}{4e^2}A_{\mu\nu}^2$ with $e^2=\frac{g^2g'^2}{g^2+g'^2}$. It is clear, that A_μ can be interpreted as electromagnetic field with electric charge given by e the ω-action having meaning of electromagnetic gauge transformation.

Thus in new variables the list of fields consists of real positive field ρ, neutral abelian fields Z_μ and A_μ and charged vector field $W_\mu^\pm$. The lagrangian assumes the form

$$\begin{aligned}\mathscr{L}=&\partial_\mu\rho\partial_\mu\rho+\frac{\rho^2}{4}(Z_\mu^2+W_\mu^+W_\mu^-)+\frac{1}{4g^2}(\nabla_\mu W_\nu^+-\nabla_\nu W_\mu^+)(\nabla_\mu W_\nu^--\nabla_\nu W_\mu^-)\\ &+\frac{1}{4(g^2+g'^2)}Z_{\mu\nu}^2+\frac{1}{4e^2}A_{\mu\nu}^2+\frac{2}{4g^2}(H_{\mu\nu},W_{\mu\nu}^3)+\frac{1}{4g^2}H_{\mu\nu}^2,\end{aligned}$$

where W_μ^3 should be changed to its expression via Z_μ and A_μ. Now we can begin discussion.

The change of variables, which I undertook, eliminates 3 degrees of freedom, leaving positive field ρ instead of four real components of scalar Φ. The functional measure

$$d\mu = \prod_x d\phi_1\, d\bar{\phi}_1\, d\phi_2\, d\bar{\phi}_2\, dY_\mu\, dB_\mu^a$$

used before gauge fixing, looks in new variables as

$$d\mu = \prod_x \rho^2 d\rho^2\, dZ_\mu dW_\mu^+\, dW_\mu^-\, dA\, dg,$$

where $\prod_x dg$ is volume of the gauge group, which is completely separated from measure without any gauge fixing. We are just to drop it to write nonsingular functional integral.

We see, that ρ^2 is not an ordinary scalar field. Besides being positive, it enters the functional integral with local factor. This requires some interpretation. In particular the reason for nontrivial expectation value

$$\langle \rho^2 \rangle = \Lambda^2,$$

supplying mass to vector fields Z_μ and $W_\mu^\pm$, must be elucidated.

In [1] we proposed to interpret ρ^2 as conformal factor of the metric in space-time

$$g_{\mu\nu} = \rho^2 \delta_{\mu\nu}.$$

Indeed, in 4-dimensional space-time we have $\sqrt{g} = \rho^4$, and contravariant vector and tensors have factors

$$\chi^\mu = \rho^{-2}\chi_\mu, \quad \chi^{\mu\nu} = \rho^{-4}\chi_{\mu\nu},$$

so that $\rho^2 Z_\mu^2 = Z_\mu Z^\mu \sqrt{g}$, $H_{\mu\nu}^2 = H_{\mu\nu}H^{\mu\nu}\sqrt{g}$, etc. Moreover the scalar curvature is given by

$$R = \frac{1}{6}\frac{\partial_\mu \rho\, \partial_\mu \rho}{\rho^4} + \text{divergence}.$$

Finally, the Christoffel's symbols, entering the definition of the field strengths $A_{\mu\nu}$, $Z_{\mu\nu}$, $W_{\mu\nu}^\pm$ via covariant derivatives, cancel due to antisymmetry. Thus the lagrangian can be rewritten in manifestly covariant form.

In this interpretation it is natural to require, that

$$\rho^2|_{r\to\infty} \to \Lambda^2$$

at spacial infinity to maintain the asymptotical flatness. Parameter Λ^2 enters as a new parameter of the model.

An alternative argument for nontrivial expectation value Λ^2 looks as follows. The field ρ enters the lagrangian either via derivatives or being multiplied by another field. So the classical vacuum configuration, given by

$$\rho^2 = \Lambda^2, \quad Z_\mu = 0, \quad W_\mu^\pm = 0, \quad A_\mu = 0$$

is degenerate. The choice of particular value of Λ^2 corresponds to the concrete choice of the vacuum. All this looks as noncompact analogy of ferromagnetism.

Thus, one way or another we see, that the nonzero expectation value for the ρ^2 can be envoked without the Higgs potential. The fundamental question which remains, is the origin of the excitations for the field ρ. In both interpretations the most natural answer is massless scalar–analogy of dilaton in the first interpretation or kind of Goldstone mode in the second.

I hope, that more experienced phenomenologist can consider seriously this hypothesis.

References

1. M.N. Chernodub, L. Faddeev, and A. Niemi, Non-abelian Supercurrents and Electroweak Theory, UUITP-04-08, ITEP-LAT-2008-10, arXiv:0804.1544 [hep-th].
2. V.V. Vlasov, V.A. Matveev, A.N. Tavkhelidze, S.Y. Khlebnikov, and M.E. Shaposhnikov, Fiz. Elem. Chast. Atom Yadra **18** (1987) 5.

A Lorentz Invariant Gauge for the Yang–Mills Field Without Gribov Ambiguity

A.A. Slavnov

Abstract A new formulation of the Yang–Mills theory which avoids the problem of Lorentz invariant gauge fixing without Gribov ambiguity is proposed.

Keywords: Yang–Mills field, Gribov ambiguity, Lorentz invariance, gauge invariance, Faddeev–Popov ghosts, Coulomb gauge, Abelian theory

1 Introduction

Non-Abelian gauge theories suffer from the problem of Gribov ambiguity. It is impossible to fix a Lorentz invariant gauge which selects a unique representative in the class of gauge equivalent configurations. For perturbation theory this problem is irrelevant, but for large fields Gribov copies appear, which makes questionable using the standard Faddeev–Popov procedure [1] as a starting point for nonperturbative calculations.

I propose a procedure which preserves in the quantum Yang–Mills theory the manifest Lorentz invariance and at the same time the gauge fixing used in the present paper is free of Gribov ambiguity. In perturbation theory our formulation leads to the same results as the standard quantization procedure.

The paper is organized as follows. In the next section the model is described and its equivalence to the standard Yang–Mills theory is demonstrated. In the third section a new Lorentz invariant gauge condition free of Gribov ambiguity is introduced and the diagram technique is analyzed. The relations between the Green functions are derived. In Conclusion I discuss the results obtained in this paper and their possible applications.

A.A. Slavnov
GSP-1, Vavilov Str., 42, RU-117 966 Moscow,
e-mail: slavnov@mi.ras.ru

V. Begun et al. (eds.), *Progress in High-Energy Physics and Nuclear Safety*,

2 The model

We start with the usual path integral representation for the S-matrix in the Coulomb gauge

$$S = \int \exp\{i \int [L_{YM} + \lambda^a \partial_i A_i^a] dx\} d\mu, \tag{1}$$

where

$$L_{YM} = -\frac{1}{4} F_{\mu\nu}^a F_{\mu\nu}^a, \tag{2}$$

$$F_{\mu\nu}^a = \partial_\mu A_\nu^a - \partial_\nu A_\mu^a + g\varepsilon^{abc} A_\mu^b A_\nu^c, \quad a,b,c,= 1,2,3. \tag{3}$$

The measure $d\mu$ includes differentials of all the fields as well as the Faddeev–Popov determinant $\det M$. This determinant is conveniently presented as the integral over anticommuting ghost fields

$$\det M = \int \exp\left\{ i \int \bar{c} \partial_i D_i c dx \right\} d\bar{c} dc, \tag{4}$$

where D_i is a covariant derivative. For simplicity I assume that we are considering the $SU(2)$ model. Generalization to other groups makes no problem.

The effective action in the integral (1) is not gauge invariant. Contrary to the Abelian case the gauge invariance is broken not only by the gauge fixing term but also by the Faddeev–Popov ghost Lagrangian. To avoid this complication I propose the following construction.

Let us consider the path integral

$$S = \int \exp\{i \int [L_{YM} + (D_\mu \varphi)^* (D_\mu \varphi) - (D_\mu \chi)^* (D_\mu \chi) +$$

$$+ i[(D_\mu b)^* (D_\mu e) - (D_\mu e)^* (D_\mu (b))]] \} dx \delta(\partial_i A_i) d\mu'. \tag{5}$$

The measure $d\mu'$ differs of $d\mu$ by the product of differentials of the scalar fields $(\varphi, \varphi^*, \chi, \chi^*, b, b^*, e, e^*)$.

We assume that the scalar fields comprise complex $SU(2)$ doublets, the fields φ, χ are commuting and b, e are anticommuting. The integration goes over the scalar fields with radiation (Feynman) boundary conditions, which corresponds to considering the matrix elements between states which do not include excitations corresponding to the scalar ghost fields. The gauge fields in the integral (5) satisfy the boundary conditions

$$A_i^{tr} \to A_i^{tr}(in,out), \quad t \to \mp\infty, \tag{6}$$

where A_i^{tr} are the three dimensionally transversal components of A_i, other fields having vacuum boundary conditions. Obviously due to the presence of $\delta(\partial_i A_i)$, $\partial_i A_i = 0$ at any time.

Performing explicitly the integration over the scalar fields in the Eq. (5), we get the factor $(|D|^2)^{-2}$ from the integration over commuting fields φ and χ, and the factor $(|D|^2)^2$ from the integration over the anticommuting fields b and e. Hence the

integral (5) coincides with the integral (1), which justifies the using in the l.h.s. of Eq. (5) the same symbol S.

Let us make in the integral (5) the shift of the integration variables1

$$\varphi \to \varphi + g^{-1}\hat{a}, \quad \chi \to \chi - g^{-1}\hat{a}, \quad \hat{a} = (0, \frac{a}{\sqrt{2}}), \tag{7}$$

a is a constant parameter. Instead of the Eq. (5) now we have

$$\tilde{S} = \int \exp\{\int [L_{YM} + (D_\mu\varphi)^*(D_\mu\varphi) + g^{-1}(D_\mu\varphi)^*(D_\mu\hat{a}) +$$

$$+ g^{-1}(D_\mu\hat{a})^*(D_\mu\varphi) + g^{-1}(D_\mu\chi)^*(D_\mu\hat{a}) + g^{-1}(D_\mu\hat{a}^*)(D_\mu\chi) +$$
$$-(D_\mu\chi)^*(D_\mu\chi) + i[(D_\mu b)^*(D_\mu e) - (D_\mu e)^*(D_\mu b)]dx]\}\delta(\partial_i A_i)d\mu'. \tag{8}$$

Notice that the choice of the negative sign of the kinetic term for the χ field is crucial for our construction. Due to the different signs of kinetic terms for φ and χ fields the shift (7) does not generate a mass term for the Yang–Mills field and preserves the equivalence of the modified theory to the original Yang–Mills model.

The action in the exponent (8) is invariant with respect to "shifted" gauge transformations

$$\begin{aligned}
\delta A^a_\mu &= \partial_\mu \eta^a - g\varepsilon^{abc} A^b_\mu \eta^c \\
\delta\varphi^0 &= \frac{g}{2}\varphi^a\eta^a \\
\delta\varphi^a &= -\frac{a\eta^a}{2} - \frac{g}{2}\varepsilon^{abc}\varphi^b\eta^c - \frac{g}{2}\varphi^0\eta^a \\
\delta\chi^a &= \frac{a\eta^a}{2} - \frac{g}{2}\varepsilon^{abc}\chi^b\eta^c - \frac{g}{2}\chi^0\eta^a \\
\delta\chi^0 &= \frac{g}{2}\chi^a\eta^a \\
\delta b^a &= -\frac{g}{2}\varepsilon^{adc} b^d\eta^c - \frac{g}{2} b^0\eta^a \\
\delta b^0 &= \frac{g}{2} b^a\eta^a \\
\delta e^a &= -\frac{g}{2}\varepsilon^{adc} e^d\eta^c \\
\delta e^0 &= \frac{g}{2} e^a\eta^a,
\end{aligned} \tag{9}$$

where we introduced the representations of the scalar fields in terms of Hermitian components, e.g.

$$\varphi = (\frac{i\varphi_1 + \varphi_2}{\sqrt{2}}, \frac{\varphi_0 - i\varphi_3}{\sqrt{2}}). \tag{10}$$

This action is also invariant with respect to the supersymmetry transformations

$$\delta\varphi^\alpha(x) = i\varepsilon b^\alpha(x)$$

$$\delta\chi^{\alpha}(x) = -i\varepsilon b^{\alpha}(x)$$
$$\delta e^{\alpha}(x) = \varepsilon(\varphi^{\alpha}(x) + \chi^{\alpha}(x))$$
$$\delta b = 0, \tag{11}$$

where ε is an anticommuting constant parameter. This invariance is closely related to the fact that the integral (5) in the sector which does not contain excitations corresponding to the scalar fields coincides with the Yang–Mills scattering matrix. Moreover the renormalization of our model may require introduction of new counterterm structures. To remove ultraviolet infinities generated in the perturbative expansion of the integral (8) mass renormalization of the type

$$i\delta m_g(e^*b - b^*e), \quad \delta m_{\varphi}\varphi^*\varphi, \quad \delta m_{\chi}\chi^*\chi \tag{12}$$

may be needed, as well as new four point vertices

$$\gamma(e^*b - b^*e)^2, \quad \mu(\varphi^*\varphi)^2, \quad \rho(\chi^*\chi)^2. \tag{13}$$

In general any counterterms compatible with the symmetries of the theory may arise. Nevertheless the invariance of the action in the exponent (8) with respect to the transformations (9, 11) provides the unitarity of the S-matrix (8) in the physical subspace which includes only transversal spin one excitations. The proof goes in analogy with the construction given in the papers [2–4].

The invariance of the action with respect to the supersymmetry transformations (11) leads to existence of the conserved charge Q and one can separate the physical subspace by requiring its annihilation by the charge Q. For asymptotic states we shall have

$$Q^0|\psi\rangle^{as}_{ph} = 0, \tag{14}$$

where Q^0 is the asymptotic conserved charge. The asymptotic charges has a form

$$Q^0 \sim \int [\partial_0 b^{\alpha}(\varphi + \chi)^{\alpha} - \partial_0(\varphi + \chi)^{\alpha} b^{\alpha}] d^3x. \tag{15}$$

I recall that we are working in perturbation theory and assume that the interaction is asymptotically turned off. That means all the terms $\sim g$ do not contribute to the asymptotic charge. Being written in terms of creation and annihilation operators the asymptotic charge looks as follows

$$Q^0 \sim \int [a_b^{\alpha+}(a_{\chi}^{\alpha-} + a_{\varphi}^{\alpha-}) + (a_{\chi}^{\alpha+} + a_{\varphi}^{\alpha+})a_b^{\alpha-}] d^3k, \tag{16}$$

where the operators $a^{\pm}$ satisfy the following (anti)commutation relations

$$a_b^{\alpha-}(\mathbf{k})a_e^{\beta+}(\mathbf{k}') + a_e^{\beta+}(\mathbf{k}')a_b^{\alpha-}(\mathbf{k}) = \delta^{\alpha\beta}\delta(\mathbf{k} - \mathbf{k}')$$
$$a_e^{\alpha-}(\mathbf{k})a_b^{\beta+}(\mathbf{k}') + a_b^{\beta+}(\mathbf{k}')a_e^{\alpha-}(\mathbf{k}) = \delta^{\alpha\beta}\delta(\mathbf{k} - \mathbf{k}'), \tag{17}$$

$$a_{\varphi}^{\alpha-}(\mathbf{k})a_{\varphi}^{\beta+}(\mathbf{k}')-a_{\varphi}^{\beta+}(\mathbf{k}')a_{\varphi}^{\alpha-}(\mathbf{k})=\delta^{\alpha\beta}\delta(\mathbf{k}-\mathbf{k}')$$
$$a_{\chi}^{\alpha-}(\mathbf{k})a_{\chi}^{\beta+}(\mathbf{k}')-a_{\chi}^{\beta+}(\mathbf{k}')a_{\chi}^{\alpha-}(\mathbf{k})=-\delta^{\alpha\beta}\delta(\mathbf{k}-\mathbf{k}'). \tag{18}$$

The operator Q^0 is obviously nilpotent as the operators a_b^+, a_b^- are anticommuting and the operators $(a_\chi^- + a_\varphi^-), (a_\chi^+ + a_\varphi^+)$ are mutually commuting.

Nonnegativity of the subspace annihilated by the operator Q^0 may be proven in the usual way (see [5]). Introducing the number operator for unphysical scalar modes

$$\hat{N}=\int\{a_{\varphi}^{+}(\mathbf{k})a_{\varphi}^{-}(\mathbf{k})-a_{\chi}^{+}(\mathbf{k})a_{\chi}^{-}(\mathbf{k})+a_{b}^{+}(\mathbf{k})a_{e}^{-}(\mathbf{k})+a_{e}^{+}(\mathbf{k})a_{b}^{-}(\mathbf{k})\}d^3k, \tag{19}$$

we see that this operator may be presented as the anticommutator

$$\hat{N}=[Q^0,K^0]_+, \tag{20}$$

where

$$K^0=\int\{a_e^+(\mathbf{k})(a_\chi^-(\mathbf{k})-a_\varphi^-(\mathbf{k}))+(a_\chi^+(\mathbf{k})-a_\varphi^+(\mathbf{k}))a_e^-(\mathbf{k})\}d^3k. \tag{21}$$

Applying the number operator (19) to an arbitrary vector we get

$$\hat{N}|\psi\rangle=N|\psi\rangle; \tag{22}$$

if $N\neq 0$ it follows that

$$N|\psi\rangle=Q^0K^0|\psi\rangle+K^0Q^0|\psi\rangle \tag{23}$$

and any vector annihilated by Q^0 has a form

$$|\tilde{\psi}\rangle=|\psi\rangle_{A,c}+Q^0|\omega\rangle, \tag{24}$$

where $|\psi\rangle_{A,c}$ does not contain the excitations corresponding to the ghost fields φ,χ,b,e. Recollecting that this vector contains only three dimensionally transversal excitations of the Yang–Mills field we conclude that

$$|\psi\rangle_{ph}^{as}=|\psi\rangle_{tr}+|N\rangle. \tag{25}$$

Here the vector $|\psi\rangle_{tr}$ depends only on the three dimensionally transversal Yang–Mills field excitations and $|N\rangle$ is a zero norm vector orthogonal to $|\psi\rangle_{tr}$. Factorizing this subspace with respect to the vectors $|N\rangle$ we see that the S-matrix (8) with the counterterms respecting the gauge invariance (9) and supersymmetry (11) is unitary in the subspace which contains only three dimensionally transversal excitations of the Yang–Mills field.

3 An unambiguous Lorentz covariant gauge with gauge invariant ghost interaction

Up to now we considered the Yang–Mills theory in the Coulomb gauge and our reformulation did not give any advantages in comparison with the standard one. In particular the Gribov ambiguity was present. However we may pass in the integral (8) to some other gauge, which avoids the problem of existence of Gribov copies for large fields.

We consider the gauge

$$\varphi^a - \chi^a = 0. \tag{26}$$

Obviously this condition selects a unique representative in the class of gauge equivalent configurations.

To pass to this gauge we shall use the standard Faddeev–Popov trick, multiplying the integral (8) by "one"

$$\Delta \prod_a \int \delta(\varphi^\Omega - \chi^\Omega)^a d\Omega. \tag{27}$$

At the surface $\varphi^a - \chi^a = 0$ the gauge invariant functional Δ is equal to

$$\Delta^{-1} = \prod_x (a + \frac{g}{2}(\varphi^0 - \chi^0))^{-3}. \tag{28}$$

Hence in the gauge (26) the S-matrix generating functional may be written as follows

$$S = \int \exp\{i \int [L_{YM} + (D_\mu \varphi)^*(D_\mu \varphi) - (D_\mu \chi)^*(D_\mu \chi) +$$
$$+ g^{-1}[(D_\mu \varphi)^* + (D_\mu \chi)^*](D_\mu \hat{a}) + g^{-1}(D_\mu \hat{a})^*(D_\mu \varphi + D_\mu \chi) + i[(D_\mu b)^*(D_\mu e) -$$
$$- (D_\mu e)^*(D_\mu b)] + \lambda^a(\varphi^a - \chi^a)]dx\} \Delta d\tilde{\mu}. \tag{29}$$

The measure $d\tilde{\mu}$ is the product of all the fields differentials and does not include any dynamical ghost determinants. All the terms in the exponent except for the gauge fixing term $\int \lambda^a(\varphi^a - \chi^a)dx$ are invariant with respect to the gauge transformations (9).

The part of the effective Lagrangian which describes the interaction of bosonic scalars with the Yang–Mills field looks as follows

$$L_1 = \partial_\mu \varphi^{0+} \partial_\mu \varphi^{0-} + a \partial_\mu \varphi^{a+} A_\mu^{a+} + \frac{g^2}{8} A_\mu^2 (\varphi^{0=} \varphi^{0-}) +$$
$$+ \frac{ag^2}{4} A_\mu^2 \varphi^{0+} - \frac{g}{2} \partial_\mu \varphi^{0-} \varphi^{a+} A_\mu^a + \frac{g}{2} \varphi^{0-} \partial_\mu \varphi^{a+} A_\mu^a, \tag{30}$$

where we used natural notations $\varphi^{\alpha\pm} = \varphi^\alpha \pm \chi^\alpha$.

The integral (29) includes a local measure, which may be formally presented as an addition to the action having a form

$$\delta A = \int \delta^4(0) \ln(1 + \frac{g(\varphi^0 - \chi^0)^3}{2a}) d^4x. \tag{31}$$

This term compensates some ultraviolet divergencies present in the diagrams generated by the expansion of the integral (29). We shall not analyze this cancellation in details and assume that this integral is calculated by using a regularization similar to the dimensional one, that is we omit all counterterms proportional to $\delta(0)$ or $D_c(0)$.

The free action determining the propagators for the perturbative expansion of the integral (29) looks as follows

$$A_0 = \int [-\frac{1}{4}(\partial_\mu A_\nu - \partial_\nu A_\mu)^2 + \frac{1}{2}\partial_\mu \varphi^0 \partial_\mu \varphi^0 -$$

$$-\frac{1}{2}\partial_\mu \chi^0 \partial_\mu \chi^0 + a\partial_\mu \varphi^a A^a_\mu + \frac{1}{2}\partial_\mu b^\alpha \partial_\mu e^\alpha] dx, \tag{32}$$

where we used the gauge condition $\varphi^a = \chi^a$.

One sees that the propagators $\varphi^0, \varphi^0; \chi^0, \chi^0; b^\alpha, e^\beta; A^{tr}_\mu, A^{tr}_\nu$ have a standard form and for large k decrease as k^{-2}, whereas the mixed propagator $\varphi^a, \partial_\mu A^a_\mu$ is a constant $\sim a^{-1}$. The free field A_μ satisfies the condition $\partial_\mu A^a_\mu = 0$.

Account of the interaction leads to modification of this condition. Variation of the Lagrangian (30) with respect to φ^a leads to the following condition on the interacting field A_μ

$$(a + \frac{g}{2}(\varphi^0 - \chi^0))\partial_\mu A^a_\mu = -gA^a_\mu(\partial_\mu \varphi^0 - \partial_\mu \chi^0). \tag{33}$$

Renormalization of our model is not quite trivial, because the propagator of the fields φ^a,A^b_μ decreases at infinity as k^{-1}. This problem will be discussed elsewhere, now we only indicate that perturbative renormalization is most easily performed in the gauge $\partial_\mu A_\mu = 0$, considered above which as was shown defines the same scattering matrix.

The relations between Green functions which replace the standard Slavnov–Taylor (ST) identities [6,7], may be obtained in the same way as the Ward identities in Abelian theories [8–10]. We consider the Green function generating functional given by the integral

$$Z = \int \exp\{i \int [\tilde{L}(A_\mu, \varphi, \chi, b, e) + \lambda^a(\varphi^a - \chi^a) +$$

$$+ J^a_\mu A^a_\mu + \zeta^\alpha(\varphi^\alpha - \chi^\alpha) + \xi^\alpha(\varphi^\alpha + \chi^\alpha) + \kappa^* b + b^* \kappa + \sigma^* e + e^* \sigma] dx\} d\mu, \tag{34}$$

where $\tilde{L}$ is the gauge invariant Lagrangian standing in the exponent of the integral (29), and $J_\mu, \zeta, \xi, \kappa, \sigma$ are external sources. Let us make the change of variables given by the Eq. (9). Due to the gauge invariance of the Lagrangian $\tilde{L}$ the only terms

which change under this transformation are the source terms and the gauge fixing term. Using the fact that the integral (34) does not change under this transformation we get

$$\int \exp\{i\int [\tilde{L}+\lambda^a(\varphi^a-\chi^a)+s.t.]dx\{\lambda^a(y)[a+\frac{g}{2}(\varphi^0(y)-\chi^0(y))]+$$

$$+i\partial_\mu J^a_\mu(y)+\zeta^a(y)[a+\frac{g}{2}(\varphi^0(y)-\chi^0(y))]+\ldots\}d\mu=0. \tag{35}$$

Here $s.t.$ stands for the source terms and $\ldots$ denote the variation of all remaining source terms. It is convenient to make further redefinitions:

$$\lambda^a(a+\frac{g}{2}(\varphi^0-\chi^0))=\lambda'^a, \tag{36}$$

$$\varphi^a-\chi^a=(\varphi^a-\chi^a)'(a+\frac{g}{2}(\varphi^0-\chi^0)). \tag{37}$$

After such redefinition the Eq. (35) acquires the form

$$\int \exp\{i\int [\tilde{L}(A_\mu,(\varphi^a+\chi^a),(\varphi^a-\chi^a)(a+\frac{g}{2}(\varphi^0-\chi^0),\varphi^0,\chi^0,b^\alpha,e^\alpha)+$$

$$+\lambda^a(\varphi^a-\chi^a)+J^a_\mu A^a_\mu+\zeta^a(\varphi^a-\chi^a)(a+\frac{g}{2}(\varphi^0-\chi^0))+\ldots]dx\}\times$$

$$\times\{\lambda^a(y)+\partial_\mu J^a_\mu(y)+\zeta^a(y)(a+\frac{g}{2}(\varphi^0(y)-\chi^0(y))+\ldots\}d\mu=0. \tag{38}$$

Here $\ldots$ denote all remaining source terms and their variations under transformation (9).

This equation replaces the standard system of ST identities. In particular the simplest identity, which follows from the Eq. (38) is

$$\langle\lambda^a(x)A^b_\mu(y)\rangle=\partial_\mu\delta(x-y)\delta^{ab}. \tag{39}$$

As follows from our previous discussion the S-matrix defined by the Eq. (29) coincides with the Coulomb gauge scattering matrix given by the Eq. (1). The Eq. (1) strictly speaking defines a unique S-matrix for the Yang–Mills theory only in perturbation theory. However one can perform the canonical quantization directly in the gauge $\varphi^a-\chi^a=0$, and prove the unitarity of the scattering matrix. Of course beyond the perturbation theory, the proof of unitarity becomes a bit formal.

4 Discussion

The main goal of this paper was to show that Yang–Mills theory allows a manifestly Lorentz invariant formulation without Gribov ambiguity. In this formulation Yang–Mills theory demonstrates a remarkable similarity to QED. The relations between the Green functions which replace in this case the standard ST-identities also

may be derived in a way similar to QED. Gauge invariance of the effective action simplifies the construction of invariant regularization and may be helpful for invariant regularization of non-Abelian supersymmetric models. Finally this construction may be useful for a nonperturbative analysis of the Green functions on the basis of Dyson–Schwinger equations having in mind that the gauge condition (26) does not introduce Gribov ambiguity. This problem requires further investigation.

Acknowledgements I wish to thank the organizers of the Conference and in particular L. Jenkovzsky for hospitality and support. I also acknowledge a partial support by RBRF, under grant 08-01-00281a, and by the grant for support of leading scientific schools -795.2008.1

References

1. L.D. Faddeev, V.N. Popov, Phys. Lett. B **25** (1967) 30
2. A.A. Slavnov, Phys. Lett. B **258** (1991) 391
3. A.A. Slavnov, Phys. Lett. B **620** (2005) 97
4. A.A. Slavnov, TMP **154** (2008) 213
5. M. Henneaux, Proceedings of the Meeting on Quantum Mechanics of Fundamental Systems (Santjago, Plenum Press, 1986)
6. A.A. Slavnov, TMP **10** (1972) 99
7. J.C. Taylor, Nucl. Phys. B **333** (1971) 436
8. J.C. Ward, Phys. Rev. **77** (1950) 2931
9. E.S. Fradkin, JETP **29** (1955) 288
10. Y. Takahashi, Nuovo Cim. **6** (1957) 370

Phenomenology of the Heavy Flavored Spin 3/2 Baryons in Light Cone QCD

T.M. Aliev, K. Azizi, and A. Ozpineci

Abstract Motivated by the results of the recent experimental discoveries for charm and bottom baryons, the masses and magnetic moments of the heavy baryons with $J^P = 3/2^+$ containing a single heavy quark are studied within light cone QCD sum rules method. Our results on the masses of heavy baryons are in good agreement with predictions of other approaches, as well as with the existing experimental data.

Keywords: Magnetic moments, Light cone QCD sum rules, heavy bottom baryons, heavy charm baryons

1 Introduction

In the recent years, considerable experimental progress has been made in the spectroscopy of baryons containing a single heavy quark. The CDF Collaboration has observed four bottom baryons $\Sigma_b^{\pm}$ and $\Sigma_b^{*\pm}$ [1]. The DO [2] and CDF [3] Collaborations have seen the Ξ_b. The BaBar Collaboration discovered the Ω_c^* state [4]. The CDF sensitivity appears adequate to observe new heavy baryons. Study of the electromagnetic properties of baryons can give noteworthy information on their internal structure. One of the main static electromagnetic parameters of the baryons is their magnetic moments. Magnetic moments of the heavy baryons in the framework of different approaches are widely discussed in the literature. In the present work, we study the magnetic moments and masses of the ground state baryons with total angular momentum 3/2 and containing one heavy quark within light cone QCD sum rules. The paper is organized as follows. In section 2, the light cone QCD sum rules for mass and magnetic moments of heavy baryons are calculated. Section 3 is devoted to the numerical analysis of the mass and magnetic moment sum rules

T.M. Aliev, K. Azizi, A. Ozpineci
Department of Physics, Middle East Technical University, 06531, Ankara, Turkey,
e-mail: taliev@metu.edu.tr; e146342@metu.edu.tr; ozpineci@metu.edu.tr

V. Begun et al. (eds.), *Progress in High-Energy Physics and Nuclear Safety*,

and discussion. Detailed analysis of the mass and magnetic moments of the baryons containing single heavy quark is presented in the original work in [5].

2 Light cone QCD sum rules for the mass and magnetic moments of the heavy flavored baryons

To calculate the magnetic moments of the heavy flavored hadrons, we start considering the correlation function which is the basic object in LCSR method. In this correlator, the hadrons are represented by their interpolating quark currents.

$$T_{\mu\nu} = i \int d^4x e^{ipx} \langle 0 \mid T\{\eta_\mu(x)\bar{\eta}_\nu(0)\} \mid 0\rangle_\gamma, \tag{1}$$

where η_μ is the interpolating current of the heavy baryon and γ means the external electromagnetic field. In QCD sum rules method, this correlation function is calculated in two different ways: (1) In terms of quark-gluon language (QCD side), (2) In terms of hadrons, where the correlator is saturated by a tower of hadrons with the same quantum numbers as their interpolating currents (phenomenological side). The magnetic moments are determined by matching two different representations of the correlation function, i.e., theoretical and phenomenological forms, using the dispersion relations.

From Eq. (1), it follows that to calculate the correlation function from QCD side, we need the explicit expressions of the interpolating currents of heavy baryons with the angular momentum $J^P = 3/2^+$. The main condition for constructing the interpolating currents from quark field is that they should have the same quantum numbers of the baryons under consideration. For the heavy baryons with $J^P = 3/2^+$, the interpolating current is chosen in the following general form

$$\eta_\mu = A\varepsilon_{abc}\left\{(q_1^{aT}C\gamma_\mu q_2^b)Q^c + (q_2^{aT}C\gamma_\mu Q^b)q_1^c + (Q^{aT}C\gamma_\mu q_1^b)q_2^c\right\}, \tag{2}$$

where C is the charge conjugation operator and a, b and c are color indices. The value of A and quark fields q_1 and q_2 for each heavy baryon is given in Table 1.

Table 1 The value of A and quark fields q_1 and q_2 for the corresponding baryons

	A	q_1	q_2
$\Sigma_{b(c)}^{*+(++)}$	$1/\sqrt{3}$	u	u
$\Sigma_{b(c)}^{*0(+)}$	$\sqrt{2/3}$	u	d
$\Sigma_{b(c)}^{*-(0)}$	$1/\sqrt{3}$	d	d
$\Xi_{b(c)}^{*0(+)}$	$\sqrt{2/3}$	s	u
$\Xi_{b(c)}^{*-(0)}$	$\sqrt{2/3}$	s	d
$\Omega_{b(c)}^{*-(0)}$	$1/\sqrt{3}$	s	s

The phenomenological part of the correlation function can be obtained by inserting the complete set of states between the interpolating currents in (1) with quantum numbers of heavy baryons.

$$T_{\mu\nu} = \frac{\langle 0 \mid \eta_\mu \mid B(p_2)\rangle}{p_2^2 - m_B^2}\langle B(p_2) \mid B(p_1)\rangle_\gamma \frac{\langle B(p_1) \mid \bar{\eta}_\nu \mid 0\rangle}{p_1^2 - m_B^2}, \tag{3}$$

where $p_1 = p + q$, $p_2 = p$ and q is the photon momentum. The vacuum to baryon matrix element of the interpolating current is defined as

$$\langle 0 \mid \eta_\mu(0) \mid B(p,s)\rangle = \lambda_B u_\mu(p,s), \tag{4}$$

where λ_B is the residue and $u_\mu(p,s)$ is the Rarita–Schwinger spinor. The matrix element $\langle B(p_2) \mid B(p_1)\rangle_\gamma$ entering Eq. (3) can be parameterized in terms of the form factors f_i and G_i as follows

$$\begin{aligned}\langle B(p_2) \mid B(p_1)\rangle_\gamma = \varepsilon_\rho \bar{u}_\mu(p_2) \Bigg\{ -g_{\mu\nu}\left[\gamma_\rho(f_1+f_2) + \frac{(p_1+p_2)_\rho}{2m_B} f_2 + q_\rho f_3\right] \\ - \frac{q_\mu q_\nu}{(2m_B)^2}\left[\gamma_\rho(G_1+G_2) + \frac{(p_1+p_2)_\rho}{2m_B} G_2 + q_\rho G_3\right]\Bigg\} \bar{u}_\nu(p_1),\end{aligned} \tag{5}$$

where ε_ρ is the photon polarization vector and $q^2 = (p_1 - p_2)^2$. To obtain the explicit expressions of the correlation function, summation over spins of the spin 3/2 particles is performed. Using the above equations in principle one can write down the phenomenological part of the correlator. But, the following two drawbacks appear: (a) all Lorentz structures are not independent, (b) not only spin 3/2, but spin 1/2 states also contribute to the correlation function. Indeed the matrix element of the current η_μ between vacuum and spin 1/2 states is nonzero and is determined as

$$\langle 0 \mid \eta_\mu(0) \mid B(p, s = 1/2)\rangle = \alpha(4p_\mu - m\gamma_\mu)u(p, s = 1/2), \tag{6}$$

where the condition $\gamma_\mu \eta^\mu = 0$ is imposed.

There are two different ways to remove the unwanted spin 1/2 contribution and retain only independent structures in the correlation function: (1) Introduce projection operators for the spin 3/2 states, which kill the spin 1/2 contribution, (2) Ordering Dirac matrices in a specific order and eliminate the structures that receive contributions from spin $1/2$ states. In this work, we will follow the second method and choose the ordering for Dirac matrices as $\gamma_\mu \not{p} \not{\varepsilon} \not{q}\gamma_\nu$. With this ordering for the correlator, we get

$$\begin{aligned}T_{\mu\nu} = \lambda_B^2 \frac{1}{(p_1^2 - m_B^2)(p_2^2 - m_B^2)} \Bigg[g_{\mu\nu}\, \not{p}\, \not{\varepsilon}\, \not{q} \frac{g_M}{3} \\ + \text{ other structures with } \gamma_\mu \text{ at the beginning and } \gamma_\nu \text{ at the end} \\ \text{or which are proportional to } p_{2\mu} \text{ or } p_{1\nu} \Bigg],\end{aligned} \tag{7}$$

where $g_M/3 = f_1 + f_2$ and at $q^2 = 0$, g_M is the magnetic moment of the baryon in units of its natural magneton. The factor 3 is due the fact that in the non-relativistic limit the interaction Hamiltonian with magnetic field is equal to $g_M B = 3(f_1 + f_2)B$.

On QCD side, the correlation function (1) can be evaluated using operator product expansion. After simple calculations, we get the following expression for the correlation function in terms of quark propagators

$$\begin{aligned}\Pi_{\mu\nu} &= -iA^2\varepsilon_{abc}\varepsilon_{a'b'c'}\int d^4x e^{ipx}\langle 0[\gamma(q)]\mid\{S_Q^{ca'}\gamma_\nu S'^{bb'}_{q_2}\gamma_\mu S_{q_1}^{ac'} \\ &+ S_Q^{cb'}\gamma_\nu S'^{aa'}_{q_1}\gamma_\mu S_{q_2}^{bc'} + S_{q_2}^{ca'}\gamma_\nu S'^{bb'}_{q_1}\gamma_\mu S_Q^{ac'} + S_{q_2}^{cb'}\gamma_\nu S'^{aa'}_{Q}\gamma_\mu S_{q_1}^{bc'} \\ &+ S_{q_1}^{cb'}\gamma_\nu S'^{aa'}_{q_2}\gamma_\mu S_Q^{bc'} + S_{q_1}^{ca'}\gamma_\nu S'^{bb'}_{Q}\gamma_\mu S_{q_2}^{ac'} + Tr(\gamma_\mu S_{q_1}^{ab'}\gamma_\nu S'^{ba'}_{q_2})S_Q^{cc'} \\ &+ Tr(\gamma_\mu S_Q^{ab'}\gamma_\nu S'^{ba'}_{q_1})S_{q_2}^{cc'} + Tr(\gamma_\mu S_{q_2}^{ab'}\gamma_\nu S'^{ba'}_{Q})S_{q_1}^{cc'}\}\mid 0\rangle, \end{aligned} \tag{8}$$

where $S' = CS^TC$ and $S_Q(S_q)$ is the full heavy (light) quark propagator. In calculation of the correlation function from QCD side, we take into account terms linear in m_q and neglect quadratic terms. The correlator contains three different contributions: (1) Perturbative contributions, (2) Mixed contributions, i.e., the photon is radiated from freely propagating quarks at short distance and at least one of quark pairs interact with QCD vacuum non-perturbatively. The last interaction is parameterized in terms of quark condensates. (3) Non-perturbative contributions, i.e., when photon is radiated at long distances. In order to calculate the contributions of the photon emission from large distances, the matrix elements of nonlocal operators $\bar{q}\Gamma_i q$ between the photon and vacuum states are needed, $\langle\gamma(q)\mid\bar{q}\Gamma_i q\mid 0\rangle$. These matrix elements are determined in terms of the photon distribution amplitudes (DA's). For these matrix elements and also the photon DA's see [6].

Using the expressions of the light and heavy full propagators and the photon DA's and separating the coefficient of the structure $g_{\mu\nu}\not{p}\not{\varepsilon}\not{q}$, the expression of the correlation function from QCD side is obtained. Separating the coefficient of the same structure from phenomenological part and equating these representations of the correlator, sum rules for the magnetic moments of the $J^P = 3/2^+$ heavy baryons is obtained. In order to suppress the contribution of higher states and continuum, Borel transformation with respect to the variables $p_2^2 = p^2$ and $p_1^2 = (p+q)^2$ is applied.The sum rules for the magnetic moments is obtained as

$$-\lambda_B^2\frac{\mu_{B_Q}}{3}e^{\frac{-m_{B_Q}^2}{M^2}} = A^2\Pi^{B_Q}. \tag{9}$$

The functions $\Pi_i(q_1, q_2, Q)$ can be written as

$$\Pi_i = \int_{m_Q^2}^{s_0} e^{\frac{-s}{M^2}}\rho_i(s)ds + e^{\frac{-m_Q^2}{M^2}}\Gamma_i, \tag{10}$$

where the explicit expressions for the ρ_i and Γ_i functions are given in [5]. In the above relations M^2 and s_0 are the Borel mass square and continuum threshold, respectively.

For calculation of the magnetic moments of the considered baryons, their residues λ_B as well as their masses are needed (see Eq. (9)). Note that many of the considered baryons are not discovered yet in the experiments. The residue is determined from analysis of the two point sum rules. For the interpolating current given in Eq. (2), we obtain the following result for λ_B^2:

$$\lambda_B^2 e^{\frac{-m_{B_Q}^2}{M^2}} = A^2 \left[\Pi' + \Pi'(q_1 \longleftrightarrow q_2) \right], \tag{11}$$

where the explicit expression for Π' is presented in [5]. The masses of the considered baryons can be determined from the sum rules. For this aim, one can get the derivative from both side of Eq. (11) with respect to $-1/M^2$ and divide the obtained result to the Eq. (11), i.e.,

$$m_{B_Q}^2 = \frac{-\frac{d}{d(1/M^2)} \left[\Pi' + \Pi'(q_1 \longleftrightarrow q_2) \right]}{\left[\Pi' + \Pi'(q_1 \longleftrightarrow q_2) \right]}. \tag{12}$$

3 Numerical analysis

In this section, we perform numerical analysis for the mass and magnetic moments of the heavy flavored baryons. Firstly, we present the input parameters used in the analysis of the sum rules: $\langle \bar{u}u \rangle (1\ GeV) = \langle \bar{d}d \rangle (1\ GeV) = -(0.243)^3\ GeV^3$, $\langle \bar{s}s \rangle (1\ GeV) = 0.8 \langle \bar{u}u \rangle (1\ GeV)$, $m_0^2 (1\ GeV) = (0.8 \pm 0.2)\ GeV^2$ [7], $\Lambda = 1\ GeV$ and $f_{3\gamma} = -0.0039\ GeV^2$ [6]. The value of the magnetic susceptibility was obtained in various papers as $\chi(1\ GeV) = -3.15 \pm 0.3\ GeV^{-2}$ [6], $\chi(1\ GeV) = -(2.85 \pm 0.5)\ GeV^{-2}$ [8] and $\chi(1\ GeV) = -4.4\ GeV^{-2}$[9].

Before proceeding to the results for the magnetic moments, we calculate the masses of heavy flavored baryons predicted from mass sum rule. Obviously, the masses should not depend on the Borel mass parameter M^2 in a complete theory. However, in sum rules method the operator product expansion (OPE) is truncated and as a result the dependency of the predictions of physical quantities on the auxiliary parameter M^2 appears. For this reason one should look for a region of M^2 such that the predictions for the physical quantities do not vary with respect to the Borel mass parameter. This region is the so called the "working region" and within this region the truncation is reasonable and meaningful. The upper limit of M^2 is determined from condition that the continuum and higher states contributions should be small than the total dispersion integral. The lower limit is determined by demanding that in the truncated OPE the condensate term with highest dimension remains small than sum of all terms, i.e., convergence of OPE should be under control.

These both conditions conditions for bottom (charmed) baryons are satisfied when M^2 varies in the interval $15\ GeV^2 < M^2 < 30\ GeV^2$ ($4\ GeV^2 < M^2 < 12\ GeV^2$). In Figs. 1–5, we presented the dependence of the mass of the heavy flavored baryons on M^2. From these figures, we see very good stability with respect to M^2.

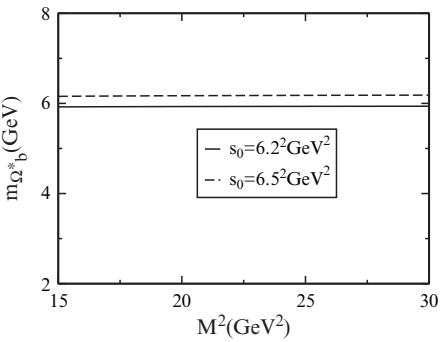

Fig. 1 The dependence of mass of the Ω_b^* on the Borel parameter M^2 for two fixed values of continuum threshold s_0

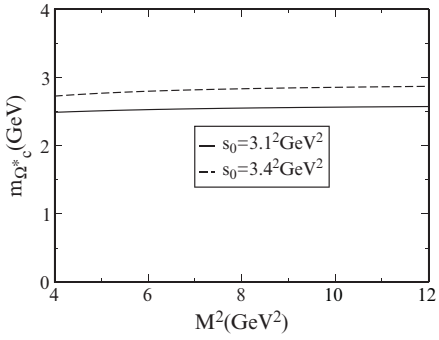

Fig. 2 The dependence of mass of the Ω_c^* on the Borel parameter M^2 for two fixed values of continuum threshold s_0

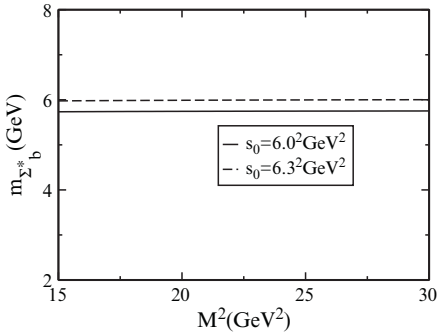

Fig. 3 The same as Fig. 1, but for Σ_b^*

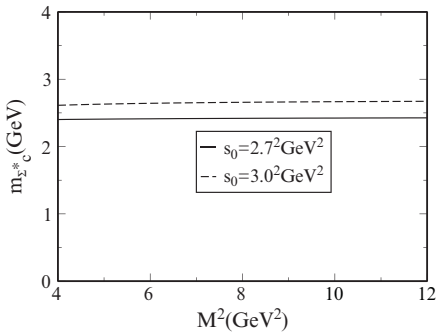

Fig. 4 The same as Fig. 2, but for Σ_c^*

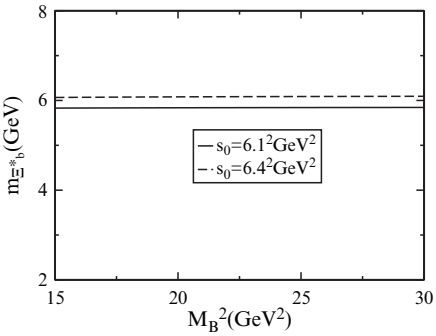

Fig. 5 The same as Fig. 1, but for Ξ_b^*

Table 2 Comparison of mass of the heavy flavored baryons in *GeV* from present work and other approaches and with experiment

	$m_{\Omega_b^*}$	$m_{\Omega_c^*}$	$m_{\Sigma_b^*}$	$m_{\Sigma_c^*}$	$m_{\Xi_b^*}$	$m_{\Xi_c^*}$
This work	6.08 ± 0.40	2.72 ± 0.20	5.85 ± 0.35	2.51 ± 0.15	5.97 ± 0.40	2.66 ± 0.18
[10]	$6.063^{+0.083}_{-0.082}$	$2.790^{+0.109}_{-0.105}$	$5.835^{+0.082}_{-0.077}$	$2.534^{+0.096}_{-0.081}$	$5.929^{+0.088}_{-0.079}$	$2.634^{+0.102}_{-0.094}$
[11]	6.088	2.768	5.834	2.518	5.963	2.654
[12]	-	-	5.805	2.495	-	-
[13]	6.090	2.770	5.850	2.520	5.980	2.650
[14]	-	2.768	-	2.518	-	-
[15]	6.083	2.760	5.840	-	5.966	-
[16]	6.060	2.752	5.871	2.5388	5.959	2.680
Exp[17]	-	2.770	5.836	2.520	-	2.645

The sum rule predictions of the mass of the heavy flavored baryons are presented in Table 2 in comparison with some theoretical predictions and experimental results. Note that the masses of the heavy flavored baryons are calculated in the framework of heavy quark effective theory (HQET) using the QCD sum rules method in [10].

After determination of the mass as well as residue of the heavy flavored baryons our next task is the calculation of the numerical values of their magnetic moments. For this aim, from sum rules for the magnetic moments it follows that the photon DAs are needed [6]. The sum rules for magnetic moments also contain the auxiliary parameters: Borel parameter M^2 and continuum threshold s_0. Similar to mass sum rules, the magnetic moments should also be independent of these parameters. In the general case, the working region of M^2 and s_0 for the mass and magnetic moments should be different. To find the working region for M^2, we proceed as follows. The upper bound is obtained requiring that the contribution of higher states and continuum should be less than the ground state contribution. The lower bound of M^2 is determined from condition that the highest power of $1/M^2$ be less than say 30% of the highest power of M^2. These two conditions are both satisfied in the region $15\ GeV^2 \leq M^2 \leq 30\ GeV^2$ and $4\ GeV^2 \leq M^2 \leq 12\ GeV^2$ for baryons containing b and c-quark, respectively. The working region for the Borel parameter for mass and magnetic moments practically coincide, but again we should stress that, this circumstance is accidental.

In Figs. 6–16, we present the dependence of the magnetic moment of heavy flavored baryons on M^2 at two fixed values of continuum threshold s_0. From these figures, we see that the magnetic moments weakly depend on s_0. The maximal change of results is about 10% with variation of s_0. The magnetic moments also are practically insensitive to the variation of Borel mass parameter when it varies in the working region. We should also stress that our results practically don't change considering three values of χ which we presented at the beginning of this section. Our final results on the magnetic moments of heavy flavored baryons are presented in Table 3. For comparison, the predictions of hyper central model [18] are also presented. The quoted errors in Table 3 are due to the uncertainties in m_0^2, variation of s_0 and M^2 as well as errors in the determination of the input parameters.

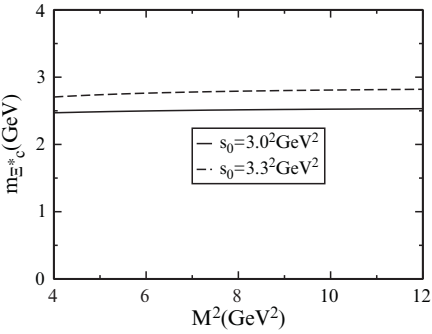

Fig. 6 The same as Fig. 2, but for Ξ_c^*

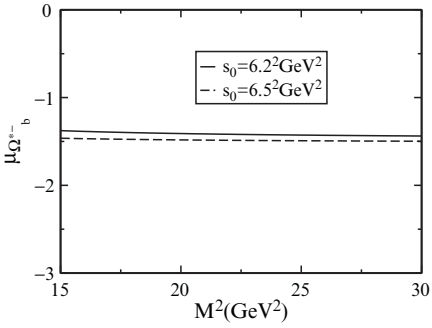

Fig. 7 The dependence of the magnetic moment of Ω_b^{*-} on Borel parameter M^2 (in units of nucleon magneton) at two fixed values of s_0

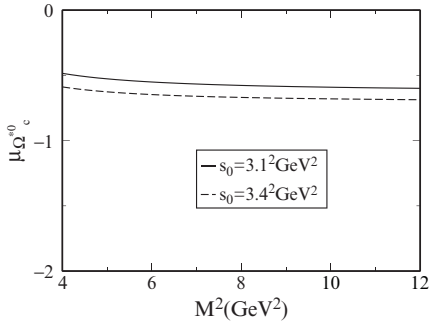

Fig. 8 The dependence of the magnetic moment of Ω_c^{*0} on Borel parameter M^2 (in units of nucleon magneton) at two fixed values of s_0

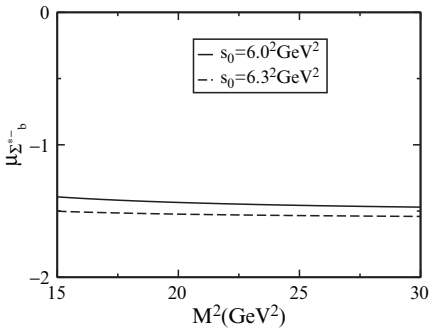

Fig. 9 The same as Fig. 7, but for Σ_b^{*-}

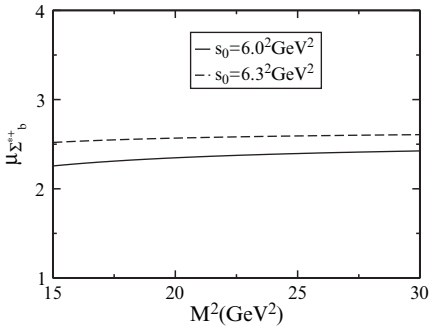

Fig. 10 The same as Fig. 7, but for Σ_b^{*+}

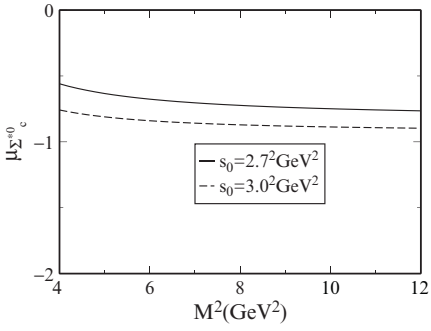

Fig. 11 The same as Fig. 8, but for Σ_c^{*0}

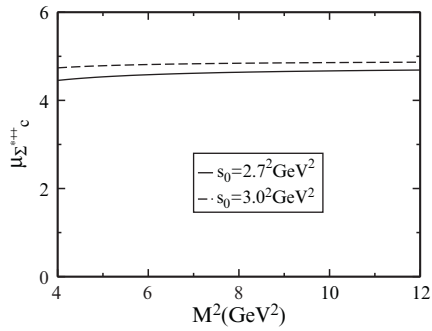

Fig. 12 The same as Fig. 8, but for Σ_c^{*++}

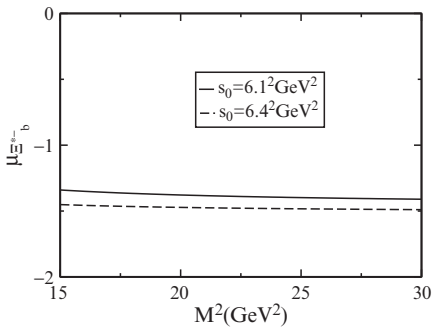

Fig. 13 The same as Fig. 7, but for Ξ_b^{*-}

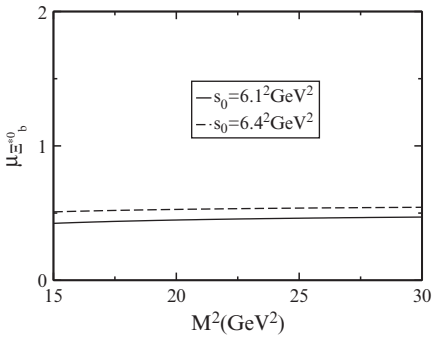

Fig. 14 The same as Fig. 7, but for Ξ_b^{*0}

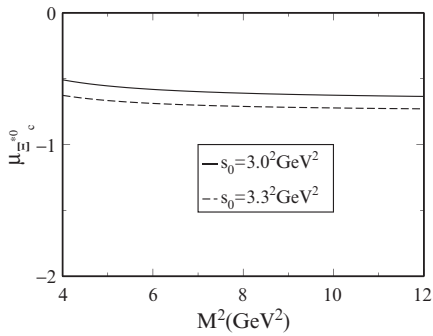

Fig. 15 The same as Fig. 8, but for Ξ_c^{*0}

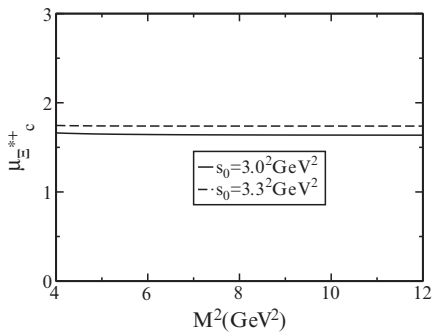

Fig. 16 The same as Fig. 8, but for Ξ_c^{*+}

Table 3 The magnetic moments of the heavy flavored baryons in units of nucleon magneton

	Our results	Hyper central model[18]
$\mu_{\Omega_b^{*-}}$	-1.40 ± 0.35	$-1.178\div-1.201$
$\mu_{\Omega_c^{*0}}$	-0.62 ± 0.18	$-0.827\div-0.867$
$\mu_{\Sigma_b^{*-}}$	-1.50 ± 0.36	$-1.628\div-1.657$
$\mu_{\Sigma_b^{*0}}$	0.50 ± 0.15	$0.778\div0.792$
$\mu_{\Sigma_b^{*+}}$	2.52 ± 0.50	$3.182\div3.239$
$\mu_{\Sigma_c^{*0}}$	-0.81 ± 0.20	$-0.826\div-0.850$
$\mu_{\Sigma_c^{*+}}$	2.00 ± 0.46	$1.200\div1.256$
$\mu_{\Sigma_c^{*++}}$	4.81 ± 1.22	$3.682\div3.844$
$\mu_{\Xi_b^{*-}}$	-1.42 ± 0.35	$-1.048\div-1.098$
$\mu_{\Xi_b^{*0}}$	0.50 ± 0.15	$1.024\div1.042$
$\mu_{\Xi_c^{*0}}$	-0.68 ± 0.18	$-0.671\div-0.690$
$\mu_{\Xi_c^{*+}}$	1.68 ± 0.42	$1.449\div1.517$

Although the $SU(3)_f$ breaking effects have been taken into account through a nonzero s-quark mass and different strange quark condensate, we predict that $SU(3)_f$ symmetry violation in the magnetic moments is very small, except the relations $\mu_{\Sigma_c^{*+}}=\mu_{\Xi_c^{*+}}$ and $\Pi^{\Sigma_c^{*++}}+\Pi^{\Omega_c^{*0}}=2\Pi^{\Xi_c^{*+}}$, where the $SU(3)_f$ symmetry violation is large. For the values of the magnetic moments, our results are consistent with the results of [18] except for the $\mu_{\Omega_b^{*-}}$, $\mu_{\Xi_b^{*-}}$ and especially for the $\mu_{\Sigma_c^{*+}}$, $\mu_{\Xi_b^{*0}}$ which we see a big discrepancy between two predictions.

In summary, inspired by recent experimental discovery of the heavy and flavored baryons [1–3], the mass and magnetic moments of these baryons with $J^P=3/2^+$ are calculated within the QCD sum rules. Our results on the masses are consistent with the experimental data as well as predictions of other approaches. Our results on the masses of the Ω_b^*, and Ξ_b^* can be tested in experiments which will be held in the near future. The predictions on the magnetic moments also can verified in the future experiments.

Acknowledgements K.A thanks the organizers of the Crimean conference (2008) for their hospitality. Two of the authors (K.A. and A.O.), would like to thank TUBITAK and TUBA for their partial financial support.

References

1. T. Aaltonen et al., CDF Collaboration, Phys. Rev. Lett. **99** (2007) 202001.
2. V. Abazov et al., DO Collaboration, Phys. Rev. Lett. **99** (2007) 052001.
3. T. Aaltonen et al., CDF Collaboration, Phys. Rev. Lett. **99** (2007) 052002.
4. B. Aubert et al., BaBar Collaboration, Phys. Rev. Lett. **97** (2006) 232001.
5. T.M. Aliev, K. Azizi, A. Ozpineci, doi:10.1016/j.nuclphysb.2008.09.018; arXiv:0807.3481v2 [hep-ph].

6. P. Ball, V.M. Braun, N. Kivel, Nucl. Phys. B **649** (2003) 263.
7. V.M. Belyaev, B.L. Ioffe, JETP **56** (1982) 493.
8. J. Rohrwild, JHEP **0709** (2007) 073.
9. V.M. Belyaev, I.I. Kogan, Yad. Fiz. **40** (1984) 1035.
10. X. Liu, H.X. Chen, Y.R. Liu, A. Hosaka, S.L. Zhu, arXiv: 07100123 (hep-ph).
11. D. Ebert, R.N. Faustov, V.O. Galkin, Phys. Rev. D **72** (2005) 034026.
12. S. Capstick, N. Isgur, Phys. Rev. D **34** (1986) 2809.
13. R. Ronaglia, D.B. Lichtenberg, E. Predazzi, Phys. Rev. D **52** (1995) 1722.
14. M.J. Savage, Phys. Lett. B **359** (1995) 189.
15. E. Jenkins, Phys. Rev. D **54** (1996) 4515; ibid **55** (1997) R10.
16. N. Mathur, R. Lewis, R.M. Woloshyn, Phys. Rev. D **66** (2002) 014502.
17. C. Amsler et al. (Particle Data Group), Phys. Lett. B **667** (2008) 1.
18. B. Patel, A.K. Rai, P.C. Vinodkumar, J. Phys. G **35** (2008) 065001.

First DAMA/LIBRA Results and Beyond

R. Bernabei, P. Belli, F. Montecchia, F. Nozzoli, F. Cappella, A. d'Angelo, A. Incicchitti, D. Prosperi, R. Cerulli, C.J. Dai, H.L. He, H.H. Kuang, J.M. Ma, X.D. Sheng, and Z.P. Ye

Abstract The DAMA project is an observatory for rare processes and it is operative deep underground at the Gran Sasso National Laboratory of the I.N.F.N. Its main apparatus is the DAMA/LIBRA set-up, consisting of $\simeq$250 kg highly radiopure NaI(Tl) detectors. Its first results – obtained by exploiting over four annual cycles the model independent annual modulation signature for Dark Matter (DM) particles – confirm by those of the former DAMA/NaI, supporting the evidence for Dark Matter presence in the galactic halo at 8.2 σ C.L.. The DAMA/NaI and DAMA/LIBRA data, in fact, satisfy all the many peculiarities of the DM annual modulation signature. Neither systematic effects nor side reactions able to account for the observed modulation amplitude and to contemporaneously satisfy all the several requirements of the DM signature are available. Future perspectives are also addressed.

Keywords: Scintillation detectors, elementary particle processes, Dark Matter

1 The DAMA project

DAMA is an observatory for rare processes and it is operative deep underground at the Gran Sasso National Laboratory of the I.N.F.N.. The DAMA project is mainly based on the development and use of low background scintillators [1–16]; the main

R. Bernabei, P. Belli, F. Montecchia, F. Nozzoli
Dip. di Fisica, Università di Roma "Tor Vergata" and INFN, sez. Roma "Tor Vergata", I-00133 Rome, Italy,
e-mail: rita.bernabei@roma2.infn.it

F. Cappella, A. d'Angelo, A. Incicchitti, D. Prosperi
Dip. di Fisica, Università di Roma "La Sapienza" and INFN, sez. Roma, I-00185 Rome, Italy

R. Cerulli
Laboratori Nazionali del Gran Sasso, I.N.F.N., Assergi, Italy

C.J. Dai, H.L. He, H.H. Kuang, J.M. Ma, X.D. Sheng, Z.P. Ye
IHEP, Chinese Academy, P.O. Box 918/3, Beijing 100039, China

V. Begun et al. (eds.), *Progress in High-Energy Physics and Nuclear Safety*,

aim is the direct detection of DM particles in the galactic halo by investigating the model independent annual modulation signature. of the low background features of these set-ups, many rare processes are also investigated obtaining very competitive results. The main experimental set-ups are: (i) DAMA/NaI ($\simeq$100 kg of highly radiopure NaI(Tl)) which completed its data taking on July 2002 [1, 12]; (ii) DAMA/LXe ($\simeq$6.5 kg liquid Kr-free Xenon enriched either in ^{129}Xe or in ^{136}Xe) [17, 18]; (iii) DAMA/R&D, devoted to tests on prototypes and to small scale experiments [19]; (iv) the new second generation DAMA/LIBRA set-up ($\simeq$250 kg highly radiopure NaI(Tl)) in operation since March 2003 [15, 16]. Moreover, in the framework of devoted R&D for radiopure detectors and photomultipliers, sample measurements are carried out by means of the low background DAMA/Ge detector (installed deep underground since more than 10 years); the detector has also been used for some small scale experiments [20].

In the following we will just briefly summarize the first results on the Dark Matter particles obtained by DAMA/LIBRA, exploiting over four annual cycles the model independent DM annual modulation signature (exposure of 0.53 ton $\times$ year). The result has also been combined together with the previous data collected over seven annual cycles by DAMA/NaI (0.29 ton $\times$ year). The whole available data correspond to 11 annual cycles for a total exposure of 0.82 ton $\times$ year.

2 DM model independent annual modulation signature

With the present technology the only reliable signature able to point out the presence of DM particles in the galactic halo and sensitive to wide ranges both of DM candidates and of interaction types, is the DM annual modulation signature. This signature – originally suggested in the middle of 1980s by Ref. [21] – exploits the effect of the Earth revolution around the Sun on the number of events induced by the Dark Matter particles in a suitable low-background set-up placed deep underground. In fact, as a consequence of its annual revolution, the Earth should be crossed by a larger flux of Dark Matter particles around $\sim$2 June (when its rotational velocity is summed to the one of the solar system with respect to the Galaxy) and by a smaller one around $\sim$2 December (when the two velocities are subtracted). This offers an efficient model independent signature, able to test also a large interval of cross sections and of halo densities.

The expected differential rate as a function of the energy, dR/dE (see also Refs. [4–6, 8–11] for some discussions), depends on the DM particle velocity distribution and on the Earth's velocity in the galactic frame, $\mathbf{v}_e(t)$. Projecting $\mathbf{v}_e(t)$ on the galactic plane, one can write: $v_e(t) = v_\odot + v_\oplus \cos\gamma\cos\omega(t-t_0)$. Here $v_\odot$ is the Sun's velocity with the respect to the galactic halo ($v_\odot \simeq v_0 + 12$ km/s and v_0 is the local velocity whose value is in the range 170–270 km/s [22, 23]); $v_\oplus = 30$ km/s is the Earth's orbital velocity around the Sun on a plane with inclination $\gamma = 60^\circ$ with the respect to the galactic plane. Furthermore, $\omega = 2\pi/\mathrm{T}$ with $\mathrm{T} = 1$ year and roughly t_0 $\simeq$2 June (when the Earth's speed is at maximum). The Earth's velocity can be con-

veniently expressed in unit of v_0: $\eta(t) = v_e(t)/v_0 = \eta_0 + \Delta\eta \cos\omega(t - t_0)$, where – depending on the assumed value of the local velocity – $\eta_0 = 1.04 - 1.07$ is the yearly average of η and $\Delta\eta = 0.05$–0.09. Since $\Delta\eta \ll \eta_0$, the expected counting rate can be expressed by the first order Taylor approximation:

$$\frac{dR}{dE}[\eta(t)] = \frac{dR}{dE}[\eta_0] + \frac{\partial}{\partial\eta}\left(\frac{dR}{dE}\right)_{\eta=\eta_0} \Delta\eta \cos\omega(t - t_0). \quad (1)$$

Averaging this expression in a k-th energy interval one obtains:

$$S_k[\eta(t)] = S_k[\eta_0] + [\frac{\partial S_k}{\partial\eta}]_{\eta_0}\Delta\eta \cos\omega(t - t_0) = S_{0,k} + S_{m,k}cos\omega(t - t_0); \quad (2)$$

the contribution from the highest order terms less than 0.1%. The DM annual modulation signature is very distinctive since the corresponding signal must simultaneously satisfy all the following requirements: the rate must contain a component modulated according to a cosine function (1) with 1 year period (2) and a phase that peaks roughly around $\simeq$2 June (3); this modulation must only be found in a well-defined low energy range, where DM particle induced events can be present (4); it must apply only to those events in which just one detector of many actually "fires" (*single-hit events*), since the DM particle multi-interaction probability is negligible (5); the modulation amplitude in the region of maximal sensitivity must be $\lesssim$7% for usually adopted halo distributions (6), but it can be larger in case of some possible scenarios such as e.g. those in Refs. [24, 25]. Only systematic effects able to fulfil these six requirements and to account for the whole observed modulation amplitude could mimic this signature[1]; thus, no other effect investigated so far in the field of rare processes offers a so stringent and unambiguous signature.

It is worth noting that the corollary questions related to the exact nature of the DM particle(s) (detected by means of the DM annual modulation signature) and to the astrophysical, nuclear and particle Physics scenarios require instead subsequent model dependent corollary analyses, as those performed e.g. in Refs. [4–11]. On the other hand, one should stress that it does not exist any approach in direct and indirect DM searches which can offer information on the nature of the candidate independently on assumed astrophysical, nuclear and particle Physics scenarios.

3 DAMA/LIBRA: First results

Highly radiopure NaI(Tl) scintillators have offered and offer many competitive features to effectively investigate the DM annual modulation signature, such as e.g.: (i) high duty cycle; (ii) well known technology; (iii) large masses; (iv) no safety

[1] It is worth noting that the DM annual modulation is not – as often naively said – a "seasonal" variation and it is not a "winter-summer" effect. In fact, the DM annual modulation is not related to the relative Sun position, but it is related to the Earth velocity in the galactic frame. Moreover, the phase of the DM annual modulation (roughly 2 June) is well different than those of physical quantities (such as temperature of atmosphere, pressure, other meteorological parameters, cosmic rays flux, ...) instead correlated with seasons.

problems; (v) the lowest cost with the respect to every other considered technique; (vi) necessity of a relatively small underground space; (vii) reachable high radiopurity by material selections and protocols, by chemical/physical purifications, etc.; (viii) feasibility of well controlled operational conditions and monitoring, (ix) feasibility of routine calibrations down to few keV in the same conditions as the production runs; (x) high light response (that is keV threshold reachable); (xi) absence of the necessity of re-purification or cooling down/warming up procedures (implying high reproducibility, high stability, etc.); (xii) absence of microphonic noise and an effective noise rejection at threshold (time decay of NaI(Tl) pulses is hundreds ns, while that of noise pulses is tens ns); (xiii) wide sensitivity to both high and low mass DM candidates and to many different interaction types and astrophysical, nuclear and particle Physics scenario; (xiv) possibility to effectively investigate the DM annual modulation signature in all the needed aspects; (xv) possibility to achieve significant results on several other rare processes; (xvi) etc.

These arguments motivated the development and use of highly radiopure NaI(Tl) scintillators for the DAMA/NaI and DAMA/LIBRA target-detectors. The competitivity of these set-ups is based on the reached intrinsic radiopurity (obtained after very long and accurate work for the selection of all low radioactive materials, for the definition of suitable protocols, etc.), on the large sensitivity to many of the DM candidates, of the interaction types and of astrophysical, nuclear and particle Physics scenarios, to the granularity of the set-ups, to the data taking up to the MeV scale (even though the optimization is made for the lowest energy region), to the full control of the running conditions, etc.

The DAMA/NaI set up and its performances are described in Refs.[2–5], while DAMA/LIBRA set-up and its performances in Ref. [15]. Here we just summarized that: (i) the detectors' responses range from 5.5 to 7.5 photoelectrons/keV; (ii) the hardware threshold of each PMT is at single photoelectron (each detector is equipped with two low background photomultipliers working in coincidence); (iii) energy calibration with X-rays/γ sources are regularly carried out down to few keV; (iv) the energy threshold of the experiment is 2 keV. The DAMA/NaI experiment collected an exposure of 0.29 ton $\times$ year over 7 annual cycles [3–5], while DAMA/LIBRA has released so far an exposure of 0.53 ton $\times$ year collected over four annual cycles [16]; thus, the total exposure of the two experiments is 0.82 ton $\times$ year, which is orders of magnitude larger than the exposure typically collected in the field.

Several analyses on the model-independent investigation of the DM annual modulation signature have been performed (see Ref. [16] and references therein); here just few arguments are reminded. In particular, Fig. 1 shows the time behaviour of the experimental residual rates for *single-hit* events collected by DAMA/NaI and by DAMA/LIBRA in the (2–4), (2–5) and (2–6) keV energy intervals. The superimposed curves represent the cosinusoidal functions behaviors $A\cos\omega(t-t_0)$ with a period $T=\frac{2\pi}{\omega}=1$ year and with a phase $t_0=152.5$ day (2 June), while the modulation amplitudes, A, have been obtained by best fit over the DAMA/NaI and DAMA/LIBRA data. When the period and the phase parameters are released in the fit, values well compatible with those expected for a DM particle induced effect are

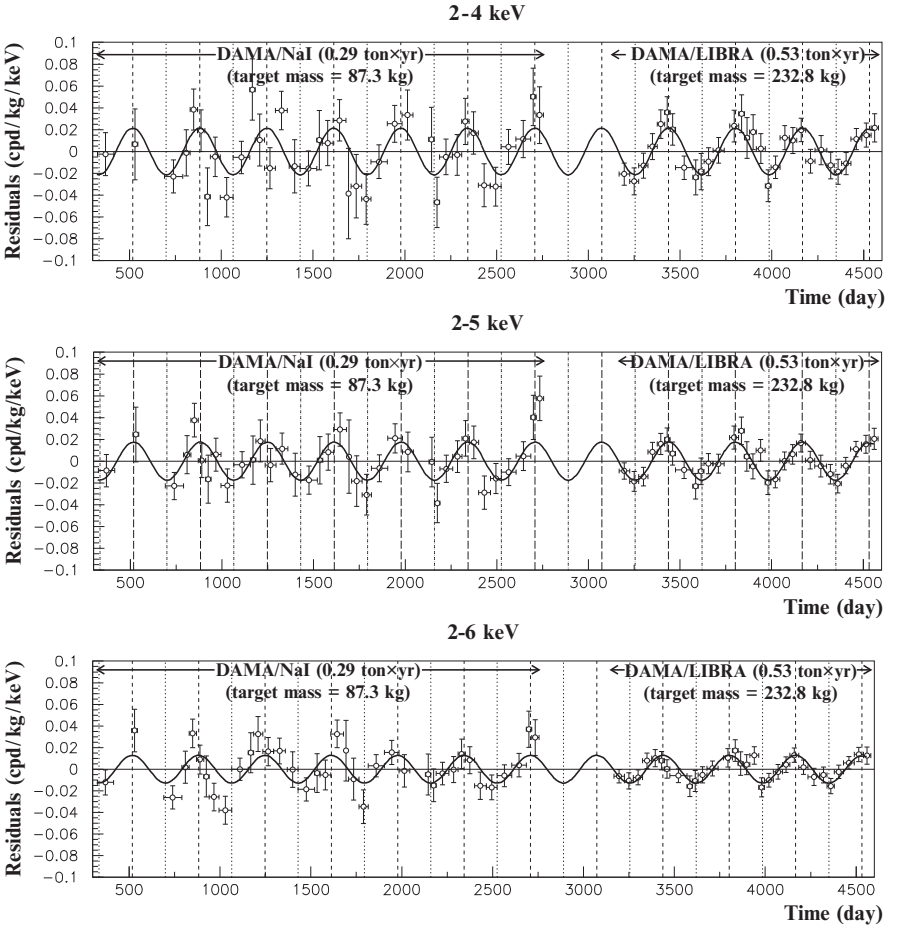

Fig. 1 Experimental model-independent residual rate of the *single-hit* scintillation events, measured by DAMA/NaI and DAMA/LIBRA in the (2–4), (2–5) and (2–6) keV energy intervals as a function of the time. The zero of the time scale is 1 January of the first year of data taking of DAMA/NaI. The experimental points present the errors as vertical bars and the associated time bin width as horizontal bars. The superimposed curves are the cosinusoidal functions behaviors $A\cos\omega(t-t_0)$ with a period $T=\frac{2\pi}{\omega}=1$ year, with a phase $t_0=152.5$ day (2 June) and with modulation amplitudes, A, equal to the central values obtained by best fit over the whole data, that is: (0.0215 ± 0.0026) cpd/kg/keV, (0.0176 ± 0.0020) cpd/kg/keV and (0.0129 ± 0.0016) cpd/kg/keV for the (2–4) keV, for the (2–5) keV and for the (2–6) keV energy intervals, respectively. The dashed vertical lines correspond to the maximum of the signal (2 June), while the dotted vertical lines correspond to the minimum. The total exposure is 0.82 t $\times$ year. For details see [16].

obtained [16]. Summarizing, the cumulative analysis of the *single-hit* residual rate favours the presence of a modulated cosine-like behaviour with proper features at 8.2 σ C.L. [16].

The same data of Fig. 1 have also been investigated by a Fourier analysis, obtaining a clear peak corresponding to a period of 1 year [16]. For comparison the

power spectrum of the (6–14) keV energy interval has also been investigated; it shows instead only aliasing peaks. Similar result is obtained when comparing the *single-hit* residuals in the (2–6) keV with those in the (6–14) keV energy interval; in fact, a clear modulation is present in the lowest energy interval, while it is absent just above [16]. Moreover, in order to verify absence of annual modulation in other energy regions and, thus, to also verify the absence of any significant background modulation, the energy distribution measured during the data taking periods in energy regions not of interest for DM detection has also been investigated. In fact, the background in the lowest energy region is essentially due to "Compton" electrons, X-rays and/or Auger electrons, muon induced events, etc., which are strictly correlated with the events in the higher energy part of the spectrum. Thus, if a modulation detected in the lowest energy region would be due to a modulation of the background (rather than to a signal), an equal or larger modulation in the higher energy regions should be present. The data analyses have allowed to exclude the presence of a background modulation in the whole energy spectrum at a level much lower than the effect found in the lowest energy region for the *single-hit* events [16].

A further relevant investigation has been done by applying the same hardware and software procedures, used to acquire and to analyse the *single-hit* residual rate, to the *multiple-hits* one. In fact, since the probability that a DM particle interacts in more than one detector is negligible, a DM signal can be present just in the *single-hit* residual rate. Thus, this allows the test of the background behaviour in the same energy interval of the observed positive effect. In particular, Fig. 2 shows the residual rates of the *single-hit* events measured over the four DAMA/LIBRA annual cycles, as collected in a single annual cycle, together with the residual rates of the *multiple-hits* events, in the considered energy intervals. A clear modulation is present in the *single-hit* events, while the fitted modulation amplitudes for the *multiple-hits* residual rate are well compatible with zero: $-(0.0004 \pm 0.0008)$ cpd/kg/keV, $-(0.0005 \pm 0.0007)$ cpd/kg/keV, and $-(0.0004 \pm 0.0006)$ cpd/kg/keV in the energy regions (2–4), (2–5) and (2–6) keV, respectively. Similar results were previously obtained also for the DAMA/NaI case [5]. Thus, again evidence of annual modulation with proper features as required by the DM annual modulation signature is present in the *single-hit* residuals (events class to which the DM particle induced events belong), while it is absent in the *multiple-hits* residual rate (event class to which only background events belong). Since the same identical hardware and the same identical software procedures have been used to analyse the two classes of events, the obtained result offers an additional strong support for the presence of a DM particle component in the galactic halo further excluding any side effect either from hardware or from software procedures or from background.

The annual modulation present at low energy has also been shown by depicting the differential modulation amplitudes, $S_{m,k}$, as a function of the energy; the $S_{m,k}$ is the modulation amplitude of the modulated part of the signal (see above) obtained by maximum likelihood method over the data, considering $T = 1$ year and $t_0 = 152.5$ day. In Fig. 3 the measured $S_{m,k}$ for the total exposure (0.82 t $\times$ year, DAMA/NaI and DAMA/LIBRA) are reported as function of the energy. It can be inferred that positive signal is present in the (2–6) keV energy interval, while $S_{m,k}$

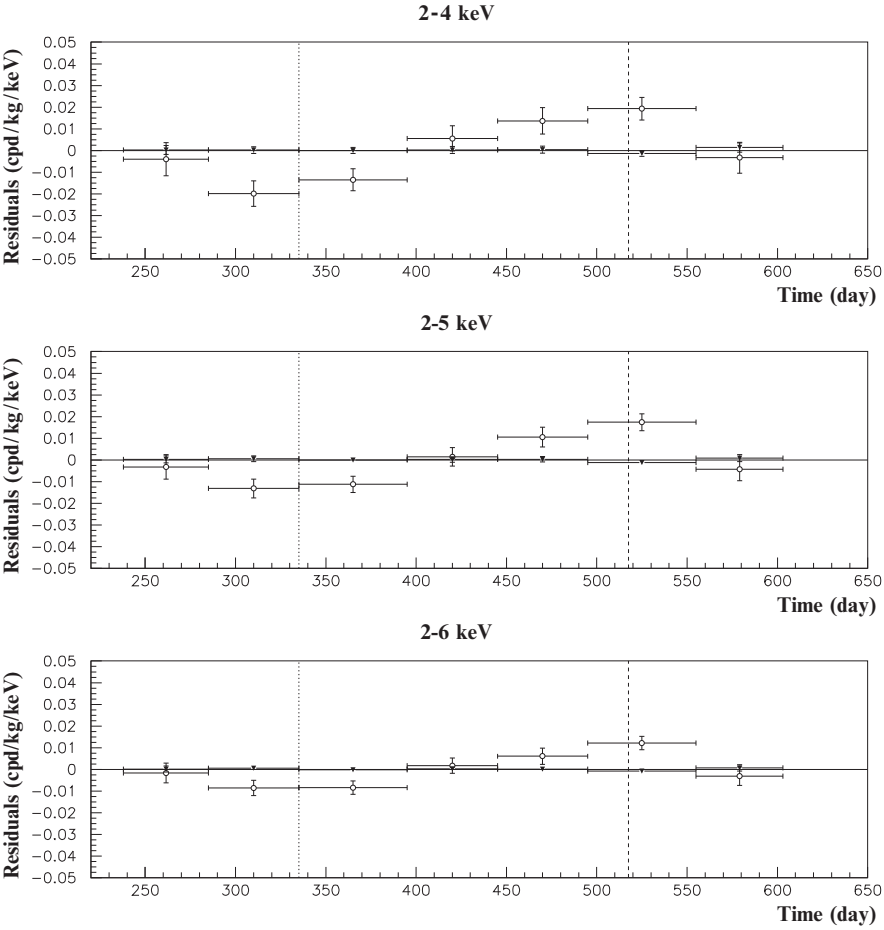

Fig. 2 Experimental residual rates over the four DAMA/LIBRA annual cycles for *single-hit* events (open circles) (class of events to which DM events belong) and for *multiple-hits* events (filled triangles) (class of events to which DM events do not belong), in the energy regions (2–4), (2–5) and (2–6) keV, respectively. They have been obtained by considering for each class of events the data as collected in a single annual cycle and by using in both cases the same identical hardware and the same identical software procedures. The initial time of the scale is taken on 7 August. The experimental points present the errors as vertical bars and the associated time bin width as horizontal bars. See Ref. [16]. Analogous results were obtained for the DAMA/NaI data [5].

values compatible with zero are present just above. In fact, the $S_{m,k}$ values in the (6–20) keV energy interval have random fluctuations around zero with χ^2 equal to 24.4 for 28 degrees of freedom. All this confirms the other analyses.

It has also been verified that the measured modulation amplitudes are statistically well distributed in all the crystals, in all the annual cycles and in the energy bins; these and other discussions can be found in Ref. [16].

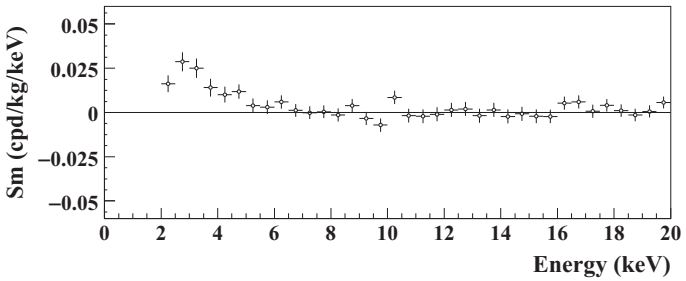

Fig. 3 Energy distribution of the $S_{m,k}$ variable for the total exposure of DAMA/NaI and DAMA/LIBRA: 0.82 t $\times$ year. A clear modulation is present in the lowest energy region, while $S_{m,k}$ values compatible with zero are present just above. In fact, the $S_{m,k}$ values in the (6–20) keV energy interval have random fluctuations around zero with $\chi^2/d.o.f.$ equal to 24.4/28. See Ref. [16].

It is also interesting the results of the analysis performed by releasing the assumption of a phase $t_0 = 152.5$ day in the maximum likelihood procedure to evaluate the modulation amplitudes from the data of the seven annual cycles of DAMA/NaI and the four annual cycles of DAMA/LIBRA. In this case alternatively the signal has been written as: $S_{0,k} + S_{m,k}\cos\omega(t-t_0) + Z_{m,k}\sin\omega(t-t_0) = S_{0,k} + Y_{m,k}\cos\omega(t-t^*)$. Obviously, for signals induced by DM particles one would expect: (i) $Z_{m,k} \sim 0$ (because of the orthogonality between the cosine and the sine functions); (ii) $S_{m,k} \simeq Y_{m,k}$; (iii) $t^* \simeq t_0 = 152.5$ day. In fact, these conditions hold for most of the dark halo models; however, it is worth noting that slight differences can be expected in case of possible contributions from non-thermalized DM components, such as e.g. the SagDEG stream [7] and the caustics [26].

Figure 4–*left* shows the 2σ contours in the plane (S_m, Z_m) for the (2–6) keV and (6–14) keV energy intervals and Fig. 4–*right* shows, instead, those in the plane (Y_m, t^*). The best fit values for the (2–6) keV energy interval are (1σ errors): $S_m = (0.0122 \pm 0.0016)$ cpd/kg/keV; $Z_m = -(0.0019 \pm 0.0017)$ cpd/kg/keV; $Y_m = (0.0123 \pm 0.0016)$ cpd/kg/keV; $t^* = (144.0 \pm 7.5)$ day; while for the (6–14) keV energy interval are: $S_m = (0.0005 \pm 0.0010)$ cpd/kg/keV; $Z_m = (0.0011 \pm 0.0012)$ cpd/kg/keV; $Y_m = (0.0012 \pm 0.0011)$ cpd/kg/keV and t^* obviously not determined (see Fig. 4). These results confirm those achieved by other kinds of analyses. In particular, a modulation amplitude is present in the lower energy intervals and the period and the phase agree with those expected for DM induced signals. For more discussions see Ref. [16].

Both the data of the first four annual cycles of DAMA/LIBRA and of the seven cycles of DAMA/NaI fulfil all the requirements of the DM annual modulation signature.

As previously done for DAMA/NaI [4, 5], careful investigations on absence of any significant systematics or side reaction effect in DAMA/LIBRA have been quantitatively carried out and reported in details in Ref. [16].

In order to continuously monitor the running conditions, several pieces of information are acquired with the production data and quantitatively analyzed.

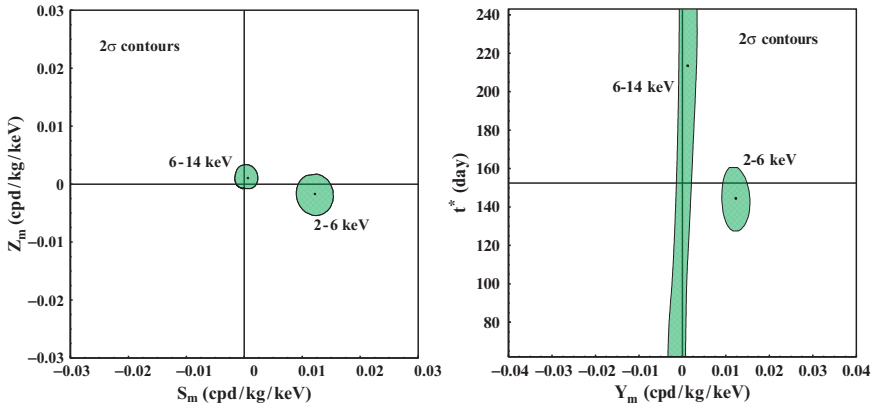

Fig. 4 2σ contours in the plane (S_m, Z_m) (*left*) and in the plane (Y_m, t^*) (*right*) for the (2–6) keV and (6–14) keV energy intervals. The contours have been obtained by the maximum likelihood method, considering the seven annual cycles of DAMA/NaI and the four annual cycles of DAMA/LIBRA all together. A modulation amplitude is present in the lower energy intervals and the period and the phase agree with those expected for DM induced signals. See Ref. [16].

No modulation has been found in any possible source of systematics or side reactions for DAMA/LIBRA as well; thus, cautious upper limits (90% C.L.) on the possible contributions to the DAMA/LIBRA measured modulation amplitude have been estimated and are summarized in Table 1. It is important to stress that – in addition – none able to mimic the signature has been found or suggested by anyone over more than a decade. In fact, they cannot account for the measured modulation amplitude and contemporaneously satisfy all the requirements of the signature. For detailed quantitative discussions on all the related topics and for results see Ref. [16] and Refs. therein.

Summarizing, DAMA/LIBRA has confirmed the presence of an annual modulation satisfying all the requirements of the DM annual modulation signature, as previously pointed out by DAMA/NaI; in particular, the evidence for the presence of DM particles in the galactic halo is cumulatively supported at 8.2 σ C.L..

4 On corollary quests and comparisons

As regards the corollary investigation on the nature of the DM candidate particle(s) and related astrophysical, nuclear and particle Physics scenarios, it has been shown – on the basis of the DAMA/NaI result – that the obtained model independent evidence at 8.2 σ C.L. can be compatible with a wide set of possibilities (see e.g. Refs. [4–6, 8–11] and in literature, for example see [27]); many others are also open. Obviously, this is also the case when the DAMA/NaI and DAMA/LIBRA data are considered all together (see e.g. [16]); an updating of previous corollary investigations and some new ones are in progress.

Table 1 Summary of the results obtained by investigating all possible sources of systematics and side reactions in the data of the DAMA/LIBRA four annual cycles. None able to give a modulation amplitude different from zero has been found; thus cautious upper limits (90% C.L.) on the possible contributions to the measured modulation amplitude have been calculated and are shown here. For details see Ref. [16]. Analogous results were obtained for DAMA/NaI [4, 5]

Source	Main comment (also see Ref.[15])	Cautious upper limit (90%C.L.)
Radon	Sealed Cu Box in HP Nitrogen atmosphere, 3-level of sealing	$<2.5\times10^{-6}$ cpd/kg/keV
Temperature	Air conditioning + huge heat capacity	$<10^{-4}$ cpd/kg/keV
Noise	Efficient rejection	$<10^{-4}$ cpd/kg/keV
Energy scale	Routine + intrinsic calibrations	$<1-2\times10^{-4}$ cpd/kg/keV
Efficiencies	Regularly measured	$<10^{-4}$ cpd/kg/keV
Background	No modulation above 6 keV; no modulation in the (2–6) keV *multiple-hit* events; this limit includes all possible sources of background	$<10^{-4}$ cpd/kg/keV
Side reactions	From muon flux variation measured by MACRO	$<3\times10^{-5}$ cpd/kg/keV
In addition: No effect can mimic the signature		

It is worth noting that no other experiment exists, whose result can be directly compared in a model-independent way with those by DAMA/NaI and DAMA/LIBRA. In particular, let us also point out that results obtained with different target materials and/or different approaches cannot intrinsically be directly compared among them even when considering the same kind of candidate and of coupling, although apparently all the presentations generally refer to cross section on nucleon.

Moreover, we remark e.g. that other existing activities: (1) are insensitive to the annual modulation signature; (2) use different target materials; (3) often provide model-dependent exclusion limits without accounting for the existing experimental, theoretical and phenomenological uncertainties and for the existing alternative choices; (4) often use crude approximation in the calculations; (5) have a disfavoured sensitivity with respect to DAMA/NaI and DAMA/LIBRA in several scenarios; moreover, scenarios exist (see literature) to which the others are not only disfavoured with respect to the DAMA experiments, but even blind. Furthermore, considering the difficulties of exploiting relative new techniques in this very low-energy and low-rate field, additional limitations in the model-dependent sensitivities (just for "nuclear recoils" and a single assumed scenario and parameters set) also

arise from some of their experimental features Moreover, the implications of the DAMA model-independent results are generally quoted in an incorrect, partial and unupdated way. Some arguments have been addressed e.g. in Refs.[4–11,28,29] and in some literature.

In conclusion, claims for contradiction have intrinsically no robust scientific bases.

Regarding the indirect detection searches, let us stress that also no direct model-independent comparison can be performed between the results obtained in direct and indirect activities. Anyhow, if possible excesses in the positron flux and in the γ rays flux from the center of the Galaxy with respect to some simulations of the hypothesized contribution, which should be expected from standard sources, would be interpreted in terms of Dark Matter, this could also be not in conflict with the effect observed by DAMA experiments.

5 Toward the future

The large merits of highly radiopure NaI(Tl) have been demonstrated in the practice by the DAMA set-ups which have been/are the highest radiopure set-ups available in the field, have effectively pursued a model independent approach to investigate the presence of DM particles in the galactic halo collecting exposures several orders of magnitude larger than those usually available in the field and have obtained and/or are in progress to obtain many other complementary or by-products results.

The highly radiopure DAMA NaI(Tl) set-ups are powerful tools for the investigation on the Dark Matter particle component in the galactic halo having all the intrinsic merits already mentioned and large exposed mass, an high overall radiopurity, an high duty-cycle and particular performances. Moreover, it is worth noting that an increase of the exposure and a possible lowering of the energy threshold below 2 keV will improve the discrimination capability among different astrophysical, nuclear and particle Physics scenarios.

In 1996 DAMA proposed to INFN to realize a ton set-up [14] and a new R&D project for highly radiopure NaI(Tl) detectors was funded at that time and carried out for several years in order to realize DAMA/LIBRA, as an intermediate step.

The collection of a much larger exposure will allow to further investigate the model independent evidence with an increased sensitivity. Moreover, it will also offer an increased sensitivity to improve corollary quests on the nature of the candidate particle, trying to disentangle at least among some of the many different possible astrophysical, nuclear and particle physics models as well as to investigate other new possible scenarios.

In the following some of the many topics – not yet well known at present and which can affect whatever model dependent result and comparison – will be summarized.

- *The velocity and spatial distribution of the Dark Matter particles in the galactic halo*. It has been shown that the naive description of the galactic halo as an

isothermal halo is an unphysical and non-realistic approximation which significantly affects model dependent evaluations (exclusion plots, allowed regions, etc.) and comparisons. Other modelings (not exhaustive at all), many of them based on N-bodies simulations, have been considered in literature and some of them have been discussed at some extent in [4, 30] and references therein. Some of these models can be significantly discriminated when larger exposure (larger mass and/or much longer running time) will be available.

- *The effects induced on the Dark Matter particles distribution in the galactic halo by contributions from satellite galaxies tidal streams*. It has been pointed out [25] that contributions to the Dark Matter particles in the galactic halo should be expected from tidal streams from the Sagittarius Dwarf elliptical galaxy. Considering that this galaxy was undiscovered until 1994 and considering galaxy formation theories, one has to expect that also other satellite galaxies do exist and contribute as well. In particular, the Canis Major satellite Galaxy has been pointed out as reported in 2003 in Ref. [31]; it can, in principle, play a very significant role being close to our galactic plane. Some debate on these arguments is present. Anyhow, at present, the best way to investigate the presence of a stream contribution is to determine in accurate way the phase of the annual modulation, t_0, as a function of the energy; in fact, for a given halo model t_0 would be expected to be (slightly) different from 152.5 day and to vary with energy [7].
- *The effects induced on the Dark Matter particles distribution in the galactic halo by the existence of caustics*. It has been shown that the continuous in-fall of Dark Matter particles in the galactic gravitational field can form caustic surfaces and discrete streams in the Dark Matter particles halo [26]. The phenomenology to point out a similar scenario is analogous to that in the previous item.
- *The detection of possible "solar wakes"*. As an additional verification of the possible presence of contributions from streams of Dark Matter particles in our galactic halo, It can also be investigated the gravitational focusing effect of the Sun on the Dark Matter particle of a stream. In fact, one should expect two kinds of enhancements in the Dark Matter particles flow: one named "spike", which gives an enhancement of Dark Matter particle density along a line collinear with the direction of the incoming stream and of the Sun, and another, named "skirt", which gives a larger Dark Matter particle density on a surface of cone whose opening angle depends on the stream velocity [26]. Thus, such a possibility can be investigated with high sensitivity through second-order time-energy correlation analyses.
- *The investigation of possible diurnal effects*. Beyond the diurnal variation expected only in case of high cross section WIMP/WIMP-like candidates (see [32] and ref. therein), also other sidereal daily effect can be considered.
  In particular, a very interesting effect, which holds for a wide range of DM candidates, is – in principle – the diurnal modulation due to the Earth rotation velocity contribution. In fact, considering a detector on the Earth surface at the latitude ζ; the velocity of the detector in the galactic frame can be written as:

$$v_d(t) = v_\odot + v_\oplus \cos\gamma \cos\omega(t - t_0) + v_{rot} cos\zeta sin\beta \cos\Omega(t - t_d). \qquad (3)$$

Here $v_{rot} \simeq 0.46$ km/s is the Earth rotational velocity at the equator, $\beta \simeq 42^o$ is the angle between the Earth axis and the DM flux (approximatively the Cygnus constellation declination), $\Omega = 2\pi/d_s$ (were d_s is 1 sidereal day) and t_d is a phase depending on detector longitude. Applying a Taylor expansion – as already done in Eqs. (1) and (2) – the expected signal counting rate in a given $k-th$ energy bin can be written as:

$$S_k[\eta(t)] \simeq S_k[\eta_0] + [\frac{\partial S_k}{\partial \eta}]_{\eta_0} (\Delta\eta \cos\omega(t-t_0) + \delta\eta \cos\Omega(t-t_d)) \qquad (4)$$

Were $\delta\eta = \frac{v_{rot}\cos\zeta\sin\beta}{v_0}$. The interest in this second-order signature is that the ratio R_{dy} of this diurnal modulation amplitude over the annual modulation amplitude is a fully model independent constant; considering the LNGS latitude ($\zeta \simeq 42.5^o$) one has:

$$R_{dy} = \frac{\delta\eta}{\Delta\eta} = \frac{v_{rot}\cos\zeta\sin\beta}{v_\oplus\cos\gamma} \simeq 0.015 \qquad (5)$$

This signature can allow a powerful decoupling from the models. However, considering that the annual modulation amplitude observed in DAMA in the (2–6) keV energy interval is roughly 0.013 cpd/kg/keV [16], the expected diurnal modulation amplitude is 2×10^{-4} cpd/kg/keV; this amplitude can be relevantly investigated just when a much larger exposure will be available (e.g. many years of running of DAMA/1ton).

- *The study of possible structures as clumpiness with small scale size*. Possible structures as clumpiness with small scale size could, in principle, be investigated by exploiting a large exposure and searching for distinctive peculiarities in the time distribution of the data.
- *The coupling(s) of the Dark Matter particle with the ^{23}Na and ^{127}I and its nature*. As mentioned, several large uncertainties are linked to the coupling(s) between the Dark Matter particle and the target-nuclei. A suitably large exposure will allow to better constrain the related aspects.
- *The scaling laws and cross sections*. At present just simple scaling laws are used to scale all the nuclear cross sections to a common nucleon cross section; however, they are a large source of uncertainties in model dependent results and comparisons. For example, it has been pointed out [33] that, even for the neutralino candidate, these assumptions (which hold in the case of model with one-nucleon current) are arbitrary when two-nucleon current with pion exchange are introduced. Thus, the presence of two target-nuclei in the NaI(Tl) detectors could in principle offer a probe for that in the large exposure this experiment will collect and with the increasing of the knowledge on the related aspects.

At present a third generation R&D effort toward the possible highly radiopure NaI(Tl) ton set-up has been funded and the DAMA collaboration has already performed various related works.

Finally, it is worth noting that ultra low background NaI(Tl) scintillators can also offer the possibility to achieve significant results on several other rare processes as

already done e.g. by the former DAMA/NaI apparatus such as [12–14]: (i) possible violation of Pauli exclusion principle in ^{127}I and in ^{23}Na; (ii) electron stability; (iii) charge non-conserving processes; (iv) search for solar axions; (v) search for exotic matter; (vi) search for spontaneous transition of nuclei to a superdense state; (vii) search for spontaneous emission of heavy clusters in ^{127}I; (viii) search for possible nucleon, di-nucleon and tri-nucleon decays into invisible channels with new approach; etc.

6 Conclusions

The highly radiopure NaI(Tl) DAMA set-ups have investigated the aspects related to the presence of DM particles in the galactic halo by exploiting the DM annual modulation signature and achieving a model independent evidence at 8.2 σ C.L.

During September 2008, an upgrade of the DAMA/LIBRA set-up has been realized, in order to restore a photomultiplier, to replace the transient digitizers with those of higher performances, and to install a new more-performing DAQ system with optical fibers. Moreover, it is foreseen the replacement of all the photomultipliers with new ones, having larger quantum efficiency, around the end of year 2009; this would allow us to lower the energy threshold of the experiment below 2 keV. Hence, an increase of the exposure and a lowering of the energy threshold will allow us to further investigate the model-independent evidence with an increased sensitivity; moreover, it will also improve the discrimination capability among different astrophysical, nuclear and particle Physics scenarios.

In conclusion, the collection of larger exposures (with DAMA/LIBRA or with the possible DAMA/1ton, which is at R&D stage) will allow to significantly investigate several open aspects on the nature of the candidate particle(s) and on the various related astrophysical, nuclear and particle Physics as well as to investigate with high sensitivity other DM features and second order effects.

References

1. R. Bernabei et al., Phys. Lett. B 389 (1996) 757; R. Bernabei et al., Phys. Lett. B 424 (1998) 195; R. Bernabei et al., Phys. Lett. B 450 (1999) 448; P. Belli et al., Phys. Rev. D 61 (2000) 023512; R. Bernabei et al., Phys. Lett. B 480 (2000) 23; R. Bernabei et al., Phys. Lett. B 509 (2001) 197; R. Bernabei et al., Eur. Phys. J. C 23 (2002) 61; P. Belli et al., Phys. Rev. D 66 (2002) 043503.
2. R. Bernabei et al., Il Nuovo Cim. A 112 (1999) 545.
3. R. Bernabei et al., Eur. Phys. J. C 18 (2000) 283.
4. R. Bernabei el al., La Rivista del Nuovo Cimento 26 n.1 (2003) 1-73.
5. R. Bernabei et al., Int. J. Mod. Phys. D 13 (2004) 2127.
6. R. Bernabei et al., Int. J. Mod. Phys. A 21 (2006) 1445.
7. R. Bernabei et al., Eur. Phys. J. C 47 (2006) 263.
8. R. Bernabei et al., Int. J. Mod. Phys. A 22 (2007) 3155.

9. R. Bernabei et al., Eur. Phys. J. C 53 (2008) 205.
10. R. Bernabei et al., Phys. Rev. D 77 (2008) 023506.
11. R. Bernabei et al., Mod. Phys. Lett. A 23 (2008) 2125.
12. R. Bernabei et al., Phys. Lett. B408 (1997) 439; P. Belli et al., Phys. Lett. B460 (1999) 236; R. Bernabei et al., Phys. Rev. Lett. 83 (1999) 4918; P. Belli et al., Phys. Rev. C60 (1999) 065501; R. Bernabei et al., Il Nuovo Cimento A112 (1999) 1541; R. Bernabei et al., Phys. Lett. B 515 (2001) 6; F. Cappella et al., Eur. Phys. J.-direct C14 (2002) 1; R. Bernabei et al., Eur. Phys. J. A 23 (2005) 7.
13. R. Bernabei et al., Eur. Phys. J. A 24 (2005) 51.
14. R. Bernabei et al., Astrop. Phys. 4 (1995) 45; R. Bernabei, in the volume *The identification of Dark Matter*, World Sc. Pub. (1997) 574.
15. R. Bernabei et al., Nucl. Instr. & Meth. A 592 (2008) 297.
16. R. Bernabei et al., Eur. Phys. J. C 56 (2008) 333.
17. P. Belli et al., Astropart. Phys. 5 (1996) 217; P. Belli et al., Nuovo Cim. C 19 (1996) 537; P. Belli et al., Phys. Lett. B 387 (1996) 222; Phys. Lett. B 389 (1996) 783 (err.); P. Belli et al., Phys. Lett. B 465 (1999) 315; P. Belli et al., Phys. Rev. D 61 (2000) 117301; R. Bernabei et al., New J. of Phys. 2 (2000) 15.1; R. Bernabei et al., Phys. Lett. B 493 (2000) 12; R. Bernabei et al., Nucl. Instrum. Meth A 482 (2002) 728; R. Bernabei et al., *Eur. Phys. J. direct* C11 (2001) 1; R. Bernabei et al., Phys. Lett. B 527 (2002) 182; R. Bernabei et al., Phys. Lett. B 546 (2002) 23. R. Bernabei et al., in the Volume "Beyond the Desert 2003", Springer, Berlin (2003) 365; R. Bernabei et al., Eur. Phys. J. A 27, s01 (2006) 35.
18. R. Bernabei et al., Phys. Lett. B 436 (1998) 379.
19. R. Bernabei et al., Astropart. Phys. 7 (1997) 73; R. Bernabei et al., Nuovo Cim. A 110 (1997) 189; P. Belli et al., Astropart. Phys. 10 (1999) 115; P. Belli et al., Nucl. Phys. B 563 (1999) 97; R. Bernabei et al., Nucl. Phys. A 705 (2002) 29; P. Belli et al., Nucl. Instrum. Meth A 498 (2003) 352; R. Cerulli et al., Nucl. Instrum. Meth A 525 (2004) 535; R. Bernabei et al., Nucl. Instrum. Meth A 555 (2005) 270; R. Bernabei et al., Ukr. J. Phys. 51 (2006) 1037; P. Belli et al., Nucl. Phys. A 789 (2007) 15; P. Belli et al., Phys. Rev. C 76 (2007) 064603; P. Belli et al., Phys. Lett. B 658 (2008) 193; P. Belli et al., Eur. Phys. J. A 36 (2008) 167;
20. P. Belli et al., Nucl. Instrum & Meth. A 572 (2007) 734; Nucl. Phys. A 806 (2008) 388; to appear on the Proceed. of NPAE 2008, INR-Kiev.
21. K.A. Drukier et al., Phys. Rev. D 33 (1986) 3495; K. Freese et al., Phys. Rev. D 37 (1988) 3388.
22. P. Belli et al., Phys. Rev. D 61 (2000) 023512.
23. P.J.T. Leonard and S. Tremaine, *Astrophys. J.* 353 (1990) 486; C.S. Kochanek, *Astrophys. J.* 457 (1996) 228; K.M. Cudworth, *Astron. J.* 99 (1990) 590
24. D. Smith and N. Weiner, *Phys. Rev. D* 64 (2001) 043502; D. Tucker-Smith and N. Weiner, *Phys. Rev. D* 72 (2005) 063509.
25. K. Freese et al. astro-ph/0309279; *Phys. Rev. Lett.* 92 (2004) 11301.
26. F.S. Ling, P. Sikivie and S. Wick, *Phys. Rev. D 70* (2004) 123503.
27. A. Bottino, N. Fornengo, and S. Scopel, *Phys. Rev. D* 67 (2003) 063519; A. Bottino, F. Donato, N. Fornengo, and S. Scopel, *Phys. Rev. D* 69 (2003) 037302 and *Phys. Rev. D* 78 (2008) 083520.
28. R. Bernabei for DAMA coll. and A. Bottino, Nature 449 (2007) 24.
29. R. Bernabei et al., arXiv0806.0011
30. P. Belli et al., *Phys. Rev. D* 66 (2002) 043503.
31. R.A. Ibata et al., *Mon. Not. Roy. Astr. Soc.* 348 (2004) 12.
32. R. Bernabei et al., *Nuovo Cimento A* 112 (1999) 1541.
33. G. Prezeau et al., *Phys. Rev. Lett.* 91 (2003) 231301.

Issues of Reggeization in qq' Backward Scattering

M.V. Bondarenco

Abstract The Kirschner–Lipatov result for the DLLA of high-energy qq' backward scattering is re-derived without the use of integral equations. It is shown that part of the inequalities between the variables in the logarithmically divergent integrals is inconsequential. The light-cone wave-function interpretation under the conditions of backward scattering is discussed. It is argued that for hadron–hadron scattering in the valence-quark model the reggeization should manifest itself at full strength starting from $s_{hh} = 50\ \mathrm{GeV}^2$.

Keywords: Quark–quark scattering, double-log asymptotics, Regge behavior

1 Introduction

Backscattering of high and intermediate energy, weakly radiating[1] particles (protons, X-ray) is known as a clean tool for atomic material structure analysis [1]. The clarity of the analysis owes exactly to the low scattered particle fraction. With the initial macroscopic luminosity, that poses no problem for detectability, but, more importantly, the relative background (actually, all the diverse kinds thereof) is suppressed.

In case when wave nature of the scattered particles is relevant, the backward scattering can sometimes get enhanced as compared with that at other large angles – due to some or the other kinematical symmetry (coherent backscattering).

M.V. Bondarenco
NSC Kharkov Institute of Physics & Technology, Kharkov 61108, Ukraine,
e-mail: bon@kipt.kharkov.ua

[1] Weakness of the radiation is, rather, a wish than a necessary condition. Backscattering, or large-angle scattering of electrons, of course, is widely applied, too, but requires proper calculation of radiative corrections.

V. Begun et al. (eds.), *Progress in High-Energy Physics and Nuclear Safety*,

For hadrons, which are objects composed of quarks, one can detect the events of single quark backscattering by separating (single-) flavor exchange reactions to high energy. Thereat, most probably, only one pair of quarks (of different flavor) scatters backwards and then recombines with the forward-moving hadron remnants. There is no external gluonic radiation in the fully exclusive reaction, because of color confinement. Besides, there is no necessity to rise the energy to extremely high values, where some internal radiative effects should eventually become important.

Owing to the hardness present in the process, a plausible approximation for it is one-gluon exchange. The latter is impact parameter conserving, which is convenient for the overlap representation of the scattering matrix element in terms of quark wave functions of hadrons, as was partially discussed elsewhere [2].

But yet, at energies high enough, the energy dependence of flavor-exchange reactions departs notably from the one-gluon-exchange prediction $\sigma \sim s^{-2}$, which is referred to as reggeization phenomenon. It is desirable to get it incorporated in the theory, within the impulse approximation treatment.

In 1967, Gorshkov, Gribov, Lipatov, and Frolov [3] (see also textbook [4]) had evaluated double-leading-logarithmic asymptotics (DLLA) of Feynman integrals corresponding to $e^-\mu^-$ backward scattering in QED, and resumed to all orders. They had found a power falloff slowdown (basically, t-independent).

Later, Kirschner [5], being generally interested in DLLA of QCD elementary scattering processes, examined quark-quark backward scattering, and quark-antiquark forward/backward annihilation, paralleling the framework of [3]. The negative signature amplitude was thereafter computed by Kirschner and Lipatov [6].

The amplitude of qq' backward scattering, which is the kernel of the hadron binary reaction overlap matrix element, has the asymptotics

$$M_{qq'\to q'q}\left(s_{qq'}\right) = \frac{1}{N_c}\delta_{m'l}\delta_{l'm}\sqrt{\frac{2\pi\alpha_s}{C_F}}\frac{8\pi}{\ln s_{qq'}}I_1\left(\sqrt{\frac{2\alpha_s C_F}{\pi}}\ln s_{qq'}\right) \qquad (\texttt{DLLA}) \quad (1)$$

$$\sim \frac{1}{\ln s_{qq'}}s_{qq'}^{\sqrt{\frac{2\alpha_s C_F}{\pi}}} \qquad (s\to\infty) \quad (2)$$

with I_1 the modified Bessel function, and

$$C_F = \frac{N_c^2-1}{2N_c}. \quad (3)$$

(Account of single logarithms can somewhat change the index in (1), but the effect of that correction is rather uncertain in view of our poor knowledge of the coupling constant α_s, anyway.)

Letting numerically $N_c = 3$, $\alpha_s \simeq 0.1 \div 0.2$, and assuming that for reactions such as $np \to pn$ small Feynman-x contribution is moderate (given that constituent quark models work rather well for nucleon), one obtains an estimate

$$\frac{d\sigma_{np\to pn}}{dt} \propto \frac{1}{s^2}\left|M_{du\to ud}\right|^2 \sim s^{-1.4\div -1.2}. \quad (4)$$

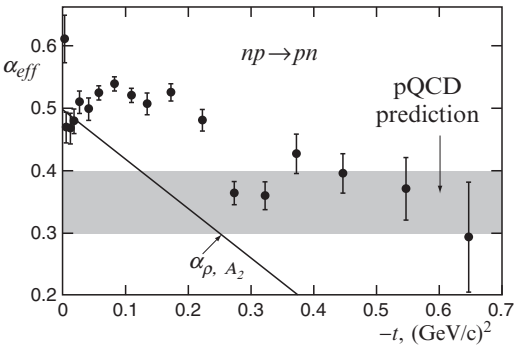

Fig. 1 Regge trajectory for $np \to pn$ reaction. Data taken from [7]. The straight line shown for comparison is the conventional ρ, A_2-trajectory $0.5 + 0.8t$

This asymptotics is expected to hold when $\sqrt{\frac{2\alpha_s C_F}{\pi}} \ln\left(s_{qq'} = \frac{s_{hh}}{N_1 N_2}\right) \gg 1$, where N_1, N_2 are valence quark numbers in the colliding hadrons. That numerically implies

$$s_{hh} \gg 50 \div 100 \text{ GeV}^2. \tag{5}$$

The correspondence of (4) with the experimental behavior is *not* too bad.

The best experimental representative of flavor exchange reactions is $np \to pn$, given the detailed data available for $d\sigma/dt$ and even some data for polarization for this reaction, and in addition – nucleon form-factors as an independent constraint for the wave function.

The Regge trajectory slope for $np \to pn$ is small (see Fig. 1). In contrast, for meson flavor exchange, particularly for $\pi^- p \to \pi^0 n$ (usually quoted as having an examplary linear Regge trajectory) the slope seems to be close to Chew–Frautchi substantial value 0.8 GeV^{-2}. But it is to be minded that in the pion charge exchange case there are cancelations between $ud \to du$ scattering and $u\bar{u} \to d\bar{d}$ annihilation, and in itself, pion is a more relativistic system then nucleon, probably, with a larger contribution from small x. Altogether, this makes the dynamics more intricate, and we refrain from discussing it here.

In this contribution we shall focus only on reggeization of two-free-quark scattering. That was the subject of Kirschner and Lipatov, but it is desirable to give it more dynamical interpretation, which can in future prove useful for scattering treatment in the spectator quark surroundings.

2 The origin of enhancements

Consider an ultra-relativistic collision of a free d-quark carrying momentum p_d with a free u-quark of momentum p_u, resulting in a near-backward elastic scattering to momenta p'_d, p'_u:

$$d(p_d) + u(p_u) \to u(p'_u) + d(p'_d),$$
$$\Delta_\perp = p_d - p'_d = p'_u - p_u \sim 1 \text{ GeV}.$$

As long as no other particles are concerned in the initial or final state, we shall throughout designate inter-quark kinematic invariants without hats or subscripts:

$$s = (p_d + p_u)^2 \gg \Delta_\perp^2.$$

Quark bispinors will be denoted as u for initial and u' for the final u-quark, and d, d' – the same for d-quark.

2.1 Loop structure. Collinear vs. infra-red large logarithms

The tree-level amplitude of quark–quark backward scattering is the single-gluon exchange:

$$M^{(1)} \approx -\frac{4\pi\alpha}{s}\left(\bar{d}'\gamma^\mu d\right)\left(\bar{u}'\gamma^\mu u\right) t^A_{l'l} t^A_{m'm}. \tag{6}$$

It scales with the collision energy $\sqrt{s}$ as s^0, which corresponds to cross-section decreasing as s^{-2}. But in higher orders there can arise loop enhancements of logarithmic kind, which are conventionally classified by two categories – soft and collinear ones. Soft divergences originate when some mass ratio tends to be large, $\frac{m}{\lambda} \to \infty$. Collinear ones require the high-energy limit $\frac{s}{m^2} \to \infty$; they correspond to an effective phase space extension with the energy.[2]

In general, a collinear divergence is encountered when a soft virtual particle connects two high-energy lines, provided the latter are sufficiently close to the mass-shell. Then, the high-energy line propagators admit eikonal approximation,[3] $\sim\frac{1}{pk}$ (p being the momentum of the high-energy line, and k – the momentum of the soft one), whereas the soft particle propagator decreases as $\sim\frac{1}{k^2}$ if it is a boson, or $\sim\frac{\not{k}}{k^2}$ if it is a fermion. When covered with 4d integration, by k-power counting it is seen to produce logarithmic divergences – in a triangle loop with two eikonal (fermion) and one soft boson lines (not counting possible hard propagators, which may be regarded as momentum-independent, and graphically represented as contracted into a point), and in quadrangular loops with two eikonal (boson) lines and two soft fermion lines.

In the first case, of triangular loops, the collinear divergence is merging with the soft one (IR). Although those can be given independent meaning, physically they both are related to emission and reabsorption of bremsstrahlung photons, with the energy smaller then the mass of the radiating particle (in the IR soft case), or then the

[2] An often quoted definition of collinear divergence type is that it is inherent to the massless case, when the singularity of the integrand is encountered not in a single point (that would characterize soft divergence), but along an entire line. But from the viewpoint of initially massive, physical case, one yet needs to specify, in which order the massless limit is achieved. The answer is that ratios of all the masses stay finite and non-zero, while their ratios to the energy tend to zero – in contrast to the soft case when some mass ratio turns small. Again, that is equivalent to the growth of the effective phase space, in mass units. As for the method of identifying soft and collinear divergences by $\frac{d\omega}{\omega}$ and $\frac{d\theta}{\theta}$ factors, it is not manifestly Lorentz-invariant.

[3] The eikonal condition ($pk \gg k^2, p^2 - m^2$) is exactly the criterion of the line proximity to the mass shell.

collision energy (in the IR collinear case). So, it is natural that they obey the same cancelation principles. For backward scattering of equal-charge particles, or with perfect charge (color) exchange, IR cancelations must be working at full strength.

The second case, of quadrangular loop, instead, has no soft counterpart. Moreover, virtual corrections of that kind upon resummation should lead to enhancement rather then suppression of the cross-section, as we shall discuss in detail below.

In higher orders of perturbation theory, in order to obtain the leading logarithmic contribution, there must be an eikonal condition for each gluon line. Denoting by q_i – d-quark momenta on its course from p_d to p'_d (see Fig. 2 below),

$$-(q_{i-1}-q_i)^2 \approx 2q_{i-1}q_i \gg q_{i-1}^2, q_i^2. \tag{7}$$

Fulfilment of these conditions is possible if the intermediate quark (and gluon) momenta approximately belong to the plane formed by initial and final momenta. For backward scattering this plane approximately coincides with that of collision, and it may unequivocally be called longitudinal. It is profitable to define in it light-cone coordinates, and expand any vector $a^\mu = a^\mu_\parallel + a^\mu_\perp$, $a^\mu_\parallel = (a^0, a^3)$, $a^\mu_\perp = (a^1, a^2)$

$$a^\pm = \frac{a^0 \pm a^3}{\sqrt{2}},$$

$$a \cdot b = a^+ b^- + a^- b^+ + a_\perp \cdot b_\perp.$$

Then, Eq. (7) requires[4]

$$p_d^+ \gg q_1^+ \gg q_2^+ \ldots \gg q_{n-1}^+ \gg p'^+_d, \tag{8}$$

$$p_d^- \ll q_1^- \ll q_2^- \ldots \ll q_{n-1}^- \ll p'^-_d, \tag{9}$$

$$q_{i\perp}^2 \ll q_{i-1}^+ q_i^-, q_i^+ q_{i+1}^-. \tag{10}$$

In fact, Eq. (10) will be satisfied automatically if

$$q_{i\perp}^2 < 2q_i^+ q_i^- = q_{i\parallel}^2, \qquad q_i^2 > 0. \tag{11}$$

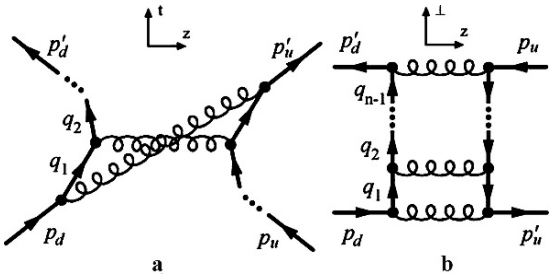

Fig. 2 The diagram giving leading logarithmic contribution in $2n$-th order: a – the temporal ordering representation; b – the spatial projection

[4] Presuming that there are no fine cancelations between $\parallel$ and $\perp$ components in momentum squares, which would reduce the integration volume.

This is nothing but the usual multi-peripheral kinematics – the same as for the reggeization at forward scattering. That is quite natural, since the denominator structure for those cases is the same (for instance, in a scalar theory, with no propagator numerators, and all the particles identical, there would be no difference between forward and backward scattering).

2.2 The Feynman diagram topology

The ordering in rapidity guarantees uniqueness of the Feynman diagram, and the temporal order of boson emission from one fermion should be reverse to that of their absorption by the other fermion. Thereby, the concept of near-neighbor interaction in the phase space finds support.

The amplitude corresponding to the n-rung diagram (see Fig. 2) is

$$M^{(n)} = i(-4\pi i\alpha_s)^n \mathsf{C}^{(n)} \int \frac{d^4q_1}{(2\pi)^4} \dots \frac{d^4q_{n-1}}{(2\pi)^4} \frac{\mathscr{N}^{(n)}}{\mathscr{D}^{(n)}} \tag{12}$$

with

$$\mathsf{C}^{(n)} = \left(t^{A_n} \dots t^{A_1}\right)_{l'l} \left(t^{A_1} \dots t^{A_n}\right)_{m'm}, \tag{13}$$

$$\mathscr{N}^{(n)} \approx \left[\bar{d}'\gamma^{\mu_n} \not{q}_{n-1} \dots \gamma^{\mu_2} \not{q}_1 \gamma^{\mu_1} d\right] \left[\bar{u}'\gamma^{\mu_1} \not{q}_1 \gamma^{\mu_2} \dots \not{q}_{n-1}\gamma^{\mu_n} u\right], \tag{14}$$

$$\mathscr{D}^{(n)} \approx (-2p_d q_1 + i0)(-2q_1q_2 + i0)(-2q_{n-1}p'_d + i0) q_1^2 (q_1-\Delta)^2 \dots q_n^2 (q_n-\Delta)^2. \tag{15}$$

At this stage, certain insight can already be gained from the topology of Feynman diagrams. Drawing Feynman diagrams in accord with the process spatial projection, when the initial particle momentum directions are opposite, an arbitrary order diagram is depicted as a ladder, each cell of which is dissectible by two lines in the t-channel (for backward scattering, $|t| \ll s \approx |u|$). On the other hand, drawing Feynman diagrams according to the event temporal ordering, either the two fermion lines, or all the boson lines must cross. In any way, the diagram cannot be cut by two lines in the s-channel (which might be utilized for evaluation by unitarity). This is in contrast with the IR boson attachment order, where triangle loops (though not necessarily the entire diagram) can always be cut by two lines in the s-channel, and the concept of correspondence with the emitted real bosons through unitarity is useful.

2.3 Classical interpretation

In classical terms, the mechanism of enhancement may be thought of, roughly, as follows. In a high-energy collision, charged particles can shed their proper fields with the impart to them of the bulk of their energy, and slow down. In the slow state, they are turned around on a larger mutual distance, which results in the increase of

the scattering differential cross-section. Upon the reflection, the charged particles can again pick up each the comoving proper field from the other particle, and thus restore the high relative energy up to the initial value.

3 Numerators

Let us, in the first place, analyze matrix numerators, determining all the speciality of quark–quark scattering.

3.1 Spin factors

As long as fermion masses are neglected, their helicity must be conserved. But, in addition, we shall acquire strict correlation of helicities of colliding particles.

In addition to the light-cone decomposition, it is convenient to introduce chiral vector basis in the transverse plane:

$$a^R = -\frac{a^1 + ia^2}{\sqrt{2}}, \qquad a^L = \frac{a^1 - ia^2}{\sqrt{2}}, \qquad a_\perp \cdot b_\perp = a^R b^L + a^L b^R. \tag{16}$$

Using in capacity of basic γ-matrices

$$\gamma^\pm = \frac{\gamma^0 \pm \gamma^3}{\sqrt{2}}, \qquad \gamma^R = -\frac{\gamma^1 + i\gamma^2}{\sqrt{2}}, \qquad \gamma^L = \frac{\gamma^1 - i\gamma^2}{\sqrt{2}} \tag{17}$$

makes the covariant anticommutation relation $\{\gamma^\mu, \gamma^\nu\} = 2g^{\mu\nu}$ look like

$$\{\gamma^+, \gamma^-\} = 2, \qquad \{\gamma^R, \gamma^L\} = 2, \tag{18}$$

with all other anticommutators zero:

$$(\gamma^+)^2 = (\gamma^-)^2 = (\gamma^R)^2 = (\gamma^L)^2 = 0, \tag{19}$$

$$\{\gamma^\pm, \gamma^{R,L}\} = 0. \tag{20}$$

Important for the future practice are cubic relations

$$\gamma^R \gamma^L \gamma^R = 2\gamma^R, \qquad \gamma^L \gamma^R \gamma^L = 2\gamma^L, \tag{21}$$

and Dirac conjugation properties

$$\bar{\gamma^\pm} = \gamma^\pm, \qquad \bar{\gamma}^R = -\gamma^L, \qquad \bar{\gamma}^L = -\gamma^R. \tag{22}$$

For in- and out-quark bispinors, which satisfy (massless) Dirac equations

$$\gamma^- d = 0, \qquad \bar{u}'\gamma^- = 0, \qquad \bar{d}'\gamma^+ = 0, \qquad \gamma^+ u = 0, \tag{23}$$

further, define polarization states as those of definite helicity (left and right):

$$\gamma^L d_R = \sqrt{2} d_L, \qquad \gamma^R d_L = \sqrt{2} d_R, \tag{24}$$

$$\bar{u}'_R \gamma^R = -\overline{\gamma^L u'_R} = -\sqrt{2}\bar{u}'_L, \qquad \bar{u}'_L \gamma^L = -\sqrt{2}\bar{u}'_R, \tag{25}$$

$$\gamma^R u_R = -\sqrt{2} u_L, \qquad \gamma^L u_L = -\sqrt{2} u_R, \tag{26}$$

$$\bar{u}'_R \gamma^L = \sqrt{2}\bar{d}'_L, \qquad \bar{d}'_L \gamma^R = \sqrt{2}\bar{d}'_R, \tag{27}$$

and the normalization should be

$$\bar{d}'_L d_R = \bar{d}'_R d_L = \bar{u}'_L u_R = \bar{u}'_R u_L = \sqrt{s}. \tag{28}$$

The important consequence of Eqs. (25–28) and (19) is

$$\gamma^R d_R = 0, \qquad \gamma^L d_L = 0. \tag{29}$$

$$\bar{u}'_R \gamma^L = 0, \qquad \bar{u}' \gamma^R = 0. \tag{30}$$

(The factor $\sqrt{2}$ in (25–28) comes from the relation $\left\{\gamma^R, \gamma^L\right\} = 2$, and the sign at it is the matter of bispinor normalization convention.)

We shall nowhere need the use of matrix γ_5, for which the chirality bispinors are eigenvectors. Thanks that all the momenta are contained in one hyper-plane, one can manage with matrices γ^R, γ^L alone, playing the role of (nilpotent) angular momentum raising and lowering operators.

Now, the smallest block in the matrix element

$$\gamma^\mu d_R \bar{u}'_R \gamma^\mu = -2 d_L \bar{u}'_L, \tag{31}$$

$$\gamma^\mu d_R \bar{u}'_L \gamma^\mu = 0. \tag{32}$$

Eq. (31) implies that fermion angular momentum projection onto the collision axis must flip after the vector boson exchange, and the spins of the opposing fermions must exactly correlate. Physically, that is natural, since a vector boson emitted by a $M_z = +\frac{1}{2}$ fermion has $M_z = +1$, so after the vector boson emission the fermion acquires $M_z = -\frac{1}{2}$, and the opposite fermion must initially have $M_z = -\frac{1}{2}$ to be able to absorb the $M_z = +1$ boson.

Hence,

$$\mathscr{N}^{(1)}_{RR,RR} = \mathscr{N}^{(1)}_{LL,LL} = -2s, \tag{33}$$

whereas all the other helicity amplitudes equal zero.

The next larger block

$$\gamma^\nu \not{q}_1 \gamma^\mu d_R \bar{u}'_R \gamma^\mu \not{q}_1 \gamma^\nu = -2\gamma^\nu \not{q}_1 d_L \bar{u}'_L \not{q}_1 \gamma^\nu = 4 \not{q}_1 d_R \bar{u}'_R \not{q}_1. \tag{34}$$

The non-zero part of r. h. s. of (34)

$$\not{q}_1 d_R \bar{u}'_R \not{q}_1 = \left(q_1^- \gamma^+ + q_1^R \gamma^L\right) d_R \bar{u}'_R \left(q_1^- \gamma^+ + q_1^L \gamma^R\right). \tag{35}$$

Now, matrix-vectors $\not{q}_i$ sandwiching this expression have components q_i^+ at γ^-, which are negligible as compared to then $q_{i\perp}$. Then, it is possible to (anti-)commute the matrices γ^+ in (36) outwards to a position next to on-mass-shell bispinors $\bar{d}'$ and u, action on which, by virtue of (23), gives zero. So, block (34) equals

$$\not{q}_1 d_R \bar{u}'_R \not{q}_1 = q_1^R q_1^L \gamma^L d_R \bar{u}'_R \gamma^R = \mathbf{q}_\perp^2 d_L \bar{u}'_L, \tag{36}$$

which is proportional to (31).

Ultimately, it is understood that in the arbitrary order

$$\mathscr{N}^{(n)}_{RR,RR} = \mathscr{N}^{(n)}_{LL,LL} = (-2)^n s\, \mathbf{q}_{1\perp}^2 \dots \mathbf{q}_{n-1\perp}^2. \tag{37}$$

Note that the $2\mathbf{q}_\perp^2$ factors emerge here without the appeal to the azimuthal averaging, or reasoning that $q_\parallel$ components cancel the logarithmic singularities in the integral (cf. [3]). As is known, vector interaction at hard momentum transfers (compared to the mass) is predominantly magnetic – similarly to the conventional separation of electric and magnetic form-factors:

$$J^\mu_{fi} = \bar{u}_f \left[F_e\left(Q^2\right)\gamma^\mu_\parallel + F_m\left(Q^2\right)\gamma^\mu_\perp\right] u_i. \tag{38}$$

Since in our case polarizations of all the virtual particles are completely fixed by that of initial ones, the problem is equivalent to some scalar field theory. The vector character of the bosons does not entail any momentum-dependent numerators, and merely secures helicity conservation.

3.2 Color matrix factor

As had been discussed in [3], [5, 6], in the perfect charge (color) exchange situation the infra-red vector boson exchange contributions mutually cancel. Here, let us neglect them altogether, and consider only the hard ladder.

Embarking on the Fierz-type identity for color generators

$$t^A_{l'l} t^A_{m'm} = \frac{1}{2}\delta_{l'm}\delta_{m'l} - \frac{1}{2N_c}\delta_{l'l}\delta_{m'm}, \tag{39}$$

by induction one proves[5]

[5] Here, C_F and $-\frac{1}{2N_c}$ are just the values of Kirschner's matrix τ_2 (defined in a basis of convenience for him [5]), and $\delta_{m'l}\delta_{l'm}$ together with $t^A_{m'l} t^A_{l'm} - \frac{1}{2N_c}\delta_{m'l}\delta_{l'm}$ are its eigenvectors.

$$\mathsf{C}^{(n)} = \left(t^{A_n}\dots t^{A_1}\right)_{l'l}\left(t^{A_1}\dots t^{A_n}\right)_{m'm}$$
$$= C_F^n\frac{1}{N_c}\delta_{m'l}\delta_{l'm} + 2\left(-\frac{1}{2N_c}\right)^n\left[t^A_{m'l}t^A_{l'm} - \frac{1}{2N_c}\delta_{m'l}\delta_{l'm}\right], \qquad (40)$$

with C_F given by Eq. (3). Obviously, $C_F > -\frac{1}{2N_c}$, both by sign, and in magnitude. At $n \geq 2$, i.e., in any loop, it suffices to keep only the first term in the r.h.s. of (40). As the Kronecker symbols indicate, the leading term requires exchange of color.[6]

The underlying reason for the law that the color exchange is assured at the given ordering of gluon emission and re-absorption, and when $N_c \to \infty$, is also transparent. For each quark, the first ladder gluon emitted by it carries away its color, and in addition has arbitrary (except at the tree level) anticolor. The final quark moving in the same direction will absorb this gluon last of all, and must annihilate its anticolor whatever it is (by color conservation), and accept its color. Thereby, the color of the final quark will coincide with that of the comoving initial one.

Summarizing this section, re-absorption of gauge bosons in the inverse order stipulates transfer of all the quantum numbers between the scattered quarks. The large-N_c limit here is sufficiently robust, and within it the picture is equivalent to that of QED, the coupling constant correspondence being $\alpha_{QED} \to \alpha_s C_F$.

4 Loop integrals in DLLA

Using the numerator kinematical factors, we are in a position to treat the loop integrals.

4.1 One-loop integral reduction. Wave-function interpretation

By far the simplest approach for of high-energy asymptotics derivation and understanding is infinite momentum frame quantum field theory. One might anticipate its applicability for the backward scattering, as well, inasmuch as the denominator structure in Feynman integrals is the same as for forward scattering. But, because of the occurrence of factors $\mathbf{q}_\perp^2$ in the numerator (see section 3.1), application of LCPT is obstructed by the divergence of the eikonal integral, over $d^2q_\perp$. To keep the treatment consistent, one may, first, straightforwardly carry out the q^- integration in Feynman integrals. In one loop,

$$M^{(2)}/\mathsf{C}^{(2)} \approx -2is(4\pi\alpha)^2\int\frac{d^4q}{(2\pi)^4}\frac{2q_\perp^2}{(2p'_dq-i0)(2p_dq-i0)q^2(q-\Delta)^2}$$
$$\approx (4\pi\alpha)^2\int\frac{dq^-}{2\pi i(q^- - i0)}\frac{dq^+}{2\pi q^+}\frac{d^2q_\perp}{(2\pi)^2}\frac{2q_\perp^2}{q_\perp^2(\Delta_\perp - q_\perp)^2}.$$

[6] The second term of (40), in fact, is not yet related to a self-consistent scattering amplitude since it is devoid of infra-red DL corrections.

Upon the integration (in the exact expression) over q^-, reducing, essentially, to taking residue in a single pole $q^- \approx 0$, we derive a restriction on q^+: $p_d^- \le q^+ \le p_d^+$. Then, one can pass to the eikonal approximation. At that, the condition

$$-(p'_d - q)^2 \approx 2p'_d q \approx 2p'^-_d q^+ \gg q^2, q_\perp^2$$

yields ordering of $q_\perp^2$ and q^+, which secures convergence of the integral over $q_\perp^2$ at large $q_\perp^2$. Within the (double-) logarithmic accuracy,

$$M^{(2)}/\mathsf{C}^{(2)} \approx \frac{(4\pi\alpha)^2}{(2\pi)^2} \int_{p'^+_d}^{p^+_d} \frac{dq^+}{q^+} \int_1^{p'^-_d q^+} \frac{dq_\perp^2}{q_\perp^2} \tag{41}$$
$$= \frac{(4\pi\alpha)^2}{8\pi^2} \ln^2 s = \frac{\alpha}{4\pi} \ln^2 s \cdot M^{(1)}/\mathsf{C}^{(1)}.$$

In the final representation (41) valuable is the separation of hard and soft physics, which does not in fact depend on our choice of prior integration over q^-, or q^+. The longitudinal hard gluons pertain to hard physics, whereas the braking fermions – to the soft. Soft physics is most conveniently interpreted in terms of wave functions and their overlaps. If one invokes the analogy with the non-relativistic (or old-fashioned) perturbation theory, Eq. (41) may be compared with the expression for the second-order transition matrix element

$$\langle 2|\, V\, |1\rangle = \sum_n \frac{\langle 2|\, V\, |n\rangle \langle n|\, V\, |1\rangle}{E_0 - E_n}. \tag{42}$$

The role of the perturbation operator V in our case is played by the coupling constant $4\pi\alpha$. The energy denominator finds an analog in the factor $\frac{1}{q^+}$, which, however, is positive, not negative, i.e., the intermediate states reside *under* the mass-shell. As for the intermediate state wave functions $|n\rangle$, their counterparts are the factors $\frac{\sqrt{2}}{q^1 \pm iq^2}$. Finally, the phase space volume element is $\frac{dq^+ d^2 q_\perp}{(2\pi)^3}$. It should be noted that the phase space available for $q_\perp^2$ is restricted by the value of the "energy" q^+. That reflects the circumstance that soft and hard physics are not separated absolutely, but only within the logarithmic accuracy. A similar situation (not encountered at forward scattering) is often met at description of exclusive hadronic processes with a large momentum transfer (see, e.g., [9]).

In conclusion, let us remark that in [3] the extraction of DLLA contributions is conducted by prior integration over $d^2 q_\perp$, in analogy with the Sudakov's vertex asymptotic treatment [10]. That renders the framework more symmetric appearance, but the wave-function interpretation gets obscured.

4.2 All-order treatment

Integrals for higher orders of perturbation theory may also be calculated via first q^--integration, but it requires more detailed considerations (cf. [8]). Instead of the

variables q_i^-, $q_{i\perp}^2$, in the present case it is convenient to introduce

$$q_i^-, \quad \kappa_i = \frac{\mathbf{q}_{i\perp}^2}{2q_i^-}, \tag{43}$$

and only then carry out the q_i^- integration. Then, a strong ordering condition ensues

$$\kappa_i \gg \kappa_{i+1} \tag{44}$$

(corresponding to the multiperipheral condition $q_i^- \ll q_{i+1}^-$ for q_i^-, which have been integrated over), and

$$\kappa_i < q_i^+ \tag{45}$$

(corresponding to the eikonal condition $\mathbf{q}_{i\perp}^2 < 2q_i^+ q_i^-$). The integral of the $2n$-th order of perturbation theory, in DLLA assumes the form

$$M^{(n)}/\mathsf{C}^{(n)} = \left(M^{(1)}/\mathsf{C}^{(1)}\right)\left(\frac{\alpha}{2\pi}\right)^{n-1}\int_{p'^+_d}^{p^+_d}\frac{dq_1^+}{q_1^+}\int_{p'^+_d}^{q_1^+}\frac{d\kappa_1}{\kappa_1}\ldots$$
$$\ldots\int_{p'^+_d}^{q^+_{n-3}}\frac{dq_{n-2}^+}{q_{n-2}^+}\int_{p'^+_d}^{\min(q^+_{n-2},\kappa_{n-3})}\frac{d\kappa_{n-2}}{\kappa_{n-2}}\int_{p'^+_d}^{q^+_{n-2}}\frac{dq_{n-1}^+}{q_{n-1}^+}\int_{p'^+_d}^{\min(q^+_{n-1},\kappa_{n-2})}\frac{d\kappa_{n-1}}{\kappa_{n-1}}. \tag{46}$$

For evaluation of this integral, it is convenient to recast the i-th pair of integrations

$$\int_{p'^+_d}^{q^+_{i+1}}\frac{dq_i^+}{q_i^+}\int_{p'^+_d}^{\min(q_i^+,\kappa_{i+1})}\frac{d\kappa_i}{\kappa_i}\ldots = \int_{p'^+_d}^{q^+_{i+1}}\frac{dq_i^+}{q_i^+}\int_{p'^+_d}^{\kappa_{i+1}}\frac{d\kappa_i}{\kappa_i}\ldots - \int_{p'^+_d}^{\kappa_{i+1}}\frac{dq_i^+}{q_i^+}\int_{q_i^+}^{\kappa_{i+1}}\frac{d\kappa_i}{\kappa_i}\ldots$$
$$\equiv \int_{p'^+_d}^{q^+_{i+1}}\frac{dq_i^+}{q_i^+}\int_{p'^+_d}^{\kappa_{i+1}}\frac{d\kappa_i}{\kappa_i}\ldots - \int_{p'^+_d}^{\kappa_{i+1}}\frac{d\kappa_i}{\kappa_i}\int_{p'^+_d}^{\kappa_i}\frac{dq_i^+}{q_i^+}\ldots \tag{47}$$

(the integral over a trapezium represented as an integral over the rectangle minus the integral over the triangle). But, as is easy to demonstrate by changing the order of variables,

$$\int_{p'^+_d}^{\kappa_{i+1}}\frac{d\kappa_i}{\kappa_i}\int_{p'^+_d}^{\kappa_i}\frac{dq_i^+}{q_i^+}\left\{\int_{p'^+_d}^{q_i^+}\frac{dq_{i-1}^+}{q_{i-1}^+}\int_{p'^+_d}^{\kappa_i}\frac{d\kappa_i}{\kappa_{i-1}} - \int_{p'^+_d}^{\kappa_i}\frac{d\kappa_{i-1}}{\kappa_{i-1}}\int_{p'^+_d}^{\kappa_{i-1}}\frac{dq_{i-1}^+}{q_{i-1}^+}\right\}\ldots \equiv 0, \tag{48}$$

so, we can drop the terms $-\int_{p'^+_d}^{\kappa_{i+1}}\frac{d\kappa_i}{\kappa_i}\int_{p'^+_d}^{\kappa_i}\frac{dq_i^+}{q_i^+}$ at all the $dq_i^+ d\kappa_i$ integrations but the $(n-1)$-th.[7] The $(n-1)$-th double integration gives

$$\int_{p'^+_d}^{q^+_{n-2}}\frac{dq_{n-1}^+}{q_{n-1}^+}\int_{p'^+_d}^{\kappa_{n-2}}\frac{d\kappa_{n-1}}{\kappa_{n-1}} - \int_{p'^+_d}^{\kappa_{n-2}}\frac{d\kappa_{n-1}}{\kappa_{n-1}}\int_{p'^+_d}^{\kappa_{n-1}}\frac{dq_{n-1}^+}{q_{n-1}^+} =$$

[7] This means that inequalities (45) are inconsequential, except for the first and the last one.

$$= \ln\frac{q_{n-2}^{+}}{p'^{+}_{d}} \ln\frac{\kappa_{n-2}}{p'^{+}_{d}} - \frac{1}{2}\ln^2\frac{\kappa_{n-2}}{p'^{+}_{d}}. \tag{49}$$

Passing to the self-suggestive variables

$$\eta_i = \ln\frac{q_i^{+}}{p'_d}, \quad \xi_i = \ln\frac{\kappa_i}{p'_d}, \tag{50}$$

the DLLA amplitude of $2n$-th order is calculated quite trivially:

$$\begin{aligned} M^{(n)}/\mathrm{C}^{(n)} &= \left(M^{(1)}/\mathrm{C}^{(1)}\right)\left(\frac{\alpha}{2\pi}\right)^{n-1} \\ &\times \int_0^{\ln s} d\eta_1 \ldots \int_0^{\eta_{n-3}} d\eta_{n-2} \int_0^{\ln s} d\xi_1 \ldots \int_0^{\xi_{n-3}} d\xi_{n-2} \left\{\eta_{n-2}\xi_{n-2} - \frac{1}{2}\xi_{n-2}^2\right\} \\ &= \left(M^{(1)}/\mathrm{C}^{(1)}\right)\left(\frac{\alpha}{2\pi}\ln^2 s\right)^{n-1} \left\{\frac{1}{[(n-1)!]^2} - \frac{1}{(n-2)!n!}\right\} \\ &= \left(M^{(1)}/\mathrm{C}^{(1)}\right)\left(\frac{\alpha}{2\pi}\ln^2 s\right)^{n-1} \frac{1}{(n-1)!n!}. \end{aligned} \tag{51}$$

Invoking the series expansion for the modified Bessel function of first order,

$$I_1(z) = \sum_{n=1}^{\infty} \frac{\left(\frac{z}{2}\right)^{2n-1}}{(n-1)!n!}, \tag{52}$$

we arrive at the result of [3], which we have thus re-derived by straightforward resummation, without the recourse to the formalism of integral equations.

Post factum, it is important to check the self-consistency of the adopted multi-peripheral approximation (8–10). When $z = \sqrt{\frac{2\alpha C_F}{\pi}}\ln s \gg 1$, the largest terms in sum (52) have numbers

$$\bar{n} \sim \frac{z}{2}. \tag{53}$$

Equally, and independently of the overall energy, one can say that each gluon typically shifts the quark rapidity by

$$\Delta y = \frac{Y = \ln s}{\bar{n}} \sim \sqrt{\frac{2\pi}{\alpha C_F}} \simeq 5 \div 7. \tag{54}$$

This implies that for the given problem the multi-peripheral approximation is very safe.

The transverse motion of quarks in the ladder rails is usually regarded as random walk. At that, the rung gluons propagate nearly forward (since, in the eikonal approximation, their propagators do not depend on transverse momenta), and so, impact parameters of the final u-quark must coincide with that of the initial d-quark, and impact parameter of the final d-quark – with that of the initial u-quark. Thereby,

the walk is not completely random. Yet, the walk step is small as compared to typical hadronic radius (recall that large $\mathbf{q}_\perp^2$ dominate), so the initial quark impact parameters must be close to one another, anyway.

5 Discussion and summary

The mechanistic picture of reggeization is observed to fall into certain contrast with the analyticity and duality expectations. In particular, transversal hardness excludes exact analogy with meson exchange in the t-channel, and yet suggests that the quark-exchange reggeization phenomenon, and the relevant intercept, may be universal, or there can be a few universal reggeons (much less numerous then the host of mesons). The similarity of the Regge ladder diagram with that of the Bethe-Salpeter equation must not be deluding, given the dominance in the present case of large $q_\perp$ (let alone the excessive hardness of the ladder u-channel gluons). In their own turn, mesons, being strongly bound relativistic states, for which the interaction radius is not small compared to the average inter-constituent distance must not necessarily obey a Bethe–Salpeter-like equation at all.

In what concerns the hadron wave function overlap representation, the hardness of the Regge ladder implies that one can rather safely exploit the notion of coincidence of colliding quark impact parameters – unless the energy becomes super-high, giving the short-step transverse random walk eventually a spread comparable to the hadron size. Another feature important at hadron wave function overlap computations is that the reggeized kernel (1) is not scale-invariant, and does not factorize in terms of Feynman-x of the active quarks:

$$M_{qq'\to q'q}\left(s_{qq'}=s_{hh}x_q x_{q'}\right)\neq f_1\left(s_{hh}\right)f_2\left(x_q\right)f_3\left(x_{q'}\right), \tag{55}$$

and it is only in far asymptotics (2), where some noninteger-power scaling law and factorization set in. Finally, note that amplitude (1) is neither even, nor odd function of s, in contrast to the kernel in Born approximation. The latter property matters at calculations of meson flavor exchange amplitudes.

References

1. Feldman, L.C., and Mayer, J.W.: Fundamentals of Surface and Thin Film Analysis. North-Holland, Amsterdam (1986) 352 p.
2. Bondarenco M.V. arXiv: hep-ph/0809.2573
3. Gorshkov, V.G., Gribov, V.N., Lipatov, L.N., and Frolov, G.V., Yad. Fiz. **6**, 129–140 (1967)
4. Berestetsky, V.B., Lifshitz, E.M., and Pitaevsky, L.P.: Quantum Electrodynamics. Pergamon Press, Oxford (1982) 667 p.
5. Kirschner, R. Yad. Fiz. **34**, 546–553 (1981); Phys. Let. B **98**, 451–455 (1981)
6. Kirschner, R., and Lipatov, L.N. Zh.E.T.F. **83**, 488–501 (1982); Phys. Rev. D **26**, 1202 – 1205 (1982); Nucl. Phys. B **213**, 122–148 (1983)

7. Barton, H.R. et al. Phys. Rev. Lett. **37**, 1656–1659, 1659–1662 (1976)
8. Cheng, H., Wu, T.T.: Expanding Protons: Scattering at High Energies. MIT Press, Cambridge, MA (1987) 285 p.
9. Lepage, G.P., and Brodsky, S.J. Phys. Rev. D **22**, 2157–2198 (1980)
10. Sudakov, V.V. Zh. E.T.F. **30**, 87–95 (1956)

$\pi\pi$ Scattering Length Measurements from Ke4 and $K^{\pm} \to \pi^{\pm}\pi^0\pi^0$ Decays at NA48/2

F. Bucci

Abstract We report here the preliminary results on the $\pi\pi$ scattering lengths a_0 and a_2 at NA48/2. We determine a_0 and a_2 by studying two different kaon decay modes. In the $K^{\pm} \to \pi^+\pi^- e^{\pm}\nu$ decays (K_{e4}) we measure the form factors of the hadronic current (F, G, H) and the $\pi\pi$ phase difference ($\delta = \delta_s - \delta_p$) in ten independent bins of the $\pi\pi$ mass spectrum to investigate their variation. Taking into account the isospin simmetry breaking effects and using numerical solutions of the Roy equations we obtain a_0 and a_2. In the $K^{\pm} \to \pi^{\pm}\pi^0\pi^0$ events we determine the $a_0 - a_2$ difference and a_2 from a fit to the $\pi^0\pi^0$ invariant mass distribution (M_{00}) around $M_{00} = 2m_{\pi^+}$.

Keywords: Charged kaon, cusp, Ke4, scattering length

1 Introduction

The single-flavor quark condensate $< 0|\overline{q}q|0 >$ is a fundamental parameter of the chiral perturbation theory (ChPT), determining the relative size of mass and momentum terms in the expansion. Since it cannot be predicted theoretically, its value must be experimentally determined by measuring, for example, the $\pi\pi$ scattering lengths a_0 and a_2 whose values are precisely predicted within the framework of the ChPT, assuming a big quark condensate [1], or of a generalised ChPT, where the quark condensate is a free parameter [2].

The K_{e4} decay is a very clean environment for the measurement of the $\pi\pi$ scattering lengths since the two pions are the only hadrons in the final state and they are produced close to the threshold. In the past years, only two experiments collected significant samples of K_{e4} decays [3,4], large enough to study their properties

F. Bucci
Università di Firenze, via G. Sansone 1, 50019 Sesto Fiorentino, Firenze,
e-mail: francesca.bucci@fi.infn.it

V. Begun et al. (eds.), *Progress in High-Energy Physics and Nuclear Safety*,

but without reaching the same precision level as the theoretical predictions. An alternative way to study the $\pi\pi$ interactions through a measurement of the lifetime of the $\pi\pi$-atom was followed in the DIRAC experiment at CERN [1]. An additional method for the determination of the $\pi\pi$ scattering length a_2 and the $a_0 - a_2$ difference is based on the study of the $\pi^0\pi^0$ invariant mass spectrum in the $\boldsymbol{K}^{\pm} \to \pi^{\pm}\pi^0\pi^0$ decays.

We present here the preliminary results on $\pi\pi$ scattering lengths based on about $1.2 \cdot 10^6$ K_{e4} events and $6 \cdot 10^7$ $\boldsymbol{K}^{\pm} \to \pi^{\pm}\pi^0\pi^0$ decays collected by the NA48/2 experiment.

2 Experimental setup

The NA48/2 experiment beam line has been designed to measure the CP violating charged asymmetry in the $K \to 3\pi$ decay [6]. Simultaneous K^+ and K^- beams are produced by 400 GeV protons from the CERN Super Proton Synchrotron (SPS) impinging on a beryllium target. Kaons are deflected in a front-end achromat to select the momentum band of (60 ± 3) GeV/c and then focused at the beginning of the detector $\sim$200 m downstream, at the end of the $\sim$100m long decay region. The NA48 detector and its performances are described in detail elsewhere [7]. The K_{e4} analysis is essentially based on the magnetic spectrometer, consisting of four drift chambers and a dipole magnet located between the second and the third chamber. Each chamber consists of four staggered double planes of sense wires along the horizontal, vertical and $\pm 45°$ directions. The momentum resolution of the spectrometer is $\sigma_p/p = (1.02 \oplus 0.044 \cdot p)\%$ (with p in GeV/c). The $\boldsymbol{K}^{\pm} \to \pi^{\pm}\pi^0\pi^0$ analysis uses the liquid-krypton calorimeter (LKr) to identify the photons produced in the π^0 decay. The transverse segmentation and the 27 radiation lenght thickness result in an energy resolution $\sigma_E/E = (3.2/\sqrt{E} \oplus 9.0/E \oplus 0.42)\%$ (with E in GeV) and a space resolution for isolated showers $\sigma_x = \sigma_y = (0.42/\sqrt{E} \oplus 0.06)$ cm (with E in GeV). Furthermore, a hodoscope consisting of two planes of scintillators segmented into horizontal and vertical strips is used to trigger the detector readout on charged track topologies. Its time resolution is $\sim$150 ps.

3 The K_{e4} decay

3.1 Formalism

The kinematics of the K_{e4} decay is fully described by five variables introduced by Cabibbo and Maksymowicz [8]: $M^2_{\pi\pi}$, the squared invariant mass of the dipion system; $M^2_{e\nu}$, the squared invariant mass of the dilepton; θ_π, the angle of the pion with the same charge as the kaon in the dipion rest frame ($\Sigma_{\pi\pi}$) with respect to

the direction of flight of the dipion in the K rest frame (Σ_K); θ_e, the angle of the electron in the dilepton rest frame ($\Sigma_{e\nu}$) with respect to the direction of flight of the dilepton system in Σ_K; ϕ, the angle between the plane formed by the two pions and the corresponding plane formed by the two leptons. Three axial (F, G, R) and one vector (H) dimensionless complex form factors contribute to the transition amplitude and can be developed in partial wave expansions of s, p, d waves [9]:

$$\begin{aligned} F &= F_s e^{i\delta_s} + F_p e^{i\delta_p} + d\ wave \\ G &= G_p e^{i\delta_p} + d\ wave \\ H &= H_p e^{i\delta_p} + d\ wave \end{aligned} \tag{1}$$

where we assumed the same phase for F_p, G_p and H_p. The third axial form factor R is suppressed by a factor $m_e^2/M_{e\nu}^2$. Neglecting d wave terms, F_s, F_p, G_p and H_p can be further [10] expanded in powers of $q^2 = (M_{\pi\pi}^2/4m_\pi^2) - 1$:

$$\begin{aligned} F_s &= f_s + f_s^{'} q^2 + f_s^{''} q^4 + ... \\ F_p &= f_p + f_p^{'} q^2 ... \\ G_p &= g_p + g_p^{'} q^2 + ... \\ H_p &= h_p + h_p^{'} q^2 ... \end{aligned} \tag{2}$$

3.2 Selection and fitting procedure

The K_{e4} events are selected by requiring three charged tracks within the detector acceptance. Two opposite sign pions and one electron or positron are required. Particle identification is mainly based on the E/p ratio between the energy as measured by the LKr calorimeter and the momentum as measured by the magnetic spectrometer. The reconstructed three tracks invariant mass (assigning a pion mass to each track) and the transverse momentum p_t relative to the beam axis have to be outside an ellipse centered on the kaon mass and zero p_t, allowing missing energy and p_t for the undetected neutrino. The kaon momentum p_K is obtained by imposing energy-momentum conservation in the Ke4 decay, under the assumption of an undetected neutrino and fixing the kaon mass and the beam direction to their nominal value. If a solution exists in the range between 50 and 70 GeV/c, the event is kept and the solution closer to 60 GeV/c is assigned to p_K. The background comes from $K^{\pm} \to \pi^+\pi^-\pi^{\pm}$ decays with a pion misidentified as an electron or the subsequent $\pi \to e\nu$ decay and $K^{\pm} \to \pi^{\pm}\pi^0(\pi^0)$ decays with $\pi^0 \to e^+e^-\gamma$, an electron misidentified as a pion and photon(s) undetected. The background is evaluated by studying the "wrong-sign" events, i.e. events for which the $\Delta S = \Delta Q$ rule is violated (the electron charge is opposite to the total one) and it results to be at 0.5% level.

We define 15,000 iso-populated boxes in the 5-dimension space of $M_{\pi\pi}$, M_{ev}, $cos\theta_\pi$, $cos\theta_e$ and ϕ. The form factors F_s, F_p, G_p, H_p and the phase shift $\delta = \delta_s - \delta_p$ are extracted by minimizing a log-likelihood estimator in the ten independent $M_{\pi\pi}$ bins. Actually, only relative form factors F_p/F_s, G_p/F_s and H_p/F_s are accessible since the branching fraction is not measured. Their variation with $M_{\pi\pi}$ is then fitted to extract the form factors $f_s^{'}/f_s$, $f_s^{''}/f_s$, $f_e^{'}/f_s$, f_p/f_s, g_p/f_s, $g_p^{'}/f_s$ and h_p/f_s.

3.3 Results

Preliminary results on form factors data are shown in Table 1. The systematic errors are quoted by comparing two independent analysis and taking into account the effect of reconstruction method, acceptance, fit method, uncertainty on background estimate, electron-ID efficiency, radiative corrections and bias due to the neglected M_{ev} dependence.

Dispersion relations and data at intermediate energies give the functional relation between the phase shift δ and $M_{\pi\pi}$ with the scattering lenghts a_0 and a_2 as parameters [11–13]. Figure 1 shows the measured variation of δ with $M_{\pi\pi}$. After correcting for the isospin simmetry breaking effects, the a_0 and a_2 values are extracted by performing a fit to the phase shift variation. The $\pi\pi$ scattering data above 0.8 GeV and the dispersion relations restrict the a_0 and a_2 values to a band in the (a_0, a_2) plane called the Universal Band (UB); the width of the allowed band is considerably reduced if the $a_2 = f(a_0)$ relation given by the chiral perturbation theory [14] is imposed in addition. Exploiting the ChPT constraint, $a_2 = f(a_0)$, we also perfom a one paramater fit. Fit results are reported in Table 2.

Table 1 Form factors preliminary results based on $1.2 \cdot 10^6$ K_{e4} events

				Stat		Syst
$f_s^{'}/f_s$	=	0.158	±	0.007	±	0.006
$f_s^{''}/f_s$	=	−0.078	±	0.007	±	0.007
$f_e^{'}/f_s$	=	0.067	±	0.006	±	0.009
f_p/f_s	=	−0.049	±	0.003	±	0.004
g_p/f_s	=	0.869	±	0.010	±	0.012
$g_p^{'}/f_s$	=	0.087	±	0.017	±	0.015
h_p/f_s	=	−0.402	±	0.014	±	0.008

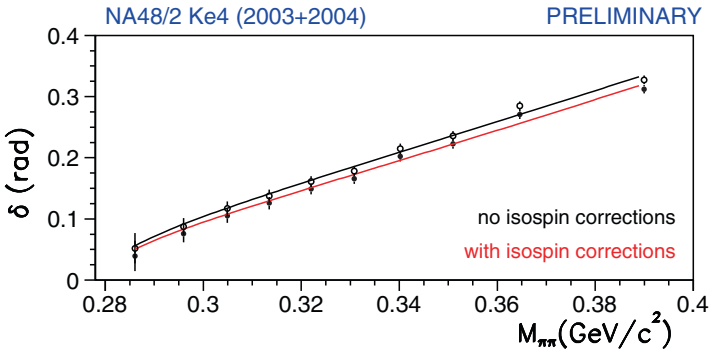

Fig. 1 Phase shift variation as a function of $M_{\pi\pi}$ with (full circle) and without (empty circle) taking into account the isospin symmetry breaking effects

Table 2 Scattering lengths preliminary results on $1.2 \cdot 10^6$ K_{e4} events

Without ChPT constraint	With ChPT constraint
$a_0 m_{\pi^+} = 0.218 \pm 0.013_{stat} \pm 0.007_{syst}$ $a_2 m_{\pi^+} = -0.0457 \pm 0.0084_{stat} \pm 0.0041_{syst}$	$a_0 m_{\pi^+} = 0.220 \pm 0.005_{stat} \pm 0.002_{syst}$

4 The $K^{\pm} \to \pi^{\pm}\pi^0\pi^0$ decay

4.1 The cusp effect

The study of $2.4 \cdot 10^7$ $K^{\pm} \to \pi^{\pm}\pi^0\pi^0$ decays showed a change of slope in the squared invariant mass distribution of the $\pi^0\pi^0$ system (M_{00}) at the $\pi^+\pi^-$ threshold [15]. This anomaly, never observed in the previous experiments, was theoretically interpreted as an effect due to the charge-exchange scattering process $\pi^+\pi^- \to \pi^0\pi^0$ in $K^{\pm} \to \pi^{\pm}\pi^+\pi^-$ decays. Cabibbo [16] proposed a simple rescattering model desribing the $K^{\pm} \to \pi^{\pm}\pi^0\pi^0$ decay amplitude as the sum of two terms: the unperturbed decay amplitude $\mathscr{M}_0$ and the contribution $\mathscr{M}_1$ from the $K^{\pm} \to \pi^{\pm}\pi^+\pi^-$ decay amplitude through the $\pi^+\pi^- \to \pi^0\pi^0$ charge-exchange with the renormalization condition $\mathscr{M}_1 = 0$ at $M_{00} = m_{\pi^+\pi^-}$. $\mathscr{M}_1$ is proportional to $a_0 - a_2$ and changes from real to imaginary at the $\pi^+\pi^-$ threshold with the consequence that it interferes destructively with $\mathscr{M}_0$ below the threshold while it adds quadratically above it. The experimental measurement of this effect thus provides a precise determination of $a_0 - a_2$ (including its sign). Subsequently, Cabibbo and Isidori (CI) [17] have extended the amplitude calculation at two loops level adding five terms proportional to the scattering lenghts. This model allows to extract $a_0 - a_2$ and a_2. A different model was developed by Colangelo et al. (CGKR) [18] which includes the electromagnetic effects and introduces a different correlation between the parameters with respect to the CI approach.

4.2 Selection and fitting procedure

The analysis was redone on $6 \cdot 10^7$ $K^{\pm} \to \pi^{\pm}\pi^0\pi^0$ decays. Signal events are selected by requiring one charged track and at least four energy clusters in the LKr. We assume that each possible pair of photons originates from $\pi^0 \to \gamma\gamma$ and we calculate the longitudinal position of the corresponding neutral vertex. We choose the two vertices combination with the closest vertices and the arithmetic average of the two π^0 vertices is taken as the kaon decay vertex. This choice gives the best M_{00} resolution at $M_{00} = 2m_{\pi^+}$. The r.m.s. of the M_{00}^2 resolution curve increases with M_{00}^2, varying between $\sim$0.0002 GeV^2 and $\sim$0.001 GeV^2. The cusp in the M_{00}^2 distribution is clearly visible in Fig. 2 at $M_{00} = 2m_{\pi^+}$. At this point the resolution on M_{00}^2 is $\sim$0.0003 GeV^2.

Both the CI and CGKR formulations are used to fit the squared invariant mass distribution of the $\pi^0\pi^0$ system. The resolution and the detector response matrix are obtained using an accurate Geant3 based simulation. For the unperturbed amplitude $\mathcal{M}_0$ the PDG parameterization is taken:

$$\mathcal{M}_0 = A_0(1 + \frac{1}{2}g_0 u + \frac{1}{2}h_0' u^2 + \frac{1}{2}k_0' v^2) \tag{3}$$

where u and v are the Dalitz variables.

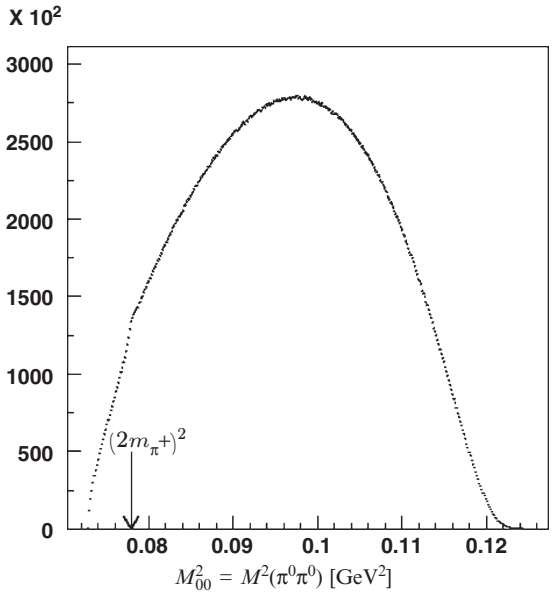

Fig. 2 $\pi^0\pi^0$ invariat mass distribution in $K^{\pm} \to \pi^{\pm}\pi^0\pi^0$ decays. A cusp at $M_{00} = 2m_{\pi^+}$ is clearly visible

The fit parameters are g_0, $h_0^{'}$, $a_0 - a_2$, a_2 and the normalization factor N. $k_0^{'}$ and the unperturbed amplitude of the $K^{\pm} \to \pi^{\pm}\pi^+\pi^-$ decay which is present in $\mathscr{M}_1$ are fixed to the values previously measured by NA48/2 [19]. The fit is performed excluding a small region around the threshold where the theoretical treatment of the electromagnetic interaction is still missing.

4.3 Results

The preliminary results obtained on $6 \cdot 10^7$ $\boldsymbol{K}^{\pm} \to \pi^{\pm}\pi^0\pi^0$ events are:

$$\begin{aligned}
CI \quad &: (a_0 - a_2) m_{\pi^+} = \quad 0.266 \pm 0.005_{stat} \pm 0.002_{syst} \pm 0.001_{ext} \\
&\quad a_2 \; m_{\pi^+} = -0.039 \pm 0.009_{stat} \pm 0.006_{syst} \pm 0.002_{ext} \\
CGKR &: (a_0 - a_2) m_{\pi^+} = \quad 0.273 \pm 0.005_{stat} \pm 0.002_{syst} \pm 0.001_{ext} \\
&\quad a_2 \; m_{\pi^+} = -0.065 \pm 0.015_{stat} \pm 0.010_{syst} \pm 0.002_{ext} \qquad (4)
\end{aligned}$$

If we impose the constraint between a_0 and a_2 due to analiticity and chiral symmetry [14], we obtain:

$$\begin{aligned}
CI \quad &: (a_0 - a_2) m_{\pi^+} = \quad 0.268 \pm 0.003_{stat} \pm 0.002_{syst} \pm 0.001_{ext} \\
CGKR &: (a_0 - a_2) m_{\pi^+} = \quad 0.266 \pm 0.003_{stat} \pm 0.002_{syst} \pm 0.001_{ext} \qquad (5)
\end{aligned}$$

The external error originates from the uncertainty on the branching ratio $\Gamma(K^{\pm} \to \pi^{\pm}\pi^+\pi^-)/\Gamma(\boldsymbol{K}^{\pm} \to \pi^{\pm}\pi^0\pi^0)$. Cabibbo and Isidori also assign a 5% theoretical error on $(a_0 - a_2)m_{\pi^+}$ to take into account the missing orders and the Coulomb corrections. Recent results both in radiative corrections [20] and in the next order preliminary calculations allow to decrease this contribution to the total error at 1% level.

5 Comparison and conclusions

Two statistically independent analysis have been performed by the NA48/2 collaboration to measure the $\pi\pi$ scattering lenghts: one, based on the high-statistics measurement of the $\pi^0\pi^0$ invariant mass distribution in the $\boldsymbol{K}^{\pm} \to \pi^{\pm}\pi^0\pi^0$ decay; the other, on the measurement of the phase shift variation with the $\pi^+\pi^-$ invariant mass in the $K^{\pm} \to \pi^+\pi^- e^{\pm}\nu$ decay. In Fig. 3 the agreement between these two independent measurements is shown together with other experimental results.

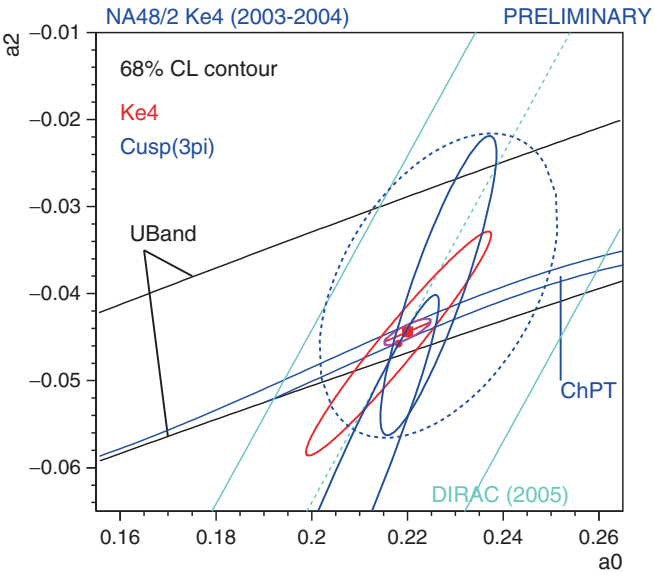

Fig. 3 Results for the $\pi\pi$ scattering lengths a_0 and a_2 in m_π^+ units. The black solid curves are the universal band boundaries and the narrow blue band is the restricted area using the ChPT constraint. The ellipses correspond to 68% CL in a two-parameter fit to $K^\pm \to \pi^\pm\pi^0\pi^0$ events (blue ellipses) and Ke4 events (red ellipse). The upper blue ellipses represent the result with the CI theory assuming a 5% (dotted) and a 1% (solid) theoretical error, respectively. The lower blue ellipse is the CGKR fit result. The red square is the result of 1-paramenter fit to Ke4 data, to be compared with the ChPT predictions (purple ellipse). The result form the DIRAC experiment (cyan) is also shown

References

1. G. Colangelo *AIP Conf. Proc.* **756**, 60 (2005).
2. M. Knecht et al., *Nucl. Phys.* **B4570**, 513 (1995).
3. L. Rosselet et al., *Phys. Rev.* **D15**, 574 (1977).
4. S. Pislak et al., *Phys. Rev. Lett.* **87**, 221801 (2001), *Phys. Rev.* **D67** 072004 (2003).
5. B. Adeva et al., [DIRAC Collaboration], *Phys. Lett.* **B619**, 50 (2005).
6. J.R. Batley et al., [NA48/2 Collaboration], *Eur. Phys. J.* **C52**, 875 (2007).
7. V. Fanti et al., [NA48 Collaboration], *Nucl. Instrum. Meth.* **A574**, 433 (2007).
8. N. Cabibbo and A. Maksymowicz, *Phys. Rev.* **B438**, 137 (1965).
9. A. Pais and S. Treiman, *Phys. Rev.* **168**, 1858 (1968).
10. G. Amoros, J. Bijnens, *J. Phys.* **G25**, 1607 (1999).
11. S. Roy, *Phys. Lett.* **B36**, 353 (1971).
12. B. Ananthanarayan, G. Colangelo, J. Gasser and H. Leutwyler, *Phys. Rep.* **353**, 207 (2001).
13. N. Fuchs, L. Girlanda and J. Stern, *Eur. Phys. J.* **C24**, 469 (2002).
14. G. Colangelo, J. Gasser and H. Leutwyler, *Nucl. Phys.* **B603**, 125 (2001).
15. J.R. Batley et al., [NA48/2 Collaboration], *Phys. Lett.* **B633**, 173 (2006).
16. N. Cabibbo, *Phys. Rev. Lett.* **93**, 121801 (2004).
17. N. Cabibbo and G. Isidori, *JHEP* **0503**, 21 (2005).
18. G. Colangelo, J. Gasser, B. Kubis and A. Rusetsky, *Phys. Lett.* **B638** 187 (2006).
19. J.R. Batley et al., [NA48/2 Collaboration], *Phys. Lett.* **B649**, 349 (2007).
20. M. Bissegger, A. Fuhrer, J. Gasser, B. Kubis and A. Rusetsky, *arXiv:087.0515*.

Measurement of the Proton-Longitudinal-Structure Function F_L at HERA

G.W. Buschhorn

Abstract The longitudinal structure function $F_L(x, Q^2)$ of the proton has been measured at the HERA collider in positron–proton deep inelastic scattering in the H1 and ZEUS experiment. Protons of 920 GeV, 575 GeV and 460 GeV have been collided with positrons of 27.5 GeV. In the H1 experiment (ZEUS experiment) the Q^2 range 12 GeV$^2 < Q^2 <$ 800 GeV^2(24 GeV$^2 < Q^2 <$ 110 GeV^2) corresponding to $0.00028 < x < 0.0353\,(6.10^{-4} < x < 0.005)$ was covered. The results are consistent with each other and with NLO QCD predictions. Parton distribution functions derived from a combined fit of the H1 and ZEUS measurements of $F_2(x, Q^2)$ are compared with recent global fits.

Keywords: structure function, HERA, proton, deep inelastic scattering, ZEUS, NLO QSD, parton distribution function, global fit

1 Deep inelastic electron–proton scattering and the proton structure

In the scattering of electrons/positrons on protons the structure of the proton can be investigated. While in elastic scattering integral properties of the proton like the distribution of the electric charge and magnetic moment are measured, at increasing momentum transfer to the proton the inelastic cross section where the proton is fragmented into secondary hadrons is dominating the scattering process. At high energies of the electron/positron the inelastic scattering ("deep inelastic scattering" DIS) is described by the parton model as the interaction of a photon with the constituents of the proton i.e. the quarks and gluons in terms of structure function. At not too high momentum transfers two structure functions completely describe the structure of the proton.

G.W. Buschhorn
Max-Planck-Institute for Physics (Werner-Heisenberg-Institute), Munich, Germany,
e-mail: gwb@mppmu.mpg.de

V. Begun et al. (eds.), *Progress in High-Energy Physics and Nuclear Safety*,

The structure functions are functions of the kinematic variables of the scattering process: the squared 4-momentum transfer $q^2 = (k-k')^2 = -Q^2$ from the scattered electron (4-momenta k, k') to the scattering parton, the fractional 4-momentum x of this parton with respect to the 4-momentum P of the proton with $x = Q^2/2q.P$ and the ineleasticity y of the scattering reaction with $y = Q^2/sx$ where s is the electron–proton squared centre-of-mass energy $s = (k+P)^2$.

The differential cross section for the inclusive inelastic scattering process $ep \rightarrow eX$ where X is the hadronic final state is given by

$$\frac{d^2\sigma}{dxdQ^2} = \frac{2\pi\alpha^2}{Q^4 x}\left[Y_+ F_2 - y^2 F_L\right] , \tag{1}$$

with the fine structure constant α, the longitudinal structure function $F_L = F_2 - 2xF_1$ and the electron helicity factor $Y_+ = 1-(1-y)^2$. (1) is often given in the form of the reduced cross section.

$$\sigma_r(x,Q^2,y) = F_2(x,Q^2) - \frac{y^2}{Y_+} F_L(x,Q^2) . \tag{2}$$

The DIS cross section can be expressed in terms of the total photoproduction cross section of transversely T or longitudinally L polarized virtual photons on protons: $F_2/x \sim \sigma_T + \sigma_L, F_L/x \sim \sigma_L$ with $R = \sigma_L/\sigma_T = F_L/F_2 - F_L$.

In the quark parton model QPM one has

$$F_2 = \sum_i e_i^2 x f_i(x,Q^2);\ F_L = F_2 - 2xF_1 = 0 , \tag{3}$$

whereas in Quantum Chromo Dynamics QCD gluon and quark/antiquark emission results in

$$F_L \sim \alpha_s\, xg(x,Q^2) . \tag{4}$$

(α_s = strong coupling constant) in next-to-leading order approximation.

F_2 has been extensively measured in the HERA experiments H1 and ZEUS. With increasing Q^2 it is strongly rising towards low x values where it is dominated by the gluon density. In contrast little is known about the detailed behaviour of F_L. In fixed target experiments (SLAC, EMC, BCDMS, NMC Ref. [2]) it was found that F_L is small at $x > 0.2$. At higher Q^2 the H1-experiment estimated F_L (Ref. [3]) using assumptions on the extrapolated behaviour of F_2 and concluded that F_L is expected to differ significantly from zero.

At HERA $F_L(x,Q^2)$ can be directly measured using the linear dependence of σ_r on y^2/Y_+ which requires a variation of s i.e. the proton energy.

The kinematics of the scattering process can be derived from the scattered electron/positron via

$$y = 1 - \frac{E'_e}{E_e}\sin^2\frac{\theta}{2} ; \qquad Q^2 = 4E_eE'_e\cos^2\frac{\theta}{2} ; \qquad x = Q^2/sy . \tag{5}$$

Since the sensitivity of σ_r to F_L is largest at high y this implies a detection of the scattered electron at low energies.

From the measurements of F_2 at HERA a prediction of F_L can be derived. The H1-data are fitted with parton densities xf_i which are parametrized as functions of x and evolved in Q^2 applying the Dokshitzer–Gribov–Lipatov–Altarelli–Parisi equations. The resulting prediction of F_L can be compared with the measured F_L.

The combination of the F_2 data from H1 and ZEUS results in an improved fit of the parton densities of the proton which can be compared with global fits of the parton densities.

2 The HERA collider and the H1- and ZEUS-detector

The HERA collider has been designed for colling 27.5 GeV electrons/positrons with 920 GeV protons allowing a maximum momentum transfer Q^2 of 10^5 GeV^2. The peak luminosity reached 5.10^{31} cm^{-2}s^{-1}. In a later stage the possibility for longitudinal polarization of the electrons/positrons was added. A total of about 1 fb^{-1} equally shared between the H1- and ZEUS experiment, electrons and positrons and positive and negative beam polarization was collected befor the early shutdown of the collider in July 2007. Dedicated runs at reduced proton energies serving the measurement of F_L (see below) were performed in 2007.

The components of the H1 detector essential for the F_L measurement are shown in Fig. 1. The interaction point in the centre of the detector is almost completely surrounded by sets of wire chambers and a liquid argon calorimeter which is split into an electromagnetic section followed by a hadronic section; the opening of the argon calorimeter in the positron beam direction (defined as the backward direction

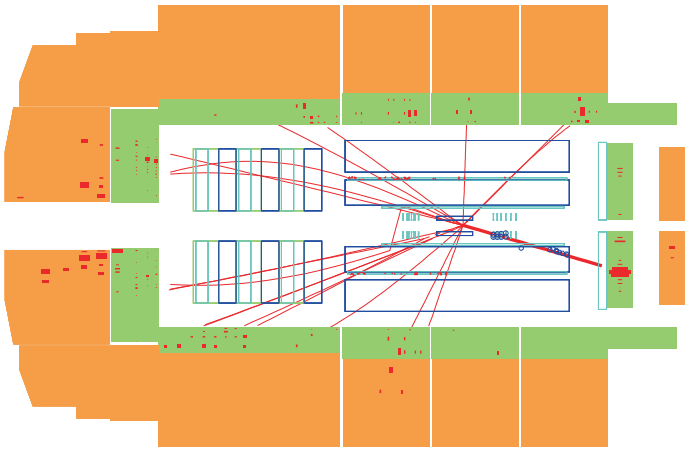

Fig. 1 H1 detector at HERA

of the protons) is covered by a scintillator calorimeter of the spaghetti type (SpaCal) also split into an electromagnetic and a hadronic section. The small angle forward and backward direction is covered by silicon counter telescopes.

Triggers for the F_L measurement are derived from the inner proportional chambers and the calorimeters; fast electronics provided on-line triggers for reconstructed tracks in the inner wire chambers (fast track tigger FTT) and energy-clusters (jet trigger JT) in the liquid argon calorimeter.

Monte Carlo simulations were performend for the three proton beam energies with the DJANGO program in which the hadronic final state was simulated with ARIADNE and the hadron fragmentation with JETSET; the detector response was simulated with a GEANT based code.

The ZEUS detector is similar to the H1 detector in its general layout with the main difference that a uranium/scintillator calorimeter is used. Inside is central tracking detector and surrounding the beam pipe a micro-vertex-detector of silicon-counters is placed.

3 F_L Measurements at HERA

First the measurement of F_L are presented which have been performed with the H1 detector in 2007 at proton beam energies of 920 GeV (corresponding to an integrated luminosity of $46.3 pb^{-}1), 575$ GeV$(7$ pb$^{-}1)$ and 460 GeV$(13 pb(-^{1})$ and the standard positron energy of 27.5 GeV.

For a medium Q^2 range of 12 GeV$^2 < Q^2 < 90$ GeV^2 the scattered positron was detected in the SpaCal ($\theta_e > 153^\circ$) with a minimum energy of the scattered electron of 3.4 GeV. The trigger efficiency for these high y events was determined as >98%. The main background for these events is due to photoproduction. By comparing the measured SpaCal energy with the measured momentum of the showering particle this background can be subtracted with a small correction applied for low-energy antiprotons from photoproduction which can result in a large SpaCal signal. An additional suppression of the photoproduction background results from requiring for DIS candidates longitudinal energy- momentum conservation $\Sigma_i(E_i - p_{zi}) > 35$ GeV with the sum running over all particles i in the final state including the scattered positron (for genuine non-radiative DIS events the corresponding value is $\sim 2E_e = 55$ GeV). The data for the medium Q^2 range have been published (Ref. [4]).

In the high Q^2 range of 35 GeV$^2 < Q^2 < 800$ GeV^2 the scattered positron was detected in the liquid argon calorimeter ($\theta_e < 153^\circ$) with a minimum energy of $E'_e > 3$ GeV. The combined trigger efficiency of the LAr calorimeter, the SpaCal, the LAr Jet trigger and the Fast Track Trigger reached 97% at $E'_e = 3$ GeV and $\sim$100% at >6 GeV.

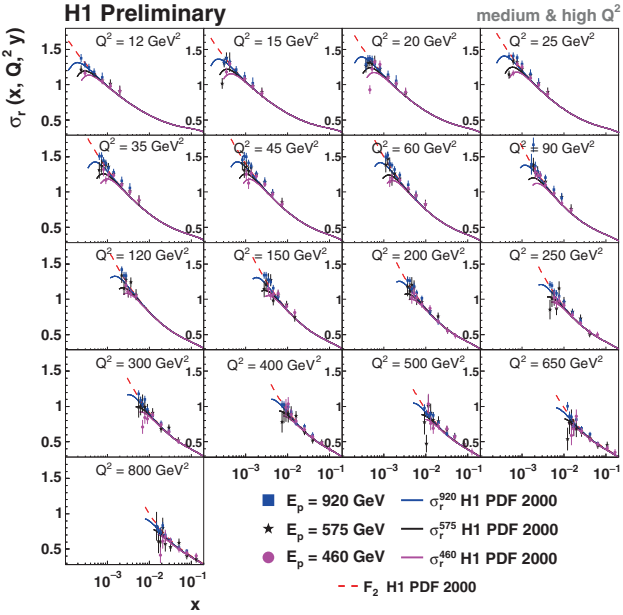

Fig. 2 Reduced cross section σ_r from H1 at medium and high Q^2 as function of x

The reduced cross section for the full range of medium and high Q^2 as a function of x is shown in Fig. 2. The data from different beam energies are normalized to each other at low y values where the cross sections are determined by $F_L(x,Q^2)$ with minor corrections only for residual F_L contributions. Straight line fits to σ_r at the same x and Q^2 but different proton beam energies resp. values of $y^2/(1+1-y)^2)$ are shown in Fig. 3 where measurements from the LAr calorimeter and the SpaCal are combined.

In Fig. 4 the resulting $F_L(x,Q^2)$ – measurements at different Q^2 are shown as function of x. In Fig. 5 these data averaged in x are shown as function of Q^2 in comparison with the prediction of F_L resulting from the QCD fit (H1 PDF 2000) to the F_2 measurements from H1 (Ref. [3]) and with global fits (CTEQ Ref. [5] and MSTW Ref. [6]). Within experimental uncertainties the H1 results are consistent also with a NNLO QCD fit by S. Alekhin (Ref. [7]).

The ZEUS collaboration has presented results of the runs at 575 GeV$(14\ \mathrm{pb}^{-}1$ and 920 GeV$(32.8\ \mathrm{pb}^{-}1)$ (Ref. [8]). The results of F_L for $\theta_e < 168^\circ$ and $E'_e > 6$ GeV corresponding to 24 GeV$^2 < Q^2 <$ 110 GeV$^2(6.10^{-4} < x < 0.005)$ are shown in Fig. 6 in comparison to a QCD fit based an ZEUS jet measurements in DIS.

Within the Q^2 range covered by the H1- and ZEUS-experiment the data are compatible with each other and also with QCD predictions.

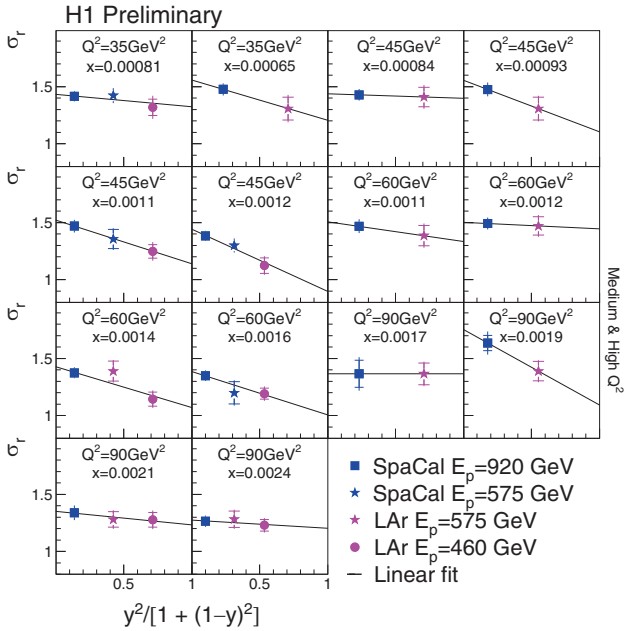

Fig. 3 Reduced cross section σ_r from H1 as function of $y^2/1+(1-y)^2$ at selected Q^2 values where both LAr- and SpaCal-data are available

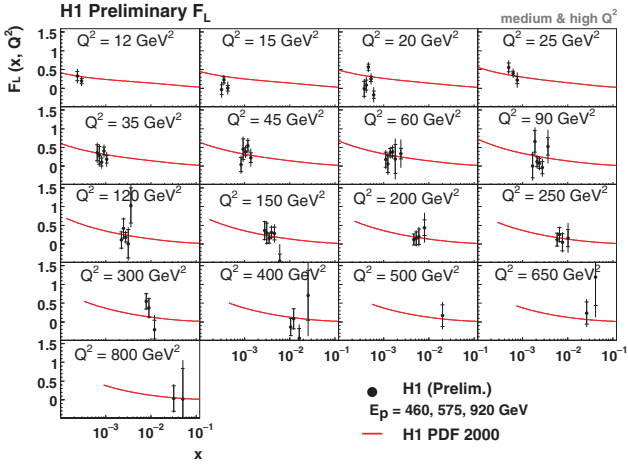

Fig. 4 From H1 at medium and high Q^2 as function of x

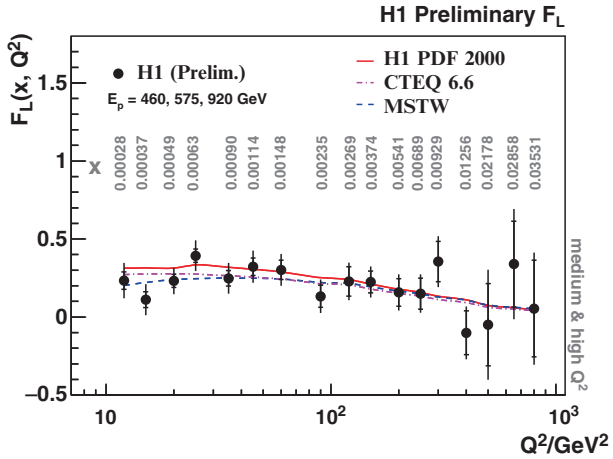

Fig. 5 F_L from H1 at medium and high Q^2 averaged in x as function of Q^2

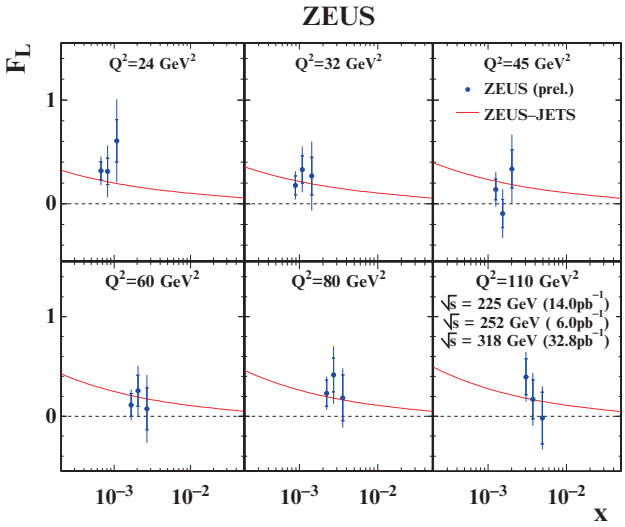

Fig. 6 Preliminary F_L from ZEUS as function x

4 Parton distribution functions

The combined H1 fit and ZEUS fit of the parton distribution functions xu_v, xd_v, xS and xg ("HERA-1 PDF" Ref. [9]) for $Q^2 = 10$ GeV^2 is shown in Fig. 7. The comparison with a global fit (CTEQ 6.5 M) is shown in Fig. 8. Such fits will be of importance to the evaluation of the coming LHC experiments.

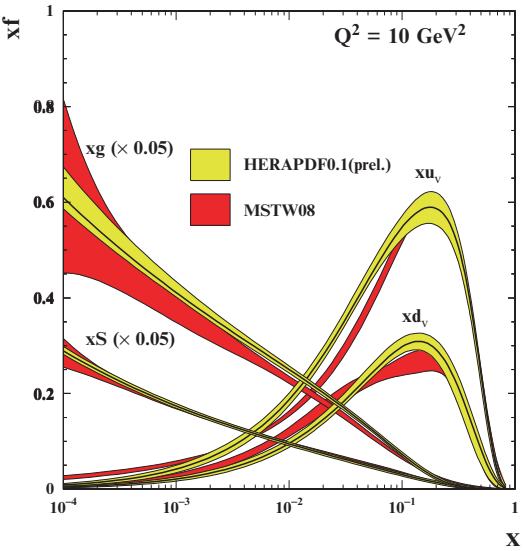

Fig. 7 Parton distribution function xf from combined fit to H1 and ZEUS ("HERAPDF 0.1")

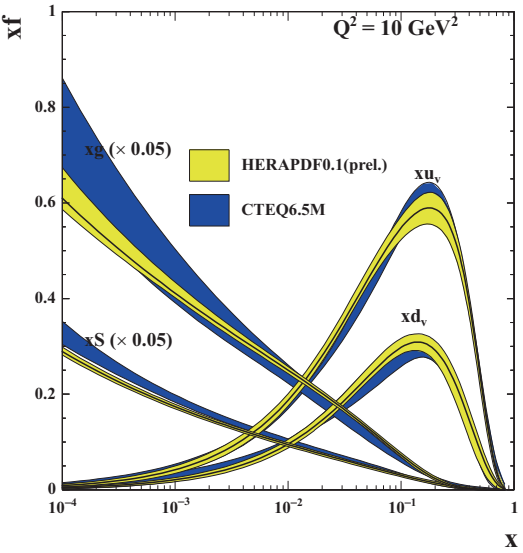

Fig. 8 Parton distribution functions xf from combined fit to H1 and ZEUS (HERAPDF = 0.1 in comparison to a global fit (CTEQ 6.5M) at $Q^2 = 10$ GeV^2 as function of x

References

1. P. Berge et al., Z. Phys. C **49** (1991) 187
2. C. Adloff et al., H1 Coll., Phys. Lett. B **393** (1997) 452; Eur. Phys. C **21** (2001) 33
3. C. Adloff et al., H1 Coll., Eur. Phys. J. C **30** (2003) 1
4. F.D. Aaron et al., H1 Coll., DESY 08-053
5. J. Pumplin et al., Phys. Rev. D (2007) 054029; P.M. Nadolsky et al., hep-ph/0802.0007
6. A.D. Martin et al., Phys. Lett B **652** (2007) 292
7. S. Alekhin, K. Melnikov, F. Petriello, Phys. Rev. D74/054033 (2006)
8. D. Kollar, ZEUS Coll., ZEUS-prel-08-001
9. H1 and ZEUS Coll., H1 prelim-08-045/ZEUS-prel-08003

Cuoricino Results and Perspectives for CUORE

M.A. Carrettoni on the behalf of the CUORE collaboration [1]

Abstract CUORE will be one of the next generation experiments designed for the search of a rare nuclear events such as Neutrinoless Double Beta Decay. It will be a closely packed array of TeO_2 crystals operating at the cryogenic temperature of 10 mK. While presenting the main reasons and ideas behind CUORE, the results of its smaller scaled prototype, Cuoricino, will be shown. Cuoricino consists of an array of 62 bolometric detectors operating in anti-coincidence to reduce background events: it took datas for 4 years, being the largest bolometric experiment who operated until now in the search for rare events.

Keywords: Neutrinoless Double Beta Decay, radioactivity, bolometers, cryogenics, neutrinos, Majorana

1 Introduction

Since their discovery neutrinos have always puzzled the scientific world. Given the precious informations from oscillation experiments, there are still many open questions concerning their nature. Massive neutrinos can in fact be described either by a Dirac field or by a Majorana field and we can't still point out their mass hierarchy.

A probe which is very sensitive to the neutrino nature is Neutrinoless Double Beta Decay.

Double Beta Decay (DBD) is a rare transition, in which an even nucleus (A, Z) decays in its isobar (A, Z+2) with the emission of two electrons and two antineutrinos. The search for its neutrinoless variant (DBD0ν) is a powerful and sensitive way to investigate the neutrino nature and mass. The next generation experiments have the possibility to reach down to a few meV scale. The signature for DBD0ν

M.A. Carrettoni
Università degli Studi di Milano-Bicocca, p.zza delle Scienze 3,
e-mail: marco.carrettoni@mib.infn.it

V. Begun et al. (eds.), *Progress in High-Energy Physics and Nuclear Safety*,

is a sharp peak in the energy spectrum at the Q-value of the transition due to the energy released by the two electrons emitted in the decay with no energy carried away by neutrinos. The measurement of the rate of the DBD0ν decay is related to the effective Majorana neutrino mass by $\Gamma_{0\nu} = G_{0\nu}(Q,Z)|M_{nucl}|^2\langle m_{ee}\rangle^2$, where $G_{0\nu}(Q,Z)$ is the phase space factor, $|M_{nucl}|$ are the nuclear matrix elements, and $\langle m_{ee}\rangle = \Sigma_k|U_{ek}|^2 m_k e^{i\alpha_k}$, where U_{ek} are the mixing matrix elements for the mass eigenstates m_k and $e^{i\alpha_k}$ are the CP Majorana phases. A search for DBD0ν in several nuclei is imperative [3] due to the theoretical uncertainties in $|M_{nucl}|$.

One of the promising nuclei is ^{130}Te. Its high natural isotopic abundance of 34% alleviates the requirement for isotopic enrichment, and its high Q-value of 2530.3 keV results in a large phase space for the decay and lies in a relatively background free region between the Compton edge and the full peak of the ^{208}Tl 2615 keV line. The large phase space contributes to a decay rate that is four or five times higher for ^{130}Te than for ^{76}Ge.

Two main approaches are used to search for DBD0ν: homogeneous and non-homogeneous. In the non-homogeneous approach, an external source of the chosen DBD candidate is placed in the form of thin foils inside the detector. In the homogeneous approach, the detector material is chosen to be a compound containing the DBD candidate, providing a high efficiency and in many cases, high resolution technique.

2 Cuoricino

Cuoricino has a total TeO_2 mass of 40.2 kg consisting of an array of 62 TeO_2 crystals, arranged in a tower of 13 planes. Eleven of the planes are made of four crystals of 5 cm cube, while two of the remaining planes have nine crystals of $3 \times 3 \times 6$ cm^3. Cuoricino uses a bolometric technique to search for DBD0ν of ^{130}Te, in which an energy deposition in the crystals induces temperature increase. A measurable temperature increase can be achieved in dielectric and diamagnetic materials such as TeO_2 when operated at very low temperatures. The operating temperature of Cuoricino is 10 mK. The temperature change of each crystal is detected using neutron transmutation doped Ge thermistors, thermally coupled to each crystal with glue spots.

The detector has a series of shields designed to reduce the background radioactivity. The inner-most lead shield is made of roman lead with ^{210}Pb content of less than 4 mBq/kg (90% confidence level), 1.5 cm around the side and 10 cm on the top and the bottom of the tower. The background from the cryostat contamination is reduced by the copper shields, and 20 cm of commercial lead shielding and 10 cm of borated PET shielding surround the cryostat to reduce environmental gammas and neutrons in the detector volume.

2.1 Results

Cuoricino took datas form April 2003 to June 2008 at the underground laboratory at LNGS (Gran Sasso National Laboratory). The data used for this analysis are from two separate runs, taken from April 2003 to September 2003 and from May 2004 to the end of the experiment. The total statistics consists of 15.83 kg year of ^{130}Te. The average FWHM resolution at the ^{208}Tl gamma line is 8 keV for the $5 \times 5 \times 5$ cm^3 crystals, and 11 keV for the $3 \times 3 \times 6$ cm^3 crystals.

The detected events are run through pulse-shape analysis for noise rejection, then through software filtering to optimize energy resolution (Optimum filter) and to reject pile-ups (Wiener filter). Coincident events were used to reduce and study the background. The detection efficiency for fully contained DBD0ν events is 86% as evaluated by Monte Carlo simulations. Rejecting coincident events reduces the background by roughly 20%. The total measured background in the DBD0ν region is 0.18 +/– 0.01 cnts/keV/kg/year.

In evaluating the limit for the ^{130}TeDBD0ν half-life ($T^{0\nu}_{1/2}$) the background spectra collected in the two runs are kept separate, due to the different measured FWHM and background. A maximum likelihood procedure is applied in the 2475–2550 keV energy interval to evaluate the maximum number of DBD0ν events possible with a flat continuum plus the 2505 keV ^{60}Co gamma line. The Q-value for the DBD0ν peak is set at 2530.30 keV and a peak shape obtained by summing up N gaussians is considered, in order to account for the different detectors energy resolutions. The obtained limit is of 3.1×10^{24}year at 90% C.L. (Fig. 1), corresponding to a limit for $\langle m_{ee} \rangle$ between 0.2 and 0.68 eV (with nuclear matrix elements from [4]). Limit variations on the order of 10% were observed when the expected peak was shifted by ± 3 keV around the Q-value and for different models for the background fitting function and for the peak shape of the ^{60}Co.

DBD0ν evidence for ^{76}Ge have been claimed [2] with a best value for $\langle m_{ee} \rangle$ of 0.44 eV, in the degenerate region of the neutrino mass spectrum.

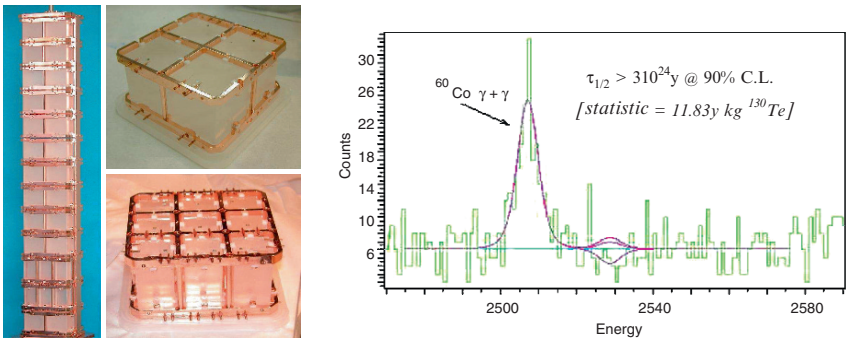

Fig. 1 Cuoricino set-up and DBD0ν limit evaluation

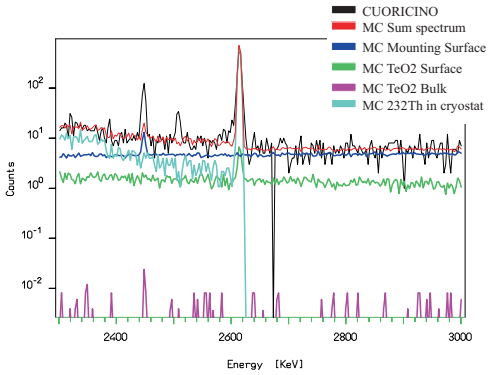

Fig. 2 CUORICINO DBD0ν background contributions

Given the present sensitivity, it is not possible for CUORICINO to confirm the claimed evidence however, in fact a null result will not rule it out due to the uncertainty in the nuclear matrix element calculations.

Next generation experiments, with $\sim$1 t of detector mass, and with a background in the DBD0ν region down to 0.01–0.001 c/keV/kg/year, are necessary to increase the sensitivity enough to reach the inverted hierarchy region of the neutrino mass spectrum.

2.2 Background analysis

An accurate knowledge of the radioactive sources, responsible of the background measured in CUORICINO in the DBD0ν region, is fundamental, in order to be able to reduce it to the wanted level in CUORE. The study of the coincidence and anticoincidence spectra, together with a comparison with Monte Carlo simulations of different radioactive contaminations in the bulk and surfaces of the various detector components, allowed us to identify the main sources of background in the DBD0ν region. They are β and α decays from ^{238}U ,^{232}Th and ^{210}Pb contaminations on the crystal surface (20% $\pm$ 5%), α decays from the same contaminats on the surface of the mounting structure (50% $\pm$ 10%) and ^{208}Tl multi-Compton events due to ^{232}Th contaminations of the cryostat shields, far away from the detectors (30% $\pm$ 5%) (Fig. 2).

3 CUORE

The next generation experiment CUORE will be made of 19 Cuoricino-like towers, 52 $5 \times 5 \times 5$ cm^3 crystals each, arranged in a tight cylindrical structure (Fig. 3), for a total TeO_2 mass of $\sim$741 kg. CUORE is expected to start at the beginning of 2011

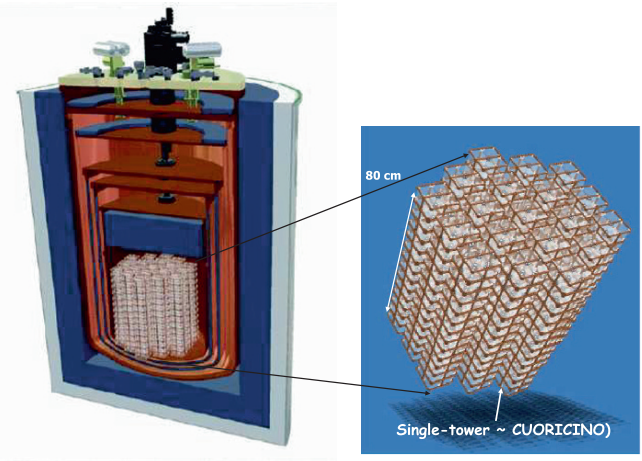

Fig. 3 CUORE set-up: Internal Pb and Cu shields and external Pb and borated PET shields are present

with a sensitivity goal for $\langle m_{ee} \rangle$ down to the inverted hierarchy region of the neutrino mass spectrum. CUORE is expected to probe the range between 29 and 150 $\times t^{1/4}$ meV for a background level in the DBD0ν region of 0.01 c/keV/kg/year and between 16 and 85 $\times t^{1/4}$ meV for a background level of 0.001 c/keV/kg/year. The high granularity of the detector will provide an effective reduction of the background by employing anticoincidence cuts. The detector shieldings have been designed in order to completely eliminate the contribution from environmental gamma radioactivity and from cryostat contaminations.

3.1 R&D for background reduction

The technical feasibility of CUORE has been proven by the good performances of Cuoricino. The true challenge, as in all the next generation DBD0ν experiments, will be the background achievement. The background knowledge acquired with Cuoricino was a helpful starting point for the background reduction R&D towards CUORE, aimed to reduce the background in the DBD0ν region to a level between 0.01 and 0.001 c/keV/kg/year.

The shielding is designed to reduce the contribution from ^{208}Tl multi-Compton events, due to ^{232}Th sources in the cryostat shields, to a negligible level. The dominant background appears to be the surface contamination both of the crystals and the copper parts facing them. A "Radioactivity study Array Detector" (RAD), was built at the end of summer 2004. The detector consists of two planes of $5 \times 5 \times 5$ cm^3 TeO_2 crystals, with a structure almost identical to that of Cuoricino.

The tests were performed in a second cryostat, housed in the Hall C of LNGS, provided with 5 cm thick internal copper shields and a 10 cm thick external lead shield. Due to the limited space in the cryostat, there is less shielding against the multi-Compton events from ^{208}Tl in the DBD0ν region than in Cuoricino. This results in higher background in the DBD0ν region in the RAD runs and direct comparison between RAD run and Cuoricino is only possible above 3 MeV where no gamma lines from the U or Th are present. We were able to isolate the alpha decays occurring in the crystals bulk (peaks at the transition energy) and surfaces (broader and asymmetric peaks at the transition energy and at the alpha energy), and on the surfaces facing the crystals, whose largest one is due to copper (flat continuum from alpha energy down to low energies).

A series of RAD runs were performed. In the first run, the crystals were etched with nitric acid, removing about 10 μm of the surfaces, then polished with SiO_2 powder. The copper mounting structure was also etched and successively treated through electroerosion, removing from 10 to 20 μm of the surfaces. All the operations were performed in a clean environment. In the second run, all copper parts facing the crystals were fully covered with polyethylene film. The result was quite successful from the point of view of crystal cleaning: the TeO_2 surface contamination in ^{238}U and ^{232}Th was drastically reduced (a factor $\sim$5), as proven by the reduction of the correspondent alpha peaks (Fig. 4). The extremely low background reached allowed us for the first time to disentangle the bulk vs. surface contamination of the crystals. Once the broader peaks due to surface contamination had disappeared, the Gaussian and sharp peaks due to crystals bulk contamination became visible.

From the observed peaks and assuming secular equilibrium, TeO_2 bulk impurities have been evaluated: ^{232}Th and ^{238}U are present at a level of $\sim\times 10^{-13}$ g/g, ^{210}Pb concentration is of $\sim 10^{-5}$ g/g. The background due to surface contamination of the copper was reduced by a factor 1.8 in the 3–4 MeV region by improved surface treatment and covering its surfaces with polyethylene film (Fig. 4).

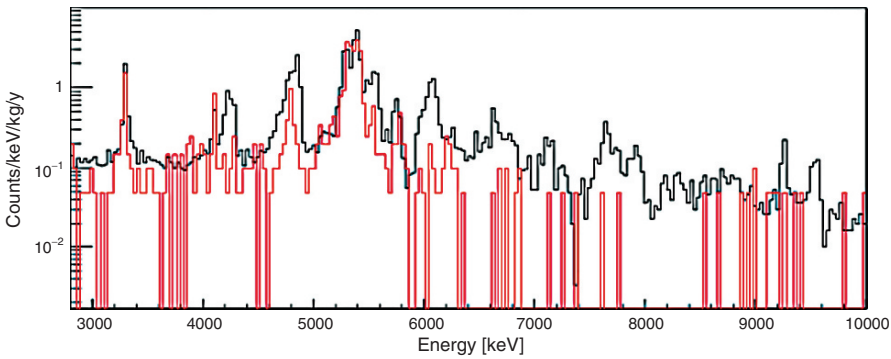

Fig. 4 Comparison between CUORICINO (black) and RAD (red) alpha background

With the surface treatment techniques, material reduction and shielding developed in the R&D program towards CUORE, the dominant sources of background are expected to be crystal surfaces (7×10^{-3} c/keV/kg/year) and copper surfaces (2.5×10^{-2} c/keV/kg/year). A small contribution is expected from crystal bulk impurities (10^{-4} c/keV/kg/year).

Additional R&D is underway to further reduce the background. One novel approach is the use "surface sensitive bolometers" (SSB) [5] where the main bolometer crystal is completely surrounded by and thermally coupled to six thin bolometers. Surface events either from the crystal or the surrounding, would deposit energy on both the main crystal and a surrounding bolometer, and these events can be excluded via anticoincidence analysis. Unfortunately several wires were lost during our test run however, we were able to reduce the background by a factor of 2 between 3 and 4 MeV with respect to the first RAD. This technique has the possibility to serve as a valuable R&D tool that allows us to unambiguously identify the origins of the background observed in Cuoricino.

4 Conclusions

CUORICINO set a limit on the half-life of ^{130}Teof 3.1×10^{24}year at 90% C.L. and $\langle m_{ee} \rangle$ between 0.2 and 0.68 eV. It demonstrated the technical feasibility of CUORE, the next generation experiment on the 1-t scale, and has given us important insight into the sources of background. An R&D program is underway to achieve a background of below 0.01 counts/keV/kg/year.

Acknowledgements This work has been partially supported by the EU FP6 programme, C.N. RII3-CT-2004-506222

References

1. The complete list of authors can be found at http://crio.mib.infn.it/wig/Cuorepage/CUORE.php
2. Klapdor Kleingrothaus HV. et al., *Phys. Lett.* B**586** (2004) 198–212
3. S.M. Bilenky and S.T. Petcov (hep-ph/0405237)
4. C. Arnaboldi et al., *Phys. Rev. Lett.* **95** (2005) 142501
5. M. Pedretti et al. (the CUORE Collaboration) AIP conference proceedings vol. 897, p. 59–64, "Topical workshop on low radioativity techniques" LRT (2006) Aussois, France

OPERA Experiment – Status Report

A. Chukanov, for the OPERA Collaboration

Abstract OPERA (Oscillation Project with Emulsion tRacking Apparatus) is an international collaboration between Europe and Asia, aiming to give the first direct proof of tau neutrino appearance in a pure muon neutrino beam, in order to validate the hypothesis for atmospheric neutrino oscillations. The first European long baseline neutrino beam called CNGS is produced at CERN and sent in the direction of the Gran Sasso underground laboratory 732 km away, where the OPERA detector is located. Since 2006 the electronic detector part is fully commissioned and running. Neutrino beam events have been recorded and partly analysed in the target elements made of very precise emulsion films and lead sheets during the 2007–2008 run. This paper reviews the status of the detector, the beam performances, the first results from the neutrino event analysis and the prospects.

Keywords: Neutrino oscillation

1 Introduction

OPERA [1] is a long baseline neutrino experiment located in the Gran Sasso underground laboratory (LNGS) in Italy. The experiment is a massive hybrid detector with nuclear emulsions used as very precise tracking devices and electronic detectors to locate the neutrino interaction events in the emulsions. It is designed to primarily search for ν_τ appearance in the CERN high energy ν_μ beam CNGS [2] at 732 km from the neutrino source, in order to establish unambiguously the origin of the neutrino oscillations observed at the "atmospheric" Δm^2 scale. The preferred hypothesis to describe this phenomenon is $\nu_\mu \rightarrow \nu_\tau$ oscillation. Combining all the present known neutrino data the best fit values of a global three flavour analysis of neutrino oscillations [3] give for $\nu_\mu \rightarrow \nu_\tau$ oscillation parameters

A. Chukanov
Joint Institute for Nuclear Research, Dubna, Russia,
e-mail: chukanov@nusun.jinr.ru

V. Begun et al. (eds.), *Progress in High-Energy Physics and Nuclear Safety*,

$\Delta m^2 = 2.39 \times 10^{-3}\text{eV}^2$ and $\sin^2 2\theta = 0.995$. The range of allowed values at 3σ is $2.06 \times 10^{-3} < \Delta m^2 < 2.81 \times 10^{-3}\text{eV}^2$. In addition to the dominant $\nu_\mu \rightarrow \nu_\tau$ oscillation in ν_μ beam, it is possible that a sub-leading $\nu_\mu \rightarrow \nu_e$ transition occurs as well. This process will also be investigated by OPERA profiting from its excellent electron identification capabilities to asses a possible improvement on the knowledge of the third yet unknown mixing angle θ_{13}.

The ν_τ direct appearance search is based on the observation of events produced by charged current interaction (CC) with the τ decaying in leptonic and hadronic modes. In order to directly measure the τ production and decay kinematics, the principle of the OPERA experiment is to observe the τ trajectories and the decay products in emulsion films composed of two thin emulsion layers (44 μm thick) put on either side of a plastic base (205 μm thick). The detector concept which is described in the next section combines micrometer and milliradian tracking resolution, large target mass together with good lepton identification. This concept allows to reject efficiently the main topological background coming from charm production in ν_μ charged current interactions.

2 Detector overview

The OPERA detector is installed in the Hall C of the Gran Sasso underground laboratory. Figure 1 shows a recent picture of the detector which is 20 m long with a cross section of about 8×9 m^2 and composed of two identical parts called super modules (SM). Each SM has a target section and a muon spectrometer.

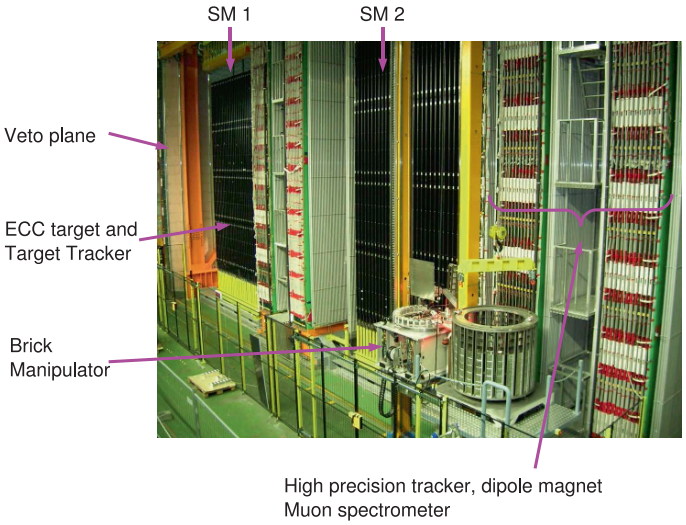

Fig. 1 View of the OPERA detector in Hall C of the Gran Sasso Underground Laboratory

The spectrometer allows a determination of the charge and momentum of muons going through by measuring their curvature in a dipolar magnet made of 990 t of iron, and providing 1.53 T transverse to the neutrino beam axis. Each spectrometer is equipped with six vertical planes of drift tubes as precision tracker together with 22 planes (8×8 m^2) of RPC bakelite chambers reaching a spatial resolution of $\sim$1 cm and an efficiency of 96%. The precision tracker planes are composed of four staggered layers of 168 aluminium tubes, 8 m long with 38 mm outer diameter. The spatial resolution of this detector is better than 500 µm. The physics performance of the complete spectrometer should reduce the charge confusion to less than 0.3% and gives a momentum resolution better than 20% for momentum less than 50 GeV. The muon identification efficiency reaches 95% adding the target tracker information for the cases where the muons stop inside the target.

The target section is composed of 31 vertical light supporting steel structures, called walls, interleaved with double layered planes of 6.6 m long scintillator strips in the two transverse directions. The main goals of this electronic detector are to provide a trigger for the neutrino interactions, an efficient event pattern recognition together with the magnetic spectrometer allowing a clear classification of the ν interactions and a precise localisation of the event. The electronic target tracker spatial resolution reaches $\sim$0.8 cm and has an efficiency of 99%.

The walls contain the basic target detector units, called Emulsion Cloud Chamber or ECC brick, sketched in Fig. 2 which are obtained by stacking 56 lead plates with 57 emulsion films. This structure provides many advantages like a massive target coupled to a very precise tracker, as well as a standalone detector to measure electromagnetic showers and charged particle momentum using the multiple coulomb scattering in the lead. The ECC concept has been already succesfully used for the direct ν_τ observation, perfomed in 2000 by the DONUT experiment [4], also electron identification and low energy muon/pion separation.

Behind each brick, an emulsion film doublet, called Changeable Sheet (CS) is attached in a separate enveloppe. The CS can be detached from the brick for analysis to confirm and locate the tracks produced in neutrino interactions and reconstructed by the electronic detectors.

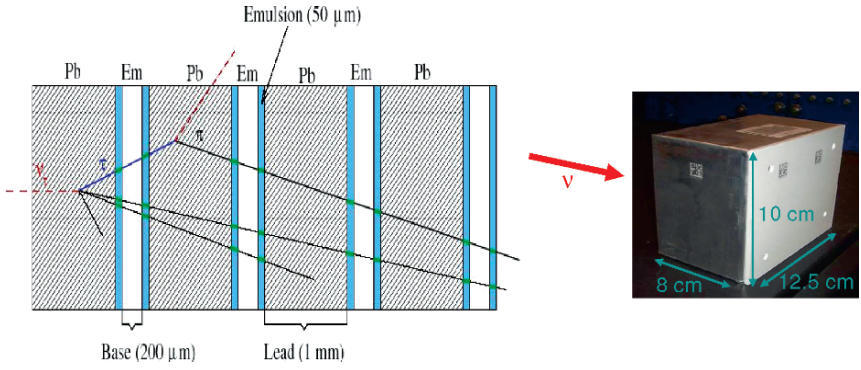

Fig. 2 Schematic structure of an ECC cell (*left*). Picture of an assembled brick (*right*). Each brick weighs about 8.6 kg and has a thickness of 10 radiation length X_0

The number of bricks in the OPERA detector is around 150,000 (1.35 kt of target). Bricks were inserted with the help of two automated manipulator systems (BMS) running on each side of the experiment.

When a candidate brick has been located by the electronic detectors, the brick is removed using the BMS and the changeable sheet is detached and developped. The film is then scanned to search for the tracks originating from the neutrino interaction. If none are found then the brick is left untouched and another one is removed. When a neutrino event is confirmed the brick is exposed to cosmics to collect enough alignment tracks before going to the development. After development the emulsions are sent to the scanning laboratories hosting automated optical microscopes in Europe and Japan [5, 6]. This step is the start of the detailed analysis consisting of finding the neutrino vertex and looking for a decay kink topology in the vertex region.

3 The CNGS beam

The CNGS neutrino beam [2] is a high energy ν_μ beam optimised to maximise the ν_τ charged current interactions at Gran Sasso produced by oscillation mechanism at the atmospheric Δm^2 . The mean neutrino energy is about 17 GeV with a contamination of 4% $\bar{\nu}_\mu$, 0.9% ν_e and less than 0.06% of $\bar{\nu}_e$. Using the CERN SPS accelerator in a shared mode with fixed target experiments together with LHC, 4.5×10^{19} protons on target (pot) per year should nominally be delivered, assuming 200 days of operation. The number of charged current and neutral current interactions expected in the Gran Sasso laboratory from ν_μ are then about 19,500 and 5,900 for 5 years respectively. If the $\nu_\mu \rightarrow \nu_\tau$ oscillation hypothesis is confirmed, the expected number of τ's produced via charged current interaction at the Gran Sasso is 150 for $\Delta m^2 = 2.5 \times 10^{-3}\text{eV}^2$ at full mixing. The number of ν_τ approximately scales like $(\Delta m^2)^2$.

For the conference time (21 September, 2008), 4,512 events correlated in time with the beam and coming from neutrino interactions in the surrounding rock and inside the detector have been recorded. The number of candidates interaction in the bricks are equal to 728 which is consistent with the expected value 768 ± 28. The delivered intensity correponded to 8.16×10^{18} pot. The reconstructed zenith angle distribution from penetrating muon tracks was showing a clear peak centered around 3.4^{o} as expected for neutrinos originating from CERN. Details and results can be found in [7].

For each registered neutrino event the electronic detector hits were used to find the most probable brick where the neutrino interaction may have occured. The Fig. 3 shows an event display of the neutrino interaction located in the OPERA detector. The event is a charged current event with a clear muon track traversing both target and spectrometer sections. The Fig. 4 shows the result of the detailed analysis of the emulsions after scanning the identified brick where a clear reconstructed interaction vertex is visible.

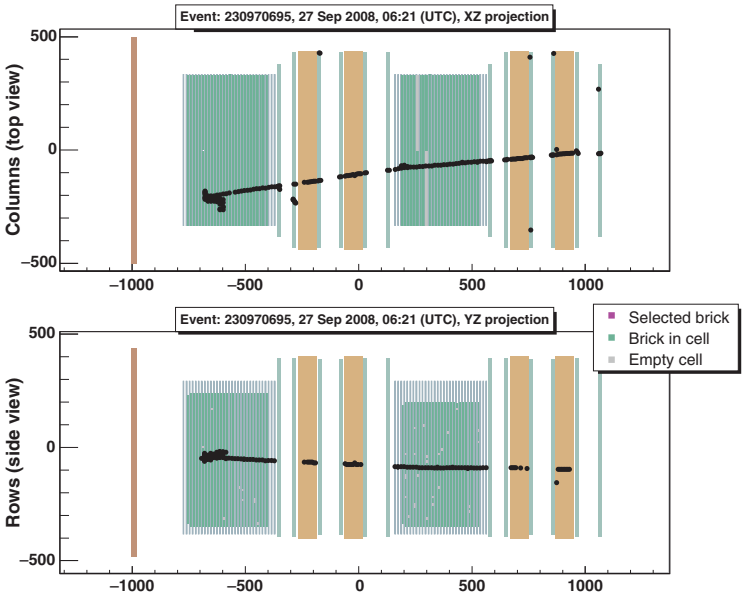

Fig. 3 Charged current neutrino interaction recorded in OPERA. The event display shows the hits left in the electronic detectors

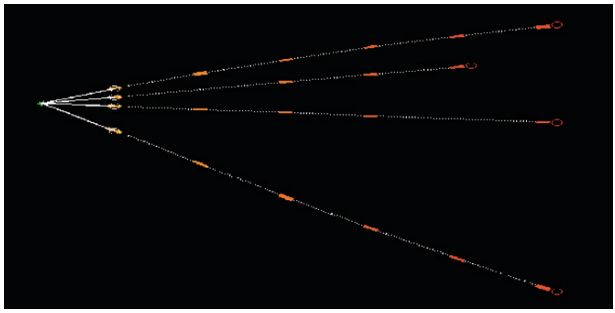

Fig. 4 Emulsion reconstruction of the neutrino interaction vertex in the target brick

The extensive study of the recorded events have confirmed the OPERA performances and the validity of the methods and algorithms used which, for example, give impact parameter resolution of the order of a few microns, particle momentum estimation, shower detection for e/π separation. Figure 5 shows the longitudinal and transverse views of another reconstructed event vertex where a clear neutral particle decay topology is visible. From the angular and distance analysis the most favorable hypotesys is the neutral charm production and decay.

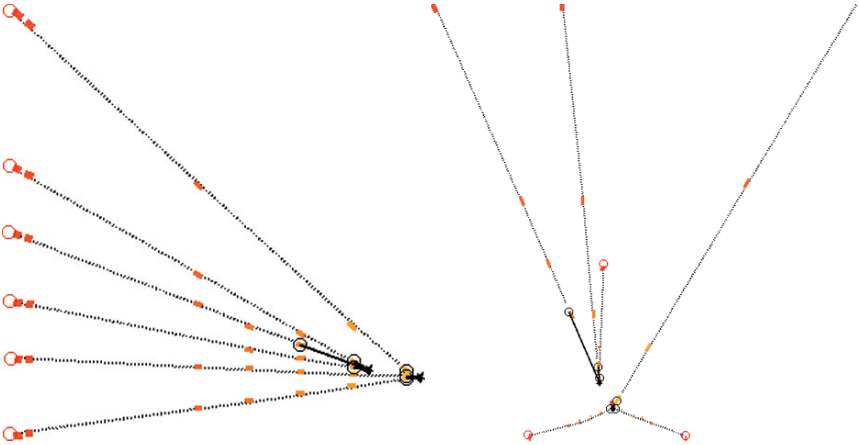

Fig. 5 Longitudinal and transverse view of reconstracted neutrino interaction vertex with a charm candidate decay topology

4 Conclusion

The OPERA detector is completed and is now massive with 1.35 kt of lead-emulsion target offering a huge and precise tracking device. With the cosmic data taking and the CNGS neutrino runs in 2006–2008, the design goals and detector perfomances were reached, the reconstruction software and the first level of analysis tools were validated.

During 89 days of 2008 run with CNGS beam intensity 8.16×10^{18} pot with the average intensity of 1.8×10^{13} pot/extraction it was collected 728 on time candidates of the neutrino interactions in the bricks.[1]

In 5 years of CNGS running at 4.5×10^{19} pot per year, OPERA should be able to observe 10–15 ν_τ events after oscillation at full mixing in the range $2.5 \times 10^{-3} < \Delta m^2 < 3 \times 10^{-3}\text{eV}^2$, with a total background less than 0.76 events.

References

1. OPERA Collaboration, M. Guler *et al.*, Experiment proposal, CERN-SPSC-2000-028 and LNGS P25/2000 (2000); Status Report on the OPERA experiment, CERN-SPSC-2001-025 and LNGS-EXP 30/2001 (2001).
2. CNGS references on line: *http* : *//proj* − *cngs.web.cern.ch/proj* − *cngs/Publications/ Publicationsproject.htm.*

[1] At the moment of writing these minutes, the 2008 run is completed. During 120 days of 2008 run with total CNGS beam intensity 1.57×10^{19} pot it was collected ∼1,500 on time candidates of the neutrino interactions in the bricks.

3. G.L. Fogli et al., Phys. Rev. **D 78**, 033010 (2008), arXiv:0805.2517v3 [hep-ph].
4. K. Kodama et al., The DONUT collaboration, Phys. Lett. **B 504** (2001) 218-224.
5. S. Aoki et al., Nucl. Instrum. Meth. **B 51** (1990) 466; T. Nakano, Proceedings of International Europhysics Conference HEP2001 *http* : *//pos.sissa.it/arhive/conferences/* 007/269/*hep*2001.269.*pdf*.
6. N. Armenise et al., Nucl. Instrum. Meth. **A 551** (2005) 261.
7. R. Acquafredda et al., [OPERA Collaboration], New Journal of Physics **8** (2006) 303.

Precise Measurement of the $\pi^+ \to e^+\nu$ Branching Ratio

E. Frlež, L.P. Alonzi, V.A. Baranov, W. Bertl, M. Bychkov, Yu. M. Bystritsky, N.V. Khomutov, A.S. Korenchenko, S.M. Korenchenko, M. Korolija, T. Kozlowski, N.P. Kravchuk, N.A. Kuchinsky, D. Mekterović, D. Mzhavia, A. Palladino, D. Počanić, P. Robmann, A.M. Rozhdestvensky, V.V. Sidorkin, U. Straumann, I. Supek, P. Truöl, A. van der Schaaf, E.P. Velicheva, and V.V. Volnykh

Abstract The PEN Collaboration is conducting a new measurement of the $\pi^+ \to e^+\nu$ branching ratio at the Paul Scherrer Institute, with the goal uncertainty of $\delta B/B_{\pi e2} = 5 \times 10^{-4}$ or lower. At present, the combined accuracy of all published π_{e2} decay measurements lags behind the theoretical calculation by a factor of 40. In this contribution we report on the PEN detector configuration and its performance during two development runs done in 2007 and 2008.

Keywords: Leptonic decays of charged pions and muons, meson properties, charged particle tracking detectors, pure CsI calorimeters

---

E. Frlež
ph.: 434-924-6786,
e-mail: frlez@virginia.edu

E. Frlež, L.P. Alonzi, M. Bychkov, A. Palladino, D. Počanić
Department of Physics, University of Virginia, Charlottesville, VA 22904-4714, USA

V.A. Baranov, Yu. M. Bystritsky, N.V. Khomutov, A.S. Korenchenko, S.M. Korenchenko, N.P. Kravchuk, N.A. Kuchinsky, D. Mzhavia, A.M. Rozhdestvensky, V.V. Sidorkin, E.P. Velicheva, V.V. Volnykh
Joint Institute for Nuclear Research, RU-141980 Dubna, Russia

W. Bertl
Paul Scherrer Institut, CH-5232 Villigen PSI, Switzerland

M. Korolija, D. Mekterović, I. Supek
Rudjer Bošković Institute, HR-10000 Zagreb, Croatia

T. Kozlowski
Institute for Nuclear Studies, PL-05-400 Swierk, Poland

D. Mzhavia
IHEP, Tbilisi, State University, GUS-380086 Tbilisi, Georgia

P. Robmann, U. Straumann, P. Truöl, A. van der Schaaf
Physik Institut der Universität Zürich, CH-8057 Zürich, Switzerland

V. Begun et al. (eds.), *Progress in High-Energy Physics and Nuclear Safety*,

1 Introduction

The PEN Collaboration is performing a new measurement of the $\pi^+ \to e^+\nu(\gamma)$ branching ratio ($B_{\pi e2}$) with a relative uncertainty of $\sim 5\times 10^{-4}$ or lower, at the Paul Scherrer Institute (PSI) [1].

The amplitude for this rare pion decay is a textbook example of the $V-A$ nature of the electroweak interaction with the branching ratio understood at the level of less than one part in 10^4.

Recent independent theoretical calculations of the ratio of the decay rates $\Gamma(\pi \to e\bar{\nu}(\gamma))/\Gamma(\pi \to \mu\bar{\nu}(\gamma))$ are in a very good agreement and give,

$$B^{\mathrm{SM}}_{e/\mu} = \frac{\Gamma(\pi \to e\bar{\nu}(\gamma))}{\Gamma(\pi \to \mu\bar{\nu}(\gamma))}\Big|_{\mathrm{the}} = \begin{cases} (1.2352 \pm 0.0005)\times 10^{-4}, & \text{Ref. [2]},\\ (1.2354 \pm 0.0002)\times 10^{-4}, & \text{Ref. [3]},\\ (1.2352 \pm 0.0001)\times 10^{-4}, & \text{Ref. [4]}. \end{cases} \quad (1)$$

Work of Marciano and Sirlin's [2] and Finkemeier [3] took into account radiative corrections, higher order electroweak leading logarithms, short-distance QCD corrections and structure-dependent effects, while Cirigliano and Rosell [4] arrived at the value using the two-loop Chiral Perturbation Theory.

The two most recent competitive experiments completed 15 years ago at the TRIUMF cyclotron [5] and the PSI ring accelerator [6] are also mutually consistent, but are exceeded in accuracy by a factor of 40 by the latest theoretical calculations (Eq. 1):

$$B^{\mathrm{exp}}_{e/\mu} = \begin{cases} (1.2265 \pm 0.0034(\mathrm{stat}) \pm 0.0044(\mathrm{sys}))\times 10^{-4}, & \text{Ref. [5]},\\ (1.2350 \pm 0.0035(\mathrm{stat}) \pm 0.0036(\mathrm{sys}))\times 10^{-4}, & \text{Ref. [6]}. \end{cases} \quad (2)$$

These two π_{e2} measurements, though inadequate in precision when compared with the theoretical accuracy, represent the best experimental test of μ-e universality at present. The improved measurement would, in addition, be a very sensitive probe of all Standard Model extensions that induce pseudoscalar currents [7] and serve as a test of possible supersymmetric corrections to the lepton couplings [8].

2 Experimental apparatus

The PIBETA detector, used from 1999 to 2004 in a series of rare pion and muon decay measurements [9–12], was upgraded to meet the needs of the new experiment. The PEN apparatus is a large solid angle non-magnetic detector optimized for detection of photons and electrons emanating from the pion and muon decays in the centrally located stopping target. The main detector elements of the apparatus, shown in two panels of Fig. 1, are:

1. A thin upstream beam counter, and an active degrader all made of plastic scintillator material, used for the beam definition

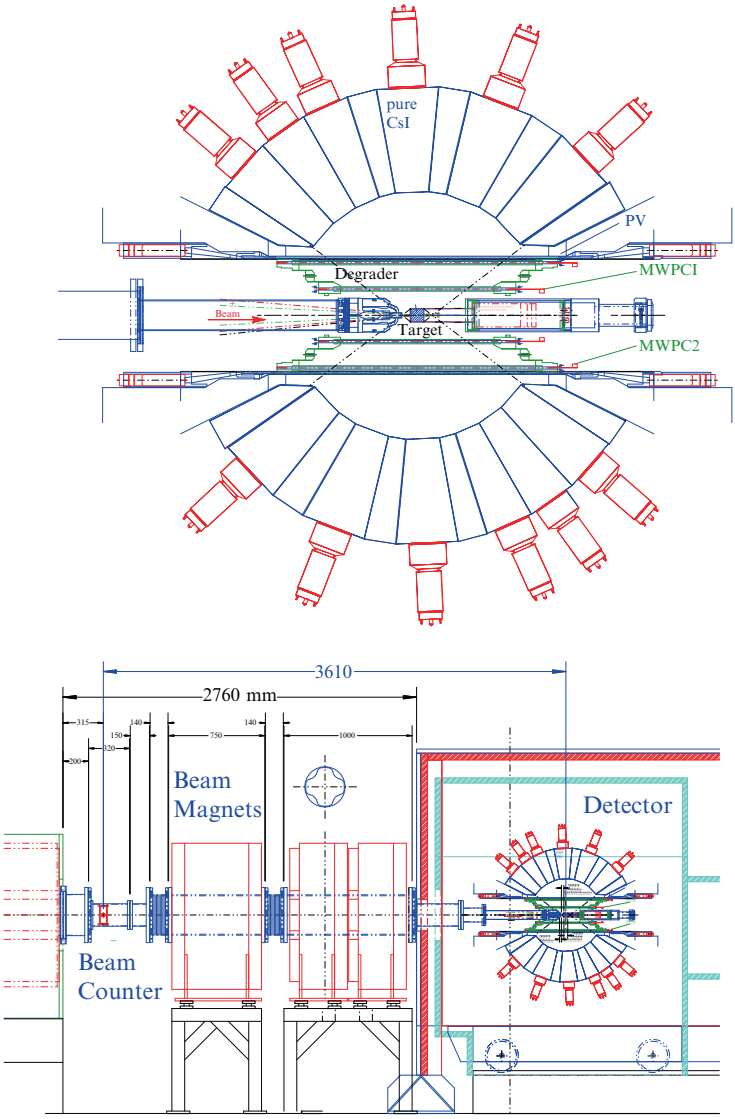

Fig. 1 Cross sections through the PEN set up in the 2008 configuration. Top panel shows the central tracking region, including the 4-wedge tracking degrader, active target, segmented plastic scintillator, a pair of cylindrical MWPC's, and modular CsI calorimeter. Bottom panel depicts the detector in the experimental area with the upstream beam-tagging counter inside the vacuum pipe and the triplet of focusing quadrupole magnets

2. An active plastic scintillator target, used to stop and detect the beam particles, and record their charged decay products
3. Two concentric low-mass cylindrical multi-wire proportional chambers for charged particle tracking, surrounding the active target

4. A 20-piece fast plastic scintillator hodoscope, surrounding the MWPC's, used for particle identification and fast timing
5. A high-resolution segmented fast shower CsI calorimeter, surrounding the target region and tracking detectors in a near-spherical geometry

The electromagnetic calorimeter is made of 240 pure CsI scintillator modules covering a $\sim 3\pi$ sr solid angle, with openings allowing for beam entry and detector readout. The inner radius of the hollowed CsI sphere is 26 cm and its thickness of 22 cm corresponds to 12 radiation lengths.

The key element of the fast electronic logic is the one-arm calorimeter trigger defined by discriminated analog signal sum of any one or more of 60 groups of 9 CsI calorimeter modules. The high discrimination threshold (HT) is adjustable and was set at around 44 MeV in the PEN experiment. In parallel, we have also used the pre-scaled (1:16 or 1:64) low level threshold (LT) trigger set by a discriminated sum of the plastic scintillator hodoscope signals. The calorimeter energy spectrum for LT trigger extends well below 0.5 MeV, being limited only by the ADC pedestal widths of the individual CsI detectors.

The PEN experiment completed two development runs in 2007 and 2008. The total number of recorded π^+ stops was 8.1×10^{10}, while the total number of collected triggers was 4.7×10^6 for HT and 180,000 for LT events.

3 Experimental method

The π_{e2} events are collected primarily by means of the one-arm high-threshold calorimeter trigger. The threshold value was chosen so as to minimize the fraction of events in the π^+ energy spectrum "tail" caused by the electromagnetic shower leakage in the CsI calorimeter, while keeping the data acquisition live time fraction at $\sim 0.8 - 0.9$.

The $\pi \to e\nu$ branching ratio can be evaluated as

$$B_{\pi e2} = \frac{N_{\mathrm{HT}}(1+\varepsilon)}{A_{\pi e2} N_{\pi^+} f_{\pi e2}(T)}, \tag{3}$$

where N_{HT} is the number of recorded π_{e2} events above the E_{HT} energy, $\varepsilon = N_t/N_{\mathrm{HT}}$ is the ratio of the "tail" to "HT" π_{e2} events, $A_{\pi e2}$ is the detector acceptance, N_{π^+} is the number of stopped beam pions recorded during the experiment, while $f_{\pi e2}(T)$ is the pion decay probability between the pion stop time, $t = 0$, and the end of the trigger gate, $t = T \simeq 220$ ns. The most precise stopped pion count is obtained by recording the sequential (Michel) $\pi \to \mu \to e$ chain decay:

$$B_{\pi\mu e} = \frac{N_{\pi\mu e}}{A_{\pi\mu e} N_{\pi^+} f_{\pi\mu e}(T)}, \tag{4}$$

where $B_{\pi\mu e} \simeq 1$ is the branching ratio for the $\mu \to e\nu\bar{\nu}(\gamma)$ decay, $A_{\pi\mu e}$ and $N_{\pi\mu e}$ are the detector acceptance and the number of muon decays, and $f_{\pi\mu e}$ is the trigger gate decay probability.

Combining the two expressions to eliminate N_{π^+} gives:

$$B_{\pi e2} = \frac{N_{\rm HT}(1+\varepsilon)}{N_{\pi\mu e}} \cdot \frac{A_{\pi\mu e}}{A_{\pi e2}} \cdot \frac{f_{\pi\mu e}(T)}{f_{\pi e2}(T)} B_{\pi\mu e}, \tag{5}$$

which conveniently factorizes into quantities that share many of the same systematic uncertainties.

A detailed analysis of the optimum choice of trigger parameters (T, $E_{\rm HT}$, LT/HT prescaling, DAQ rates, etc.), presented in Ref.[1], has demonstrated that the PEN detector system is capable of reaching statistical uncertainty levels in π_{e2} decay that are an order of magnitude better than those obtained in previous experiments in about six months of beam time.

The systematic uncertainties relevant to the PEN measurements are:

1. Discrimination of pion and muon events: Due to low μ decay pile-up and the digitized target waveforms misidentified events will be kept at the level below 10^{-4}.
2. The pion and muon decay normalization: The well determined Michel parameter ρ controlling the shape of the μ^+ decay positron energy spectrum, in conjunction with the low energy threshold below 1 MeV, and the absolute calorimeter energy calibration attained in previous measurements, are projected to yield $\Delta N_{\pi\mu e}/N_{\pi\mu e} = 1 \times 10^{-4}$.
3. The ratio of acceptances for π_{e2} and Michel decay events: Shared systematics of the signal and normalization decay limits the uncertainties to $\sim 1 \times 10^{-4}$.
4. A correction for radiative muon decays: In-situ measurement of the radiative decays leads to sub-10^{-4} accuracy.
5. Nuclear interactions correction: Suppressed in the HT data sample via analysis cuts, will be simulated for the LT "tail" in the full detector Monte Carlo calculation to 10 % accuracy. It will also be measured with our LT trigger.
6. The zero time definition: 5 ps accuracy in the mean value for $t = 0$ is achievable with digitized waveforms.

Thus, an overall systematic uncertainty in the range of $2 - 4 \times 10^{-4}$ is an attainable goal in the PEN experiment.

4 Preliminary results

Tightly focused π^+ beam tunes were developed for a dozen beam momenta between 67 and 85 MeV/c, with the pion stopping rates ranging from 1,000 to 20,000 π^+/s. The beam particles are first detected in a thin upstream beam counter made of plastic

scintillator, 3.61 m upstream of the detector center. The beam pions are subsequently slowed down in the active degrader and stopped in the active target.

We have used several cylindrical-shaped degraders of different thicknesses, the final one being a 4-wedge scintillator capable of lateral beam particle tracking. It consisted of two pairs of plastic scintillators with the thicknesses tapering from 5 to 1.5 mm along the horizontal and vertical directions. The lateral beam particle coordinates were determined by the ratios of energy depositions in the pairs of wedges. The points of closest approach (PCA) of the reconstructed beam particle paths and the back-tracked decay positron hits recorded by the MWPC's define the π^+ or μ^+ decay vertex inside the target. Comparison of a Monte Carlo simulation of the PCA distributions with the experimental histograms reveals that the vertex resolution root-mean-square is better than 2 mm.

The reconstructed π^+/μ^+ vertex allows, in turn, the calculation of the e^+ path length in the target and the prediction of the positron contribution to the measured target signal.

The PMT signals for the upstream beam detector, active degrader and active target were digitized in conventional FASTBUS and CAMAC ADC and TDC units as well as by a waveform digitizer, the Acqiris DC282 four-channel unit operated at 2 GS/s sampling rate (2 channels/ns), and yielding an effective 7-bit resolution.

Examples of the recorded beam counter waveforms are given in the six panels of Fig. 2. The data quality is illustrated in the π^+ time-of-flight (TOF) spectrum (Fig. 3), representing the time differences between the target and the degrader hits.

By applying a cut on the monoenergetic 4.1 MeV μ^+ peak in the active target waveform, one can discriminate between the π_{e2} signal events and $\pi \to \mu \to e$ background events after the e^+-in-target energy contribution has been subtracted. The total energy spectrum of the π_{e2} decay positron identified by such a cut is shown in Fig. 4 for a subset of 2008 HT data.

Finally, the time spectra of the π_{e2} signal and Michel background events with respect to the stopping π^+ time are shown in the Fig. 5. The *rms* time resolution between the target and degrader is 78 ps for beam pions. Similarly, the *rms* time resolution between the upstream beam detector and the active degrader is approximately 120 ps. These time resolutions correspond to $O(10\,\%)$ of the bin width of the waveforms from which the timing was deduced.

5 Conclusion and future plans

We have upgraded the PIBETA detector to optimize it for the task of a precise measurement of the $\pi^+ \to e^+\nu$ decay ratio at PSI. Two development runs were successfully completed in 2007 and 2008, with the beam stop and DAQ rates ramped up to the design specifications. To date we have recorded 4.7×10^6 raw $\pi \to e\nu$

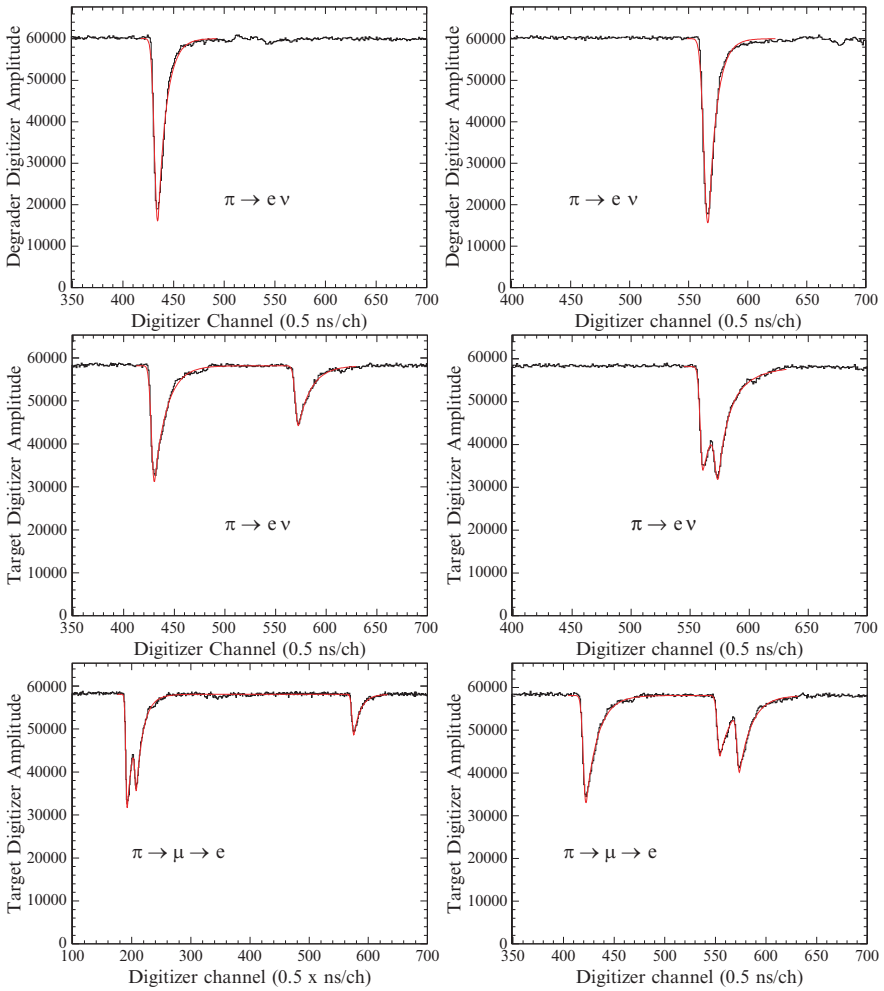

Fig. 2 Digitized PMT waveforms of the single-piece active degrader counter (top panels) and the corresponding active target waveforms for two $\pi \to e\nu$ decay events (middle panels) and two Michel $\pi \to \mu \to e$ chain decay events (bottom panels) from the 2007 development run. The time scale is 2 channels/ns

events, before analysis cuts are applied, corresponding to the statistical uncertainty of $\delta B/B = 5 \times 10^{-4}$. The replay of the data set collected so far is under way as of this writing, in preparation for a production run in 2009 that is planned to complete the required statistics [13].

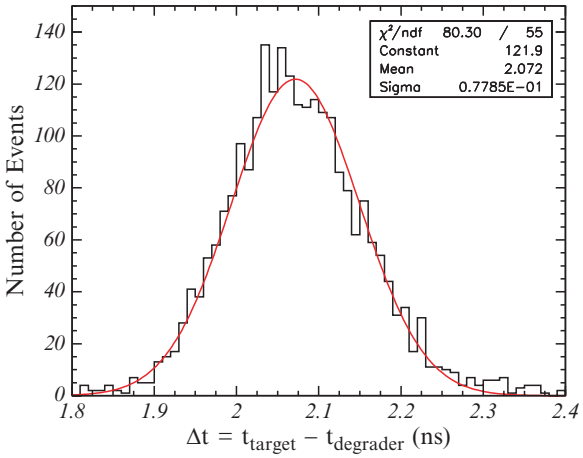

Fig. 3 Time-of-flight spectrum between the degrader and target with *rms* = 78 ps. The contributions to *rms* come from the beam momentum spread and instrumental resolution

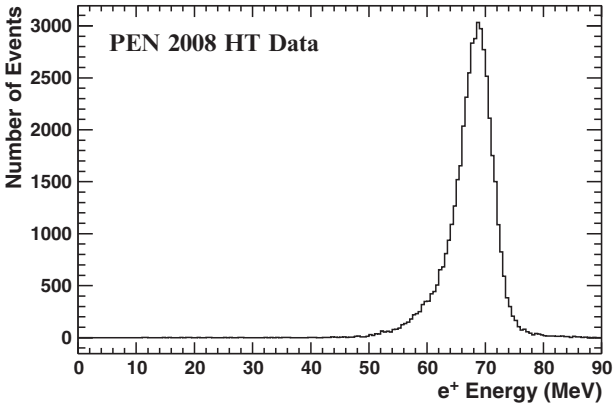

Fig. 4 The high threshold $\pi^+ \to e^+\nu$ energy spectrum for a subset of the 2008 data. Michel background has been suppressed by the cut on the total energy deposited in the target

The PEN experiment has been supported by the National Science Foundation (NSF PHY-0653356), the Paul Scherrer Institute and the Russian Foundation for Basic Research (Grant No. 08-02-00652a).

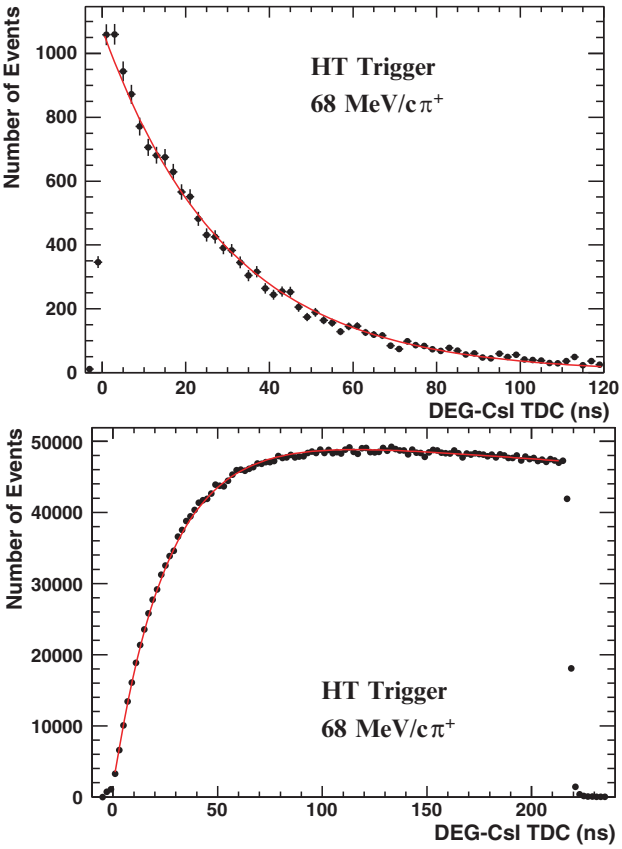

Fig. 5 Calorimeter time distributions with respect to the π^+ stop time for $\pi \to e\nu$ events (top panel) and $\pi \to \mu \to e$ decay chain events (bottom panel) for a subset of 2007 data

References

1. PEN Collaboration: Precise Measurement of the $\pi^+ \to e^+\nu$ Branching Ratio. Paul Scherrer Institute Proposal R-05-01. Available at http://pen.phys.virginia.edu/proposal/pen_proposal.pdf.
2. W. J. Marciano, A. Sirlin: Radiative corrections to π_{l2} decays. Phys. Rev. Lett. **71**, 3629–3632 (1993)
3. M. Finkemeier: Radiative corrections to π_{l2} and K_{l2} decays. Phys. Lett. B **387**, 391–394 (1996)
4. V. Cirigliano, I. Rosell: Two-Loop Effective Theory Analysis of $\pi(K) \to e\bar{\nu}_e[\gamma]$ Branching Ratios. Phys. Rev. Lett. **99**, 231801–4 (2007)
5. D.I. Britton, S. Ahmad, D.A. Bryman, R.A. Burnham, E.T.H. Clifford, P. Kitching, Y. Kuno, J.A. Macdonald, T. Numao, A. Olin, J-M. Poutissou, M.S. Dixit: Measurement of the $\pi^+ \to e^+\nu$ branching ratio. Phys. Rev. Lett. **68**, 3000–3003 (1992)
6. G. Czapek, A. Federspiel, A. Flükiger, D. Frei, B. Hahn, C. Hug, E. Hugentobler, W. Krebs, U. Moser, D. Muster, E. Ramseyer, H. Scheidiger, P. Schlatter, G. Stucki, R. Abela, D. Renker, E. Steiner: Branching ratio for the rare pion decay into positron and neutrino. Phys. Rev. Lett. **70**, 17–20 (1993)

7. D.A. Bryman, $\pi \to e\nu$ decay: window on the generation puzzle. Comments Nucl. Part. Phys. **21**, 101–122 (1993)
8. A. Masiero, P. Paradisi, R. Petronzio, Probing new physics through μ-e universality in $K \to \tilde{l}\nu$. Phys. Rev. D **74**, 011701–5(R) (2006)
9. E. Frlež, D. Počanić, Assamagan, et al.: Design, commissioning and performance of the PIBETA detector at PSI. Nucl. Inst. and Meth. A **526**, 300–347 (2004)
10. E. Frlež, D. Počanić, V. A. Baranov, et al.: Precise Measurement of the Pion Axial Form Factor in the $\pi^+ \to e^+\nu_e\gamma$ Decay. Phys. Rev. Lett. **93**, 181804-1-4 (2004)
11. D. Počanić,, E. Frlež, V.A. Baranov, et al.: Precise Measurement of the $\pi^+ \to \pi^0 e^+\nu$ Branching Ratio. Phys. Rev. Lett. **93**, 181803-1-4 (2004)
12. M. Bychkov, D. Počanić, B.A. VanDevender, et al.: New Precise Measurement of the Pion Weak Form Factors in the $\pi^+ \to e^+\nu\gamma$ Decay. hep-ph arXiv:0804.1815v1 (2008)
13. PEN Collaboration Home Page, http://pen.phys.virginia.edu/.

Performances of the CMS Tracker

Ch. Genta on behalf of the CMS Tracker Collaboration

Abstract With a total area of almost 200 m^2, about 15,000 silicon modules, and nearly ten million readout channels, the CMS Silicon Strip Tracker is by far the largest silicon strip detector ever built. Inside the Strip Tracker, a Pixel Detector made of three barrel layers closed by two forward/backward disks on each side of the interaction region, provides a crucial contribution to pattern recognition, as well as primary and secondary vertices reconstruction. Altogether the Tracker reconstructs the trajectories of charged particles, measures their momentum, and plays a major role in lepton identification and heavy quark tagging. The strip detector has been integrated and commissioned in a dedicated assembly hall on the surface, then inserted in CMS, and re-commissioned using cosmic triggers from the CMS muon system. Excellent results have been achieved in terms of detector performance and preliminary alignment results. The pixel barrel and forward detectors have been built and commissioned separately, and then integrated in CMS. Re-commissioning with the rest of the detector has been done with cosmic triggers.

Keywords: LHC, CMS, tracker, silicon, micro-strip, pixel

1 Introduction

The Compact Muon Solenoid (CMS)[4] is one of the two general-purpose experiments installed at the Large Hadron Collider (LHC) situated at CERN (Geneva). CMS was designed for a wide range of physics goals, including: the discovery of Higgs boson, elucidation of the electroweak symmetry breaking mechanism, and the search for physics beyond the Standard Model. The accelerator will provide pp

Ch. Genta
INFN and University of Florence, via Sansone 1 - I50019 Sesto Fiorentino (FI) - Italy,
e-mail: genta@fi.infn.it

V. Begun et al. (eds.), *Progress in High-Energy Physics and Nuclear Safety*,

collisions at $\sqrt{s} = 14$ TeV with a design luminosity of 10^{34} cm^{-2}s^{-1} and a bunch crossing frequency of 40 MHz.

Due to the expected high multiplicity of tracks per event, the tracker will play a very important role in the experiment.

2 The CMS tracker

The CMS collaboration opted for a tracker made entirely of silicon modules. In the innermost region a pixel detector is installed, while the outer part is instrumented with $\sim$15,000 silicon micro-strip modules corresponding to a total active area of almost 200 m^2. The tracker occupies a volume of 5.4 m length and 2.4 m diameter and is immersed in a magnetic field of $\sim$4 T in order to obtain the design charged-particle transverse momentum resolution of $1-2\%$ at $P_T \sim 100$ GeV/c. The whole tracker covers the pseudorapidity, η region between -2.5 and 2.5.

2.1 The silicon pixel detector

The pixel tracker is the detector closer to the beam pipe. Its purpose is to reconstruct with high precision primary and secondary vertices, determine with high accuracy the track impact parameter and to provide a robust seeding for the track pattern-recognition. The pixel detector therefore will have a key role in identifying jets from b quarks.

The detector consists of three barrel layers (BPix) with two end-cap disks (FPix) on each side of the barrel as shown in Fig. 1.

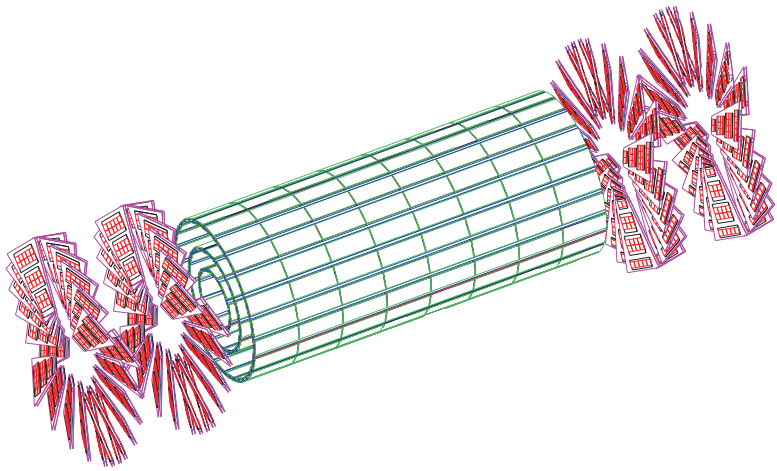

Fig. 1 Three-dimensional view of the silicon pixel detector

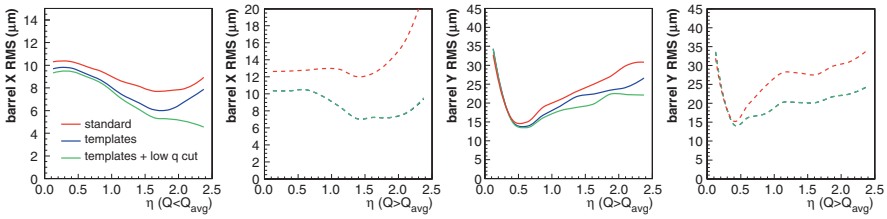

Fig. 2 Pixel $r-\phi$ (labelled as "X") and z (labelled as "Y") resolutions as a function of eta on simulated data. Q is the cluster charge and Q_{avg} the average cluster charge

The 53 cm long BPix layers are located at mean radii of 4.4, 7.3, and 10.2 cm. The FPix disks extending from 6.1 to 15.0 cm in radius are placed on each side at $z = \pm 34.5$ cm and $z = \pm 46.5$ cm. The sensors are n-on-n with n^+ implants on 300 μm thick n bulk silicon and contain arrays of pixels with a cell size of 100×150 μm^2. The total number of channels is 48 million in the barrel and 18 million in the forward. Sensors are connected to the read out chips (ROC) [9] with indium (barrel) and lead-tin (forward) bump bonding. Each ROC provides an analog readout with zero suppression of a 52×80 pixel-matrix, organized in 26 double columns. The forward detectors are tilted at 20° in a turbine-like geometry in order to exploit the Lorentz drift in the magnetic field. The effect of the Lorentz angle (∼25° on unirradiated sensors) is to spread the charge on more pixel and therefore improve the spatial resolution by charge interpolation. A position resolution of about 10 (15) μm in $r-\phi$ (z) coordinates can be achieved thanks to charge sharing and template reconstruction [11]. In Fig. 2 the pixel resolution in $r\phi$ and z coordinates on simulated data is shown.

2.2 The silicon strip detector

The Silicon Strip Tracker (SST) consists of four major subsystems, shown in Fig. 3: four layers form the Inner Barrel (TIB) complemented by the Inner Disks (TID) – formed of three disks on each side – cover the 24 cm $< r <$ 55 cm and $|z| <$ 120 cm region; the six layers of the Outer Barrel (TOB) covering approximately 55 cm $< r <$ 120 cm and the same z range as the Inner part and 2×9 disks the two End Caps (TEC), which complete the pseudorapidity coverage up to $|\eta| < 2.5$.

The subdetectors are instrumented with microstrip modules in 27 different sizes and shapes. In the barrel modules are rectangular while in the TID and TEC discs are wedge shaped. The strips are p^+ implants on a n-type bulk sensors. In the innermost layers (in the barrel) and rings (in the forward) modules are 320 μm thick, while in the outer layers are 500 μm thick.

In addition, some layers and innermost rings are equipped with special stereo modules, made of sandwiches of sensors with strips tilted by 100 mrad with respect to each other, such providing also z information for barrel detectors and r information for disks.

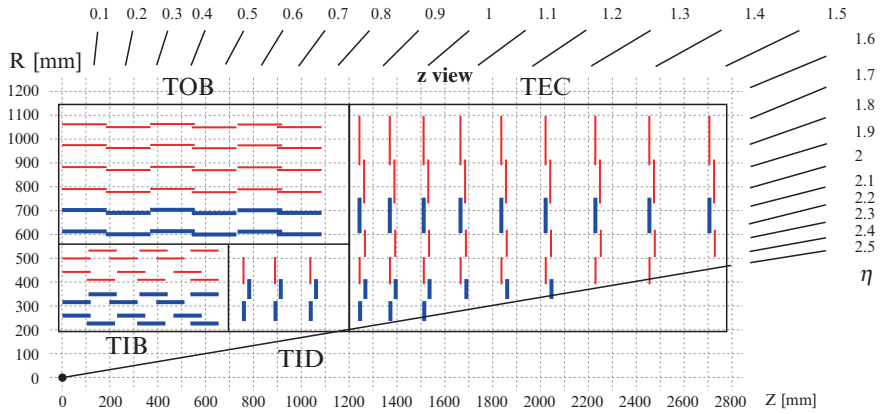

Fig. 3 Layout of one quarter of the CMS silicon strip tracker in the $R-Z$ plane showing the position of the active sensors. Dimensions are in mm. The pseudorapidity coverage is also shown

Groups of 128 strips are connected though a pitch adapter to the front-end readout chips (APV25) [7] mounted on the multilayer kapton hybrid circuit. The APV25 is a 128-channel chip built in radiation hard 0.25 μm CMOS technology [10]. Each channel consists of a preamplifier coupled to a shaping amplifier which produces a 50 ns CR-RC pulse shape. The output of each channel is sampled at 40 MHz and sent to a 192 cell deep pipeline. The pipeline depth allows a programmable level 1 trigger latency of up to 4.8 μs, with 32 locations reserved for buffering events awaiting readout [2].

2.3 Tracker material budget

Once the assembly of the SST was complete, it was possible to include in the simulation a realistic description of the material used in the integration.

One of the drawbacks of having such a high number of channels in the tracker is a high material budget due to the subdetector services (power cables, cooling pipes). As shown in Fig. 4 the active sensors contribute only for a small amount to the total material. The most critical region is around $1.2 < |\eta| < 1.8$ where the thickness of the tracker reaches 1.8 radiation lengths (X_0). As can be seen in Fig. 3 this region corresponds to the gap between the barrel and the forward parts of the strip tracker were the service connections are routed. However in the central part of the tracker ($|\eta| < 1$) the material keeps below 0.6 X_0.

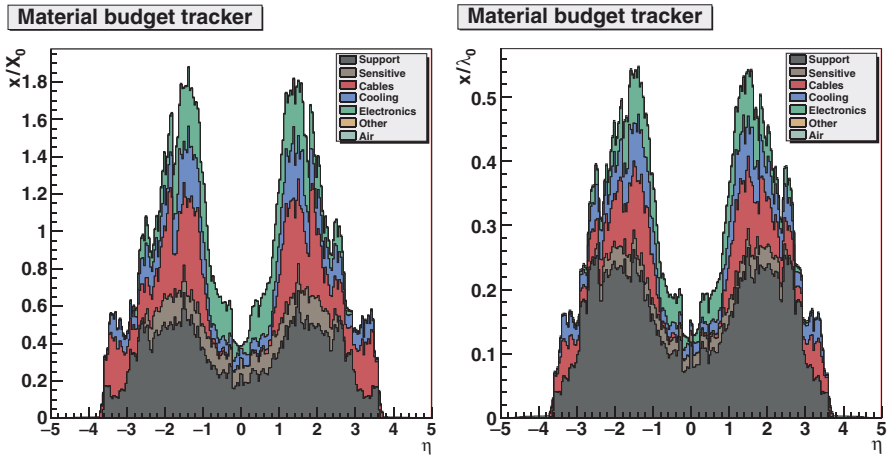

Fig. 4 Material budget in units of radiation lengths (left) and interaction lengths (right) as a function of η. The contribution of the different materials is also shown

3 Tracker integration facility

The modular structure of the tracker made possible to assemble the subdetectors in different institutes all over the world. The construction of the silicon strip tracker was performed during 2006. The final assembly of the Silicon Strip Tracker (STT) in the Support Tube was carried out in March 2007 at CERN in a large, purpose-built, clean area: the Tracker Integration Facility (TIF). After the installation a sector of the SST on the $+z$ side corresponding to the 15% of the entire detector was cabled and read out, and finally commissioned with cosmic rays in the so called "Sector Test".

For this purpose scintillators put on top and bottom of the tracker were put in coincidence to deliver a cosmic muon as trigger. Between the tracker and the bottom scintillator 5 cm lead bricks were placed in order to filter very low energy particles. The thickness of the bricks was limited by the clearance below the tracker. During the tests, the scintillators area was gradually increased, allowing to cover larger portions of the tracker, while keeping the 15% of it readout. In the final configuration the trigger rate was 6.5 Hz, but since the Data Acquisition software (DAQ) was limited to about 3 Hz by the Front End Driver board (FED) readout [2], a trigger veto was implemented to keep the rate under that level. Five million of events were recorded between March and June 2007 at different temperatures (from $+15$°C to -15 °C). The test progressed in an incremental way, beginning with testing separately the sub-systems, then proceeding to a test of the barrel systems, and finally incorporating one endcap.

During the Sector Test, practical experience of the operation of the systems (Data Acquisition, Data Quality Monitoring, Control, Safety, Cooling, etc.) was achieved. In the following paragraphs some of the results achieved by the analysis of the data will be shown.

3.1 Noise performances

In the silicon strip modules a linear dependence of the noise from the strip length is expected. In the Sector Test the modules were mounted on the final structure and also other effects like grounding loops, cross talk with other modules, digital noise, could contribute.

Pedestals and noise were measured on daily basis before any cosmic data taking run (physics run). In order to compare noise from different APVs, a gain correction factor was applied, such that the different responses of the electro-optical readout chain were taken into account. The gain factor was obtained by measuring the height of the APV of the synchronization pulse called tick mark. Since the height of the tick mark depends on the module operating voltages, a systematic spread of 5% between different layers is expected.

Noise studies permitted to identify noisy strips and bad behaving modules or broken fibers. Modules with known problems were removed either from DAQ or from the data analyses. The resulting fraction of missing modules was at the 0.5% level. Dead fibers were identified during a synchronization run on the basis of low tick mark height. The number of missing fibers in the Tracker was at the 0.1% level. The number of dead channels was very constant among several runs for all subdetectors, showing that the identification of these channels is clear and stable: the majority of the dead strips (70%) were flagged in all runs [5]. The noisy components were instead subject to fluctuations and only a small fraction of the noisy strips were noisy throughout the Sector Test.

3.2 Signal-to-noise performances

The signal-to-noise ratio should be largely independent on the different gain corrections, therefore this quantity can be used to compare the performances of the modules in the different layers. Since the signal depends on the path length of the track in silicon, it was normalized to the detector thickness [5]. The noise N was defined as: $N = \sqrt{\sum_i N_i^2 / n_{\text{strips}}}$ where N_i is the noise of the i-th strip of the cluster and n_{strips} is the number of strips of the cluster. The signal-to-noise was measured for different cooling temperatures and, as expected, improves with lower temperatures. As can be seen in Fig. 5 the signal-to-noise is stable within runs taken at the same temperature.

3.3 Hit efficiency

The efficiency of a Tracker module to observe a hit when traversed by a particle, was measured for all modules of a given layer at a time. The pattern recognition

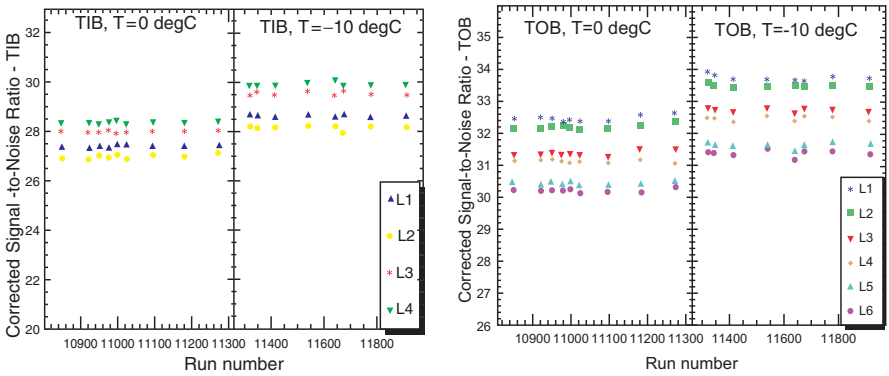

Fig. 5 Signal over noise in the TIB (left) and TOB (right) corrected for the track angle as a function of the run number

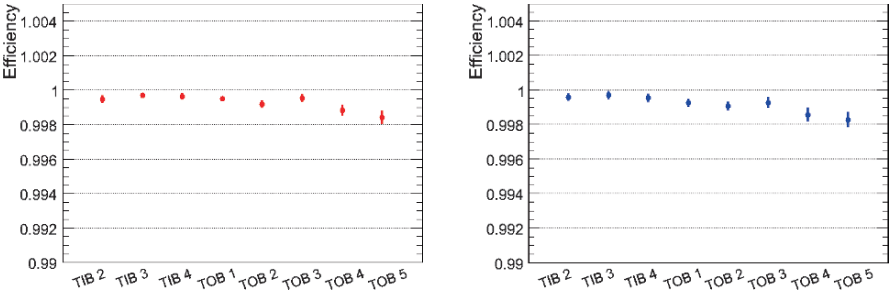

Fig. 6 Summary of the layer efficiency at room temperature (left) and −10°C (right)

was performed with the Combinatorial Kalman Filter (CKF) [1] excluding the hit on the modules of the layer where the efficiency is calculated. A sample of high quality events was selected by requiring only one track reconstructed by the CTF algorithm, one hit in the first TIB layer, one hit in each of the two outermost TOB layers, and at least four reconstructed hits of which at least three in double sided layers. The efficiency for a module was measured by asking for an intersection with the interpolated track and by checking for the presence of a hit. For increased robustness in the presence of residual misalignment the distance between the hit and the predicted track position was not used in the selection. An upper cut of 30° on the angle of incidence of the track with respect to the normal to the module plane, applied in TIB layer 2, selected topologies similar to the ones expected from collisions. In order to avoid artificial inefficiencies at the edge of the sensitive region a fiducial area was used to restrict the region in which efficiency is measured. The hit reconstruction efficiency exceeds 99.8% for all measured layers, as it is shown in Fig. 6.

3.4 Track efficiency

Due to the absence of an external reference other than the scintillators used for triggering it was not possible to measure the absolute efficiency of the tracker. Therefore tracks in TIB and TOB were reconstructed independently and two efficiencies were computed: $\varepsilon(TOB|TIB)$, the probability to find a matching TOB track for a given TIB track, and, vice versa, $\varepsilon(TIB|TOB)$. The track used as reference was required to have at least two hits in double sided modules and its extrapolation to be fully contained in the other subdetector. The match between tracks was based on a comparison of the azimuthal angles. The difference was required to be smaller than five times the resolution determined from simulation. Obtained results are in the range 90–99% (Table 1) for the three track reconstruction algorithms used in the Sector Test [1]; the small discrepancies observed with respect to Monte Carlo are due to a different acceptance between reconstructed and simulated data.

3.5 Alignment

Alignment analysis with tracks is based on the minimization of the track-hit residuals. More precisely, one can minimize the χ^2 function which includes the covariance matrix V of the measurement uncertainties:

$$\chi^2 = \sum_{i}^{\text{tracks}} r_i^T(p,q) V_1^{-1} r_i(p,q) \tag{1}$$

where p represents the position and orientation of the modules and q the track parameters.

At the sector test three different track based alignment methods were employed [6]:

- Hits and Impact Points (HIP): An iterative procedure to find a local analytical solution for p only [8]
- Kalman filter fit method: A sequential procedure updating alignment parameters after adding every track [12]

Table 1 Average conditional track efficiencies and corresponding statistical uncertainties for all three track reconstruction algorithms in data and Monte Carlo simulation

	ε(TIB|TOB) [%]		ε(TOB|TIB) [%]	
	Data	MC	Data	MC
Combinatorial Kalman filter	94.0 ± 0.2	98.66 ± 0.04	97.7 ± 0.1	98.76 ± 0.04
Cosmic track finder	93.1 ± 0.2	94.46 ± 0.09	96.9 ± 0.1	97.36 ± 0.06
Road search	89.9 ± 0.2	89.08 ± 0.12	99.0 ± 0.1	99.39 ± 0.03

- MillePede minimization: A method to find a global solution for p and q, taking into account all possible correlations [3]

Due to the absence of the magnetic field during the sector test it was not possible to estimate the track momentum. For this reason and the low momentum spectrum of the cosmic muons, the alignment accuracy was limited by the uncertainty on the multiple scattering. Moreover due to the angular distribution of the cosmic rays the alignment of the endcaps was very difficult and it was only possible to align the TEC at the disk level. The typical achieved precision on module position measurement in the local x coordinate is estimated to be about 50 μm and 80 μm in the Tracker Outer and Inner Barrels, respectively.

4 The global run

In December 2007 the SST was installed underground in CMS and the full cabling and piping was completed in March 2008. Almost all the Silicon Strip Tracker (TIB, TID, TOB and TEC+) participated to the CMS global run starting from July 2008. By the end of July also the installation of the pixel detector was completed and starting from 22 August all the tracker was included in the global data acquisition. The re-commissioning of all the tracker is now completed, and the tracker performances are excellent. A huge amount of cosmic data has been taken both with and without magnetic field. In Fig. 7 a cosmic event recorded during a run with magnetic field on is shown.

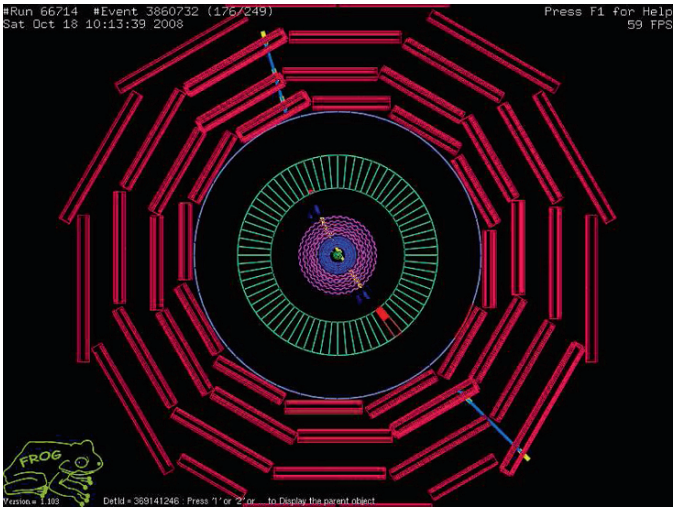

Fig. 7 Cosmic track crossing the CMS detector including all the tracker layers, shown in the innermost parts of the picture

The analysis of the data is ongoing. The data with magnetic field will permit to calibrate the Lorentz angle and will improve the track reconstruction and the alignment.

5 Conclusions

The complete commissioning of the tracker and the analysis of the sector test data has demonstrated the good quality of the pixel and strip modules. The data taken since August 2008 until November 2008 during the global run will improve the understanding of the detector and will provide the first calibration constants that will be used with collision data.

References

1. W. Adam et al., Track Reconstruction with Cosmic Ray Data at the Tracker Integration Facility, CMS NOTE in preparation.
2. S.A. Baird et al., The Front-End Driver card for the CMS Silicon Strip Tracker Readout, Eighth Workshop on Electronics for LHC Experiments, CERN/LHCC/2002-034.
3. V. Blobel, Software Alignment for Tracking Detectors, Nucl. Instrum. Meth. A566 (2006) 5.
4. M. Della Negra et al., CMS Physics Technical Design Report: Volume 1, Detector Performance and Software, CERN LHCC-2006-001, 2006
5. L. Demaria et al., Silicon Strip Tracker Detector Performance with Cosmic Ray Data at the Tracker Integration Facility, CMS NOTE-2008/032.
6. G. Flucke et al., CMS Tracker Alignment at the Integration Facility, CMS NOTE in preparation.
7. M.J. French et al., "Design and results from the APV25, a deep sub-micron CMOS front-end chip for the CMS tracker," *Nucl. Instrum. Meth.*, vol. A466, pp. 359–365, 2001.
8. V. Karimaki, T. Lampen, F.-P. Schilling, The HIP Algorithm for Track Based Alignment and its Application to the CMS Pixel Detector, CMS NOTE-2006/018.
9. H.C. Kastli et al., Design and performance of the CMS pixel detector readout chip, Nucl. Instrum. Meth. A565:188–194, 2006.
10. A. Marchioro, Deep submicron technologies for HEP, Proceedings of 4th workshop on electronics for LHC experiments, CERN/LHCC/98-36, 40–46.
11. M. Swartz, D. Fehling, G. Giurgiu, P. Maksimovic, V. Chiochia, A new technique for the reconstruction, validation, and simulation of hits in the CMS Pixel Detector, CMS NOTE-2007/033.
12. E. Widl, R. Frühwirth, W. Adam, A Kalman Filter for Track-based Alignment, CMS NOTE-2006/022.

Nuclear Track Detectors. Searches for Exotic Particles

G. Giacomelli and V. Togo

Abstract We used Nuclear Track Detectors (NTD) CR39 and Makrofol for many purposes: (i) Exposures at the SPS and at lower energy accelerator heavy ion beams for calibration purposes and for fragmentation studies. (ii) Searches for GUT and Intermediate Mass Magnetic Monopoles (IMM), nuclearites, Q-balls and strangelets in the cosmic radiation. The MACRO experiment in the Gran Sasso underground lab, with $\sim$1,000 m^2 of CR39 detectors (plus scintillators and streamer tubes), established an upper limit for superheavy GUT poles at the level of 1.4×10^{-16} cm^{-2} s^{-1} sr^{-1} for $4 \times 10^{-5} < \beta < 1$. The SLIM experiment at the high altitude Chacaltaya lab (5,230 m a.s.l.), using 427 m^2 of CR39 detectors exposed for 4.22 years, gave an upper limit for IMMs of $\sim 1.3 \times 10^{-15}$ cm^{-2} s^{-1} sr^{-1}. The experiments yielded interesting upper limits also on the fluxes of the other mentioned exotic particles. (iii) Environmental studies, radiation monitoring, neutron dosimetry.

Keywords: Nuclear track detectors, Magnetic Monopoles, nuclearites, Q-balls

1 Introduction

Nuclear Track Detectors are used in many branches of science and technology [1]. The isotropic poly-allyl-diglycol carbonate polymer, commercially known as CR39, is the most sensitive NTD; also Makrofol and Lexan polycarbonates are largely employed.

G. Giacomelli
University of Bologna and INFN Bologna, Italy,
e-mail: giacomelli@bo.infn.it

V. Togo
INFN, Sezione di Bologna, Italy,
e-mail: togo@bo.infn.it

V. Begun et al. (eds.), *Progress in High-Energy Physics and Nuclear Safety*,

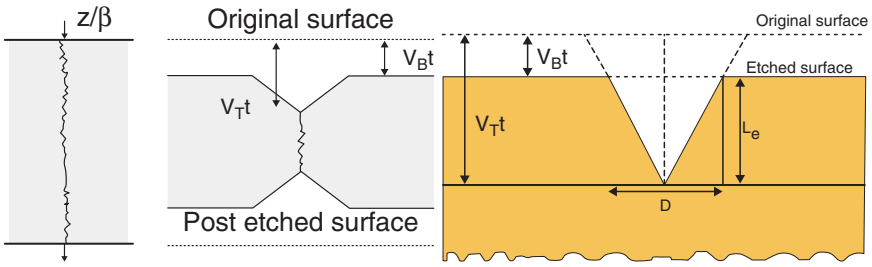

Fig. 1 Sketch of: (a) The latent track formation by a charged particle passing in a NTD. (b) Situation after etching. (c) Parameters of an etched track for a normally incident fast ion in a NTD

A nuclear track detector records the passage of highly ionizing particles via their Restricted Energy Loss (REL). The latent damage trail formed in NTDs may be enlarged by a suitable chemical etching and made visible under an optical microscope. The latent track develops into a conical-shaped etch-pit (Fig. 1) when the etching velocity along the particle trajectory (v_T) is larger than the bulk etching velocity of the material (v_B) [2]. The sensitivity of NTDs crossed by particles with constant energy loss is characterized by the ratio $p = v_T/v_B$ (reduced etch rate) which is determined by measuring the bulk etch rate v_B and either the etch-pit diameter or height. Two methods were used to determine v_B. The first is the common one based on the mean thickness difference before and after etching. The second method is based on both cone height and base diameter measurements of the etched tracks.

The measured track diameter D and track length L_e are expressed in terms of the velocities v_T and v_B

$$D = 2v_B t\sqrt{\frac{(v_T - v_B)}{(v_T + v_B)}} \tag{1}$$

$$L_e = (v_T - v_B)t \tag{2}$$

from which one obtains

$$p = \frac{v_T}{v_B} = 1 + \frac{L_e}{v_B t} = \frac{1 + (\frac{D}{2v_B t})^2}{1 - (\frac{D}{2v_B t})^2} \tag{3}$$

Experiments in different fields require an accurate detector calibration [3, 4]. More than 4,000 m^2 of CR39 detectors were used in the MACRO and SLIM experiments which searched for new massive particles in the cosmic radiation (Magnetic Monopoles, nuclearites, Q-balls) [5–13].

In this note will be summarized the technical work on NTDs and results on fragmentation studies, on the search for MMs, nuclearites and Q-balls in the cosmic radiation, underground or at high altitudes, and environmental monitoring.

2 Experimental. Calibrations

Stacks composed of CR39 and Makrofol foils of size 11.5 × 11.5 cm^2 with several targets were exposed to 158 A GeV In^{49+} ions in 2003 at the CERN-SPS, at normal incidence and a total ion density of ∼2,000 /cm^2. The detector foils downstream of the target recorded the beam ions as well as their nuclear fragments [14–16] see Fig. 2. The CR39 polymer sheets were manufactured by Intercast Europe Co., Parma, Italy, where a scientific production line was set up in order to achieve a lower detection threshold, a higher sensitivity in a larger range of energy losses, a high quality of the post-etched surfaces after prolonged etching [17, 18]. The Makrofol detectors were manufactured by Bayer A.G., Germany.

After exposures, CR39 and Makrofol foils located after the target were etched in 6N NaOH + 1% ethyl alcohol at 70°C for 40 h and 6N KOH + 20% ethyl alcohol at 50°C for 8 h that are the optimum etching condition for CR39 and Makrofol, respectively. The addition of ethyl alcohol in the etchant improves the etched surface quality, reduces the number of surface defects and background tracks, increases the bulk etching velocity, speeds up the reaction, but raises the detection threshold [11, 19]. The etching was performed in a stainless steel tank equipped with internal thermo-resistances and a motorized stirring head. A continuous stirring was applied; the temperature was stable to within ±0.1°C.

Figure 3a shows the etch-pit base area distribution for indium ions and their fragments in CR39 measured with the Elbek image analyzer system [20]; averages were computed from measurements made on the "front sides" of two detector sheets. The fragment peaks are well separated, from Z/β ∼7 to 45; the charge resolution for the average of two measurements is σ_Z ∼0.13e at Z/β ∼15. The resolution close to the indium peak (Z = 49) can be improved by measuring the heights of the etch-pit cones [21].

They were measured with a Leica microscope coupled to a CCD camera and a video monitor; the L_e distribution is shown in the insert in Fig. 3a [19]. For each nuclear fragment we computed the REL and the reduced etch rate p using Eq. 3; p vs REL is plotted in Fig. 3b; the CR39 detection threshold is at REL∼50 MeV cm^2 g^{-1} (corresponding to a relativistic fragment with Z/β∼7).

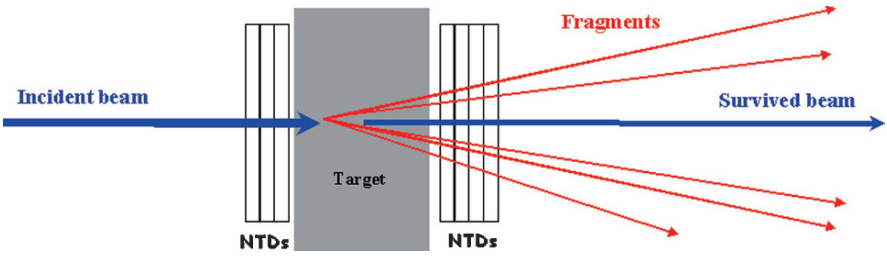

Fig. 2 Exposure set-up for the calibration of CR39 and Makrofol NTDs

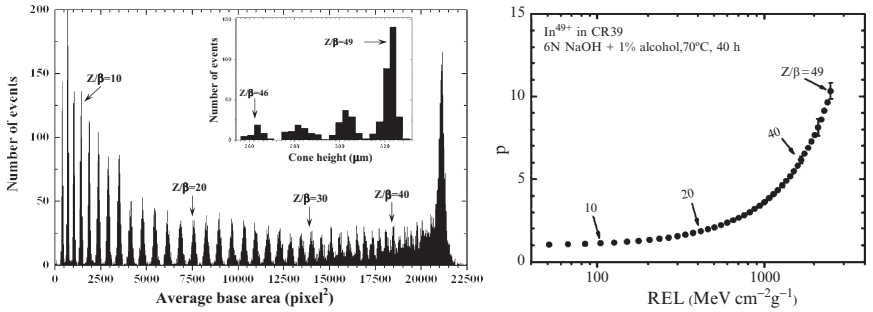

Fig. 3 (a) Base area distributions of etched cones in CR39 from 158 A GeV In^{49+} ions and their fragments. In the insert are shown the cone height distribution for $46 \leq Z/\beta \leq 49$. (b) p vs REL for CR39; statistical standard deviations are shown at $Z/\beta = 40, 45, 49$; for $Z/\beta < 37$ the errors are smaller than the size of the points

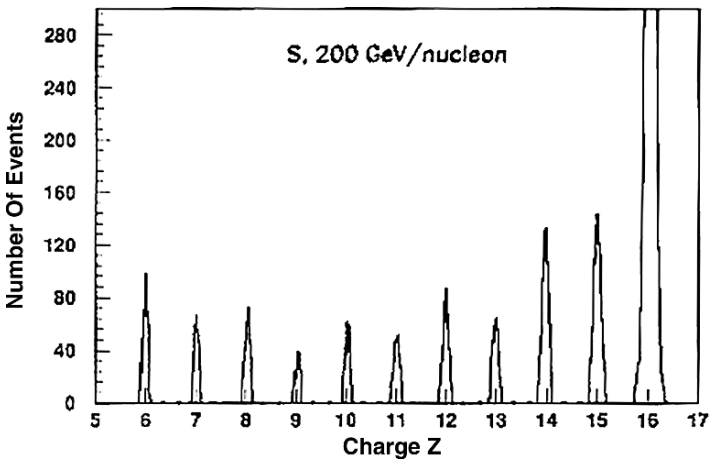

Fig. 4 Search for nuclear fragments with fractional charges in CR39 detectors (12 measurements were made on the same track)

Measurements of *Makrofol detectors* exposed to Pb ions and their fragments yield fragmentation peaks well separated from $Z/\beta \sim 51$ to ~ 77. The threshold is at $Z/\beta \sim 50$; the charge resolution for 2 face measurement is $\sigma_Z \sim 0.18$e at $Z/\beta \sim 55$.

Figure 4 shows the results of repeated precision measurements on the same track (12 times) in CR39 detectors exposed to 200 GeV/nucleon S ions and their fragments. The charge resolution is adequate to allow a search for fragments with fractional charges. The limits on fractional charge fragments are at the level of 10^{-4} [22].

3 Fragmentation cross sections

The availability of ion beams at CERN, BNL and Chiba (HIMAC) made possible to investigate the projectile fragmentation on different targets and for rather different projectile energies. The total charge changing cross sections were determined from the survival fraction of ions using the following relation

$$\sigma_{tot} = \frac{A_T \ln(N_{in}/N_{out})}{\rho\ t\ N_{Av}} \tag{4}$$

where A_T is the nuclear mass of the target; N_{in} and N_{out} are the numbers of incident ions before and after the target, respectively; ρ (g/cm^3) is the target density; t (cm) is the target thickness and N_{Av} is Avogadro number.

At low energies the total fragmentation cross sections are essentially energy independent and are in agreement with semi-empirical formula [23]. At high energies the fragmentation cross section depends on the target mass as $\sim A_T^{1/3}$. The partial fragmentation cross sections increase with decreasing ΔZ and the cross sections leading to even Z fragments are slightly larger than those leading to odd Z [14, 15].

4 Searches for magnetic monopoles

GUT theories of the electroweak and strong interations predict the existence of superheavy MMs produced in the Early Universe when the GUT gauge group breaks into separate groups, one of which is U(1):

$$SU(5) \underset{10^{-35}\ \mathrm{s}}{\overset{10^{15}\ \mathrm{GeV}}{\longrightarrow}} SU(3)_C \times [SU(2)_L \times U(1)_Y] \underset{10^{-9}\ \mathrm{s}}{\overset{10^{2}\ \mathrm{GeV}}{\longrightarrow}} SU(3)_C \times U(1)_{EM} \tag{5}$$

MMs should be generated as topological point defects in the GUT phase transition $SU(5) \longrightarrow U(1)_Y$, about one pole for each causal domain. In standard cosmology this leads to too many poles (*the monopole problem*). A rapid expansion of the early Universe (*inflation*) would defer the GUT phase transition; in the simplest inflation version the number of generated MMs is small. However if there was a reheating phase one may have MMs produced in high energy collisions, like $e^+e^- \rightarrow M\bar{M}$.

Figure 5 shows a sketch of the energy loss of a MM in liquid H.

The structure of a GUT MM: a very small core, an electroweak region, a confinement region, a fermion–antifermion condensate (which may contain 4-fermion baryon–number–violating terms); for $r \geq$ few fm a GUT pole behaves as a point particle generating a field $B = g/r^2$, Fig. 6 [9].

A flux of cosmic GUT MMs may reach the Earth with a velocity spectrum in the range $4 \times 10^{-5} < \beta < 0.1$, with possible peaks corresponding to the escape velocities from the Earth, the Sun and the Galaxy. Searches in the Cosmic Rays (CR) performed with superconducting induction devices yielded a 90% CL limit of 2×10^{-14} cm^{-2} s^{-1} sr^{-1} independent of β [24].

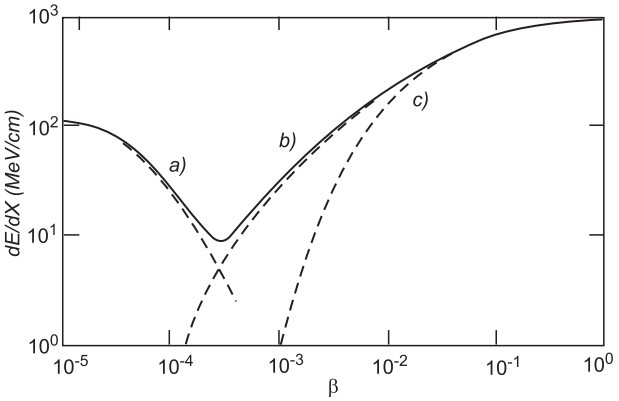

Fig. 5 The energy losses of $g = g_D$ MMs in liquid hydrogen due to (a) elastic collisions; (b) excitation and Drell effect; (c) ionization

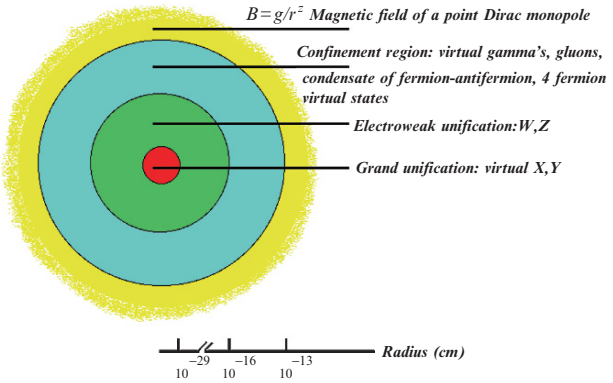

Fig. 6 Extended picture of a GUT Magnetic Monopole

Direct searches were performed above ground and underground [9, 25, 26]. MACRO made a search with liquid scintillators, limited streamer tubes and NTDs; the 90% CL flux limits obtained with the NTDs are shown in Fig. 7a. Figure 7b shows the limits for $g = g_D$ obtained with all the subdetectors; they are at the level of 1.4×10^{-16} cm^{-2} s^{-1} sr^{-1} for $\beta > 4 \times 10^{-5}$ [5, 27]. The figure shows also the limits from the Ohya, Baksan, Baikal, and AMANDA experiments [28].

Indirect GUT MM searches used ancient mica which is a NTD with a very high threshold. It is assumed that a pole passing through the Earth captures an Al nucleus and drags it through subterranean mica causing lattice defects, which survive as long as the mica is not reheated. Only small sheets were analyzed (13.5 and 18 cm^2), but they recorded tracks for $4 \div 9 \times 10^8$ year. The flux limits are at the level of $\sim 10^{-17}$ cm^{-2} s^{-1}sr^{-1} for $10^{-4} < \beta < 10^{-3}$ [29]. But these indirect experiments might not be really so sensitive.

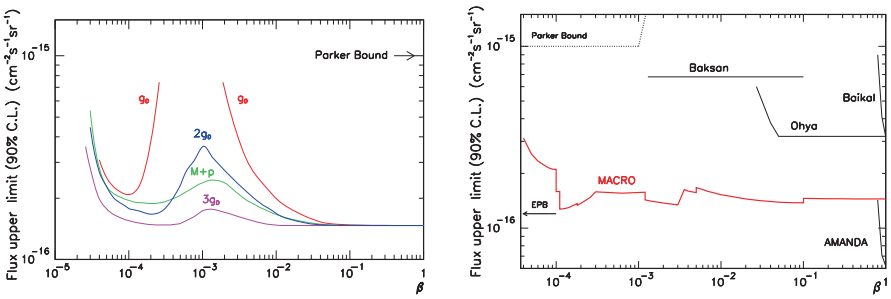

Fig. 7 (a) Upper limits (90%) for an isotropic flux of MMs obtained with the CR39 subdetector of MACRO for poles with magnetic charge g = g_D, 2g_D, 3g_D and for M+p composites. (b) Global limit obtained by MACRO for GUT poles with g = g_D, using all its subdetectors

Intermediate Mass Magnetic Monopoles may appear as topological point defects at a later time in the Early Universe, *i.e.* if the GUT group yields the U(1) group of the Standard Model in the following two steps:

$$SO(10) \xrightarrow[10^{-35}\ \mathrm{s}]{10^{15}\ \mathrm{GeV}} SU(4)\times SU(2)\times SU(2) \xrightarrow[10^{-23}\ \mathrm{s}]{10^{9}\ \mathrm{GeV}} SU(3)\times SU(2)\times U(1) \qquad (6)$$

This would lead to MMs with masses of $\sim 10^{10}$ GeV; they would survive inflation, be stable, "doubly charged" ($g = 2g_D$) and do not catalyze nucleon decay [30]. The structure of an IMM is similar to that of a GUT MM, but the core is larger.

Relativistic IMMs with masses, $10^7 < m_M < 10^{13}$ GeV, may be present in the cosmic radiation, and may be accelerated to high γ factors in one domain of the galactic magnetic field. Detectors at the Earth surface may detect downgoing IMMs if $m_M > 10^5$ GeV [9]; lower mass MMs may be detected at high mountain altitudes, in balloons and in satellites.

SLIM at 5230 m a.s.l. [6] was based on 427 m^2 of CR39 and Makrofol detectors exposed for 4.27 years to the CR. The detectors were organized in modules of 24 × 24 cm^2, each consisting of three layers of CR39 interleaved with three layers of Makrofol and 1 mm Al absorber. Each module was packed in an aluminized polyethylene envelope at 1 atm of dry air to prevent the CR39 loss in sensitivity at a reduced oxygen content in the air (0.5 atm). The 90% CL flux upper limits for downgoing IMMs with $g = g_D,\ 2g_D,\ 3g_D$ and M+p are plotted in Fig. 8 vs β ($2g_D$ is the theoretically preferred value).

5 Searches for nuclearites, strangelets, Q-balls

Strange Quark Matter (SQM) consists of aggregates of *u, d* and *s* quarks in almost equal proportions (the number of *s* quarks is lower than the number of *u* or *d* quarks and SQM should have a relatively small positive integer charge).

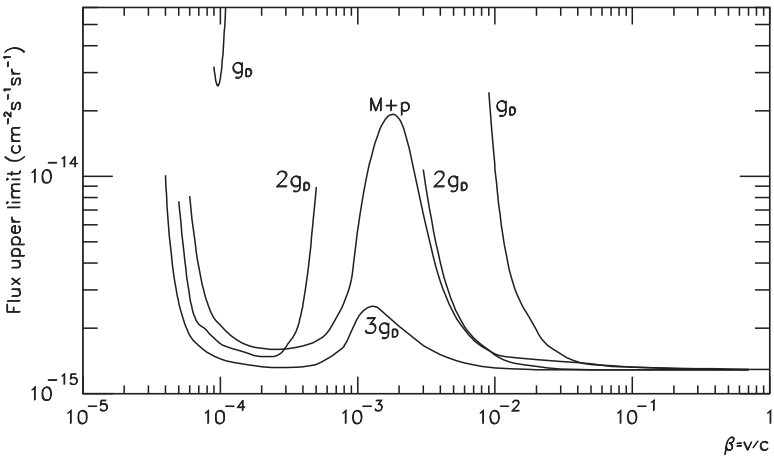

Fig. 8 90% CL upper limits from the SLIM experiment on IMMs in the cosmic radiation

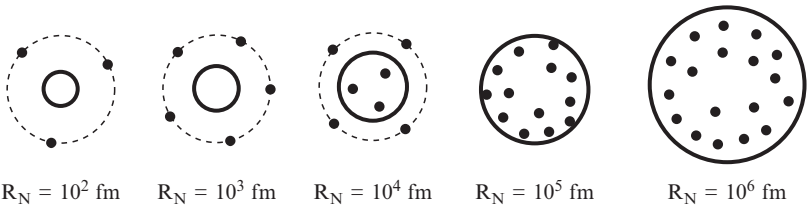

Fig. 9 Sketch of nuclearite structure: the quark bag radius R_N and the core plus electron system (indicated by dashed lines); the electrons are indicated by black points

The overall neutrality of SQM is ensured by an electron cloud which surrounds it, forming a sort of atom, see Fig. 9 [9, 31–33]. SQM has a constant density $\rho_N = M_N/V_N \simeq 3.5 \times 10^{14}$ g cm^{-3}, slightly larger than that of atomic nuclei, and it should be stable for all baryon numbers between ordinary heavy nuclei and neutron stars. SQM with baryon number $A < 10^6 - 10^7$ are called "*strangelets*"; the word "*nuclearite*" was introduced to indicate larger lumps of SQM, which may be present in the Cosmic Radiation [12,31,32]. SQM may have been produced shortly after the Big Bang and may have survived as remnants. SQM may contribute to the cold Dark Matter (DM) in the Universe.

The main energy loss for low velocity nuclearites is due to elastic or quasi-elastic collisions with ambient atoms. The loss is large; therefore nuclearites may be easily detected in scintillators and CR39 NTDs. Nuclearites should have typical galactic velocities, $\beta \sim 10^{-3}$, and for masses >0.1 g could traverse the Earth.

Most nuclearite searches were made as byproducts of CR MM searches; the flux limits are similar to those for MMs. Direct flux limits for nuclearites come from large area experiments with CR39 NTDs; Mt. Norikura at 2,770 m a.s.l. [28]; at the depth of $\sim 10^4$ g cm^{-2} in the Ohya mine [28]; MACRO, at a depth of 3,700 hg cm^{-2}, used also liquid scintillators [33]. Experimental limits for heavy nuclearites are at

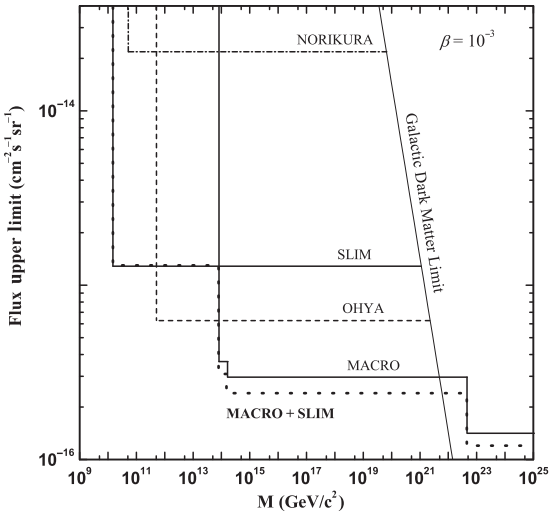

Fig. 10 Flux limits at 90% CL for downgoing nuclearites vs mass

the level of those presented in Fig. 7b for GUT MMs: $\sim 1.4 \times 10^{-16}$ cm^{-2} s^{-1} sr^{-1}. For Intermediate Mass Nuclearites the limits are at the level indicated in Fig. 7a. For small nuclearites, $A < 8{,}000$, the predicted flux in the cosmic radiation is expected to increase with decreasing mass. The present status of the search for galactic nuclearites is summarized in Fig. 10 [13,32]. Indirect searches may yield lower limits, but they are affected by systematic uncertainties. Some exotic cosmic ray events were interpreted as due to incident nuclearites, f. e. the "Centauro" events and the anomalous massive particles, but the interpretation is not unique [34].

Q-balls should be aggregates of squarks $\tilde{q}$, sleptons $\tilde{l}$ and Higgs fields [35]. The scalar condensate inside a Q-ball core has a global baryon number Q (and may be also a lepton number). Protons, neutrons and electrons may be absorbed in the condensate. There may be neutral and charged Q-balls: Supersymmetric Electrically Neutral Solitons (SENS) (more massive and may catalyse proton decay); SENS may obtain a positive electric charge when absorbing a proton in their interaction with matter yielding SECS (Supersymmetric Electrically Charged Solitons), which have a core electric charge and lower masses; the Coulomb barrier may prevent the capture of nuclei. SECS have only integer charges because they are color singlets. Figure 11 [32] shows sketches of SECS and SENS. A SENS which enters the Earth atmosphere could absorb a nitrogen nucleus and become a SECS with charge $Z_Q = 7$. Q-balls could be cold DM candidates. SECS with $\beta \sim 10^{-3}$ and $M_Q < 10^{13}$ GeV may reach an underground detector from above. SENS may be detected by their large emission of pions; SECS may be detected by scintillators, NTDs and ionization detectors. Figure 12 shows the present status of the searches for galactic charged Q-balls with a net charge $Z_Q = 1$.

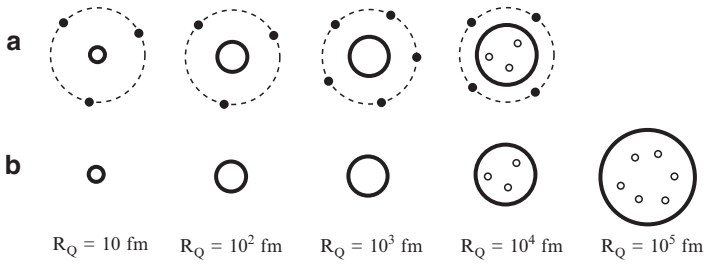

Fig. 11 Sketch of supersymmetric Q-ball structure: (a) for SECS and (b) for SENS. The black points are electrons, the empty dots are s-electrons

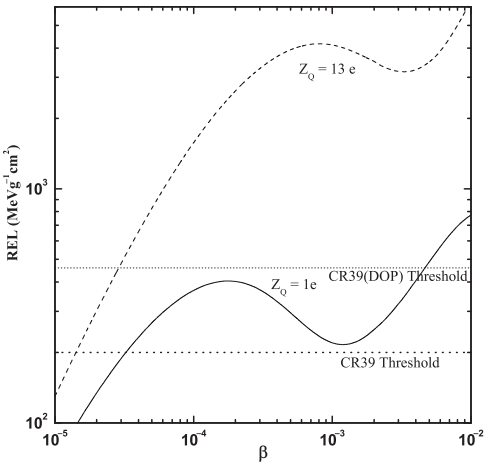

Fig. 12 REL vs β for downgoing charged Q-balls (SECS)

6 Conclusions. Outlook

The NTDs CR39 and Makrofol were calibrated with different ions of different energies. For each type of detector a unique curve of p vs REL describes their response.

The total fragmentation cross sections for low energy ions on different targets do not show any observable energy dependence and are in agreement with similar data in the literature.

Direct and indirect accelerator searches for classical Dirac MMs placed limits for $m_M \leq 800$ GeV. Future improvements may come from LHC experiments [36]. Searches performed for GUT poles in the penetrating cosmic radiation yielded 90% CL flux limits at the level of $\sim 1.4 \times 10^{-16}$ cm^{-2} s^{-1} sr^{-1} for $\beta \geq 4 \times 10^{-5}$. Present limits on IMMs with high β, in the downgoing cosmic radiation are at the level of 1.3×10^{-15} cm^{-2} s^{-1} sr^{-1}. As a byproduct of GUT MM searches some experiments obtained stringent limits on nuclearites, strangelets and Q-balls.

In the past, a number of monopole and of other exotic candidates were thought to have been observed and some results were published [34, 37]. But they were

not confirmed and most of them are now neglected. In 2006 the SLIM experiment faced a problem of this type when analysing the top faces of the top CR39 layers. A sequence of etch-pits was found along a ∼20 cm line; each one of them looked complex and very different from usual ion tracks. Since the "candidate event" was rather peculiar, a thorough study was made in all the sheets of the module, and in all NTD sheets in the modules within a ∼1 m distance. Short soft etching periods were used so as to follow the evolution of the etch-pits. It was concluded that they originated in a rare manufacturing defect involving 1 m^2 of CR39 [38].

We measured the radon concentration in the houses of the city of Bologna, in the Gran Sasso Underground Laboratory and in some thermal sites. In the first two cases the radon level was globally low, and changed with the floor and ventilation [39]. At the 2008 24th Int. Conf. on Nuclear Tracks in Solids, in Bologna, new results were presented in Radiation Environment Monitoring (mainly radon), Neutron Dosimetry and Medical Applications (see proceedings in Radiation Measurements).

Acknowledgements We acknowledge several discussions with many colleagues. We thank Drs. M. Errico, M. Giorgini and I. Traoré for their cooperation.

References

1. S.A. Durrani et al., Solid State Nuclear Track Detection, Pergamon, Oxford (1987).
2. D. Nikezic et al., Material Science Eng. R **46** (2004) 51.
3. Y. Uchihori et al., J. Radiat. Res. **43** (Suppl. S81-5) (2002).
4. S. Kodaira et al., Jpn. J. Appl. Phys. **43** (2004) 6358.
5. M. Ambrosio et al., Eur. Phys. J. C **25** (2002) 511; Nucl. Instrum. Meth. A **486** (2002) 663.
6. S. Balestra et al., Eur. Phys. J. C **55** (2008) 57; hep-ex/0506075; hep-ex/0602036. V. Togo and I. Traoré, arXiv:0811.2885 [physics.ins-det].
7. S. Cecchini et al., astro-ph/0510717 (2005).
8. S. Cecchini et al., Radiat. Meas. **40** (2005) 405.
9. J. Derkaoui et al., Astropart. Phys. **10** (1999) 339. D. Bakari et al., hep-ex/0004019.
10. G. Giacomelli et al., hep-ex/0702050 (2007).
11. S. Manzoor et al., Nucl. Phys. B (Proc. Suppl.) **172** (2007) 296.
12. E. Medinaceli, arXiv:0811.1111 [hep-ex].
13. Z. Sahnoun, 24th Int. Conf. Nucl. Tracks in Solids, (2008) Bologna, Radiat. Meas.
14. S. Cecchini et al., Nucl. Phys. A **807** (2008) 206.
15. M. Giorgini, arXiv:0812.0236 [nucl-ex]; arXiv:0812.0685 [physics.ins-det].
16. V. Togo et al., Nucl. Instrum. Meth. A **580** (2007) 58.
17. L. Patrizii et al., Nucl. Tracks Radiat. Meas. **19** (1991) 641.
18. E. Vilela et al., Radiat. Meas. **31** (1999) 437.
19. S. Balestra et al., Nucl. Instrum. Meth. B **254** (2007) 254.
20. A. Noll et al., Nucl. Tracks Radiat. Meas. **15** (1988) 265.
21. G. Giacomelli et al., Nucl. Instrum. Meth. A **411** (1998) 41.
22. S. Cecchini et al., Astropart. Phys. **1** (1993) 369.
23. H.L. Bradt et al., Phys. Rev. **77** (1950) 54. S. Cecchini et al., Nucl. Phys. A **707** (2002) 513.
24. G. Giacomelli et al., hep-ex/011209; hep-ex/0302011; hep-ex/0211035; hep-ex/0506014.
25. J. Ruzicka and V.P. Zrelov JINR-1-2-80-850 (1980).
26. G. Giacomelli et al., hep-ex/0005041.

27. M. Ambrosio et al., Phys. Lett. B **406** (1997) 249; Astropart. Phys. **18** (2002) 27.
28. S. Orito et al., Phys. Rev. Lett. **66** (1991) 1951. Yu.F. Novoseltsev et al., Nucl. Phys. B **151** (2006) 337. V. Aynutdinov et al.,astro-ph/0507713. A. Pohl et al., astro-ph/0701333.
29. P.B. Price, Phys. Rev. D **38** (1988) 3813. D. Ghosh et al., Europhys. Lett. **12** (1990) 25.
30. T.W. Kephart and Q. Shafi, Phys. Lett. B **520** (2001) 313.
31. E. Witten, Phys. Rev. D **30** (1984) 272. A. De Rujula and S. Glashow, Nature **31** (1984) 272.
32. S. Cecchini et al., arXiv:0805.1797 [hep-ex].
33. M. Ambrosio et al., Eur. Phys. J. C **13** (2000) 453. S. Ahlen et al., Phys. Rev. Lett. **69** (1992) 1860.
34. M. Rybczynski et al., hep-ph/0410064. D. P. Anderson et al., astro-ph/0205089
35. S. Coleman, Nucl. Phys. B **262** (1985) 293. A. Kusenko et al., Phys. Lett. B **418** (1998) 46.
36. G. Abbiendi et al., Phys. Lett. B **663** (2008) 37.
37. P.B. Price et al., Phys. Rev. Lett **35** (1975) 487; Phys. Rev. D **18** (1978) 1382.
38. S. Balestra et al., arXiv:0802.2056 [hep-ex].
39. G. Giacomelli et al., Il Nuovo Saggiatore **4** (1990) 5; Acqua Aria **4** (1990) 371. C. Arpesella et al., Health Phys. **72** (1997) 629.

The ANTARES Neutrino Telescope

G. Giacomelli, for the Antares Collaboration

Abstract The ANTARES underwater neutrino telescope, at a depth of 2,475 m in the Mediterranean Sea, near Toulon, is taking data in its final configuration of 12 detection lines. Each line is equipped with 75 photomultipliers (PMT) housed in glass pressure spheres arranged in 25 triplets at depths between 100 and 450 m above the sea floor. The PMTs look down at 45° to have better sensitivity to the Cherenkov light from upgoing muons produced in the interactions of high energy neutrinos traversing the Earth. Such neutrinos may arrive from a variety of astrophysical sources, though the majority are atmospheric neutrinos. The data from five lines in operation in 2007 yielded a sufficient number of downgoing muons with which to study the detector performances, the vertical muon intensity and reconstruct the first upgoing neutrino induced muons.

Keywords: Neutrino Astronomy, neutrino, ANTARES

1 Introduction

The effort to build large sea water Cherenkov detectors was pioneered by the Dumand Collaboration with a prototype at great depths close to the Hawaii islands [1]; the project was eventually cancelled. Then followed the fresh water lake Baikal detector at shallow depths, which was later enlarged [2]. Considerable progress was made by the Amanda and Icecube ice telescopes in Antarctica [4,5]. In the Mediterranean sea the NESTOR collaboration tested a deep line close to the Greek coast [5] and the NEMO Collaboration close to Sicily [6]; the ANTARES neutrino telescope at 2,475 m below sea level was deployed in the Mediterranean sea, close to Toulon, France, see Figs. 1, 2, 3 [7,8].

G. Giacomelli
University of Bologna and INFN Bologna,
e-mail: giacomelli@bo.infn.it

V. Begun et al. (eds.), *Progress in High-Energy Physics and Nuclear Safety*,

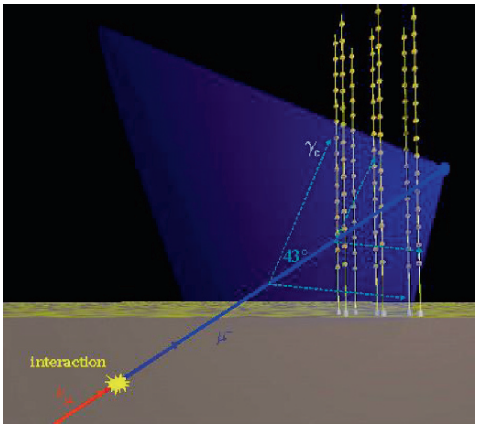

Fig. 1 Optical detection of ν_μ neutrinos interacting in the rock below the sea and giving an upgoing muon which yields Cherenkov radiation in the detector

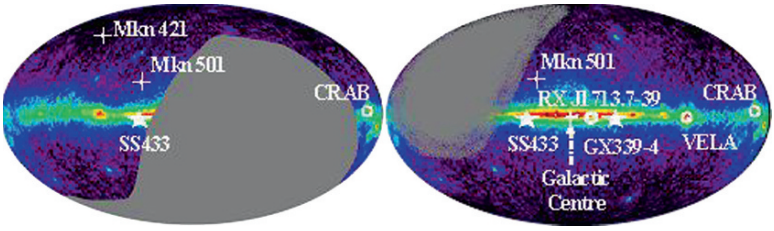

Fig. 2 Left: Regions of sky observable by neutrino telescopes at the South Pole (Amanda, IceCube); Right: In the Mediterranean sea (Antares at 43° North)

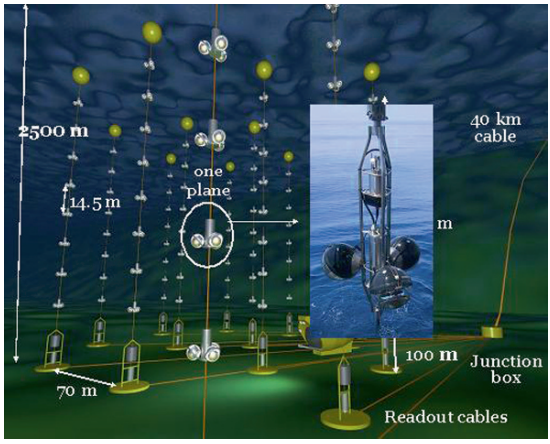

Fig. 3 Scheme of the Antares completed detector

The completed ANTARES neutrino telescope, at 2,475 m below sea level, is presently taking data with 12 detection lines, held vertical by buoys and anchored at the sea floor. The lines are connected to the Junction Box (JB) that distributes power and data from/to shore. The instrumented part of each line starts at 100 m

above the sea floor, so that Cherenkov light can be seen also from upgoing muons coming from neutrino interactions in the rock below the sea, Fig. 1. The lines are separated by $\sim$70 m, and are on an approximate octagonal structure. Each line has 25 floors (storeys), each with 3 Hamamatsu 10" Photomultipliers (PMT) looking downward at 45° from the vertical, housed inside pressure resistant glass spheres (Optical Module (OM)), Fig. 3. The storeys include frontend electronics for signal processing and digitization [9–12].

One of the main reasons to build neutrino telescopes is to study high energy muon neutrino astronomy. Neutrinos may be produced in far away sources, where charged pions are produced and decay, like very high energy photons from π^0 decay, and reach the earth undisturbed. Instead the photons interact with the Cosmic Microwave Background (CMB) radiation and with matter, protons are deflected by magnetic fields and neutrons are unstable. The main drawback of neutrinos is that one needs very large detectors. Neutrino telescopes may also allow dark matter searches [13], searches for exotic particles (fast magnetic monopoles, nuclearites, etc. [14–17], may contribute to the study of atmospheric neutrino oscillations [18]) and test conservation laws [19].

It is worthwhile to recall that neutrino telescopes in the Northern hemisphere have access, can see, the center of our galaxy, while neutrino telescopes in Antarctica cannot see it, Fig. 2. Thus a large telescope in the Mediterranean sea (KM3) [20], and one in Antarctica (Icecube) are complementary and scientifically justified.

2 The ANTARES experiment

Figure 3 shows an artistic illustration of the 12 lines Antares detector; Fig. 4 shows the detector as seen by downgoing muons. The main features of ANTARES were recalled in the Introduction; here we shall recall some other features.

The water properties at the site were extensively studied and are given in Ref. [7]: the absorption length in blue light is $\sim$60 m, the effective scattering length is $\sim$250 m. Several prototype lines and an instrumentation line were deployed in 2003–2005 [9, 10]. The final first two lines were deployed in 2006; in early 2008 the telescope was completed. The electro-optical cable to shore was repaired in mid 2008.

Large photomultipliers, optical modules and the data acquisition system (DAQ) were extensively studied [8, 9, 13]. Each OM has a mu-metal schield for the Earth magnetic field, and contains a system of LED and laser optical beacons for calibrations and relative calibrations of different OMs. Precision timing is distributed via a 200 MHz clock sygnal with a precision of $\sim$100 ns. The final timing precision is $\sim$0.5 ns, which yields an angular resolution of 0.3° for muons with energies $>$10 TeV. The readout system assigns time-stamps to PMT signals, digitizes their charges and merges the data from the 75 PMTs on each detection line in a single fiberoptic [13]. The data which satisfy a minimal requirement, L0 hits, above a threshold of 1/3 photoelectron, are sent to shore. The reconstruction of muon tracks is based on ns measurements of the arrival times of Cherenkov photons at the

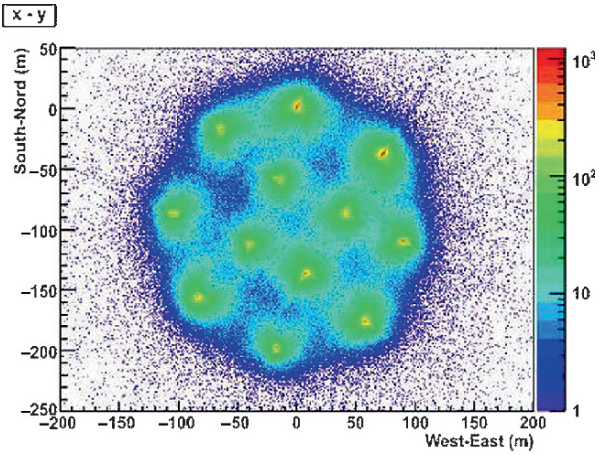

Fig. 4 The 12 line Antares detector as seen by downgoing atmospheric muons

PMTs. This requires precise knowledge of the relative positioning of OMs. An array of acoustic trasponders is deployed on the sea floor; they transmit sound signals to hydrophones mounted at five different altitudes on each detection line. Several special triggers are available ($\sim$7.5 Gb/s). A filter removes excessive noise from bioluminescence and β decays from K^{40} decays. Usually this noise is at the level of $\sim$60 kHz, but there was a higher rate in the first data taking periods, in 2006 and part of 2007, characterized by large sea currents.

For the 12 line detector, Figs. 5 and 6 show the on line event display examples of one muon bundle and of one neutrino candidate event, respectively. The present rate of neutrino induced upgoing muons is $\sim$5 events/day.

3 Preliminary results

The first Antares detector line was deployed in February 2006 and took data alone till October 2006. During this period the background rates were often high and one had to select data over a more limited time [21] and several problems were solved, like the reconstruction software. The downgoing muon data were used to calculate the vertical muon intensity versus depth, Fig. 7: Note the good agreement with previously measured data which were taken with different types of detectors.

Thanks to its modular project Antares was able to take data in a non complete configuration: it took data with a five line configuration in the period February-November 2007. This period of data taking was adequate to obtain a good sample of downgoing atmospheric muons, to improve the track recontruction software with several lines, to improve and test several Monte Carlo codes [31–34].

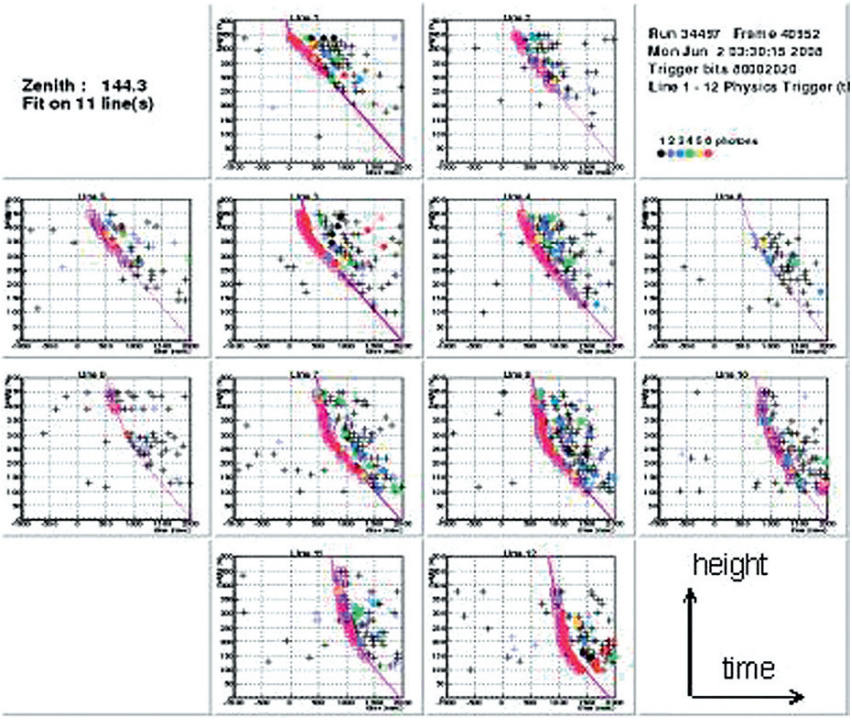

Fig. 5 Example of a muon bundle seen by the 12 line Antares telescope

Figures 8 and 9 show the zenith and azimuth distributions of reconstructed downgoing and upgoing muon tracks. A loose quality cut was applied, that is not able to remove all the badly reconstructed tracks, which are still dominant in the upgoing track region ($0^\circ < \vartheta < 90^\circ$). The black points are the data; the solid line refers to MC expectations obtained using the full CORSIKA simulation with QGSJET01 for the hadronic interaction description [32], and the Horandel model [33] of primary cosmic rays: a good agreement is evident both in shape and in absolute normalization. The shadowed band is an estimate of the systematic effects due to the uncertainties on environmental and geometrical input parameters in the Monte Carlo simulation. In Fig. 8, the dotted line is obtained with CORSIKA QGSJET01 and the NSU model of primary cosmic rays [32]. The difference between the two MC expectations can be ascribed to the different composition models. The dashed-dotted line refers to the fast parametric simulation using MUPAGE [34]. This simulation is based on an all-particle CR flux obtained in underground experiments. The difference with respect to the predictions obtained with the NSU model are likely due to the different hadronic interaction description (DPMJET). Globally, data and MC show a good agreement in shape and are in agreement within 30 – 40% in absolute normalization.

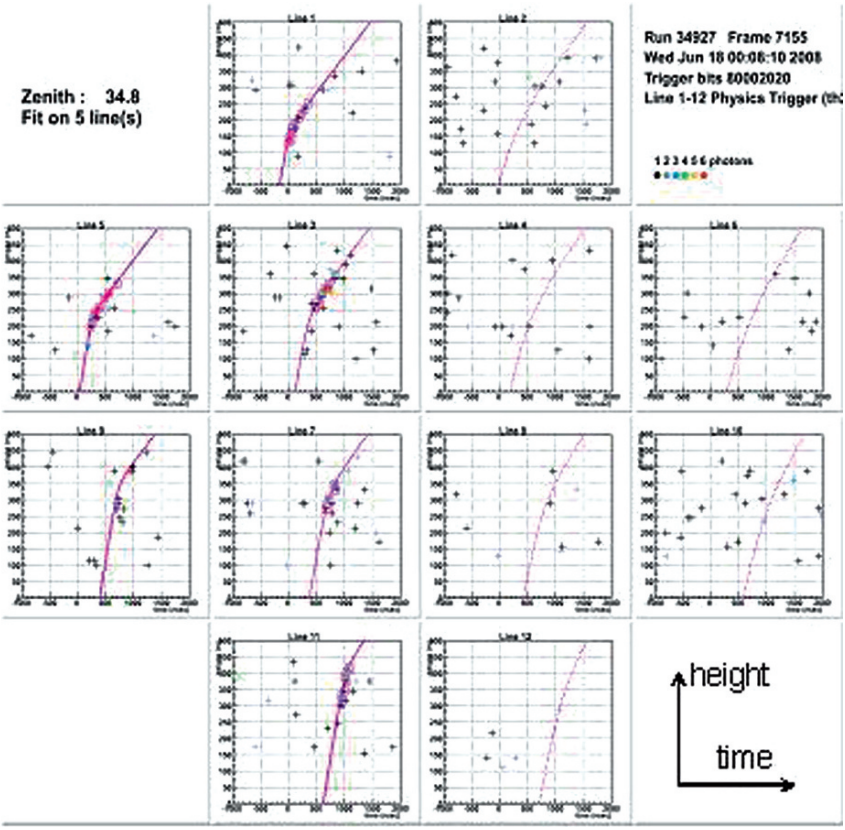

Fig. 6 Example of a neutrino candidate seen by the 12 line Antares telescope

In Fig. 9 some peaks are visible in the azimuth data distribution, which are well reproduced by the MC simulation (CORSIKA-QGSJET-Horandel model). They correspond to the enhancement of the muon reconstruction efficiency for tracks lying on a plane defined by two or more ANTARES strings. The good superposition between data and MC expectations indicates that the positioning systems are working well and that MCs can reproduce the main geometrical features of the detector.

4 Conclusions

The Antares neutrino telescope is running in its final configuration of 12 detection lines. The preliminary results obtained with a single line and with five lines allowed checking and improving the reconstruction programs, and testing of MC codes.

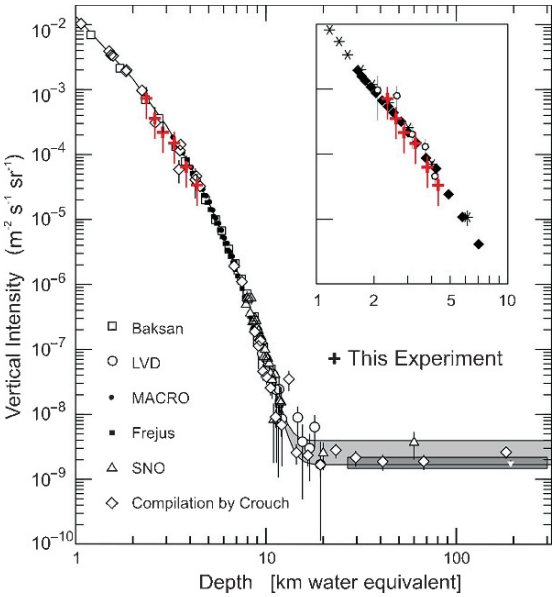

Fig. 7 Vertical muon intensity versus depth. Crosses are from the first Antares line [21]; other data are from: the compilations of Crouch [22], Baksan [23], LVD [24], MACRO [25], Frejus [26], and SNO [27]. The shaded area at large depths represents neutrino induced muons of energy above 2 GeV. In the insert the Antares data are compared to other water or ice data [28–30]

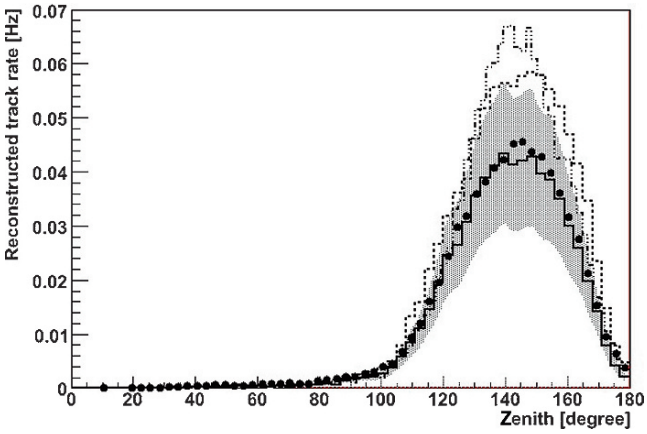

Fig. 8 Zenith distribution of reconstructed tracks with five Antares lines. Black points are data, lines refer to MC predictions: the solid line histogram is the full simulation with CORSIKA, QGSJET01 and the Horandel model for CR composition; the dotted line is the same MC reweighed for the NSU CR model. The dashed-dotted line is the parametric simulation with MUPAGE. The shadowed band is the systematic uncertaintys due to environmental and geometrical parameters

The data taken with line 1 measured the vertical atmospheric muon intensity as a function of depth: the distribution agrees well with previous measurements.

The zenith and azimuth distributions of atmospheric downgoing muons measured with five lines agree with MC expectations, which have a $\sim$30% systematic uncertainty; the main source of uncertainty lies in the primary cosmic ray model.

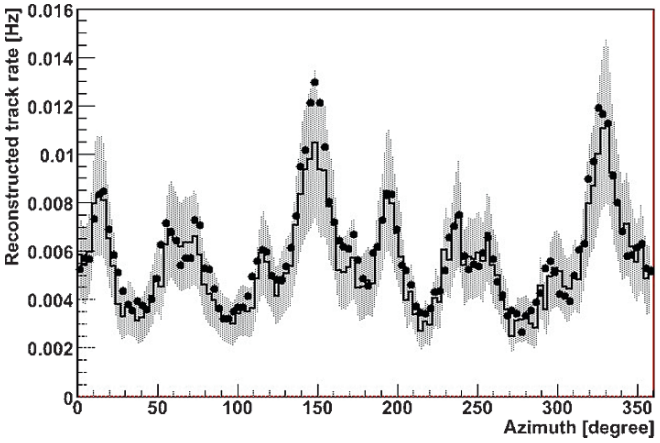

Fig. 9 Azimuth distribution of reconstructed tracks with five Antares lines. Black points are data. The solid line histogram is the MC expectation with the CORSIKA code + QGSJET01 for air shower simulation plus Horandel model for CR composition. The shadowed band is an estimate of the systematics uncertanty due to environmental and geometrical parameters

Acknowledgements I thank Drs. S. Cecchini, A. Margiotta, M. Errico and Prof. M. Spurio for their cooperation. I thank Dr. M. Errico for typing and correcting the manuscript.

References

1. J. Babson et al., (DUMAND Collab.) Phys. Rev. D **42** (1990) 3613.
2. I.A. Belolaptikov et al., (Baikal Collab.) Astropart. Phys. **7** (1997) 263.
3. C. Amsler et al., Data Particle Book, Phys. Lett. B **667** (2008) 1.
4. R. Abbasi et al., (AMANDA-II, IceCube Collab.) arXiv:0809.1646 (2008).
5. G. Aggouras et al., (NESTOR Collab.) Astropart. Phys. **23** (2005) 377.
6. E. Migneco et al., (NEMO Collab.) Nucl. Instrum. Meth. A **588** (2008) 111.
7. J.A. Aguilar et al., (ANTARES Collab.) Astropart. Phys. **23** (2005) 131.
8. P. Amram et al., (ANTARES Collab.) Nucl. Instrum. Meth. A **484** (2002) 369.
9. J.A. Aguilar et al., (ANTARES Collab.) Nucl. Instrum. Meth. A **555** (2005) 132.
10. J.A. Aguilar et al., (ANTARES Collab.) Astropart. Phys. **26** (2006) 314.
11. J.A. Aguilar et al., (ANTARES Collab.) Nucl. Instrum. Meth. A **581** (2007) 695.
12. P. Amram et al., (ANTARES Collab.) Astropart. Phys. **19** (2003) 253.
13. J.A. Aguilar et al., (ANTARES Collab.) Nucl. Instrum. Meth. A **570** (2007) 107.
14. M. Ambrosio et al., Phys. Rev. D **60** (1999) 082002.
15. M. Ambrosio et al., Eur. Phys. J. C **25** (2002) 511.
16. S. Balestra et al., (SLIM Collab.) arXiv: 0801.4913 [hep-ex].
17. S. Cecchini et al., arXiv: 0805.1797 [hep-ex].
18. M. Ambrosio et al., Phys. Lett. B **434** (1998) 451; Phys. Lett. B **517** (2001) 59.
19. G. Battistoni et al., Phys. Lett. B **615** (2005) 14.
20. P. Bagley et al., (KM3NeT Collab.) http://km3net.org/CDR/CDR-KM3NeT.pdf.
21. M. Ageron et al., Performance of the first ANTARES line, to be published.
22. M. Crouch, Proc. 20th Int. Cosmic Ray Conf., Moscow, 6 (1987) 165.

23. Y.M. Andreev et al., (Baksan Collab.) 20th ICRC, Moscow, 6 (1987) 200.
24. M. Aglietta et al., (LVD Collab.) Astropart. Phys. **3** (1995) 311.
25. M. Ambrosio et al., (MACRO Collab.) Phys. Rev. D **52** (1995) 3793.
26. Ch. Berger et al., (Frejus Collab.) Phys. Rev. D **40** (1989) 2163.
27. C. Waltham et al., (SNO Collab.) Proc. 27th ICRC, Hamburg, (2001) 991.
28. E. Andres et al., Astropart. Phys. **13** (2000) 1.
29. I.A. Belolaptikov et al., Astropart. Phys. **7** (1997) 263.
30. J. Babson et al., Phys. Rev. D **42** (1990) 41.
31. M. Ageron et al., Angular distribution of atmospheric muons measured with 5 lines.
32. Y. Becherini et al., Astropart. Phys. **25** (2006) 1.
33. J. Horandel et al., Astropart. Phys. **19** (2003) 193.
34. G. Carminati et al., arXiv: 0802.0562 [physics ins -det].

HSD Transport Model as a Tool for Studying Fluctuations in Nucleus-Nucleus Collisions

V.P. Konchakovski

Abstract The multiplicity fluctuations in nucleus-nucleus collisions at SPS and RHIC energies within the HSD transport approach and statistical model have been studied. Both energy and system size dependences of the scaled variances have been analyzed for proton–proton and central nucleus–nucleus collisions. The importance of rigid centrality trigger has been discussed additionally.

Keywords: Nucleus–nucleus collisions, fluctuations, transport models, statistical models

1 Introduction

The study of event-by-event fluctuations in high energy nucleus-nucleus (A+A) collisions opens new possibilities to investigate the phase transition between hadronic and partonic matter as well as the QCD critical point (cf. the reviews [31, 33]). By measuring the fluctuations one might observe anomalies from the onset of deconfinement [25, 27, 29] and dynamical instabilities when the expanding system goes through the 1-st order transition line between the quark-gluon plasma and the hadron gas [32,40]. Furthermore, the QCD critical point may be signaled by a characteristic pattern in the fluctuations as pointed out in Refs. [42, 43]. However only recently, due to a rapid development of experimental techniques, first measurements of the event-by-event fluctuations of particle multiplicities [2,4,6–8,23,41] and transverse momenta [1,3,5,9,10] in nucleus–nucleus collisions have been performed.

From the theoretical side such event-by-event fluctuations for charged hadron multiplicities (in nucleus-nucleus collisions) have been studied in statistical models

V.P. Konchakovski
Helmholtz Research School, Frankfurt, Germany;
Bogolyubov Institute for Theoretical Physics, Kiev, Ukraine,
e-mail: voka@fias.uni-frankfurt.de

V. Begun et al. (eds.), *Progress in High-Energy Physics and Nuclear Safety*,

[11–17, 30] and in dynamical transport approaches [35–38], which have been used as important tools to investigate high-energy nuclear collisions (see, e.g., Refs. [18–22, 24, 44]).

2 Fluctuations in the number of participants

The centrality selection is an important aspect of fluctuation studies in A+A collisions. At the SPS fixed target experiments the samples of collisions with a fixed number of projectile participants N_P^{proj} can be selected to minimize the participant number fluctuations in the sample of collision events. This selection is possible due to a measurement of the number of nucleon spectators from the projectile, N_S^{proj}, in each individual collision by a calorimeter which covers the projectile fragmentation domain. However, even in the sample with $N_P^{proj} = const$ the number of target participants fluctuates considerably. In the following the variance,

$$Var(n) \equiv \langle n^2 \rangle - \langle n \rangle^2 \,, \tag{1}$$

and scaled variance,

$$\omega \equiv \frac{Var(n)}{\langle n \rangle} \,, \tag{2}$$

where n stands for a given random variable and $\langle \cdots \rangle$ for event-by-event averaging, will be used to quantify fluctuations. In each sample with $N_P^{proj} = const$ the number of target participants fluctuates around its mean value, $\langle N_P^{targ} \rangle = N_P^{proj}$, with the scaled variance ω_P^{targ} (Fig. 1). Within the HSD transport models it was found in Refs. [36–38] that the fluctuations of N_P^{targ} strongly influence the charged hadron fluctuations. To minimize this influence only very central collisions have to be considered where fluctuations of participants are small (this statement is also valid for

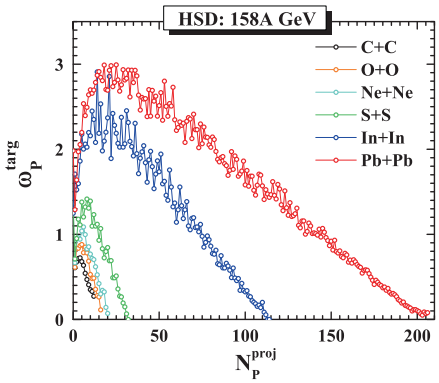

Fig. 1 The HSD simulations for the scaled variances ω_P^{targ} as functions of N_P^{proj} for different nuclei

the collider type experiment as discussed in [34]). The constant values of N_P^{proj} and fluctuations of N_P^{targ} lead also to an asymmetry between the multiplicity fluctuations in the projectile and target hemispheres. The consequences of this asymmetry depend on the A+A dynamics as discussed in [26].

3 Energy dependence of multiplicity fluctuations in N+N and central A+A

To compare central collisions of heavy nuclei and N+N collisions within the HSD model we construct the multiplicity and scaled variance of negatively charged particles in N+N using the HSD results for p+p, p+n and n+n collisions:

$$\langle N_-^{NN} \rangle = \alpha_{pp} \langle N_-^{pp} \rangle + \alpha_{pn} \langle N_-^{pn} \rangle + \alpha_{nn} \langle N_-^{nn} \rangle , \tag{3}$$

$$\omega_-^{NN} = \frac{1}{\langle N_-^{NN} \rangle} \left[\alpha_{pp}\, \omega_-^{pp} \langle N_-^{pp} \rangle + \alpha_{pn}\, \omega_-^{pn} \langle N_-^{pn} \rangle + \alpha_{nn}\, \omega_-^{nn} \langle N_-^{nn} \rangle \right] , \tag{4}$$

where α_{pp}, α_{pn}, α_{nn} are the probabilities of proton-proton, proton-neutron, and neutron-neutron collisions in Pb+Pb (A = 208, Z = 82) or Au+Au (A = 197, Z = 79) reactions.

In the left panel of Fig. 2 the HSD model results in full acceptance are shown for the the scaled variances, ω_-, in central collisions (zero impact parameter, $b = 0$) of Pb+Pb at $E_{lab} = 10,\ 20,\ 30,\ 40,\ 80,\ 158$ AGeV and Au+Au at $\sqrt{s_{NN}} = 62,\ 130,\ 200$ GeV. One can conclude that the HSD results for the scaled variances in central A+A collisions are close to those in N+N collisions. For the SPS energy region all scaled variances in central A+A collisions are slightly below the N+N results. The reversed situation is observed for RHIC energies (for more details see Ref [35]).

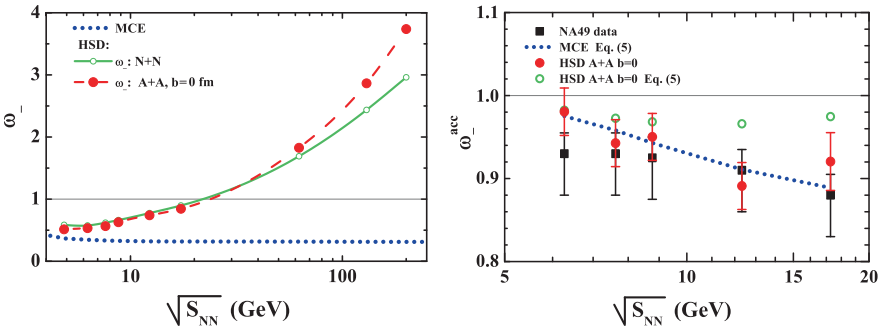

Fig. 2 *Left:* The scaled variance for negative charged particles, ω_- in full acceptance. The solid lines are the HSD results for N+N collisions according to Eq. (3). The full circles are the HSD results for central A+A collisions for zero impact parameter, $b = 0$. The dotted lines are the MCE HG model results for ω_- [14]. *Right:* Results for ω_- in experimental acceptance in comparison to NA49 data [39] (full squares). See [35] for the details

On the other hand in the statistical model the scaled variances $\omega_- = 1$ for the ideal Boltzmann gas in the grand canonical ensemble (GCE). The deviations of ω_- from unity in the hadron-resonance gas (HG) model stem from Bose and Fermi statistics, resonance decays, and exactly enforced conservations laws within the canonical ensemble (CE) or micro-canonical ensemble (MCE) [12, 14]. In Fig. 2 the scaled variances ω_- calculated within the MCE HG model along the chemical freeze-out line (see Ref. [14] for details) are presented by the dotted lines: ω_- reach their asymptotic values at RHIC energies. The HSD results for ω_- in central A+A collisions are very different. They remain close to the corresponding values in p+p collisions and, thus, increase with collision energy as $\omega_- \propto n_-$. One observes no indication for 'thermalization' of fluctuations in the HSD results.

A rigid centrality selection has been recently done for the NA49 data [39] by fixing the number of projectile participants, $N_P^{proj} \cong A$. Only very central, $\leq 1\%$, collisions have been selected. The HG model was compared in Ref. [14] with the NA49 data [39]. It was found that the MCE results for ω_- are very close to the data, they are shown by the dashed lines in Fig. 2. In the statistical model the scaled variances ω_-^{acc} for the accepted particles are calculated from ω_- in the full space according to the acceptance scaling formulae (ASF) (see Ref. [14] for details):

$$\omega_-^{acc} = 1 - q + q\,\omega_-. \tag{5}$$

Thus HSD predicts that the scaled variances ω_- in central A+A collisions increase with collision energy as the multiplicity per participating nucleon, i.e. $\omega_- \propto n_-$. The scaled variances ω_- calculated within the statistical HG model along the chemical freeze-out line show a rather different behavior: ω_- approach finite values at high collision energy. At the top RHIC energy $\sqrt{s_{NN}} = 200$ GeV the HSD values of ω_i(HSD) is already about 10 times larger than the corresponding MCE HG values of ω_-(MCE). So, the HSD and HG scaled variances ω_- show a different energy dependence and are very different numerically at high energies. However, a comparison with preliminary NA49 data of very central, $\leq 1\%$, Pb+Pb collisions at the SPS energy range does not distinguish between the HSD and MCE HG results. This happens because of two reasons. First, the MCE HG and HSD results for ω_i at SPS energies are not too much different from each other and from ω_i in p+p collisions. Second, small experimental values of the acceptance, $q = 0.04 \div 0.16$, make the difference between the HSD and MCE HG results almost invisible. New measurements of ω_- for the samples of very central A+A collisions with large acceptance at both SPS and RHIC energies are needed to allow for a proper determination of the underlying dynamics.

4 Multiplicity fluctuations: energy and system size dependence

An ambitious experimental program for the search of the QCD critical point has been started by the NA61 Collaboration at the SPS [28]. The program includes a variation in the atomic mass number A of the colliding nuclei as well as an energy

scan. This allows to scan the phase diagram in the plane of temperature T and baryon chemical potential μ_B near the critical point as argued in Ref. [28]. One expects to 'locate' the position of the critical point by studying its 'fluctuation signals'. High statistics multiplicity fluctuation data will be taken for p+p, C+C, S+S, In+In, and Pb+Pb collisions at bombarding energies of $E_{lab} = 10$, 20, 30, 40, 80, and 158 AGeV.

We will consider C+C, S+S, In+In, and Pb+Pb collisions at the bombarding energies of 10, 20, 30, 40, 80, 158 AGeV within HSD transport approach. For a comparison and reference we also present the results of multiplicity fluctuations in p+p collisions at the same energies. The study thus is in full correspondence to the experimental program of the NA61 Collaboration [28]. The same calculations in UrQMD transport model were performed in [37].

The importance of a selection of the most central collisions for studies of hadron multiplicity fluctuations has been stressed in papers [34–36, 38]. Due to its convenience in theoretical studies (e.g., in hydrodynamical models) one commonly uses the condition on impact parameter b, for the selection of the 'most central' collisions in model calculations. However, the number of participant even at $b = 0$ is not strictly fixed, and fluctuates according to some distributions. It should be stressed that the conditions $b < b_{max}$ can not be fixed experimentally since the impact parameter itself can not be measured in a straightforward way. Actually, in experiments one accounts for the 1%, 2% etc. most central events selected by the measurement of spectators in the Veto calorimeter, which corresponds to the event class with the largest N_P^{proj}. As it will be shown below the multiplicity fluctuations are very sensitive to the centrality selection criteria.

The charged multiplicity fluctuations are closely related to the fluctuations of the number of participants [34, 38]. Therefore, it is useful to estimate the average number of participants, $\langle N_P \rangle$, and the scaled variances of its fluctuations, ω_P, in $A + A$ collision events which satisfy the $b = 0$ condition and for 1% most central collisions selected by the largest values of N_P^{proj}. The left panel in Fig. 3 shows the ratio, $\langle N_P \rangle / 2A$, for different nuclei at collision energies $E_{lab} = 10$ and 158 AGeV. The fluctuations of the number of participants ω_P are shown on the right panel of Fig. 3. For heavy nuclei, like In and Pb, one finds no essential differences between these two criteria of centrality selection. However, the 1% centrality trigger defined by the largest values of N_P^{proj} looks much more rigid for light ions (S and C). In this case, the ratio $\langle N_P \rangle / 2A$ is larger, and ω_P is essentially smaller than for the criterion $b = 0$. As a result, the 1% centrality trigger by the largest values of N_P^{proj} leads to a rather weak A-dependence of ω_P.

Results of HSD transport model calculations for the scaled variance of negative hadrons, ω_-, are shown in Fig. 4 at different collision energies, $E_{lab} = 10$, 20, 30, 40, 80, 158 AGeV, and for different colliding nuclei, C+C, S+S, In+In, Pb+Pb. The transport model results correspond to collision events for zero impact parameter, $b = 0$. To make the picture more complete, the transport model results for inelastic p+p collisions are shown too, for reference.

Figure 4 (*left*) corresponds to the full 4π acceptance, i.e. all particles are accepted without any cuts in phase space. In actual experiments the detectors accept charged

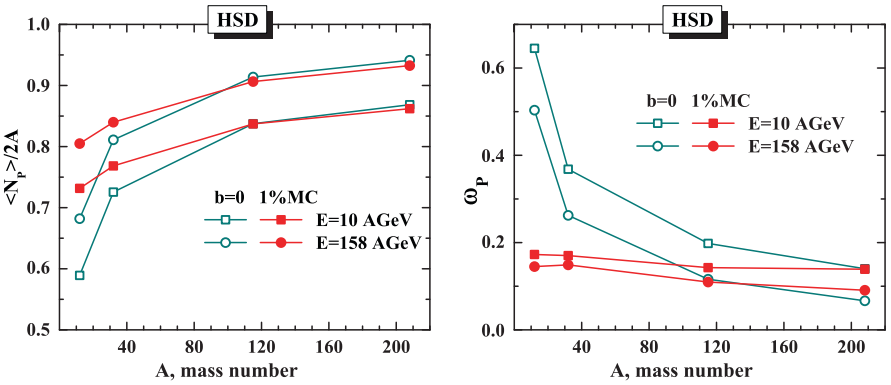

Fig. 3 The HSD results for the ratio $\langle N_P \rangle / 2A$ (*left*) and the scaled variance of the participant number fluctuations, ω_P (*right*), for the 1% most central collisions selected by the largest values of N_P^{proj} (full symbols), for different nuclei at collision energies $E_{lab} = 10$ and 158 AGeV. The open symbols present the results for $b = 0$

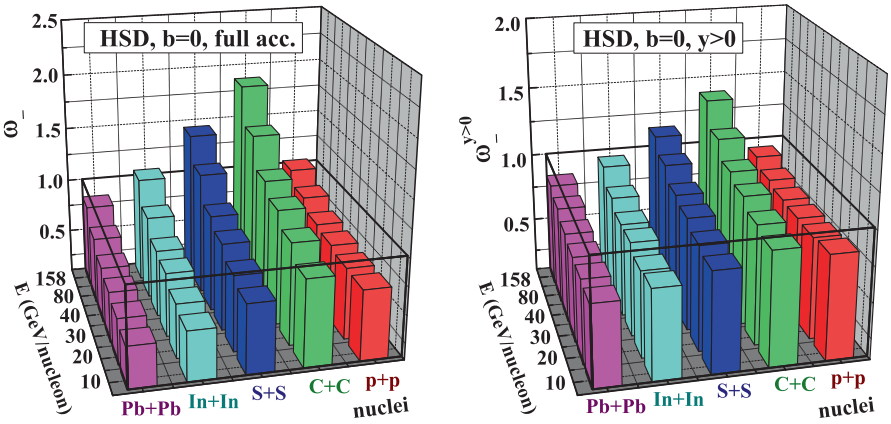

Fig. 4 The results of HSD simulations for ω_- in p+p and central C+C, S+S, In+In, Pb+Pb collisions at $E_{lab} = 10$, 20, 30, 40, 80, 158 AGeV. The condition $b = 0$ is used here as a criterium for centrality selection. Left panel corresponds for full 4π acceptance and right one for hadrons with positive c.m. rapidities, $y > 0$

hadrons in limited regions of momentum space. Figure 4 (*right*) shows the HSD results for multiplicity fluctuations in the projectile hemisphere (i.e. positive rapidities, $y > 0$ in the c.m. frame). This corresponds to the maximal possible acceptance, up to 50% of all charged particles, by the optimized detectors of the NA61 Collaboration [28]. One observes from Fig. 4 (*right*) that the energy and system size dependencies of the multiplicity fluctuations in the projectile hemisphere $(y > 0)$ become less pronounced than in full 4π acceptance. Note also that the centrality selection criterium $b = 0$ keeps the symmetry between the projectile and target hemispheres. Thus, the results for a $y < 0$ acceptance are identical to those for $y > 0$ presented in Fig. 4 (*right*).

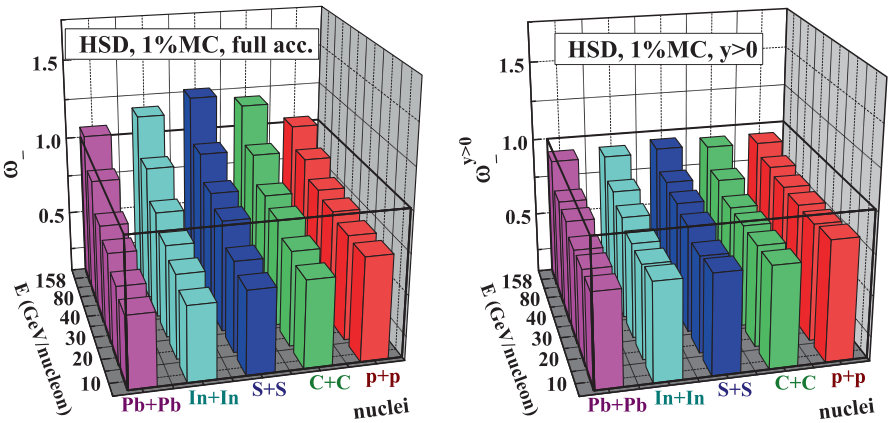

Fig. 5 The HSD results for ω_- in $A+A$ and p+p collisions for the full 4π acceptance (*left*) and for final hadrons accepted in the projectile hemisphere, $y > 0$ (*right*). The 1% most central C+C, S+S, In+In, and Pb+Pb collisions are selected by choosing the largest values of N_P^{proj} at different collision energies E_{lab} = 10, 20, 30, 40, 80, 158 AGeV

For the 1% most central $A+A$ collision events – selected by the largest values of N_P^{proj} – the HSD multiplicity fluctuations are shown in Fig. 5 for full 4π and $y > 0$ acceptance. For light nuclei (S and C) the multiplicity fluctuations in the samples of 1% most central collisions are smaller than in the $b = 0$ selection and the atomic mass number dependencies become less pronounced (compare Fig. 5 with Fig. 4). This is because the participant number fluctuations ω_P have now essentially smaller A-dependence, as seen in Fig. 3.

Figure 5 (*right*) shows that HSD predicts a monotonic dependence of the charge particle multiplicity with energy. So, the hadronic 'background' for the NA61 experiments is expected to be a smooth monotonic function of beam energy.

5 Summary

Our analysis shows that the fluctuations in the number participants strongly influence observed multiplicity fluctuations. To avoid them one should consider the most central collisions with rigid events selection.

We have found a qualitative difference in the behavior of the scaled variances of multiplicity distributions in statistical and transport models. The transport models predict that the scaled variances in central nucleus–nucleus collisions remain close to the corresponding values in proton–proton collisions and increase with collision energy in the same way as the corresponding multiplicities, whereas in the statistical models the scaled variances approach finite values at high collision energy, i.e. become independent of energy. New measurements at higher energies and with larger acceptance can clarify the situation.

We conclude that the condition $b = 0$ corresponds to 'most central' $A+A$ collisions only for nuclei with large atomic mass number (In and Pb). In this case the average number of participants is close to its maximum value and its fluctuations are rather small. However, in the studies of event-by-event multiplicity fluctuations in the collisions of light nuclei (C and S) the criterium $b = 0$ is far from selecting the 'most central' $A+A$ collisions.

We have considered C+C, S+S, In+In, and Pb+Pb nuclear collisions from $E_{lab} =$ 10, 20, 30, 40, 80, 158 AGeV. The influence of participant number fluctuations on hadron multiplicity fluctuations has been emphasized and studied in detail. To make these 'trivial' fluctuations smaller, one has to consider the most central collisions. Indeed, one needs to make a very rigid selection – 1% or smaller – of the 'most central' collision events. In addition, one wants to compare the event-by-event fluctuations in these 'most central' collisions for heavy and for light nuclei. Different centrality selections are not equivalent to each other. We have defined the 1% most central collisions by selecting the largest values of the projectile participants N_P^{proj}. The multiplicity fluctuations calculated in these samples show a much weaker dependence on the atomic mass number A than for criterium $b=0$. A monotonic energy dependence for the multiplicity fluctuations are obtained in the HSD transport model. Thus, the expected enhanced fluctuations – attributed to the critical point and phase transition – can be observed experimentally on top of a monotonic and smooth 'hadronic background'. The most promising signature of the QCD critical point would be an observation of a non-monotonic dependence of the scaled variances on bombarding energy E_{lab} for central A+A collisions with fixed atomic mass number. Our findings should be helpful for the optimal choice of collision systems and collision energies for the experimental search of the QCD critical point.

Acknowledgements I would like to thank E.L. Bratkovskaya, M.I. Gorenstein and B. Lungwitz for fruitful collaboration.

References

1. Adamova, D., et al.: Event-by-event fluctuations of the mean transverse momentum in 40-a-gev/c, 80-a-gev/c, and 158-a-gev/c pb - au collisions. Nucl. Phys. **A727**, 97–119 (2003). DOI 10.1016/j.nuclphysa.2003.07.018
2. Adams, J., et al.: Multiplicity fluctuations in au + au collisions at s(nn)**(1/2) = 130-gev. Phys. Rev. **C68**, 044,905 (2003). DOI 10.1103/PhysRevC.68.044905
3. Adams, J., et al.: Event-by-event fluctuations in au au collisions at s(nn)**(1/2) = 130-gev. Phys. Rev. **C71**, 064,906 (2005). DOI 10.1103/PhysRevC.71.064906
4. Adare, A., et al.: Charged hadron multiplicity fluctuations in au+au and cu+cu collisions from s(nn)**(1/2) = 22.5 to 200 gev. Phys. Rev. **C78**, 044,902 (2008). DOI 10.1103/PhysRevC.78.044902
5. Adler, S.S., et al.: Measurement of non-random event-by-event fluctuations of average transverse momentum in s**(1/2) = 200-gev au + au and p + p collisions. Phys. Rev. Lett. **93**, 092,301 (2004). DOI 10.1103/PhysRevLett.93.092301

6. Afanasev, S.V., et al.: Event-by-event fluctuations of the kaon to pion ratio in central pb + pb collisions at 158-gev per nucleon. Phys. Rev. Lett. **86**, 1965–1969 (2001). DOI 10.1103/PhysRevLett.86.1965
7. Aggarwal, M.M., et al.: Event-by-event fluctuations in particle multiplicities and transverse energy produced in 158-a-gev pb + pb collisions. Phys. Rev. **C65**, 054,912 (2002). DOI 10.1103/PhysRevC.65.054912
8. Alt, C., et al.: Centrality and system size dependence of multiplicity fluctuations in nuclear collisions at 158-a-gev. Phys. Rev. **C75**, 064,904 (2007). DOI 10.1103/PhysRevC.75.064904
9. Anticic, T., et al.: Transverse momentum fluctuations in nuclear collisions at 158-a-gev. Phys. Rev. **C70**, 034,902 (2004). DOI 10.1103/PhysRevC.70.034902
10. Appelshauser, H., et al.: Event-by-event fluctuations of average transverse momentum in central pb + pb collisions at 158-gev per nucleon. Phys. Lett. **B459**, 679–686 (1999). DOI 10.1016/S0370-2693(99)00673-5
11. Begun, V.V., Gazdzicki, M., Gorenstein, M.I.: Power law in micro-canonical ensemble with scaling volume fluctuations. Phys. Rev. **C78**, 024,904 (2008). DOI 10.1103/PhysRevC.78.024904
12. Begun, V.V., Gazdzicki, M., Gorenstein, M.I., Zozulya, O.S.: Particle number fluctuations in canonical ensemble. Phys. Rev. **C70**, 034,901 (2004). DOI 10.1103/PhysRevC.70.034901
13. Begun, V.V., Gorenstein, M.I.: Bose-einstein condensation of pions in high multiplicity events. Phys. Lett. **B653**, 190–195 (2007). DOI 10.1016/j.physletb.2007.07.059
14. Begun, V.V., Gorenstein, M.I., Hauer, M., Konchakovski, V.P., Zozulya, O.S.: Multiplicity fluctuations in hadron-resonance gas. Phys. Rev. **C74**, 044,903 (2006). DOI 10.1103/PhysRevC.74.044903
15. Begun, V.V., Gorenstein, M.I., Kostyuk, A.P., Zozulya, O.S.: Particle number fluctuations in the microcanonical ensemble. Phys. Rev. **C71**, 054,904 (2005). DOI 10.1103/PhysRevC.71.054904
16. Begun, V.V., Gorenstein, M.I., Zozulya, O.S.: Fluctuations in the canonical ensemble. Phys. Rev. **C72**, 014,902 (2005). DOI 10.1103/PhysRevC.72.014902
17. Begun, V.V., et al.: Multiplicity fluctuations in relativistic nuclear collisions: statistical model versus experimental data. Phys. Rev. **C76**, 024,902 (2007). DOI 10.1103/PhysRevC.76.024902
18. Bratkovskaya, E.L., Cassing, W., Stoecker, H.: Open charm and charmonium production at rhic. Phys. Rev. **C67**, 054,905 (2003). DOI 10.1103/PhysRevC.67.054905
19. Bratkovskaya, E.L., Soff, S., Stoecker, H., van Leeuwen, M., Cassing, W.: Evidence for non-hadronic degrees of freedom in the transverse mass spectra of kaons from relativistic nucleus nucleus collisions. Phys. Rev. Lett. **92**, 032,302 (2004). DOI 10.1103/PhysRevLett.92.032302
20. Bratkovskaya, E.L., et al.: Strangeness dynamics and transverse pressure in relativistic nucleus nucleus collisions. Phys. Rev. **C69**, 054,907 (2004). DOI 10.1103/PhysRevC.69.054907
21. Bratkovskaya, E.L., et al.: Strangeness dynamics in relativistic nucleus nucleus collision. Prog. Part. Nucl. Phys. **53**, 225–237 (2004). DOI 10.1016/j.ppnp.2004.02.015
22. Cassing, W., Bratkovskaya, E.L.: Hadronic and electromagnetic probes of hot and dense nuclear matter. Phys. Rept. **308**, 65–233 (1999). DOI 10.1016/S0370-1573(98)00028-3
23. Das, S.: Event-by-event fluctuation in k / pi ratio at rhic. J. Phys. **G32**, S541–S545 (2006). DOI 10.1088/0954-3899/32/12/S73
24. Ehehalt, W., Cassing, W.: Relativistic transport approach for nucleus nucleus collisions from sis to sps energies. Nucl. Phys. **A602**, 449–486 (1996). DOI 10.1016/0375-9474(96)00097-8
25. Gazdzicki, M., Gorenstein, M.I.: On the early stage of nucleus nucleus collisions. Acta Phys. Polon. **B30**, 2705 (1999)
26. Gazdzicki, M., Gorenstein, M.I.: Transparency, mixing and reflection of initial flows in relativistic nuclear collisions. Phys. Lett. **B640**, 155–161 (2006). DOI 10.1016/j.physletb.2006.07.044
27. Gazdzicki, M., Gorenstein, M.I., Mrowczynski, S.: Fluctuations and deconfinement phase transition in nucleus nucleus collisions. Phys. Lett. **B585**, 115–121 (2004). DOI 10.1016/j.physletb.2004.01.077

28. Gazdzicki, M., et al.: A new sps programme. p. 016 (2006)
29. Gorenstein, M.I., Gazdzicki, M., Zozulya, O.S.: Fluctuations of strangeness and deconfinement phase transition in nucleus nucleus collisions. Phys. Lett. **B585**, 237–242 (2004). DOI 10. 1016/j.physletb.2004.01.080
30. Hauer, M.: Multiplicity fluctuations in limited segments of momentum space in statistical models. Phys. Rev. **C77**, 034,909 (2008). DOI 10.1103/PhysRevC.77.034909
31. Heiselberg, H.: Event-by-event physics in relativistic heavy-ion collisions. Phys. Rept. **351**, 161–194 (2001). DOI 10.1016/S0370-1573(00)00140-X
32. Heiselberg, H., Jackson, A.D.: Anomalous multiplicity fluctuations from phase transitions in heavy ion collisions. Phys. Rev. **C63**, 064,904 (2001). DOI 10.1103/PhysRevC.63.064904
33. Jeon, S., Koch, V.: Event-by-event fluctuations (2003)
34. Konchakovski, V.P., Gorenstein, M.I., Bratkovskaya, E.L.: Multiplicity fluctuations in au + au collisions at rhic. Phys. Rev. **C76**, 031,901 (2007). DOI 10.1103/PhysRevC.76.031901
35. Konchakovski, V.P., Gorenstein, M.I., Bratkovskaya, E.L.: Multiplicity fluctuations in proton proton and nucleus nucleus collisions. Phys. Lett. **B651**, 114–118 (2007). DOI 10.1016/j.physletb.2007.06.032
36. Konchakovski, V.P., Gorenstein, M.I., Bratkovskaya, E.L., Stoecker, H.: Baryon number and electric charge fluctuations in pb+pb collisions at sps energies. Phys. Rev. **C74**, 064,911 (2006). DOI 10.1103/PhysRevC.74.064911
37. Konchakovski, V.P., Lungwitz, B., Gorenstein, M.I., Bratkovskaya, E.L.: Multiplicity fluctuations in nucleus-nucleus collisions: Dependence on energy and atomic number. Phys. Rev. **C78**, 024,906 (2008). DOI 10.1103/PhysRevC.78.024906
38. Konchakovski, V.P., et al.: Particle number fluctuations in high energy nucleus nucleus collisions from microscopic transport approaches. Phys. Rev. **C73**, 034,902 (2006). DOI 10. 1103/PhysRevC.73.034902
39. Lungwitz, B., et al.: Energy dependence of multiplicity fluctuations in heavy ion collisions. p. 024 (2006)
40. Mishustin, I.N.: Non-equilibrium phase transition in rapidly expanding QCD matter. Phys. Rev. Lett. **82**, 4779–4782 (1999). DOI 10.1103/PhysRevLett.82.4779
41. Mitchell, J.T.: Fluctuation results from phenix. J. Phys. Conf. Ser. **27**, 88–97 (2005)
42. Stephanov, M.: The phase diagram of qcd and the critical point. Acta Phys. Polon. **B35**, 2939–2962 (2004)
43. Stephanov, M.A., Rajagopal, K., Shuryak, E.V.: Signatures of the tricritical point in QCD. Phys. Rev. Lett. **81**, 4816–4819 (1998). DOI 10.1103/PhysRevLett.81.4816
44. Weber, H., Bratkovskaya, E.L., Cassing, W., Stoecker, H.: Hadronic observables from sis to sps energies: Anything strange with strangeness? Phys. Rev. **C67**, 014,904 (2003). DOI 10. 1103/PhysRevC.67.014904

First Results on the Interactions of Relativistic ^{9}C Nuclei in Nuclear Track Emulsion

D.O. Krivenkov, D.A. Artemenkov, V. Bradnova, M. Haiduc, S.P. Kharlamov, V.N. Kondratieva, A.I. Malakhov, A.A. Moiseenko, G.I. Orlova, N.G. Peresadko, N.G. Polukhina, P.A. Rukoyatkin, V.V. Rusakova, V.R. Sarkisyan, R. Stanoeva, T.V. Shchedrina, S. Vokál, P.I. Zarubin, and I.G. Zarubina

Abstract First results of the exposure of nuclear track emulsions in a secondary beam enriched by ^{9}C nuclei at energy of 1.2 A GeV are described. The presented statistics corresponds to the most peripheral ^{9}C interactions. For the first time a dissociation $^{9}\mathrm{C} \rightarrow 3^{3}\mathrm{He}$ not accompanied by target fragments and mesons is identified.

Keywords: relativistic nuclei, nuclear track emulsion, carbon nuclei, peripheral interaction, meson, BECQUEREL Collaboration

1 Introduction

The most peripheral processes of the fragmentation of relativistic nuclei on heavy nuclei of the emulsion composition (i.e., Ag and Br) proceed without production of target fragments and mesons. They are called "white" stars aptly reflecting the images of events [1, 2]. The fraction of such events that are induced by electromagnetic diffraction and nuclear interactions is a few percent of inelastic interactions. The statistics of various configurations of relativistic fragments reflects the cluster features of light nuclei due to minimal transferred excitation [3–10]. The use of emulsion provides a complete monitoring of relativistic fragments with an excellent angular resolution. This approach to the study of the nucleon clustering is used by the BECQUEREL collaboration [11] for the study of light nuclei at the proton drip line. Exploration of the dissociation of lighter nuclei ^{7}Be [8] and ^{8}B [9] formed the basis for the progress in the study of the next nucleus - ^{9}C. One can expect that in

D.O. Krivenkov, D.A. Artemenkov, V. Bradnova, M. Haiduc, S.P. Kharlamov, V.N. Kondratieva, A.I. Malakhov, A.A. Moiseenko, G.I. Orlova, N.G. Peresadko, N.G. Polukhina, P.A. Rukoyatkin, V.V. Rusakova, V.R. Sarkisyan, R. Stanoeva, T.V. Shchedrina, S. Vokál, P.I. Zarubin, and I.G. Zarubina
Joint Insitute for Nuclear Research, J.Curie, 6, Dubna, 141980 Russia,
e-mail: krivenkov@lhe.jinr.ru; zarubin@lhe.jinr.ru

V. Begun et al. (eds.), *Progress in High-Energy Physics and Nuclear Safety*,

the peripheral ^{9}C dissociation the picture hitherto obtained for ^{8}B and ^{7}Be with the addition of one or two protons, respectively, should be reproduced.

The ^{3}He based clustering plays an equally important role in these nuclei as the α-particle one does. For the ^{9}C nucleus a cluster excitation 3^{3}He with a relatively low threshold (around 16 MeV) becomes available. In this case, a rearrangement of a neutron from the α-particle cluster into the emerging ^{3}He nucleus should occur. The search for the dissociation $^{9}\mathrm{C} \rightarrow 3^{3}\mathrm{He}$ without accompanying fragments of the target and mesons, i.e. "white" stars, becomes the main task of this study. In principle, this bright channel could be identified by a trident of doubly charged fragments. But the real situation with emulsion exposure in the secondary beams of relativistic radioactive nuclei is more complicated. There should be a detailed analysis of events of the "white" star type as the most clearly interpreted interactions for a reliable determination of the used beam composition. In what follows, first results on ^{9}C identified interactions are described.

2 Experiment

The fragmentation of 1.2 A GeV ^{12}C nuclei, accelerated at the JINR Nuclotron, was used to form a secondary beam with low magnetic rigidity for the best selection of ^{9}C nuclei [12]. The momentum acceptance of the separating channel was about 3%. The amplitude spectrum of a scintillation monitor of the secondary beam is presented Fig. 1. It shows that the major contribution comes from C nuclei. The main background was an admixture of nuclei ^{3}He, which have the same ratio of the charge Z_{pr} to the atomic mass A_{pr}, as ^{9}C ones have. ^{4}He nuclei could not penetrate into the channel because of a much greater magnitude of this ratio. A small admixture of

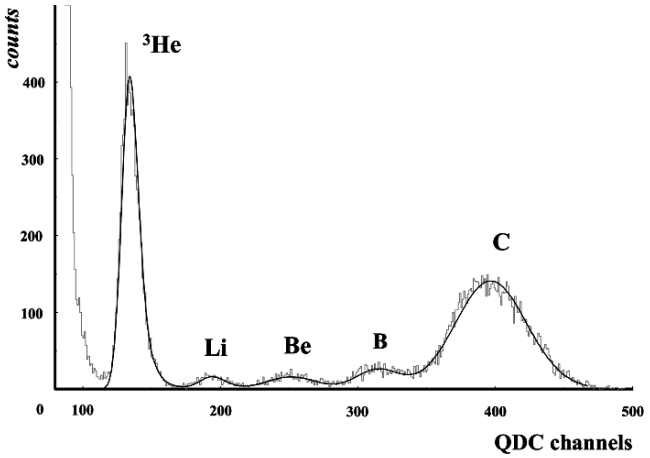

Fig. 1 Charge spectrum of nuclei produced in the fragmentation of $^{12}\mathrm{C} \rightarrow {}^{9}\mathrm{C}$ at secondary beam tuning $Z_{pr}/A_{pr} = 2/3$

fragments ^{7}Be and ^{8}B with slightly higher magnetic rigidity than that of ^{9}C entered the beam. These spectrum features indicate the correctness of the channel tuning.

The exposed stack consisted of 19 layers of BR-2 nuclear track emulsion with a relativistic sensitivity. The layer thickness and dimensions were 0.5 μm and 10×20 cm^2. Stack exposure was performed in a beam directed in parallel to the plane of the stack along the long side. The presented analysis is based on a complete scanning of 13 layers along the primary tracks with charges visually assessed as $Z_{pr} > 2$. ^{3}He nuclei were rejected at the primary stage of selection. The ratio of intensities $Z_{pr} > 2$ and $Z_{pr} = 2$ was about 1:10. The presence of particles $Z_{pr} = 1$ in the ratio $Z_{pr} > 2$ 1:1 was also detected. The $Z_{fr} = 1$ fragments were separated visually from the $Z_{fr} = 2$ fragments, because their ionization was four times smaller. Over the viewed length of 167.1 m traces one found 1217 interactions mostly produced by C nuclei. Thus, it was obtained that the mean free path was equal to $\lambda_C = 13.7 \pm 0.4$ cm. This value corresponds to the estimate based on the data for the neighboring cluster nuclei.

The relativistic fragments H and He can be identified in the cases of small variations in their values $p\beta c$, derived from measurements of multiple scattering, where p is the full momentum, and β the speed. It is assumed that the projectile fragments conserve their momentum per nucleon, i.e., $p\beta c \approx A_{fr} p_0 \beta_0 c$, where A_{fr} the fragment atomic number. To achieve the required precision one needs to measure the deflection of the track coordinates in more than 100 points. Despite the workload, this method provides a unique completeness of the information on the composition of the systems of few lightest nuclei.

The presence of ^{3}He nuclei in the beam composition was found to be helpful to calibrate the identification conditions for secondary fragments. The distribution of the $p\beta c$ measurements for 30 nuclei ^{3}He from the beam is presented in Fig. 2 (solid histogram). The average value of the distribution is $<p\beta c> = 5.1 \pm 0.2$ GeV

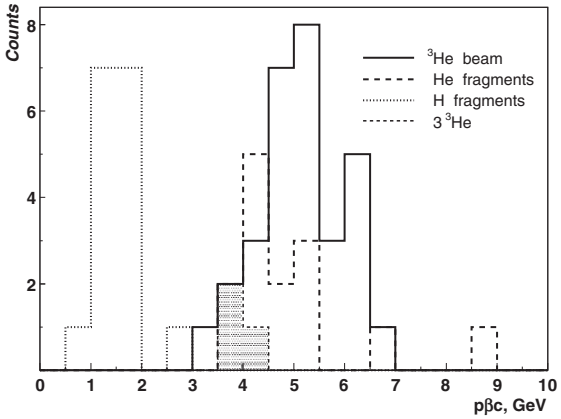

Fig. 2 Distribution of the measurements $p\beta c$ for beam ^{3}He nuclei (30 tracks, solid histogram), singly charged fragments of the "white" stars $\Sigma Z_{fr} = 5+1$ and $4+1+1$ (15 tracks, dot histogram), doubly charged fragments of the "white" stars 3He (14 traces, dotted histogram) and from the 3^{3}He event (shaded histogram)

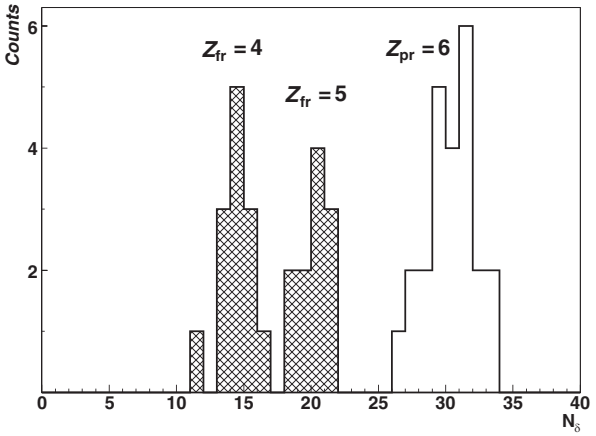

Fig. 3 Distributions by the mean number of δ-electrons per 1 mm length for beam particles (solid histogram) and relativistic fragments with charges $Z_{fr} > 2$ (shaded histogram) from "white" stars $\Sigma Z_{fr} = 5+1$ and $4+1+1$

in the mean scattering $\sigma = 0.8$ GeV. The absolute value is somewhat different from the expected value of 5.4 GeV for ^{3}He nuclei (for ^{4}He - 7.2 GeV) and is defined by the traditionally used constants. The σ value can be assumed to be satisfactory for the separation of isotopes ^{3}He and ^{4}He, and especially their systems.

The contribution of the C, Be and B isotopes was separated via the charge configurations of secondary fragments ΣZ_{fr} in "white" stars and subsequent measurements of the primary charges Z_{pr}. The charges of the projectile nuclei and fragments $Z_{fr} > 2$ were determined by counting of δ-electrons on tracks. The measurement of the charges of the primary nuclei and fragments of the events $\Sigma Z_{fr} = 5+1$ and $4+1+1$, presented in Fig. 3, allows one to conclude that all the events are originated from nuclei $Z_{pr} = 6$. There is an expected shift in the distribution for interaction fragments.

3 Fragment charged configurations

The distribution of 123 "white" stars N_{ws} in the charge configurations ΣZ_{fr} is presented in Table 1. Events with fragments $Z_{fr} = 5$ and 4 and identified charges $Z_{pr} = 6$, accompanied by protons, are interpreted as channels ^{9}C $\rightarrow$ ^{8}B+p and ^{7}Be+2p, due to the absence of stable isotopes ^{9}B and ^{8}Be. These two channels are relative to the most low-threshold dissociation of the nucleus ^{9}C and constitute about 30% of the events of $\Sigma Z_{fr} = 6$. The ratio of ^{8}B "white" stars with heavy fragments (^{8}B $\rightarrow$ ^{7}Be+p) and stars containing only H and He are shown to be approximately equal [9]. Therefore, one can expect that the statistics of the Table 1 contains a large fraction of events produced exactly by the ^{9}C nuclei.

Table 1 Distribution of "white" stars N_{ws} in charge configurations ΣZ_{fr}

ΣZ_{fr}	Z_{fr}						N_{ws}
	6	5	4	3	2	1	
7	–	–	–	–	1	5	2
7	–	–	–	–	2	3	4
$6(Z_{pr}=6)$	–	1	–	–	–	1	11
$6(Z_{pr}=6)$	–	–	1	–	–	2	13
6	–	–	–	–	3	–	13
6	–	–	1	–	1	–	1
6	–	–	–	1	1	1	2
6	–	–	–	1	–	3	2
6	–	–	–	–	1	4	22
6	–	–	–	–	2	2	21
6	–	–	–	–	–	6	5
5	–	–	1	–	–	1	2
5	–	–	–	1	–	2	2
5	–	–	–	–	1	3	13
5	–	–	–	–	2	1	7
4	–	–	–	–	1	2	4

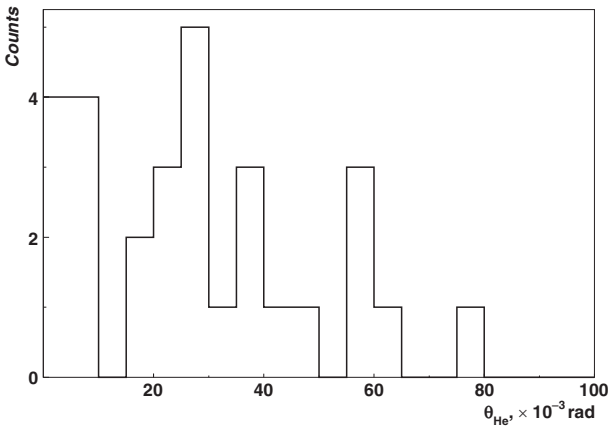

Fig. 4 Distribution by polar angles θ for doubly charged fragments in the "white" stars C→3He

The result of identification of fragments $Z_{fr}=1$ in this group of events is presented in Fig. 4 (dotted histogram). The distribution has $<p\beta c> = 1.5 \pm 0.1$ GeV and $\sigma = 0.4$ GeV. In fact, the identification in these cases is not necessary because of limited options, and protons can serve as a calibration mechanism in more complicated cases.

Table 1 allows one to derive useful indirect conclusions about the composition of the beam. For example, there is only one event $\Sigma Z_{fr} = 4+2$, which might arise from the dissociation ^{11}C→ ^{7}Be+^{4}He having the lowest threshold for the isotope ^{11}C. Thus, a possible presence of ^{11}C in the secondary beam is negligible. Six "white"

Table 2 Distribution of the numbers and fractions of "white" stars of ^{7}Be, ^{8}B and C nuclei, over H and He configurations

Channel	^{7}Be	Fraction, %	^{8}B(+H)	Fraction, %	^{9}C(+2H)	Fraction, %
2He	41	43	12	40	21	42
He+2H	42	45	14	47	22	44
4H	2	2	4	13	5	10
Li+H	9	10	0	0	2	4

stars with the total charge $\Sigma Z_{fr} = 7$ are associated with ^{12}N nuclei, captured in the beam. ^{12}N nuclei were produced in charge exchange processes ^{12}C→^{12}N in the producing target.

The distribution of "white" stars produced by ^{7}Be, ^{8}B and C nuclei of the charge configurations ΣZ_{fr}, which consist only of the nuclei H and He, is presented in the Table 2. One excluded from the sum ΣZ_{fr} one H nucleus for the ^{8}B cases and 2H for the C cases. There are similar fractions of the channels 2He and He + 2H, which correspond to the appearance of ^{7}Be as a core of ^{9}C.

Besides, it is possible to note the production of five "white" stars C→6H (Table 2). Events of this type in the cases of the ^{12}C and ^{11}C isotopes, requiring a simultaneous collapse of three He clusters, could not practically proceed without target fragments due to a very high threshold. Being related to an extremely high threshold, they could not proceed without the production of target fragments. In contrast, similar processes related to the breakups of cluster He pairs, were observed for the "white" stars ^{7}Be→4H [8] and ^{8}B→5H [9]. These events require a full identification of the He and H isotopes and a kinematical analysis to be performed in future. It is quite possible that one will find some cases which would correspond to the cross-border stability in the direction of nuclear resonance states ^{9}C→ ^{8}C.

The question about the contribution of ^{10}C nuclei to the statistics of the Table 1 which would be characterized by configurations consisting only of the He and H isotopes, remains open. A detailed identification and an angular analysis will be crucial in this regard.

4 Search for 3^3He events

Table 1 shows the production of 13 "white" stars with the 3He configuration. The distribution by the polar angles θ for these fragments, which illustrates the degree of collimation, is presented in Fig. 4. Angular measurements allow one to derive the opening angle distribution Θ_{2He} for fragment pairs (Fig. 5). Four narrow He pairs with $\Theta_{2He} < 10^{-2}$ rad are clearly seen due to an excellent spatial resolution. The obtained statistics permits to begin the search for the channel ^{9}C→3^{3}He as the most interesting challenge. The ^{10}C admixture could also lead to the events of a deep nucleonic regrouping ^{10}C→2^{3}He+^{4}He.

The method of the multiple Coulomb scattering was used to determine pβc values of He fragments. Such measurements were implemented only for 14 tracks because of the characteristics of the stack used and because of the fragment angular dispersions (dashed histogram in Fig. 2). The average value $<p\beta c>$ was found to be equal to 4.6 ± 0.2 GeV, with $\sigma = 0.6$ GeV. The fraction of the fragments that could be defined as ^{4}He nuclei is insignificant as compared with ^{3}He. A systematic decrease in the value $<p\beta c>$ with the respect to the beam calibration is due to energy losses in interactions.

The procedure for determining the pβc values of all three fragments became possible only in a single event C→3He (shaded histogram in Fig. 2). The values allow one to interpret the event as a triple production of ^{3}He nuclei with a total value pβc $= 12 \pm 1$ GeV. The interpretation of events as ^{10}C→3^{3}He $+ n$ is unlikely, because in this case one would need to modify not one but a pair of clusters ^{4}He by overcoming a threshold of at least 37 MeV in a peripheral interaction without target fragment production.

This event is a first identified candidate for ^{9}C→3^{3}He. Its mosaic microphotography is presented in Fig. 5. The values of the 3He transverse momenta P_t, obtained by pβc and angular measurements are equal to 318 ± 53 MeV/c, 128 ± 20 MeV/c and 110 ± 14 MeV/c. Then the total momentum ΣPt transferred to the system 3^{3}He is equal to 551 ± 60 MeV/c. By introducing the ΣP_t correction, one can get noticeably lower values of P_t^* in the 3^{3}He center of mass - 138 ± 23 MeV/c, 66 ± 10 MeV/c, and 74 ± 10 MeV/c.

The excitation energy estimated from the difference of the invariant mass M_{eff} of the 3^{3}He system and the fragment mass is equal $E_{3He} = 11.9 \pm 1.4$ MeV. The peculiarity of this event is the presence of a 2^{3}He narrow pair of an energy of $E_{2HE} = 46 \pm 8$ keV. Such a low E_{2He} value of the relativistic 2^{3}He pair is close to the decay energy from the ground state of ^{8}Be→ 2^{4}He. In the study of ^{7}Be→^{3} He $+ ^{4}$He [8] so narrow relativistic pairs 2He were not found. The discussed "white" star is one of the four 3He events with such narrow pairs (Fig. 5). This observation can motive the study of an intriguing opportunity of the existence of a 2^{3}He narrow resonant state near the threshold.

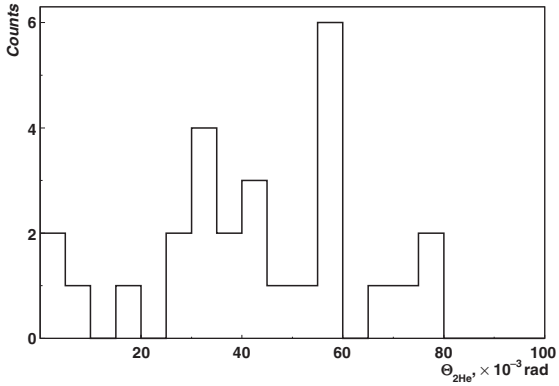

Fig. 5 Distribution by opening angles Θ_{2He} between fragments in the "white" stars C→3He.

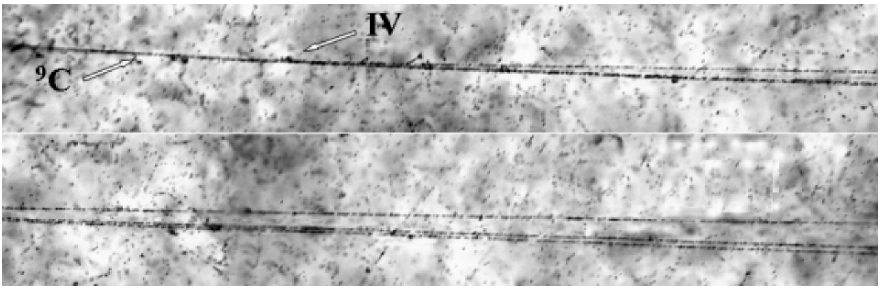

Fig. 6 Microphotography of "white" star $^9C \rightarrow 3^3He$ at 1.2 A GeV. The upper photo shows the dissociation vertex (indicated as **IV**) and fragments in a narrow cone. Three tracks of relativistic He fragments can clearly be seen in the bottom photo.

5 Conclusions

For the first time nuclear track emulsion is exposed to relativistic ^{9}C nuclei. The picture of the charge configurations of relativistic fragments is obtained for the most peripheral interactions. A dissociation event $^9C \rightarrow 3^3He$ accompanied by neither target fragments of the nucleus target nor charged mesons is identified. This paper provides a framework for further accumulation of statistics and for a detailed analysis of ^{9}C interactions.

Acknowledgements We are very grateful to the JINR Nuclotron staff for the enthusiastic work and friendly cooperation in this experiment. The authors express their particular gratitude to the JINR staff member A. M. Sosulnikova for a large and careful work on visual scanning of emulsions. This work was supported by grants – 96-1596423, 02-02-164-12a, 03-02-16134, 03-02-17079, 04-02-17151 and 04-02-16593 of Russian fund for basic researches, grants VEGA #1/2007/05 and #1/0080/08 of Agency Science of Ministry of Education of the Slovak Republic and the Slovak Academy of Sciences, as well as grants of plenipotentiaries of Bulgaria, Slovakia, the Czech Republic and Romania in 2002–2008.

References

1. G. Baroni et al., Nucl. Phys., A **516**, (1990) 673–714
2. G. Baroni et al., Nucl. Phys., A **540**, (1992) 646–658
3. N.P. Andreeva et al., Phys. At. Nucl., **68**, (2005) 455–476; arXiv:nucl-ex/0605015
4. V.V. Belaga et al., Phys. At. Nucl., **58**, (1995) 1905–1911
5. M.I. Adamovich et al., Phys. At. Nucl., **62**, (1999) 1378–1388
6. D.A. Artemenkov et al., Phys. At. Nucl., **70**, (2007) 1261–1265; arXiv:nucl-ex/0605018
7. T.V. Shchedrina et al., Phys. At. Nucl., **70**, (2007) 1230–1234; arXiv:nucl-ex/0605022
8. N.G. Peresadko et al., Phys. At. Nucl., **70**, (2007) 1266–1280; arXiv:nucl-ex/0605014
9. R. Stanoeva et al., Phys. At. Nucl., **70**, (2007) 1216–1221; arXiv:nucl-ex/0605013
10. D.A. Artemenkov et al., AIP Conf. Proc., **912**, (2007) 78–87; arXiv:0704.0384
11. Webs sites of the BECQUEREL Project http://becquerel.jinr.ru and http://becquerel.lhe.jinr.ru
12. P.A. Rukoyatkin et al., Czech. J. of Phys., Supplement **C56**, (2006) 379–384

A Precision Measurement of the Neutral Pion Life Time: Updated Results from the PrimEx Experiment

I. Larin
on behalf of PrimEx Collaboration

Abstract The PrimEx detector has been built for high precision measurement of the neutral pion lifetime via the Primakoff effect. PrimEx physics data have been collected during October 2004 run at Jefferson Lab. Detailed study of systematics performed during this year allowed to estimate systematic error more precise. The extracted preliminary result for the π^0 radiative decay has 2.1% statistical and 1.6% systematic error.

Keywords: Neutral pion life time

1 π^0 life time measurements

Width of the $\pi^0 \to \gamma\gamma$ decay is one of the most precise low energy QCD calculations. In the massless u- and d-quarks limit (so-called Leading Order approximation) it is equal to 7.725 eV. More detailed calculations give 7.92 ± 0.12 eV (QCD sum rule, [1]) and 8.10 ± 0.10 eV (chiral theory with u- and d-quark non zero masses taken into account – Next to Leading Order calculations, [2]). Simple ratio gives connection between π^0 lifetime (τ) and $\pi^0 \to \gamma\gamma$ decay width: $\Gamma(\pi^0 \to \gamma\gamma) = \frac{\hbar}{\tau} \times Br(\pi^0 \to \gamma\gamma)$, where $Br(\pi^0 \to \gamma\gamma)$ is well known decay branching ratio, close to 1. Therefore π^0 lifetime and $\pi^0 \to \gamma\gamma$ decay width measurements are almost equivalent.

The most straightforward way to measure π^0 lifetime is decay length measurement. Since it's very small (tens of microns at hundred GeV for decaying π^0 energy), this measurement is technically complicated. Nevertheless such a measurement has been performed [3] and has the smallest error reported so far ($\sim$3%). Other methods are utilizing π^0 production in $\gamma\gamma$ reaction. Measurement of differential cross section

I. Larin
Alikhanov Institute for Theoretical and Experimental Physics, Moscow, Russia,
e-mail: larin@itep.ru

V. Begun et al. (eds.), *Progress in High-Energy Physics and Nuclear Safety*,

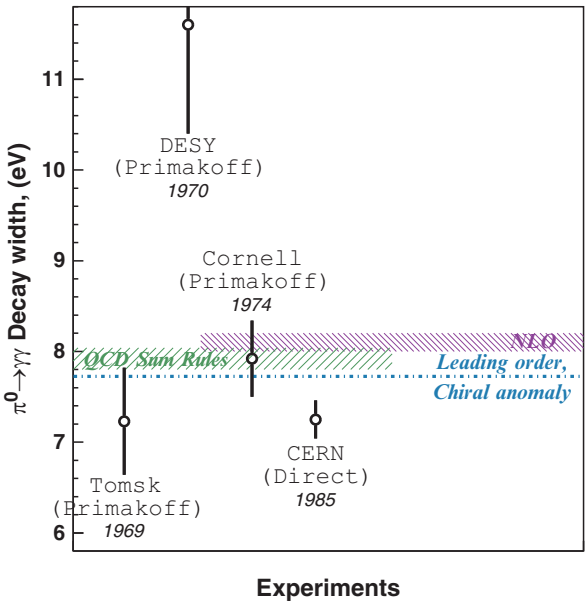

Fig. 1 Measurements of $\Gamma(\pi^0 \to \gamma\gamma)$ (with shown year of result publication) which have been made before the PrimEx experiment. Dotted line and dashed bands represent theory calculations

of such a reaction allows to calculate $\pi^0 \to \gamma\gamma$ decay width. The most "popular" method is the Primakoff production [4] in Coulomb field of nucleus and γ beam. Many experiments conducted in 1960s – 1970s ([5–9]) have used the Primakoff effect. They have utilized untagged photon beam and mostly lead glass calorimetry for γ from π^0 decay detection. Figure 1 represents theory calculations and experimental measurements of $\Gamma(\pi^0 \to \gamma\gamma)$ which have been done before PrimEx. Averaged $\Gamma(\pi^0 \to \gamma\gamma)$ measured value has $\sim$7% error and quite large scale factor $S = 3$ [10].

2 The PrimEx experiment

The PrimEx experiment [11] has been planned as a high precision $\Gamma(\pi^0 \to \gamma\gamma)$ measurement via the Primakoff effect. PrimEx has collected first π^0 photoproduction data in 2004. This advanced precision experiment is utilizing tagged photon beam with well known (at 1% level) flux and high resolution hybrid ($PbWO_4$ with lead glass outer part) electromagnetic calorimeter [12]. Schematic view of PrimEx setup is given on Fig. 2. PrimEx is using ^{12}C and ^{208}Pb high purity monoisotopic targets for π^0 production with 5% rad. length thickness [13]. Pair spectrometer magnet deflects charged component produced in the target so it can not hit calorimeter. A fraction of charged component (mostly e^+e^- pairs) hits PS counters which are serving as an additional beam flux monitor. Calorimeter with VETO system is placed 7.3 m

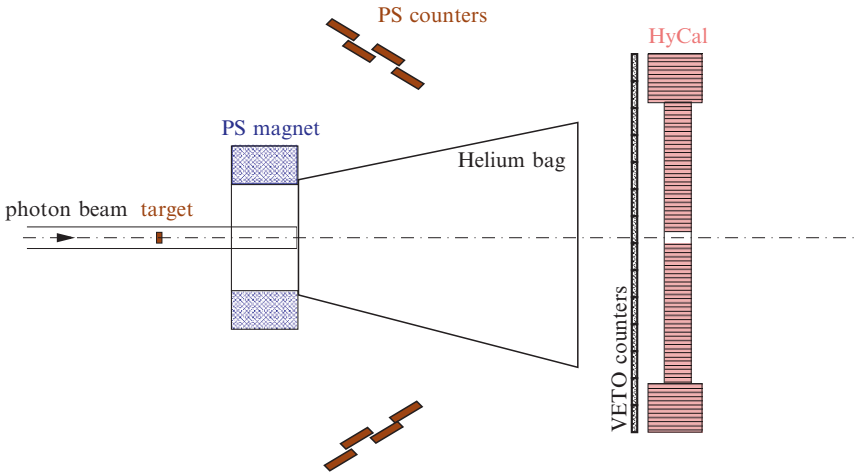

Fig. 2 PrimEx setup

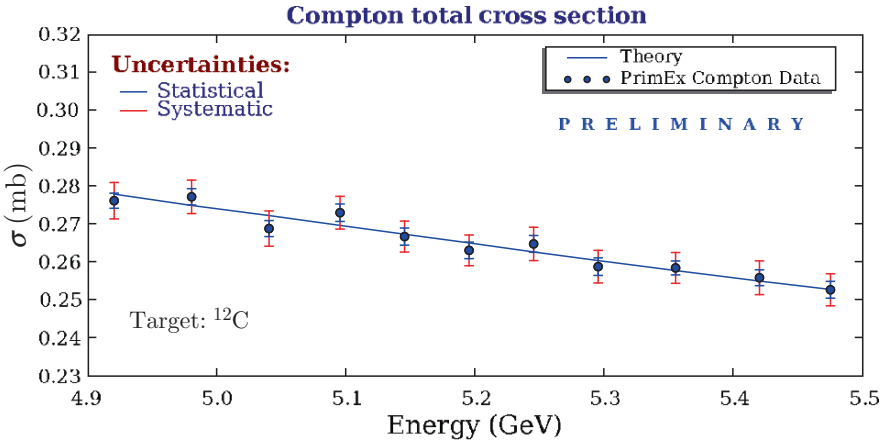

Fig. 3 Measured Compton cross section vs photon energy. QED calculation given as a solid line

downstream the target. Helium bag serves to reduce a number of beam interactions after vacuum pipe. Charged background from beam interactions after the magnet, is monitored by VETO hodoscopes.

To test PrimEx ability to high precision cross section measurements well calculable QED reactions of compton scattering and pair productions have been used as a calibration reactions. Good agreement between theory and measurement within the experimental error of 1.5–2 % have been achieved. Figure 3 shows as an example measured Compton cross section on carbon per electron as a function of photon energy and the theory calculations.

Measured elastic π^0 yield (Fig. 4) has been used to extract $\Gamma(\pi^0 \to \gamma\gamma)$ value.

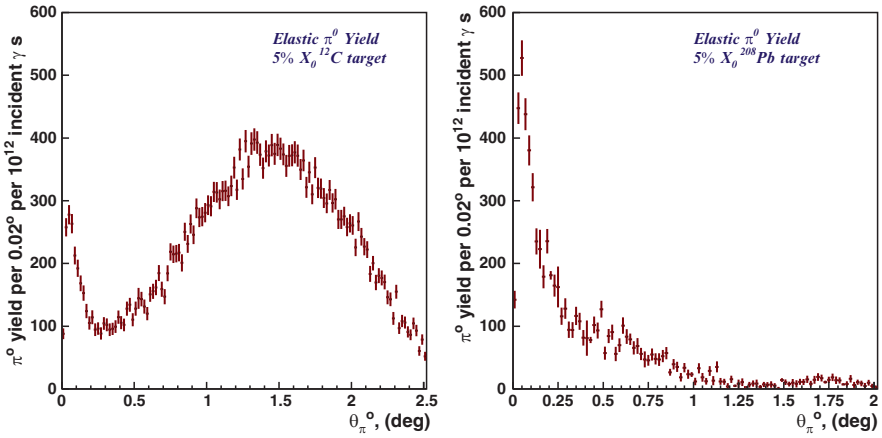

Fig. 4 Extracted elastic π^0 yield for Carbon and Lead target vs production angle

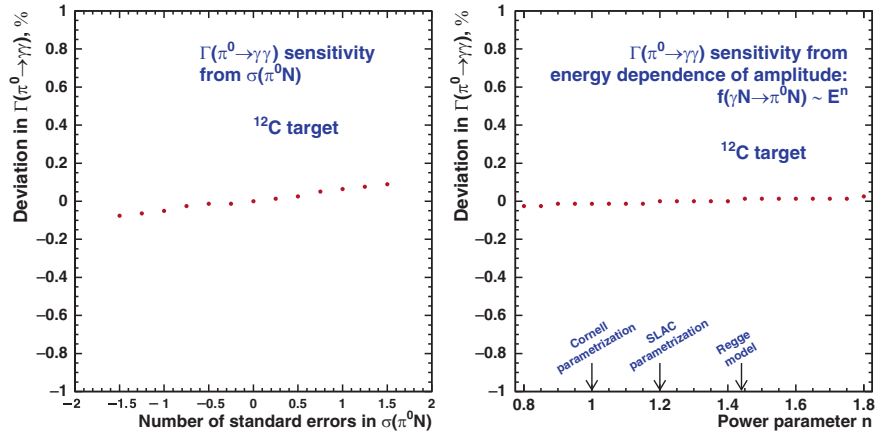

Fig. 5 $\Gamma(\pi^0 \to \gamma\gamma)$ sensitivity from pion-nucleon interaction cross section (left plot) and strong photoproduction amplitude dependence on energy power parameter

Extensive work has been performed during past year in model dependence of extracted value study. It allowed to estimate contribution to the final result systematic error from model parameters uncertainty – 0.25% (see Table 1). The following figures show examples of such estimations. Figure 5 (left plot) shows deviation (in percent) of $\Gamma(\pi^0 \to \gamma\gamma)$ value from uncertainty of pi0-nucleon interaction cross section $\sigma(\pi N)$ (in number of standard deviations from averaged value). The right plot (Fig. 5) shows deviation of $\Gamma(\pi^0 \to \gamma\gamma)$ from parameter n in strong amplitude of π^0 photoproduction (describing its dependence from photon energy $A_{strong} \sim k^n$). Values $n = 1$ and $n = 1.2$ have been used in different independent approaches.

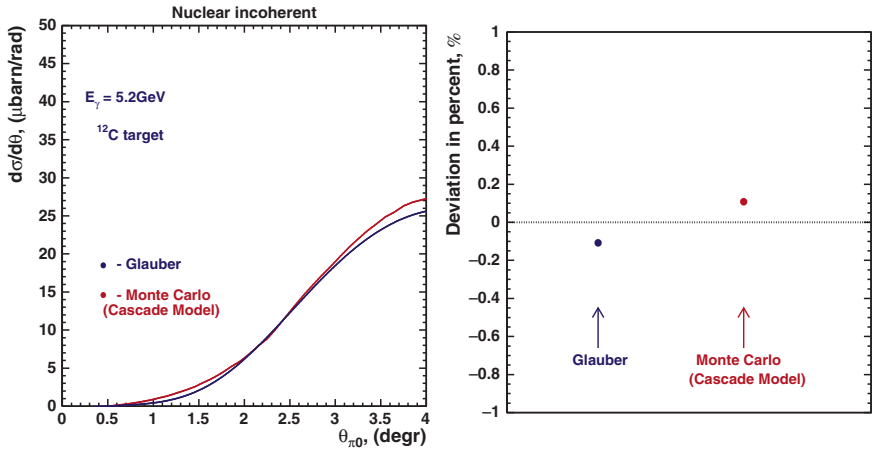

Fig. 6 Incoherent π^0 photoproduction differential cross section for two models [14] and [15] (left plot). $\Gamma(\pi^0 \to \gamma\gamma)$ sensitivity from incoherent model selection (right plot)

Table 1 Systematic error budget for $\Gamma(\pi^0 \to \gamma\gamma)$ (Preliminary)

Contributions	Errors
Photon beam flux	0.97%
Target number of atoms and absorption	0.07%
π^0 yield extraction	1.0%
Calorimeter response function	0.5%
Beam geometry parameters	0.4%
Setup acceptance	0.3%
Model errors (theory)	0.25%
Physics background (ω, ρ)	0.24%
π^0 Branching ratio (PDG)	0.03%
Total	1.6%

Two different models have been used to calculate incoherent π^0 photoproduction [14, 15]. Figure 6 shows differential cross section for them (left plot) and difference for extracted $\Gamma(\pi^0 \to \gamma\gamma)$ (in percent, right plot).

PrimEx result for $\Gamma(\pi^0 \to \gamma\gamma)$ is expected to be within 7.7 eV–7.9 eV range and will be finalized with next few months. Preliminary result has 2.1% statistical and 1.6% systematic error. Systematic error budget is given in detail in the Table 1.

3 Conclusion

A new precision experiment has been performed in 2004 at Jefferson Lab to test fundamental QCD prediction. It has utilized the high resolution tagging facility and the new state of the art hybrid calorimeter. Systematic errors are controlled by Compton

and pair production cross section measurements at 1.5% level. Preliminary result for $\Gamma(\pi^0 \to \gamma\gamma)$ has 2.1% statistical and 1.6% systematic errors. $\Gamma(\pi^0 \to \gamma\gamma)$ value will be finalized in the next few months and is expected to be within 7.7–7.9 eV range. An extension of PrimEx experiment was recently approved by Jefferson Lab Program Advisory Committee (PAC) to facilitate achieving 1.4% precision.

References

1. B.L. Ioffe, A.G. Oganesian, Phys. Lett. **B647** 389 (2007) [arXiv:hep-ph/0701077]
2. J.L. Goity, A.M. Bernstein, J.F. Donoghue, B.R. Holstein, Phys. Rev. **D66** 076014 (2002)
3. H.W. Atherton et al., "Direct Measurement of The Lifetime of The Neutral Pion", Phys. Lett. **B158** 81 (1985)
4. H. Primakoff, Phys. Rev. **81** 899 (1951)
5. G. Bellettini, C. Bemporad, P.L. Braccini, L. Foá, Nuovo Cimento **40**, 1139 (1965)
6. M. Braunschweig, W. Braunschweig, D. Husmann, K. Lübelsmeyer, D. Schmitz, Phys. Lett. **B26** 405 (1968)
7. V.I. Kryshkin, A.G. Sterligov, Yu.P. Usov, "Measurement of π^0 lifetime", ZhETF **57** 1917 (1969)
8. G. Bellettini et al., "A new measurement of the pi0 lifetime through the primakoff effect in nuclei" Nuovo Cimento **A66**, 243 (1970)
9. A. Browman, J. DeWire, B. Gittelman, K.M. Hanson, D. Larson, E. Loh, R. Lewis, "The Decay Width of the Neutral π-Meson", Phys. Rev. Lett. **33** 1400 (1974)
10. W.-M. Yao et al. (Particle Data Group), J. Phys. **G33** 540 (2006)
11. PrimEx Collaboration, "Primex Conceptual Design Report", PrimEx Note, (2000) http://www.jlab.org/primex/primex_notes/PrimEx_CDR.ps
12. M. Kubantsev, I. Larin, A. Gasparian, "Performance of the PRIMEX Electromagnetic Calorimeter", *Proc. of conf. "Calor 2006", Chicago, 2006*
13. P. Martel et al., "Nuclear Targets for a Precision Measurement of the Neutral Pion Radiative Width" arXiv:0811.2132 [nucl-ex]
14. S. Gevorkyan et al., "Incoherent Photoproduction of π^0 Mesons off Nuclei", PrimEx Note, (2007) http://www.jlab.org/primex/primex_notes/inc.pdf
15. T. Rodrigues, "Incoherent π^0 photoproduction in the PrimEx kinematics via the MCMC intranuclear cascade model", PrimEx Note, (2007) http://www.jlab.org/primex/primex_notes/PrimEx_Note_52.pdf

New Heavy Gauge Boson Searches with CMS

M. Malberti, on the behalf of the CMS Collaboration

Abstract New heavy gauge bosons, like W' and Z', are foreseen by several extensions of the Standard Model. The large luminosity and center of mass energy available at the LHC will allow to probe such bosons with masses above 1 TeV already in the very first period of data taking. Here the sensitivity to searches for new gauge bosons with the CMS experiment is discussed. These studies are based on detailed detector simulation with realistic start up conditions and are focused on possible early discoveries. The expected CMS discovery/exclusion potential as a function of luminosity is presented as well.

Keywords: Gauge bosons, BSM

1 Introduction

The Standard Model (SM) successfully describes the fundamental fermions and their interactions through gauge bosons. However, far to be considered a complete theory, it leaves many open questions (e.g. the naturalness and hierarchy problem, the dark matter problem...), for which a number of models, introducing new symmetries, new interactions or new dimensions, have been proposed. New heavy neutral (Z') or charged (W') gauge bosons appear in several extensions of the Standard Model, such as Left-Right Symmetric Models (LRSM) [1], E_6 based GUTs (giving rise to Z'_ψ, Z'_ξ, Z'_η) [2], Little Higgs Models [3], Extra Dimensions [4]. Moreover, the Altarelli Reference Model [5], also known as Sequential Standard Model (SSM), is often considered as a benchmark by experimentalists: in this model, the new heavy gauge bosons $Z'(W')$ are considered as heavy carbon copy of the corresponding SM ones, $Z(W)$, with the same coupling constants.

M. Malberti
INFN Milano-Bicocca, Piazza della Scienza 3, I-20126, Milano, Italy,
e-mail: martina.malberti@mib.infn.it

V. Begun et al. (eds.), *Progress in High-Energy Physics and Nuclear Safety*,

Current limits by the Tevatron experiments CDF and D0 exclude new heavy gauge bosons up to about 1 TeV, depending on the model assumed. At the Large Hadron Collider (LHC), the large luminosity (10^{34} cm^{-2} s^{-1} designed luminosity, and $\sim 10^{32}$ cm^{-2}s^{-1} in the initial phase) and the large center of mass energy of 14 TeV will allow a good potential for new gauge bosons searches already with the very first data, i.e. with luminosity of the order of 100 pb^{-1}. In this paper the discovery potential of the Compact Muon Solenoid (CMS) experiment is discussed. The central feature of CMS is a superconducting solenoid, providing a 4 T magnetic field. Both the inner tracker and the calorimeters are contained within the solenoid. The tracker consists of silicon pixel and strip detectors. The electromagnetic calorimeter (ECAL) is made of $PbWO_4$ scintillating crystals and it is surrounded by a brass/scintillator sampling hadron calorimeter. Muons are measured in gas chambers embedded in the iron return yoke. Besides the barrel and endcap detectors, CMS has extensive forward calorimetry. A detailed description of the CMS experiment can be found in [6].

The discussion is focused on analyses based on detailed simulations of the CMS detector, assuming realistic start-up calibration and alignment conditions. Emphasis is given to analysis strategies relevant for an early data-taking.

2 Events selections and backgrounds in leptonic searches

Leptonic channels $Z' \to l^+l^-$ and $W' \to l\nu$, with electrons or muons in the final state, provide the cleanest signatures for new gauge bosons searches at hadron colliders.

2.1 $Z' \to l^+l^-$ signature and backgrounds

$Z' \to l^+l^-$ events are characterized by two high (O(TeV)) transverse momentum leptons with opposite charge. $Z' \to e^+e^-$($Z' \to \mu^+\mu^-$) are selected by requiring events passing an electron (muon) trigger and two well reconstructed and isolated electrons (muons) within the detector acceptance, $|\eta| < 2.5$ for electrons and $|\eta| < 2.4$ for muons [7,8]. The main background is represented by SM Drell-Yan events, while minor contributions come from $t\bar{t}$, W+jets, γ+jets, as shown in Fig. 1.

Table 1 summarizes the production cross section times the branching ratio of $Z' \to e^+e^-$ for two different values of the SSM Z' mass and the corresponding number of events expected within the detector acceptance for an integrated luminosity of 100 pb^{-1}.

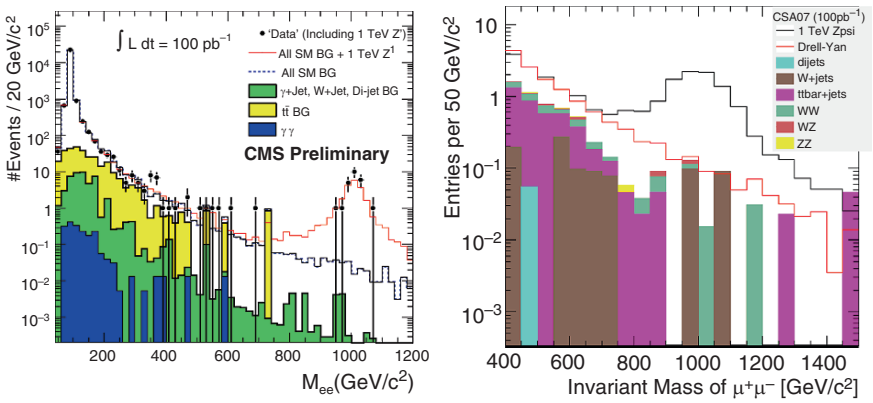

Fig. 1 Invariant mass distribution for a $Z' \rightarrow ee$ (left) and $Z' \rightarrow \mu\mu$ (right) with M = 1 TeV. The main backgrounds from Standard Model processes are also shown

Table 1 Production cross section times branching ratio for $pp \rightarrow Z' \rightarrow e^+e^-$ and number of events expected in 100 pb^{-1} with both leptons within the detector acceptance

SSM Z'	M = 1000 GeV	M = 2000 GeV
$\sigma\times$ BR (fb)	458	20
n. of events in 100 pb^{-1} with 2 electrons in $\lvert\eta\rvert$ <2.5	38	1.8
Drell-Yan background	**M > 600 GeV**	**M > 1600 GeV**
$\sigma\times$BR (fb)	50	0.76
n. of events in 100 pb^{-1} with 2 electrons in $\lvert\eta\rvert$ <2.5	4	0.07

2.2 $W' \rightarrow l\nu$ signature and backgrounds

$W' \rightarrow l\nu$ events present a straightforward signature, with one high p^T lepton and missing transverse energy (MET) due to the neutrino; moreover, as the boson transverse momentum is expected to be small, the lepton and the MET are almost balanced in the transverse plane. This signature is identical to the SM $W \rightarrow l\nu$ one, that represents an irreducible background. Other sources of backgrounds, giving much smaller contributions, are $t\bar{t}$, Drell-Yan, di-bosons and di-jet events in which one jet is misidentified as a lepton and the other is mismeasured giving rise to missing transverse energy. Beyond the trigger and lepton identification requirements, two dedicated selections can be applied in order to enhance the signal in the high p^T region. They exploit the W' kinematics: the angle between the lepton and the MET has to be close to 180° and their transverse energy must be balanced (this is accomplished by requiring $0.5 < E_l^T/MET < 1.5$). The transverse mass spectrum ($M^T = \sqrt{2E_l^T E_\nu^T(1-cos\phi_{l-MET})}$, where ϕ_{l-MET} is the angle between the lepton direction and the MET direction in the transverse plane) of the lepton–neutrino pair is shown in Fig. 2 for the electron channel, normalized to an integrated luminosity of 100 pb^{-1} [9].

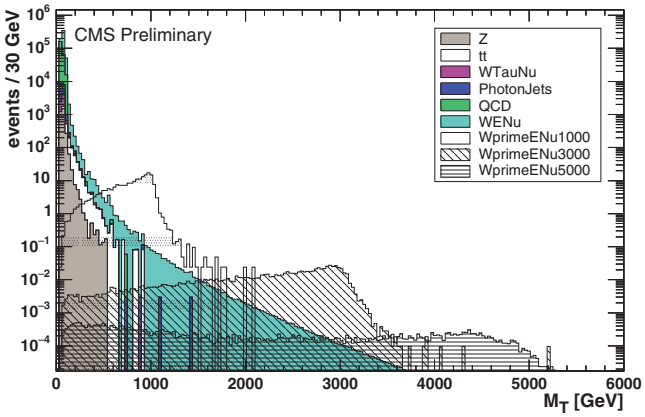

Fig. 2 Transverse mass distribution of $W' \to e\nu$ events for three different W' mass values and main backgrounds

3 Electron and muon reconstruction at high energies

The reconstruction of electrons and muons at high energies presents several experimental issues. Electrons are reconstructed as energy deposits in the electromagnetic calorimeter linked to a track in the tracker. The identification criteria, based on the shape of the electromagnetic shower, track matching and isolation, are robust against start-up conditions and are optimized for high energy electrons, in order to keep a high efficiency ($\sim$80%) and to guarantee a low rate of jets faking electrons.

An important issue related to the energy measurement at very high energy is related to the saturation of the ECAL electronics, that occurs for energy deposits of 1.7 TeV (3 TeV) in one single crystal in the barrel (endcaps). The energy can be, however, efficiently recovered by using the energy deposits in the crystals surrounding the saturated one, with a resolution of about 10% for 1 TeV electrons [10].

Concerning the muon reconstruction, the Muon System and Tracker alignment plays an important role, because it has a large impact on the mass resolution: for a 1 TeV (2 TeV) Z', the mass resolution is 7–8% (10%) for a misalignment scenario corresponding to 100 pb^{-1} [8], nearly doubled with respect to ideal conditions (Fig. 3). Misalignment doesn't affect efficiency, which is around 94% for di-muons.

There are two important issues that are specific of the TeV muon reconstruction: the first is the low bending in the magnetic field at such high energies that requires a very precise measurement of the position, and the second one is the high probability of bremsstrahlung. Dedicated algorithms have been developed in order to get the best performances in terms of efficiency and resolution.

Lepton reconstruction and identification efficiencies will be measured using the so called "Tag and probe" method [11], which exploits Drell-Yan events: in events containing two electron (muon) candidates, one lepton is reconstructed with tight criteria and used as "tag", the second one is identified as "probe"; in this way, a sample of high purity probes can be selected and used to measure efficiencies. In

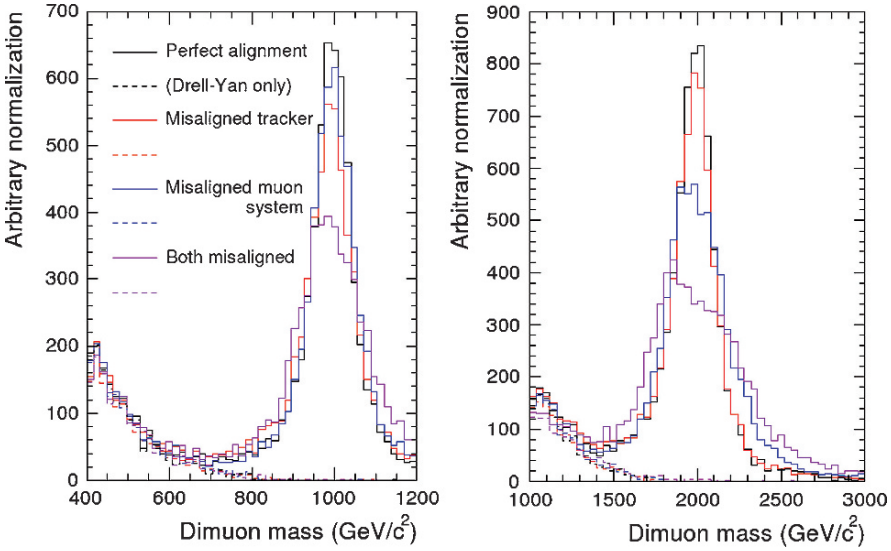

Fig. 3 Di-muon Invariant mass spectra for 1 TeV and 2 TeV SSM in different alignment conditions

the case of high energy leptons, the method will be applied in two different mass regions: at the Z pole (in a region 70 GeV $<$ M(ll) $<$ 110 GeV) and in the high invariant mass range (e.g. M(ll) $>$ 200 GeV). The first one, thanks to the tight mass cut, is characterized by high purity, but allows to probe lepton transverse momentum ranges only up to about 150 GeV and requires a MC based extrapolation to high energies; the second one, on the contrary, covers higher momentum ranges, but is affected by larger backgrounds. Both will be used for cross checks and to reduce systematic errors.

4 Background determination and uncertainties

New heavy gauge boson searches are characterized by small SM backgrounds, that anyway must be understood carefully in order to establish the significance of events found in the signal region. It is desirable, especially in a start-up scenario, to determine backgrounds from the data themselves whenever possible. In particular, data driven techniques have been studied for $t\bar{t}$ and QCD background.

The $t\bar{t}$ background can be determined with two approaches: one is the b-tag method, exploiting events containing exactly one b-tagged and two b-tagged jets, in order to measure simultaneously the b-tagging efficiency and the total number of $t\bar{t}$ events; the second one is the e-μ method, exploiting events with one electron and one muon, with appropriate corrections for acceptances and electron/muon efficiencies [7]. These methods have been tested on simulated datasets containing signal and background events, showing a good agreement between the extracted number of $t\bar{t}$ events and the one expected from the simulation (Fig. 4).

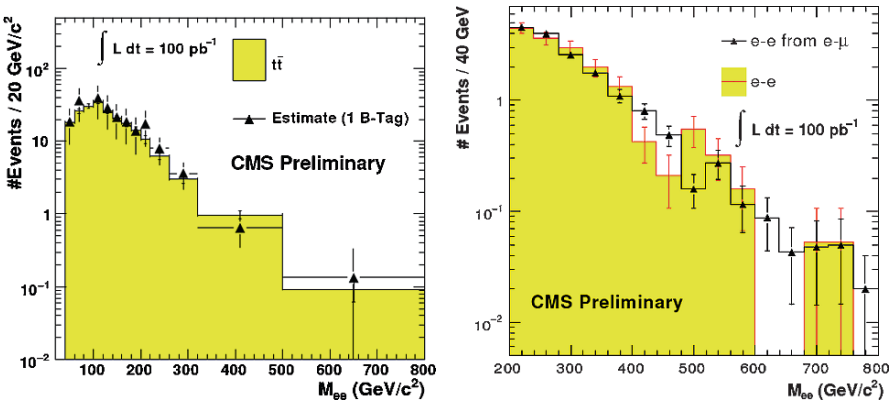

Fig. 4 $t\bar{t}$ background to $Z' \rightarrow ee$ events estimated using the b-tag method (left) and the $e - \mu$ method (right)

The QCD background, is almost negligible, but can be controlled using different techniques. For $Z' \rightarrow ee$ events, it can be obtained by measuring the lepton fake rate, i.e the probability that a jet fakes a lepton, on jet triggered events. In the case of $Z' \rightarrow \mu\mu$ searches, the use of same-sign di-leptons has been considered, exploiting the fact that no charge correlation between two lepton candidates is expected in events containing jets faking electrons. In $W' \rightarrow e\nu$ searches, a technique already applied at Tevatron, has been investigated: it uses a sample of non-isolated electrons and normalizes the transverse mass spectrum in the low, background dominated, transverse mass region.

SM Drell-Yan and W events , which constitute the most important and irreducible backgrounds to Z' and W' respectively, will be controlled by normalizing the simulation to the Z peak or W transverse mass peak. Several theoretical uncertainties have been considered, like PDFs (see Fig. 5), renormalization and factorization scales, higher order QCD and QED corrections [7, 8].

5 Expected significance and exclusion limits

The CMS experiment is expected to have a very good potential for searches of new neutral gauge bosons even with low integrated luminosities. A discovery, in the di-electron or di-muon channel, is possible up to masses of about 1.5 TeV for a SSM Z' and 1.2 TeV for a Z'_{ψ} with an integrated luminosity of 100 pb^{-1} (Fig. 6).

The $W' \rightarrow e\nu$ discovery sensitivity is shown in Fig. 7 and indicates that a discovery is possible up to W' masses of about 2.2 TeV with an integrated luminosity of 100 pb^{-1}. Systematic effects such as uncertainties on the detector calibration (2% on the electron energy scale, 10% on the MET), backgrounds (10%), luminosity (10%) and PDFs (10%) are taken into account. In case no discovery is possible, an

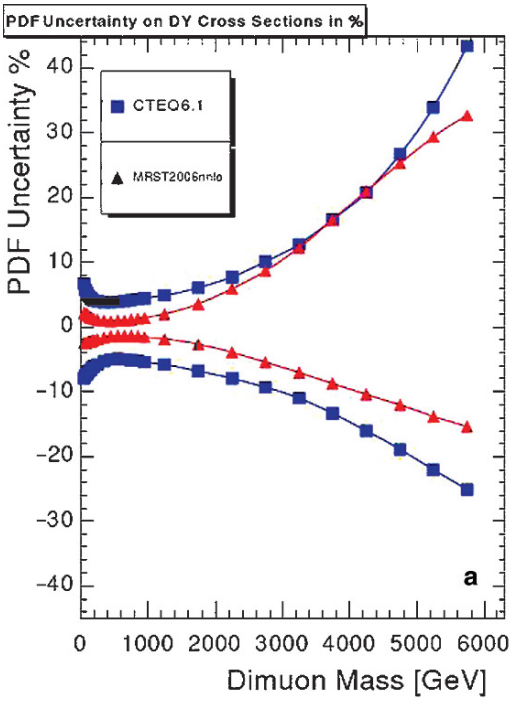

Fig. 5 PDF uncertainties on the absolute Drell–Yan cross section as a function of the di-muon mass [8]

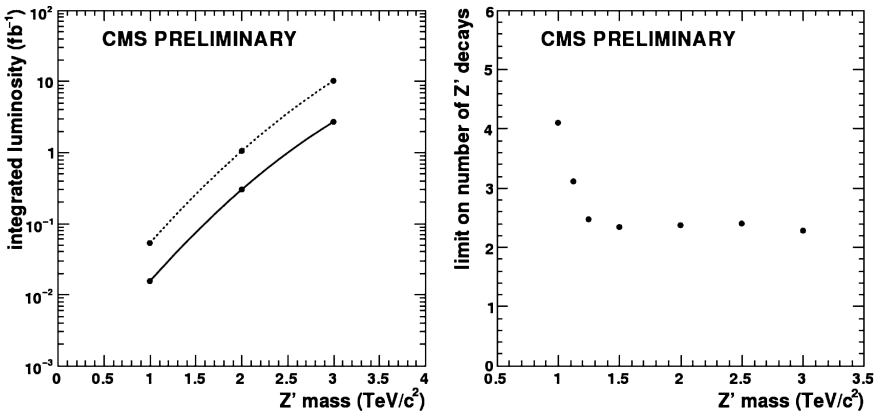

Fig. 6 Left: Integrated luminosity needed to reach a 5σ significance in the electron channel as a function of resonance mass for two different models, Sequential Standard Model (full line) and Z'_{ψ} (dashed line). Right: Expected 95% CL limit on the number of events as a function of the resonance mass

exclusion limit can be set up to W' masses of about 2.5 TeV with 100 pb^{-1}. For comparison the current best limit from the D0 experiment in the electron channel is 1 TeV with about 1 fb^{-1} [12]. Increasing the integrated luminosity up to 100 fb^{-1}, the CMS exclusion potential rises up to about 4.5 TeV (Fig. 8).

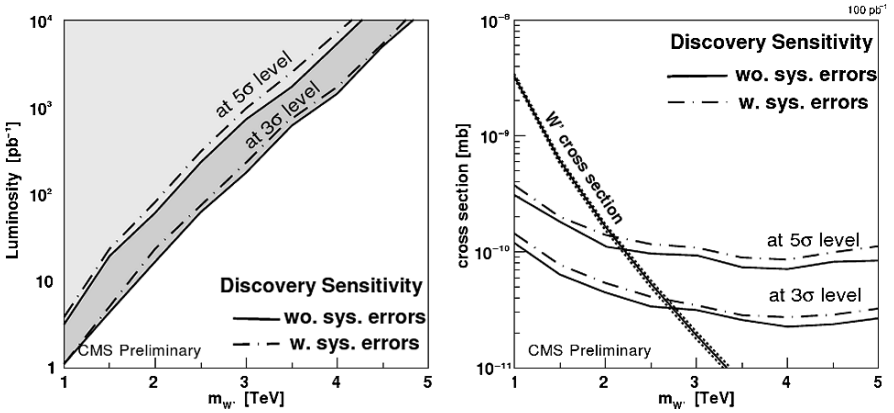

Fig. 7 Discovery potential of $W' \rightarrow e\nu$ as a function of the mass and of the integrated luminosity

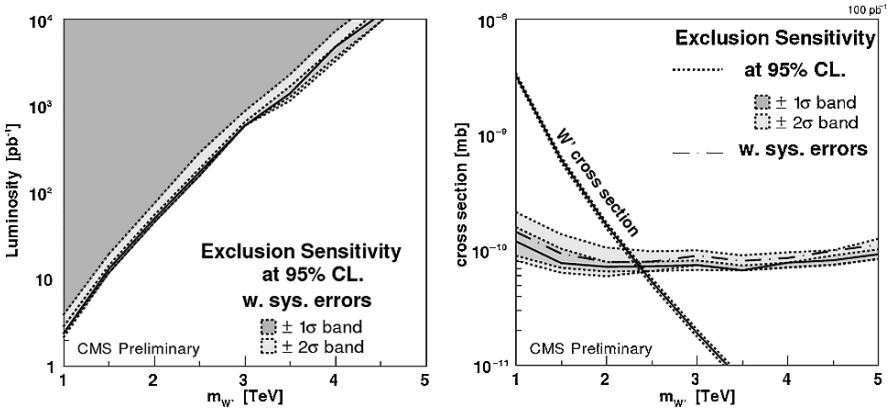

Fig. 8 Exclusion sensitivity as a function of the mass and of the integrated luminosity

6 Searches in the di-jets channel

Beyond leptonic searches, searches involving jets measurements are feasible. Di-jet events are sensitive to new physics and, for example, the di-jet ratio has been found to be a useful observable to search for the evidence of a new resonance [13]. The di-jet ratio is defined as the ratio between the number of di-jet events with $|\eta| < 0.7$ and the number of events with $0.7 < |\eta| < 1.3$. Spin 1 gauge bosons, as well as other spin 1/2 or spin 2 resonances, have more isotropic angular decays than QCD (Fig. 9–left) and the di-jet ratio is larger than for QCD events. Figure 9 shows the di-jet ratio as a function of the di-jet mass: a signal can be observed with 100 pb^{-1} for masses around 2 TeV, while with higher integrated luminosities the di-jet ratio is expected to be useful in order to determine the resonance spin.

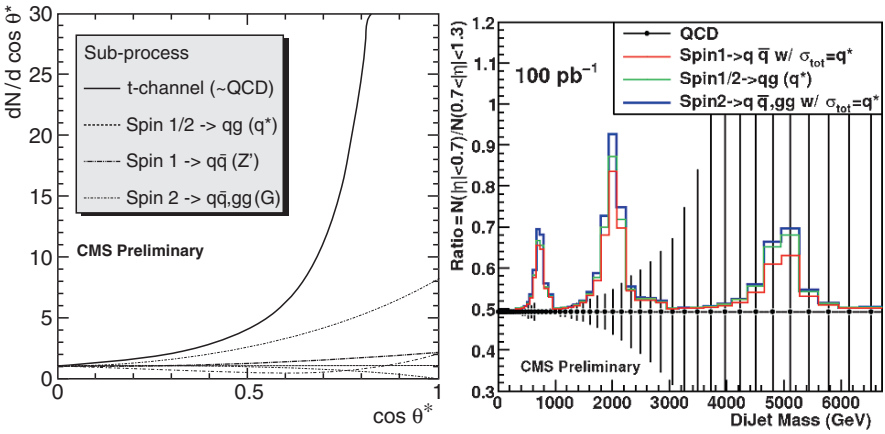

Fig. 9 Left: angular distribution of resonances compared to the angular distribution of QCD events. Right: Di-jet ratio as a function of di-jet mass

7 Conclusions

The potential of the CMS experiment for new heavy neutral or charged gauge bosons searches has been presented. Analysis strategies have been defined to be ready for real data, including realistic start-up detector conditions. A good sensitivity, probing the region above 1 TeV, is reachable already with integrated luminosities of about 100 pb^{-1}.

References

1. R.N. Mohapatra and J.C. Pati, Phys. Rev. **D11** (1975) 566–571
2. R.N. Mohapatra, *Unification and supersimmetry*, Springer (2003)
3. T. Han, H.E. Logan, B. McElrath, L.-T. Wang, Phys. Rev. **D67** (2003) 095004
4. L. Randall and R. Sundrum, Phys. Rev. Lett. **83** (1999) 3370-3373, hep-ph/9905221
5. G. Altarelli, B. Mele and M. Ruiz-Altaba, Z. Phys. **C45** (1989) 109
6. CMS Collaboration, *Physics TDR volume I, The CMS Physics Technical Design Report Volume 1*, CERN-LHCC-2006-001 (2006)
7. CMS Collaboration, *Search for high mass resonance production decaying into an electron pair in the CMS experiment*, CMS PAS EXO-08-001 (2008)
8. CMS Collaboration, *Search for new high mass resonances decaying to muon pairs in the CMS experiment*, CMS PAS SBM-07-002 (2007)
9. CMS Collaboration, *Discovery potential of* $W' \rightarrow e\nu$ *at CMS*, CMS PAS EXO-08-004 (2008)
10. B. Clerbaux, S. Elgammal, T, Mahmoud and P. Marage, *Saturation and energy corrections for TeV electrons and photons*, CMS NOTE 2006-149 (2006)
11. CMS Collaboration, *Measuring electron efficiencies at CMS with early data*, CMS PAS EGM-07-001 (2007)
12. D0 Collaboration, arXiv:hep-ex/0710.2966v1 (2007)
13. CMS Collaboration, *CMS search plans and sensitivity to new physics using dijets*, CMS PAS SBM-07-001 (2007)

CMS Tracker Upgrade Issues and Plans: A Short Review

S. Mersi, on behalf of the CMS Tracker Collaboration

Abstract The consolidation and upgrade of the LHC accelerators complex is expected to yield a progressive increase in peak luminosity $\mathscr{L}$, exceeding the value of $\mathscr{L} = 10^{34}\,\mathrm{cm}^{-2}\,\mathrm{s}^{-1}$ (original design figure) after about 5 years of operation, to eventually reach values close to $\mathscr{L} = 10^{35}\,\mathrm{cm}^{-2}\,\mathrm{s}^{-1}$ (the so-called Super-LHC). All the experiments will have to make some upgrades to be able to operate at Super-LHC. This article makes a short review of the CMS tracker sub-detector research activities in this direction: we will show the time framework of the evolution plan of LHC, what are the limiting factors of the present-day detector and which requirements come from the luminosity upgrade. We will also describe the main results of the research activities already in place in the field of: sensors, power supply, cooling, layout design and simulations.

Keywords: CMS, LHC, upgrade luminosity, Super-LHC, tracker, sensors, cooling, simulations

1 The LHC upgrade

The Large Hadron Collider (LHC) project just started its operations, with the first beam circulating on September 10, 2008. No collision was achieved yet at the tine of writing of this article, so it is difficult to foresee the outcomes of its first years of life. Nevertheless, it is already possible to sketch the main steps of its future evolution: the nominal luminosity of $10^{34}\ \mathrm{cm}^{-2}\ \mathrm{s}^{-1}$ will be reached after some upgrades of the machine. These will require about 5 years, during which the accelerator complex will be tuned and the experiments will optimize their performance and collect physics data corresponding to a integrated luminosity of a few hundreds of fb^{-1}.

S. Mersi
European Organization for Nuclear Research (CERN), CH-1211 Genève 23 Switzerland,
e-mail: stefano.mersi@cern.ch

V. Begun et al. (eds.), *Progress in High-Energy Physics and Nuclear Safety*,

If the LHC will then undergo no major upgrade the integrated luminosity delivered to the experiments would be around 1,000 fb^{-1} by 2019 but then it will be difficult to increase significantly the collected statistics in the time framework of this project. For this reason it was proposed a luminosity upgrade in order to further exploit this accelerator [11], with a target figure of $\mathscr{L} = 10^{35}\,\text{cm}^{-2}\,\text{s}^{-1}$ to be achieved around 2016–2017 (the so-called Super-LHC, or S-LHC).

The luminosity enhancement is foreseen to be achieved by increasing the number of interactions per bunch crossing, rather than the collision frequency: the commonly accepted upgrade scenario foresees a *decrease* of the bunch crossing frequency (from 40 to 20 MHz), with an increase of a factor 20 in colliding protons per event.

In this scenario, the experiments will have to modify (part of) their detectors to cope with the higher irradiation and particle density, to avoid sensor irradiation damage and signal pile-up.

2 Current CMS tracker

The silicon tracker [1, 2] is the innermost detector of CMS. It extends in the region of pseudo-rapidity[1] $|\eta| < 2.5$, radius $r < 120$ cm, length[2] $|z| < 270$ cm and it is completely based on silicon detectors, covering a surface of $\sim$200 m^2, the largest Si detector ever built. Its aim is to reconstruct the tracks and vertices of charged particles in the highly congested LHC environment.

The present tracker was designed to operate at luminosities up to about $\mathscr{L} = 10^{34}\,\text{cm}^{-2}\,\text{s}^{-1}$. Significant robustness and redundancy in the tracking capability was implemented in the detector layout, to ensure optimal performance for several years of operation (up to an integrated luminosity of about 500 fb^{-1}), with basically no maintenance/repairs, except for the innermost pixel vertex detector.

The key aspects to solve the tracking pattern recognition problem are a low cell occupancy and a large number of hits per track. To achieve these goals the tracker is structured in two distinct parts: a silicon pixel vertex detector and an outer silicon micro-strip tracker (see Table 1).

The pixel detector is composed of three barrel layers and two end-cap disks per side, and is quickly removable for beam pipe bake-out or replacement.

The Strip Tracker is composed of ten layers of detectors in the barrel region, four of which are double-sided and provide also the z-coordinate measurement. It comprises end-caps made of wedge-shaped detectors matching the types of the corresponding modules in the barrel region (see Fig. 1).

The low occupancy is obtained by using high granularity detectors, and fast primary charge collection, obtained using thin detectors operated with over-depleted

[1] Pseudo-rapidity η is defined as $\eta = -\ln\left[\tan\left(\frac{\theta}{2}\right)\right]$, with θ polar coordinate in the cylindric reference.

[2] Along the beam direction axis z.

Table 1 Some parameters of LHC and Super-LHC

	LHC	S-LHC
Peak luminosity	$\mathscr{L} = 10^{34}\,\mathrm{cm}^{-2}\,\mathrm{s}^{-1}$	$\mathscr{L} = 10^{35}\,\mathrm{cm}^{-2}\,\mathrm{s}^{-1}$
Integrated luminosity	$100\,\mathrm{fb}^{-1}$/year	$1\,000\,\mathrm{fb}^{-1}$/year
C.M. energy	14 TeV	14 TeV
Bunch crossing interval	25 ns	50 ns
# pp events / crossing	∼20	∼400
# particles in tracker	∼1 000	∼20 000

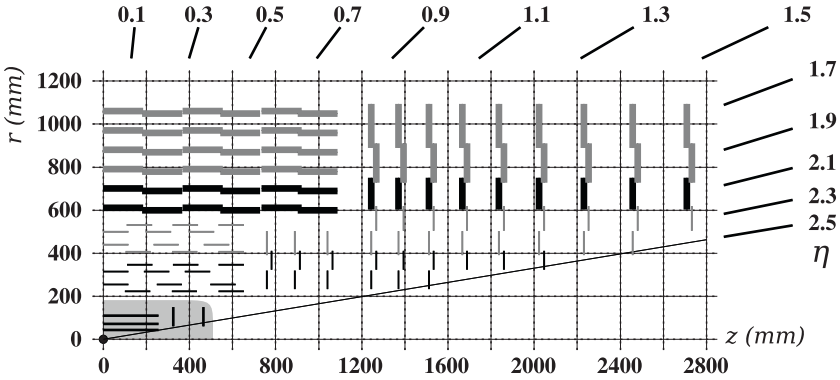

Fig. 1 Schematic view of a quarter of the CMS silicon tracker. The sensor position in the r,z plane is shown here. The inner grayed area is instrumented with pixel sensors. The outer strip tracker is build with single sided (gray) and double sided (black) detectors. Thin lines represent 300 μm-thick sensors, whereas the thick lines represent 500 μm-thick ones

silicon bulks and fast readout electronics. The redundancy is guaranteed by the overall design of the tracker, which allows to measure 10–14 points per track, depending on the pseudo-rapidity.

To reduce the effects of radiation damage and limit the leakage current, the silicon detectors, once irradiated, will be operated at -10°C and kept below 0°C also during maintenance.

Results from data collected with the real detector to date [3], during the assembly and commissioning phase, confirm that the detector is operational, with minor (nominal) inefficiencies.

The tracker is characterized by an excellent performance, according to the latest simulations [9], which make use of all the information coming from the construction tests and early data taking:

- Track reconstruction: An excellent track finding efficiency for single muons (details below), with a good fake rejection (high purity)
- Transverse momentum resolution: 0.5% in the barrel region and 3% in the endcap region for tracks with $p_{\mathrm{T}} = 10$–$100\ \mathrm{GeV}/c$
- Tagging and reconstruction of b jets, fundamental requirement for new physics studies ($\mathrm{H} \rightarrow \mathrm{b\bar{b}}$), for top quark physics and CP violation measurements, is also

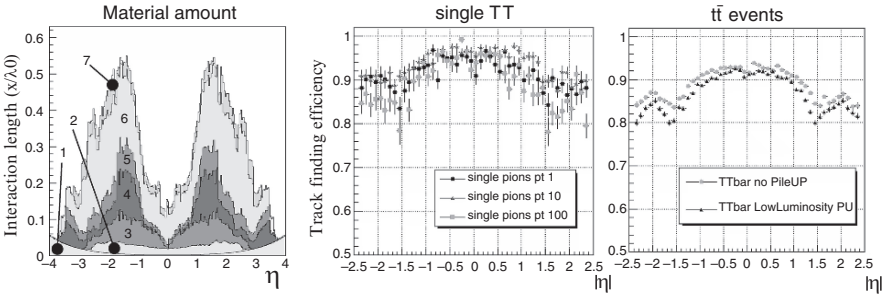

Fig. 2 *Left:* Material amount (in nuclear interaction lengths) break down by function: (1) Beam pipe, (2) Sensors, (3) Electronics, (4) Cables, (5) Cooling, (6) Support, (7) Other. *Center and Right:* Track reconstruction efficiency for single-π and in $t\bar{t}$ events. The drop in efficiency corresponds to material amount peak

based on the good secondary vertex reconstruction: 50–60 μm error in the transverse plane for $p_T = 1\ \mathrm{GeV}/c$, increased to 10 μm for $p_T = 100\ \mathrm{GeV}/c$

This performance is possible mainly because of a highly segmented detector, which both gives the high position resolution and a low occupancy, which is lowest in the pixel vertex detector ($\sim 10^{-4}$) and maximum in the inner layers of the strip tracker (where it reaches 3×10^{-2}).

The large amount of material affects the ultimate performance of the tracker itself (in particular in the momentum resolution at low p_T and the track reconstruction efficiency) as well as electron and photon detectability, and need to be improved in the new tracker design. That can be seen by comparing the track reconstruction efficiency for muons, which is found to be larger than 98% in the whole pseudo-rapidity range ($|\eta| < 2.5$), with that of pions, which is as low as 80% around $|\eta| \simeq 1.5$. Such behavior is due to the interaction of pions with the material present in the tracker, that peaks in the regions where the reconstruction efficiency is lowest, as shown in Fig. 2.

Although the material breakdown is somewhat arbitrary (as in the case of the ledges supporting the modules, which serve both as cooling contact and as supporting structures), we can see that the material is largely driven by the amount of conductors needed to bring in and out the large current ($\sim$15 kA) required to operate the front-end electronics, and by the need of removing the power dissipated ($\sim$40 kW inside the tracker volume) in a capillary way, to keep all silicon sensors below the temperature limits imposed by the high radiation environment.

3 Tracker upgrade goals and plans

The first upgrade of the LHC to deliver a higher luminosity is foreseen to happen in $\sim$2013. The following period of running is known as **Upgrade Phase I** and is foreseen to feature a luminosity ramp up to $\sim 2 \times 10^{34}\ \mathrm{cm}^{-2}\ \mathrm{s}^{-1}$.

The strip tracker is designed in such a way that it will be capable of sustain the increased particle flow, but the Pixel detector will need to be replaced, mainly because of the integrated radiation damage.

Thanks to a specific design requirement, the replacement of the pixel detector is feasible during a winter shutdown. The design and realization of a new detector allows to test new technologies and open the road for the next upgrade.

The "Phase I" Pixel will probably feature: a different pixel size, a fourth barrel layer and a third end-cap disk. It may also feature: a different sensor material (p-type bulk) and pixel size, larger read-out buffers, micro-twisted pair cables instead of Kapton® cables to reduce the amount of material, CO_2 cooling and a fourth barrel layer.

At peak luminosities much higher than $\mathscr{L} = 10^{34}\,\mathrm{cm}^{-2}\,\mathrm{s}^{-1}$ also the outer tracker will have to be upgraded, to enhance radiation hardness and granularity. Currently plans are being developed to build a new complete upgraded Tracker around 2018 for the so-called **Upgrade Phase II**.

3.1 Required features for the strip tracker upgrade phase II

For the phase II of the LHC upgrade there is almost no margin of improvement on the ϕ coordinate and momentum measurement precision of the strip tracker, but there are many requirements and constraints in the design. The main ones are mentioned below.

The new detector will have to cope with **higher particle density** ($\sim \times 20$), maintaining the present tracking and vertexing performance. This will certainly lead to a change of the sensor design, with a higher granularity (finer strip pitch, shorter strips), but it will also be possible to allow for a higher channel occupancy (from present $\sim$1% to $\sim$5%), as the present simulations show that an efficient tracking is still achievable with a slightly higher occupancy.

The sensors will have to withstand **higher radiation doses**, thus it is necessary to optimize the choice of sensor material (in details below in section 3.3). The ASICs will profit from new process technologies which were not accessible at the time when the present tracker was designed, with lower power consumption.

An important constraint is that the new tracker will have to **reuse most of the present services** (power cables, cooling pipes, readout and control optical fibers). This means, for example, that the total power supply current is limited and that the bandwidth of each data link must be increased. Such limits can be overcome implementing novel data links and powering schemes (section 3.4).

An additional requirement is the **reduction of the material** inserted in the tracker, in terms of radiation and interaction length, especially in the region around $\eta \simeq 1.5$ (as shown in section 2).

Finally, tracking information must be made available to the **Level-1 trigger**, in order to keep constant the trigger rate without loosing efficiency for physics channels (section 3.2)

While various groups are working to define feasibility and design principles of the components, and different options are proposed, some benchmark simulations are required to compare alternative solutions, keeping in mind that the final layout design will have to be optimized for track finding, reduced material amount and trigger contribution from tracker.

3.2 Design ideas for including tracking information in the trigger

The CMS detector will probably change only its tracking device, with all the other components undergoing only minor improvements/changes. If all the front-end electronics must be kept for the S-LHC upgrade, then the maximum Level-1 trigger rate must be kept to the designed 100 kHz, otherwise one overflows the on-board memory buffers. The problem with this is that the data actually available to the Level-1 trigger do not allow it to reduce the rate down to 100 kHz with the S-LHC parameters, not even by increasing the triggering thresholds on muons and e-γ jets. In Fig. 3 it is reported the foreseen frequency of triggered e-γ jets and muons as a function of the threshold energy and momentum, respectively. The left scale shows the frequencies foreseen for the start-up scenario (LHC nominal $\div$ 5), while the right scale shows the S-LHC scenario (LHC nominal $\times$ 10). It is clear that jet and μ triggers easily saturate the available 100 kHz rate at S-LHC.

If the tracker was able to provide some information to the trigger, this would greatly help in reducing the fake rate, and would allow to keep the rate of accepted events below 100 kHz with a reasonable efficiency.

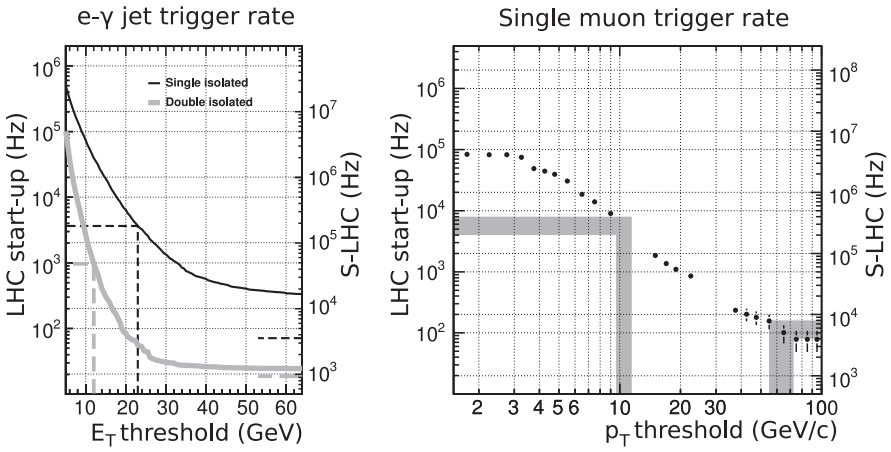

Fig. 3 Level-1 trigger rates as a function of the threshold. Left scale: Low luminosity start-up scenario. Right scale: S-LHC scenario. The marked rates represent the allocated bandwidth for each trigger for the start-up scenario

The tracker trigger information could be used to confirm isolated muons with high transverse momentum and to reduce the fake e/γ candidates by matching the calorimeter signal with inner track/vertex. Moreover the signature of high-p_T particles close to/in jets could help identifying τ- and b-jets.

The approach to this solution is to have *some* information at the Level-1 trigger in order to reduce data volume by applying p_T cuts, as the time constraints (of a few μs) do not allow to perform a complete tracking.

Providing information for the L1 trigger involves sending out data at 20 MHz, and therefore reducing the data volume at the front-end by a large factor (e.g. $\sim$100), to keep the number of links reasonable. Reduction of the data volume must be achieved by rejecting signals from low-momentum particles. Three methods have been proposed so far, none of which is fully proven, but in all cases the idea is to measure the local track angle with respect to the sensor plane to deduce the particle's transverse momentum.

1. Reconstruction of "track stubs" from the correlation of signals in pairs of modules segmented in long pixels. Simulation studies [8] indicate that sufficient rejection of low momentum particles can be achieved with pairs of detectors spaced by $\sim$2 mm placed at a radius of 20–25 cm. High granularity is required, as the method currently relies on the assumption of one hit per readout chip per event, therefore a granularity well below 1%. The approach is in principle applicable also to detectors oriented in the "forward" configuration, by expanding the spacing between the two sensors of the pair by a factor $1/\tan(\theta)(\simeq 5)$.
2. Reconstruction of "track stubs" from the correlation of signals in pairs of strip detectors wire-bonded to the same readout hybrid, which implements correlation functionalities
3. Discrimination on the basis of the cluster size in single sensors [5, 10]. This method has the advantage of not requiring two sensing layers (nor a data link between the two), and therefore it is a priori less demanding in terms of cost, material and power dissipation, but it imposes a constraint in the ratio between pitch and sensor thickness.

For all these methods advantages, disadvantages and feasibility are being evaluated. Also it is of paramount importance to clearly identify the physics requirement for the triggering information, so to avoid a so-called design overkill, which would be not optimal in terms of cost, material amount and thus performance.

3.3 Sensors research & development

The goal of the research on sensors for the strip tracker is to identify one single Silicon sensor type in planar technology for the outer region and one more pixelated (i.e. short strips) for the inner layers.

Studies are being carried out to determine which process is favored for the production for sensors which will have to withstand the intense radiation at the S-LHC:

after half the life of S-LHC (equivalent to 2,500 fb^{-1} delivered integrated luminosity) the expected fluence (Φ) at the inner layer of the strip tracker is $\sim 10^{15}$ cm^{-2} for charged hadrons $\sim 10^{14}$ cm^{-2} for neutrons [7].

The defects created by hadron irradiation cause an increase of the bias voltage needed to completely deplete the sensor and a decrease of the bulk resistance. With the silicon sensors used today and the hadron fluence foreseen at S-LHC, one would expect an increase of the dissipated energy in the sensor bulk, eventually causing a thermal runaway. Studies [6] show that the magnetic Czochralski method allows a much lower bias voltage than the traditional Floating-Zone method for $\Phi > 10^{14}$ n cm^{-2}.

Another negative effect of sensor irradiation is the loss of Charge Collection Efficiency (CCE) due to the trapping of charge carriers by radiation-induced bulk defects. It was recently shown [4] that n-on-p structures behaves better than p-on-n for $\Phi > 5 \times 10^{14}$ cm^{-2}, independently of the crystal production method. A choice of n-on-p has a few drawbacks, namely a higher minimum strip pitch achievable of 50 μm, with respect to 25 μm for the p-on-n, and a larger Lorentz angle. The latter could be compensated by using thinner sensors, which also helps reducing the material amount and the energy dissipation in the bulk.

Innovative readout schemes are under study to cope with the use of shorter strips, which is required to increase the channel granularity. For the inner layers, in order to have the requested granularity, more than two strip segments along the sensors will be needed. This requires special readout techniques like double metal layers or bump bonding.

3.4 Power delivery

A major constraint on upgraded system is the routing of services: all the services to the tracker lying outside the detector volume follow complex congested routes, entangled with other services and with other detectors. Thus it will be impossible to replace external cables and cooling pipes for S-LHC.

The heat load of cables must be removed, and in the present design about 40% of the power is dissipated in external cabling.

$$P_{front-end} \simeq 33\ \text{kW} \qquad P_{cables} \simeq 20\ \text{kW} \qquad I_{cables} \simeq 15\ \text{kA}$$

The foreseen design choices for the upgrade tracker imply an increase of the supply current. Even if the power per readout channel will decrease for the next generation readout chips ($2.7\ \text{mWch} \rightarrow 0.5\ \text{mW/ch}$), the number of channels will increase in order to be compatible with tracking requirements, so the total readout power is expected to be at least in same range as for the present system. Smaller feature size of the front-end chips will result in smaller readout chip supply voltage (1.2 V for the 0.13 μm technology), so larger currents at front-ends will be required. This is not possible without changing the powering scheme, as the external cabling is

already at the limit of current it can withstand, and a decrease of a factor x in the front-end voltage at fixed power delivered corresponds to an increase of a factor x^2 in the power dissipated in external cabling.

The proposed solutions up to now involve either DC/DC conversion at the modules or the serial powering of the modules themselves, both techniques would allow to deliver a higher voltage to the front-ends, but neither are proven. The option of powering serially the front-end devices is likely to bring significant complications for very large systems. The technological challenge of DC/DC conversion, instead, consists in developing low-mass, high-efficiency, radiation-hard and magnetic-field tolerant devices, that can be integrated in the front-end without inducing noise in the readout system; different options are being considered, like air-core inductors or switched capacitors.

Also the increased radiation damage plays a role in the power supply scenario: the sensor power will become more important; in order to control it thinner sensors and lower temperatures will be useful.

Reaching lower working temperature, instead, requires a higher cooling power to be delivered with the same external services as the present ones. The most promising solution to this seems to be the two-phase CO_2 cooling, which offers a number of attractive features, like low mass, low viscosity, high latent heat, high heat transfer coefficient, giving in principle the opportunity to realize a system with a smaller number of independent cooling lines and cooling pipes of smaller size compared to the present mono-phase fluorocarbon, possibly coping with higher power dissipation.

3.5 First layout studies and simulation

Some studies on the possible layouts already started: estimates on important parameters like power consumption per channel and expected particle density allow to describe different possible tracker geometries and compare them in terms of foreseen channel occupancy per layer, total power consumption, amount of sensor surface, etc...

It is assumed that a pixel detector with four barrel layers and corresponding end-caps will be placed in the same region as the present-day tracker, so the studies started addressing the outer tracker. The present-day 10-layer configuration is largely redundant; given the material reduction requirement, it will be probably possible to lower the number of barrel layers down to 6. In this case it could be possible also to keep the power consumption in the same range as the present tracker.

Full simulation of possible layouts also already started, these are aimed mainly at validating the tracking with different conditions with respect to the present-day tracker and estimate the potential of trigger information from the tracker. The simulation group is working to develop a set of software tools to assist studies on different layouts, in order to be able to have common benchmarks for comparisons. This is

done trying to maximize the overlap of these common software tools with standard CMS Software, which was already extensively validated and can provide a solid framework to study the new features.

4 Conclusions

The LHC upgrade (S-LHC) is foreseen to increase the luminosity of a factor 10 with respect to the nominal LHC. The vertex pixel detector of CMS will have to be replaced 5 years after the start-up (or $\sim$250 fb^{-1}), while whole tracking detector will need a replacement when the major instantaneous luminosity upgrade will be implemented (foreseen about 10 years after the start-up), in order to cope with higher irradiation and higher density of tracks, which will require new radiation-hard sensors and enhanced readout channels density.

If no other sub-detector of CMS will be changed, information from the tracker will be needed at the Level-1 trigger, to keep the rate compatible with the electronics of all the CMS sub-detectors. Thus strategies are being explored to provide some information to the trigger from the tracker.

The requirement to increase the granularity and to create trigger primitives, combined with the need of moderating (and possibly reducing) the material in the tracking volume, constitute a formidable challenge. The task is further complicated by the fact that the new tracker will have to be integrated in the existing CMS detector, with no margin to modify volumes available for detectors and services; in particular, the section of the services going from the tracker external surface to the back-end shall be reused. In order to help achieving such goals while coping with all the constraints, in addition to considering a variety of options in terms of detector layout and readout architecture, innovative powering schemes and cooling technologies are under study.

References

1. CMS: The Tracker Project Technical Design Report (1998). CERN-LHCC-98-06.
2. Addendum to the CMS Tracker TDR (2000). CERN-LHCC-2000-016.
3. Adam,W., et al.: Silicon Strip Tracker Detector Performance with Cosmic Ray Data at the Tracker Integration Facility (2008). CMS NOTE-2008/032.
4. Affolder, A., Allport, P., Casse, G.: Charge collection, power, and annealing behaviour of planar silicon detectors after reactor neutron, pion and proton doses up to 1.6 10–16 neq cm-2. In: 13th RD50 Workshop, CERN, 10–12 November 2008 (2008).
5. Barbagli, G., Palla, F., Parrini, G.: Track momentum discrimination using cluster width in silicon strip sensors for slhc. In: TopicalWorkshop on Electronics for Particle Physics, Prague, Czech Republic, 03 – 07 Sep 2007, pp. 282286. CERN, CERN, Geneva (2007).
6. H.ark.onen, J., Tuovinen, E., Luukka, P., Tuominen, E., Li, Z., Ivanov, A., Verbitskaya, E., Eremin, V., Pirojenko, A., Riihimaki, I., Virtanen, A.: Particle detectors made of high-resistivity czochralski silicon. Nuclear Instruments and Methods in Physics Research Section A **541**(1-2), 202–207 (2005). DOI: 10.1016/j.nima.

2005.01.057. URL http://www.sciencedirect.com/science/article/B6TJM-4FDJ4BC- 11/2/33fb50b54ffdcd2a31da88ef7b7a5b50. Development and Application of Semiconductor Tracking Detectors – Proceedings of the 5th International Symposium on Development and Application of Semiconductor Tracking Detectors (STD 5).
7. Huhtinen, M.: Radiation considerations (2004). CMS Workshop on Detectors and Electronics for SLHC, available at http://indico.cern.ch/conferenceDisplay.py?confId=a036368.
8. Jones, J.A.: Development of Trigger and Control Systems for CMS. Ph.D. thesis, High Energy Physics Blackett Laboratory, Imperial College, London, UK (2007). CERN-THESIS-2007-041.
9. Mangano, B.: CMS track reconstruction performance and latest results with cosmic muons. In: Proceedings of Science. Vertex 2008, Uto Island, Sweden, July 28–August 1, 2008 (2008). To be published.
10. Palla, F., Parrini, G.: Tracking in the trigger: from the CDF experience to CMS upgrade. PoS VERTEX2007, 034 (2007).
11. Scandale, W., Zimmermann, F.: Scenarios for slhc and vlhc. Nuclear Physics B - Proceedings Supplements **177-178**, 207–211 (2008). DOI: 10.1016/j.nuclphysbps.2007.11.110. URLhttp://www.sciencedirect.com/science/article/B6TVD-4S0J4RD-1C/2/4bc67c35920881d5939baf9f4ebfff95. Proceedings of the Hadron Collider Physics Symposium 2007, Proceedings of the Hadron Collider Physics Symposium 2007.

Search for Lepton Flavour Violation with the MEG Experiment

A. Papa, on behalf of the MEG collaboration

Abstract The aim of the MEG experiment is to measure the branching ratio of the rare muon decay $B = \frac{\mu^+ \to e+\gamma}{\mu^+ \to TOT}$ at a sensitivity of $\approx 10^{-13}$.To reach this goal, the experiment must use the most intense continuous muon beam available ($\approx 10^8 \mu/s$) and obtain the highest energy, time and space resolutions, today reachable. A description of the main properties of each subdetector is given and the detector performances during the first engineering run are presented.
PACS 11.30.Hv; PACS 29.40.Mc; PACS 29.40.Gx; PACS 06.20.fb; PACS 29.20.Ba; PACS 25.20.Lj; PACS 29.40.Mc

Keywords: Flavor symmetries, scintillation detectors, tracking and position-sensitive detectors, calibration and monitoring methods, Cockroft–Walton accelerator, liquid xenon.

1 Brief historical overview

The motivations for a search of the $\mu^+ \to e^+\gamma$ decay changed in the course of time, but the process always maintained a fundamental role.

The search for the $\mu^+ \to e^+\gamma$ decay started in 1947 [1, 2]. Pontecorvo was the first to raise the question: *"is the electron emitted by the meson with a mean life of about 2.2 microseconds accompanied by a photon of about 50 MeV?"* [3]. A first upper limit was reached: $B(\mu^+ \to e^+\gamma) < 10\%$ [4]. The result also excluded the emission of a new type of meson in muon decay and it supported the evidence for a muon decay to an electron and two neutrinos (requiring 1/2 spin for the μ-meson).

The assumption was at the same time made of a universal interaction acting among spin-$\frac{1}{2}$ particles and, as a consequence, what was known for the β decay applied also to the muon process [5, 6].

A. Papa
Università degli studi di Pisa and INFN, I-56127 Pisa, Italy,
e-mail: angela.papa@pi.infn.it

V. Begun et al. (eds.), *Progress in High-Energy Physics and Nuclear Safety*,

The hypothesis that two like neutrinos were ejected in μ decay had now a theoretical support. The observable secondary electron spectrum was predicted by Michel [7].

Although the theory could adequately explain the experimental observations, it could not equally well explain what was not observed. In particular the decay of a muon into an electron and a photon was not observed despite being a perfectly valid electromagnetic transition. The $\mu^+ \to e^+\gamma$ search went on and a new upper limit, four order of magnitude better was achieved $\mathrm{B}(\mu^+ \to e^+\gamma) < 2 \times 10^{-5}\%$ at 90% C.L. [8].

This result and the prediction of $B(\mu^+ \to e^+\gamma) \approx 10^{-4}$ [9], based on the hypothesis of a universal Fermi interaction mediated by a charged vector boson, proposed by Feynman and Gell-Mann [10], seemed inconsistent. However the fashionable intermediate vector boson of the weak interaction is not ruled out if some selection rules apply forbidding $\mu^+ \to e^+\gamma$. Such selection rules were first proposed by Konopinski and Mahmoud supposing that μ and e have opposite quantum numbers [5]. Later on, additive or multiplicative conservation laws were proposed involving two sorts of neutrinos: one associated with electrons, the other with muons [11]. The electron-type neutrinos ν_e can never trasform into muons, nor muon-type neutrinos ν_μ into electrons. All this means that the lepton conservation law is associated with that of the lepton type (flavour) conservation; both the electron number and the muon number must be separately conserved in each reaction.

Meanwhile a new upper limit was reached: $B(\mu^+ \to e^+\gamma) < 6 \times 10^{-8}$ at 90% C.L. [12], supporting the selection rule hypotesis. After that a new upper limit: $B(\mu^+ \to e^+\gamma) < 3.6 \times 10^{-9}$ at 90% C.L. [13] was obtained at TRIUMF. A new generation of $\mu^+ \to e^+\gamma$ decay experiments started in the eighties, by using muon beams instead of pion beams. A new upper limit was obtained: $B(\mu^+ \to e^+\gamma) < 1 \times 10^{-9}$ [14]. Another order of magnitude was gained at LAMPF [15] ($B(\mu^+ \to e^+\gamma) < 1.7 \times 10^{-10}$ at 90%C.L.).

Always in the 1980s the Standard Model predictions were thoroughly studied at CERN. The vector bosons were discovered (1982) and all SM predictions were confirmed at a high level of precision. The model had nevertheless no explanation for the replication of fermion families and had no prediction for fermion masses and weak mixings, etc. In this framework, the conservation of lepton flavour appeared as an accidental conservation law, not associated with either a space–time symmetry or with the existence of a massless gauge boson[16].

On the experimental side, the usage of muon beams of increasing intensity and the development of detectors with increasingly improved performances allowed higher and higher sensitivities. An upper limit: $B(\mu^+ \to e^+\gamma) < 4.9 \times 10^{-11}$ was established [17] before the last one, reched by the MEGA experiment ($B(\mu^+ \to e^+\gamma) < 1.2 \times 10^{-11}$ at 90% C.L.[18]).

The $\mu^+ \to e^+\gamma$ chronicle stops here, having reached the birth of the MEG experiment. Figure 1 summarizes the evolution of $\mu^+ \to e^+\gamma$ decay search.

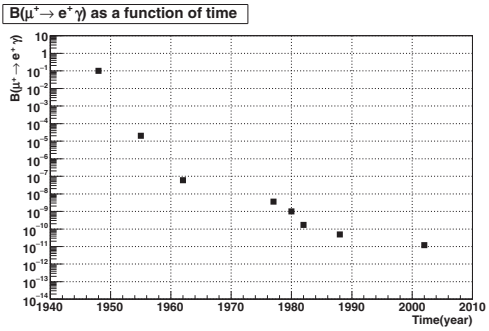

Fig. 1 Branching ratios for the $\mu^+ \to e^+\gamma$ decay measured during the time until now.

2 The theoretical framework

The discovery of the $\mu^+ \to e^+\gamma$ decay is today thought to be a significant signature of supersymmetric unification ([20–24] and references therein). These models have attracted much attention because the three gauge coupling constants determined at LEP and SLC are consistent with $SU(5)$ GUT predictions and with other larger groups, as $SO(10)$ GUT. The three coupling constants are then unified at 2×10^{16} GeV. The contributions from the SUSY particles play a fundamental rule in the renormalization-group evolution of the coupling constants. For this reason the $SU(5)$ *or* $SO(10)$ $SUSY - GUT$ groups appear a well-motivated extensions of the Standard Model.

In the $SU(5)$ or $SO(10)$ $SUSY - GUT$ framework the LVF is induced by a mismatch of the lepton and slepton diagonalization. The diagonal terms of the slepton mass matrix can be examined in the basis where the Yukawa coupling constant for lepton is diagonalized. The off-diagonal elements of the right-handed slepton mass matrix in this basis become a source of LVF.

Large LVF are expected in $SO(10)$ SUSY GUT model. In the minimal $SO(10)$ SUSY GUT both the left-handed and the right-handed sleptons show LVF effects. A large contribution is coming from the diagrams of Fig. 2 where the m_τ is involved. The prediction of the branching ratio of $\mu^+ \to e^+\gamma$ decay is enhanced for this scheme by $(m_\tau/m_\mu)^2$, compared to the minimal $SU(5)$ SUSY GUT. The branching ratio of the muon LFV processes as a function of the right-handed slepton mass is shown in the Fig. 3, where the SUSY input parameters are the $SU(2)$ gaugino mass, indicated as $M_{1/2}$ and the ratio of the two Higgs vacuum expectation values, tan β. Here the branching ratio become comparable to the present experimental upper bounds.

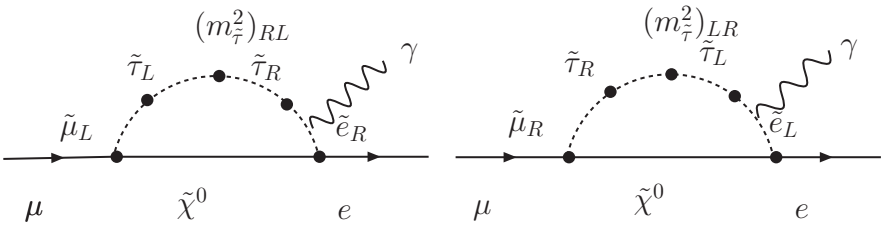

Fig. 2 Feynman diagrams in the $SO(10)$ *SUSY GUT* model, which give dominant contributions to the $\mu^+ \to e^+\gamma$ decay

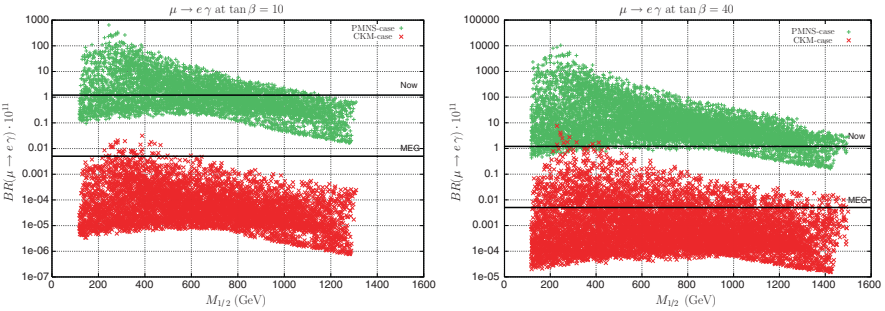

Fig. 3 Scaled BR($\mu \to e\gamma$) vs. $M_{1/2}$. Scaled branching ratio predictions for the $\mu^+ \to e^+\gamma$ decay in the $SO(10)$ *SUSY GUT* model. The plots are obtained by scanning the LHC accessible SUSY–GUT parameter space at fixed values of $\tan\beta$. The horizontal lines are the present (MEGA) and the future (MEG) experimental sensitivities. (pictures by [24]).

3 The event signature

The event signature of the $\mu^+ \to e^+\gamma$ decay at rest is a positron and a photon in coincidence, moving collinearly back-to-back with their energies equal to half the muon mass ($m_\mu/2 = 52.8$ MeV). If we assume CPT invariance, this decay is equivalent to $\mu^- \to e^-\gamma$ but the former is more convenient from the experimental point-of-view because the μ^+ can be stopped in a target without being captured by a nucleus.

Two kinds of background are present.

The prompt background from the radiative muon decay, $\mu^+ \to e^+\nu_e\overline{\nu}_\mu\gamma$, when the positron and the photon are emitted in opposite directions and the two neutrinos take away a small amount of energy. We evaluate this prompt background corresponding to a branching ratio of 10^{-14} by using the expected detector resolutions.

The accidental background due to an accidental coincidence between a positron from the normal muon decay, $\mu^+ \to e^+\nu_e\overline{\nu}_\mu$, and a high energy photon from the radiative muon decay $\mu^+ \to e^+\nu_e\overline{\nu}_\mu\gamma$ (or annihilation in flight and external bremsstrahlung of positrons from normal muon decay). We evaluate an effective branching ratio of the accidental background of 2.5×10^{-13}: the accidental background is more important than the prompt background.

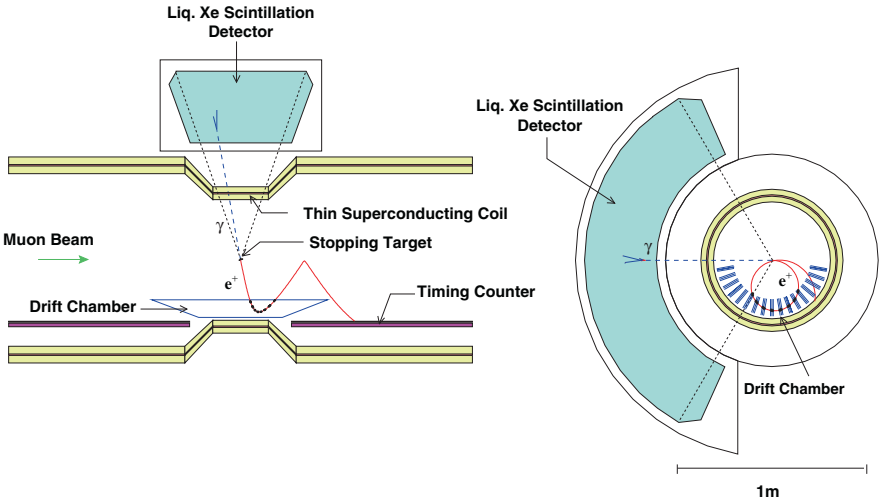

Fig. 4 MEG experiment layout.

4 The MEG experimental set-up

The ability of an experiment to identify the signal and to reject background depends on the detector resolutions in measuring the relevant four-momenta, in our case: the ones of the positron and of the photon.

The precise measurement of the positron relies on a magnetic spectrometer (drift chambers + superconducting magnet). This is similar to what MEGA did, but MEG has a magnet with an additional field gradient getting rid of low momentum positrons and to reducing the number of unwanted hits in the drift chambers. Good timing is obtained by fast scintillation counters.

Standard photon calorimetry, based on NaI(Tl) crystal arrays, provides a good energy measurement, but poor timing. MEG decided to develop an innovative calorimetry based on the use of liquid xenon. The new detector couples a good γ momentum determination with an optimum timing resolution.

Figure 4 shows the MEG experiment layout. The MEG detector is described in more detail in the following sections. Table 1 summarizes the upper limits on the $\mu^+ \to e^+\gamma$ branching ratio, obtained by the last experiments. The associated experimental resolutions and the expected MEG resolutions are also reported.

5 The muon beam and the target

We used the most intense continuous muon beam in the world to reach the best possible sensitivity on $\mu^+ \to e^+\gamma$ decay search. Muons are extracted from a thick graphite production target (thickness = 40 or 60 mm), where the primary proton

Table 1 Progresses in the $\mu \to e\gamma$ search. The resolutions are given as Full Width Half Maximum (FWHM)

Laboratory	Year	ΔE_e	ΔE_γ	$\Delta t_{e\gamma}$ (ns)	$\Delta\theta_{e\gamma}$ ($mrad$)	Upper limit	Ref
TRIUMF	1977	10%	8.7%	6.7		3.6×10^{-9}	[13]
SIN	1980	8.7%	9.3%	1.4		1.0×10^{-9}	[14]
LANL	1982	8.8%	8%	1.9	37	1.7×10^{-10}	[15]
LANL	1988	8%	8%	1.8	87	4.9×10^{-11}	[17]
LANL	2002	1.2%	4.5%	1.6	15	1.2×10^{-11}	[18]
PSI	2008	0.7 – 0.9%	4%	0.15	17 – 20.5	$\approx 10^{-13}$	[19]

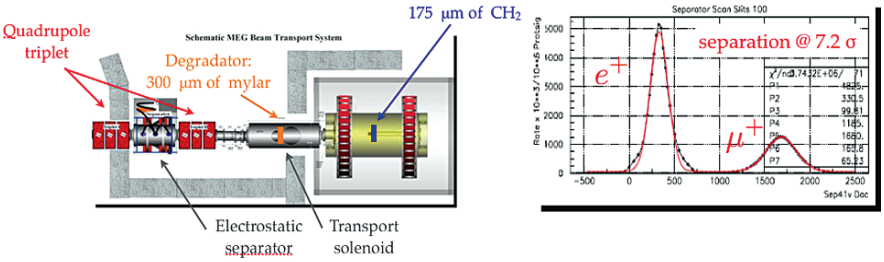

Fig. 5 Muon beam line elements inside the πE5 area (in the left). Muons and positrons separation by means of the Wien filter (in the right).

beam impinges (proton energy = 590 MeV, proton current = 2 mA). The muons of the MEG experiment are the so-called *surface*-muons [25–27]. The kinetic energy and the momentum of these surface-muons are $\approx$3.6 MeV and 29 MeV/c respectively, and their range in graphite is $\approx$1mm: only muons produced by π^+-pion decaying at the target skin are selected. The advantage of using a low momentum muon beam when muon decays at rest are required is directly associated with a better identification of the muon stopping region.

The last part of the beam line, inside the πE5 area where the experiment is mounted, is optimized to satisfy the following points: (a) reducing the contaminants (positrons coming from μ^+-decays in flight); (b) coupling the μ^+-beam with the high magnetic field region of the COBRA magnet; (c) reducing the momentum to stop muons in a thin target. A quadrupole triplet, an electrostatic separator, a second triplet and a transport solenoid are the last muon-beam elements. In the middle of the transport solenoid, at a beam focus, a degrader (Mylar sheet of 300 μm thickness) is mounted to reduce the μ^+ momentum. In these conditions a muon beam of $3 \times 10^8 \mu^+$/s was obtained at the COBRA center, with an ellipsoidal spot with σ_x = 10 mm and σ_y = 11 mm (see Fig. 5).

The muons are stopped in a thin ellipsical CH_2-target (210×70 mm^2 and 175 μm of thickness), mounted in an He atmosphere, at an angle of 22° relative to the muon beam direction. This angle maximizes the CH_2 thickness along the beam direction and minimizes the positron energy loss through it. This target + degrader

system was considered the best material from both a background suppression and beam quality point of view, mainly because of its larger radiation length. Finally the target depolarizes the muon beam, which is highly polarizated as consequence of the $\pi^+ \rightarrow \mu^+ \nu_\mu$ decay at rest.

6 The positron spectrometer

The positron momentum and flight direction are measured by the COBRA spectrometer (COBRA superconducting magnet and 16 Drift Chambers); the time of flight is measured by a scintillation counter system, called the Timing Counter.

6.1 The cobra magnet

The magnetic field map, the Drift Chamber and Timing Counter positionis were chosen to fulfil to conditions:

a. Low momentum positrons are swept away from the MEG detector center, without hitting chambers and counters. A large number of Michel positrons comes from the muon standard decay; a non-homogeneous magnetic field can be shaped as to make the projected radius dependent on the absolute value of momentum, and not on the transverse part only. Low momentum tracks are confined inside a cylindrical shell and the occupancy of the drift chamber is reduced.

b. Monocromatic positrons follow trajectories with the projected radius indipendent of the emission angle. The number of multi-turns in the chamber system is minimized and the reconstruction of the higher momentum tracks is greatly simplified.

Figure 6 shows the positron trajectory evolution in the case of a uniform solenoidal magnetic field and in the case of a gradient magnetic field.

6.2 The drift chambers

Positron trajcectories are measured with 16 drift chamber sectors radially aligned at 10.5^o intervals in azimuthal angle (see Fig. 7, in the left). Each sector consists of two trapezoidal staggered arrays of drift cells. The sensitive area of the chamber extends from a radius of 19.3−27.0 cm. In the z direction the active region extends up to z ± 50 cm, at the innermost radius, and z = ±21.9 cm, at the outermost. Positrons of 29 MeV/c emitted from the target with $|\cos\theta < 0.35|$ and $-60^o < \phi < 60^o$ are accepted by this geometry. Momentum and angular resolutions are primarly limited by multiple scattering in the chamber materials and in the gas. Particular attention was psid to two items. The structure of a chamber sector and its measurement principle are shown in Fig. 7 (right). The chamber wall is made of an extremely thin foil,

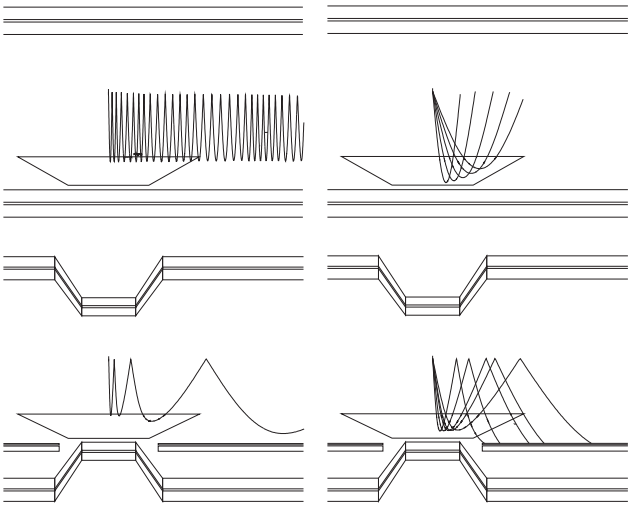

Fig. 6 Problems with a uniform solenoidal magnetic field (top) and advantages of a gradient magnetic field (bottom): r–z view of the COBRA spectrometer shown with the trajectory of a particle emitted at 88^o (left); Trajectories of monochromatic particles emitted at various angles (right).

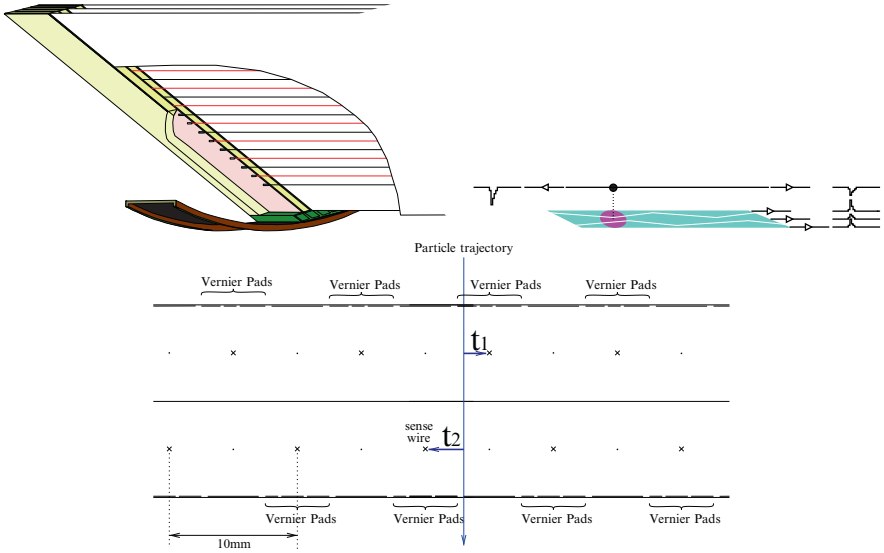

Fig. 7 Schematic view of the drift chambers (top, left). A schematic view of the Vernier pad method (top,right). A cross-sectional view of a part of chamber sector (bottom). It consists of two layers of drift cells staggered by half-cell.

12.5 μm thick polymide, with an aluminum deposition (250 nm), which acts as a chatode. An array of sense (anode) and potential wires are mounted inside the chambers and fixed at a carbon fiber frame (open towards the target). This *open-frame* makes wire/foil-stretching more challenging. Thanks to such precautions, the overall material in the fiducial tracking volume amounts to 0.002 X_0 on average for the positron (52.8 MeV/c) trajectory.

The chamber sectors are filled with a 50% He−50 % C_2H_6 gas mixture and the outer volume with pure He, both at 1 atm. Such a mixture and the pure helium are chosen to have a sufficient ionization loss in the gas (≈65 e^-/cm for minimum ionizing particles) as well as to minimize multiple Coulomb scattering.

The staggered-cell configuration allows the simultaneous measurement of the r-coordinate and of the absolute time of the track. The difference between the drift times $t_1 - t_2$ in the adjacent cells measures the r-coordinate of the track with 100–200 μm accuracy, while the mean time $(t_1 + t_2)/2$ measures the absolute time of the track with ≈5 ns accuracy. This excellent timing resolution is important for the pattern recognition.

The z-coordinate (muon beam direction) along the wire can be initially located with an accuracy of ≈1 cm, by the ratio of the charges observed at both ends of a sensitive wire. The thin layer of aluminum deposit on the four cathode foils is patterned to make a 5 cm period *Zig-Zag*-strip, called *Vernier pattern* as shown in Fig. 7 (bottom,left). Consequentely, the ratio of charges induced on each pad measures the z-coordinate precisely, with an accuracy of 300–500 μm.

The expected resolutions of the spectrometer have been studied with GEANT simulations. Positrons of 52.8 MeV were generated and their trajectories were reconstructed by using several methods. Depending on the method, the momentum resolution ranged from 0. 7% to 0.9% (FWHM) and the angular one from 9 to 12 mrad (FWHM). The positron origin can be reconstructed with a resolution ranging from 2.1 to 2.5 mm.

6.3 The timing counter

The Timing Counter (TC) was designed to measure the positron timing with a resolution of 100 ps (FWHM). Thanks to its rapidity it is used, at the trigger level, for selecting positron and gamma events coincident in time and collinear in direction with a photon identified in the electromagnetic calorimeter.

The TC hodoscope arrays of plastic scintillators are placed on both sides of the positron spectrometer (see Fig. 8), at a radius of 29.5 cm, covering 145° in ϕ and with $25 < |z| < 95$ cm. The $\mu^+ \to e^+\gamma$ positrons emitted in the angular range $0.08 < |\cos\theta| < 0.35$ are incident on the timing counter after completing ≈1.5 turns in the r-ϕ plane.

The longitudinal layer precisely measures the incident particle timing, as well as a fast estimation of the emission angle ϕ. Each longitudinal detector is an assembly

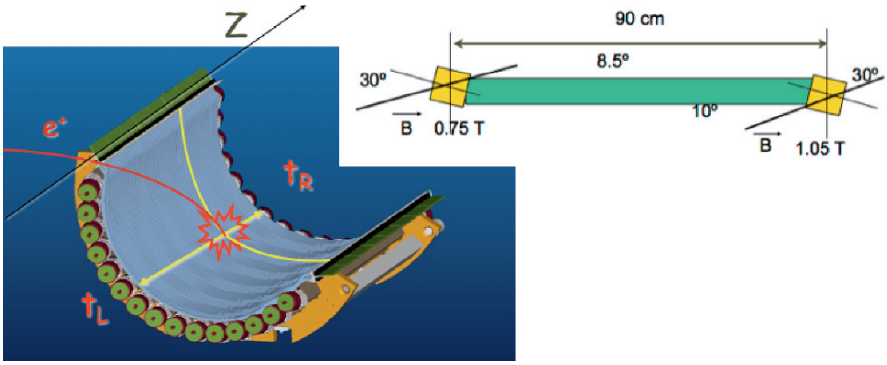

Fig. 8 The timing counter layout and its working principle. The positron hits on the transverse detector (scintillating fibers and APDs), which determines its position and crosses the scintillator bars of the longitudinal detector, which determines the time of the impact.

of 15 scintillator bars whose light output is collected by two photomultiplier tubes (PMTs). The bars are BC404 plastic scintillator of dimensions $40 \times 40 \times 780$ mm^3. The PMTs are Hamamtsu 2" fine mesh R5924, selected for operating in an intense magnetic field region.

Each PMT at the ends of each bar measures the pulse height as well the arrival time of the scintillation light (t_L and t_R). The mean time gives the absolute impact time, the time difference $t_R - t_L$ and the pulse-height ratio provides a measurement of the impact point along the bar (z coordinate), with an accuracy of ± 1 cm.

The transverse detector is made of two layer of 128 scintillating fibers (BCF20) with square cross-section (5×5 mm^2), read at both ends by Avalanche Photo Diodes (APDs). The usage of fibers coupled with the APDs is compatible with the high magnetic field. The transverse module provides the impact point z on the TC. This is used for a first raw determination of the positron trajectory, allowing the fast rejection of events with unmatched kinematic parameters. The z point also constraints the track reconstruction and is used in the data analysis.

7 The gamma liquid Xenon calorimeter

The MEG gamma detector is a C-shaped homogeneous Liquid Xenon calorimeter, which represents the most innovative part of the experiment.

A schematic layout of the γ detector is shown in Fig. 9. The detector is external to magnet coil. The surface of the liquid Xenon is at 65 cm from the target center and the detector thickness is 47 cm, sufficient to contain γ's of 52.8 MeV momentum. The fiducial volume of the detector covers a solid angle $\Delta\Omega/4\pi \approx 12\%$ ($|\cos\theta| < 0.35$ and 120^o in ϕ).

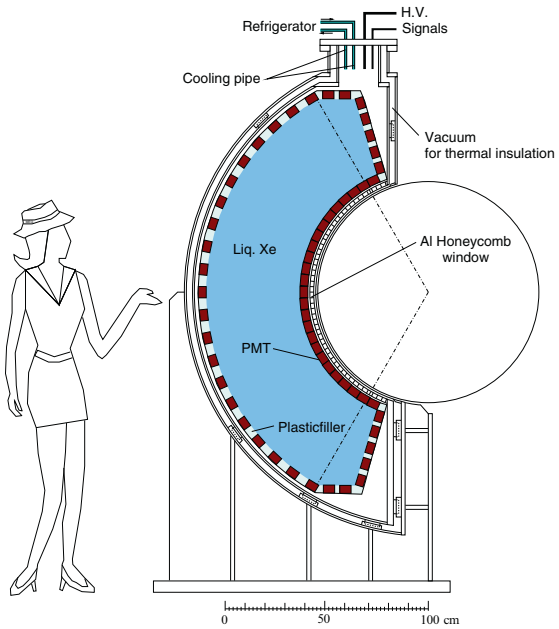

Fig. 9 Schematic view of the Liquid Xenon photon detector.

The LXe calorimeter measures the energy, the timing and the position of the gamma coming from the $\mu^+ \to e^+\gamma$ decay. Eight hundred liters of pure liquid xenon are used and only the scintillation light, without any attempt to collect the ionization, is collected by 846 photomultipliers, immersed in liquid xenon. An R&D was necessary to ensure that these photomultipliers (Hamamatsu R9869) correctly work at cryogenic temperature (at the Xe liquid temperature of $\approx -108^{\circ}$C), in the vacuum ultra-violet region (where Xenon emits at $\lambda_{\text{scin}} = 178$nm), at high signal rate (photomultipliers anodic current $\approx 4\,\mu$A).

The high number of scintillation photons (40,000 ph/MeV), the small time constant (three components $\tau_1 = 4$ ns, $\tau_2 = 22$ ns and $\tau_3 = 45$ ns), the high atomic number ($Z = 54$), the high density ($2.95\ \text{g}/\text{cm}^3$) are desirable characteristics for the use of Xe as a highly performing detector medium.

The energy is measured by the scintillation light collected by the PMTs. The γ is supposed to come from the same vertex of a companion positron, and its direction is determined by looking at the interaction point on the calorimeter, derived from the distribution on the light calorimeter front face. The light arrival time on the all PMTs is used to measure the photon timing.

Since the calorimeter has a big homogeneous volume, we expect a high rate of low energy gammas: it is therefore necessary digitize every PMT waveform to reject events in which pileup is present.

The large dimentions of the calorimeter make the determination of the optical properties of the xenon important understanding for the calorimeter performance.

In particular the Xe trasparency to the scintillation light strongly affects the energy resolution. Dedicated calibration methods were developed to measure, monitor the Xe optical properties and to check the general detector performance, as discussed in the next section.

A detailed Monte Carlo simulation was developed. One obtained for the final calorimeter an energy resolution $\Delta E_\gamma/E_\gamma$(FHWM) $= 4.5\%$, a time resolution Δt_γ(FHWM) $\approx$ 120 ps and a position resolution Δx(FWHM) $= \Delta y$(FWHM) $\approx$1.5 cm.

8 The calibration methods

The performance of a big scintillation detector depends on the light propagation in the medium, in other words, on its optical properties [28,29]. We must also take into account the amount of photocathode coverage and the PMT characteristics (quantum efficiency QE, gain g, transit time spread σ_{tt} etc.). The understanding of the detector means: (1) to know and to control the Xe purity, the light emission spectrum, the refractive index n_{Xe}, the Rayleigh diffusion length λ_R, the absorption length λ_{abs}. They determine all physical processes from scintillation photons to photo-electrons; (2) to measure the characteristics of all PMTs.

The apparatus must be continuously monitored. Its stability must be checked, under the high beam intensity and its possible time variations. The only way to ensure that the required performances are reached and maintained during the MEG run is by the use of several complementary and redundant methods. This is a must for a reliable experiment searching for rare decays .

We studied and developed different calibration and monitoring methods (CMM).

In order to measure the LXe optical properties, we used radioactive Am-sources mounted on tungsten wires (WS), immersed in the detector volume [30]. These are also used to evaluate the quantum efficiency QE of all PMTs. The gain equalization among the PMTs is obtained by using LEDs, mounted on the lateral faces of the detector.

The energy calibration and the linear response of the LXe calorimeter as a function of energy are checked with γ's of different energy from several physical process [31]. We used 9 MeV γ's from Am or Cf neutron capture on Ni. 17.6 MeV γ's are obtained by the proton capture nuclear reaction ${}^{7}_{3}\mathrm{Li}(\mathrm{p},\gamma){}^{8}_{4}\mathrm{Be}$. A check of the LXe detector at the 54.9 MeV, close to the γ's energy from the muon decay, is obtained by the charge exchange reaction $\mathrm{p}(\pi^-,\pi^0)\mathrm{n}$, followed by the decay $\pi^0 \rightarrow \gamma\,\gamma$.

Two simultaneous γ's, at 4.4 MeV and 11.7 MeV, are emitted from the proton nuclear reaction ${}^{11}_{5}\mathrm{B}(\mathrm{p},\gamma){}^{12}_{6}\mathrm{C}$, useful to study the timing between the LXe calorimeter and the timing counter (TC).

A single reaction is not sufficient to solve all problems. The implementation of some of these methods has required the coupling of a 1 MeV Cockcroft–Walton (C-W) to the MEG experiment (see Fig. 10). The use of such a machine for an elementary particle experiment is rather exceptional. The excitation of several

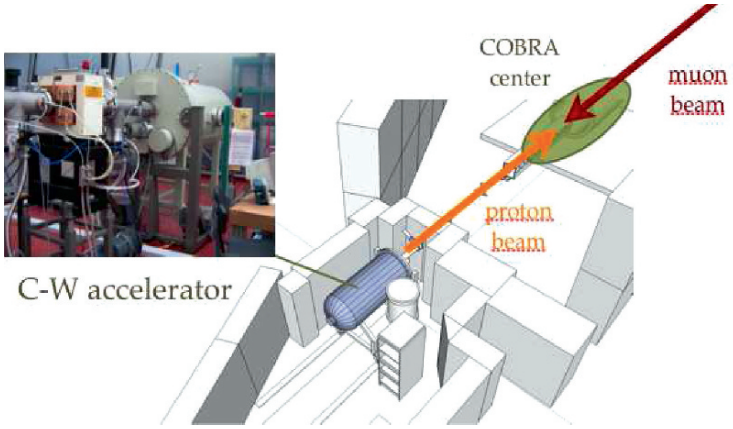

Fig. 10 The Cockcroft–Walton accelerator at the MEG experiment.

exothermic nuclear reactions producing γ-rays opens a full range of calibration possibilities. These can be used to keep the apparatus tuned, even during periods in which the MEG μ-beam is not available.

9 The trigger and DAQ systems

9.1 The trigger system

The trigger system uses the signals coming from the fast detectors (Liquid Xenon calorimeter and timing counter) to select the $\mu^+ \to e^+\gamma$ candidate events with the highest efficiency on the signal selection and to efficiently reject the background. As consequence, the useful variables for the trigger are: (a) the γ energy, time and direction from the LXe calorimeter; (b) the positron timing and impact point from the Timing Counter. The signal selection efficiency of each variable is equal or greater then the 98%, the background power rejection is (a) $f_\gamma = 8\times10^{-3}$ for the γ's, normalized to the muon radiative decay probability with the γ's energy greater than 10 MeV; (b) $f_\theta = 0.2$ and $f_\phi = 0.5$, for the positron-gamma direction; the positron-gamma time coincidence is fixed in a time window of $|\Delta T| < 10$ ns. Taking into account the expected gamma and positron rate (R_γ and R_{e^+} respectevely) at $R_\mu = 3 \times 10^8 \mu^+/s$ the expected trigger rate is:

$$R_{trigger} = R_\gamma R_{TC} f_\theta f_\phi 2\Delta T \approx 10\, events/s. \quad (1)$$

All these were evaluated with a Monte Carlo simulation.

From the hardware point of view, the trigger system is based on two different electronics boards.

A first board (Type 1, with 16 FADCs and 1 FPGA) receives the analogic signal and digitizes it at a frequency of 100 MHz by means of Flash Analog-to-Digital Converter (FADC). The digitized signals can then be manipolated, by using the Fast Programmable Gate Array (FPGA), in order to apply the different algorithms in a simple and flexible way. The combining of the informations coming from the Type 1 boards and other complex operations is made by the second board (Type 2, with 2 FPGAs). Finally a third board (Ancillary) is added to the trigger system provide the clock and the syncronization signals to all the boards.

9.2 Front-end electronics and DAQ

The signal digitization is made by means of a 2 GHz waveform sampling CMOS chip. The waveform sampling was adopted to overcome the expected pile-up events separated in time by less than 30–40 ns (mandatory for the LXe PMT signals). The standard usage of ADCs and TDCs for signal digitization is not sufficient.

The chip consists of 1,024 capacitors, which sample the PMT signal at a frequency of 2 GHz (500 ps bin width), necessary to obtain a timing resolution of 50 ps via interpolation. A domino wave constantly runs in a circular fashion and it is only stopped by the trigger. For this reason the chip is called the Domino Ring Sampler [32].

Eight data channels and two auxiliary channels are integrated in a single chip, which is housed and read out by a custom made VME board using 12 bit flash ADCs and FPGAs. Thanks to the FPGAs the algorithms for the data acquisition can be changed and optimized during the set-up of the experiment.

The DAQ system of the MEG experiment exclusively use the DRS chip on all 1,000 PMT channels (LXe calorimeter and TC) at 2 GHz and on all 3,000 drift chamber channels (cathodes and anodes) at 500 MHz, delivering an excellent pile-up rejection. A timing calibration signal is distributed and sampled in all DRS chip, in order to meet the experiment requirement of a 100 ps timing accuracy.

An on-line cluster of about 10 PC's is operating for on-line waveform processing, resulting in a data rate below 2 MB/s for an event rate of 100 Hz.

Figure 11 shows a scheme of the Trigger and DAQ system.

10 The detector performances

The 2007 engineering run was the first occasion for switching on all detectors together. Preliminary results are reported here.

The Americium α wire sources is a beautiful and effective method to calibrate and monitor liquid detectors. It is based on a set of thin wires (diameter 100 μm) mounted inside the sensitive volume of the LXe calorimeter. The point-like ^{241}Am α-sources are fixed on the wire. A thin gold layer ($\approx$1.5 μm) protects them. The

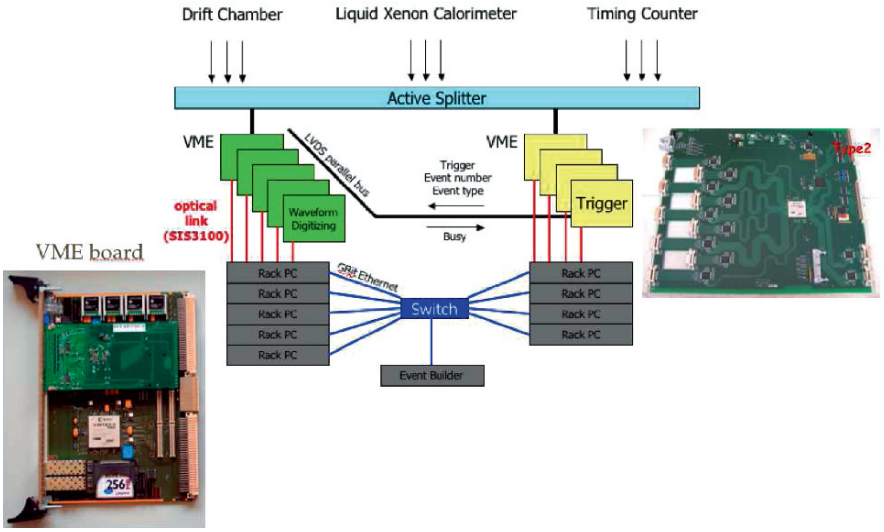

Fig. 11 A scheme of the Trigger and DAQ systems. A zoom of the Type 2 Trigger board and the VME board is given.

activity of each α-sources is $\approx$200 Bq. The α-events are at known positions, the α-energy is known ($E_\alpha = 5.4$ MeV) and the Am-source is stable since its half-life is very long ($t_{1/2} = 432.7$ years). These properties make the WS the most effective method for determining the relative QE of all PMTs and for monitoring the optical properties of LXe.

The Fig. 12 shows the well reconstructed 25 ^{241}Am-sources during the Xe liquefaction. The reconstructed bulbs (Xe gaseous phase) and rings (Xe liquid phase) are related to the different α-range R_α in GXe and LXe ($R_\alpha = 7$ mm and $R_\alpha = 40$ µm respectively): in the liquid phase a large amount of the scintillation light is lost on the wire than in the gas phase. The reconstructed position is affected by this process and the rings are the consequence.

The LXe purification monitoring, the detector stability check, the calorimeter uniformity study, the energy resolution determination, at an energy only a factor three lower than 54.9 MeV, was obtained by illuminating the whole LXe detector with 17.6 MeV γ's from the proton capture nuclear reaction $^7_3\mathrm{Li}(\mathrm{p},\gamma)^8_4\mathrm{Be}$, by means of the C-W accelerator. Figure 13 shows the lithium line at the beginnig and after about 120 h of Xe purification and the obtained energy resolution. The energy resolution extrapoled at 52.8 MeV is $\Delta E_\gamma/E_\gamma$(FHWM) = 5.0 – 5.5%, without implementing the QE corrections. The lithium and alpha peak evolution are shown in the Fig. 14.

The Xe calorimeter energy resolution was measured at 54.9 MeV with π^o-decay photons from the exchange reaction $\mathrm{p}(\pi^-,\pi^0)\mathrm{n}$. An energy resolution

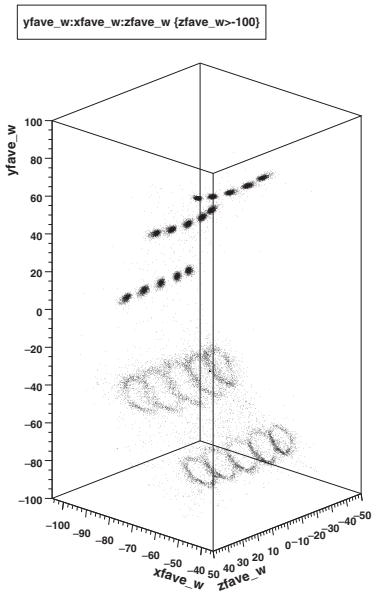

Fig. 12 The reconstructed position of the 25 sources inside the LXe calorimeter during the Xe liquefaction: in gas Xe (the bolbs, at the top), in liquid Xe (the rings, at the bottom).

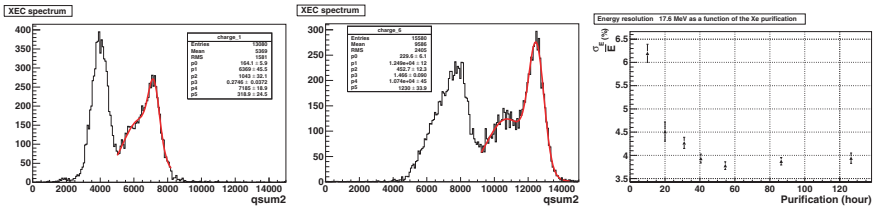

Fig. 13 The Lithium γ-lines immediately after the Xe liquefaction (at left) and after about 120 of Xe purification (at center). The energy resolution as a function of the purification time is reported (at right)

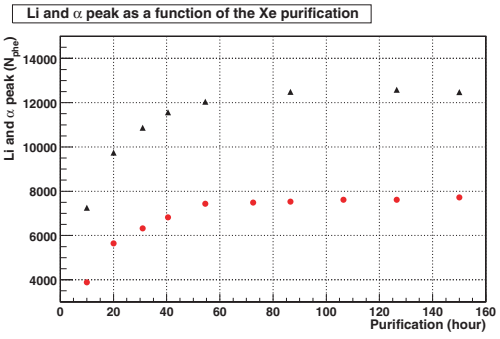

Fig. 14 The Lithium-γ (black triangle) and alpha (red circle) peak evolution as a function of the Xe purification.

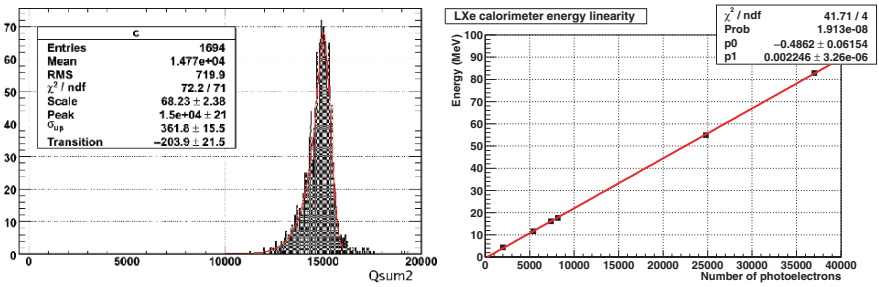

Fig. 15 LXe energy resolution at 54.9 MeV with π^o-decay γ's from the exchange reaction $p(\pi^-,\pi^0)n$ (at left). The LXe calorimeter energy linearity, with the calorimeter illuminated by photons at different energies (at right).

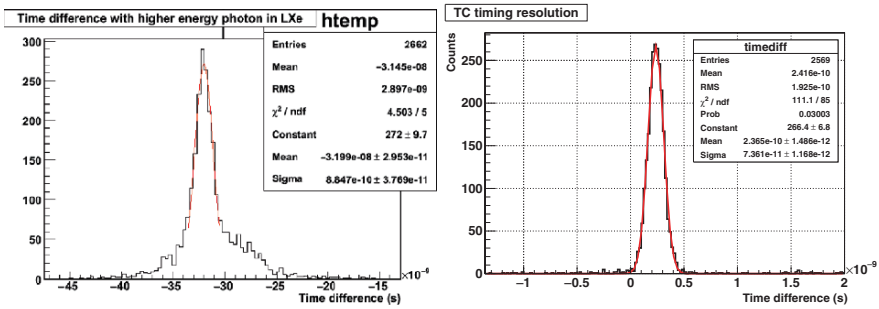

Fig. 16 The LXe time resolution evaluated at 54.9 MeV (at left) and the TC time resolution evaluated by using Michel-e^+ with an energy end-point of 52.8 MeV (at right).

$\Delta E_\gamma/E_\gamma(\text{FHWM}) = 6.5\,\%$ was measured, without yet introducing the quantum efficiency corrections (see Fig. 15 (left)). Introducing the QE we expect that $\Delta E_\gamma/E_\gamma(\text{FHWM}) < 5\%$.

The LXe calorimeter energy linearity, with the calorimeter illuminated by γ's at different energies is summarized in Fig. 15 (right).

The timing resolution of the LXe calorimeter was evaluated at 54.9 MeV with π^o-decay photons, selecting PMTs mounted at the center of the inner face. We measured $\Delta t_\gamma(\text{FHWM}) \approx 270$ ps (see Fig. 16 (left)).

The timing resolution of the timing counter and the drift chamber momentum resolution were measured with Michel positrons. We achieved a $\Delta t_{e^+}(\text{FHWM}) \approx 120$ ps (see Fig. 16 (right)) and $\Delta p_{e^+}/p_{e^+}(\text{FHWM}) \approx 2\,\%$ (Fig. 17).

The relative timing between the LXe calorimeter and the timing counter was obtained by using the two simultaneous γ's, at 4.4 MeV and 11.7 MeV, emitted from the proton nuclear reaction ${}^{11}_{5}\text{B}(p,\gamma){}^{12}_{6}\text{C}$. The Fig. 18 shows the measured (preliminary) LXe-TC timing, without any position selection.

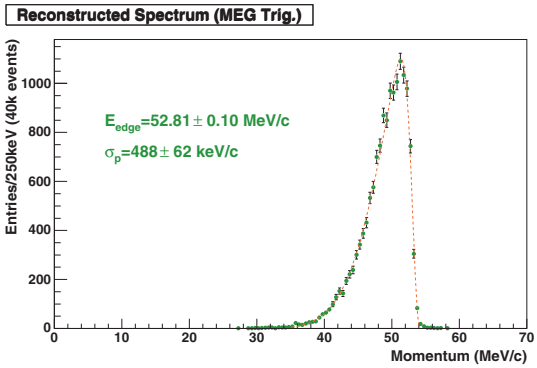

Fig. 17 The Drift Chamber momentum resolution evaluated by using Michel-e^+ coming from the μ^+-decay at rest, with an energy end-point of 52.8 MeV. We measured $\Delta p_{e^+}/p_{e^+}$ (FHWM) $\approx 2\%$.

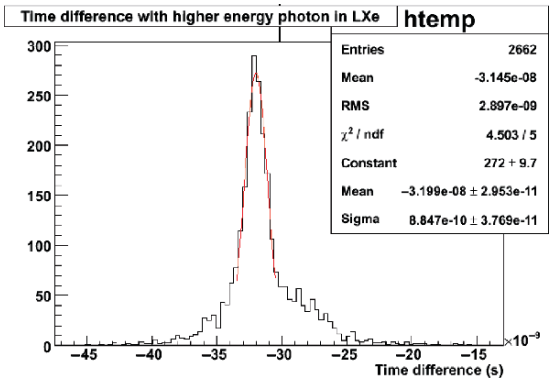

Fig. 18 The LXe-TC timing obtained by using the two simultaneous γ's, at 4.4 MeV and 11.7 MeV, emitted from the proton nuclear reaction $^{11}_{5}\mathrm{B}(\mathrm{p},\gamma)^{12}_{6}\mathrm{C}$. We measured $\sigma_{\gamma e^+} \approx 850$ ps, without any position selection.

11 The conclusion

We successfully ran the whole experiment during the engineering run 2007. All the detectors were installed and operated smoothly. All triggers were implemented and worked at the expected rates. A full set of calibration and data were taken. The detector performances were measured and are closer to the expected ones. We successfully restarted with the calibrations at May of this year and we started with the data acquisition at the end of September and we will go on for almost 3 years to reach the final sensitivity. We expect to improve the present upper bound on the $\mathrm{B}(\mu^+ \to e^+\gamma)$ at the end of this year if no candidate events are observed.

References

1. E.P. Hincks and B. Pontecorvo *Phys. Rev.*, Vol. 73, 257 (1948).
2. E.P. Hincks and B. Pontecorvo *Phys. Rev.*, Vol. 73, 1122 (1948).
3. B. Pontecorvo *Phys. Rev.*, Vol. 72, 246 (1947).
4. E.P. Hincks and B. Pontecorvo *Phys. Rev.*, Vol. 77, 102 (1950).
5. E.J. Konopinski and H. M. Mahmoud *Phys. Rev.*, Vol. 92, 1045 (1953).
6. E.J. Konopinski *Rev. Mod. Phys.*, Vol. 27, 254 (1955).
7. L. Michel *Phys. Rev.*, Vol. 86, 814 (1952).
8. S. Lokanathan and J. Steinberger *Phys. Rev.* Vol. 98, 240 (1955).
9. G. Feinberg *Phys. Rev.*, Vol. 110, 1482 (1958).
10. R. Faynman and R.P. Gell-Mann *Phys. Rev.*, Vol.109, 1482 (1958).
11. G. Feinberg and S. Weinberg *Phys. Rev. Lett.* Vol. 6, 381 (1961).
12. D. Bartlett, S. Devons and A.M. Sachs *Phys. Rev. Lett.* Vol. 8, 120 (1962).
13. P. Depommier et al. *Phys. Rev. Lett.* Vol. 39, 1113 (1977).
14. A. Van der Schaaf et al *Nucl. Phys. A* Vol. 340, 249 (1979).
15. W.W. Kinnison et al *Phys. Rev. D* Vol. 25, 2846 (1982).
16. A. De Rújula, H. Georgi and S.L. Glashow *Phys. Rev. D* Vol. 12, 147 (1975).
17. R.D. Bolton et al *Phys. Rev. D* Vol. 38, 2077 (1988).
18. M.L. Brooks et al. (MEGA collaboration) *Phys. Rev. Lett.*, Vol. 83, 1521 (1999).
19. A.Baldini et al. *Research Proposal to INFN* (2002).
20. R. Barbieri and L.J. Hall *Phys. Lett. B* Vol. 338, 212 (1994).
21. R. Barbieri, L.J. Hall and A. Strumia *Nucl. Phys. B* Vol. 445, 219 (1995).
22. Y. Kuno and Y. Okada *Rev. Mod. Phys.*, Vol. 73, 151 (2001).
23. M. Raidal et al. *arXiv:0801.1826v1*, "Flavour physics of leptons and dipole moments".
24. L. Calibbi et al. *hep-ph/0605139*, "Lepton flavour violation from SUSY-GUTs: where do we stand for MEG,PRISM/PRIME and a super flavour factory".
25. A.E. Pifer et al. *Nucl. Instr. Meth*, Vol. 35, 39 (1976).
26. H.W. Reist et al. *Nucl. Instr. Meth*, Vol. 153, 61 (1978).
27. A. Badertscher et al. *Nucl. Instr. Meth. A*, Vol. 238, 200 (1985).
28. A. Baldini et al. *Nucl. Instr. Meth. A*, Vol. 545, 753(2005).
29. A. Baldini et al. *IEEE Tans. Diel. Elec. Ins.*, Vol. 13, 547(2006).
30. A. Baldini et al. *Nucl. Instr. Meth. A*, Vol. 565, 589 (2006).
31. A. Papa *Il Nuovo Cimento B*, Vol.122, 627 (2007).
32. S. Ritt *Nucl. Instr. Meth. A*, Vol. 494, 520 (2002).

The Study of Ultra High Energy Cosmic Rays in the Pierre Auger Observatory

M. Pimenta, for the Pierre Auger Collaboration

Abstract The present status of the Pierre Auger Observatory and its recent results on Ultra High Energy Cosmic Rays are shortly reported. The following topics are discussed: (i) the energy spectrum above $\sim 4 \times 10^{18}$ eV, (ii) the arrival directions, (iii) the depth of the shower maximum, (iv) the upper limit on the primary photon flux, (v) the upper limit on the diffuse neutrino flux.

Keywords: Ultra High Energy Cosmic Rays, Pierre Auger Observatory

1 Ultra high energy cosmic rays

The energy spectrum of cosmic rays extends over more than 11 decades of energy, following an almost perfect power law (see Fig. 1) [18]. The fluxes are quite high at low energies (up to 1 particle/m^2/s for energies of the order of the GeV), but extremely small at the highest energies ($\sim$1 particle/km^2/century at 10^{20} eV). The Pierre Auger Observatory aims at measuring the far end of the spectrum, the Ultra High Energy Cosmic Rays (UHECR) region (Fig. 2)[7]where just a few events have been observed. The first event with an energy greater than 10^{19} eV was observed by John Linsley in 1962 at Volcano Ranch [13]. Until 2005 $\sim$20 events were collected mainly by the AGASA [15] and HiRes [8] experiments.

UHECR are of relevance for a wide range of astronomy/astrophysics and particle physics subjects. At energies above 10^{19} eV the deflection of UHECR by the galactic magnetic field is small and so it is possible to use UHECR as an astronomy channel. UHECR are the most energetic particles ever accessible. The centre-of-mass energy of a $10^{19} - 10^{20}$ eV UHECR collision in the atmosphere is around 100$-$400 TeV, which is well above the energy of present and future man made accelerators. The

M. Pimenta
LIP/IST, Av. Elias Garcia 14, 1. P-1000-149 Lisboa, Portugal,
e-mail: pimenta@lip.pt

V. Begun et al. (eds.), *Progress in High-Energy Physics and Nuclear Safety*,

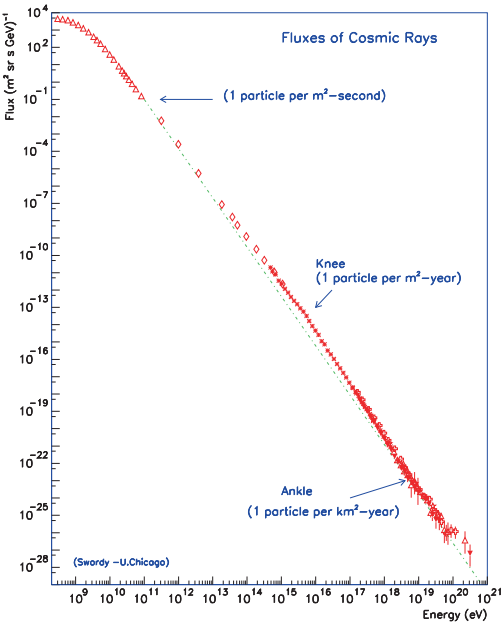

Fig. 1 The cosmic ray spectrum

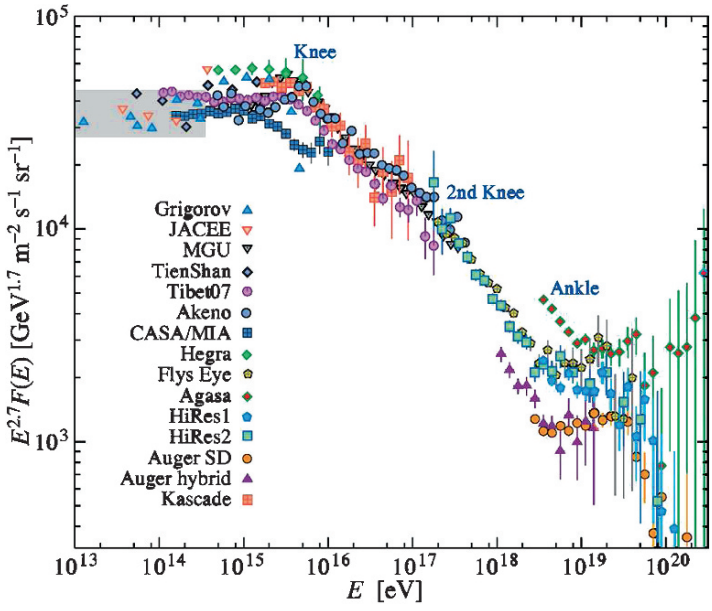

Fig. 2 The far end of the cosmic ray spectrum

study of UHECR is thus an unique opportunity to access energy scales beyond the LHC. However, fluxes are small, the accessible kinematic region is very narrow (very forward region) and the detection capability is poor. Finally, UHECR travel at speeds near the speed of light, with huge Lorentz boost factors ($\sim 10^{11}$), and are therefore ideal probes to test fundamental physics postulates as Lorentz invariance.

There is an intense debate on the possible acceleration mechanisms able to produce particles with such energies. The sources where these acceleration may occur can be characterized by two variables: its size and the intensity of its magnetic fields. High energy particles can be confined either in small regions, if there is an intense magnetic field, or, if the magnetic field is weak, in extensive regions. Such a feature is usually summarized in the so-called Hillas plot (Fig. 3) [12]. There are still some possible sources for UHECR up to 10^{20} eV, but at higher energies it is much more difficult to find good candidates. Furthermore, energy losses due to Bremsstrahlung have to be taken into account whenever the accelerations are very large [14].

The observed UHECR have to propagate through very large distances before reaching the Earth. But there is no empty space. The space is, as it is well known, filled with the Cosmic Microwave Background (CMB). The interaction of the UHECR with the CMB photons can be quite dramatic if the centre-of-mass energy is above the first inelastic channel threshold. The net result is that UHECR

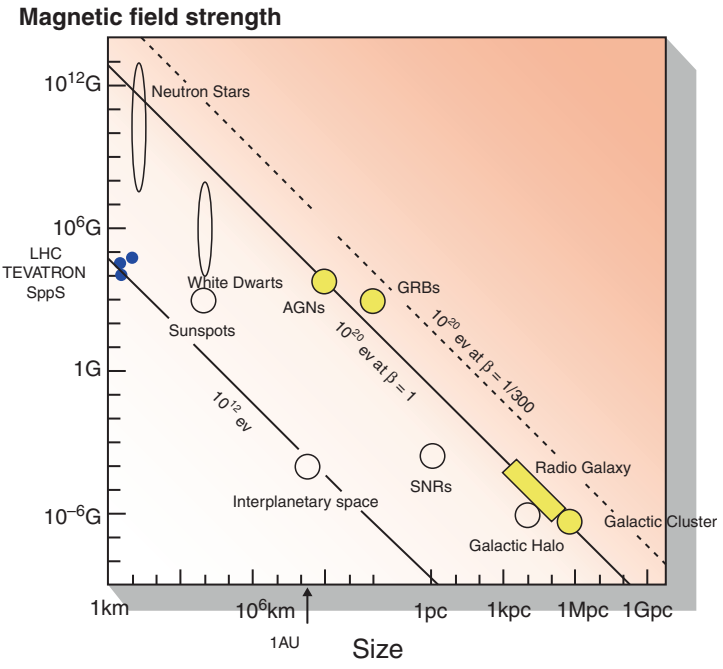

Fig. 3 The Hillas plot. The intensity of the magnetic field (B) of the possible astrophysical sources is plotted against its size (R). The straight lines represent the Larmor relation $E \propto \beta \cdot B \cdot R$ where β is an efficiency factor

produced at far-away sources with energies well above 10^{20} eV, would reach Earth with energies of about 10^{20} eV. This is the famous Greisen-Zatsepin-Kuzmin (GZK) effect [10, 19]. GZK does not create however a real cut-off as it depends on many parameters (the type of sources and their distribution in space, the existing magnetic fields, the particle type, ...).

Arriving at the Earth UHECR interact with the atmosphere, originating Extensive Air Showers (EAS) composed by billions of particles (mainly electrons and photons). If the primary particle is a proton or a nuclei then hadronic interactions play a determinant role in the first stages of the EAS development. However, there is no computable theory for soft hadronic interactions and one must deal with phenomenological models and the corresponding systematic uncertainties. There is thus no direct or unambiguous way to determine the UHECR hadronic mass composition. Only photons and neutrinos can be discriminated with certainty.

2 Pierre Auger Observatory

The construction of the southern site of the Pierre Auger Observatory [1] in Malarge, province of Mendoza, Argentina, has just reached completion. It covers 3,000 km^2, combining the technique of sampling the shower particles reaching the Earth surface, using 1,600 water Cherenkov tanks, with the technique of detecting the fluorescence light produced by the shower in the atmosphere, using four groups (eyes) of six fluorescence telescopes. The atmosphere above the Auger site in Mendoza is permanently monitored by several complementary instruments, including radiosondes, laser facilities and Lidars. Many thousands of events per year (several tens above 10^{20} eV) will be collected. About 10% of the collected events will have, in addition to the information from the Surface Detector (SD), information from the Fluorescence Detector (FD). The data collected so far (in the last 4 years, during construction) corresponds roughly to 1 year of operation of the complete southern observatory. The UHECR arrival directions, in events recorded only by the SD (SD events), are basically obtained from the time measurements registered by the individual stations, assuming a reasonable description of the shower front geometry. The obtained angular resolution for energies above 10^{19} eV is 1°. In events with information from the FD (FD events) the shower axis can be reconstructed and a similar angular resolution is obtained. For Hybrid events, with both FD and SD information (at least one SD station near the shower core) the angular resolution is clearly improved to values of the order of 0.2°. The UHECR energy is directly measured by the FD. The fluorescence light, emitted by the de-excitation of the N_2 molecules, is proportional to the number of the charged particles in the shower. A systematic uncertainty of 22% is presently assigned, coming mainly from the uncertainties on the determination of the fluorescence light yield (14%) and from the shower reconstruction (10%). In SD events a more indirect energy estimator, the $S38$, is built using the EAS lateral density distribution at a distance of 1,000 m from the core, $S(1{,}000)$, and rescaling it to zenith angles of 38°. This rescaling, made

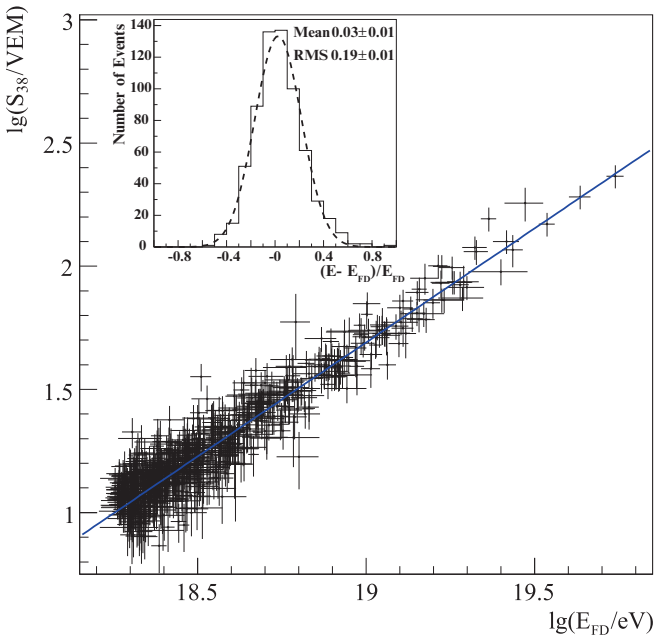

Fig. 4 Correlation between $\log S38$ and $\log E_{\mathrm{FD}}$ for the 661 hybrid events used in the fit. The full line is the best fit to the data. The fractional differences between the two energy estimators are shown in the inset plot

through the so called Constant Intensity Cut method, assumes that the cosmic ray intensity is, at a given energy, the same for all directions [11]. The $S38$ is then calibrated using a clean set of Hybrid events. The good correlation between the $S38$ and the direct FD energy measurement is shown in Fig. 4. The spread around the best fit is 19% which is compatible with the uncertainties on the $S38$ and on the FD energy scale. The UHECR mass composition is, as mentioned before, an important but difficult measurement. One of the most sensitive observable is the X_{max}, the depth in the atmosphere at which the number of electrons in a shower reaches a maximum. In Auger, X_{max} is measured in selected hybrid events with an accuracy better than $20\,\mathrm{g\,cm^{-2}}$ [16].

An enhancement program of the Pierre Auger southern site is now under way. The aims are: to lower the present energy threshold of the experiment, increasing the SD station density in a small area of the array and to improve the muon detection capabilities by introducing new muon detectors in the infill region (AMIGA – Auger Muons and Infill for the Ground Array); to enlarge the vertical field of view of the fluorescence detectors (HEAT – High Elevation Atmospheric Telescope); and to test the radio detection technique. Radio detection of showers with an external trigger from the array has already been achieved.

The complete sky coverage by the Pierre Auger Observatory implies the construction of a second site in the northern hemisphere. At the time of the original

design report, the two sites were foreseen to be built simultaneously and covering the same surface area (3,000 km^2). Later, it was decided to build the southern site and take into account its first results in the elaboration of the final Auger North design. This design is presently being finalized. Lamar, in Colorado, USA, was chosen as the Auger northern site, after a detailed evaluation based on criteria such as land access, climate, atmosphere, available surface and local support. In the present preliminary design Auger North is optimized for the highest energies (above 10^{20} eV) and a much larger surface area (20,000 km^2) is being considered.

3 Pierre Auger results

The Pierre Auger Observatory has recently published its first results on the UHECR energy spectrum [4] and arrival directions [2,3] as well as on the depth of the shower maximum [16]. Upper limits on the primary photon flux [5] and on the diffuse neutrino flux [6] were also reported.

The energy spectrum based on ∼20,000 SD events with energy above 2.5×10^{18} eV is displayed in Fig. 5. The reported exposure of ∼7,000 km^2 sr year is twice that of HIRes. The measured flux [4], above 4×10^{19} eV is suppressed, with a significance of 6 standard deviations, in relation to what would be expected in a non-GZK

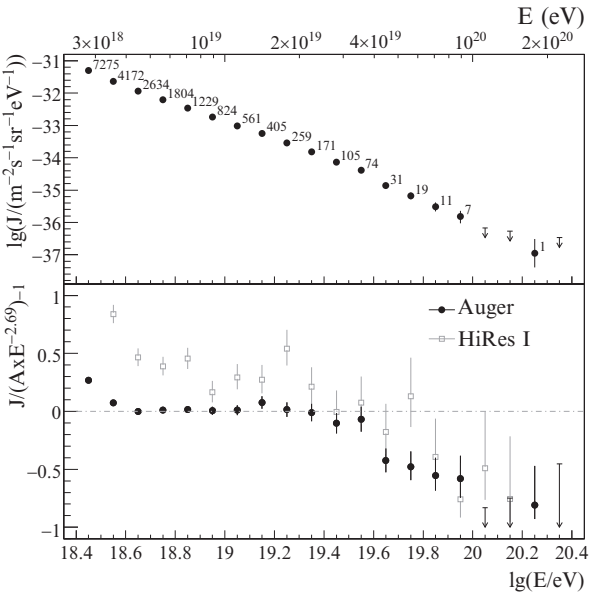

Fig. 5 Upper panel: The energy spectrum of CRs obtained with 20,000 SD events with $\theta < 60^\circ$. The numbers on top of each point indicate the number of events in the bin. Lower Panel: The fractional differences between Auger and HiRes I data compared with a spectrum with an index of 2.69

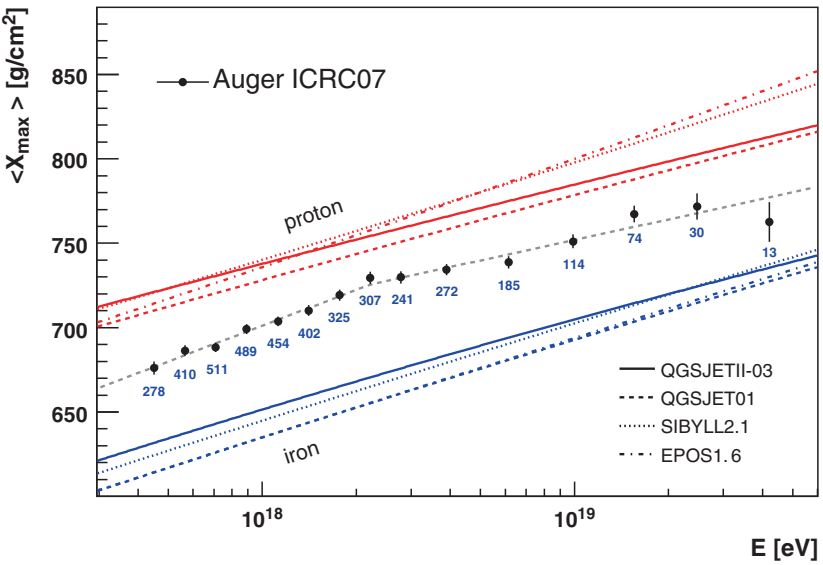

Fig. 6 $\langle X_{\max} \rangle$ as a function of energy compared to predictions from hadronic interaction models. The dashed line is a fit with two constant elongation rates and a break-point. Event numbers are indicated below each data point

scenario. However, no claim of the discovery of the GZK can be yet firmly stated as the acceleration mechanisms and the sources are basically unknown. As can be seen in the same figure the previously reported HIRes spectrum is softer but presents the same suppression features.

The depth in the atmosphere at which the number of electrons in the EAS reaches the maximum, $X_{\max}$, is shown in Fig. 6. The expected mean $X_{\max}$ for iron and protons showers, assuming different hadronic models, are also shown. The comparison of the Pierre Auger Observatory data with the predictions of the most popular hadronic models indicates that at the highest energies the average mass composition increases, which is in contradiction to what is usually assumed. The other possibility is a deep change on the hadronic interaction models at this high energy scale, not accessible at man-made accelerators.

The arrival directions of the events with energy larger than 57 EeV collected by the Pierre Auger Observatory until August 2007 are displayed in galactic coordinates in Fig. 7. The events are shown as small circles of 3.1° and the red crosses indicate the position of nearby AGNs (distance less than 75 Mpc) taken from the 12th edition of the Vron-Cetty and Veron catalog [17]. The white region of the sky is not accessible from the Auger southern site and the darker blue regions indicate larger relative exposures. These results are not compatible with an isotropic distribution of the arrival directions of the very high energy cosmic rays and show a significant correlation with the positions of nearby AGNs. However other sources that may have similar spatial distribution within the GZK horizon may also lead to significant cor-

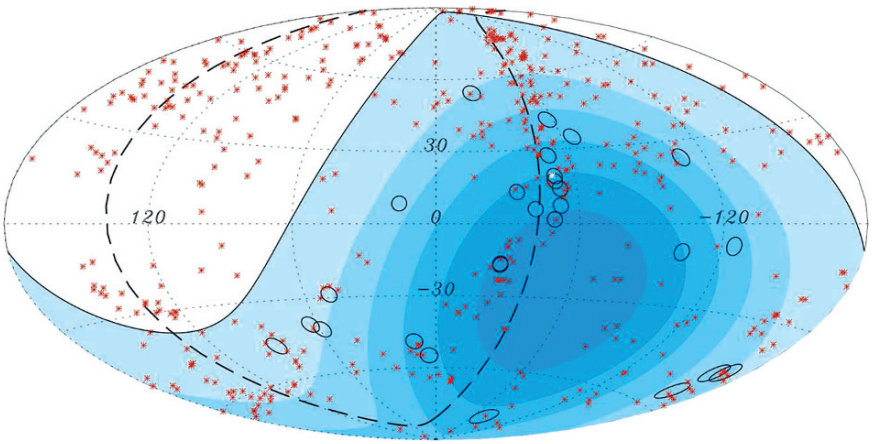

Fig. 7 Aitoff projection of the celestial sphere in galactic coordinates with circles of radius 3.1° centered at the arrival directions of the 27 cosmic rays with highest energy detected by the Pierre Auger Observatory. The positions of the 472 AGN with redshift $z \leq 0.018$ ($D < 75$ Mpc) from the 12th edition of the catalog of quasars and active nuclei are indicated by red asterisks. The solid line represents the border of the field of view. Darker color indicates larger relative exposure. The dashed line is the supergalactic plane. Centaurus A, one of our closest AGN, is marked in white

relations. The correlation angle of 3.1° between the cosmic ray arrival directions and the AGNs positions may also give some insight on the cosmic ray composition and/or on the strength of the galactic and extra-galactic magnetic fields. While protons may be deflected just a few degrees by the galactic magnetic field, nuclei should have much higher deflections. A light composition at high energies may then be favored, in apparent contradiction with the indication given by the evolution of $X_{\max}$ as discussed above.

The 95% confidence level upper limits on the primary flux of primary photons obtained by the Pierre Auger Observatory are compared in Fig. 8 to previous results and theoretical predictions. The corresponding limits on the cosmic ray fraction of photons are 2%, 5.1% and 31% at 10^{19} eV, 2×10^{19} eV and 4×10^{19} eV, respectively. These results are based on the different longitudinal development of the photon and of the hadronic showers, namely in the depth of the maximum of the shower, $X_{\max}$, measured by the FD, and on the signal rise time and on the curvature of the shower front at the Earth surface, measured by the SD. These upper limits can already exclude several top-down models of UHECR [9]. After some years of data taking the level of fluxes due to GZK photons can be attained.

The 90% confidence level upper limits on the diffuse neutrino flux reported by the Pierre Auger Observatory are compared in Fig. 9 to previous results and theoretical predictions. These results are based on the capability of discriminating quasi-horizontal neutrino induced air showers, which have a significant electromagnetic component, from the normal hadronic showers at large zenith angles, where the only surviving particles are high energy muons concentrated in a thin and quasi-planar front. In particular, the Pierre Auger Observatory is able to detect the so-called

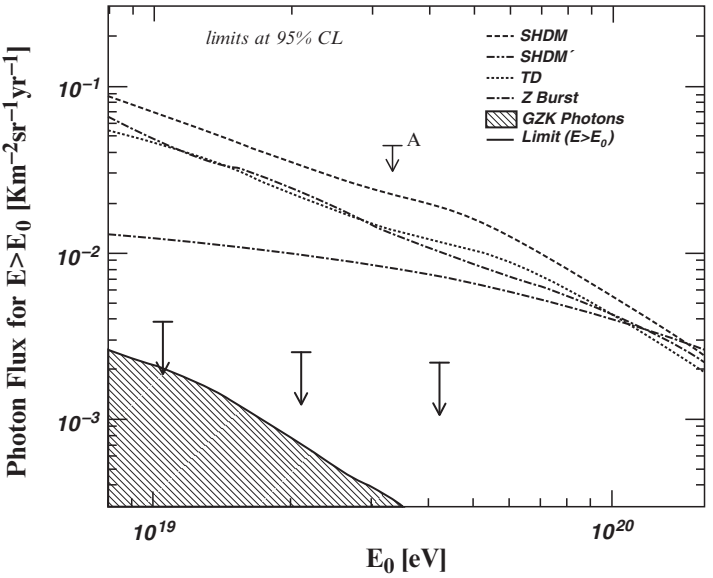

Fig. 8 The Auger upper limits on the integral flux of photons (black arrows) along with predictions from top-down models (SHDM, TD and ZB, SHDM) and with predictions of the GZK photon flux. A flux limit derived indirectly by AGASA ("A") is shown for comparison

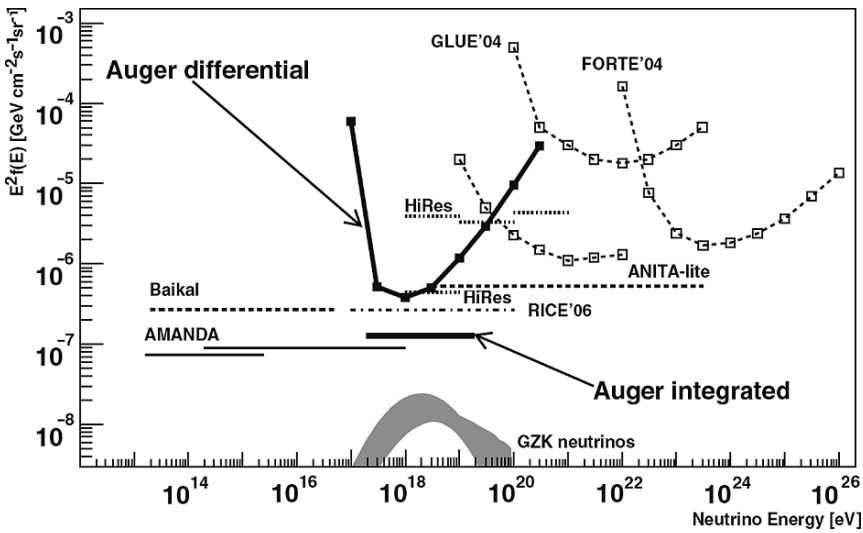

Fig. 9 Limits at 90% C.L. for a diffuse flux of ν_τ from the Pierre Auger Observatory. Limits from other experiments are converted to a single flavour assuming a 1:1:1 ratio of the three neutrino flavours and scaled to 90% C.L. where needed. Two different formats are used: differential (squares) and integrated (constant lines). The shaded curve shows the range of expected fluxes of GZK neutrinos calculated

Earth skimming τ neutrinos where a τ neutrino moving upwards interacts inside the Earth producing a EeV τ lepton which, after traveling tens of kilometers, decays in the atmosphere giving birth to a nearly horizontal air shower. No candidate was found up to August 31, 2007.

4 Conclusion

The Pierre Auger Observatory has recently published results on the arrival directions and on the energy spectrum of UHECR. In fact, the anisotropy of the arrival directions of the highest-energy cosmic rays and their extragalactic origin was demonstrated. The observations are consistent with the hypothesis that the rapid decrease of flux measured by the Pierre Auger Observatory above 6×10^{19} eV is due to the interactions with the cosmic microwave background (the GZK effect) and that most of the cosmic rays reaching Earth in that energy range are protons from nearby astrophysical sources, either AGN or other objects with a similar spatial distribution. Meanwhile, results on the depth along the atmosphere at which the number of electrons and positrons in the extensive air showers reaches its maximum were also presented by the Pierre Auger Observatory and are in contradiction with the current expectations assuming a light composition. Upper limits of the photon fraction in the UHECR spectrum, as well as on the diffuse flux of high-energy τ neutrinos, were also reported. These results open a new astronomy channel to the nearby Universe and also represent a unique window to study Particle Physics at energies well beyond the LHC.

Acknowledgements I would like to warmly thank the organization and in particular László Jenkovszky for the hospitality and a very interesting meeting. Thanks are due to Sofia Andringa, Pedro Assis, Ruben Conceio, Catarina Esprito Santo and Bernardo Tom for reading the manuscript and helping in the preparation of these proceedings.

References

1. http://www.auger.org/.
2. Abraham, J., et al.: Correlation of the Highest-Energy Cosmic Rays with Nearby Extragalactic Objects. Science. **318**, 938–943 (2007).
3. Abraham, J., et al.: Astrop. Phys. **29** 188 (2008).
4. Abraham, J., et al.: Observation of the suppression of the flux of cosmic rays above 4×10^{19}eV. Phys. Rev. Lett. **101**, 061101 (2008).
5. Abraham, J., et al.: Upper limit on the cosmic-ray photon flux above 10^{19} eV using the surface detector of the Pierre Auger Observatory. Astroparticle Phys. **29**, 243–256 (2008).
6. Abraham, J., et al.: Upper Limit on the Diffuse Flux of Ultrahigh Energy Tau Neutrinos from the Pierre Auger Observatory. Phys. Rev. Lett. **100**, 211101 (2008).
7. Amsler, C., et al.: Review of Particle Physics. Phys. Lett. B **667**, 1 (2008).
8. Bird, D., et al.: Astrophys. J. **511**, 739 (1999).

9. Semikoz, D.: In: Proc. 30th ICRC. P. 1035 (Merida, Mexico, 2007).
10. Greisen, Kenneth: Phys. Rev. Lett. **16**, 748 (1966).
11. Hersil, J., Escobar, I., Scott, D., Clark, G., and Olbert, S.: Observations of Extensive Air Showers near the Maximum of Their Longitudinal Development. Phys. Rev. Lett. **6**, 22 (1961).
12. Hillas, A.M.: Ann. Rev. Astron. Astrophys. **22**, 425 (1984).
13. Linsley, J.: Phys. Rev. Lett. **10**, 146 (1963).
14. Medvedev, M.V.: Phys. Rev. E **67**, 045401 (2003).
15. Takeda, M.: Astro. Part. Phys. **19**, 499 (2003).
16. Unger, M.: In: Proc. 30th ICRC. P. 594 (Merida, Mexico, 2007).
17. Véron-Cetty, M.-P. and Véron, P.: A catalogue of quasars and active nuclei: 12th edition. Astronomy and Astrophysics **455**, 773–777 (2006).
18. Watson, A.A. and Nagano, M.: Rev. Mod. Phys. **72**, 689 (2000).
19. Zatsepin, G. T. and Kuz'min, V.A.: Sov. Phys. JETP Lett. **4**, 78 (1966).

The MoEDAL Experiment – Searching for Highly Ionizing Particles at the LHC

J.L. Pinfold

Abstract The MoEDAL experiment designed to search for magnetic monopoles and other highly ionizing particles at the LHC. The MoEDAL experiment employs nuclear track etch detectors deployed in the VELO vertex region of the LHCb experiment. A description of this experiment is given in addition to a brief discussion of the physics program and data taking plans.

Keywords: Nuclear track detectors, magnetic monopoles, heavy stable particles, black hole remnants, LHC, LHCb, proton–proton collisions

1 Introduction

In 2009 the LHC will open up a new energy regime where it will be possible to observe envisaged physics beyond the Standard Model. The search strategy for exotics planned for the main LHC detectors can be extended with dedicated experiments designed to enhance, in a complementary way, the physics reach of the LHC. The MoEDAL (Monopole and Exotics Detector at the LHC) experiment is such an experiment. The prime motivation of MoEDAL is to directly search for highly ionizing Stable Massive Particles (SMPs) at the LHC that fall into three main categories. The first is that of massive magnetically charged particles such as the magnetic monopole [1, 2] or the dyon [3]. The second class of hypothetical particle has multiple electric charge such as the black hole remnant [4], strangelet [5–8], Q ball [9], or long-lived doubly charged Higgs boson [10]. Last, but not least, are the very heavy conventionally charged particles that are heavily ionizing by virtue of their small speed (β = v/c) such as charge R-hadrons [11] or long lived charge sleptons predicted in the framework of GMSB models [12].

J.L. Pinfold
Centre for Particle Physics Research, Edmonton, Alberta T6G 0V1, Canada,
e-mail: pinfold@phys.ualberta.ca

V. Begun et al. (eds.), *Progress in High-Energy Physics and Nuclear Safety*,

A particle with a very large effective charge such as the magnetic monopole may be absorbed before reaching of fully traversing the calorimetry of the general purpose LHC experiments, particularly if the magnetic charge is greater than one. For those monopoles that are registered by ATLAS and CMS, little work has been done to estimate the sensitivity of ATLAS and CMS to direct detection of these particles. However, as described below a Dirac monopole will typically lose several thousand times as much ionisation energy as a MIP. A detailed dE/dx calibration is therefore not necessary to observe them. However, detector and readout electronic saturation effects due to the enormous ionisation energy must be carefully studied in any search. Furthermore, customized track-finding algorithms would have to be written to account for the parabolic track trajectory followed by a magnetic monopole in a magnetic field. It is also important to employ GEANT simulations to calculate the stopping of magnetic monopoles in detector material and the energy deposition of profiles of magnetic monopoles which progress to the calorimeters. A comprehensive search must consider the full mass and magnetic charge range which is experimentally available.

The main LHC experiments are designed to detect conventionally charge particles produced with a β large enough to fall into LHC trigger window of 25 ns. one of the principal constraints on the design of a collider experiment and its ability to measure slow-moving SMPs is the bunch crossing time.[1] For a SMP at the LHC to be detected or triggered in a certain detector system and be associated to the correct bunch crossing, it should arrive at most 25 ns after the default arrival time of a particle traveling at the speed of light [13, 14]. Later arrival would imply triggering or detection within the next crossing time window. The large size of the ATLAS and CMS detectors[2] ensures that this will be an important source of inefficiency in detecting SMPs. For example, it is only possible to reconstruct the track of a slowly moving SMP in the ATLAS central muon chambers within the correct bunch crossing window if $\beta \geq \sim 0.5$ [13].

Even if the SMP travels within the appropriate timing window, additional problems may arise from its slowness. The sampling time and reconstruction software of each sub-detector is optimised assuming particles travelling at luminal speed. Hence, the quality of the read-out signal or reconstructed track or cluster may be degraded for an SMP, especially for sub-systems far away from the interaction point. Detector simulations so far suggest that it will still be possible to trigger and measure slowly moving particles at ATLAS and CMS [13, 15]. However, this is an area which must continue to be studied as the simulation programs are further developed and the detectors better understood.

The MoEDAL experiment bypasses the problems described above of detecting magnetic monopoles with active detectors, by using the passive plastic track technique that does not require a trigger. Also, as we shall see below, track-etch detectors provide a tried and tested method to detect and accurately measuring the track of a highly ionizing particle, but also its Z/β. Importantly, heavy-ion beams

[1] The LHC crossing time of 25 ns, is considerably shorter than that at LEP (25 μs), the Tevatron (396 ns) or HERA (96 ns).

[2] The central ATLAS and CMS muon chambers extend to 10 and 7 m, respectively.

provide a demonstrated calibration technique using energy depositions very similar to that of the hypothetical particles sought. Current acceptance calculations indicate that MOEDAL will be sensitive to monopoles with: masses up to near 7 TeV; and, a magnetic charge as high as 3g. MOEDAL offers the most promising method of hunting for magnetic monopoles at the LHC. However, this depends on the magnetic monopole production cross section since MOEDAL would be exposed to integrated luminosity around 100 times lower than that collected by ATLAS and CMS. Having said this the detection of even one magnetic monopole that penetrated a MoEDAL NTD stack would be distinctive, as the background from conventionally charged tracks is negligible.

In this paper we shall concentrate on main physics aim of the MoEDAL experiment, that is the search for the magnetic monopole in the new energy regime opened up by the LHC.

2 The search for the monopole

In 1931 Dirac introduced the magnetic monopole in order to explain the quantization of the electric charge, which follows from the existence of at least one free magnetic charge [16]. He established the basic relationship between the elementary electric charge e and the basic magnetic charge:

$$eg = n\hbar c/2 = ng_D \tag{1}$$

where n is an integer, n = 1, 2, ... The magnetic charge is $g = ng_D$; $g_D = \hbar c/2e = 68.5e$ is called the unit Dirac charge. The existence of magnetic charges and of magnetic currents would symmetrize in form the Maxwells equations, but the symmetry would not be perfect since $e \neq g$. But if the couplings are be energy dependent they could converge to a single common value at very high energies [17].

There is no real prediction of the mass of classical Dirac magnetic monopole. One may have a rough estimate assuming that the classical monopole radius is equal to the classical electron radius: from which $r_M = g^2/(m_M c^2) = r_e = e^2/m_e c^2$ from which $m_M = g^2 m_e/e^2 \approx n.4700.m_e = n.2.4$ GeV/c^2. Thus the mass should be relatively large and even larger if the basic charge is e/3 and if n > 1.

Grand Unification magnetic monopoles, with masses of the order of 10^{15} GeV are well beyond the reach of any presently conceivable man-made accelerator. Never-the-less there are models where monopoles could appear in a mass range accessible to the LHC. Examples include: the electroweak Cho–Maison monopole [19]; the Troost–Vinciarelli monopole [18] with mass that depends on the matter field (10^4 GeV/c^2 with IVB matter fields, 10^2 GeV with ρ matter fields and 50 GeV with spin-1/2 matter fields; and a Superstring model [20] where in principle, monopoles/dyons with a mass low enough ($\sim$1 TeV/c^2) to be detected at the LHC are hypothesized.

Since 1931 searches for classical Dirac monopoles were carried out at every new accelerator using mainly relatively simple experiments, and recently also large collider detectors [2]. Searches at the Fermilab collider [21] seem to exclude MMs with masses up to 850 GeV. Experiments at the LEP2 collider exclude masses below 102 GeV [22]. The limits produced on magnetic monopole production depend on the physical process by which the monopole is presumed to be produced. Monopole searches have been carried out in e^+e^-, $p\bar{p}$, and pp interactions at various high energy colliders.

For example, for Dirac monopoles the most obvious mechanism is annihilation and pair production via the electromagnetic interaction. If one assumes a single-photon production process, then the amplitude for pair production is proportional to the magnetic charge. Ignoring higher order effects, one can then formulate a naive pair production cross section for monopoles of mass m, $\sigma_{D(m)}$, by multiplying the cross section for production $\mu^+\mu^-$ pair with invariant mass greater than $2m$ by the square of the charge ratio and making a phase space correction:

$$\sigma_{D(m)} = \left(\frac{g_D}{e}\right)^2 \times \sigma_{\mu\mu}(> 2m) \times (1 - 4\frac{m^2}{s}) \tag{2}$$

2.1 Magnetic monopole pair production cross-section at the LHC

Due to the high coupling constant of the magnetic monopole perturbative calculations of the magnetic monopole cross section cannot be made. Instead a Drell–Yan mechanism [23] is used for the cross section calculation. Figure 1 shows a Feynman diagram of the Drell-Yan mechanism for dimuons and monopole-antimonopole production. These two diagrams shows annihilation of the quark-antiquark via the intermediate virtual photon and later photon decay into the two leptons (left) and monopole-antimonopole pair (right). This simple production mechanism allows qualitative cross section estimates in the absence a reasonable field formulation of monopole production. The Drell–Yan cross section depends on strong

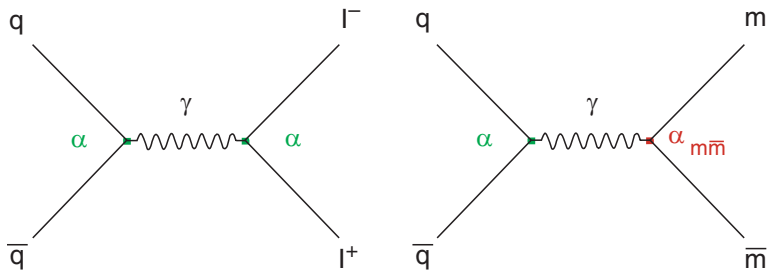

Fig. 1 Drell–Yan process for dimuon production (left) and monopole-pair production (right)

interaction between the initial pair of quarks. In the high energy limit, the quarks are treated like free charged particles and their interaction is purely electromagnetic. This is a very good approximation for reasonably high energies ($E \gg m_q$), where E is the total energy of the incident particles in the centre-of-mass system. The cross-section $\sigma(qq \to l^+l^-)$ is related to $\sigma(e^+e^- \to \mu^+\mu^-)$, which is given by: $\sigma(e^+e^- \to \mu^+\mu^-) = 4\pi\alpha^2/3E_{cm}^2$, (for $E \gg m_\mu$. The electron charge e is replaced by the quark charge $Q|e|$ and all possible colour orintations of the quark are averaged,

$$\sigma(qq \to l^+l^- = \frac{Q^2}{3} \times \frac{4\pi\alpha^2}{3E_{cm}^2} \tag{3}$$

The complete cross-section takes into account the quark structure of the hadrons.

We can use this formulation to attempt to calculate the production cross-section for magnetic monopoles once the proper coupling of the magnetic charge to the electromagnetic field is incorporated. This is derived by combining the Dirac quantization condition with the definition of the coupling constant ($\alpha \sim e^2$) $\alpha_{mm} = \alpha(ng/e)$, which gives for the cross-section:

$$\sigma(qq \to m\bar{m} = \frac{ng}{e} \times \sigma(qq \to l^+l^-) \tag{4}$$

Thus, to get the monopole-pair cross-section the Drell–Yan cross-sections are scaled by a factor $(ng/e)^2$.

For pp collisions there exists data on the differential cross-section for production of massive virtual photons, which exhibits scaling and falls of exponentially with $x \equiv 2M_m/\sqrt{s}$, [24] where $\sqrt{s}$ is the available centre-of-mass energy andM_m is the magnetic monopole mass[3] to this end we have predicted monopole-pair cross-sections at LHC energies by the formula:

$$\frac{d\sigma}{dmdy}|_{y=0} = \frac{44 \times 10^{-30}}{s^{\frac{3}{2}}} \times e^{\frac{-25.3m}{\sqrt{s}}} cm^2/GeV/c^2 \tag{5}$$

To obtain the cross-section for monopole pair production with mass $M = (s/2)^{1/2}$ we integrate the cross-section above $m = 2M_m$. Assuming no phase space suppression:

$$\sigma M = (68.5)^2 \times \frac{1.74}{s} \times e^{\frac{-25.3m}{\sqrt{s}}} \times 10^{-30} \tag{6}$$

Running for 1 year (10^7 s) at a luminosity of 5×10^{32} cm^{-2}s^{-1}, the search sensitivity is $\sim 2 \times 10^{-39}$ cm^2, when convoluted with the MoEDAL acceptance and detection efficiency, which corresponds to single event production with a mass of $\sim$3.5 TeV.

The cross-section given above is intended to be a rough point of reference cross-section for the production of magnetic monopoles via the electromagnetic interaction. This estimate is conservative since higher order diagrams with more than one

[3] For pp collisions this cross-section is about an order of magnitude smaller than for $p\bar{p}$ collisions at the same centre-of-mass energy [25].

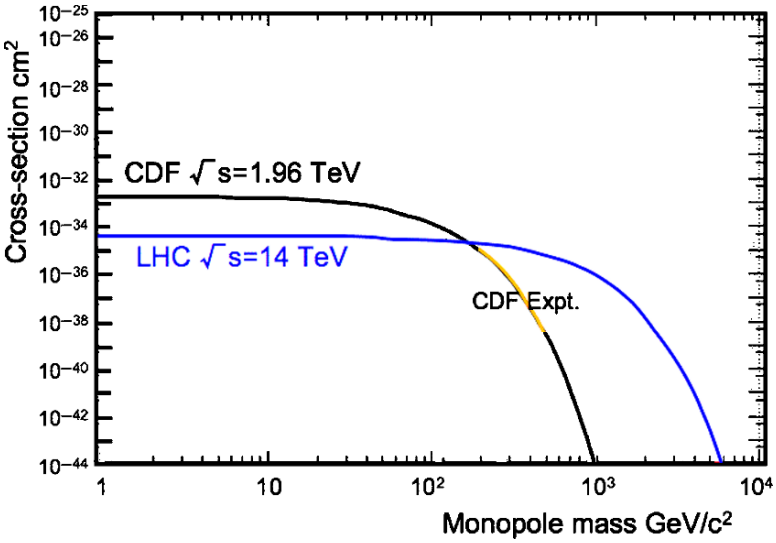

Fig. 2 The Drell–Yan cross-section versus magnetic monopole mass for the Tevatron and LHC Energies

virtual photon in the intermediate state will also contribute. Production via gluon-gluon fusion may be more likely still [26]. The variation of the predicted Drell–Yan cross-section with magnetic monopole mass is shown in Fig. 2. We find excellent agreement with the Drell–Yan curve for the mass interval 200-600 HeV published by the authors of the CDF experiment [27], as is shown by the orange curve which fits the black predicted curve well.

3 The MoEDAL detector

The MoEDAL detector is comprised of an array of plastic Nuclear Track Detectors (NTDs) deployed around the (Point-8) intersection region of the LHCb detector, in the VELO[4] cavern. The array consists of NTD stacks, nine layers deep, in Aluminium housings attached to the walls and ceiling of the VELO cavern. The maximum possible surface area available for detectors is around 25 m^2, although the final deployed area could be somewhat less due to the developing requirements of the LHCb detector. A depiction of the (maximal) MoEDAL array is given in Fig. 3.

The plastic NTDs employed by MoEDAL, consisting on nine layers of CR39 (3), MAKFROFOL (3) and Lecxan (3), record the passage of heavily ionizing particles which leaves an invisible damage zone along its trajectory in the plastic. The latent track of a highly ionizing particle such as a that of a magnetic monopole, is

[4] VErtex LOcator

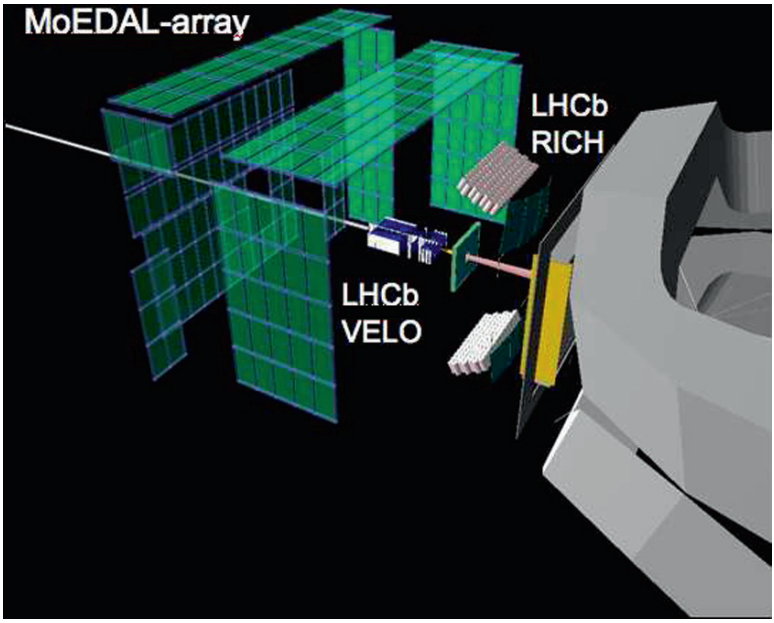

Fig. 3 A GEANT4 generated depiction of the MoEDAL array and is deployment in the VELO cavern of LHCb

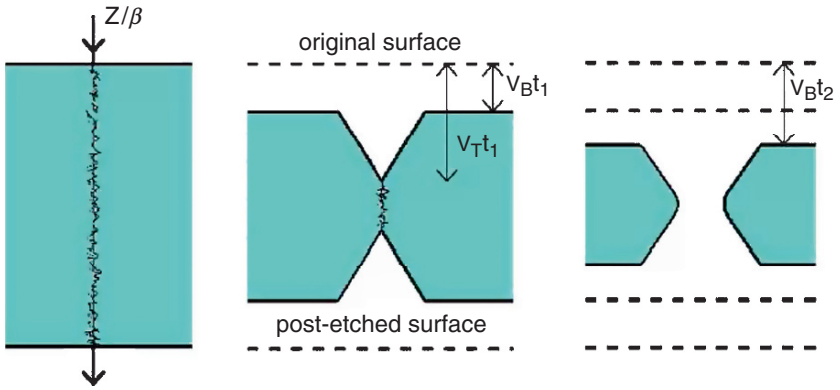

Fig. 4 The formation of a damage zone in a plastic NTD by the passage of a highly ionizing particle (left) and the subsequent etching (middle and right) to reveal the damage zone

manifested by etching v_B is the bulk rate v_T is the faster rate along the track. The damage zone is revealed as a cone shaped etch-pit, when the surface of the plastic detector is etched in a controlled manner using an etchant such as hot sodium hydroxide (NAOH) solution. The depth of the etch-pit is an increasing function of the Z/β of the particle, where Z is a particle charge and β its velocity. A schematic picture of the etching process is shown in Fig. 4. The reduced etch rate, p, is given by

v_T/v_B. The reduced etch rate is simply related to the restricted energy loss (REL), which is the fraction of the total energy loss which remains localized in a cylindrical region with about 10 nm diameter around the particle trajectory. Both the electronic and the nuclear energy losses contribute to REL. It was shown [28] that both are effective in producing etchable tracks in a CR39 nuclear track detector. NTD detectors comprised of CR39 can have a threshold as low as $Z/\beta \approx 5$ making it the most sensitive NTD and it allows to search for magnetic monopoles with one unit Dirac charge ($g = g_D$) for β around 10^{-4}, for $\beta > 10^{-3}$ and the whole β-range of $4 \times 10^{-5} < \beta < 1$ for magnetic monopoles with $g \leq 2g_D$ [29, 30]. The Lexan and Makrofol polycarbonates have a threshold at $Z/\beta \sim 50$; thus they are sensitive only to relativistic and/or multiply charged magnetic monopoles.

After etching, the MoEDAL NTDs will be scanned using manually controlled and/or computer controlled optical scanners which, with special dowel-pin marker holes, allow the determination of hole position with accuracy better than $\sim$20 μm in the multilayered NTDs stack used in the experiments. The response of track etch detectors versus REL can only be established by a calibration performed using ions of different charges and energies, where the calibration is dependent on the etching conditions. A typical calibration set-up at an ion beam accelerator includes a fragmentation target and nuclear track detector foils in front of and behind a target. After exposure the detector sheets are etched in standard conditions. The measured base areas of the etch-pit cones (tracks) increase with increasing ion charges. The trajectory of each highly ionizing particle is reconstructed by tracking the etch cones successively through the stack. This multiple measurement can be exploited to achieve a charge resolution that is to separate individual fragments from the calibration beam.

The etching process will, for one sheet of the CR39 stack, be continued for a sufficient length of time for holes resulting from a highly ionizing track to be formed in the sheet. Any holes so formed can be detected using the ammonia technique [31] where the plastic sheet is placed on top of sensitive blueprint paper and the two are sealed around the edge with tape. This package is then exposed to ammonia vapour. Each hole in the plastic is then revealed by a blue spot. The spotted blueprint paper can then be used as a map to define corresponding regions in accompanying sheets in the detector stack, that can be etched with greater care.

4 Conclusion

The MoEDAL experiment will use Nuclear Track Detector Arrays, deployed in the LHCb intersection region, to search for magnetic monopoles and other highly ionizing particles at the LHC. This detection technique is favoured for the following reasons:

- *Sensitivity to magnetic monopoles*: Monopoles with n = 1 will be detectable in CR-39 provided that $\beta \gtrsim 0.1$ and in Lexan for $\beta \gtrsim 0.85$. Highly ionizing particles with Z/β as low as 10- can be detected by CR39, depending on the etching conditions.

- *Insensitivity to MIPs*: CR-39, Lexan and UG-5 are totally insensitive to normally ionizing particles. For example with a luminosity of $\int$Ldt = 10^{40} cm^{-2} and a rapidity interval of Δy = 2, there will be 10^{16} MIPs passing through the detector. Nonetheless, with NTDs, we will still be able to pick out the signal from one monopole.
- *Solid angle coverage*: It is relatively easy to cover the full solid angle with stacks of NTDs.
- *Trigger*: As NTDs are always sensitive to monopoles and yet insensitive to normal hadronic events, no trigger is necessary (nor possible) with these devices. This is very useful in the search for very heavy stable particles whose time of flight to, say, the muon counters of an LHC experiment could exceed the trigger time allocated for each beam crossing.
- *Monopole Properties*: The measurement of the detailed shape of the conical etch pit produced on each side of the plastic or glass sheet gives information on the particle trajectory as well as the equivalent $Z/beta$. In a multi-sheet stack detector, the position and direction information from individual pits can be combined to give a very precise trajectory and the Z/β values can be used to determine the change in ionization energy loss as the particle looses energy passing through the detector (dE/dx should increase for electrically charged particles but decrease for a monopole). Showing that the candidate track comes from the interaction region and has consistent dE/dx values will be important checks.
- Radiation Resistance: The radiation resistance of track-etch detectors is examined in reference [32]. CR-39 is the most sensitive being able to stand a dose of around 2 MRads, Lexan/Makrofol can withstand around 200 MRads and UG-5 around a GigaRad. Thus NTDs are relatively radiation hard. Moreover, as the material is inexpensive, compared to usual electronic detector technology, it can be replaced when necessary.
- Cost: Both the cost of the mechanical structure required to hold the plastic NTD stacks and the plastic NTD themselves cost very little when compared to the electronic detectors designed to do the same job with the same coverage.

References

1. P.A.M. Dirac, Proc. R. Soc. London, Set. A, **133**, 60 (1931); P.A.M. Dirac, Phys. Tev., **24**, 817 (1948).
2. G. Giacomelli and M. Sioli (Astroparticle Physics), Lectures at the 2002 Int. School of Physics, Constantine, Algeria, hep-ex/0211035; G. Giacomelli and L. Patrizii, hep-ex/011209; G.R. Kalbfleisch, Phys. Rev. Lett. **85**, 5292 (2000); hep-ex/0005005 ; K.A. Milton et al. (New limits on the production of magnetic monopoles at Fermilab), hep-ex/0009003; B. Abbott et al., hep-ex/9803023, Phys. Rev. Lett. **81**, 524 (1998); G. Giacomelli, Riv. Nuovo Cimento **7** N.12, 1 (1984); M. Acciarri et al., Phys. Lett. B345, 609 (1995); L. Gamberg et al. (Direct and indirect searches for low-mass MMs), hep-ph/9906526;
3. J. Schwinger, A Magnetic Model of Matter, Science, **165**, Issue 3895, 757 (1969).
4. B. Koch, Marcus Bleicher and Sabine Hossenfelder, JHEP **0510**, 053, (2005); H. Stoecker, Int. J. Mod. Phys. D **16**, 185 (2007); S. Hossenfelder, B. Koch, M. Bleicher, e-Print: hep-ph/0507140, (2005).

5. H. Heiselberg, Phys. Rev. D **48**, 1418 (1993).
6. J. Madsen, Phys. Rev. Lett **81**, 53 (1998).
7. G. Wilk et al., J. Phys. G **22**, L105 (1996).
8. S. Banerjee et al., Phys. Rev. Lett. **85** (2000) 1384.
9. S. Coleman, Nucl. Phys. B **262**, 263 (1985); erratum: B **269**, 744 (1986); A. Kusenko and M. Shaposhnikov, Phys. Lett. B **418**, 46 (1998); D. A. Demir, arXiv:hep-ph/9810453v2, (1998).
10. G.B. Gelmini and M. Roncadelli, Phys. Let B **99**, 411 (1981); R.N. Mohaptra and J.D. Vergados, Phys. Rev. Lett. **47**, 1713 (1981); V. barger, H. Baer, W.Y. Keung and R.J.N. Philips, Phys. Rev. D26, 218 (1982); H.F. Gunion, H.E. Haber, G.L. Kane and S. Dawson, The Higgs Hunters Guide. Addison, Wesley (1990); J. A. Grifols, A. Mendez and G.A. Schuler, Mod. Phys. Lett. A **4**, 1485 (1989).
11. A. Arvanitaki, S. Dimopolous, A. Pierce, S. Rajendran and J. Wacker, arXiv:hep-ph/0506242v2, (2005); S. Bressler, arXiV:hep-ex/0710.2111v3, (2007).
12. A. Ambosanio et al., arXiv:hep-ph/0012192 (2000).
13. A.C. Kraan, J.B. Hansen and P. Nevski, (2005), hep-ex/0511014.
14. R. Hauser, Eur. Phys. J. C **34**, s173 (2004).
15. P. Zalewski, CMS Conference Note, CMS-CR-1999-019.
16. P.A.M. Dirac, Proc. R. Soc. London **133**, 60 (1931); Phys. Rev. **74**, 817 (1948).
17. A. De Rujula, Nucl. Phys. B **435**, 257 (1995).
18. Walter Troost and Patrizio Vinciarelli (CERN). CERN-TH-2195, Jul 1976. 15pp
19. Y.M. Cho and D. Maison, Phys. Lett. B **391**, 360–365 (1997).
20. T. Banks, M. Dine, H. Dykstra and W. Fischler, Phys. Lett. B **212**, 45 (1988).
21. M. Bertani et al., Europhys. Lett. **12**, 613 (1990).
22. G. Abbiendi et al., Phys. Lett. B **663**, 37 (2008).
23. I.R. Kenyont, Rep. Prog. Phys. **45** (1982).
24. J.K. Yoh et al. Phys. rev. Lett. **41**, No. 10, 684 (1978).
25. F. Halzen and D.M. scott, Phys. rev. D **21**, 131 (1980).
26. L.E. Roberts, Nuov Cimento **92A**, 247 (1986).
27. A. Abulencia, Phys. Rev. Lett. **49**, 102 (1982).
28. S. Cecchini et al., Nuovo Cim. A **109**, 1119 (1996).
29. J. Derkaoui et al., Astrop. Phys. **9**, 173 (1998).
30. J. Derkaoui et al., Astrop. Phys. **9**, 339 (1999).
31. R.L. Fleischer et al., Nuclear Tracks in Solid (U. Berkeley) (1975).
32. P.B. Price, Proc. Of the Workshop on Experiments, Detectors, and Experimental Areas for the Supercollider. World Scientific, 899 (1987).

Radiative Kaon Decays and ChPT Test with the NA48/2 Experiment at CERN

G. Ruggiero

Abstract The NA48/2 experiment at CERN SPS carried out data taking in 2003 and 2004. The analysis of selected data samples of $K^{\pm} \to \pi^{\pm}\gamma\gamma$, $K^{\pm} \to \pi^{\pm}e^{+}e^{-}\gamma$, $K^{\pm} \to \pi^{\pm}e^{+}e^{-}$, and $K^{\pm} \to \pi^{\pm}\mu^{+}\mu^{-}$ allowed precise tests of the ChPT theory predictions.

Keywords: Radiative kaon decay, NA48/2 Experiment, CERN SPS, non leptonic decays, chiral perturbation theory, Standard Model

1 Introduction

The non leptonic radiative kaon decays offer the possibility to study the structure of the weak interactions at low energies and to test the predictions of the Chiral Perturbation Theory (ChPT). The current paper summarizes the analysis on $K^{\pm} \to \pi^{\pm}\gamma\gamma$, $K^{\pm} \to \pi^{\pm}e^{+}e^{-}\gamma$, $K^{\pm} \to \pi^{\pm}e^{+}e^{-}$ and $K^{\pm} \to \pi^{\pm}\mu^{+}\mu^{-}$ performed by the NA48/2 experiment at CERN SPS.

All the above mentioned decays are flavour changing neutral current processes which arise at one loop level in the Standard Model. In the framework of the ChPT theory, their decay rates have been computed at the leading $O(p^4)$ and next-to-leading order $O(p^6)$. The $K^{\pm} \to \pi^{\pm}\gamma\gamma$ [1, 2] and $K^{\pm} \to \pi^{\pm}e^{+}e^{-}\gamma$ [3] decay rates turn out to depend on theoretically unknown weak couplings, which mainly affect the $\gamma\gamma$ invariant mass spectrum. Before the NA48/2 experiment only few $K^{\pm} \to \pi^{\pm}\gamma\gamma$ candidates were observed [4], while the $K^{\pm} \to \pi^{\pm}e^{+}e^{-}\gamma$ decay was not observed at all. The decay rate of the $K^{\pm} \to \pi^{\pm}l^{+}l^{-}$ ($l = e, \mu$) [5,6] depends on form factors which affect the $l^{+}l^{-}$ invariant mass spectrum. Before NA48/2 the $K^{\pm} \to \pi^{\pm}e^{+}e^{-}$ has been studied experimentally at CERN [7] and at BNL by the E777 [8] and E865 [9] experiments; the $K^{\pm} \to \pi^{\pm}\mu^{+}\mu^{-}$ decay has been observed at BNL by the E787 [10] and E865 [11] experiments and by the HyperCP experiment [12].

G. Ruggiero
Scuola Normale Superiore, Pisa, Italy,
e-mail: giuseppe.ruggiero@cern.ch

V. Begun et al. (eds.), *Progress in High-Energy Physics and Nuclear Safety*,

This paper is organized as follows: in section 2 a description of the NA48/2 detector is given. Section 3 describes the analysis of the $K^{\pm} \to \pi^{\pm}\gamma\gamma$ decay. Section 4 presents the final published results about the $K^{\pm} \to \pi^{\pm}e^{+}e^{-}\gamma$ decay [13]. Section 5 summarizes the status of the analysis of the $K^{\pm} \to \pi^{\pm}e^{+}e^{-}$ and $K^{\pm} \to \pi^{\pm}\mu^{+}\mu^{-}$ decays.

2 The NA48/2 experiment

The NA48/2 was a fixed target experiment located at CERN. A primary proton beam of 400 GeV/c momentum, extracted from the SPS accelerator, impinged with zero angle on a beryllium target and produced a secondary charged beam. About 5–6% of all the charged particles in the secondary beam were $K^{\pm}$. The secondary beam was transported along a 100 m long beam line, depicted in Fig. 1.

The front-end achromat made by four dipoles and two collimators (tax 17 and 18) split the positive and negative particles in the vertical plane, selected the particles with momentum of (60 ± 3) GeV/c and recombined them on a common axis. Then the secondary beam passed through a set of defining collimators, focusing quadrupoles and through three stations forming a spectrometer (KABES1-3). Finally the beam entered in a decay volume, housed in a 100 m long vacuum tank with a diameter increasing from 1.9 m to 2.4 m.

With a primary beam intensity of about 7×10^{11} protons per SPS spill of 4.8 s duration, the positive (negative) beam flux at the entrance of the decay volume was 3.8×10^{7} (2.6×10^{7}) particles per pulse. The K^{+}/K^{-} flux ratio was about 1.8. The fraction of kaons decaying in the decay volume was about 22%.

The detector was designed to see the charged and neutral products of the kaons decaying in the vacuum region. A magnetic spectrometer tracked the charged particles. It was housed in a tank containing He and separated from the vacuum region

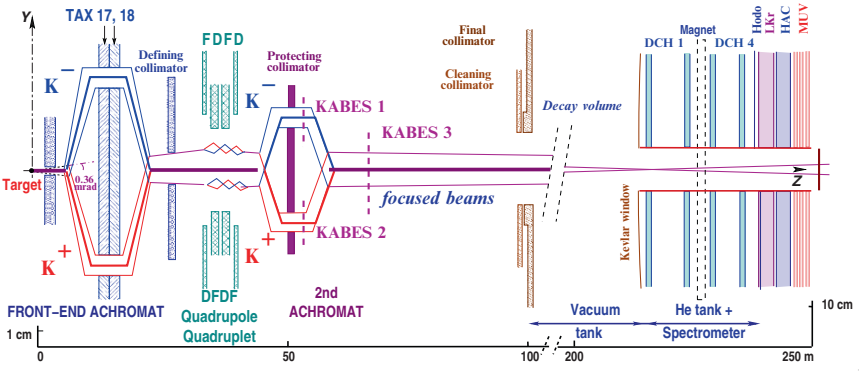

Fig. 1 Schematic lateral view of the NA48/2 beam line, decay volume and detector. The vertical scales are different in the two parts of the figure

by a Kevlar window, 0.31% X_0 thick. An aluminium beam pipe of 16 cm diameter with vacuum inside, traversed the spectrometer and allowed the not decayed beam particles to pass through, without touching the sensitive detector volume. The spectrometer consisted of four drift chambers (DCH1-4) separated by a dipole magnet, which gave to the charged particles an horizontal transverse momentum kick of 120 MeV/c. The spatial resolution of the spectrometer was about 90 μm in the x and y coordinates and the momentum resolution was $\sigma_p/p = (1.02 \oplus 0.044 \times p)\%$ (p in GeV/c).

An hodoscope (HOD), made by two planes of 64 plastic scintillator slabs each, followed the magnetic spectrometer. It provided the time reference for the other detectors and the main trigger for the events with charged particles.

An electromagnetic calorimeter (LKr), placed after the hodoscope, was used for photon detection and particle identification. It was a quasi-homogeneous calorimeter with liquid kripton as active material. A system of Cu-Be ribbons electrodes allowed the collection of the ionization signal. In total 13,248 projective cells segmented the active volume transversally to the beam axis. The total length of the detector corresponded to about 27 X_0. The measured energy resolution was $\sigma(E)/E = 0.032/\sqrt{(E)} \oplus 0.09/E \oplus 0.0042$ (E in GeV).

An hadronic calorimeter (HAC) and a muon detector (MUV) followed the electromagnetic calorimeter.

A detailed description of the NA48/2 detectors can be found elsewhere [14].

The NA48/2 experiment took data in 2003 and 2004. About 18×10^9 triggers were recorded in total. Its main goal was the study of the direct CP violation in the $K^\pm \to 3\pi$ [15]. The high statistics collected, however, made this experiment well suited to study also rare decays.

A detailed GEANT-based Monte Carlo simulation [16] was employed to simulate the detector response. Radiative corrections to kaon decays were applied using the PHOTOS package [17].

3 $K^\pm \to \pi^\pm\gamma\gamma$ analysis

The decay rate of the $K^\pm \to \pi^\pm\gamma\gamma$ can be written as [2]:

$$\frac{\partial^2\Gamma}{\partial y \partial z} = \frac{m_{K^\pm}}{(8\pi)^3}\left[z^2(|A+B|^2+|C|^2) + \left(y^2 - \frac{1}{4}\lambda(1,r_\pi^2,z)\right)^2(|B|^2+|D|^2)\right] \quad (1)$$

Here $y = p\cdot(q_1-q_2)/m_K^2$ and $z = (q_1-q_2)^2/m_K^2$ where $p, q_{1,2}$ are the four-momenta of the kaon and the two photons, respectively. The parameter $r_\pi = m_\pi/m_K$ and the explicit form of the functions A, B, C, D and $\lambda(1,r_\pi^2,z)$ can be found in [2]. At the order $O(p^4)$ in ChPT $A = A(z,\hat{c})$, where $\hat{c}$ depends on several strong and weak coupling constants. It is expected of $O(1)$, but is largely unknown. ChPT predicts a cusp-like behaviour of the $m_{\gamma\gamma}$ spectrum at the $\pi\pi$ threshold, independently on the value of $\hat{c}$. This parameter, however, has an impact on the shape of the $\gamma\gamma$ spectrum.

It also affects the branching ratio, which, at $O(p^4)$, is $(5.26 + 1.64 \cdot \hat{c} + 0.32 \cdot \hat{c}^2 + 0.49) \times 10^{-7}$. The function C depends on z and is about 10% of A, while B and D are zero. At $O(p^6)$ unitarity corrections [2] are at work and increase the branching ratio of 30-40%, depending on $\hat{c}$. At this order D can be still neglected, but not B which depends on both y and z like A.

The experimental analysis of $K^{\pm} \to \pi^{\pm}\gamma\gamma$ implies the measurement of the branching ratio and the extraction of $\hat{c}$ from the shape of the $\gamma\gamma$ invariant mass spectrum.

The NA48/2 experiment measured the rate of $K^{\pm} \to \pi^{\pm}\gamma\gamma$ relatively to the $K^{\pm} \to \pi^{\pm}\pi^0$ normalization channel using data taken in 2003 and 2004. The following preliminary results refer to the analysis of 40% of the total sample. The signal and the normalization channels had identical particle composition of the final states. The signature in both cases was one track and two photons. The trigger of the data used for this analysis involved a minimal requirement of energy deposition in the LKr and kinematic cuts on spectrometer variables reconstructed on-line using a dedicated PC-farm.

The basic requirements at the analysis level were: one track reconstructed in the spectrometer and two photons not associated to the track in the LKr. The track had to pass through the geometrical acceptance of the detector and to cross the line connecting the beginning of the decay region and the position of the center of gravity computed at the LKr, with a distance of closest approach less than 2 cm. In order to be a pion, the track had to release the in the LKr less than 80% of its energy, which was known from the track momentum measured in the spectrometer. The photons had to be in time with the track. Cuts on kinematic variables, like the $\gamma\gamma$ invariant mass distinguished among the signal and normalization channel. These cuts rejected also the backgrounds of the signal due to decays with lost or overlapping photons in the LKr or with accidental photons. The cut $m_{\gamma\gamma} > 0.2$ GeV/c^2 defined the signal region.

In total 1,164 $K^{\pm} \to \pi^{\pm}\gamma\gamma$ had been selected with a background of about 3.3%, mainly due to $K^{\pm} \to \pi^{\pm}\pi^0\gamma$ events, as estimated from Monte Carlo simulations. For comparison, 31 candidates were used in the previous measurement [4]. The normalization channel contained about 6×10^6 events corresponding to about 2.06×10^{10} kaon flux.

The reconstructed $\gamma\gamma$ invariant mass in the accessible kinematic region is presented in Fig. 2, along with a Monte Carlo expectation, assuming ChPT $O(p^6)$ distribution with $\hat{c} = 2$. The observed spectrum provides the first clean experimental evidence for the cusp-like shape of $m_{\gamma\gamma}$.

The partial width of the decay was measured using the Monte Carlo simulation to compute the signal acceptance. Suitable control samples collected during the data taking allowed a precise measurement of the trigger efficiency. The background subtraction procedure made use of the Monte Carlo simulation. The preliminary result for the branching ratio was:

$$BR = (1.07 \pm 0.04_{stat} \pm 0.08_{syst}) \times 10^{-6}. \quad (2)$$

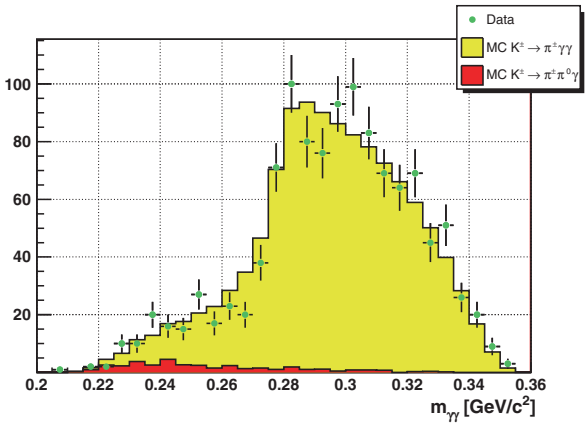

Fig. 2 Invariant $\gamma\gamma$ mass of $K^{\pm} \to \pi^{\pm}\gamma\gamma$ events; data (dots) and Monte Carlo expectation assuming ChPT $O(p^6)$ and $\hat{c} = 2$ (filled area)

The main contribution to the systematic uncertainty came from the overlap of pion and photon clusters in the LKr and from the measurement of the trigger efficiency. The above result depended on the value of $\hat{c}$ used in the simulation through the acceptance correction. A combined fit of the $m_{\gamma\gamma}$ spectrum shape and decay rate is foreseen to measure $\hat{c}$.

4 $K^{\pm} \to \pi^{\pm}e^{+}e^{-}\gamma$ analysis

The theoretical description of the $K^{\pm} \to \pi^{\pm}e^{+}e^{-}\gamma$ [3] is close to the $K^{\pm} \to \pi^{\pm}\gamma\gamma$ one, shortly summarized in section 3. The first non trivial order in ChPT is the $O(p^4)$, which predicts a cusp-like behaviour of the $m_{\gamma\gamma}$ spectrum at the $\pi\pi$ threshold. The overall shape of the spectrum, instead, depends on the largely unknown parameter $\hat{c}$. The $O(p^6)$ corrections account for about 40% of the total branching ratio. The ChPT prediction for the branching ratio is $0.92 \div 1.7 \times 10^{-8}$, depending on the value of $\hat{c}$.

The NA48/2 experiment measured the branching ratio of $K^{\pm} \to \pi^{\pm}e^{+}e^{-}\gamma$ relatively to $K^{\pm} \to \pi^{\pm}\pi^{0}_{D}$ (here π^{0}_{D} means $\pi^0 \to \gamma e^{+}e^{-}$) and the $\hat{c}$ parameter. The signal and the normalization channels had identical particle composition of the final states. The signature in both cases was three tracks and one photon. This analysis made used of the data collected with the main trigger of the 2003 and 2004 runs, optimized for events with three charged particles in the final state [15].

At the analysis level each event had to have at least one combination of three tracks with a total charge of ± 1 and one cluster in the LKr not associated with any track. The three tracks had to pass through the geometrical acceptance of the detectors and come from the same decay vertex. One of them had to be recognized as

a pion using the same technique described in section 3. The other two tracks had to be compatible with an electron hypothesis. As a consequence a track was required to release more than 94% of its energy in the LKr. Backgrounds from decays with more than one photon were rejected by cutting events with other unassociated clusters in time with the tracks. In order to select signal events cuts on kinematic variables, like $m_{ee\gamma}$ and $m_{\pi ee\gamma}$ were used to suppress backgrounds due to $K^{\pm}$ decays with a π^0_D in the final state. A cut on the maximum angle between the photon and the electrons allowed the rejection of $K^{\pm} \to \pi^{\pm}e^+e^-$ with a γ internally or externally radiated. The cut $m_{e^+e^-\gamma} > 260$ MeV/c^2 defined the signal region.

In total 120 events had been observed with a background of about 6%, as estimated from Monte Carlo. This is the first observation of such a decay mode. The normalization channel contained about 13×10^6 events corresponding to about 1.5×10^{11} kaon flux. Here the branching fraction of the normalization was $BR(K^{\pm} \to \pi^{\pm}\pi^0_D) = (2.51 \pm 0.07) \times 10^{11}$ [12].

The reconstructed $\gamma\gamma$ invariant mass in the accessible kinematic region is presented in Fig. 3 along with a fit assuming ChPT $O(p^4)$ distribution. A model independent branching ratio was measured in bins of $m_{e^+e^-\gamma}$. The computation of the acceptance and the subtraction of the background made use of the Monte Carlo simulation. The result was:

$$BR(m_{ee\gamma} > 260 \text{ MeV/c}^2) = (1.19 \pm 0.12_{stat} \pm 0.04_{syst}) \times 10^{-8}. \quad (3)$$

The main uncertainty on systematics came from the background subtraction procedure and the branching ratio of the normalization channel. A least squared fit to $m_{ee\gamma}$ gave $\hat{c} = 0.90 \pm 0.45$. This number is compatible with the only existing measurement of $\hat{c}$, which is 1.8 ± 0.6, obtained from the analysis of $K^{\pm} \to \pi^{\pm}\gamma\gamma$ decays [4].

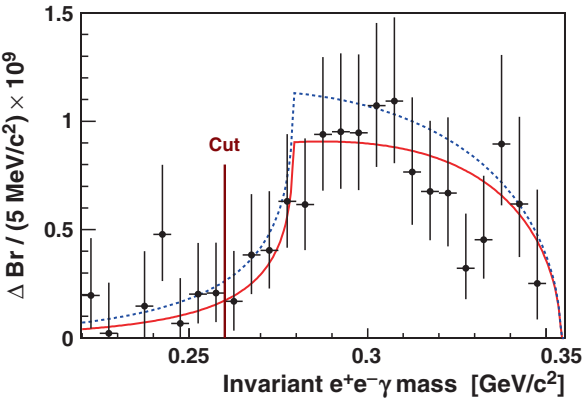

Fig. 3 Distribution of $m_{e^+e^-\gamma}$ in the kinematic accessible region for the selected $K^{\pm} \to \pi^{\pm}e^+e^-\gamma$; best fit of the distribution using $\hat{c}$ as a free parameter and the $O(p^4)$ theoretical description (solid line); theoretical predication with $\hat{c} = 1.8$ (dotted line)

5 The $K^{\pm} \to \pi^{\pm} l^+ l^-$ analysis

The decay rate of the $K^{\pm} \to \pi^{\pm} l^+ l^-$, with $l = e, \mu$, is [6]:

$$\frac{d\Gamma}{dz} = \frac{\alpha^2 m_K}{12\pi(4\pi)^4} \lambda^{3/2}(1, z, r_\pi^2) \sqrt{1 - 4\frac{r_l^2}{z}} \left(1 + 2\frac{r_l^2}{z}\right) |W(z)|^2, \tag{4}$$

where $z = (m_l/m_K)^2$, $r_l = m_l/m_K$, $r_\pi = m_\pi/m_K$ and $\lambda(a,b,c) = a^2 + b^2 + c^2 - 2ab - 2ac - 2bc$. The distribution of the angle $\theta_{\pi e}$ between π and e^+ in the e^+e^- rest frame is proportional to $\sin^2\theta_{\pi e}$ and is not sensitive to $W(z)$.

The following parametrization $W(z)$ are considered:

1. Linear: $W(z) = G_F m_K^2 f_0(1 + \delta z)$, with the free parameters δ and f_0
2. ChPT: $W(z) = G_F m_K^2 (a_+ + b_+ z) + W^{\pi\pi}(z)$, with free parameters a_+, b_+ and an explicit calculated pion loop term $W^{\pi\pi}(z)$ [6]
3. A Dubna version of ChPT: $W(z) \equiv W(M_a, M_\rho, z)$, with the resonance masses M_a and M_ρ treated as free parameters [19]

These form factors are predicted equal for electron and muons.

The experimental analysis of $K^{\pm} \to \pi^{\pm} l^+ l^-$ aimed to measure the branching ratio and the form factors both for the electron and muon channel.

5.1 $K^{\pm} \to \pi^{\pm} e^+ e^-$

The NA48/2 experiment measured preliminarily the rate of $K^{\pm} \to \pi^{\pm} e^+ e^-$ relatively to the $K^{\pm} \to \pi^{\pm} \pi^0_D$ normalization channel using data from 2003 and 2004. The final states of the two decay modes contained the same charged particles. This allowed a first order cancellation of the systematics coming from the particle identification inefficiencies. The data used in this analysis had been recorded with the main trigger of the 2003 and 2004 run.

In both the signal and normalization events selection, three tracks reconstructed in the spectrometer and coming from a common vertex were required. These tracks had to pass through the geometrical detector acceptance. One track had to be compatible with the pion hypothesis and the others with the electron hypothesis, as described in Section 4. Cuts on the total momentum, on the transverse momentum with respect to the beam trajectory and on the $\pi^{\pm} e^+ e^-$ invariant mass, were applied to select the $K^{\pm} \to \pi^{\pm} e^+ e^-$ events. Finally the kinematic cut $z < 0.08$ allowed the suppression of the $K^{\pm} \to \pi^{\pm} \pi^0_D$ and $K^{\pm} \to \pi^{\pm} \pi^0_{DD}$ backgrounds (π^0_{DD} means $\pi^0 \to e^+e^-e^+e^-$). This cut corresponded to $m_{ee} > 140$ MeV/c^2. The presence of a cluster in the LKr not associated to the track and such that $m_{ee\gamma}$ was compatible with m_{π^0}, tagged the $K^{\pm} \to \pi^{\pm} \pi^0_D$ events.

In total 7,146 $K^{\pm} \to \pi^{\pm} e^+ e^-$ candidates (Fig. 4 left) had been selected with a background of 0.6% mainly due to kaon decays with particles mis-identified (i.e. $e^{\pm}$ identified as $\pi^{\pm}$ and vice versa). The background was estimated selecting the

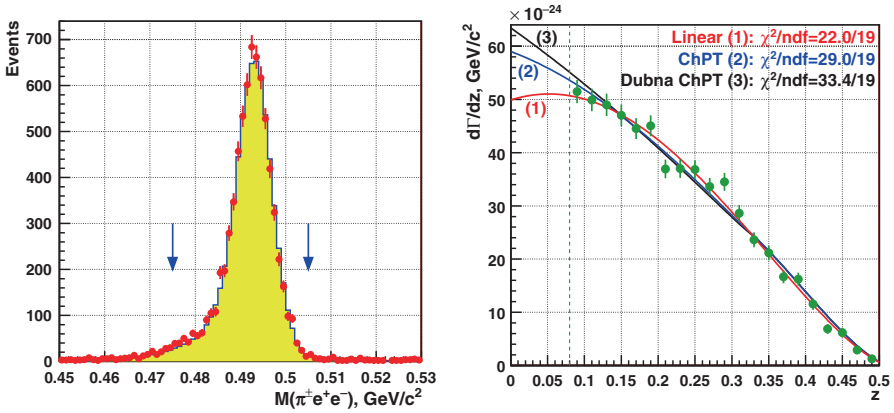

Fig. 4 Left: Reconstructed spectrum of $K^{\pm} \to \pi^{\pm}e^{+}e^{-}$ invariant mass; data (dots) and Monte Carlo simulation (filled area). Right: Measured $d\Gamma/dz$ and the results of fits according to the considered models (see text)

strongly suppressed lepton number violating decay $K^{\pm} \to \pi^{\mp}e^{\pm}e^{\mp}$. This method was cross checked with the Monte Carlo simulation. About 12.2×10^6 $K^{\pm} \to \pi^{\pm}\pi^0_D$ events were selected, corresponding to about 1.7×10^{11} kaon flux. The branching fraction of the normalization was $BR(K^{\pm} \to \pi^{\pm}\pi^0_D) = BR(K^{\pm} \to \pi^{\pm}\pi^0) \cdot BR(\pi^0)$ with $BR(K^{\pm} \to \pi^{\pm}\pi^0_D) = (20.64 \pm 0.08)\%$ [20] and $BR(\pi^0_D)$ from [12].

The partial decay rate $d\Gamma/dz$ was measured using the Monte Carlo simulation to account for signal acceptance, the data to subtract the background and the data recorded with control triggers to correct for trigger efficiency. The preliminary result is shown in Fig. 4 right. The model independent branching ratio, related to the accessible kinematic region, was:

$$BR(z > 0.08) = (2.26 \pm 0.03_{stat} \pm 0.03_{syst} \pm 0.06_{ext}) \times 10^{-7}. \quad (5)$$

The form factors were extracted by performing a fit to the $d\Gamma/dz$ spectrum. Table 1 summarizes the preliminary results. The systematic uncertainties came from particle identification, beam simulation, background subtraction, radiative corrections and trigger efficiency measurement. The external uncertainty came from the errors on the PDG values used. The statistics collected was not sufficient to distinguish between the models considered. The obtained form factor slope δ is in agreement with the previous measurements based on $K^{\pm} \to \pi^{\pm}e^{+}e^{-}$ [8,9] and $K^{\pm} \to \pi^{\pm}\mu^{+}\mu^{-}$ [11, 12] samples. It also confirms the contradiction of the data with the meson dominance models [21]. The f_0, a_+ and b_+ parameters are in agreement with the only previous measurements [9]. The parameters M_a and M_ρ are a few persentage away from the nominal masses of the resonances [12].

The branching ratio in the full kinematic range was computed for each of the considered form factor parameterizations. The preliminary average branching ratio in the full kinematic region was:

Table 1 Results of fits to the three considered models for the extraction of the form factors of the $K^{\pm} \to \pi^{\pm} e^{+} e^{-}$ decay

δ	=	2.35 ±	0.15$_{\text{stat.}}$ ±	0.09$_{\text{syst.}}$ ±	0.00$_{\text{ext.}}$ =	2.35 ±	0.18
f_0	=	0.532 ±	0.012$_{\text{stat.}}$ ±	0.008$_{\text{syst.}}$ ±	0.007$_{\text{ext.}}$ =	0.532 ±	0.016
$\text{BR}_1 \times 10^7$	=	3.02 ±	0.04$_{\text{stat.}}$ ±	0.04$_{\text{syst.}}$ ±	0.08$_{\text{ext.}}$ =	3.02 ±	0.10
a_+	=	−0.579 ±	0.012$_{\text{stat.}}$ ±	0.008$_{\text{syst.}}$ ±	0.007$_{\text{ext.}}$ =	−0.579 ±	0.016
b_+	=	−0.798 ±	0.053$_{\text{stat.}}$ ±	0.037$_{\text{syst.}}$ ±	0.017$_{\text{ext.}}$ =	−0.798 ±	0.067
$\text{BR}_2 \times 10^7$	=	3.11 ±	0.04$_{\text{stat.}}$ ±	0.04$_{\text{syst.}}$ ±	0.08$_{\text{ext.}}$ =	3.11 ±	0.10
M_a/GeV	=	0.965 ±	0.028$_{\text{stat.}}$ ±	0.018$_{\text{syst.}}$ ±	0.002$_{\text{ext.}}$ =	0.965 ±	0.033
M_ρ/GeV	=	0.711 ±	0.010$_{\text{stat.}}$ ±	0.007$_{\text{syst.}}$ ±	0.002$_{\text{ext.}}$ =	0.711 ±	0.013
$\text{BR}_3 \times 10^7$	=	3.15 ±	0.04$_{\text{stat.}}$ ±	0.04$_{\text{syst.}}$ ±	0.08$_{\text{ext.}}$ =	3.15 ±	0.10
$\text{BR}_{\text{mi}} \times 10^7$	=	2.26 ±	0.03$_{\text{stat.}}$ ±	0.03$_{\text{syst.}}$ ±	0.06$_{\text{ext.}}$ =	2.26 ±	0.08

$$BR = (3.08 \pm 0.04_{stat} \pm 0.04_{syst} \pm 0.08_{ext} \pm 0.07_{model}) \times 10^{-7}, \tag{6}$$

where the model error came from the difference between the various parameterizations. A comparison to the precise BNL E865 measurement dismissing correlated uncertainties due to external branching ratios and model dependence, and using the same external input, showed a 1.4σ difference [9].

Finally a preliminary measurement of the direct CP violating asymmetry of K^+ and K^- gave:

$$(BR^+ - BR^-)/(BR^+ + BR^-) = (-2.1 \pm 1.5_{stat} \pm 0.3_{syst})\%. \tag{7}$$

Its precision, however, is far from the 10^{-5} theoretical expectation [6].

5.2 Status of the $K^{\pm} \to \pi^{\pm}\mu^{+}\mu^{-}$ analysis

Less than 800 events exist in the world up to now[10–12]. The agreement on the various branching ratio measurements reported by PDG is poor. The form factors measured using the linear parametrization, however, are in agreement with the ones extracted from the $K^{\pm} \to \pi^{\pm} e^{+} e^{-}$ decay.

The NA48/2 experiment could select $K^+ \to \pi^{\pm}\mu^{+}\mu^{-}$ events using the 2003 and 2004 data. The selection was similar to the one applied for the electron channel. In the present case, however, muons were identified using the Muon Veto detector. Up to now the analysis is still in a preliminary stage. Few thousands of signal events had been selected (Fig. 5) with a background of the order of 1%, mainly due to $K^{\pm} \to \pi^{\pm}\pi^{+}\pi^{-}$ decays with two pions decaying. The extraction of the form factors and the measurement of the branching ratio are foreseen.

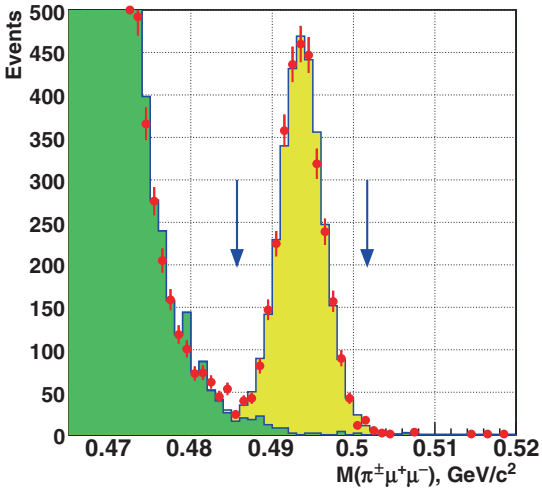

Fig. 5 Invariant mass distribution for selected $K^{\pm} \to \pi^{\pm}\mu^{+}\mu^{-}$ events; data (dots) and Monte Carlo simulation (filled area). The peak on the left is due to the $K^{\pm} \to \pi^{\pm}\pi^{+}\pi^{-}$ events

References

1. G. Ecker, A. Pich, and E. de Rafael, Nucl. Phys. B **303** (1988) 665.
2. G. D'Ambrosio and J. Portoles, Phys. Lett. B **386** (1996) 403.
3. F. Gabbiani, Phys. Rev. D **59** (1999) 094022.
4. P. Kitching et al., Phys. Rev. Lett. **79** (1997) 4079.
5. G. Ecker, A. Pich, and E. de Rafael, Nucl. Phys. B **291** (1987) 692.
6. G. D'Ambrosio et al., JHEP **8** (1998) 4.
7. P. Bloch et al., Phys. Lett. B **56** (1975) 201.
8. C. Alliegro et al., Phys. Rev. Lett. **68** (1992) 278.
9. R. Appel et al., Phys. Rev. Lett. **83** (1999) 4482.
10. G. Adler et al., Phys. Rev. Lett. **79** (1997) 4756.
11. H. Ma et al., Phys. Rev. Lett. **84** (2000) 2580.
12. H.K. Park, Phys. Rev. Lett. **88** (2002) 111801.
13. J.R. Batley et al., Phys. Lett. B **659** (2007) 493.
14. V. Fanti et al., Nucl Inst. Methods A **574** (2007) 433.
15. J.R. Batley et al., Eur. Phys. J. C **52** (2007) 875.
16. GEANT detector description and simulation tool, CERN program library long writeup W5013 (1994).
17. E. Barberio and Z. Was, Comp. Phys. Comm. **79** (1994) 291.
18. W.M. Yao et al., J. Phys. G **33** (2006) 1.
19. A.Z. Dubnickova et al., Phys. Part. Nucl. Lett. **5**, vol 2 (2008) 76.
20. M. Antonelli et al., arXiv:0801.1817.
21. P. Lichard, Phys. Rev. D **60** (1999) 053007.

New results for $K^+ \to \pi^+ \nu\bar{\nu}$ at low π^+ Momentum from BNL E949

A. Shaykhiev, for E949 Collaboration

Abstract The BNL E949 experiment was a successor to BNL E787 and was aimed to measure the branching ratio of the $K^+ \to \pi^+ \nu\bar{\nu}$ decay. After detector upgrades were made, data equivalent to 1.7×10^{12} K^+ decays at rest were collected in a 2002 physics run. The data were analyzed via a blind analysis with a technique called the "Bifurcation Method". In this report we present the results of a search for $K^+ \to \pi^+ \nu\bar{\nu}$ in the pion momentum region below $K^+ \to \pi^+ \pi^0$ peak. Three new candidate events were observed with an estimated background of $0.93 \pm 0.17^{+0.32}_{-0.24}$ events. Combining these observation with previously reported results yields a branching ratio of $BR(K^+ \to \pi^+ \nu\bar{\nu}) = (1.73^{+1.15}_{-1.05}) \times 10^{-10}$ consistent with the standard model prediction.

Keywords: BNL, E949 Experiment, branching ratio, K^+ decay, blind analysis, Bifurcation Method, Standard Model

1 Introduction

The Standard Model (SM) in particle physics has accounted for almost all particles and their processes have observed.

CP violation was discovered in the middle of the 1960s and reasonable explanations for the mechanism of CP violation have been explored for years. Kobayashi and Maskawa explained CP violation by introducing 3×3 unitary matrix with imaginary phase. The unitary matrix has four independent parameters, which in the Wolfenstein parameterization are A, λ, ρ and η. In terms of these parameters, the Cabbibo-Kobayashi-Maskawa (CKM) matrix can be written as

A. Shaykhiev
Institute for Nuclear Research RAS, 60 October Revolution Pr. 7a, 117312 Moscow, Russia,
e-mail: shaykhiev@inr.ru

V. Begun et al. (eds.), *Progress in High-Energy Physics and Nuclear Safety*,

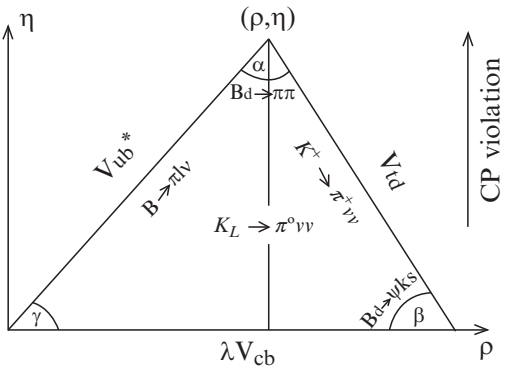

Fig. 1 Unitary triangle in the ρ–η plane

$$\begin{pmatrix} V_{ud} & V_{us} & V_{ub} \\ V_{cd} & V_{cs} & V_{cb} \\ V_{td} & V_{ts} & V_{tb} \end{pmatrix} \simeq \begin{pmatrix} 1-\lambda^2/2 & \lambda & A\lambda^3(\rho - i\eta) \\ -\lambda & 1-\lambda^2/2 & A\lambda^2 \\ A\lambda^3(1-\rho-i\eta) & -A\lambda^2 & 1 \end{pmatrix} \tag{1}$$

CP invariance of the Lagrangian for weak interaction is violated when the CKM matrix is a complex one. The parameter η describes CP violation in the SM. One of the most important goals of experimental physics is to determine the CKM matrix elements.

All of direct and indirect information concerning the CKM matrix elements can be summarized in terms of "unitary triangles". Applying the unitary property $V^{\dagger}V = 1$ to the CKM matrix in (1) implies

$$V_{ub}^* V_{ud} + V_{cb}^* V_{cd} + V_{tb}^* V_{td} \simeq V_{ub}^* - \lambda V_{cb}^* + V_{td} = 0, \tag{2}$$

where the approximations $V_{ud} \simeq V_{tb}^* \simeq 1$ and $V_{cd} \simeq -\lambda$ have been made. This equation is represented graphically in Fig. 1.

Powerful tests of our understanding of CP violation and quark mixing will come from comparisons of the results from B meson and kaon decays:

- A comparison of angle β from the ratio $BR(K_L^0 \to \pi^0 \nu\bar{\nu})/BR(K^+ \to \pi^+ \nu\bar{\nu})$ and from CP violation asymmetry in the decay $B_d^0 \to J/\psi K_s^0$
- A better determination of $|V_{td}|$ from $K^+ \to \pi^+ \nu\bar{\nu}$ and from the mixing frequencies of B_s and B_d mesons will provide sensitive test of the SM and probe new physics.

1.1 Physics beyond the SM

Among the many rare kaon and B meson decays, the $K \to \pi\nu\bar{\nu}$ modes are unique since their SM branching ratios can be computed to an exceptionally high degree of precision, not matched by any flavour-changing neutral current process involving quarks. A possible discrepancy between the measured branching ratio and the SM

Table 1 Previous results of the search for $K^+ \to \pi^+ \nu\bar{\nu}$

π^+momentum (MeV/c)	(211,229)	(140,199)
Years	1995–98(E787) and 2002(E949)	1996–97(E787)
Stopped K^+	7.7×10^{12}	1.7×10^{12}
Candidates	3	1
BR($K^+ \to \pi^+ \nu\bar{\nu}$)	$(1.47^{+1.30}_{-0.89}) \times 10^{-10}$ (68% CL)	$< 22 \times 10^{-10}$ (90% CL)

prediction would indicate the existence of new physics beyond the SM. For the $K^+ \to \pi^+ \nu\bar{\nu}$ decay SM branching ratio is $(0.85 \pm 0.07) \times 10^{-10}$ [8].

Several SM extensions to new physics would affect the $K^+ \to \pi^+ \nu\bar{\nu}$ branching ratio. For example, in the "Minimal Flavor Violation" model, where the origin of CP violation and quark mixing comes from the CKM matrix, as in the SM, the $K^+ \to \pi^+ \nu\bar{\nu}$ branching ratio is allowed to be as large as 1.9×10^{-10} [9].

1.2 Previous results of the search for $K^+ \to \pi^+ \nu\bar{\nu}$

A detailed history of the search for $K^+ \to \pi^+ \nu\bar{\nu}$ can be found in [3]. The first attempt to measure this decay was a heavy liquid bubble chamber experiment [10] at the Argonne Zero Gradient Synchrotron. The result of this experiment was a 90% CL upper limit on the branching ratio of 5.7×10^{-5}. About a decade later an experiment at KEK Proton Synchrotron improved the limit to 1.4×10^{-7} [7]. Previous results for BNL E787/E949 are summarized in Table 1.

2 Experiment BNL E949

The experimental signature of the $K^+ \to \pi^+ \nu\bar{\nu}$ decay is a single pion track and no other particle from a K^+ decay, because two neutrinos in the final state cannot be detected in the apparatus. $K^+ \to \pi^+ \nu\bar{\nu}$ is a three-body decay and the pion has the momentum $P_\pi < 227$ MeV/c.

2.1 The E949 detector

The K^+ beam is produced by a high-intensity proton beam from the Alternating Gradient Synchrotron (AGS) at Brookhaven National Laboratory (BNL). Protons are accelerated to a momentum of 21.5 GeV/c and hit the platinum target.

Incoming ~710 MeV/c kaons with 3/1 K^+/π^+ ratio are identified by Čerenkov counter and two proportional wire chambers then slowed down by an inactive degrader and an active degrader (AD), passing through a beam hodoscope and stopping in the scintillating fiber target as shown schematically in Fig. 2.

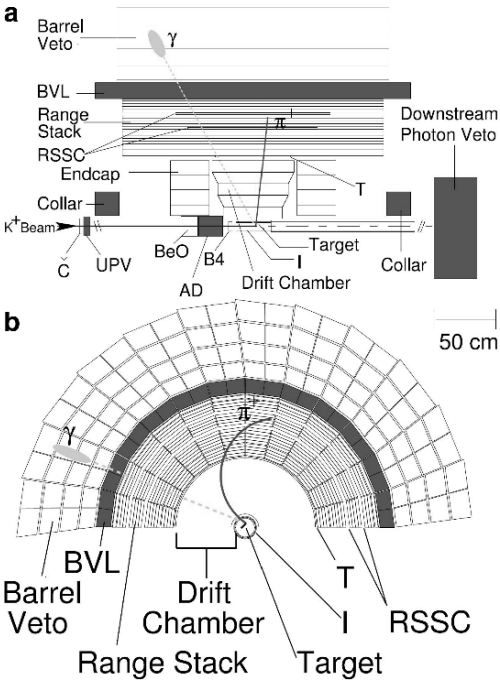

Fig. 2 Schematic side (a) and end (b) views of the upper half of the E949 detector. An incoming kaon is shown traversing the beam instrumentation stopping in the target and decaying to $\pi^+\pi^0$. The outgoing charged pion and one photon from $\pi^0 \to \gamma\gamma$ decay are illustrated. Elements of the detector are described in the text

The Čerenkov light from kaons and pions is unreflected and reflected at the inner surface of the radiator, respectively. The light from a kaon exits the radiator and is reflected by a parabolic mirror to the outer ring of 14 photomultiplier (PMT) tubes, while that from pion is internally reflected within the radiator and detected in the inner ring of 14 PMTs. Behind the Čerenkov counter, two beam wire chambers (BWPCs) are located. BWPCs allow to monitor beam profile and to identify multiple incoming particles. Downstream of BWPCs cylindrical degraders are located for slowing down the kaons so that come to rest in the center of the target. The inactive degrader is made of 11.1 cm long BeO and 4.76 mm Lucite. The AD consists of 40 layers of 2 mm thick scintillator disks (139 mm diameter) alternating with 2 mm thick copper disks (136 mm diameter). The AD is split into 12 azimuthal segments. The scintillation lights in the each segment are sent to a single PMT through wavelength shifting fibers and read out by ADCs, TDCs and CCDs. Using this information the AD allows to identify the beam particles and to detect the activities coincident with kaon decays. After passing through the degraders, just in front of the target, a beam hodoscope (B4) detects the incoming particle and identifies it as a kaon by measuring the energy deposit.

The target consists of 413 5 mm square and 3.1 m long plastic scintillating fiber that are bundled to form 12 cm diameter cylinder. A number of smaller fibers ("edge" fibers) fill in the gaps near the outer edge of the target. Each 5 mm fibers is connected to a PMT, whereas the edge fibers are grouped into 12 and each group of the edge fibers is connected to a single PMT. The PMTs are read out by

ADCs, TDCs and CCDs. The fiducial region of the target is defined by two layers of 6 plastic-scintillating counters that surround the target. The inner counters (IC) tag decay products for a trigger before they enter the drift chamber. The outer counters (VC) overlap the downstream edge of the IC by 6 mm and serve to detect particles that decay downstream of the fiducial region.

The drift chamber, called "Ultra Thin Chamber" (UTC), is located just outside of the IC. The whole E949 spectrometer is in a 1 Tesla magnetic field. Positively charged particles are bent clockwise in view from downstream. The primary functions of UTC are momentum measurement of charged particles and to provide a matching between the tracks in the target and in the range stack. The UTC consists of 3 superlayers. Each superlayer contains four layers of axial anode wires that provide *xy* position information between two cathode foil strips that provide *z* position information. The UTC has a length of 51 cm and inner and outer radii of 7.85 cm and 43.31 cm, respectively.

The range stack (RS) is located just outside the UTC at an inner radius of 45.08 cm and an outer radius of 84.67 cm. It consists of 19 layers of plastic scintillators azimuthally segmented into 24 sectors (Fig. 2). The scintillators of layers 2–18 have a thickness of 1.905 cm and a length of 182 cm. The scintillators of 19 layer have a thickness of 1 cm and are mainly used to veto charged particles with long range by requiring that they do not reach the 19 layer. The innermost counters, called T-counters, serve to define the fiducial volume for kaon decay products. The scintillation light is led by light guides to PMTs. Each PMT of RS counters is read out by an ADC and a TDC. The primary functions of the RS are energy and range measurements of charged particles and their identification.

The detection of any activities coincident with the charged track is very important for suppressing the backgrounds for $K^+ \to \pi^+ \nu\bar{\nu}$ decay. Photons from $K_{\pi 2}$ and other radiative decays are detected by hermetic photons detectors with 4π solid angle coverage. Photon veto is performed by the Barrel Veto (BV), the Barrel Veto Linear (BVL), the upstream and downstream End Caps (ECs), the upstream and downstream Collar detectors (CO), the downstream Microcollar detector (MC), as well as the target and RS. The BV and BVL with a thickness of 14.3 and 2.29 radiation lengths (r.l.) at normal incidence, respectively, provide photon detection over 2/3 of 4π solid angle. The photon detection over the remaining 1/3 of 4π solid angle is provided by the other calorimeters in the region from $\approx 10^\circ$ to 45° of the beam axis with a total thickness from 7 to 15 r.l.

More detail description of the E949 experiment may be found in [3].

3 Data analysis

Identification of $K^+ \to \pi^+ \nu\bar{\nu}$ decays relies on detection of an incoming kaon, its decay at rest and an outgoing pion with no coincident detector activity. All other kaon decay modes could be sources of background. There are two kinematic regions to search for $K^+ \to \pi^+ \nu\bar{\nu}$ called $\pi\nu\bar{\nu}(1)$ and $\pi\nu\bar{\nu}(2)$ that lie above and

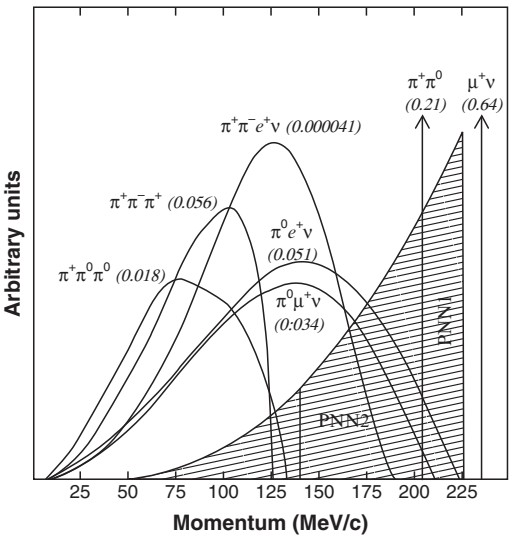

Fig. 3 Momentum spectra of charged particles from K^+ decay in the rest frame. The values in the parentheses represent the branching ratios for their decay modes. The hatched spectrum shows pion momentum in $K^+ \to \pi^+\nu\bar{\nu}$ decay assuming $V-A$ interaction

below $K^+ \to \pi^+\pi^0$ ($K_{\pi 2}$) peak, respectively (Figure 3). Searches in the $\pi\nu\bar{\nu}(1)$ region have been more sensitive to the $K^+ \to \pi^+\nu\bar{\nu}$ decay due the ability to suppress background in the $\pi\nu\bar{\nu}(1)$ region.

3.1 Analysis strategy

Since the predicted branching ratio for $K^+ \to \pi^+\nu\bar{\nu}$ in the SM is at 10^{-10}, the backgrounds should be suppressed to the level of 10^{-11}. This large suppression of the backgrounds makes a reliable estimation of the backgrounds in the signal region difficult, because any measurement involving low statistics could be subject to large statistical fluctuations. To find the candidate events we used a "blind" analysis. That is, background sources are identified a priori and a signal region is masked out until the selection criteria (cuts) development and the background estimation are finalized. For a background study the real data are divided into two portions: a uniformly sampled one-third portion of the whole data is used to develop the cuts, and the remaining two-third portion is used to measure the final background levels. The bifurcation method is used for the background estimation. The estimation is performed with two uncorrelated cuts or groups of cuts, which are independently inverted to enhance of statistics. This method is shown in Fig. 4. The number of background events in the signal region is A events. If the two cuts are uncorrelated, that is, if the rejection of a cut does not depend on the rejection of the other cut, the ratio of the number of background events in region "A" to region "B" must be equal to the ratio in region "C" to region "D". Therefore number of background events in the signal region is $A = BC/D$.

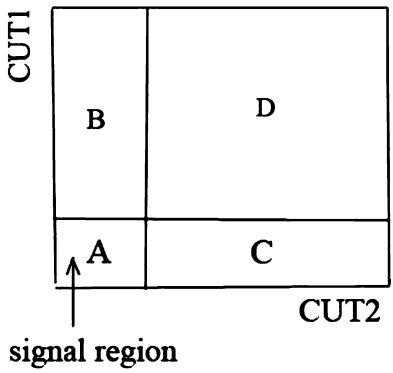

Fig. 4 Schematic of bifurcation method. The background level in signal region can be estimated from the numbers of events observed in the other regions

4 Backgrounds: Suppression and estimation

4.1 Overview

Figure 5 shows the range in a plastic scintillator versus the momentum of charged particles for the events that pass the $K_{\pi 2}$ trigger [3]. There are various sources of background in this figure. Events in the $K_{\pi 2}$ peak due to π^+ track from $K^+ \to \pi^+\pi^0$ decays with a momentum of 205 MeV/c, an energy of 108 MeV and a range of 30 cm. Events in the $K_{\mu 2}$ peak due to μ^+ track from $K^+ \to \mu^+\nu_\mu$ decays with a momentum of 236 MeV/c, an energy of 153 MeV and a range of 55 cm. Both events in the $K_{\pi 2}$ range tail and events in the $K_{\mu 2}$ range tail have ranges smaller than that expected from these decays, due to elastic (inelastic) scattering in the RS. Events in the muon band are due to multibody decays, such as $K^+ \to \mu^+\nu_\mu\gamma$ (radiative $K_{\mu 2}$ or $K_{\mu\nu\gamma}$) and $K^+ \to \mu^+\pi^0\nu_\mu$ ($K_{\mu 3}$), π^+ decay in flight in the target and the $K_{\mu 2}$ decay with inelastic scattering in the target. Events in the pion band are due to pions in the beam that scatter into the RS.

4.2 $K_{\pi 2(\gamma)}$ background

The $K_{\pi 2(\gamma)}$ background consists of three components: $K_{\pi 2}$-target scatter, $K_{\pi 2}$-range stack scatter and $K^+ \to \pi^+\pi^0\gamma$ decay ($K_{\pi 2\gamma}$). If photons from π^0 decay were missed and π^+ lose energy due to scattering, then $K_{\pi 2}$ event appears in the signal region. The positive pion from $K_{\pi 2\gamma}$ decay is not monochromatic, therefore three final-state photons should be miss for this type of event to be a background.

The main background for this analysis is $K_{\pi 2}$ decay in which the π^+ travels along the kaon fiber, loses energy and scatters in the target, while π^0 travels parallel to beam direction and photons from its decay are directed at upstream or downstream ends of the detector where the photon veto is weakest. Two cuts used for suppression of this background were photon veto and target-scatter cuts. Pion scattering

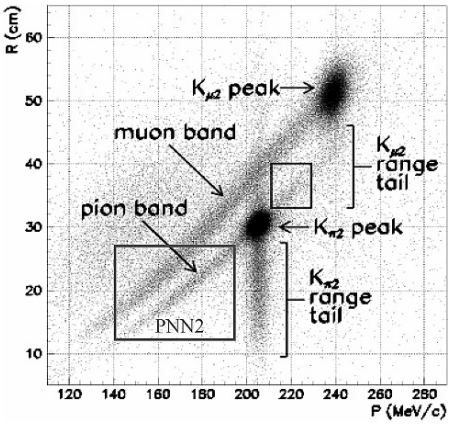

Fig. 5 Range in a plastic scintillator and the momentum of the charged particles for events that pass the $K_{\pi 2}$ trigger

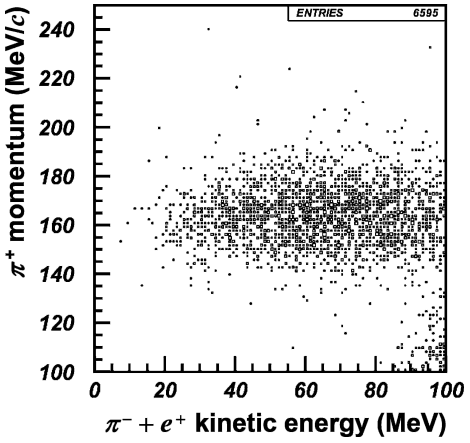

Fig. 6 Total kinetic energy of the π^- and e^+ versus the π^+ momentum for simulated K_{e4} events passed the trigger

was identified by kinks in the pattern of target fibers attributed to pion, by tracks that didn't point back to the fiber containing the kaon decay, by energy deposits inconsistent with an outgoing pion or by unexpected energy deposits at the time of the pion in fibers traversed by the kaon. There is also a much smaller background due to $K_{\pi 2}$-range stack scattering that is similarly identified by the energy deposits and pattern of RS counters attributed to the track.

$K_{\pi 2\gamma}$ background could not be distinguished from the larger $K_{\pi 2}$-scatter background based solely on the π^+ track. The rejection of this background was calculated using a combination of simulated $K_{\pi 2}$ and $K_{\pi 2\gamma}$ events and $K_{\pi 2}$ data events.

4.3 $K^+ \to \pi^+\pi^- e^+ \nu_e$ (K_{e4}) *background*

The branching ratio of the K_{e4} decay is $(4.09 \pm 0.10) \times 10^{-5}$ [12] and this process forms a background when the π^- and e^+ have little kinetic energy and interact in the target without leaving a detectable trace. Figure 6 shows the total kinetic

energy of the π^- and e^+ versus the π^+ momentum for simulated K_{e4} events passed the trigger. For these low kinetic energy events the distribution of the π^+ momentum concentrates around 160 MeV/c which is in the range of the $\pi\nu\bar{\nu}(2)$ signal region (140 MeV$<$ P_π $<$ 199 MeV). Due to low statistics and contamination by the other types of background it was not possible to make a purely data-based background sample for bifurcation analysis. So both data and simulated K_{e4} data were used to estimate this background. Positron interaction are well-modeled in EGS4-based simulation and the π^- energy deposition spectrum in scintillator measured previously in E787 [5] was used to model π^- absorption. To isolate K_{e4} sample the target pattern recognition was used. The simulated K_{e4} data supplemented by the π^- energy deposition spectrum in scintillator were used to estimate the rejection power of the target pattern recognition.

4.4 Charge exchange background

Interaction of incoming kaon in the target $K^+ n \to K^0 p$ can be a source of background when the K^0 decays as K_S^0 or K_L^0. The time condition requirement effectively removes any contribution from short-lived K_S^0 ($\tau_{life} = 0.1\ ns$). The semileptonic decays $K_L^0 \to \pi^+ e^- \bar{\nu}_e$ and $K_L^0 \to \pi^+ \mu^- \bar{\nu}_\mu$ with branching ratio of 20% and 14%, respectively, are the most likely sources of background of this type. The charge exchange event has a gap between kaon and pion fibers in the target. It is therefore suppressed by requiring no large gap between kaon and pion fibers. To identify these gaps the target pattern recognition was used. This background is also suppressed by the time condition requirement since K_L^0 that travels a short distance can be allowed by requiring no large gap. Additional suppression is provided by detecting the negative lepton. It is not possible to isolate a sufficiently pure, statistically significant sample of charge exchange events so the rejection power of the cuts was measured with simulated data.

4.5 Muon background

The main kaon decay $K^+ \to \mu^+ \nu_\mu$ (63%) can be a background if the muon interacts in the detector or is mis-reconstructed and misidentified as pion. $K^+ \to \mu^+ \pi^0 \nu_\mu$ and $K^+ \to \mu^+ \nu_\mu \gamma$ decays require two photons and one photon, respectively, must be missed in order to be a background, also muon must be misidentified as pion. Muons and pions have the different kinematic parameters (as shown in Fig. 5), therefore one of two bifurcation cuts for suppression muon background is the π/μ range-momentum separation and another one is $\pi \to \mu \to e$ decay chain identification. This decay chain identification relies almost entirely on the analysis of the transient digitizer data (TD cut). In this analysis TD cut was loosened compared to $\pi\nu\bar{\nu}(1)$ analysis [3] to increase the acceptance since the muon background is very small and continues to be much smaller than other background after loosening.

4.6 Beam background

The non-K^+ decay background contains three component: charge exchange interaction (section 4.4), Single Beam and Double Beam backgrounds.

The Single Beam background appears from single entering beam particle. If a pion in the beam scatters in the target and the enters the fiducial region of the detector, the event fakes the $K^+ \to \pi^+ \nu\bar{\nu}$ signal. The scattered pion leaves the target immediately after entering the target. This type beam background is suppressed by imposing the delayed coincidence. It is also suppressed by kaon identification in the Čerenkov counter and the beam hodoscope.

The Double Beam background can be categorized into two: kaon-kaon entering and kaon-pion entering cases. In the kaon-kaon entering case the first kaon enters and stops the target, and the second kaon entering the target decays-in-flight to π^+ and the π^+ enters the fiducial region of the detector. The kaon-pion case is the same as the kaon-kaon case, except that the second pion scatters in the target and enters the fiducial region to satisfy the kinematics of the signal. For both cases the Double Beam background can imitate $K^+ \to \pi^+ \nu\bar{\nu}$ signal, if the decay products from the first kaon are missed and the second kaon or pion is not detected in the beam line detectors. These backgrounds can be suppressed by looking for any extra activities that are coincident with the charged track in the beam instrumentation, target and range stack.

4.7 Background summary

The contribution of the each background component and the total background are presented in Table 2.

Table 2 Summary of the estimated number of events in the signal region from each background component for E787 and E949 $\pi\nu\bar{\nu}(2)$ analysis (1.73×10^{12} and 1.77×10^{12} stopped kaons, respectively). In the third column the first value is the sum of $K_{\pi 2}$-target scatter and $K_{\pi 2}$-range stack scatter events

Process	Background events (E949)	Background events (E787)
$K_{\pi 2}$-target scatter	$0.619 \pm 0.150^{+0.067}_{-0.100}$	
		1.030 ± 0.230
$K_{\pi 2}$-range stack scatter	$0.030 \pm 0.005 \pm 0.004$	
$K_{\pi 2\gamma}$	$0.076 \pm 0.007 \pm 0.006$	0.033 ± 0.004
K_{e4}	$0.176 \pm 0.072^{+0.233}_{-0.124}$	0.052 ± 0.041
Charge exchange	$0.013 \pm 0.013^{+0.010}_{-0.003}$	0.024 ± 0.017
Muon	0.011 ± 0.011	0.016 ± 0.011
Beam	0.001 ± 0.001	0.066 ± 0.045
Total	$0.927 \pm 0.168^{+0.320}_{-0.237}$	1.22 ± 0.24

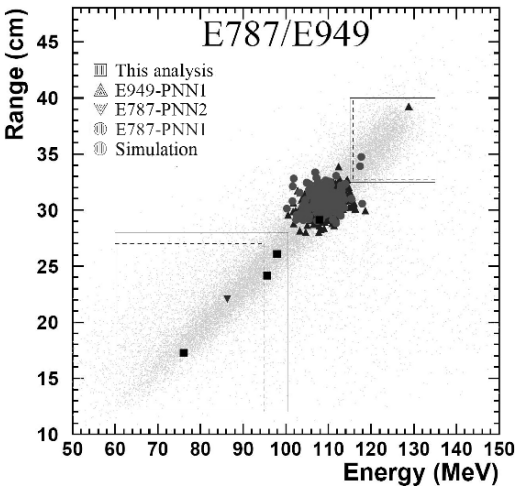

Fig. 7 The kinetic energy vs. range of all candidate events passing all other cuts. The points near $E_\pi = 108$ MeV are $K_{\pi 2}$ that survive the photon veto cuts and predominantly from the $\pi\nu\bar{\nu}(1)$ analyses due to the higher sensitivity and the less stringent photon veto cuts. No kinematic cuts are applied to the simulated $K^+ \to \pi^+ \nu\bar{\nu}$ events (light grey)

Compared to E787 $\pi\nu\bar{\nu}(2)$ analysis [2], our total background was decreased by 24% and total acceptance was increased by 63% thanks to improved background rejection due to the upgrades of the AD and BV for E949. In addition the improved knowledge of the background contributions allowed the signal region to be divided into nine sub-regions, with relative signal-to-background levels differing by a factor of 4, that were used in the likelihood method [11] to determine $BR(K^+ \to \pi^+ \nu\bar{\nu})$.

5 Results

After completion of the background studies, the signal region was examined and three candidates were found. The energy versus range for these observed candidates is shown in Fig. 7 along with the results of previous E787 [1, 2] and E949 [3, 4] analyses. From these three new candidates alone, $BR(K^+ \to \pi^+ \nu\bar{\nu}) = (7.89^{+9.26}_{-5.10}) \times 10^{-10}$ was calculated using the likelihood method [11]. The probability of these three events to be due to background only is 3.7%. When combined with the results of previous E787 and E949 analyses, $BR(K^+ \to \pi^+ \nu\bar{\nu}) = (1.73^{+1.15}_{-1.05}) \times 10^{-10}$ was measured [6]. The probability that seven candidate events were due to background only is 0.1%. These observation imply a $K^+ \to \pi^+ \nu\bar{\nu}$ branching ratio consistent with SM prediction.

6 Conclusion

For many years physics beyond the Standard Model, or new physics, has been searched for. There are two approaches: one is the direct search of new particles in a very high-energy region; the other is the observation of any possible discrepancy

between measured and predicted quantities in electroweak processes. The search for the decay $K^+ \to \pi^+ \nu\bar{\nu}$ is an attempt to utilize the latter of two approaches.

In 25 years of research with BNL E787 and E949, the search for $K^+ \to \pi^+ \nu\bar{\nu}$ decays went from a limit on the branching ratio $BR(K^+ \to \pi^+ \nu\bar{\nu}) < 1.4 \times 10^{-7}$ at 90% CL to a measurement of $(1.73^{+1.15}_{-1.05}) \times 10^{-10}$ that is twice as large as, but still consistent with, the Standard Model expectation of $(0.85 \pm 0.07) \times 10^{-10}$.

There is a letter of intent for a stopped kaon decay experiment in Japan. And analysis of E949/E787 for other K^+ decay modes still continue.

Experiment NA62 (formerly NA48/3) at CERN was approved in 2007 and is in preparation. The use of kaon decay-in-flight to measure $K^+ \to \pi^+ \nu\bar{\nu}$ has not been attempted before. NA62 aims to collect about 100 of such decays in two years of data taking using 75 GeV/c beam.

References

1. S. Adler et al., Phys. Lett. B. **537**, 211 (2002)
2. S. Adler et al., Phys. Rev. D. **70**, 037102 (2004)
3. S. Adler et al., Phys. Rev. D. **77**, 052003 (2008)
4. V.V. Anisimovky et al., Phys. Rev. Lett. **93**, 031801 (2004)
5. M. Ardebili, Ph.D. Thesis, *Princeton University* (1995)
6. A.V. Artamonov et al., Phys. Rev. Lett. **101**, 191802 (2008)
7. Y. Asano et al., Phys. Lett. B. **107**, 159 (1981)
8. J. Brod, M. Gorbahn, Phys. Rev. D. **78**, 034006 (2008)
9. A.J. Buras, Nucl. Phys. B **697**, 2004
10. U. Camerini, D. Ljung, M. Sheaff, D. Cline, Phys. Rev. Lett. **23**, 326 (1969)
11. T. Junk, Nucl. Instrum. Meth. A. **434**, 435 (1999)
12. W.M. Yao et al., J. Phys. G **33**, 1 (2006)

The sLHC and the ATLAS Detector

Chr. Zeitnitz

Abstract The LHC accelerator at CERN will collide protons at a centre-of-mass energy of 14 TeV. This will allow to discover a possible Standard Model Higgs–Boson, establish Supersymmetry or new other physics beyond the Standard Model. The physics up to a scale of approx. 1 TeV will be covered, but the precision measurements of the properties of the discovered particles and/or processes will very likely not be possible with the currently foreseen design luminosity of 10^{34} cm^{-2}s^{-1}. An upgrade of the LHC, called sLHC, will allow to increase the luminosity by an order of magnitude. The corresponding increase in statistics will allow to measure some of the expected properties with a higher precision, but will impact the detector performance substantially. This article describes some of the physics goals for the sLHC and the environment the detector has to operate in. The impact on the detector design is discussed as well as some of the currently foreseen solutions.

Keywords: LHC ATLAS upgrade sLHC calorimetry

1 Introduction

The proton–proton collider LHC at CERN will start its operation in 2009. The design parameters are a centre-of-mass energy of 14 TeV and a luminosity of 10^{34} cm^{-2}s^{-1}, which are expected to be reached in 2010/11. The experiment ATLAS aims for a total amount of collected data of approx. 500 fb^{-1} for the period up to 2015/16. These data will be sufficient to discover new particles like a Standard Model Higgs, new gauge bosons or establish Supersymmetry up to a scale of 1.5 TeV, but high precision measurements will not be possible. Current studies show, that the couplings for a SM Higgs could be measured with a precision of $10-50\%$.

Chr. Zeitnitz
Bergische Universität Wuppertal, Gaussstrasse 20 D-42119 Wuppertal,
e-mail: zeitnitz@uni-wuppertal.de

V. Begun et al. (eds.), *Progress in High-Energy Physics and Nuclear Safety*,

Higher precision or the measurement of CP-state and spin of newly discovered particles would require substantially more data. An upgrade of the LHC-accelerator, called sLHC, is therefore planned for the year 2016/17 with the goal to increase the luminosity by st least an order of magnitude to 10^{35} $cm^{-2}s^{-1}$. This would allow to increase the reach for supersymmetric particles up to 2 TeV and would open the door for other physics topics, like Flavour-Changing-Neutral-Currents in top-quark decays, as well.

The upgrade of the LHC to higher luminosity will require an upgrade of a substantial part of CERNs accelerator complex (LINAC, PS, SPS), which will start already during the next years.

At sLHC luminosities the particle flux, which the detectors have to cope with, will increase substantially as well. The current detectors have not been designed to perform well at these rates. In addition will the radiation increase for the electronics. All this will make an upgrade of the detectors mandatory as well.

2 Current LHC upgrade plans

A luminosity upgrade of the LHC accelerator would require to re-build part of pre-accelerator complex. The current plans are

2010-13	Construction of LINAC4
2012	Upgrade interaction regions, collimators and injectors of the LHC
2013	New LINAC4 starts operation
2012-16	Construction of new Low-Power superconducting proton linac (LP)SPL
2016	Modify SPS
2017	Ready for sLHC operation

The upgrade of the interaction regions and collimators of the LHC is already required to reach the design luminosity. Additional studies are performed for an energy upgrade of the LHC. Since this will require to increase the field in the dipole magnets, these would need to be replaced.

3 Experimental environment

The high rate of underlying events at the sLHC luminosity ($\approx$300) will lead to a substantial increase in the radiation background (charged particles, neutrons and gammas). Mainly effected are the tracking system (inner detector), the very forward calorimeter, the muon system and a substantial fraction of the on-detector electronics. The current ATLAS detector has not been built to cope with this level of radiation and some detector components will no longer be operational or at least will show a substantially reduced performance. Since the actual background level is currently not very well known, due to uncertainties in the background simulation, the

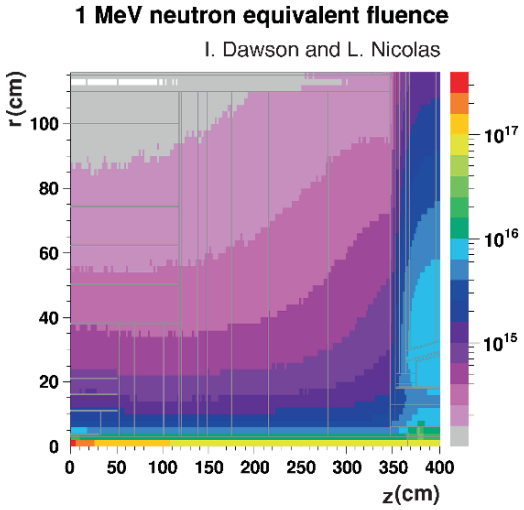

Fig. 1 The expected neutron flux at the sLHC luminosity in the ATLAS detector simulated with the FLUKA program by I. Dawson. The interaction point is located in the lower left corner of the plot

detector has been built with a safety factor of 5–10 for most components. Figure 1 shows the expected neutron flux for the sLHC luminosity of 10^{35} $cm^{-2}s^{-1}$. In order to validate the existing simulations of the background, multiple neutrons and gamma sensors have been installed inside of the detector volume. This will allow to estimate more precisely the lifetime of the electronics and the detector components within the next 1 to 1.5 years.

For some components it is already now clear, that they will not be able to cope with the high particle flux: the tracking detectors and the electromagnetic forward calorimeter. For the first a complete replacement is planned for the sLHC operation and the latter is currently studied in a high intensity proton beam at the Protvino accelerator. The result of these tests will be valuable to understand the actual limits of the current calorimeter technology utilized in the ATLAS experiment.

4 Upgrade of the ATLAS detector

The currently forseen upgrades for the sLHC operation consists of

- A complete replacement of the inner detector (tracking detectors)
- A modification of the forward calorimeter region (replacement or shielding)
- Design and construction of new front-end electronics for the inner detector and the calorimeter
- Upgrade of the trigger system
- A modified beam pipe (beryllium) in order to minimize the background rate in the forward muon chambers

The time slot foreseen for the upgrade in 2016/17 is planned to be 18 month long.

4.1 Read-out electronics

The parameters of the sLHC (bunch crossing time and rate of underlying events) makes it necessary to read-out a larger fraction of the detector. This is due to the larger occupancy. An additional reason for the new electronics is the high radiation background, which requires more radiation hard electronics to be used for the on-detector components. For the currently designed new inner detector, which is planned as a full silicon tracker, this electronics is directly integrated into the module design (sensor, read-out and transmission). For the LAr-calorimeter read-out the signals are supposed to be digitized in the front-end electronics, which requires all data to be transmitted off the detector in order to allow for the triggering of the event. This will require radiation hard optical transmission components for very high rates to be available. The current electronics of the calorimeter is summing specific analog channels to build trigger towers (≈7,200), which are fed into the trigger system. An early digitization has to build the trigger sums after the data of all cells have been transfered off the detector. This will require modifications in the triggering system as well.

4.2 Inner detector

The inner detector of the current ATLAS experiment will need a modification already in the year 2012, when the inner layer will very likely show a seriously degraded performance due to radiation damage. The development of this new layer (so-called b-layer) has already started.

For the sLHC operation the complete tracker has to be replaced. The currently foreseen baseline design is shown in Fig. 2. It consists of multiple layers of silicon

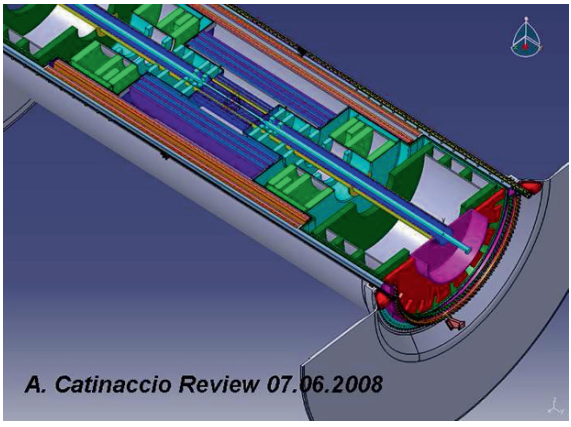

Fig. 2 Current strawman design of the full silicon inner tracker

pixel detectors for a high precision tracking and vertexing, followed by silicon strip detectors for the outer layers.

In detail the current design consists of:

- Four layers of silicon pixel detectors
- Three layers of short silicon strips (≈25 mm long)
- Two layers of long silicon strips (≈100 mm long)

The total occupancy is supposed to be below 1%.
The development for the different components of a new inner detector has started:

- Radiation hard sensors
- Front-end electronics
- Data transmission components
- Powering schemes (parallel and serial)
- Carbon structures
- Cooling system

The goal is to build a radiation hard high resolution tracker, which requires as little material as possible to minimize the energy loss and multiple scattering of the charged particles in the tracking volume.

4.3 Forward calorimeters

The calorimeter of the ATLAS experiment utilizes, for most parts, liquid argon as the active material. In a high charged particle flux environment the ionization rate becomes high and a large amount of positive Ar-ions are produced. Due to their low mobility in the liquid, these stay in the argon and shield the electric field of the ionization chamber. The calorimeter performance is degraded due to this built-up effect. The current of the high voltage is increased and the effective volume decreases. At a certain critical ionization the calorimeter stops to work. For the very forward calorimeter of the ATLAS calorimeter two effect lead to a degradation of the performance: the high current on the high voltage lines cause a voltage drop over a protection resistor and the built-up effect reduces the signal amplitude. The voltage drop of the high voltage will become severe at sLHC particle rates, even assuming that the flux is at the lower end of the expectation. Therefore the first section of the forward calorimeter will require a modification.
Two options are currently discussed:

- Replace the very forward calorimeter, the so-called FCAL or
- Shield the FCAL by placing an additional warm calorimeter in front

In addition to the actual detector performance the hadronic endcap calorimeters utilize cold GaAs electronics. It is currently not clear, if this is radiation hard enough to stand the high radiation level during sLHC operation. If this electronics fails, the two endcap cryostats have to be opened, which will make the FCAL replacement

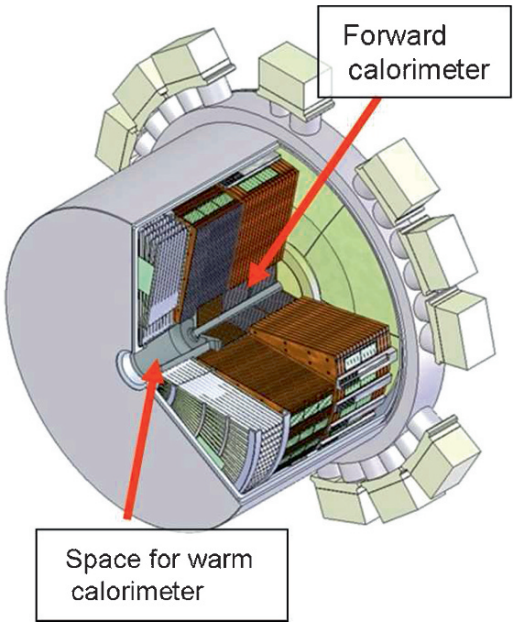

Fig. 3 Position of a warm calorimeter in the bore of the endcap cryostat

the preferred option. Otherwise a warm calorimeter in the front bore of the cryostat, as sketched in Fig. 3, becomes an option. The complication of opening the cryostats in a high radiation environment and handling highly activated components makes this operation a very time consuming enterprise and will hardly fit into the foreseen time slot of 18 month.

4.4 Muon system

Most of the muon system is well shielded by the calorimeters of the ATLAS detector. The exception is the forward region, where the shielding is not sufficient to reduce the enormous particle flux to an acceptable level, especially at small angles to the beam pipe. A major source of particle is the beam pipe itself. A significant reduction in background for the muon system could be achieved by a beam pipe made out of Beryllium. Simulations show a reduction between 30% and 60%.

5 Conclusion

The upgrade of the ATLAS detector for the super-LHC will require a substantial R&D effort and has to start in the near future. The actually required upgrades will only be clear, once the radiation level has been measured at LHC during the next 1 to

1.5 years. The inner detector will be replaced completely and the forward calorimeters will require substantial improvements in order to perform well at the foreseen luminosity. New electronic for the front-end as well as read-out and trigger has to be developped.

Part II
Nuclear Safety

Problem of Radiation Resistance of Structural Materials of Nuclear Power

I.M. Neklyudov, O.V. Borodin, V.V. Bryk, and V.N. Voyevodin

Abstract Mechanisms of radiation damage of construction materials in nuclear engineering and progress in developing radiation-resistant materials for the present and future generation nuclear reactors are reported. The analysis of the present state and of the perspectives toward a solution of the problem show that, in spite of the considerable research efforts throughout the world, economically acceptable operation standards for presently operating reactors still have not been reached. The reason is insufficient radiation resistance of the basic ingredients of the existing nuclear devices – of various classes of stainless steel and zirconium alloys. A key problem in the material sciences provision of the modern and future nuclear engineering is the study of the microstructure evolution and its impact on the degradation of the input physical and chemical characteristics.

Keywords: Nuclear energy, construction materials, radiation-resistant materials, radiation defects, heat reactors, reactors on fast neutrons, effects of transmutation, electronuclear systems

1 Introduction

Today's nuclear power is the more real in the world that possesses the humanity for the production and supply of low cost electrical and thermal power for distant prospective with guarantee of nuclear, physical, ecological and technical safety in amounts corresponding with society needs. According to the data of IAEA more than 500 nuclear power units of research and other reactors are in operation.

I.M. Neklyudov, O.V. Borodin, V.V. Bryk, V.N. Voyevodin
National Science Center "Kharkov Institute of Physics and technology", 1, Akademicheskaya Str., Kharkov 61108,
e-mail: voyev@kipt.kharkov.ua

V. Begun et al. (eds.), *Progress in High-Energy Physics and Nuclear Safety*,

The development of nuclear power had proceeded and proceeds in strict competition fight with traditional technologies of electrical power production and also with alternative (restored) sources.

The key questions of such competition in 21st century are the safety and economy (the price of produced electrical power).

It is just the behavior of structural materials of operated and developed reactors that determines the safe and economical operation of nuclear stations.

Irradiation of the materials of nuclear reactors causes the following changes of materials: hardening; low (LTRE) and high temperature (HTRE) radiation embrittlement; radiation creep; radiation growth and radiation swelling; production of induced activity.

Exactly these characteristics at the same time as corrosion resistance are the priority on the evaluation and comparison of different structural materials. On the development of new materials the main problem is the attainment of minimum or acceptable variation of these characteristic for the guarantee of safety and longevity of structural elements.

The last requirement of low activation or of fast decrease of induced activity is now necessary during the development of the design of fusion reactors (FUR) due to the higher volume of irradiated components than in the core of fission reactors.

Expediency of the use of the materials in nuclear power plants of definite type depends on special features of NPP, on used coolant, on energy spectrum of neutrons and so on.

Stainless steels and alloys on the base of nickel and chromium are used as claddings of absorption element, of springs elements of fuel elements and fuel assemblies and in some cases for distance grid of FA. For fast reactors operating at higher temperatures and power intensity high-temperature resistant solution-treated austenitic steels, chromium ferritic-martensitic steels, nickel alloys are used. For the first wall of fusion reactor with helium coolant the main material is low-activated chromium steels and on lithium cooling – alloys of vanadium alloyed by titanium and chromium. These materials are used in domestic and in foreign reactors. Differences are in alloying elements and in technologies of production that define their operational characteristics.

2 Reactors on thermal neutrons

Now thermal-neutron reactors, pressurized water reactors or boiling reactors are the base of the world nuclear power (WWER-440, WWEE-1000, PWR, BWR). The main components of thermal reactors that are subjected to the intensive radiation exposure are the pressure vessels, fuel elements claddings, pressure vessels internals.

Materials of pressure vessels must guarantee the safe operation during the whole service life. Ferritic-perlitic (Russia) and ferritic-martensitic steels (USA, France, Japan) are used for the fabrication of pressure vessels.

Table 1 Reactors on thermal neutrons: WWER, PWR, BWR (power 440–1200 Mw)

Mean density of thermal neutron flux in core	2,7-4,4.10^{-13} n/cm^2 s
Mean density of fast neutrons in core	1,9-4,0.10^{14}
The rate of dose setting-up	10^{-7}dpa/s
Temperature of coolant (pressure vessel)	On inlet 285–290°C On outlet 320–325°C
Density of fast neutron flux on pressure vessel	1.10^{17}n/cm^{2}s
Fluence of fast neutrons ($E_n > 0{,}1$ MeV) on pressure vessel during 40 years of operation	$\Phi t = 5.10^{19}$–1.10^{20}n/cm^2
Rate of damaging rate (steel)	10^{-10}dpa/s
Dose of radiation damage of pressure during 40 years	0,1 dpa

WWER-440 – 15Cr2MoA (C-0,11-0,21; Si-0,17-0,37; Mn-0,3-0,6; S-0,012-0,018; P-0,009-0,0038; Cr-2,5-3,0; Cu-0,09-0,17; Ni-0,19-0,27; Mo-0,6-0,8; V-0,25-0,35);

WWER-1000 – 15Cr2NiMoPA, 15Cr2NiMoPAA (C-0,13-0,18; Si-1; Mn-1; S<0,035; P<0,01; Cr-1,8-2,3; Ni-1,0-1,5; Mo-0,5-0,7; V-1,1-0,12);

PWR, BWR – A533-B (C<0,25; Si-o,15-0,30; Mn-0,15-1,50; S-),040; P-0,035; Ni-0,40-0,70; Mo-0,45-0.60.

Given in Table 1 data of the operational conditions of thermal neutron reactor show that rather low fluences and rather low operational temperatures are the characteristic properties of pressure vessel material operation for the reactor of such type.

All pressure vessel steels harden in the result of operation. As a rule, the increase of yield strength after irradiation at temperatures 240–290°C to the fluence 10^{22} neutrons/cm^2 makes 20–40%.

It is obvious now that radiation-induced degradation of mechanical properties of pressure vessel steels during operation is the result of microstructure changes of nanostructure scale (nm). Evolution of microstructure under neutron irradiation at temperature of operation of pressure vessel (270–300°C) depends not only on the migration of point defects formed by irradiation, on their interaction and clustering but also on complex interaction with impurities.

Three main mechanisms responsible for the change of microstructure of pressure vessel steels under irradiation are now considered:

1. Damage in the matrix due to the formation of radiation-induced clusters and dislocation loops
2. Radiation-accelerated formation of fine dispersion precipitates – precipitates enriched by copper and of carbonitrides
3. RIS on grain boundaries and interphase boundaries of embrittling elements such as phosphorus, sulphur, arsenic

Sum radiation embritterment (change of the temperature of brittle-ductile transition) is presented on Fig. 1.

It is obvious that described above radiation-induced variations are the cause of complex synergetic changes in the steel behavior, that can‘t be explained only by one mechanism.

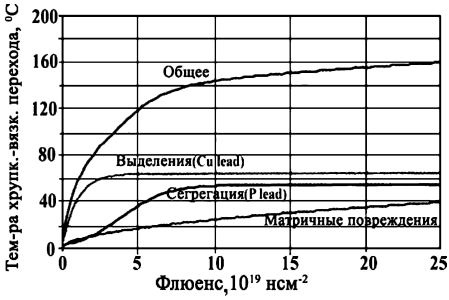

Fig. 1 Dependence of the temperature of brittle-ductile transition on neutron fluence [14]

It is supposed that evolution of radiation damage in pressure vessel steels proceeds as follows:

Formation of primary defects → nano structure evolution→ hardening → embrittlement (shift of temperature of brittle-ductile transition) [15]

Matrix defects in pressure vessel steels. Damaging in matrix of irradiated pressure vessel steels may be subdivided on:

(a) Aggregates of interstitial clusters and interstitial dislocation loops and also as vacancy clusters, microvoids and vacancy loops

(b) Mixed clusters of solute atoms and point defects

Now there is some uncertainty in the definition of matrix defects nature but experimental and theoretical results show that interstitial and vacancy defects may exist; the wide range of interpretations suppose that microstructure and irradiation conditions may strongly influence on distribution of defects [16].

Under other similar conditions the size and concentration of radiation defects increases with the increase of fast neutron dose. It was detected that matrix damaging evolves with irradiation dose, the rate of dose set up and with irradiation temperature; this damage gives the resulting hardening proportional to the square root of accumulated dose [16].

Formation of precipitates enriched by Cu and Mn-Ni, of carbonitrides and carbides of different types ($(V, Cr)_7(C,N)_3$). Elements of solid solution of pressure vessel steels have the trend to radiation-accelerated clustering and formation of precipitates with nanosize (2–3 nm).

In most cases the results show that formation of precipitates enriched by copper is one of the main causes of radiation hardening and embrittlement of pressure vessel steels [17]. It must be noted that chemical composition of these precipitates remains uncertain, different elements are present in these precipitates (Fe, Mn, Ni and possibly Si and P). Even insignificant variation in steel composition and in neutron spectrum causes the significant differences in morphology and concentration of precipitates [18]. In steels of reactor WWER-1000 precipitates are radiation-stimulated and in steels of reactor WWER-440 they are radiation-induced [18].

The role of phosphorus in the processes of radiation embrittlement of pressure vessel steels is related with its segregation on grain boundaries in the result of radiation-stimulated diffusion of atoms of phosphorus by vacancy mechanism and by the decrease of energy of boundary cohesion. On the other hand it is shown that in

irradiated steels phosphorus participates in the formation of some hardening forms in the grain body that causes the decrease of its concentration on grain boundaries and to the loss of the segregation effects. It is established that phosphorus increases the embrittling influence in the presence of considerable quantities of copper, nickel and manganese [19].

Now the question about relationship of contributions into the radiation embrittlement of different mechanisms demands the further investigation under higher irradiation doses.

Investigation of Ni role in the processes of embrittlement is of special interest because due to the technological causes in pressure vessels of nuclear reactor operating in Ukraine the content of nickel exceeds 1.5% weight. The deleterious effect of nickel on temper brittleness of steel Cr-Ni-Mo-V was known a long time ago and the existing experimental data on nickel contribution to the radiation embrittlement of reactor steels are limited.

3 Alloys of zirconium

The main structural material of cores of water-cooled thermal reactors are zirconium alloys that have the low cross section of neutron capture and high radiation and corrosion resistance.

The characteristic feature of zirconium alloys of Russian production that are used in nuclear reactors of Ukraine is the presence of niobium. Niobium is the main alloying element for binary and for multi components alloys.

Base zirconium alloys of foreign production (Zircaloy-2 (Ni-0,03-0,8%; Fe-0,07-0,2%; Sn-1,2-1,7; Cr-0,05-0,1%)) and Zircaloy-4 (Fe-0,18-0,24%; Sn-1,2-1,7%; Cr-0,07-0,13%)) are alloyed by tin, iron, chromium and nickel.

Alloys of Russian production E-110 (Zr-1% Nb), E-125 (Zr-2,5% Nb), E635 (Nb-1,0%; Fe-0,3-0,5%; Sn-1,0-1,5%) are now the base material of operating Russian reactors.

These alloys are used only in the state close to the recrystallized one that guarantees their high ductility in the initial state.

Alloy E635 has the high creep resistance that can be explained by considerable hardening of this alloy under irradiation. This alloy has also the high resistance to the radiation growth. From the point of view of microstructure, the resistance to the radiation growth may be explained by the special features of dislocation structure evolution under irradiation (Figs. 2, 3). In alloy E 635 with very high resistance to the radiation growth the high concentration of radiation-induced dislocation loops of <c> type responsible for the processes of radiation growth may be formed only under very high irradiation doses (>50 dpa) that are practically unreachable in commercial reactors. This singularity of alloy E635 evolution may be explained by the role of α-solid solution enriched by iron [20]. For alloys Zr-1% Nb of the Ukrainian production obtained by calcination the investigation of the oxygen influence on irradiation behavior of alloys is of special interest.

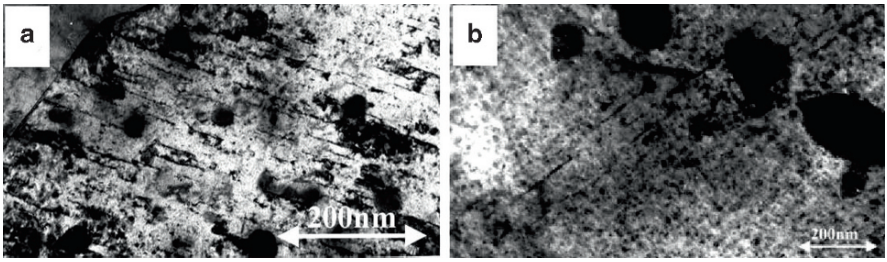

Fig. 2 c-component dislocation microstructure of alloys E-110 (a) and E-635 (b)

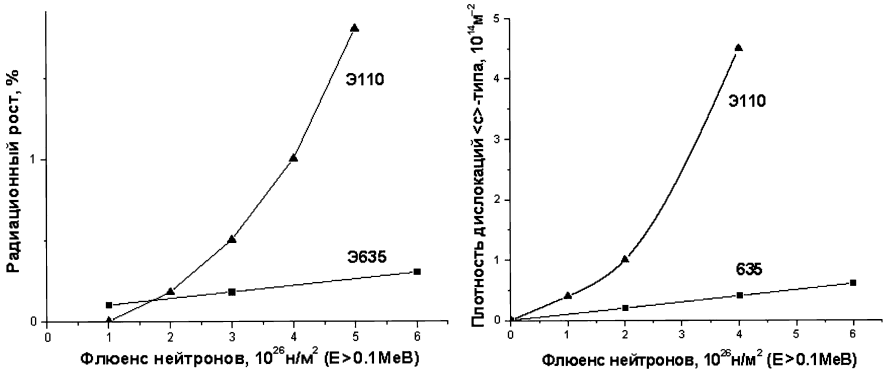

Fig. 3 Plots of the dependence of radiation growth (a) and density of dislocation loops of c-type on fluence of neutrons (E < 0,1 MeV)

4 Materials of Pressure Vessel Internal (PVI)

A new important challenge for radiation material science is now the substantiation of radiation resistance of materials of pressure vessel internal (PVI) for reactors WWER-440 and WWER-1000; PVI were designed as not replaceable element of construction with the operation delay equal to the service life of the reactor pressure vessels [21]. Characteristic property of PVI elements and, first of all of the baffle, produced for Russian reactors of steel Cr08Ni18Ti10 and for reactors of type PWR and BWR of steel 321, is that during operation they accumulate quite high fluence of neutrons and have the temperature level caused by the absorption of γ-quanta and of neutrons; the considerable volume changes of the material of PVI may occur at such temperature level due to the vacancy swelling under irradiation (Fig. 4). Early the possibility of such radiation swelling in this temperature range was rejected. Recently it became known that this phenomenon may proceed in light-water thermal reactors. In American, French, Japanese and Russian works voids were detected in PVI of reactors of PWR type (Fig. 5) [22, 23].

Distinction of swelling manifestation in conditions of thermal reactors PWR is the abrupt decrease of incubation period of swelling and considerable decrease of the temperature of void formation.

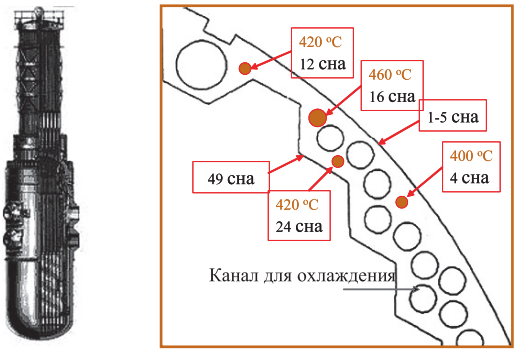

Fig. 4 Baffle and temperature field in section with maximum of neutron flux on height: (a) baffle; (b) temperature field in baffle body [23]

Fig. 5 Voids observed in pressure vessel internal of reactor WWER-1000 (steel 06Cr18Ni10Ti) RNPS –3 [23]

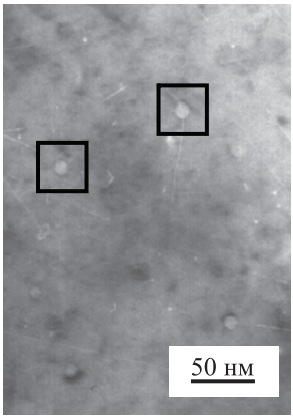

This problem is potentially more dangerous for reactors WWER-100 the baffle of which has more complicated shape and is thicker than in reactors PWR. This causes the local increase of temperature up to 460°C and leads to the void formation even without temperature shift.

It was shown that at temperature of irradiation near 335°and under doses exceeding 75 dpa the swelling of austenitic steels is higher 10% and their ductility decreases abruptly.

Now, examining the problem of service life prolongation for Ukrainian reactors WWER is necessary to consider the radiation swelling and embrittlement of PVI.

The main task for the solution of the problem of low-temperature swelling is the study of the operational conditions (rate dose, temperature, doses, environment, synergetic effect of gaseous impurities, stresses, material composition, its initial condition and others).

5 Fast-neutron reactors

Development of large-scale nuclear power is not possible without the use of fast-neutron reactors guaranteeing the nuclear fuel breeding and using in nuclear power cycle of all produced nature uranium and consequently – of thorium.

Fast reactors with fuel cycle on the base of self – supply and non spreading of nuclear materials (BN-600, BN-800, BREST and others) will be the base of large-scale nuclear power in the second half of our century. Putting into operation of reactors BN from 2040 will allow to decrease the demands of NPS in uranium to 2100 from 240 to 50,000 t/year (Fig. 6) and also organize the annihilation of long-lived isotopes.

High temperatures and irradiation doses in reactors BN (Table 2) lead to the situation that the problem of structural material production for claddings of fuel elements became the key one; such material must have the complex of mechanical and technological properties, compatibility with coolant and fuel material and also stability of properties under irradiation (see Table 3).

6 Austenitic stainless steels

Austenitic stainless steels (ASS) as structural material for the use in core of operating and developed nuclear reactors present the greatest interest.

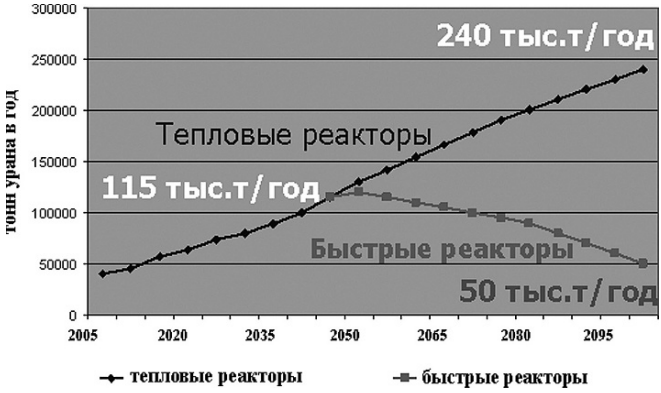

Fig. 6 Forecast of the world needs in uranium upto 2100 [24]

Table 2 Parameters of fast-neutron reactors

Density of neutron flux	3.10^{15}–10^{16}n/cm^{2}s
Rate of He generation	20–30 appm/year
Rate of dose setting	100–200 dpa/year
Temperature	400–600°C

Table 3 Chemical composition of austenitic steels used in core of nuclear reactors

Steel	Ni	Cr	Mo	C	Ti	Nb	Si	V	P	S	Mn	Others
AISI 316 USA	10,0014,00	16,0 18,0	2,03,0	≤0.08	–	–	≤1,0	–	–	–	≤2,0	B 0,0002
D9 USA	14,0–16,0	14,0	1,4–2,3	–	0,2–0,35	–	0,8–1,0	–	–	–	1,8–2,3	–
PNC316 Japan	13,8	16,5	2,5	–	0,098	0,07	0,93	–	0,031	–	1,78	B 0,0044
15/15Ti, France	14,5–15,0	14,5–15,0	1,3–1,5	–	0,45–0,5	–	0,5	–	0,007	–	1,4–1,6	B 0,0065
15/15Si, France	14,5–15,0	14,5–15,0	1,3–1,5	–	0,5	–	0,085	–	0,007	–	1,3–1,5	B 0,004
1,4981, Germany	15,5–16,0	15,5–16,0	1,6–1,8	–	0,4–0,5	0,7–0,85	0,45	–	–	–	1,3–1,4	–
FV-548,Great Britain	16,0–17,0	11,5–12,0	1,1–1,2	1,4–1,5	0,9–1,0	–	0,3–0,4	–	–	–		
09Cr16Ni15Mo 3B(EI-847), Russia	14,0–16,0	15,0–17,0	2,5–3,0	≤0,09	–	0,8–0,9	≤0,8	–	–	–	≤0,8	–
16Cr15Ni3Mo BP(EP-172), Russia	14,5–16,0	15,0–17,0	2,5–3,0	0,04–0,07	–	0,35–0,9 Nb/C=9–13	0,3–0,6	–	≤0,02	–	0,5–0,9	B≤0,008 Ce0,15
08CrCr18Ni10 T, Russia	9,0–11.0	17,0–19,0	–	0.07–0,1	≥5xC to 0,8	–	≤0.8	–	≤0,0,25	≤0.015	1.0–2.0	–
15Cr15Ni2Mo2 GTP(ChS-68) Russia	14,0–15,5	15,5–17,0	1,9–2,5	0,06–0,08	0,2–0,5	–	0,3–0,6	0,1–0,3	0,014	0,004	1,1–2,0	B≤0,005
EK-99 Ukraine	15,0–16,0	15,0–16,0	2,0–2,5	–	0,2–0,4	–	0,2–0,4	–	0,010	–	0,9–1,3	B≤0,005

* base- iron

Fig. 7 Main relations in structure of irradiated stainless steels [2]

Unfortunately, the radiation swelling is up to now the main factor limiting the use of austenitic stainless steels as structural material for fast reactors and reactors of next generations [25].

Radiation swelling in multi component ASS is the result of complex structure-phase transformations under irradiation (Fig. 7) therefore the achievement of necessary level of resistance of austenitic steels to swelling may be obtained only on the base of understanding of all phenomena involved in the processes of radiation swelling

In authors opinion the reaching of minimum level of swelling is related with the increase of stability of all structural components (dislocation structure, solid solution, systems of secondary phases precipitates) under irradiation.

In austenitic stainless steels the evolution with the irradiation dose proceeds identically for materials with FCC structure: clusters of point defects → defected Frank loops $a/3\langle 111\rangle$ → perfect prismatic loops $a/2\langle 110\rangle$ → dislocation network (Fig. 8a, b, c, d, e) moreover the majority of Frank loops are the loops of interstitial type.

Density of dislocations in network under doses 20–40 dpa reaches the saturation and makes $8–9.10^{10}\text{cm}^{-2}$.

Radiation resistance of ASS may be improved at the expense of introduction of insignificant quantities of alloying elements and subsequent thermal-mechanical treatment [2].

Component and impurity composition of steels influencing on energy of stacking fault and energy characteristics of point defects may modify the evolution of dislocation structure during irradiation. Formation of perfect loops that are mobile and can glide and climb making easy the formation of dislocation network.

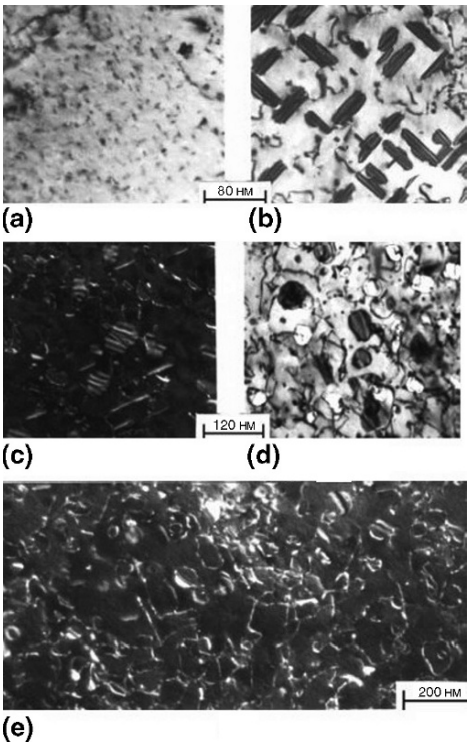

Fig. 8 Stage of dislocation structure evolution in irradiated steel EI-847 (Cr^{3+}, E = 3 MeV, $T_{ir.} = 823$ K, $K = 10^{-3}$ dpa/s), (a) D = 0,5 dpa, (b) D = 2 dpa, (c) D = 10 dpa, (d) D = 15 dpa, (e) D = 25 dpa

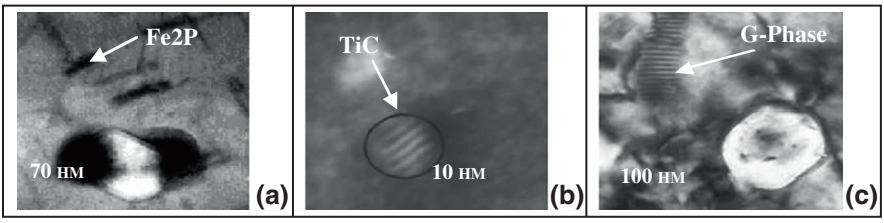

Fig. 9 Precipitates of second phases in irradiated ASS: (a) – phosphydes Fe_2P; (b) – carbides TiC; (c) – G-phase $(Ti, V, Nb, Mn)_6(ni, Co)_{16}Si_7$)

Alloying influences on the key points of evolution of dislocations from Frank loops $a/3\langle 111\rangle$ to prismatic loops $a/2\langle 110\rangle$ and subsequent formation of dislocation network; this network is the start of swelling.

It must be noted that the local variation of composition induced by RIS, leads to the decay of solid solution and forms the precipitates of two types:

- Precipitates suppressing the swelling at the expense of accelerated recombination of point defects on interface particle-matrix. These are carbides of type MC (principally TiC, NbC, VC), phosphides Fe_2P or Ni_3Ti (Fig. 9a, b);

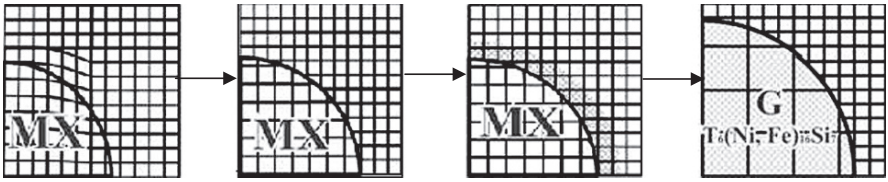

Fig. 10 Stages of transformation of precipitates of type MX (M – metal, X: C, N) under irradiation [26]

- Precipitates produced in the result of solid solution decay (especially due to the segregation of Ni and Si) are the sign of radiation resistance loss on last stages of evolution of structure – M_6C and G-phase (Fig. 9b)

Flows of point defects produced under irradiation that are very mobile at these temperatures will stimulate evolution of second phase precipitates. This evolution may proceed by several manners: (1) growth of precipitates; (2) dissolution of precipitates; (3) infiltration (transition of solid solution elements into precipitate) in precipitates (from precipitates) of other elements (from/or into) solid solution (Fig. 10).

The obtained results show:

- Reaching of acceptable level of swelling is directly related with formation of more stable microstructure under irradiation.
- Influence of alloying and treatment consists in following:
  - Production of more stable dislocation structure (conservation of low mobile Frank loops) and increase of the recombination level TD. It may be reached due to the solution treatment or by the processes of segregation of alloying elements on dislocation components that decreases their mobility.
  - Conservation of fine carbides precipitates (TiC) and phosphides (Fe_2P) (increase of their life is the m and η-carbides into the range of higher doses.

Delay of formation of G-phase and η-carbides must conserve in the solid solution the sufficient quantity of such elements as Ni, Si and P that influence on nucleation and growth of voids. Evolution of defected structure is the result of "competition" between the evolution of phases preventing the swelling, and phases produced in the result of decay of solid solution. This "competition" may be extended by the selection of optimal composition and by the thermal-mechanical treatment.

Unfortunately, the role of precipitates as the main mechanism suppressing the swelling depends on the matrix surrounding and may vary during irradiation. The alloying elements included into precipitates change the nature of precipitates and modified precipitates interact with point defects in different way under irradiation. Interaction of matrix and precipitates throughout the flows of point defects makes the processes of evolution of microstructure complex and creates some contradictions for understanding of the influence of alloying elements or the role of precipitates.

7 Ferritic-matrensitic Steels

Ferritic-martensitic steels with chromium content 9–12% are now the priority candidate materials for clad and wrapper of fast reactors, for first wall of fusion reactors because they are characterized by low induced activity, by low vacancy swelling (in comparison with austenitic steels, Figs. 11, 12) and creep, by the high degree of resistance to the high-temperature and helium embrittlement (Table 4).

There are different international program for development of prospective reactors of new four generation and also development of fusion reactors. Each of these programs foresees the use of ferritic-martensitic steels that must operate under irradiation doses not lower ∼100–200 dpa and at temperatures 650–750°C and in most cases they will be subjected to very high levels of helium and hydrogen.

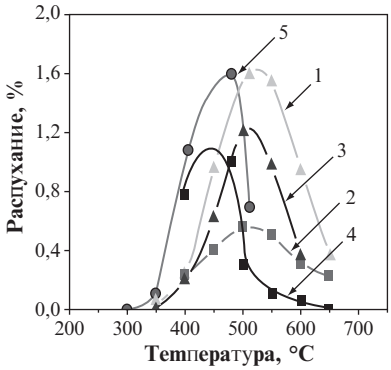

Fig. 11 Temperature dependence of swelling in materials on the base of Fe: 1 – α-Fe (D = 100 dpa); 2 – EP-450 (D = 150 dpa); 3 – Fe-12%Cr (D = 100 dpa); 4 – 01Cr13No4, Cr^{3+} (=100dpa); 5 – 01Cr13Mo4, Ar^{3+} (D = 100 dpa)

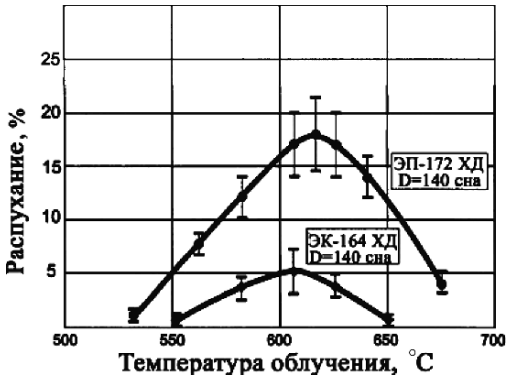

Fig. 12 Temperature dependence of swelling in austenitic steels (EP-172, EK-64) (Cr^{3+}, D = 140 dpa)

Table 4 Chemical composition of some 9–12% chromium steels [27]

Steel mark/country	C	Si	Mn	Cr	Ni	Mo	V	W	Nb	B	Other elem
EM12 Belgium/France	0,08–0,12	0,.30–0,50	0,90–1,20	9,0–10,0		1,9–2,1	0,25–0,35	0,35–0,45			
F82H Japan	0,10	0,20	0,50	8,0			0,20	2,0		0,003	Ta-0,04 N-less 0,01
JLF-1 Japan	0,1	0,05		8,0			0,2	1,95			Ti-0,002 Ta-0,09 N-0,023
ORNL9Cr, USA	0,1	0,21		8,8			0,18	1,97			Ti-0,01,Ta-0,07 N-0,023
EUROFER, Europe	0,10,–0,12	0,05	0,4–0,6	8,0–9,0			0,20–0,30	1,0–1,2		0,004–0,006	Ta-0,06-0,10; n-0,02-0,04
2Cr12Mo2, Czech Republic	0,20		11,6	0,5	2,20	0,30	0,5				
NT9, Sweden	0,20			12		1,0	0,25–0,40				
FV48, England	0,10	0,46	0,86	10,7	0,65	0,60	0,14		0,26		N-0,05
EP-450, Russia	0,10–0,15	0,60	0,60	11,0–13,5	0,05–0,30	1,2–1,4	0,10–0,30		0,30–0,60	0,004	
EP-823, Russia	0,10–0,18	1,15–1,3	0,5–0,8	11,3	0,5–0,85	0,6–0,82	0,32	0,5–0,8	0,26–0,4	0,006	Ti 0,004
EP-852, Russia	0,13	1,19	0,31	13,15	0,27	1,69	–		–	–	P=0,017
EP-900, Russia	0,14–0,18	1,0–1,3	0,6–0,9	10,0–12,0	0,5–0,8	0,6–09	0,2–0,4	0,5–8	0,2–0,4	0,006	N-0,06–0,10
MA957, France	0,01	0,05	0,050,11	14	0,13	0,3					Ti-1,05; Y_2O_3.0,25; O-0,015–0,22;P<0,005
1DK, Japan	0,045	0,019	0,013	12,87	0,16	–		2,81			P<0,005, S-0,001Ti-0,52 N-0,015 O-0,186 Y_2O_3-0,34

8 Dispersion-hardened Steels

Dispersion hardened ferritic steels are now ones of the more prospective materials for FA clad of fast reactors and first wall of fusion reactors (FR) and also as structural material of reactors of next generation due to their excellent resistance to swelling. The required increase of high-temperature strength is attained by the proper dispersion hardening of fine particles of titanium (TiO2) and/or yttrium (Y2O3). The unique combination of fine grains, of high density of dislocations and nanoclusters containing atoms of solution Y-O and Y-O-Ti supposes the production of materials with unique properties [28, 29].

The more important factor influencing on the properties of dispersion hardened steels is the provision of the deformation dissolution in steel matrix of sufficiently "coarse" oxides of yttrium with dimension 40–100 nm and their subsequent precipitation as effectively hardening nano oxides.

The necessity of the investigation of material properties under such severe operational conditions is caused by the last observations that make doubtful the serviceability of ferritic-martensitic steels for their use at high temperatures and high rates of gases generation [2]. Therefore it is necessary to analyze the evolution of microstructure and modification of composition for better understanding not only the nature of low swelling but also the cause of the embrittlement.

9 Electronuclear Systems

In energetic nuclear technologies of the next generation (4 Generation) it is supposed to use the accelerators of charged particles (of electrons or of protons) for energies from 100 to 1000 MeV for generation of neutrons in electronuclear systems (Fig. 13). The energy spectrum of emitted neutrons reaches the energies of 100 and more MeV and cross-sections of nuclear reactions of transmutation (n, 2n), (n,p) and (n,α) increase and due to this the rate of transmutation variation of element composition of steels increases also as the level of transmutation generation of gaseous transmutants.

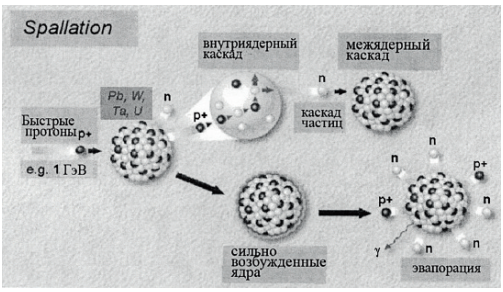

Fig. 13 Processes of "spallation"-ADS (2009–2012) [31]

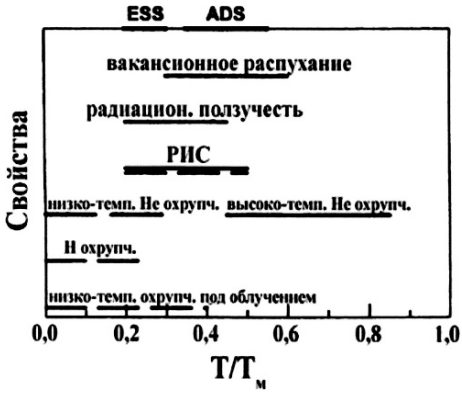

Fig. 14 Homological temperatures of the manifestation of physical-mechanical properties of austenitic steels (solid line) and of martensitic steels (dotted line)

Table 5 Parameters of electronuclear systems (ENS)

Energy of protons	350 MeV–3 GeV
Current of protons	1 mA–5mA
Rate of H generation	3500–4400 appm/year
Rate of He geberation	950–3500 appm /year
Rate dose	4,6–40 dpa/year

Damaging of structural materials of electronuclear systems occurs as the result of irradiation by high energy protons and neutrons and is aggravated by the effect of liquid metals and possibly of other coolants. This damage is similar to the damage in (t, d) fusion reactors but the transmutation effects (production of H and He) are manifested strongly. Just the high rate of light elements production will limit the lifetime of structural materials in the region of the target. It is revealed that austenitic steels have higher resistance to radiation effects at low temperature and the martensitic steels – at high temperatures of irradiation. (Fig. 14) [32].

Neutron sources on the base of the reaction of splitting ("spallation") excellently simulate the conditions of the first wall of fusion reactor and the source on the base of reaction Li(d, n) completely simulate the source with energy of neutrons 14 MeV (RTNS).

In reactions with multiple release of secondary particles: of protons (atoms of H), α-particles (atoms of He), of neutrons (solid transmutant).

1. Reactions of transmutation in fission nuclear reactors lead to the formation of more heavy elements:

$$\mathrm{Fe} \rightarrow \underline{\mathrm{Ni} \rightarrow \mathrm{Cu} \rightarrow \mathrm{Zn}} \rightarrow \ldots \tag{1}$$

2. Reactions of transmutation in fusion reactors and spallation form lighter elements

$$\mathrm{V} \leftarrow \mathrm{Cr} \leftarrow \mathrm{Mn} \leftarrow \mathrm{Fe} \leftarrow \mathrm{Co} \overset{n,2n}{\longleftarrow} \mathrm{Ni} \tag{2}$$

Materials for near-critical assemblies driven by accelerator (ADS).

Data presented in the Table 5 show that for given type of facility the behavior of structure materials will be determined by the influence of high doses of irradiation,

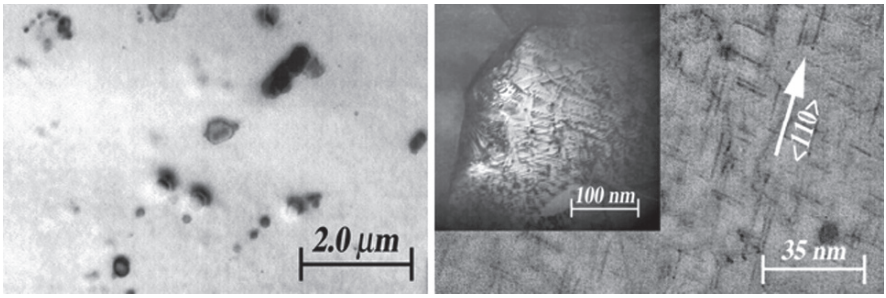

Fig. 15 Phase transformation under "spallation" irradiation in alloy Al 5052 (Al-3% Mg (a) unirradiated; (b) irradiated LASREF (D = 0,35 dpa, $T_{ir.} = 55°C$))

by generation of high quantities of helium and hydrogen in the result of transmutation reactions.

Now the investigation of physical phenomena responsible for the degradation of materials under "spallation" irradiation is focused on following phenomena:

1. Trigger swelling
2. Evolution of precipitates
3. Loss of ductility, embrittlement, failure
4. Influence of defect clusters on the strength and hardening
5. Influence of gases (H, He, He + H)

Production of gaseous and solid products of transmutation leads to the loss of ductility.

On Fig. 15 the example of second phase precipitation in the result of transmutation reactions under irradiation in LASREF to doses 0, 35 dpa is shown.

$$^{27}\mathrm{Al}(n,\gamma) \rightarrow ^{28}\mathrm{Al} \tag{3}$$

$$\mathrm{Al} \rightarrow ^{28}\mathrm{Si} + \beta, \quad 2\mathrm{Mg} + \mathrm{Si} \rightarrow \mathrm{Mg_2Si} \tag{4}$$

10 Conclusion

In spite of considerable efforts of researchers in all countries developing the nuclear power the economically necessary levels of operation of existing nuclear reactors are not reached so far.

It is determined in considerable degree by the insufficient radiation resistance of the main structural materials of existing nuclear facilities – of different classes of stainless steels and of zirconium alloys.

Challenges of the 21st century for radiation material science are the guaranteeing of the problems of security and economy of NPP.

The main of them are:

1. Substantiation of overhaul period prolongation for operating thermal reactors, that is, study of the influence of the dose, of rate dose, of processes of segregation, special features of material (composition, thermal treatment, structure) on microstructure evolution in structural materials during operational period of reactor.
2. Development of radiation-resistant materials for reactors of new generations. Study of the influence on the material physical – mechanical properties of the dose rate, of stresses, of segregation processes (fast reactors); influence of the dose, of gas concentration (He, H), of gaseous and solid transmutants (fusion reactors, electronuclear systems ("spallation").
3. Solution of ecological problems of nuclear power (development of low-activated materials, solution of the problems of nuclear fuel wastes (NFW).

The presented aims may be realized only on the base of modern understanding of the role of microstructural processes responsible for the evolution of structural state under irradiation and for degradation of initial physical-mechanical properties.

References

1. National security and defense, O. Rosumkov Ukrainian center of economic and political studies, No. 6, p. 3, Kiev, 2005 (in Ukrainian).
2. V.N. Voyevodin and I.M. Neklyudov, Evolution of the structure-phase state and radiation stability of the construction materials (Naukova Dumka, Kiev, 2006), p. 387 (in Russian).
3. Torrens I.M. Robinson M.I. and Norgett M. A proposal method of calculation displacement dose rate, Nuclear Engineering and design, **33** (1978) 50–54.
4. A.N. Orlov and Yu. V. Trushin, Energy of the point-like defects in metals (Energoatomizdat, Moscow, 1983), p. 80 (in Russian).
5. D.T. Heald and M.V. Speight, Point defect behavior in irradiated materials, Acta Metall, **23** (1975) 1389–1399.
6. P. Ehrhart, K.N. Robrock and H.R. Schober, Basic defects in metals, Physics of Radiation Effects in Crystals. Eds. Johnson R.A., Orlov A.N. (Elsevier Science Publishers, Amsterdam, 1986), pp. 3–106.
7. V. Naundorf, Diffusion in metals and alloys under irradiation, International Journal of Modern Physics B **6**, No. 18 (1992) 2925–2986.
8. T.R. Waite, General theory of bimolecular reaction rates in solids and liquids, J. Chem. Phys. **28**, No. 1 (1958) 103–106.
9. I.M. Neklyudov and V.N. Voyevodin, Features of structure-phase transformations and segregation processes under irradiation of austenitic and ferritic-martensitic steels, JNM **212–215** (1994) 39– 44.
10. J.M. Perks and S.M. Murphy, Modeling the major element radiation- induced segregation in concentrated Fe-Cr-Ni alloys, Proc. of the Conference "Materials for nuclear reactor core applications", British Nuclear Energy Society (BNES), London. v. 1 (1988) pp. 165–170.
11. L.E. Ren and P.R. Okamoto, Non-equilibrium segregation in irradiated alloys, In: Phase transformations under irradiation, Edited by F. Nolfy (Mettalurgia, Chelabinsk, 1990), p. 468 (in Russian).

12. B.A. Shilyaev, I.M. Neklyudov, L.S. Ozhigov et al., Modelling processes of nuclear transmutation of construction materials under the irradiation by protons with energy up to 100 MeV, VANT, Ser. FRP and PM **2(53)** (1990), 15.
13. C. English, J. Hyde and S. Ortner, Microstructural development in RPV steels, Fracture, Plastic Flow and Structural Integrity (2000), pp. 103–127.
14. L. Debarberis, B. Acosta, F. Sevini et. al. Role of nickel in semi-mechanistic analytical model for radiation embrittlement of model alloys, JNM **336** (2005) 210–216.
15. K. Fujii and K. Fukuya, Characterization of defect clusters in ion-irradiatedA533B steel, Institute of Nuclear. Safety System Inc., 64 Sata, Mihama-cho, Mikata-gun, Fukui 919–1205, Japan.
16. B.L. Eyre, D.M. Maher, and R.C. Perrin, Phys J. F: Metal Phys. **7**, No. 77 (1999) 1371.
17. A. Ulbricht, J. Bohmert, and H.-W. Viehrig, Microstructural and mechanical characterization of radiation effects in model reactor pressure vessel steels, Journal of ASTM International, November/ December 2005, v. 2–10, pp. 151–164.
18. E.A. Kuleshova, B.A. Gurovich, Ya.I Shtrombakh et al. Comparision of microstructural features of radiation embrittlement of VVER – 440 and VVER – 1000 reactor pressure vessel steels, JNM **300** (2002) 127–140.
19. Yu.F. Balandin, I.V. Gorynin, Yu.I. Zvezdin, and V.G. Mardkov, Construction materials for APS (Energoizdat, Moscow, 1984), p. 236.
20. A.V. Nikulina, V.A. Markelov, and V.N Voyevodin, Irradiation induced microstructural changes in Zr–Sn–Nb–Fe alloy, JNM **238** (1996) 123–127.
21. V.S. Neustroev, V.N. Golovanov, V.K. Shamardin, et al., Radiation phenomena in X18H10T steel irradiated in various reactors at conditions close to those in the operaton of VKU VVER, Collection of talks at the 6-th Russion conference on reactor material science, Dimitrovgrad, v. 3, part I, pp. 3–23 (in Russian).
22. V.S. Neustroev and V.K. Shamardin, Russian viewpoint on swelling in VVERs // 1st International Workshop on Voids in In-Core Structural Materials in LWR, December 2003, Kyoto, Japan. – issued in CD format, no page numbers.
23. F.A. Garner, Void swelling of austenitic internal components of PWRs and VVERS, and its possible impact on plant life extension, 5th International Conference on Nuclear and Radiation Physics, September 2005, Almaty, Kazakhstan, issued in CD format, no page numbers.
24. S.A. Golovinksi and A.V. Boitsov, Intl. Conf. "Progress in atomic energy based on fast neutron with a closed fuel cycle. Strategy and perspectives of the international collaboration", Moscow, Nov. 2005, available on CD.
25. F.A. Garner, Irradiation Performance of Cladding and Structural Steels in the Liquid Metal Reactors, in Material Science and Technology. Eds: R.W. Cahn, P. Haasen and E.J. Kramer (VCH Weinheim), Nuclear Materials **10A** (1994), 12–14.
26. V. Voyevodin, Research work report, Japan Nuclear Cycle Development Institute, TN 9400, O-arai, 2001, pp. 12–16.
27. K.A. Lanskaya, High-chromic heat-proof steels (Metallurgia, Moscow, 1976), p. 216.
28. M. Klimiankou, R. Lindau and A. Moslang, TEM characterization of structure and composition of nanosized ODS particles in reduced activation ferritic-martensitic steels, JNM **329–333** (2004) 347–351.
29. M.K. Miller, D.T. Hoelzer, E.A. Kenik, and K.F. Russell, Nanometer scale precipitation in ferritic MA/ODS alloy MA 957, JNM **329–333** (2004) 338–341.
30. S. Ukai, N. Akasaka and K. Hattori, The effects of phase stability on void swelling in P, Ti-modified 316 stainless steels during neutron irradiation, Proc. of 18-th Intern. Symp. "Effects of Radiation on Materials", ASTM STP 1325 (1998) 808–821.
31. P. Vladimirov and A. Moslang, Irradiation conditions of ADS beam window, Seventh International Workshop on Spallation Materials Technology, May 29 – June 3, 2005, Thun, Switzerland, issued in CD format, no page numbers.
32. P. Yung. Radiation effects in structural materials of spallation targets, JNM **301** (2002) 15–22.

Symbiotic Nuclear–Coal Systems for Production of Liquid Fuels

S. Taczanowski

Abstract The notion of safety is not confined to the technological or non-proliferation aspects. It covers also the elements of energy policy: irrational reactions of societies, emotions, egoistic interests of more or less powerful pressure of economical and external political factors. One should be conscious that the country's privilege of being equipped by the Nature with rich resources of oil or gas is not solely economical, but even more a political one. Simultaneously, the gradual depletion of world hydrocarbons that draws behind irrevocable price increase has to be expected within the time scale of exploitation of power plants (now amounted to $\sim$60 years). Therefore consequences of energy policy last much longer than the perspectives the political or economical decision makers are planning and acting within and the public is expecting successes and finally evaluating them. The world oil and gas resources are geopolitically very non-uniformly distributed, in contrast to coal and uranium. Since the level of energy self-sufficiency of the EU is highest for coal, the old idea of synfuels production from coal is recalled. Yet, in view of limits to the CO_2 emissions in the EU another method has to be used here than the conventional coal liquefaction just applied in China. Simultaneously, an interesting evolution of energy prices was be observed, namely an increase in that of motor fuels in contrast to that of electricity remaining well stable. This fact suggests that the use of electricity (mainly the off-peak load), generated without emissions of CO_2 for production of liquid fuels can prove reasonable. Thus, the essence of the presented idea of coal-nuclear symbiosis lies in the supply of energy in the form of H_2, necessary for this process, from a nuclear reactor. Particularly, in the present option H_2 is obtained by electrolytic water splitting supplying also O_2 as a precious by-product in well mature and commercially available already since decades, Light Water Reactors (LWRs). The direct coal hydrogenation (Bergius method) has been proposed as the optimum process for liquid fuels production, as distinct by the

S. Taczanowski
Faculty of Physics and Applied Computer Science, AGH University of Science and Technology, 30 059 Cracow, Poland,
e-mail: Taczanowski@novell.ftj.agh.edu.pl

V. Begun et al. (eds.), *Progress in High-Energy Physics and Nuclear Safety*,

best hydrogen economy, thus reducing the consumption of need nuclear energy. The present concept allows for simultaneous achievement of a number of aims: production of motor fuels without CO_2 emissions (thus without carbon tax) based upon domestic energy carriers – coals, supply of the electricity produced in the nuclear power plant to the national grid to cover the peak demand. Such concept broadens the palette of liquid fuels supply, thus heightens energy safety of the country or e.g. whole of the EU. In an emergency case (for instance – disturbances of gas deliveries) the supply of produced H_2 directly to the gas grid is also not excluded too. The performed preliminary cost evaluation indicates that the coal–nuclear symbiont can be well economic. Finally, the most radical option of coal-nuclear alliance is mentioned – the production of liquid fuels in the Fischer–Tropsch process from CO_2 as a raw material sequestered from a coal power plant. The latter would use the oxy-combustion technique profiting on the O_2 obtained earlier together with H_2 what would facilitate the sequestration of CO_2 at the plant. Unfortunately, this variant requires for reduction of CO_2 to C much more hydrogen, achievable effectively in High Temperature Reactors commercially still unavailable. But on the basis of coal alone great resources – natural, technological and human of the coal sector can be best utilized too. Summarizing: the coal-nuclear synergy is the optimum far-sighted concept of safe development of the EU energy and fuels sector.

Keywords: Energy safety, nuclear energy, nuclear-coal systems, motor fuels, energy prices

1 Introduction

The notion of safety is well ample, thus in the present paper we will not confine to its narrow understanding confined to the technological or non-proliferation oriented aspects of nuclear safety. For instance, to those factors that need to be taken into consideration is among others the energy policy, the making of which, is not at all that easy task, since usually it has to be a compromise between a number rather antagonistic factors [1]. A compromise that is a resultant of also rather negative elements: irrational reactions of societies, emotions, egoistic interests of more or less powerful economical lobbies and external political pressure. The attraction of fast profits and the immediate social and individual needs shorten the horizons taken into consideration for economical or political decision-making. The situation is aggravated not only because of the objective complexity and importance of this issue but also by the fact that the decision makers seem to demonstrate either wishful thinking or unsatisfactory knowledge of the subject.

In addition to this, one should remember that the country's privilege of being equipped by the Nature with rich resources of oil or gas is not solely economical, but first of all, a political one. Obviously this alternative may designate politically very different situations. The worse – the blackmail with use of energy as an effective political weapon, unfortunately, not long ago – was already applied.

Simultaneously, it is hard to expect that the relying of the world on hydrocarbons can weaken in the nearer future. But meanwhile, within the time scale of normal exploitation of power plants (i.e. now amounted to ∼60 years), the gradual depletion of hydrocarbons at global scale (drawing behind irrevocable price increase) – is unavoidable. Yet, the question is if decision makers care about something that has to happen after several 10 years. It is obvious that energy policy has much longer lasting consequences than the perspectives politicians are planning and acting within or their electorate is expecting successes and finally evaluating them. Also a global scale business is not audited only after decades but much earlier. Therefore, it seems less probable that such a long perspective will be in fact considered by real political or economical decision-makers. It is true that we have been accustomed for decades to hear that the world resources of oil would be exhausted within about 30 years and we stopped to believe in such warnings already long ago, since these decades were passing by and the perspective of exhaustion has remained that remote, or even more, as before [1]. Nevertheless, independently of our wish /or rather against it/ the day, when this gloomy forecast proved true, is close. The world has climbed the peak of the Hubbert curve. Happily one cannot say the same of other earth resources, namely, coal or uranium.

However, with the nuclear energy there are also linked some considerable risks. But rather not those ones associated with radioactivity or nuclear weapons. As already has happened several times, under pressure of negative social attitudes, complete nuclear power plants had been prevented from operation while even already operating ones had been closed. All that deprived the invested capital of any value. Thus a danger of serious financial losses is real in result of erroneous social evaluation of anthropogenic hazards.

Therefore, the investment in the enlightenment of society can prove most cost-effective action by softening the consequences of the energy crisis and thus heightening the safety of whole economy. In the long run, but not exclusively, a strategy concentrated on such development lies in the very interest of any far-conceived energy-related initiative.

The resolute initiative regarding rebirth of nuclear energy may bring its promoter great advantages on the future market. However, the maturing of a new, advanced technology is a long process that hardly can be accelerated whatever expenses would be born. Therefore, the preparations to these events should start early enough i.e. already now. Just the scientists' duty is to prepare a strategy to soften the difficulties that seem to happen.

2 Energy safety

The intention of this paper lies in the consideration of the comprehensive term of energy safety applied principally to the EU with special emphasis on the new member countries, but not being confined to them. To the contrary, this is addressed also to all European countries relying on imported liquid fuels as well as to those outside of

Europe, particularly if distinct with coal resources. The term safety does not regard the safe nuclear energy alone, but much more the security of fuel and electricity supply. Since the latter energy is the most noble, we start the discussion from the respective selected problems of safety.

2.1 Electric power safety

In the modern world the most universal and flexible form of final energy – electricity seems the most important. Its lack even during few seconds may draw behind in irreparable damage and losses. In addition to this, it is highly improbable that the demand for electricity might decrease in the future. And not due to the fast economic growth of countries of the South. In the North also further expansion of various appliances in our households is easy to forecast. In many of them – computers, faxes, printers, modems, (de)humidifiers, air conditioners, heat pumps, etc. are still lacking. Thus one should anticipate even in the industrialized countries, not mentioning the less developed ones, a further increase in the electricity demand [2].

As regards new member countries of the EU one can base upon example of e.g. Poland. Seeing the present underutilization of electricity in there (under 50% of mean EU consumption per cap. in general [3], with the mere 25% in households) one can observe an increase in its demand already at present. The deficit of electric energy may appear first during the peak load hours in cold winter time. But the frequently met suggestion of the utilization of gas for meeting the power peak demands give rise to serious doubts. However, the increase in the gas share for electricity generation is dissuaded for several reasons, at least in all regions characterized by demand for electric energy culminating in dark and cold winter evenings. The main problem is the difficulty in fulfilling this task due to perfect seasonal (winter) and daily (afternoon/evening) synchronization of demand peaks for both electricity and heating, with the latter mostly based on gas. Thus, one should look for other solutions. How to apply nuclear energy for meeting the electricity peak loads is described farther in this paper.

2.2 Fuel safety

In spite of the fact that shortages of hydrocarbon fuels do not draw behind that prompt damage like black outs due to lacking electricity, the EU security and other countries in this aspect is not unshakable. This situation can be illustrated best with independence indexes (the fraction of domestic supply of fuels) that show the scale of dependence from import of organic fuels (Table 1. [4]).

Such a state of very strong Europe's dependence on imported hydrocarbons is highly unsatisfactory. In the Table 1 one can see that the dependence on import is highest for liquid fuels, what can not be a surprise. At the same time the highest level

Table 1 Examples of fuel self-sufficiency in Europe

Energy carrier	EU			UA	PL
	Domestic production	Net import		Independence index	
	[M toe]			[%]	
Oil & derivatives	127	589	17.8	11	7
Gas	188	257	42.3	26	∼30
Coal hard & brown	195	145	57.4	100	∼100

of fuel self-sufficiency is linked to coal in the EU as well as in Ukraine and Poland in particular. This situation seems to suggest openly utilisation of this European domestic resource i.e. – coal for liquid fuels production. Yet the question how to do it remains open. In this paper an answer is just sought.

2.3 Nuclear energy safety

Unfortunately, nuclear energy still is raising very strong emotions in the most of the world societies thus selected problems of widely understood nuclear safety must not be neglected. Still frequent negative attitudes regarding nuclear energy are objective element that must be considered while shaping the energy policy. Mostly, since these are the main source of investment risk, increase the cost of bank loans and are even capable to prevent any engagement of capital i.e. the whole undertaking.

During ca. 20 years after Chornobyl disaster in 1986 one could hardly hear any positive opinion about nuclear energy. Recently, these attitudes evolved in favour of nuclear energy, particularly among young generation and are manifested still more often with the level of education.

Against common feelings a very high level of safety nuclear power must emphasized. The maturity of present Light Water Reactor (LWR) technology and exceptional achievement of ca. 10,000 reactor-years of operation without any serious accident with fatalities, convincingly prove the reliability of LWR.

Nevertheless no debate on the nuclear safety can neglect the problems of spent fuel – in view of its very high radiotoxicity. On the other hand it should be kept in mind that whole nuclear power of the world releases ca. mere 10,000 t/year (i.e. ∼30 ton from one 1GWe plant). That value compared with the emission of 11,000 million tons CO_2 from organic fuelled power plants proves to be a quantity million times lesser.

In general there are two ways of treatment of the spent fuel after an interim storage:

1. A reprocessing – for extraction of uranium and plutonium for its reuse in the MOX type fuel or –
2. Qualification for final disposal as a high level waste in selected stable geological formations.

The latter solution is unquestionably safe though not quite optimum one since enormous amount of energy is uselessly buried. Thus in spite of the advantage of safety, already now in some countries (e.g. France) up to 1/3 of spent nuclear fuel is recycled. Moreover, in not a very distant future realization of the fully closed cycle can be expected in transmutation processes carried out in subcritical systems thus safer than critical ones and intensively developed in recent two decades. In that way not sole additional burnup of the nuclear fuel can be achieved, but also a reduction of the amount of radiotoxic waste and heat generation that would facilitate its disposal.

2.3.1 Economical and political safety of nuclear energy

First, it is of interest to confront the "longevity" of world main energy resources (Table 2).

For comparison with hydrocarbons let us remind also the distribution of uranium world deposits: Australia, Canada, Kazakhstan, RSA, Namibia, Brazil, Niger, Russian Federation, USA etc. This list demonstrates that uranium resources are geopolitically distributed in the world in a much more uniform manner than oil and gas. Next, the cost of nuclear generated electricity is to be discussed.

Due to relatively cheap nuclear fuel and operation & maintenance costs of nuclear power plants the electricity price depends mostly on its front-end costs. These are caused by high construction and equipment expenses thus also depend on cost of the bank loan. The preponderance of capital costs, is rarely perceived otherwise than as a disadvantage, in spite of the fact that just fixed costs when more important make the respective forecasts and planning much more credible.

Besides the capital costs depend on a number of factors, ranging for example from US$1,000/kWe in the Czech Republic up to $2,500/kWe in Japan., at French estimations of Direction Générale de l'Énergie et des Matières Premières (DGEMP) equal to 1,280 /kWe [6]. Such data demonstrate the importance of the local labour costs.

The question of fuel costs draws attention to its raw material i.e. uranium. It is true that the scale and rapidity of its price fluctuations are striking. For instance the spot prices rose from US$36 per pound of U_3O_8 in the year 2000 upto US$140 in July 2007, then dropped to US$90 in January 2008 and further in November 2008 down to US$ 0–40? [7]. Fortunately, this volatility is not a problem, since the share of uranium cost in electricity price from nuclear power is mere several percent.

Table 2 Lifetime of the world energy reserves

Energy carrier	Oil	Gas	Coal	Uranium	
				Open [5] cycle	Closed cycle
World reserves lifetime [years]	40	60	200	85	>5000

But another question may appear, namely, how fast nuclear energy can significantly contribute into the energy supply of a country i.e. to achieve not negligible heightening of its energy safety. Certainly the necessary rate of deployment of nuclear power would require a great organizational effort and not a lesser engagement of capital. Though not easy, it is not impossible. It should be reminded here, that in the UK 21 power reactors were launched in the years 1963–1972 i.e. over 2 per year, while in France – 50 GWe in 45 units in 1978–1989, i.e. yearly over 4GWe [8]! After 30–50 additional years of nuclear experience – in the coming decade, it should be possible still more, though – provided the decision makers display a sufficient determination.

3 Selected preconditionings

There are at least several ways to energy safety enhancement. In order to select one considered as the best, one needs first to have a sufficient pertinent knowledge. Some arguments in favour of selected solutions can be found on the basis of pertinent data. Very informative is to see the observation of the prices of basic energy carriers in the USA during last 15 years (Fig. 1.).

A glance at Fig. 1 allows for some observations. Namely: the hydrocarbon prices during last 10 years increased enormously, whereas the prices of electricity remained nearly constant or even slightly lowered. Obviously, the price trajectories (unavailable to the author) in other countries may have other shapes; nevertheless the differences should not be very significant. Even present drop (November 2008) of oil prices does not change principally the general observation that can be drawn from this picture: the relation between the prices of liquid fuels and of electricity has radically changed towards much higher ones of the former. This, in turn, gives rise to the question, whether the use of electricity for production of motor fuels

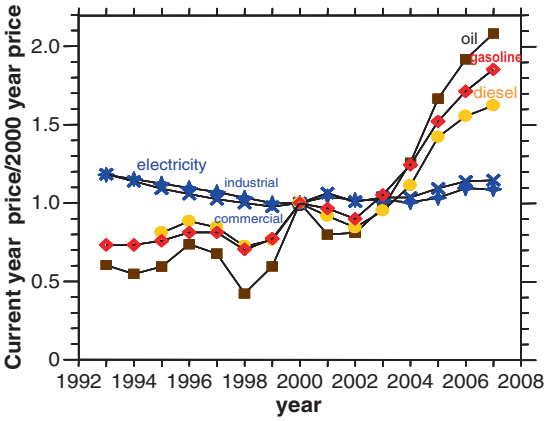

Fig. 1 Evolution of prices of energy carriers in the USA (2000 prices taken as unit)

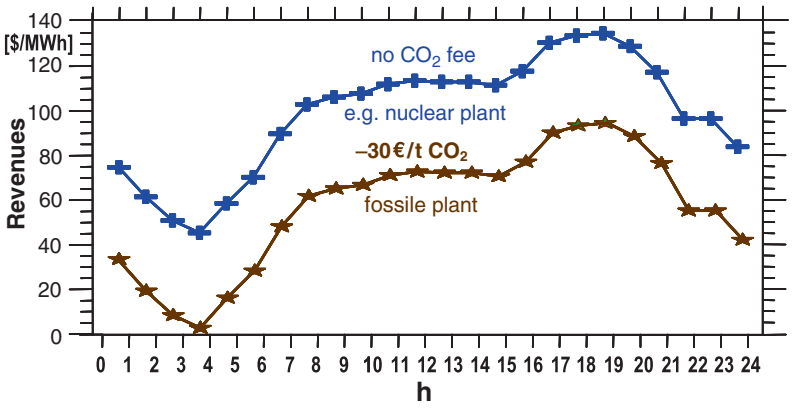

Fig. 2 Revenue from the electricity sale vs. time with deduction of the forecasted CO_2 fee

can prove reasonable i.e. economically justified. In support of this thesis stands an important difference between the character of profits that can one obtain from the sale of electricity and of motor fuels. The well known fluctuations of fuel prices in the scale of years or decades notwithstanding – the electricity price is subject to regular periodicities. The most distinct is the 24 hour one (see Fig. 2, based upon the Polish stock market [9]), the second one corresponds to the weekly ordering of human activity. There can be noticed also seasonal regularities, but usually these are of lesser importance). In contrast with these statements, within the above time scale, the motor fuel prices remain constant.

On the basis of Fig. 2 one can state that the daily distribution of electricity price is highly differentiated. In particular one can conclude that the sales at night hours are hardly profitable. It is not that easy to store electricity produced during "valley" hours 0–6 in order to sell it during evening peak hours. Classic approach would suggest using a hydro storage i.e. to pump water up at the valley and recover the stored energy at the peak load time. Here, instead of that – the production of motor fuels is recommended. The time sharing of the plant performance between the two products – fuels and electricity will depend on the relation of respective prices. Though rather the power plants based upon the fuels containing carbon are in trouble due to the CO_2 emissions, the above suggestion is addressed to nuclear plants. First of all due to providing for them the possibility of satisfying the peak load demand. This significantly broadens the tender of power of nuclear plant traditionally considered as being reduced to cover solely the base load demand.

4 Nuclear – coal symbiosis

The suggested above production of hydrogen from nuclear energy need not necessarily signify any connection with coal. One can easily imagine a confinement to the hydrogen. Anyway it may prove to be the ultimate target in the further future.

However, the lack of adequate hydrogen market in the nearer one drawing behind its relatively low prices, make the sole production of H_2 simply unprofitable. In the present world market no one offers for hydrogen alone such price as that one when it is in the form gasoline or diesel oil. Just these prove valuable enough that to assure the economy of the whole undertaking. Thus the hydrogen should be further processed for production of hydrocarbons first of all liquid since these are most expensive.

4.1 Coal liquefaction

First, it should be reminded that combustion of coal, depending on sulphur content in coal, produces SO_2, the source of acid rain. Coal also contains many highly toxic trace elements, e.g. As and Hg, as well as radioactive nuclides born in the natural decay chains of U and Th. But the coal liquefaction processes allow for removal of practically all toxic components from the fuels produced of coal, thus making such clean coal technology truly clean. Coal can be converted into liquid fuels like gasoline or diesel by several different processes. The idea of synfuels production from coal is not at all new – it was used on industrial scale first of all in Nazi Germany during World War II but in the UK as well. We concentrate on the direct synthesis of liquid hydrocarbons since this process is distinct by the best hydrogen economy. The method in question (named after its inventor Bergius process) consists in liquefaction by hydrogenation.

Recently the most striking development of coal conversion into liquid fuels is observed in China, where the most advanced installation of direct coal liquefaction Shenhua CTL Plant (Coal-To-Liquid) in China has been launched this year. The available data are as follows [10]:

- Net investment \$1500 million
- Synfuel composition: diesel oil $\sim$53%, gasoline $\sim$35%, LPG $\sim$12%
- CO_2 emission: 3.6 million tons/year, in that 3.1 million tons for H_2 production
- Profitability threshold for oil price: \$35 $\div$ 40 billion
- Synfuel yield: \$24,000 BPD (barrels per day) = 3,816 m^3/day = ca. 3340 t/day = ca.1.2 million tons/year
- 1998 – award of governmental subvention; 2002 – completion of feasibility study, 2008 – of construction

The above informations are very encouraging with one exception: the emission of CO_2; particularly while having in mind the obligatory limitations to CO_2 emissions in the EU. This restriction practically excludes classic methods of coal liquefaction. In this process, the burning of important coal quantities is needed for necessary investment of energy in the fuels just produced. As a result the classic methods are inseparable from release of large quantities of CO_2, that proves rather be insurmountable hindrance for their wider deployment.

Thus the unique energy for H_2 production seems nuclear energy.

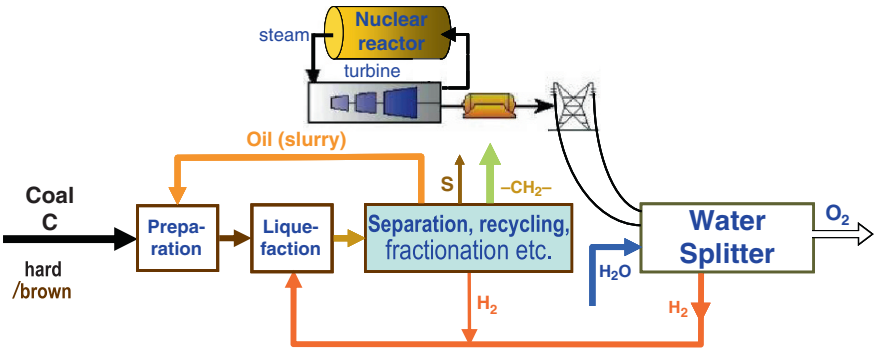

Fig. 3 Simplified scheme of the Nuclear sustained Direct Coal Liquefaction (NDCL) system

4.2 Nuclear sustained coal liquefaction

There is a number of ways and processes leading to this aim and all of them have one common element, namely, the role of nuclear energy laying in the production of H_2 by water splitting that supplies also O_2 as a precious by-product. In the present option H_2 is obtained by electrolytic water splitting supported by well mature and commercially available already since decades Light Water Reactors (LWRs). A scheme of such symbiotic system [11] is shown in Fig. 3.

In this system recycling is of importance. Hydrogen is supplied to the proper DCL plant, recycled with the products of liquefaction and then all further transferred to the proper liquid fuel factory.

The choice of just the option of electrolytic water splitting as source of indispensable H_2 has resulted from the availability of LWR right now. Besides, this approach may be recognised as the first step towards the most advanced nuclear–coal synergy i.e. the use of captured CO_2 as the raw material for liquid fuels production [12, 13].

Such idea of double use of coal enables oxy-combustion technique based on the O_2 obtained earlier together with H_2, thus facilitating the sequestration of CO_2 at the power plant. Next, from this raw material and in the reverse water gas shift reaction syngas would be obtained and the liquid fuels produced in the Fischer–Tropsch process. However, hydrogen demand must be then greater, since the reduction of CO_2 to C requires large additional energy. Thus, a nuclear reactor with proportionally higher power is needed. Sufficient yield of H_2 seems to be efficiently assured only with a High Temperature Reactor that is not yet commercially available.

4.2.1 Economical aspects

Any new technology cannot be exempted from to obligation to be economical without special privileges. Therefore an estimation of economy of Nuclear sustained Direct Coal Liquefaction (NDCL) may be of justified interest. At the same time it has to be emphasised that at present volatility of both – oil prices and currencies

Table 3 Performance of nuclear sustained production of synfuels from coal

Principal investments [M $]		Annual repayments [M $]					Annual production	Product unit cost	Annual income
		Investment	O&M	Fuel	Sum	Sum			
Nuclear Power Plant	3500	450	90	U 70	610	1200	0 [TWh]	– [$/MWh]	–
Fuel plant	2200	290	180	Coal 120	590		1.1 [Mt]	∼1.2 [$/kg]	∼1300 [M$]

(exchange rates) the reliability of the performed evaluation is obviously very limited. On the other hand any analysis concerning the time of realisation of present ideas (i.e. projected now for nearer or farther future) in no circumstances can be regarded as unquestionable.

Anyhow, providing some notion of economical side of nuclear sustained production of motor fuels from coal is necessary. The respective analysis is based on the following assumptions:

Technological:	Economical:
Coal liquefaction Method: NDCL,	Interest rate 8%,
H_2 production in electrolytic water splitting,	Repayment time 20 years,
Nuclear energy: 1 GWe Light water reactor,	Loan repayment start: 5 years after investing start,
	Uranium price US$150/kg,
	Product unit net average price US$1.3/kg.

Thus, based upon the prices from August/September 2008 and above assumptions with use of standard loan conditions [14] the performance of the enterprise has been evaluated (Table 3). At that time the prices of motor fuels were so high that no sales of electricity would have been justified.

In the above calculations some not negligible potential revenues have been omitted.

Additional income sources:		
Oxygen	1 million tons	unit price $150/ton → annual income = $150 million
LPG	0.1 million tons	unit price $700/ton → annual income = $70 million
5% w. H_2	in coal	30% reduction in H_2 use → proportional increase in the yield of fuel
Covering peak load		income depending on respective electricity price

All the year 2008 is characterised by exceptional economical instabilities. It is true that present shocking phenomena are very unpleasant; they delay the world economic growth and have undermined the credibility of banking systems in most of the world market. Nevertheless, the author's is deeply convinced that all these effects still are not able to demolish the world economy as a whole. From the present shake the world surely recovers at the time the above concept is coming true. Therefore, the validity of the estimations inserted here may be considered as preserved.

It is also worth emphasising the scale of the market for the present Clean Coal Technology that in no case is limited to Poland; to the contrary should be recommended to all EU Member States using coal: i.e. also to Germany, United Kingdom, Czech Republic, Spain, Greece etc. Obviously, to all coal rich countries out of EU too: Ukraine, Russia, Turkey, USA, China, India etc.

5 Conclusions

In view of the entire above one can recapitulate the advantages of the nuclear–coal symbiosis for production of motor fuels. In the field of energy safety for many countries it shows the way to energy self-sufficiency. It is achieved thanks to utilisation of coal for this purpose just increasing the diversity of supply of primary energy carriers. The additional objective – heightening of the supply of electricity can be attained due to inherent elasticity of the system. Any time – when needed, the peak power demand can be met by switching the current from the electrolytic water splitter to the grid.

At the same time the use of coal is the answer to societal problems of the coal sector that since decades remains under strong public pressure raised by heavy environmental impact stemming from conventional uses of coal. The proposed modern technology is a good offer directed to existing great human resources and infrastructure of the fuel & mining sector while creating demand for manpower in respective branches and regions.

In connection with the economic side of nuclear–coal symbiosis the discussed enterprise offers realisation of a competitive production of liquid fuels.

Finally, the environmental questions have to be addressed. In short: nuclear sustained production of motor fuels is a rigorously Clean option of Clean Coal Technology with zero emission. And last but not least, an appeal to world coal community: Nuclear energy proves not to be a competitor of Coal but its ally offering new areas to be taken by coal sector thus helping to solve its problems. Summarizing:

The coal–nuclear synergy is the optimum far-sighted concept of development of the energy sector.

References

1. Taczanowski, S. and Pohorecki, W.: Viewpoints on Energy Policy of a Sceptical Observer. Archiwum Energetyki. **1-2**, 3–20 (1998)
2. Taczanowski, S.: Evaluation of accelerator-driven subcritical systems for transmutations of nuclear waste. Int. J. of Energy Research. **24**, 935–951 (2000)
3. http://www.europa.eu.int/comm/energy_transport/etif/index.html
4. http://www.maygerconsult.com
5. http://www.iaea.org/cgi-bin/db.page.pl/pris.main.htm
   NewsCenter/News/2006/uranium_resources.html
6. http://www.icjt.org/npp/index.html
7. http://www.world-nuclear.org
8. http://www.uranium-stocks.net/category/uranium/
9. http://www.polpx.pl
10. Qingyun, Sun: CTL Development in China, Congressional Noontime Briefing. Washington, D.C. April (2008)
11. Taczanowski, S.: Coal-nuclear Symbiosis for Production of Liquid Fuels (in Polish) Polityka Energetyczna. **11**, 1, 499–516 (2008)

12. Bogart, S.L., et al.: Production of Liquid Synthetic Fuels from Carbon, Water, and Nuclear Power ... In: Proc. ICAPP (2006), Reno, NV, June 2006
13. Uhrig R.E., Schultz K.R., Bogart S.L.: Implementing the “Hydrogen Economy” with Synfuels. In: The Bent of Tau Beta Pi, Summer 2007
14. http://www.kellogg.northwestern.edu/faculty/hertzberg/htm/Teaching/Spring%2008

Prospects of Safe Nuclear Energy in Ukraine

V.A. Babenko, L.L. Jenkovszky, and V.N. Pavlovych

Abstract Lessons from the Chernobyl accident are summarized. The evolution of traditional nuclear reactor design, including new projects such as subcritical assemblies controlled by an external beam of particles (neutrons and protons) is presented. The Feoktistov reactor and the possibility of its realization are discussed.

Keywords: Nuclear energy, reactor, subcritical assembly, Chernobyl, Sarkofag, Feoktistov, uranium, neutrons, safety, accident, pollution, fuel

1 The Chernobyl accident and Chernobyl problems

1.1 Chernobyl problems and contaminated territories

Among the Chernobyl problems three main groups can be identified. The first one is connected with radionuclide environment pollution and its impact on the people's health, the flora and fauna of the polluted regions, the peculiarities of agricultural production in polluted territories, etc. The second group of questions is associated directly with the disintegrated 4th unit of the Chernobyl NPP (the Object Shelter (OS) or "Sarkofag"): its technical state, nuclear and radiation safety problems, and the effect of the OS on the environment in the short and long terms. The third group deals with the analysis of what caused the accident (strange as it seems).

Although reasonable enough versions of the accident exist [1], they do not consider (or explain) some details, such as witness information, seismic data, and the results of radio-physicists' studies of radio-waves transmission in atmosphere [2].

V.A. Babenko, L.L. Jenkovszky
Bogolyubov Institute for Theoretical Physics, National Academy of Sciences of Ukraine,
Kiev 143, 03680, Ukraine,
e-mail: pet@bitp.kiev.ua; jenk@bitp.kiev.ua

V.N. Pavlovych
Institute for Nuclear Research, National Academy of Sciences of Ukraine, Kiev, Ukraine,
e-mail: pavlovich@kinr.kiev.ua

V. Begun et al. (eds.), *Progress in High-Energy Physics and Nuclear Safety*,

In this paper we briefly present the first group of questions and more thoroughly examine the OS problems (for more details see also [3]). The solution of the OS problem and its convert into an ecologically secure object constitutes separate scientific, technical, and economic tasks.

The accident discharges from Chernobyl polluted 53,454 km^2 with 2,293 settlements and a population of 2.6 million with radionuclides [4]. The evaluation of the discharged fuel quantity $(3 \pm 1.5)\%$ proposed in 1986 in the report of the Soviet delegation in IAEA [5] caused some doubts, which were concerned mainly with large quantities of radioactive iodine-131 and cesium-137. Generally the discharge could be evaluated along three ways [6]: measuring the quantity and contents of active substances ejected to the environment immediately during the accident; measuring the radionuclides density contamination of the territories both directly adjoining the OS and of remote areas; and a third way connected to the fuel quantity determination directly within the different sections of the OS. Knowing the reactor total core loading, it is possible to evaluate the quantity of the fuel discharged from the difference. The best evaluation of the quantity of fuel discharged will be achieved through a combination of all three methods. The direct measurement of the ejected substance activity and content during the active phase of the accident met substantial methodological difficulties while selecting samples of aerosols above the damaged reactor. These troubles led to essential measurement errors ($\pm 50\%$) in the definition of radioactive aerosols discharged concentration. Thus the first evaluations of radioactivity emitted were rough.

The second way requires estimating the radionuclides pollution of vast territories in different countries and is a very laborious one. Nevertheless, as the remote territories were contaminated mainly by volatile radionuclides, and fine-dispersed fuel particles containing heavy transuranium elements fell out mostly within the 30-km zone around the OS, then sufficiently accurate estimates of fuel discharge could be made through the thorough studies of the alienated zone contamination. Certainly, in addition, the degree of decrease of pollution from transuranium elements as the distance from the discharge source increases has to be evaluated. These estimates were carried out in 1986 and they have constantly been improved [7, 8]. The estimates reconfirm the conclusion of [5] that more than 95% of the disintegrated fuel from the core is concentrated in the OS. The bulk of the fuel discharged (keeping in mind the uranium and transuranium isotopes) is localized in the Chernobyl alienated zone and partly in the zone of unconditionally settling out. The fission products (at this time cesium-137 and strontium-90 are still the most urgent from the point of view of external and internal irradiation of the population) are dispersed across far greater territories, mainly in the Ukraine Poles'e zone.

1.2 The object shelter

One of the basic problems of the disintegrated 4th unit of the Chernobyl NPP significantly defining nuclear and radiation security is the problem of nuclear fuel inside the Object Shelter (OS). To estimate the nuclear and radiation security within

different sections of OS, it is necessary to know the quantity of nuclear fuel in each section, the degree of its initial enrichment and burnup at the moment of accident, physical properties of fuel containing materials (FCM) and the possibility of water entering each section of the OS. It is well known (see, e.g., [9]) that at the moment of the accident some 2,14,600 kg of nuclear fuel resided in the 4th unit of the Chernobyl NPP. The bulk of this fuel (190.2 t) was loaded to the reactor core, part of the spent fuel was placed to the cooling pond (14.8 t), some was on the central hall stand where fresh fuel assemblies were prepared for core loading (5.5 t), and, lastly, some was in the section for fresh fuel preparation (4.1 t). At the moment of accident, there were 1,659 fuel assemblies in the reactor core with 0.1147 t of uranium each. The fresh fuel of the high-power channel type reactor-1000 (HPCT-1000) before the accident contained 2% of uranium-235 (after the accident the fuel enrichment was raised up to 2.5% at all HPCT-1000 reactors to avoid positive values of the steam reactivity factor).

At the moment of the accident the major part of fuel assemblies were the first loading assemblies, with a burnup within 11–15 MW·day/kgU. However, the fresh fuel was also loaded to the reactor. Rough estimates show that a burnup of $\sim$10 MW·day/kgU approximately corresponds to a uranium-235 concentration decrease of 1% and a plutonium-239 concentration increase (at the beginning of the operating period) by 0.4%. Thus, estimating on the basis of a mean burnup of 10.5 MW·day/kgU, the core content at the moment of the accident was roughly 1,900 kg of uranium-235 and 760 kg of plutonium-239. Even the first estimates conducted in 1986 [4] showed that the accident resulted by discharge beyond the 4th block of 3–5% of nuclear fuel originally concentrated in the reactor core. At present it is considered [9] that $>$96% of core fuel, plus fuel in the cooling pond and the central hall fresh fuel, remain inside the OS. After the accident, 4.1 t of fresh nuclear fuel were removed from the section for fresh fuel preparation in 1986.

To understand the physical properties of fuel-containing materials of the OS it is worth going over the basic stages leading up to the accident. The runaway of the reactor on prompt neutrons resulted in the disintegration of fuel elements shells and incandescent fuel coming in contact with coolant (water). The explosive water vapor generation caused a sharp increase of pressure inside the reactor. This first explosion led to the reactor cover (scheme E, see Fig. 14 [9]) being thrown out to the central hall up to a height of about 14 m, and the base of the reactor (scheme OP — base of the reactor BR) went down roughly by 4 m to the apparatus room 305/2, with the south-east quadrant of the scheme totally ruined. During the flight of the scheme E the second explosion came about and destroyed the drum separator section, the wall of which appeared to be inside of the reactor pit, and accordingly the reactor building itself. After the explosion the reactor cover occupied the position shown in Fig. 1. The explosions caused part of fuel to be thrown out beyond the reactor building perimeter, while that remaining in the reactor started to heat-up due to heat release of fission products and graphite combustion. This process lasted for approximately 10 days. During this period some 14,000 t of various materials: lead, dolomite, marble crumb, sand, zeolite sorbent, and boron containing neutron absorbers, were thrown down from helicopters to the central hall and reactor pit. Part of these materials,

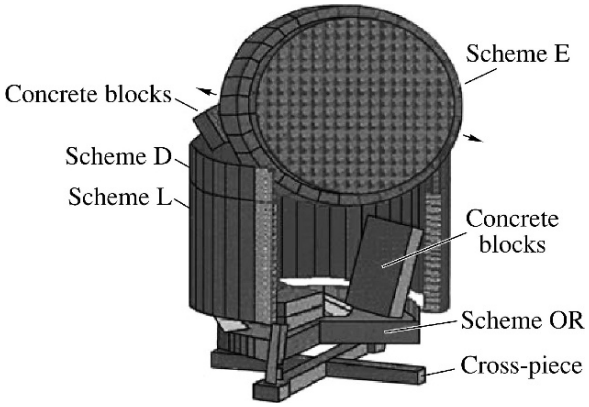

Fig. 1 Schematic picture of the destroyed reactor

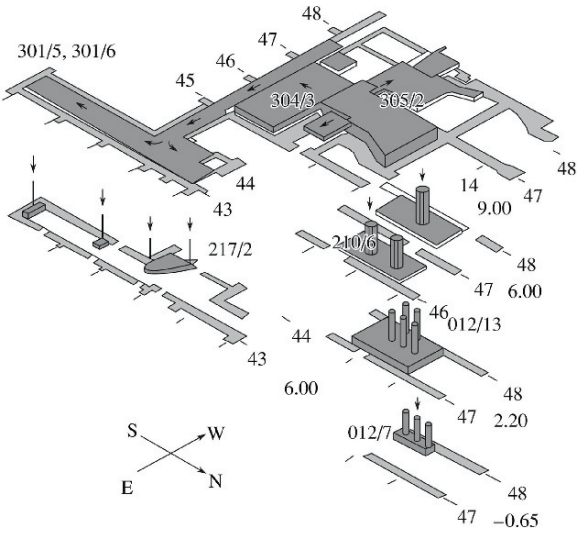

Fig. 2 Scheme of FCCM distribution within the OS sections

which fell down to the reactor pit was meltdown together with fuel, fuel elements shells, walls of process pipes, and fill up material for the scheme BR (serpentine concrete). This melt penetrated into the sections under the reactor and afterwards spread around the numerous rooms of the lower floors of the reactor building — see Fig. 2 [9]. The hardened melt formed the so-called fuel containing clinker-like masses (FCCM) in these rooms.

The clinker-like FCM of the OS comprised heterogeneous ceramics of brown or black color with inclusions of different nature. The later studies showed that the FCCM possess all properties of glass-like materials, thus we will call them ceramics

Table 1 Chemical composition of FCM in 304/3 and 305/2, and concrete, wt %

Element	FCM, 304/3	FCM, 305/2	Concrete
B	0.06	0.07	–
O	43.4	37.1	55.26
Na	4.20	3.34	0.55
Mg	2.40	3.34	0.79
Al	4.80	2.90	2.90
Si	29.8	24.7	26.44
K	1.25	1.05	0.61
Ca	5.50	3.90	8.64
Fe	1.40	0.70	3.64
Zr	3.20	4.00	3.20
C	–	–	0.40
H	–	–	0.77

for the sake of tradition. In room 304/3 resides all black ceramics, whereas in the room 305/2 both black and brown ceramics are present. The black color of the ceramics is basically caused by radiation defects, and after the annealing it assumes a bottle-green color, which is characteristic for silicate glass. Iron oxides produce the color of the brown ceramics. The averaged nuclide ceramics content in the 304/3 and 305/2 rooms, excluding actinides, is presented in Table 1. Special attention should be paid to the boron content in FCCM. It is known that boron is a burnable neutron poison; that is, the quantity of the isotope ^{10}B absorbing neutrons decreases with time in a medium of non-zero neutron flux. Additionally, the boron is well dissolved in water and can be washed out of porous FCM. We can't make the exact estimates of quantity of "burnup" and moreover "washed-out" boron because before the time of the analysis of FCCM about 15 years passed.

At present the nuclear fuel resides in the OS in several forms. First of all, there are the remaining fuel assemblies (southern cooling pond and central hall). In various locations fragments of fuel assemblies (core fragments) were also found. In some places of the under-reactor rooms unmelted pellets of uranium dioxide were found. In FCCM the fuel resides in the form of different inclusions in silicate matrix with dimensions ranging from several μm up to 300 μm of various chemical compositions [10]. Besides, the uranium is also dissolved in the FCCM silicate matrix. The concentration of the fuel dissolved and included in the FCCM matrix varies from 4% to 10% in different rooms of the OS, and the mass fraction of uranium-235 generally corresponds to the burnup [11].

Practically in each OS room the fine-dispersed fuel (fuel dust) with particles with dimensions from parts of a micron up to hundreds of microns is observed. This dust could represent the basic radioactive danger in the case of a hypothetical collapse of the OS building construction. Eventually, in 1990, it was found that in the water accumulated in certain places of the OS lower floors, some uranium, plutonium, and americium salts are dissolved. The estimates show that up to 4,000 m^3 of water per year could penetrate inside the OS through the non-hermetic OS roof, when combined with the quantity contributed by condensation from humid

air [12]. Flowing through the fuel containing materials, the water dissolves some uranium salts and brings them to the OS lower sections. The nuclear danger of each OS room is determined by the fuel quantity in the room, geometrical placing of this fuel, and the possibility of water entering the room and its penetration inside fuel containing materials.

It might seem that the third way of estimation of the thrown out of the OS nuclear fuel quantity, that is determination of fuel quantity in different rooms of the OS, is mostly precise and available. However, the number of hindrances to a detailed examination of the OS is large. The following could be named among such obstacles: high radiation fields in the OS rooms, blocks of various materials thrown down from helicopters in the central hall, heaps of hardened "fresh" (1986) concrete on the clusters of FCM, and the thickness of FCCM layer in room 305/2, where the bulk of FCCM is located. The estimation of the nuclear fuel quantity inside the OS and its distribution among sections is very important from the point of view of the OS nuclear safety and its radiation impact on the Chernobyl NPP and environment in case of possible accidents.

In [13] the authors used the results of analysis of more than hundred samples taken from room 305/2 during 1986–1997, measurements of gamma-radiation power, and the results of all video- and photo- surveys of the room 305/2 and reactor pit. Further, room 305/2 was divided into squares with 2×2 m cross-sections, and the evaluation of quantity of fuel in a FCM volume located over each square taking into account all the data was carried out. On the basis of such a detailed analysis of the whole content a computer model of room 305/2 and the reactor pit was elaborated (Fig. 3). The thorough consideration of all data on room 305/2 and the reactor

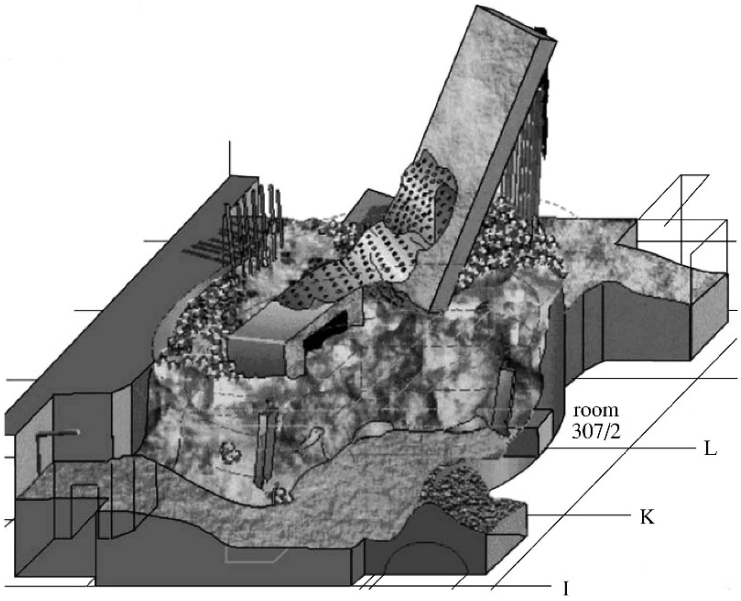

Fig. 3 Computer model of the room 305/2 and reactor pit

Table 2 Distribution of fuel-containing materials inside the OS

Room (mark)	Type of FCM and state	Quantity of uranium in FCM, estimation (on the basis of uranium metric tons)
Central hall (35.50), other rooms of upper floors	Core fragments (the majority is located under the materials thrown down from helicopters to the central hall during the active stage of accident, also FCCM could be present)	?
	plus fuel dust.	30?
	Fresh fuel assemblies	5.5
	In the area of the scheme "E"	10–30
Southern cooling pond (18.00–35.50)	Fuel assemblies spent	14.8
Under-reactor rooms 305/2 (9.00) plus 307/2 plus scheme "OR" plus reactor pit	FCCM, core fragments	75 (+25,−35) proved >60 t
304/3, 303/3, 301/5, 301/6, "elephant leg" and others	FCCM	11 ± 5
Steam distributing corridor (6.00), including FCM in valves	FCCM	25 ± 11
Bubbler pond, 2nd floor (BB-2)	FCCM	8 ± 3
Bubbler pond, 1st floor (BB-1)	FCCM	1.5 ± 0.7
Lower rooms of reactor block	Water with uranium salts dissolved	~3,000 m^3 of water <3 kg U

pit made possible the following conclusion: this section contains not less than 60 tons of fuel. From room 305/2 through the disintegrated by explosion concrete wall FCCM leaked into room 304/3 and to steam distributing corridors. The second flow of incandescent lava through steam dumping valves of different floors penetrated down to the first floor of bubbler pond. For the majority of these rooms the fuel quantity estimations do not cause debate, and they are given in Table 2 summarizing all the measurements data and estimations of fuel quantity in the OS [9]. As is shown in Table 2, the room 305/2 and central hall are suspicious from the nuclear safety point of view. In the steam distributing corridors at the marks 9 and 6 m the clinker layer is thin (maximum 0.6 m in the room 304/3) and according to evaluations the probability of a self-sustaining chain reaction onset in these rooms is insignificant despite the large quantity of fuel. At present the water in lower rooms of the OS doesn't constitute nuclear danger, but in the future, with a gradual increase of the uranium salt concentration, the risk of self-sustaining chain reaction (SSCR) onset could also rise.

There are two ways to evaluate the nuclear safety of the different sections of the OS. The first one is the calculation of the neutron multiplication factor in these sections under various conditions including the most unfavorable case of FCM flooded by water. The criticality computations should be supplemented with computations of the SSCR course scenario if the criticality calculations show the possibility that the neutron multiplication factor exceeds one. The second way is direct measurements of the neutron multiplication factor in the OS sections and possible monitoring of FCM reactivity on the basis of these measurements. The unification of the calculation and experimental methods is advisable, as the data for both precise computations and experimental results interpretation are lacking.

Nuclear safety of the OS, which actually is a problem of FCM criticality, was considered by several groups [14–18]. Criticality computations usually are conducted by numerical solution of the steady-state equation of neutron transport in the medium. The eigenvalue of this equation determines the medium multiplication factor, that is, criticality. Generally this equation is solved with the help of well-developed computer codes. Among the most known the codes SCALE, MCNP, SRAC could be noted. To carry out the calculations, the following must be known: (1) The nuclide composition of the FCM and the concrete they are located on. This concrete could act as a neutron reflector; (2) Macroscopic properties of the FCM, such as density and porosity; (3) Geometrical FCM parameters, the dimensions and configuration of FCM clusters; (4) The quantity and distribution of fuel in the FCM (this is the main question). The first three issues are investigated fairly enough, whereas the question of the quantity and spatial distribution of fuel in FCM stays open in many details: the distribution of non-meltdown core fragments and fuel pellets are still unknown. Thus, the calculation of the effective neutron multiplication factor in FCCM requires that additional ideas be drawn in.

For calculation of the greatest possible effective neutron multiplication factor in FCM of room 305/2, which poses a major danger, various models of fuel distribution were considered [17, 18]; in the paper [18] the results of a recent inspection of room 305/2 [13] were used, serving as the basis for creation of the computer model shown in Fig. 3. The fuel enrichment was calculated on the basis of mean burnup of around 11.5 MW·day/kgU. The total quantity of fuel was determined on the basis of mean and maximum values presented in Table 2. All the quantities were calculated depending on water content in the FCM. In Fig. 4 the spatial distribution of neutron flux along the vertical coordinates accounting for the lower (100 cm) and upper (ceiling, 280 cm) concrete reflectors (the layer of FCM is 80 cm) is presented. Figure 5 shows the neutron spectrum inside FCM depending on degree of FCM flooding by water, and Fig. 6 presents distribution of neutron flux in the room 305/2 implemented using the Monte Carlo method with the help of the MCNP code [18].

The results of the calculations show that taking into account the fuel heterogeneity in FCM does not always lead to the effective multiplication factor increase. The effect depends on water concentration in FCM and on the boron and gadolinium quantities, i.e., on the moderating and absorbing properties of the medium. From the computations it is also seen that the value of the effective multiplication factor slightly depends on a chosen model of non-meltdown inclusions disposition, thus

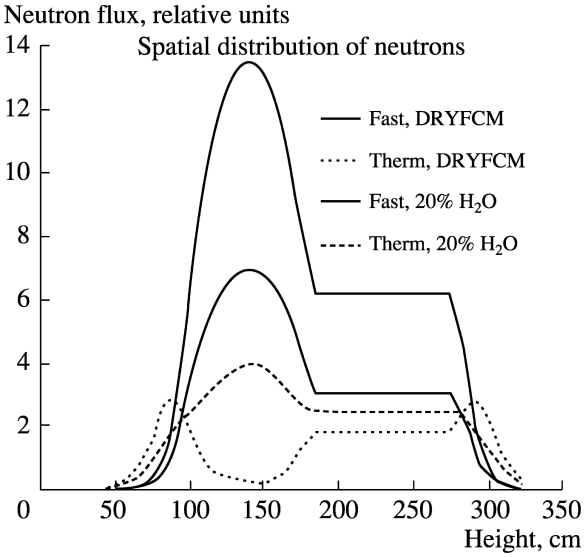

Fig. 4 Fast and thermal parts of neutron flux in the room 305/2 at two values of FCM filling with water (0% and 20%) depending on height (0–100 cm is concrete, 100–180 cm FCM, 180–280 cm air, and >280 cm concrete)

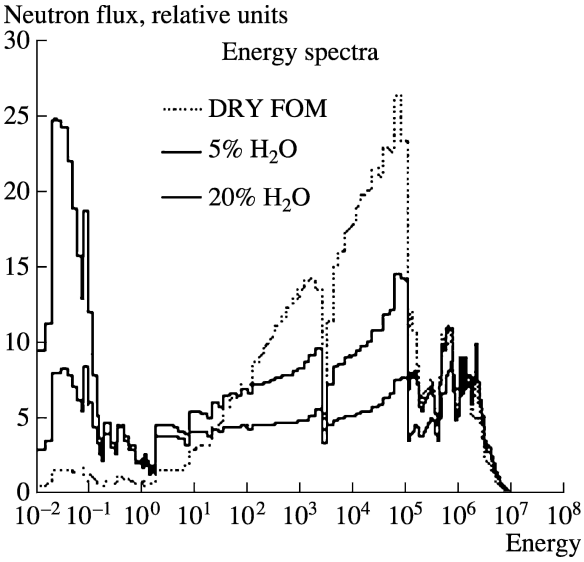

Fig. 5 Energetical spectra in the room 305/2 at different water content in FCM

giving possibility to use the lattice models in most of calculations. In all models with an average quantity of fuel the effective multiplication factor increases rapidly from values 0.25–0.35 for dry FCM up to 0.65–0.70 under 20–25% water flood. With

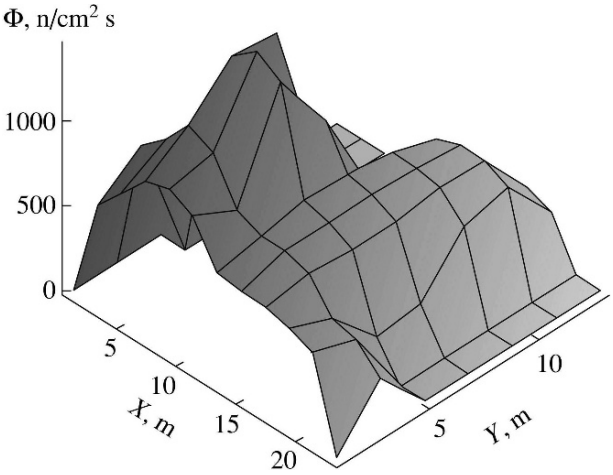

Fig. 6 The neutron flux distribution in the plane of the room 305/2 depending on coordinates (obtained on the basis of the room computer model)

further water flood of FCM the effective multiplication factor falls down to values 0.60–0.65 for the majority of models, whereas for the model with non-meltdown inclusions in the lower layer the factor gradually increases up to 0.8. In an infinite medium, FCM with the highest possible fuel quantity, and pellets cubic lattice with average burnup, the multiplication factor reaches the value of 0.81 at 20% water flood. The same model with fresh fuel gives $k_\infty \approx 0.99$ at 20% water flood, which rises up to 1.07 at 40% of water volume content in FCM. The heterogeneous models with larger thickness of wet FCM (according to estimations of [13] the thickness of the FCM layer in the room 305/2 reaches 4 m) give a value of effective multiplication factor exceeding one even for burned out fuel.

So, some models of FCM give multiplication factor exceeding one. However, such values of the multiplication factor are reached only at big enough water content in FCM. This means that with water entering into FCM from any external source (e.g., precipitation and condensation) the self-sustaining chain reaction (SSCR) of fuel nuclear fission inside FCM could start. The results of studies of the dynamics of SSCR inception and development in FCM, under different conditions of FCM filling with water and at various values of maximally possible reactivity, the effective multiplication factor taking into account possible temperature effects, including the Doppler effect [17], are given below. It is shown that depending on the rate of FCM water flood, different scenarios of SSCR are possible.

Let us assume that the heterogeneous composition with a maximum possible neutron multiplication factor exceeding one is realized (both the existence of such composition and its flood with water are fairly problematic) and consider the qualitative pattern of SSCR development. To analyze FCM behavior at the conditions of its reactivity variation due to water flood, it is necessary to solve the system of kinetic equations describing the situation. The first equation describes neutron transport in

FCM medium and it must account for the existence of delayed neutrons and variations of mean neutron lifetime and reactivity depending on quantity of water in FCM and temperature. Stationary computations show that the dependence of reactivity on water quantity is close to a square-law function reflecting moderating and absorbing properties of water. The second equation is actually an energy conservation law accounting for fission energy release, FCM heating, and FCM cooling from surface and water evaporation. The third equation is a water mass conservation law taking into account the water entering from the external source and its evaporation due to heating as fission energy is released.

These equations were investigated by qualitative methods of the stability theory in the framework of point model and were solved using numerical methods [17]. Different regimes of SSCR development were found depending on parameters values. These regimes are as follows: single neutron burst both in sub-critical and super-critical regimes (in a sense of maximum possible reactivity), and also the regimes of stable and damped neutron oscillations. The realization of one of these regimes depends on the multiplication factor value, the rate of FCM water flood, the rate of heat removal, etc. One of the most probable regimes of subcritical neutron burst is presented in Figure 7, where time profiles of neutron flux density, temperature, water density, and reactivity of FCM are given. It is necessary to note that in 1990 and 1996 two neutron bursts were registered by neutron detectors placed in the rooms 304/3 and 305/2. The reasons of these bursts were widely debated but it is obvious that both incidents happened after intense rain in the Chernobyl oblast. The pattern of bursts development resembled the picture presented in Fig. 7.

The problem of neutron multiplication factor measurements in a multiplying medium is pressing for any multiplying media, that is, for any accumulation of dangerous nuclear materials, and not only for the OS. The authorities of many countries demand from operating organizations that nuclear safety should be grounded by an exact knowledge of neutron multiplication factors in subcritical systems. In connection with the ADS ideology the exact knowledge of subcriticality in the “on-line” regime is urgent to secure the effective work of subcritical reactors. Despite the high speed and accuracy of modern computers the data on subcriticality can’t be always provided by calculations, as the computations are often lacking precise initial data. Taking the OS as an example we’ll discuss the possible ways to solve this problem below. It is necessary to note that attempts at making such measurements at the OS were carried out in 1991 [19]. These measurements were made on the basis of the pulsed neutron method with the standard geophysical instrumentation for neutron well logging. The authors didn’t have the ability to vary the frequency of neutron pulses, and also the equipment had a short detection time for the system response (2 ms). Thus, they could not measure the delayed neutrons and determine the multiplication factor with proper accuracy.

Experimental methods of reactivity measurements could be conditionally divided into two classes: active and passive methods. The active methods presuppose some effect on the multiplicative system with subsequent measurement of the system response. These methods could be realized both by introducing of redundant reactivity (positive or negative) into the system or irradiating the system by external neutron

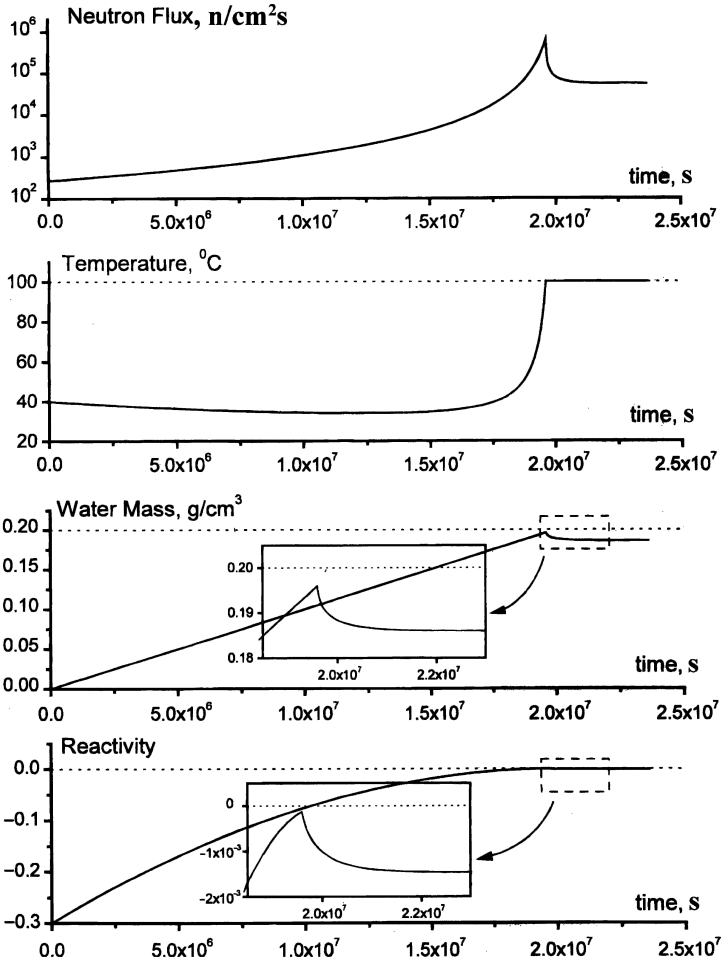

Fig. 7 Time profiles of neutron flux, temperature, water density, and reactivity of FCM in the regime of non-periodic subcritical neutron burst

source. As a rule, the active methods are unfit for practical application. The introduction of additional reactivity requires exact knowledge of this reactivity and, so, the calculations of multiplicative properties of the system we want to determine experimentally. The method of external pulse neutron source for the sake of improving accuracy requires the placement of the source inside the system to the point of the first harmonic maximum, which also needs the neutron flux density calculations to be conducted; on the other hand, the placement is not always possible technically. In turn the passive methods of reactivity definition are based on measurement and analysis of steady neutron background fluctuations, which in the majority of nuclear systems originate from transuranium elements or a stationary external neutron source. Namely, in the OS, the neutron background depends on spontaneous fission

of transuranium elements (^{244}Cu, ^{242}Cu, ^{240}Pu, and the negligibly small contribution of ^{238}U) and (α,n)-reactions. The fluctuations of the neutron background are stipulated by the statistical (probabilistic) nature of the neutron emission and their interaction with the medium nuclei. A review of statistical methods for reactivity measurements is presented in [20], and a number of measurements with various improvements [21, 22], including measurements at the OS [23, 24] have been conducted since.

It is noteworthy that modern electronics are capable of getting the initial statistical experimental information with subsequent software processing on a computer using one or another theoretical method (or all methods known). At the INR of the Ukraine NAS such equipment was developed, permitting measurement of time intervals between pulses of the neutron detector with an accuracy of 250 ns [23]. The software was also developed and the measurements of the neutron multiplication factor in the OS ($k_{eff} \approx 0.35$ in room 305/2) were performed.

It is clear from above that the OS contains significant radiation and nuclear risks. So, a pressing need exists to transform OS into ecologically safe system.

2 Nuclear reactors

2.1 General requirements for next-generation reactors

Recent recession in nuclear power engineering development rate in the 1980s–1990s is connected not only with accidents at power reactors but also with the diminishing competitiveness of electrical power produced at atomic plants. This is connected with rise in the cost of some units construction and increase of building terms. The fuel became more expensive as well. Thus, the second requirement to future atomic power plants is reduction of electricity price produced. These two demands are contradictory on the face of it, but really closely connected with each other. One should never forget that even in cases when radioactivity doesn't go out of the reactor limits, nevertheless the heavy accidents cause huge financial losses. The third requirement for next-generation nuclear power engineering is the need for a solution to the problem of nuclear waste.

We will try to formulate the main demands on developers elaborating new reactors. First of all, the reactors in new designs must be provided with the systems of passive protection. That is, in case a dangerous situation in the reactor arises the chain reaction must be damped and the core cooling started without personnel interference. The other requirement is simplification of all reactor systems designs with simultaneous increase of their reliability. The simplification is understood as diminishing of the quantity of units that could fail. The rest assemblies should be doubled and have reliable control systems. At last, the safe reactors should be less powerstressed; i.e., it is advisable that the units of lesser power that are produced and assembled directly at production sites be put into operation. Apropos, such units

will have significantly improved quality and reduce the cost of station construction. The possibility appears that the lesser power reactors cooling exclusively through natural forces usage are of coolant natural convection. Thus, the diminishing of reactor power makes possible the application of passive protection systems along with quality increase and reduction of production costs.

A contradiction arises again, as it is known that the economical efficiency of high power units is larger. That is why before the decision is taken all the financial expenses must be very well calculated, accounting for economical, ecological, and social risks. Thus the new designs of reactors are being developed now along two directions. On the one hand, the high power blocks are being developed with all possible protection systems including passive systems and sophisticated systems of operational control. On the other hand, reactors of minor power with additional cooling by the coolant convection are also being elaborated. Such improved constructions of reactors are already developed. Note that a brief review of existing types of nuclear power reactors is given in [3].

2.2 Improved reactors

We tentatively group new reactor projects into three types: improved reactors, perspective reactors, and innovative reactors. Let us call the improved reactors those that do not strongly differ from the ones operating now but have an increased safety level. This safety level is reached using all the three principles listed above, but possibly not in full measure. The projects of such reactors fully developed passed license and are ready for the serial production (see, e.g., [25]). One of the possible ways of such modernization consists in the deeper submerging of the core into a vessel containing pressurized water, so that in the case of an accident the water above the core will not boil away as quickly as in an ordinary reactor and destruction of fuel elements will be delayed. This method doesn't exclude the necessity of backup cooling systems and protective shells, but its application gives the operators more time to take adequate decisions.

There are also other fully developed projects, for instance IP-600, WWER-650, and PBR-600, having far lesser power with core and confinement cooling by the coolant convection in case of accident. Among the boiling reactors to this type could be attributed the reactor ABWR developed jointly by General Electric and Hitachi; at present 4 units of ABWR with 1,356 MW(e) power each operate in the world. A, simplified reactor on boiling water SBWR with power 600 MW(e) with the coolant natural circulation has been developed as well.

Other type of projects are perspective projects with the highest possible use of passive safety principles. The most strikingly such designs are represented by the project of ultimately safe reactor (USR) developed by Swedish company ASEA-ATOM. This project is based on a drastic change of reactors on light water construction. Its core, first cooling circuit, and steam generators are submerged into a big pool made of prestressed concrete filled with cold water and boron solution.

The pool and the first circuit are connected hydraulically, but in normal conditions the water pressure maintained by cooling pumps prevents water from entering the core. Disruptions in the cooling system lead to pressure diminishing and cold water entering the core. The boron damps nuclear reaction as a strong neutron absorber and natural convection of cold water takes away residual heat and makes the reactor shut down cooling without personnel interference or usage of electromechanical means. The second interesting project which could also be attributed to the "fully safe reactors" series is design of a compact (100 MW(e)) high temperature reactor with gaseous coolant developed by the German company KWU/Interatom. The core of such reactors consists of large quantity of graphite balls with small pieces of fuel inside covered by a layer of graphite and silicon carbide mixture. In the lower part of reactor the unit for fuel reloading, which is performed without reactor shutdown, is located. The fuel can withstand temperature up to 1,600° without fission products being released. Due to the small dimensions of the balls and, accordingly, a big surfaceto-volume ratio, the temperature in the core can't exceed the preset value even if all coolant is lost. The chain reaction will automatically stop after temperature increase due to broadening of resonant absorption levels. The radioactive fission after-heat is removed through the vessel walls, and with small reactor dimensions such removal will be sufficient for the temp! erature not to exceed a safe level.

Breeder reactors on fast neutrons were also developed. One of them is a reactor BREST (in Russia) with melted lead as coolant. This reactor could be considered sufficiently safe as it works at fairly low pressure due to the low pressure of lead saturated vapors. One of the essential drawbacks of modern reactors is a problem of radioactive waste, especially transuranium elements. For this problem to be solved there are several approaches, one of which is in the stages of an almost developed project. In this context the project PATES (in Russia) is meant (underground atomic thermal electric power plant). Recently this project was intensively advertised to be introduced to Ukraine atomic power engineering; thus, we will examine it somewhat more closely. The project envisages employment of ^{235}U with purity 99.9% as a fuel. It is true that such fuel will lessen radioactive waste and practically zero quantities of transuranium elements making bulk contribution to long-term residual activity of waste. This effect is precisely the main advantage of the approach proposed. The very station is supposed to be build on the basis of reactors KNZ (in Russian) developed for submarines. They are compact and could be produced at manufacturing plants with high quality. The plant consists of separate units placed underground. Such reactors don't need the separate protective shells to be built so construction costs will be lower. Besides after the operation lifetime is over the station could be simply buried underground. Thus the basic idea of underground station construction with use of low power units undoubtedly deserves attention.

2.3 Innovation projects

There are innovation projects of nuclear reactors, some of them only ideas, uniting the solutions to both the problems of radioactive waste and safety. We'll mention

three directions. The first is projects of subcritical reactors controlled by the charge particles accelerator (the so called ADS, accelerator driven systems); the second is molten salt reactors-breeders; and the third is the Feoktistov reactor, which is a reactor on fission auto-wave. These types of reactors are actively discussed presently, different constructions calculated, and even the concept of the first and second types of reactors symbiosis have been proposed. The main idea of the reactors with accelerator (firstly suggested more than half-century ago [26–28] reanimated at present after papers of Rubbia, Bowman, and Furukawa [29–31]) is that the core is maintained in a subcritical state with a neutron multiplication factor below one. An external source of neutrons is required to keep such reactor in steady state. The reaction of accelerated protons up to energies of around 1 GeV with target of heavy metals (bismuth, tungsten, lead, or a mixture of these) is considered to be most suitable source of neutrons. Upon attainment of high currents of the accelerator beam a sufficiently high density of neutron flux in core can be obtained ($>10^{15}$ n/cm^{2}s). At such neutron flux density and with the condition of fast neutrons spectrum in reactor (i.e., without moderators), all the transuranium isotopes turn to fissionable isotopes (or merely break down in the fast spectrum) and take part in chain reaction. Thus all transuranium waste of light water reactors could be burned out (ideal case) and, besides, in such reactions fluxes transmutate even long-life fission products. Such a reactor is a safe one, as far as chain reaction is maintained by the external neutrons source, which can be practically instantaneously switched off by electrical means of control.

A review of the possibilities and advantages of subcritical systems in comparison with reactors in operation can be found in [32, 33]. In this paper we discuss several questions that were insufficiently considered in the literature. Those are questions of choice of the external neutron source for subcritical systems and optimization of core aiming at obtaining the maximum amplification factor of neutron flux from the external source. The question of multiplication factor measurement in subcritical systems is also very important.

In contrast to traditional ADS based on protons (or deuterons) of high energies (up to 1 GeV) with beam currents reaching tens of milliamperes one may consider the possibility of usage of ordinary neutron generators based on the D–T reaction with a deuteron beam current up to 1 A. As deuteron energy on the order of 200–300 keV is quite sufficient for reaction to proceed, the creation of such neutrons generator could appear far cheaper than the construction of 1 GeV accelerators; the currents of several amperes are quite accessible for low energy accelerators. The neutrons generators could turn advisable at construction of high fluence research reactors.

Let us sketch the basic principles of the construction of neutron generators. In such generators neutrons are produced as a result of fusion reactions D–D and D–T (D is a deuteron and T is a triton). The leading is the reaction D–T, as its cross-section reaches maximum ($\sim$5.3 barn) at an energy of about 109 keV, exceeding the cross-section of the D–D reaction by more than order. The majority of neutron generators work on metallic tritium saturated targets irradiated by 300–400-keV deuteron beams. The neutron yield in such systems depends on deuterons energy

losses in targets (i.e., on material of the target), saturation of target with tritium and naturally on the deuteron beam current. For multilayered solid targets neutron yield per one accelerated particle up to 300–400 keV is on the order of 10^{-4}; i.e., at accelerator current ~ 1 neutron yield could reach 10^{14} n/s. For gaseous targets neutron yield per accelerated particle is bigger by an order, $\sim 10^{-3}$ [34]. Thus for subcritical research reactor it is advisable to construct neutron generator with particles beam current around 1 Å and a gaseous target. Such a generator will serve as an external neutron source with intensity of 10^{15} n/s for subcritical system. It is worth noting that a generator with intensity of 10^{14} n/s and accelerator current of the order 1 Å has already been constructed [35].

Apparently, the questions of core optimization have been repeatedly discussed. For instance, Daniel and Petrov [36], on the basis of one-group diffusion model, showed that it is more effective to use two-zone system with an external neutron source surrounded by a small booster with $k_\infty > 1$, which, in turn, is surrounded by a subcritical core; thus, the effective multiplication factor of the whole system $k_{eff} < 1$. Multizone systems with valve neutron connections were also considered [37, 38]. As a one-group diffusion model for complicated multizone systems does not often lead even to qualitatively correct results, than optimal parameters to be chosen (dimensions and zones enrichment) for the subcritical reactor it is advisable to conduct numerical multi-variant calculations of model systems [39, 40] and then compute the reactor real scheme. As a principal optimization parameter the amplification factor of neutrons from external source could be chosen (ratio of total quantity of neutrons passing the external boundary surface per time unit N_S to neutron source intensity I_0: $q = N_S/I_0$), as the basic purpose of research reactors construction is obtaining high-flux neutron beams.

The results of model calculations of two-zone subcritical homogeneous systems with different enrichment and zone dimensions with a neutron source 14 MeV are given below. The calculations were carried out using the neutron-physical codes SCALE and MCNP. Our results show that the amplification factor of neutron flux from external source shows nonmonotonic behavior depending on the thickness of the zones and on fuel enrichments. In Fig. 8, the results of calculations of a system with enriched uranium internal zone and a pure uranium-238 external zone are presented. The thickness of the external zone is set within 1–20 cm. For each enrichment of internal zone, its dimensions are selected so that the whole system k_{eff} equals 0.99. The internal zone enrichment as to uranium-235 varies within 8–100%. It can be seen that at the internal zone enrichment of 20% the maximum of factors is observed at any thickness of external zone. Such nonmonotonic behavior of amplification factors is observed for all the schemes computed; that is, optimal choice of zones dimensions and enrichments could secure the maximum possible neutron flux to be obtained [41]. Certainly, calculations of realistic schemes could introduce some amendments to the estimations presented, but still the research reactors of this type are promising for further development. Moreover, to get high amplification factors and so to diminish accelerators currents in power reactors, it is probably worth conducting optimization calculations with dimensions and enrichments of different zones of reactor.

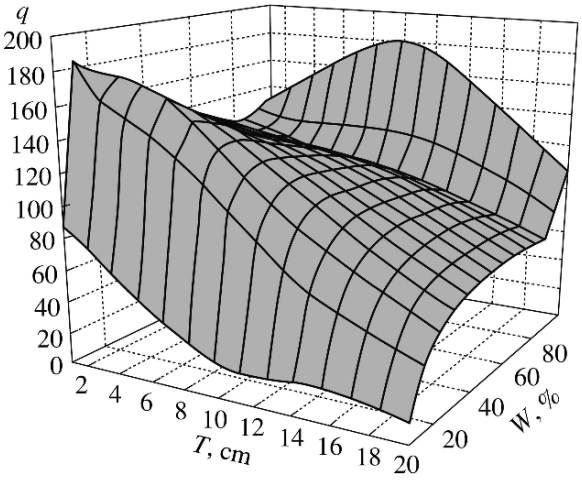

Fig. 8 Dependence of amplification factor of neutron flux q for two-zone system at various thickness of external zone T and different enrichments w for uranium-235

Let us note that an experimental subcritical assembly, namely "YALINA-B" with a neutron generator, has already been constructed at the Joint Institute for Energy and Nuclear Research (Sosny, Minsk, Belarus) [42]. The assembly consists of a deuteron ion accelerator and a titanium target saturated with tritium at which the beam is directed (keep in mind that the typical ADS scheme proposes to use a heavy metallic target irradiated by a beam of charged particles, protons or deuterons, as an external neutron source). The generator neutrons hit a lead target, which forms a neutron beam going exactly to the subcritical core. The very core, with effective multiplication factor $k_{eff} < 0.98$ consists of polyethylene moderator in the channels of which the fuel rods are placed (UO_2 with 10% enrichment to ^{235}U). All the core is placed in a graphite reflector. The subcritical assembly of the traditional scheme, in which a proton accelerator of 600 MeV with current up to 3.2 μ is directed to a lead or tungsten target to cause a stripping reaction (spallation), is being developed in Dubna, JINR, Laboratory for Nuclear Problems (SAD is subcritical assembly of Dubna) [43]. By now the project of the installation and technology of fuel pellets production have been developed. The core is assembled of fuel elements developed for the reactor BN-600 with mixed oxide fuel (UO_2+PuO_2) [44]. SAD could become the first installation ADS in the world connecting a proton accelerator with subcritical compact core filled with MOX fuel. SAD is aimed at ADS physics research in a wide subcriticality interval up to $k_{eff} \sim 0.98$. At present the SAD installation has already assembled. The works on safety provision are in final stages and technology of fuel pellets production is being adopted. In the Ukraine Kharkov "phystech" the project of a subcritical reactor on the base of an already existing 300 MeV electron accelerator is being developed. At present the work is at the stage of physical project development.

2.4 Feoktistov reactor

Innovation projects of nuclear reactors are directed both on reactors safety increase and fuel cycle improvement, the burn-out of transuranium elements and huge resources of ^{238}U and ^{232}Th usage. From our point of view the Feoktistov reactor, which is based on the origination of a slow nuclear combustion wave in a pure ^{238}U (or ^{232}Th) medium, solves both problems: ultimate nuclear safety and ^{238}U usage, but only in the case of practical realization of such a reactor. Possibly in the Feoktistov reactor not only pure ^{238}U will be used but also depleted uranium (enrichment process waste) and spent nuclear fuel (without preliminary radiochemical reprocessing). Feoktistov [45] showed that in ^{238}U medium (for the sake of definition further we will talk about a uranium–plutonium reactor) under certain conditions the neutron-fission wave could propagate. Really, if a halfspace filled with matter containing uranium is irradiated by neutrons then plutonium will be accumulated close to surface. With time, the plutonium concentration could reach critical value and then the system could become capable to self-multiplication. Neutrons emitted from reaction zone are captured by the next uranium layers in which plutonium accumulates also. Under certain conditions the core moves and plutonium accumulates in subsequent layers. As a result a steady wave forms, in the front of which uranium is processed into plutonium due to fission neutrons. It was noted in [46,47] that such a regime realization in reactor will provide its internal safety.

In the paper by Teller [48] the concept of a fast reactor working in a self-controlled regime on thorium fuel at the depth 100 m underground for 30 years running without man's direct interference was presented. Such a reactor operation is practically absolutely safe. Actually, Teller used and applied the Feoktistov idea to a thorium reactor. In [49–52], new models of perspective fast reactor development are proposed. Through mathematical simulation it was shown that the self-controlled reactor period reaches 11 days, whereas in ordinary reactors it is several minutes (reactor period is time of power increase by e times). In particular in [49, 50] was proposed a model of a reactor on metallic fuel and it was shown that without control reactor power changes by 2.5% during 2 years. Though the authors of [47, 49, 50] refer to Feoktistov, in their works the auto-wave of plutonium fission doesn't emerge and the reactors considered are not steady as their power changes with time without control. Maybe, this is due to geometrical effects or initial conditions choice.

The Kharkov group [51, 52] showed the possibility of origination and propagation of nuclear combustion wave in a critical fast reactor on metallic U–Pu fuel. The calculations demonstrated that such a reactor automatically maintained itself in a state close to critical during long time (years) due to internal feedback on reactivity which provides stable propagation of the combustion wave. In particular, the run of a cylindrical reactor with radius 100.5 cm and length 500 cm lasts around 15 years, after which the reactor reaches the stable phase of the nuclear combustion wave propagation, with the speed of its front movement constituting about 25 cm per year. The analysis done showed the stability of the combustion regime regarding the perturbations of neutron flux in the reactor.

In our opinion, the numerical calculations of such a type do not reflect the physical peculiarities of the wave reactors and, in any case, can not be the proof of stable wave existence. This is due to the fact that the main idea of the wave reactor self-aligning is loosed in such calculations: fluctuation excesses of plutonium concentration over the critical value burn during the times compared with neutron life-time (without taking the delayed neutrons into consideration) or, at least, compared with reactor period (taking the delayed neutrons into account), but new plutonium is formed approximately through three days and not simultaneously. This means that the numerical calculations should be performed with time mesh of the order of 10^{-6}–10^{-7} s without delayed neutrons and with time steps $\sim 10^{-1}$–1 s taking the delayed neutrons into account. At the same time, the most of the numerical calculations were performed with the time steps of the order of days (in the works where the step was indicated), which was connected with necessity to calculate the long-term processes of wave formation and propagation over the whole reactor. But the calculation with such time steps leads to seeming increase in multiplication factor up to 1.1–1.2 in dependence on time step, and reactor runaway is not observed. It means that such calculations have no physical sense.

It is interesting to note that taking into account the delayed neutrons is not important for formation of the nuclear burning wave at first glance. But it can be very important for the numerical calculations since adding of one or several equations to the mathematical model cannot be compared to necessity of time step decreasing to several orders. It is clear that the calculation of the reactor life-time with small time steps of the order of neutron life-time is impossible at present computers (excluding supercomputers and international grids).

The stationary auto-wave regime is very interesting, and it is necessary to analyze the conditions of its onset – first on the basis of simplified equations and then using more realistic mathematical models. One such simplified model is considered in [53, 54]. In contrast with [45], where a system of four equations for concentrations of neutrons (in one-speed approximation), uranium-238, plutonium-239, and intermediate nuclide-239 was analysed, in the papers mentioned only one equation for neutron flux density ϕ is considered, and nuclide concentration fluctuations in wave are accounted by the model quadratic dependence of multiplication factor $k_\infty(x)$ on the neutron flux $\Psi(x,t) = \int_0^t \phi(x,t')dt'$:

$$L_0^2 \frac{d^2\phi}{d\xi^2} + [k_\infty(\Psi) - 1 + \gamma\phi]\,\phi = 0,$$

where $\xi = x - ut$ is the wave variable, L_0 is the neutron diffusion length, γ is the power reactivity factor describing feedback with other reactor subsystems, and $k_\infty = k_{\max} + (k_0 - k_{\max})\left[\frac{\Psi}{\Psi_m} - 1\right]^2$.

Such an approximation can be justified if the plutonium concentration dependence on the wave variable is expanded into series in the vicinity of the maximum, and consideration is restricted to quadratic terms. As a result, the solution of the equation obtained has a well known form of diffusion soliton $\phi(\xi) = \phi_m \mathrm{sech}^2(\alpha\xi)$,

and in [53] the influence on the solution of power feedback, deviations from parabolicity, and wave initiation methods was investigated; [54] considers the effect of transverse leaks (all the [53, 54] analyses are conducted for the one-dimensional case).

The system of four equations [45] is far more complicated, but it can be analyzed in terms of the flux variable instead of neutron flux variable. Then the system of equations can be presented in the following general form:

$$\frac{\partial \Psi}{\partial t} = \nu \cdot D \cdot \Delta \Psi + G\left(\overrightarrow{N}_0, \overrightarrow{N}, \Psi\right),$$

$$\frac{\partial \overrightarrow{N}}{\partial t} = \widehat{\sigma} \cdot \overrightarrow{N} \cdot \frac{\partial \Psi}{\partial t} + \widehat{\lambda} \cdot \overrightarrow{N},$$

where $G = \int_0^{\Psi} g\left(\overrightarrow{N}\right) d\Psi$ is the flux generation function by analogy with neutron generation function $g\left(\overrightarrow{N}\right)$, which is the linear function of nuclide concentrations $\overrightarrow{N}$ and takes into account all the processes of neutron creation and absorption; $\widehat{\sigma}$ is the matrix, elements of which are the microscopic cross sections of absorption and capture, and $\widehat{\lambda}$ is the matrix, elements of which are the decay constants of the β-active nuclides; ν is the mean neutron velocity, D is the neutron diffusion coefficient (only three nuclides were taken into account in [45], but it is necessary to consider all nuclides important in the process, including fission products and external absorber).

It can be shown in quasistationary diffusion approximation, which is always fulfilled, that in order to satisfy the boundary conditions it is necessary and sufficient to satisfy the following two conditions:

$$\int_0^{\Psi} g d\Psi = 0,$$

$$\int_0^{\Psi} \left(\Psi_f - \Psi\right) \cdot g d\Psi = 0,$$

where Ψ_f is the final value of the flux. One can transform these conditions to those analogous to criticality condition of usual reactors: $k_{eff} = 1$, where k_{eff} is the effective multiplication factor. Let us disjoint for this purpose the neutron and flux generation functions into two parts:

$$g = g^+ - g^-,$$

$$G^{\pm} = \int_0^{\Psi} g^{\pm} d\Psi.$$

so that $\overline{g}^{+}$ and $\overline{g}^{-}$ are positive (the bars denote the mean values). Besides, $\overline{g}^{+}$ corresponds for neutron generation and $\overline{g}^{-}$ corresponds for neutron absorption. Then the effective multiplication factor for usual reactors has the form:

$$k_{eff} = \frac{g^{+}}{g^{-}}.$$

Let us denote the points at the flux axis with coordinates

$$\overline{\Psi}^{\pm} = \frac{\int\limits_{0}^{\Psi} \Psi g^{\pm} d\Psi}{\int\limits_{0}^{\Psi} g^{\pm} d\Psi}$$

as the "centers of neutron generation and neutron absorption application". And let us introduce the integral neutron multiplication factor for the nuclear fission wave reactor

$$k_{eff} = k_0 = \frac{\overline{g}^{+}}{\overline{g}^{-}}$$

and integral coefficient of space equilibrium

$$k_1 = \frac{\overline{\Psi}^{+}}{\overline{\Psi}^{-}}.$$

Then one can write the conditions of wave stationarity in the form

$$k_0 = k_1 = 1.$$

Summarizing the obtained results, one can make the following qualitative conclusion: in addition to integral equality of created and absorbing neutrons, the distribution of neutron creation and absorption density along the fluence coordinate is also important for the wave stationarity. One can write the corresponding condition of time-space equilibrium in the wave as the condition of generation and absorption centers of application coincidence along the fluence coordinate $\overline{\Psi}^{+} = \overline{\Psi}^{-}$, or $k_1 = 1$. So the wave should be balanced by two (not only one) parameters simultaneously, which is very important. The existence of such two conditions gives the possibility to develop the perturbation theory in order to determine the wave velocity (and also energy release and reactor power) in dependence on the different nuclide concentrations, first of all on the concentration of the external absorber, which is the control parameter of the problem. More detailed information can be found in [55].

The results obtained allow for some conclusions to be made. First, before conducting bulky numerical calculations in many-group approximation accounting for a large quantity of nuclides in realistic geometry, it is necessary to study auto-wave solution stability for such system. Second, auto-wave stability essentially depends on geometry and on the problem parameters (relationship between cross sections). Third, numerical calculations of realistic systems must be carried out with maximum

possible accuracy, because such calculations require recomputing cross sections at each step and the relation between cross sections determines wave stability. The stability study of system of parabolic equations constitutes a fairly complicated problem with no general solution found so far. Nevertheless, in some special cases the methods developed in chemical combustion theory [56] are applicable. For example, if diffusion coefficients of components participating in the reaction are equal (in our case, if the neutron diffusion coefficient is zero) it could be shown that wave solution is stable in a fast uranium–plutonium reactor in flat geometry. More complicated cases require further study.

3 Conclusions

In conclusion, one tries to answer the principal question: could nuclear power engineering be safe? The authors consider the nuclear power engineering no less safe than any other energy intensive technologies. Moreover, nuclear power engineering could be and must be more safe than other energy generating technologies because the price of potential problems is enormously high. This price consumes huge resources, especially from Ukraine because of the Chernobyl accident. Innovative approaches considered above allow for the solution of other problems of nuclear power engineering, namely, competitiveness and nuclear waste handling.

To summarize, closed fuel cycle creation relies on the availability of two essential technologies: uranium isotope enrichment and radiochemical production facilities to process spent nuclear fuel. In the project of manufacturing of fuel assemblies in Ukraine, it was supposed that the uranium enrichment will be conducted at Russian plants and the fuel pellets will be delivered from Kazakhstan. Generally speaking, the energy independence achievement supposes availability of all technological stages of fuel production inside the country and, apparently, while developing the project of nuclear fuel production in Ukraine the question of isotope uranium enrichment plant construction was also considered, and the decision not to build such a plant was reached. The authors agree that uranium enrichment on the basis of traditional technologies (centrifugation and gas diffusion) is undesirable.

However, for the past 20 years the technologies of uranium laser enrichment were being developed, which are considered more cheap and effective, as enriched fuel could be obtained in a one-cascade process (in contrast with traditional technologies where thousands of cascades are required). As far back as the beginning of the 1990s about 1,000 kg of enriched uranium at experimental industrial installation was obtained on the basis of method AVLIS (Atom Vapor Laser Isotope Separation) in the United States. There are also methods of laser enrichment in molecular beams (MOVLIS) and laser-chemical methods. Thus, in the case of a significant rise of enriched uranium costs, one of the points of atomic power engineering in Ukraine could become the development of laser enrichment technology and its introduction into fuel production.

As was already noted, a "deferred decision" strategy of spent nuclear fuel handling was adopted in Ukraine, i.e., centralized dry storage of SNF construction and possible development of own radiochemical production in future. The known technologies usage like methods of extraction by solvents are also probably undesirable. As an alternative it is worth considering the fluoride technologies developed by scientists in St. Petersburg.

In conclusion let us list some principal points. Nuclear power engineering is undoubtedly one of the energy sources with the most potential. Its effectiveness will depend on various circumstances and first of all on profitability. Nuclear safety enforcement at NPP leads to higher cost of the produced electricity. This increase could be compensated in future by development of new more safe reactors. To safe reactors we firstly attribute subcritical reactors controlled by charged particles accelerators (ADS). The other perspective direction in development of next-generation reactors is the Feoktistov reactor. Still, before its practical operation a number of essential problems are to be solved. The specific weight of NPP in Ukrainian power engineering is one of the highest in the world and state authorities intend to preserve and even enlarge the NPP share in future. Moreover, there exist in Ukraine all the preconditions to build up its own closed nuclear cycle.

This work was supported in part by the National Academy of Sciences of Ukraine (special program "Fundamental Properties of Physical Systems Under Extremal Conditions").

References

1. "INSAG-7 The Chernobyl Accident: Updating of INSAG-1", in *Report of Intern. Nuclear Safety Advisory Group* (Intern. Atomic Energy Agency, Vienna, 1992).
2. O.A. Litvinenko et al., "Some Insights about Possible Reason of Accident on Chernobyl NPP in 1986", Preprint MNTTs Ukrytie 98-9 (Chernobyl, 1998).
3. V.A. Babenko, L.L. Jenkovszky, and V.N. Pavlovych, Fiz. Elem. Chastits At. Yadra **38**, 1517 (2007) [Phys. Part. Nucl. **38**, 795 (2007)].
4. V.I. Kholosha, Yu. A. Ivanov, L. Ya. Tabachnyi, et al., in *Problems of Chernobyl Exclusion Zone* (Chernobyl, 2001), Vol. 7, p. 3 [in Russian].
5. "USSR State Committee on the Utilization of Atomic Energy — The Accident at the Chernobyl NPP and Its Consequences", in *IAEA Post Accident Meeting, Aug. 25–29, 1986, Vienna (1986)*.
6. A.A. Borovoi, "Ejection of Nuclear Fuel and Fission Products from Reactor of 4th Unit Chernobyl NPP during Accident", in *Problems of Chernobyl* (Chernobyl, 2001), Vol. 7, pp. 130–140 [in Russian].
7. A.A. Borovoi, "Fission Products and Transuranic Release during Chernobyl Accident", in *Proc. of. Intern. Conf. on the Fission of Nuclei — 50 Years* (Leningrad, 1989).
8. A.R. Sich, "The Chernobyl Accident Revisited, Part 3: Chernobyl Source Term Release Dynamics", Nuclear Safety **36** (2) (1995).
9. *The Shelter Current Safety Analysis and Situation Development Forecasts*, Updated Version (Tacis, 1998).
10. E.M. Pazukhin, "Lava-like Fuel Containing Masses of the 4th Unit of Chernobyl NPP: Topography, Physical, and Chemical Properties, Scenario of Formation", Radiokhimiya **36** (2), 97–142 (1994).

11. E.M. Pazukhin, "Some Nuclear Physical Characteristics of 4th Unit Fuel of Chernobyl NPP", Problemy Chernobylya **7**, 149–158 (2001).
12. S.A. Bogatov, A.A. Korneev, A.P. Krinitsyn, et al., "The Problem of Water in the Object "Shelter" ", Preprint 99-5 MNTTs "Ukrytie" (Chernobyl, 1999).
13. A.A. Borovoi, A.S. Lagunenko, and E.M. Pazukhin, "The Room under Operating 305/2 Room of 4th Unit of Chernobyl NPP: Its State, Estimation of Fuel Quantity", Preprint MNTTs "Ukrytie" 97-7 (Chernobyl, 1997).
14. *Nuclear and Radiation Safety during Working on "Shelter": Report*, MNTTs "Ukrytie" of Nation. Acad. Nauk Ukrainy, Arkhivn. No. 3173 (Chernobyl, 1993) [in Russian].
15. *The Elaboration of Suggestions and Recommendations on Monitoring and Diagnostics of Multiplying Properties of the LFCM of the "Shelter" of Chernobyl NPP: Report*, MNTTs "Ukrytie" Nation. Akad. Nauk Ukrainy, Arkhivn. No. 3234 (Chernobyl, 1993) [in Russian].
16. *Technical Substantiation of Nuclear Safety of Object "Shelter": Report* (Kurchatov IAE, Moscow, 1990) [in Russian].
17. V.A. Babenko, L.L. Jenkovszky, V.N. Romanov, et al., "Fuel-Containing Masses of Chernobyl Unit 4: Multiplying Properties and Neutron Characteristics", Nucl. Sci. Eng. **133**, 301–313 (1999).
18. V.A. Babenko, E.D. Vysotskii, A.A. Klyuchnikov, et al., "Models of Neutron Flux Density Distribution in Fuelcontaining Materials in 305/2 Room of Object "Shelter" ", Problemy Bezpeki Atomn. Electrostantsii i Chernobyla **2**, 55–60 (2005).
19. G.V. Lebedev and V.F. Shikalov, "Subcriticality Measurements of Fuel Containing Masses of "Shelter" ", Preprint Kurchatov IAE No. 5876/5 (Moscow, 1995) [in Russian].
20. R. Urig, *Statistical Methods in the Nuclear Reactor Physics* (Univ. of Florida, Ronald Press, New York, 1973).
21. E.F. Efimenko, V.K. Magajev, and V.A. Dulin, "Using the Fission Chamber with $^{2}52$Cf Layer in Some Physical Measurements", Atom. Energy **79** (1) (1995).
22. V. Doolin, I.P. Matveenko, and G.M. Mikhailov, "The Using of the Model of Two Group of the Prompt Neutrons to Analysis of Measurements of β_{eff} by the α-Rossy Method", Atom. Energy **80** (1) (1996).
23. V.P. Badovskii, A.A. Klyuchnikov, A.A. Kuchmagra, et al., "Development of Methods of Noise Diagnostics of Hazardous Nuclear Fissioning Materials Aggregations of Object "Shelter"", Problemi Chornobilya **9**, 76 (2002).
24. A.A. Klyuchnikov, A.A. Kuchmagra, V.T. Kotlyarov, et al., "Adaptation of Metodics of Subcriticality Statistical Measurements to Object Shelter Conditions", Problemi Chornobilya **13**, 33 (2002).
25. R.K. Lester, V Mire Nauki (Scientific American, Russian Edition) **5**, 4 (1986).
26. W. Lewis, Report AECL-968 (1952).
27. *AEC Research and Development Report, Facilities for Electronuclear (MTA) Program*, Report LWS-24736 (1953).
28. W.A. Gibson et al., ORNL-3940, Electronuclear Division, Ann. Progress Rep. (1965), p. 110.
29. F. Carminati et al., Report CERN-AT-93-47(ET) (1993).
30. C.D. Bowman et al., Nucl. Instr. Meth. A **320**, 336 (1992).
31. K. Furukawa et al., in *Japan-US Seminar on Thorium Fuel Reactors, Naora, Japan, Oct. 1982* (1982).
32. S.A. Bznuni et al., Fiz. Elem. Chastits At. Yadra **34**, 977 (2003) [Phys. Part. Nucl. **34**, 497 (2003)].
33. C.D. Bowman, Ann. Rev. Nucl. Part. Sci. **48**, 505 (1998).
34. G.I. Primenko, V. I. Strizhak, I. D. Chikai, and T. Starichkai, " Ways of Increasing Yield and Flux Stability for 14 MeV Neutrons", Izv. Vuzov. Fiz. **31** (5), 17–31 (1988).
35. J.M. Verbeke, K.N. Leung, and J. Vujic, "Development of a Sealed-Accelerator-Tube Neutron Generator", Applied Radiation and Isotopes **53**, 801–809 (2000).
36. H. Daniel and Yu. V. Petrov, "Subcritical Fission Reactor Driven by the Low Power Accelerator", Nucl. Instr. Meth. A **373**, 131 (1996).
37. R. Eiveri, in *2nd Intern. Conf. on Peaceful Use of Atomic Energy*, Fiz. Yad. Reaktorov **3**, 321–340 (1959).

38. V.F. Kolesov and B. Ya. Guzhovskii, Atomnaya Energiya **76** (1), 71 (1994).
39. V.A. Babenko, L.L. Jenkovszky, V.N. Pavlovych, and E.A. Pupirina, "Subcritical Neutron Amplifier Based on Enriched Uranium", Voprosy Atom. Nauki Tekhniki, Ser. Fiz. Radiatsion. Povrezhdenii Radiatsion. Materialoved. **6**, 13–48 (2002).
40. V.A. Babenko, L.L. Jenkovszky, V.N. Pavlovych, and E.A. Pupirina, "Study of One-Zone Subcritical Amplifiers of Neutron Flux Involving Enriched Uranium", Problems of Atom. Sci. Technology **6**, 122–126 (2005).
41. V.A. Babenko, V.I. Gulik, V.N. Pavlovych, and E.A. Pupirina, in *Proc. of Intern. Conf. on Research Reactors in XXI Century* (NIKIET, Moscow, 2006).
42. H.I. Kyavitskaya et al., in *Nuclear Science and Safety in Europe*, Ed. by T. Cechak, L. Jenkovszky, and Yu. Karpenko (Springer, London, 2006), p. 265.
43. V.N. Shvetsov et al., in *AccApp-05, Venice, 2005* (Elsevier Science, 2005); W. Gudowski et al., in *AccApp-05, Venice, 2005* (Elsevier Science, 2005).
44. S.B. Vorozhtsov and N.G. Shakun, JINR-P9-658 report (Dubna, 1983).
45. L.P. Feoktistov, "Neutron-initiated Fission Wave", Dokl. AN SSSR **309** (4), 864–867 (1989).
46. L.P. Feoktistov, "Safety: The Key to Revitalization of Nuclear Energetics", Usp. Fiz. Nauk **163** (8), 89–102 (1993) [Phys.-Usp. **36**, 733 (1993)].
47. V. Ya. Gol'din, Yu. V. Troshchiev, and G.A. Pestryakova, "On the Control of a Fast Reactor in a Type-II Self-Adjustable Regime", Dokl. RAN **369** (2), 170–172 (1999).
48. E. Teller, "Nuclear Energy for the Third Millennium", Preprint No. UCRL-JC-129547, LLNL (1997).
49. V. Ya. Gol'din and D. Yu. Anistratov, "Fast Neutron Reactor in Self-Adjustable Neutron-Nuclear Regime", Mat. Modelir. **7** (10), 12–32 (1995).
50. V. Ya. Gol'din, G. A. Pestryakova, Yu. V. Troshchiev, and E. N. Aristova, Atom. Energiya **94** (3), 184–190 (2003).
51. S. Fomin, Yu. Melnik, V. Pilipenko, and N. Shulga, Ann. Nucl. Energy **32**, 1435–1456 (2005).
52. S. Fomin, Yu. Melnik, V. Pilipenko, and N. Shulga, Probl. of Atom. Sci. Technol. Ser. Nucl. Phys. Invest. **45** (6), 106–113 (2005).
53. H. Van Dam, Ann. Nucl. Energy **30**, 1495–1504 (2003).
54. C. Xue-Nong and W. Maschek, Ann. Nucl. Energy **32**, 1377–1390 (2005).
55. V.M. Pavlovych, V.M. Khotiaintsev, and O.M. Khotiaintseva, "The Physical Bases of the Fission Wave Reactor. I, II.", Nuclear Physics and Atomic Energy **2(24)**, 39–49 (2008), **4(26)** (2008).
56. A.I. Volpert, V.A. Volpert, and V.A. Volpert, *Traveling Wave Solutions of Parabolic Systems* (Am. Math. Society, Providence, R.I., 2000).

Development of Methods for Simulation of Electronuclear Processes

A. Polański

Abstract Cascade Evaporation Model and Quantum Molecular Dynamic (QMD) model for the description of the spallation reaction is presented in this paper. The Monte Carlo code CASCADE based on cascade evaporation model [1] was prepared for the calculation of inelastic hadrons–nucleus and nucleus–nucleus interactions at energies from several tens of MeV up to several tens of GeV and for modelling of nuclear–physical processes accompanying the transport of particles and nuclei in matter. The QMD model coupled with Generalized Evaporation Model was applied for the description of fission nuclei production in p+U interactions and for a description of neutrons and isotopes production in p+Pb reactions at energies from a few MeV to a few hundred MeV. A good reproduction of the data has been reached. The spectrum of particles and residual nuclide mass and charge distributions in reactions of protons and neutrons with heavy targets (Pb, U) were calculated using these models. On the basis of the Monte Carlo CASCADE and QMD codes the neutron spectra and isotope production in target were calculated and compared with experimental data.

Keywords: Nuclear physics, heavy ions, hadrons, spallation source, quantum molecular dynamic, cascade-evaporation, neutron spectra, isotope production, accelerator driven system

1 Introduction

Data on nuclear reactions at the energies of hundred MeV and GeV are required for multiple purposes such as long-lived radioactive waste transmutation, material analysis and isotopes production. Experiments on measuring the data are costly and

A. Polański
The A. Soltan Institute for Nuclear Studies, 05-400 Otwock-Swierk, Poland,
e-mail: polanski@ipj.gov.pl

V. Begun et al. (eds.), *Progress in High-Energy Physics and Nuclear Safety*,

there are a limited number of facilities to make them. Therefore, reliable computer models for a simulation of the reactions are created to provide the necessary data. Most of them are using the ideas of the cascade-evaporation model [1–6]. At low energies (less than 250 MeV) the particle production is not a dominant mechanism and potential interaction becomes more important. In this region the Quantum Molecular Dynamic Model (QMD model) is used.

2 Development of quantum molecular dynamic model

It is assumed by many authors that the Quantum Molecular Dynamic Model (QMD model) [7] can be used for calculations of hadrons and ions interactions with nuclei. These are the Quantum Molecular Dynamics model [7] and the Quasi-Particle Dynamics (QPD) model [8]. These models simulate the reactions on an event-by-event basis and in consequence preserve the N-body correlations and fluctuations.

In the QMD model each nucleon (or quasi-particle) is assumed to be a constant width minimal wave packet (coherent state):

$$\psi_i(\mathbf{r},t) = \frac{1}{(2\pi L)^{3/4}} e^{-\frac{(\mathbf{r}\mathbf{r}_{0i}(t))^2}{4L}} e^{-\frac{i}{\hbar}\mathbf{p}_{0i}(t)\mathbf{r}},$$

where $\mathbf{r}_{0i}$ and $\mathbf{p}_{0i}$ are the mean position and momentum of the nucleon i, and the width of the wave packet is characterized by the parameter L. The N-body "wave function", ψ_N, describing the entire nucleus is taken to be a direct product of N single particle states ψ_i. This, of course, is a violation of the anti-symmetry rules. Here it is assumed that the fermionic effects, which are believed to be essential for the reasonable treatment of the dynamics, can be simulated with the use of an effective potential term (Pauli potential) and with Pauli blocking of final states of individual NN collisions. The Pauli potential plays an important role during initialisation of a cold nucleus. It prevents the nucleons of the same kind from being too close in phase space.

The quantum mechanical analogue of a classical N-body phase space density distribution function is a Wigner transform of the density matrix [9, 10].

$$f^{(N)}(\mathbf{R}_1\mathbf{R}_2,\ldots,\mathbf{R}_N,\mathbf{p}_1,\mathbf{p}_2,\ldots,\mathbf{p}_N) =$$

$$= \frac{1}{(\pi\hbar)^{3N}} e^{-\frac{1}{2L}\sum_{k=1}^{N}(\mathbf{R}_k-\mathbf{r}_{0k})^2-\frac{2L}{\hbar^2}\sum_{k=1}^{N}(\mathbf{p}_k-\mathbf{p}_{0k})^2}.$$

The one-body densities in coordinate and momentum space look like:

$$\rho(\mathbf{r}) = \int f(\mathbf{r},\mathbf{p})d^3p = \frac{1}{(2\pi L)^{3/2}} \sum_{i=1}^{N} e^{-\frac{1}{2L}(\mathbf{r}-\mathbf{r}_{0i})^2},$$

$$g(\mathbf{p}) = \int f(\mathbf{r},\mathbf{p})d^3r = \left(\frac{2L}{\pi\hbar^2}\right)^{3/2} \sum_{i=1}^{N} e^{-\frac{2L}{\hbar^2}(\mathbf{p}-\mathbf{p}_{0i})^2}.$$

The time evolution of the N-body "wave function" describing the entire system is governed by the Ritz variation principle [7]. In fact it reduces to the classical Hamilton equations of motion for the centroids of the Gaussian wave packets. Thus the mean positions and momentum of N nucleons are assumed to evolve due to mutual two and three body effective NN interactions along classical trajectory in phase space. The influence of the scattering term on the time evolution of the system is simulated by a Monte Carlo procedure. Whenever two nucleons come closer than the distance determined by the NN cross section they are assumed to scatter isotropic ally, provided the final states are not blocked. Only the elastic channel of the NN scattering is assumed (no gamma or particle production is implemented). This, together with the fact that the non-relativistic kinematics is used, the upper limit of the incident energies sets to about 150 MeV/nucleon.

The total N-body Hamiltonian has the form:

$$H = \sum_{i=1}^{N} \frac{p_{0i}^2}{2m} + U_N + U_P + U_C,$$

where U_N is the nuclear potential energy, U_P is the total energy arising from the "Pauli interaction", and U_C - the Coulomb energy of the system.

$$U_N = \int V_N \, d^3r \simeq \frac{\alpha}{2\rho_0} \sum_{i=0}^{N} \sum_{\substack{k=1 \\ k \neq i}}^{N} \tilde{\rho}_{ik} + \frac{\beta}{(\gamma+1)\rho_0^{\gamma}} \sum_{i=1}^{N} \left(\sum_{\substack{k=1 \\ k \neq i}}^{N} \tilde{\rho}_{ik} \right)^{\gamma} +$$

$$+ \frac{\omega}{2\rho_0} \sum_{i=0}^{N} \sum_{\substack{k=1 \\ k \neq i}}^{N} \xi_i \xi_k \tilde{\rho}_{ik} + \frac{G}{8L^2} \sum_{i=0}^{N} \sum_{\substack{k=1 \\ k \neq i}}^{N} (6L - r_{ik}^2) \tilde{\rho}_{ik},$$

$$\xi_i = \begin{cases} +1 \text{ for protons} \\ -1 \text{ for neutrons,} \end{cases}$$

where the last term accounts for the surface effects, the third one for symmetry energy. The two first terms are analogous to that in the Skyrme parameterisation of the nuclear potential energy density,

$$U^{\text{loc}}(\rho) = \alpha \left(\frac{\rho}{\rho_0} \right) + \beta \left(\frac{\rho}{\rho_0} \right)^{\gamma},$$

$$U_P = \frac{1}{2} V_0^P \frac{\hbar^2}{16mL^2} \sum_{i=0}^{N} \sum_{\substack{j=1 \\ j \neq i}}^{N} \frac{Q_{ij}^2}{e^{\frac{1}{4L} Q_{ij}^2} - 1} \delta_{t_i t_j} \delta_{s_i s_j},$$

$$Q_{ij}^2 = (\mathbf{r}_{0i} - \mathbf{r}_{0j})^2 + \frac{4L^2}{\hbar^2} (\mathbf{p}_{0i} - \mathbf{p}_{0j})^2,$$

where the Kronecker deltas ensure that the potential acts between like quasi-particles only. The scale factor $V_0^P > 1$ was introduced in order to reproduce the energies of three- and higher-body systems. Its value was found to be between 1.7 and 1.9 [8].

The Coulomb potential for Gaussian charge distribution can be expressed in terms of the error functions:

$$V_C^{ij} = \frac{e^2}{r_{ij}} \operatorname{erf}\left(\frac{r_{ij}}{2\sqrt{L}}\right),$$

$$r_{ij} = |\mathbf{r}_{0i} - \mathbf{r}_{0j}|,$$

$$U_C = \frac{1}{2} e^2 \sum_{i=0}^{N} \sum_{\substack{j=1 \\ j \neq i}}^{N} V_C^{ij} \left(\frac{1}{2} + t_{3i}\right) \left(\frac{1}{2} + t_{3j}\right),$$

where the last two factors exclude neutrons from the summation.

The relationship between the binding energy per particle of nuclear matter, *E/A*, and the single particle potential $U^{\mathrm{loc}}(\rho)$ is not as straightforward as one might at first guess. For the Skyrme parameterisation and density dependence of the Fermi gas momentum one obtains:

$$\frac{E}{A} = \frac{3p_F^2(\rho)}{10m} + \frac{\alpha}{2}\left(\frac{\rho}{\rho_0}\right) + \frac{\beta}{1+\gamma}\left(\frac{\rho}{\rho_0}\right)^{\gamma}.$$

The above relation i.e. the density dependence of the energy per particle in nuclear matter at temperature $T = 0$ is often referred to just as the EOS.

The compressibility constant, *K* (often also referred to as incompressibility) may be defined as a second derivative of the energy per particle with respect to the density taken at the saturation point (see e.g. [11, 12]):

$$K \equiv 9\rho^2 \frac{\partial^2 E/A}{\partial \rho^2}\bigg|_{\rho=\rho_\circ}.$$

Using now the value of nuclear matter binding energy per nucleon, $E/A = -15.48$ MeV, and applying the stationary condition at the saturation point, one can express t α, β and γ parameters as a function of *K* only.

The exact value of the nuclear matter compressibility constant is still unknown. For the hard EOS with the nuclear matter compressibility $K = 380$ MeV the parameters α, β and γ are [13]: $\alpha = -124$ MeV, $\beta = 70.5$ MeV and $\gamma = 2$. And for the soft EOS with $K = 200$ MeV: $\alpha = -356$ MeV, $\beta = 303$ MeV and $\gamma = 7/6$.

The time evolution of the centroids of the Gaussian wave packets is described by two processes: the propagation due to classical equation of motion and the stochastic short range two body scattering. The equations of motion:

$$\begin{cases} \dot{\mathbf{r}}_{0i} = \frac{\mathbf{p}_{0i}}{m} + \boldsymbol{\nabla}_{p_{0i}} U, \\ \dot{\mathbf{p}}_{0i} = -\boldsymbol{\nabla}_{r_{0i}} U, \end{cases} \qquad i = 1, \ldots, A_P + A_T,$$

The equations of motion are solved numerically with the use of the two steps Euler method of the second accuracy order:

$$\text{(I)} \quad \begin{cases} \mathbf{r}_{0i}\left(n+\frac{1}{2}\right) = \mathbf{r}_{0i}(n) + \frac{\Delta t}{2}\left(\frac{\mathbf{p}_{0i}(n)}{m} + \nabla_{\mathbf{p}_{0i}} U(n)\right) \\ \mathbf{p}_{0i}\left(n+\frac{1}{2}\right) = \mathbf{p}_{0i}(n) - \frac{\Delta t}{2}\nabla_{\mathbf{r}_{0i}} U(n) \end{cases}$$

$$\text{(II)} \quad \begin{cases} \mathbf{r}_{0i}(n+1) = \mathbf{r}_{0i}(n) + \Delta t\left(\frac{\mathbf{p}_{0i}(n+\frac{1}{2})}{m} + \nabla_{\mathbf{p}_{0i}} U(n+\frac{1}{2})\right) \\ \mathbf{p}_{0i}(n+1) = \mathbf{p}_{0i}(n) - \Delta t \nabla_{\mathbf{r}_{0i}} U(n+\frac{1}{2}). \end{cases}$$

During the evolution any two nucleons become candidates for scattering if their spatial distance is less than the distance determined by the *NN* cross. Now, the possible new moment are determined assuming isotropic scattering. The collision is allowed if the new states are not already occupied by the any nucleons. Otherwise the collision is blocked and the two nucleons continue their movement in the effective potential. Thus the scattering probability is proportional to the effective (i.e. Pauli corrected) *NN* cross section.

After a specified time (100–200 fm/c) the dynamical evolution is stopped. Now a cluster search routine is called. It is assumed that all nucleons, which are separated in the configuration space by less, then $d = 3$ fm form a single cluster. Each cluster has then assigned a mass number, atomic number, CM position, linear momentum, binding energy, temperature and spin. The binding energy allows for later determination of the excitation energy.

We incorporated evaporation model for calculations of the second stage of nuclear interaction. The results for fast stage of nuclear interactions (QMD model without evaporation) and with second stage of reaction (QMD with evaporation) are presented on Fig. 1.

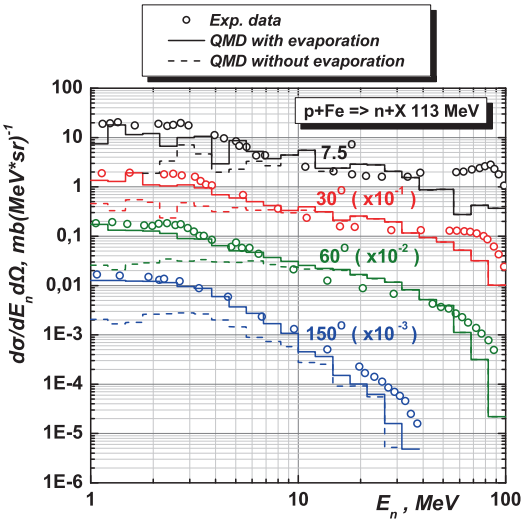

Fig. 1 Comparison of the experimental data on cross sections for neutron production with calculations using QMD model with and without evaporation

As one can see from Fig. 1 reaction cross sections calculated in QMD + evaporation model agree quite with experimental data.

There is a lot of programs implementation of the QMD model. They are different in the parameters values, in the preparation of the nuclei in the ground states (an important ingredient of the QMD calculation is how to determine the initial phase space distribution of the projectile and target nucleons), in the NN-collision scattering amplitude, and so on. We mark only some of them.

For the first time neutron emission in p-induced reactions at incident energies of 80–160 MeV within the framework of the QMD model was analysed in the paper [14]. The calculations showed a characteristic transition from weak neutron energy dependence at forward angles to an almost exponential shape at backward angles. The author conclusion was that the failure of the pre-equilibrium models to describe the angular dependence of the data is due to the neglect ion of second- and higher-order collisions.

In Ref. [15] the model was incorporated with the statistical decay model to account for hot fragment relaxation, and a good description of (*N, xN'*) reactions has been reached at energies from 100 MeV to 3 GeV. A unified description of the three major reaction mechanisms, i.e., compound, pre-equilibrium, and spallation processes, has been given. The main assumption of the authors was that the whole reaction process could be divided into two parts, i.e., the dynamical process and the statistical process, which is quite ordinary at high-energy simulations. In order to treat reactions with high bombarding energies, the authors included the nucleon, deltas (Δ (1,232), N^*(1,440))'s and pions with their isospin degree of freedom.

More detailed study of the pre-equilibrium decay was presented in Ref. [16]: the stepwise contributions to the angular distribution, comparisons with the FKK theory, and the effects of momentum distribution and surface refraction/reflection to the quasi-free scattering. A good reproduction of the measured (*p, xp'*) and *p, xn*) angular distributions has been reached in the energy region from 90 MeV to 200 MeV due to account of the Fermi motion of target nucleons, the refraction of projectile and ejective, and contribution from the multi-step processes.

Analysis of proton-induced fragment production in the QMD model coupled with the statistical decay model was given in Ref. [17]. The calculated results were compared with experimental data in the energy region from 50 MeV to 5 GeV. It was shown that the model could reproduce the production cross sections of the light and intermediate-mass to heavy fragments in a good accuracy. The analogous was done in Ref. [18].

At last, an improved QMD model has been proposed for a description fusion reaction near barrier [19].

There is a Lorentz-covariant extension of the QMD, dubbed relativistic quantum molecular dynamics (RQMD), proposed by H. Sorge et al. [20], and based on the Poincare-invariant constrained Hamiltonian dynamics. It is very popular in high-energy physics. The new modern version of the QMD model is the Ultra Relativistic Quantum Molecular Dynamic (UrQMD) model [21] proposed for simulation of heavy ion collisions in the energy range from SPS to RHIC.

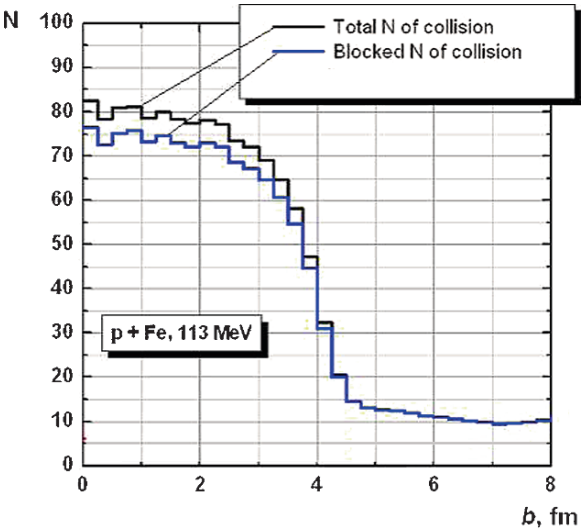

Fig. 2 Dependence of number of collisions on impact parameter

Usually the authors of the papers have omitted details of their calculations what are quite important for practical applications. We consider some of them.

The first point is a choice of allowed region of impact parameter. According to Fig. 2 at large impact parameters nearly all binary collisions are blocked. So, no ejected nucleons are presented in peripheral reactions, as it must be. If one is interesting in inelastic reactions, the natural choice of b is when $N_{\text{tot}} > N_{\text{blocked}}$. At this value a correct reaction cross section can be obtained.

Evolution time depends on many conditions. First of all, it is determined by the putting of the incident proton in the initial state. Usually at chosen impact parameter the proton is placed in distance of 3 fm from nuclear surface. After that the system evolution starts. One can obtain various final states depending on the evolution time. If the time is short, the nuclear system will not be in the equilibrium state. If the time will be longer, this will waste the computational time. Thus an optimal choice of the time is needed. In many papers the time is chosen in the range 100–200 fm/c.

According to Fig. 3, 150 fm/c is a time when the neutron spectra become stable. It is obvious that the time depends on nuclear properties, and because the nuclear density is nearly equal for all nuclei, the time does not depend on nuclear mass number.

The time step of integration is another important quantity. At first glance, it seems that the step is determined by the requested accuracy. But at integration step a check is made on possible binary collisions. If the step will be small, there will be many possible and real collisions between the same pair of nucleons. Due to this multiple collisions the effective scattering becomes isotropic one, though in free *NN* interactions it has been chosen as anisotropic one. This can reflect on the neutron spectra at large energies at forward angles. In typical calculations the step was equal to 0.5 fm/c. In Fig. 4 we show calculations with standard step (histograms), and with

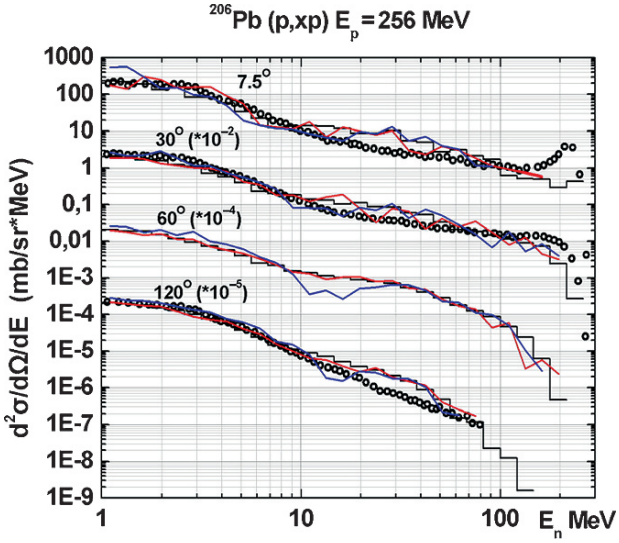

Fig. 3 Dependence of the neutron spectra on evolution time. Points – experimental data, histograms – calculations at $t = 100$ fm/c, lines – calculations at t equal 50 and 150 fm/c

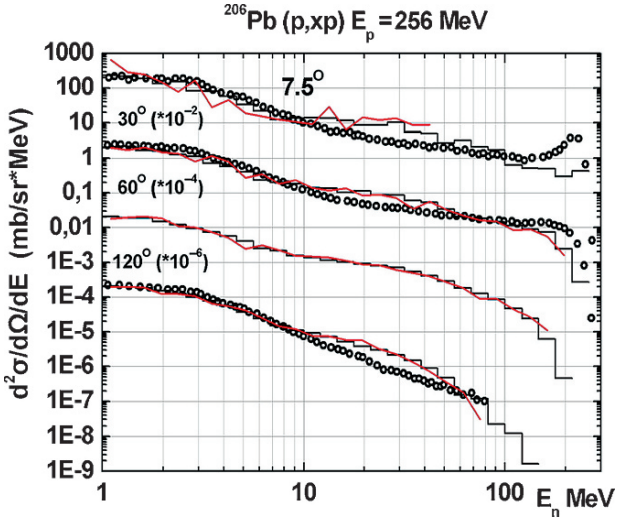

Fig. 4 Dependence of the neutron spectra on time step

the step reduced twice (line). As one can see, there is not a big difference between the calculations. Though the question about elimination of the artificial collisions need a more careful consideration.

At the end of the evolution needs to determine the mass number and charge of the residual nucleus or nuclear fragments. Usually it is assumed that two nucleons belong to the same nuclear fragment, if they are on the distance r_c shorter then

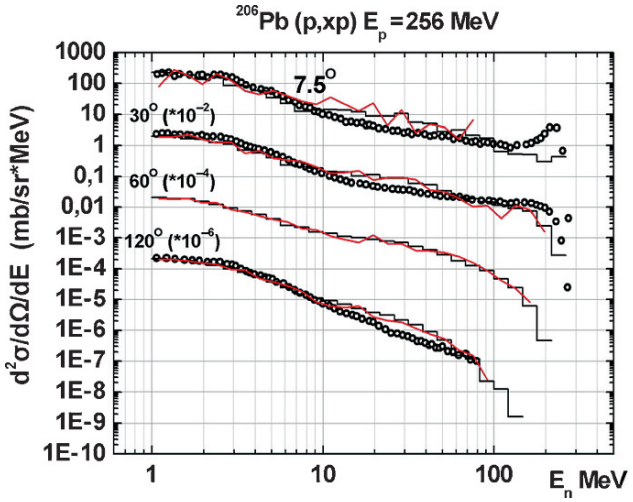

Fig. 5 Dependence of the neutron spectra on the r_c. Histograms are the calculations with $r_c = 3$ fm, red lines – with $r_c = 4$ fm

2–3 fm. The distance can not be smaller than the average distance between the nucleons in the cold nuclei. At the same time, it can not be large than the effective nucleon forces radius. The neutron spectra in hadron–nucleus reaction have a week dependence on the parameter. In Fig. 5 we show the calculations with different values of r_c. In the case of nucleus–nucleus interactions it is quite heavily to choose an appropriate value of r_c.

Summing up, we conclude that QMD model calculations for proton–nucleus reactions are rather insensitive to the model parameter.

3 Calculations of neutron and isotope production cross sections

Figure 6 shows results of calculations neutron cross sections using QMD and Cascade model. As we can see at Fig. 6, we have good agreement between QMD, Cascade and experimental data.

Figure 7 shows mass distributions of products from p(100 MeV) + ^{238}U, calculated with the combined version of QMD + evaporation compared to the available experimental data [22]. All the experimental data shown in Fig. 7 were obtained by the -spectrometry method. Only some of the produced isotopes were measured. As presented at Fig. 7 it is good agreement between results of calculation and experimental data [22]. Isotope production cross section was calculated at the time of evolution 200 fm/c and it is a time when the production of isotopes becomes stable.

The proton-induced Bi isotopes production in the natural lead target was calculated. The calculated results were compared with experimental data [23, 24].

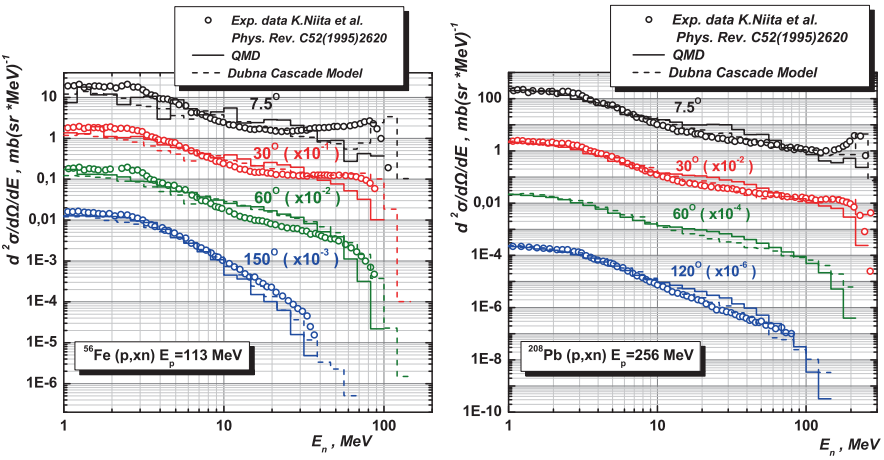

Fig. 6 Comparison of the experimental data on cross sections for neutron production [15] with calculations using QMD model and Cascade model with evaporation

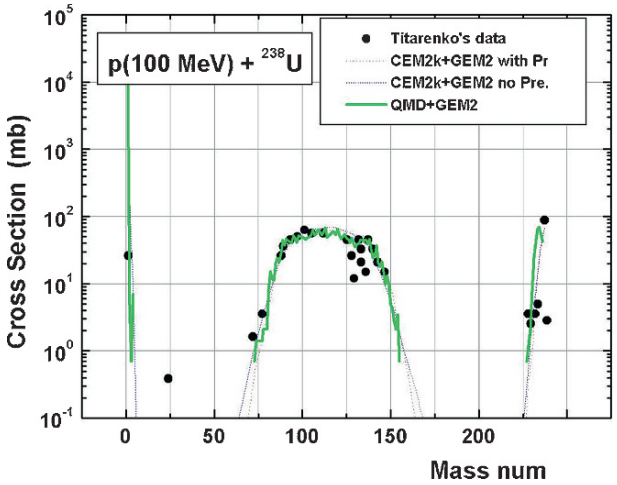

Fig. 7 Fragment mass distribution in p+^{238}U at 100 MeV

As shown at Fig. 8 we did not find peak of production cross sections in experiment data.

In Fig. 9 example of excitation functions for the production of ^{205}Bi is presented [25].

As presented at Fig. 9 the gross features of ^{205}Bi production cross-section at energies below 100 MeV is reproduced quite satisfactory. At higher energies more dynamical effect must be taken into account (cascading, π-meson production and so on). Analogous results were obtained for production of other isotopes of Bi.

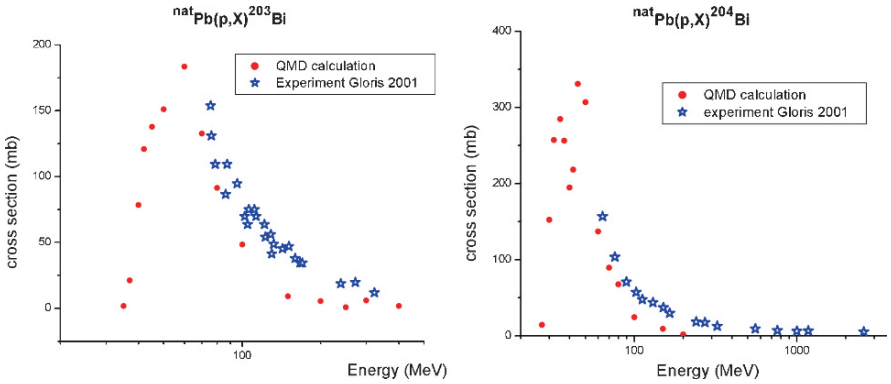

Fig. 8 ^{203}Bi and ^{204}Bi production cross section in p+Pb(nat) reaction

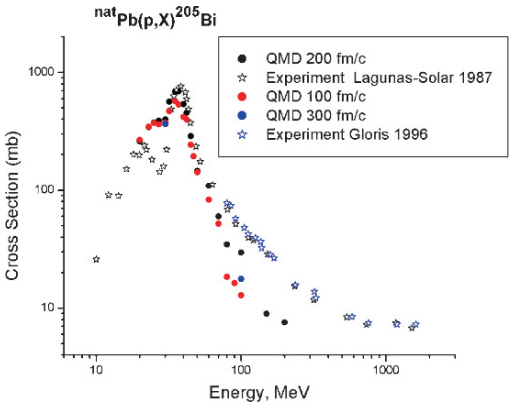

Fig. 9 ^{205}Bi production cross section in p+Pb(nat) reaction

4 Experiments on lead target

The series of experiments on lead target were performed in JINR Dubna using a 660 MeV proton beam [26–28]. The experimental target was assembled from the cylinders of natural lead. The geometry of target is presented on Fig. 10.

Target was built of several pieces of 5 cm and 1 cm thick cylindrical parts of 8 cm in diameter. The target was enclosed in a 1.5 mm thick stainless steel cylinder. Samples were placed along the lead target as presented in Fig. 10. That way we reproduced the spatial distribution of proton induced activity. In that experiment 31 pieces of 1 mm thick lead and bismuth samples were used. All parts of the target were irradiated and then the samples were counted with the use of HPGe coaxial detector. For quantitative evaluation some nuclides were selected from the ones with the identified lines in the measured y-spectra. These way axial distributions inside the lead target were obtained. In paper [28] is shown experimental and calculated data of spatial distribution of polonium produced in massive lead target irradiated

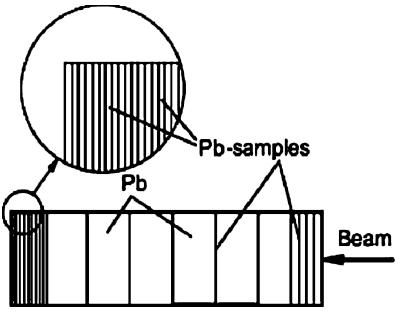

Fig. 10 Geometry of experiment and schematic view and Pb sample location

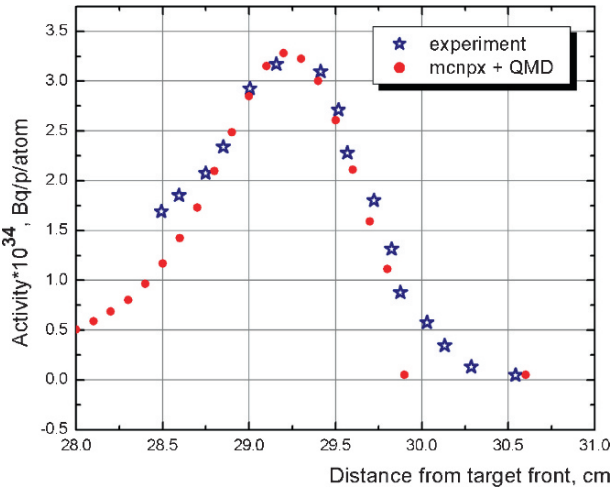

Fig. 11 Spatial distribution of ^{205}Bi production in lead target. Results of the calculations and experiment

by 660 MeV protons. In this paper we present results of calculation of spatial distribution of bismuth produced in lead samples placed in lead target.

We calculated the production of the following isotopes: ^{203}Bi , ^{204}Bi and ^{205}Bi. Two steps were applied in calculations of the induced activity: First by calculations Bi isotopes production cross sections using QMD model. Second by calculations spatial distribution of isotopes in target by using Cascade transport code [29]. The results of experiments and calculations of ^{205}Bi is presented at Fig. 11.

One can observe the results of simulation (QMD+ Cascade codes) in good agreement with the results obtained in experiment.

Activity of Bi isotopes inside the target, reached its peak at about 40 MeV near the end of the proton range in the lead. It results from the changing proton energy to 40 MeV in the end of the lead target. As we can see from Fig. 9 the maximum cross sections is for energy 40 MeV. On the basis of the presented models we calculated Accelerator Driven System (ADS) with 660 MeV proton accelerator and MOX subcritical assembly [30].

5 Conclusion

In the field of application of accelerators, such as spallation neutron sources, accelerator-based transmutation system, and shielding, the productions of neutrons and isotopes play an important role. The QMD code (QMD+ evaporation model) and Cascade code (Cascade model with evaporation and hadrons transport) can be successfully applied for these tasks. The QMD model includes, in a self-consistent way, many important aspects in understanding of the nucleon-induced reaction mechanisms at intermediate energy range, i.e., entrance/exit channel refraction, Coulomb deflection, variation of the mean-field potential, transition between unbound and bound states, energy-dependent, anisotropic *NN* elastic and inelastic scattering including the Pauli-blocking effect, and so on.

References

1. A. Polański, B. Slowinski and A. Wojciechowski, Particles and Nuclei, Letters, **3**(139), 417–427 (2007).
2. N.W. Bertini et. al., Phys. Rev. C **9**, 522 (1974).
3. N.W. Bertini et. al., Phys. Rev. C **14**, 590 (1976).
4. J.P. Bondorf et. al., Phys. Lett. **65B**, 217 (1976).
5. J.P. Bondorf et. al., Zeit. fur Phys. A **279**, 385 (1976).
6. V.D. Toneev and K.K. Gudima, Nucl. Phys. A **400**, 173 (1983).
7. J. Aichelin, Phys. Rep. **202**, 233 (1991).
8. D.H. Boal, J.N. Glosli, Phys. Rev. C **38**, 1870 (1988).
9. M. Hillery, R.F. O'Connel, M.O. Scully and E.P. Wigner, Phys. Rep. **106**, 121 (1984).
10. P. Carruthers and F. Zachariasen, Rev. Mod. Phys. **55**, 245 (1983).
11. J.P. Blaizot, D. Gogny and B. Grammaticos, Nuc. Phys. A **265**, 315 (1976).
12. B.K. Jennings and A.D. Jackson, Phys. Rep. **66**, 143 (1980).
13. J. Aichelin et. al., Phys. Rev. C **37**, 2451 (1988).
14. O. Peilert et. al., Phys. Rev. C **46**, 1457 (1992).
15. K. Niita et. al., Phys. Rev. C **52**, 2620 (1995).
16. A. Chiba et. al., Phys. Rev. C **53**, 1824 (1995).
17. A. Chiba et. al., Phys. Rev. C **53**, 1824 (1995).
18. Fan Sheng et. al., Eur. Phys. J. A **4**, 61 (1999).
19. Ning Wang et. al., nucl-th/0201079 (2002).
20. H. Sorge, H. Stocker and W. Greiner, Ann. Phys. (NY) **192**, 266 (1989); Nucl. Phys. A **498**, 567 (1989).
21. Aichelin, J. Phys. Rep. 202–233 (1991)
22. Yu.E. Titarenko et al., LA-UR-01-5346, (2001).
23. M.C. Lagunas-Solar et. al., Applied Rad. Isotopes **38**, 129 (1987)
24. M. Gloris et. al. Nucl. Instr. Meth. B **113**, 429 (1996).
25. A. Polański, S. Petrochenkov, V. Uzhinsky and M. Baznat, Radiation Protection Dosimetry **115**, No.1-4, 131–132 (2005).
26. W. Pohorecki, T. Horwacik, J. Janczyszyn, S. Taczanowski, V.P. Bamblevski, S.A. Gustov, I.V. Mirokhin, A.G. Molokanov and A. Polański, Radiation Protection Dosimetry **115**, No.1-4, 630-633 (2005).
27. W. Pohorecki, J. Janczyszyn, S. Taczanowski, and A. Polański. *Measurements of production and distribution of radionuclides in the spallation target*. In: *Proc. PHYSOR 2002 Int. Conference on the New Frontiers of Nuclear Technology: Reactor Physics, Safety and High-Performance Computing*, Seoul, Korea, October 7–10, 34 (2002).

28. A. Polański, Proton Induced Reactions. Nucl. Instr. Meth. B **171**, 252–258 (2000).
29. A. Polański, A.N. Sosnin, V.D. Toneev, JINR Preprint E1-91-562, 1 (1991).
30. A. Polański. Acta Phys. Polonica B **11**, No.1, 95 (2000).

Simulation of Energy Deposition and Neutron Spectrum of Subcritical Assembly Irradiated with Proton Beam with MCNPX Transport Code

A. Polański, P. Zhivkov, and Ch. Stoynov

Abstract The neutron and proton spectra and the energy deposition at the Subcritical Assembly in Dubna (SAD) have been studied with the Monte Carlo code MCNPX. The subcritical reactor will be used for study of transmutation of nuclear waste and energy production. The energy deposition in the reactor and in the tungsten and lead target, i.e. in the direction of the incident proton beam was calculated. Neutron spectra by separating the radiation fields into a spallation-induced and a fission-induced part was calculated. It was shown that the neutrons with energy higher than 10 MeV, originating exclusively from the proton-induced spallation reactions in the target.

Keywords: accelerator driven systems for nuclear transmutation, spallation neutron source, neutron spectra, subcritical reactor

1 Introduction

In the SAD experimental set up [1, 2] at the Joint Institute for Nuclear Research in Dubna (JINR) the various concepts and the basic physical principles of accelerator-driven systems (ADS) [3, 4] were studied extensively. In these experiments, a 660 MeV proton accelerator is coupled to a subcritical core, loaded with fast reactor MOX (Mixed Oxide) fuel assemblies. The proton beam impinges of a target, which generates a large number of neutrons via spallation reactions. The produced spallation neutrons leak out from the target, thus providing the subcritical core with a strong external neutron source.

A. Polański
Soltan Institute for Nuclear Studies, 05-400 Otwock-Swierk, Poland,
e-mail: polanski@ipj.gov.pl

P. Zhivkov, Ch. Stoynov
Institute for Nuclear Research and Nuclear Energy, Bulgarian Academy of Science,
e-mail: peter_jivkov@yahoo.com

V. Begun et al. (eds.), *Progress in High-Energy Physics and Nuclear Safety*,

This work presents numerical simulations done by MCNPX transport code [5] for target optimization of a subcritical reactor. The aim of the simulations is to solve three problems. The first is the calculation and comparison of the total and fission energy deposition in the subcritical MOX set-up with the lead and tungsten target irradiated by a proton beam with an energy interval from 660 MeV to 1500 MeV. The second is the calculation of the neutron and proton fluxes and spectra in the Pb and W targets irradiated by a proton beam with an energy interval from 660 MeV to 1200 MeV. The third is the comparison of neutron spectra calculated by different models: the Bertini, [6, 7] the INCL [8] and the CEM [8].

2 Construction of SAD

The principle of construction of such subcritical assembly SAD is illustrated in Figure 1.

The proposed ADS facility consists of the 660 MeV protons accelerator, beam bending magnets, a spallation target with different materials, a subcritical core based on MOX fuel elements, reflectors, concrete shielding, control and auxiliary systems. The proton beam is transported vertically to the target through a vacuum track provided with a concrete shielding. The proton beam interacts with the lead or tungsten target. A blanket containing MOX fuel surrounds the target. The fuel is placed in a stainless steel vessel. A lead reflector and concrete shielding surround the core. The target and the fuel elements are cooled by air.

The fuel designed for the fast breeder BN-350 reactor will be adopted for the core of the assembly. The 18 fuel elements with external diameter equal to 6.9 mm are located in a hexagonal fuel assembles. The full length of a fuel element with its end details is about 70 cm, when the core length is 57 cm. The fuel element consists of fuel pellets diameter 5.95 mm with the plutonium and uranium oxides mixture ($0.297\ ^{239}PuO_2$+$0.703\ ^{nat}UO_2$). In the core would be maximum 141 fuel element assembles. The distance between the center of the fuel assembles is equal to 36 mm.

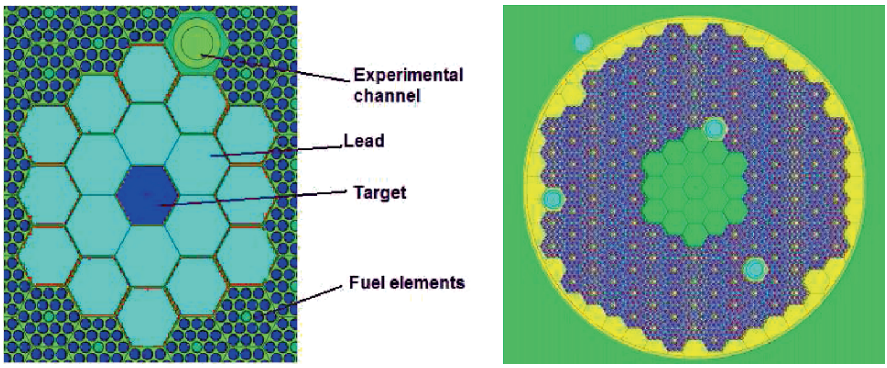

Fig. 1 Horizontal cross-section of the SAD Core: 138 fuel assemblies

3 Geometry of calculations

Geometry of calculations of a sub-critical reactor is presented at Fig. 2. It is a cylinder with a diameter of 185 cm and a length of 175 cm. The lead-tungsten target, MOX fuel, lead reflector, steel assembly with graphite layer are inside cylinder.

We calculated three kinds of targets. The first; target was a made of natural Pb, the second target was made of tungsten and the last target was multilayer made with tungsten and lead. Around the targets was lead (see Fig. 2). The length of target was from 30 cm to 80 cm and was depending on the proton beam energy. The diameter of target was 5 cm.

Geometry of targets is presented at Fig. 3.

For calculations of energy deposition and flux we used surface and volume detectors presented at Fig. 4. Surface detector is divided into small parallel cylinders (cells) with a length ranging from 1 mm to 10 mm and a diameter of 5 cm. For calculations of radial distribution all cylinders (cells) have the same length of 5 cm and a thickness of the wall of 1 mm, but the diameter changes from 2 mm to 50 mm.

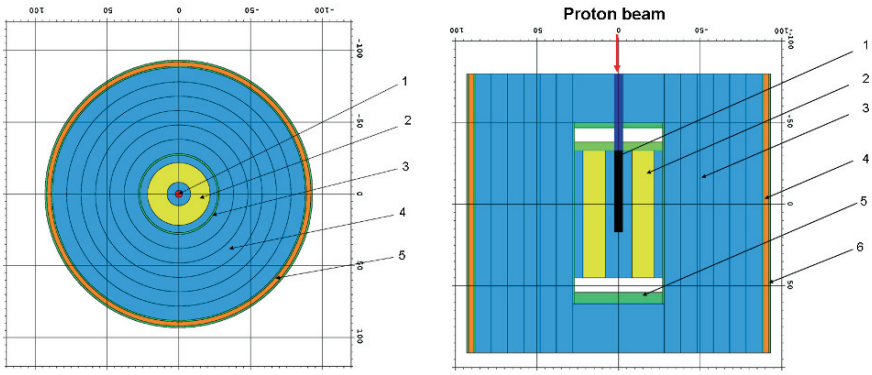

Fig. 2 Cross sections of calculated set up. 1 – Pb-W target; 2 – MOX fuel; 3 – lead reflector; 4 – graphite layer; 5 and 6 – steel. The arrow indicates the direction of the movement of a proton beam

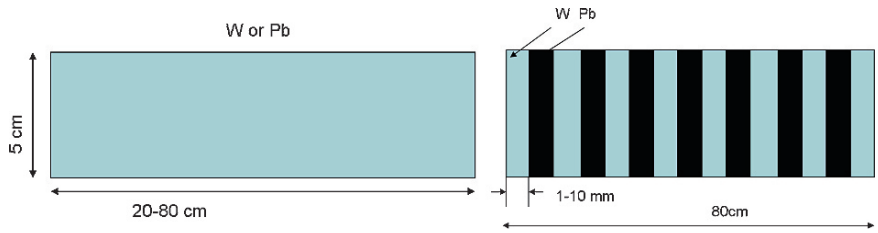

Fig. 3 Cross sections of targets: *Left* – Made of natural lead or tungsten. *Right* – Multilayer target made of layers of lead and tungsten

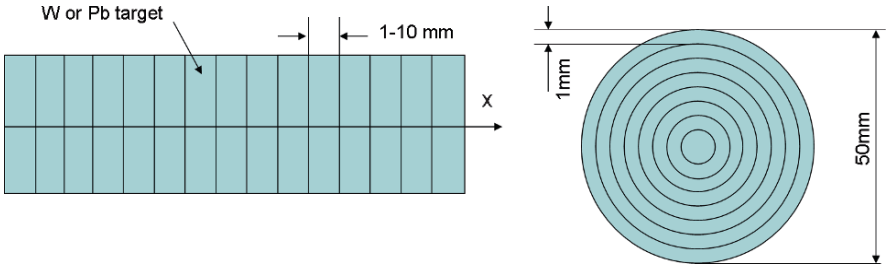

Fig. 4 Cross section of the surface and volume detectors. Target is divided into small parallel cylinders (cells) with a length and radius ranging from 1 mm to 10 mm

4 Results of simulations of energy deposition

The first step of the simulations is the optimization of the target, i.e. calculation of the total charged particles energy deposition E_{tot} and the fission energy deposition E_{fiss} in subcritical reactor. We used in the simulations proton beams with energies 660, 800, 1,000, 1,200, 1,500 MeV, interacting with heavy targets such as lead, tungsten, and the composition of Pb and W (see Fig. 3).

The experiments performed in different laboratories demonstrate that, lead and tungsten are very appropriate for a target because it has a high ratio of irradiated neutrons per proton. Some targets such us natural uranium or plutonium can generate more neutrons per proton than lead, but the activation of the U or Pu targets after irradiation can be higher than that of a lead target. If the proton beam has a high current [mA], the lead is going to melt (melting point 327° C), and this property of lead can be used for heat transportation in the sub-critical reactor system. However, tungsten has a high melting point ∼3,422° C and it is easier to remove some of the radio nuclides from the target or to remove part of the target itself (in case of slice Pb and W target).

At the beginning of the sub-critical reactor simulations the k_{eff} was calculated for all types of targets and proton beam energies and it has to be 0.98 for all cases. This value was achieved by changing the size of the Pb reflector. After that we calculated the E_{tot} and E_{fiss} by MCNPX 26c. We used a composite Pb-W multilayer target (see Fig. 3) and a proton beam with different energies. The results of these simulations are presented in Fig. 5.

We made simulations with targets of different lengths, materials and construction. This article presents some of our results. One of the most interesting cases is the calculation of E_{tot} for all slices in a composite Pb-W slice targets when they have been irradiated by different proton beams. The results are presented in Fig. 6. This graphs show the total energy deposition in all target cells per proton energy. The target was irradiated by protons with energies Ep = 660, 800, 1,000, 1,200 MeV. It is a slice target, a composition of Pb and W, which is 60 cm long and has a diameter of 5 cm. Each slice is 1 mm long and has a diameter of 5 cm.

The total energy deposition in target has two peaks – the spot where the total flux is maximum and the spot where the total proton absorption takes place (at the

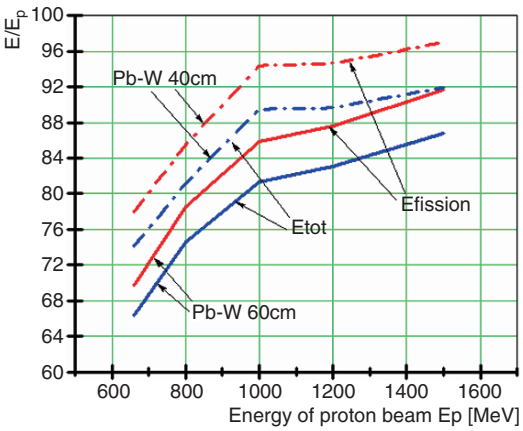

Fig. 5 Comparison of E_{tot} and E_{fiss} per proton in all cells at the sub-critical reactor. The target was irradiated by protons with energies Ep = 660, 800, 1,000, 1,200 and 1,500 MeV. The targets are 40 cm and 60 cm long and are composed of Pb and W slices of 1 mm each

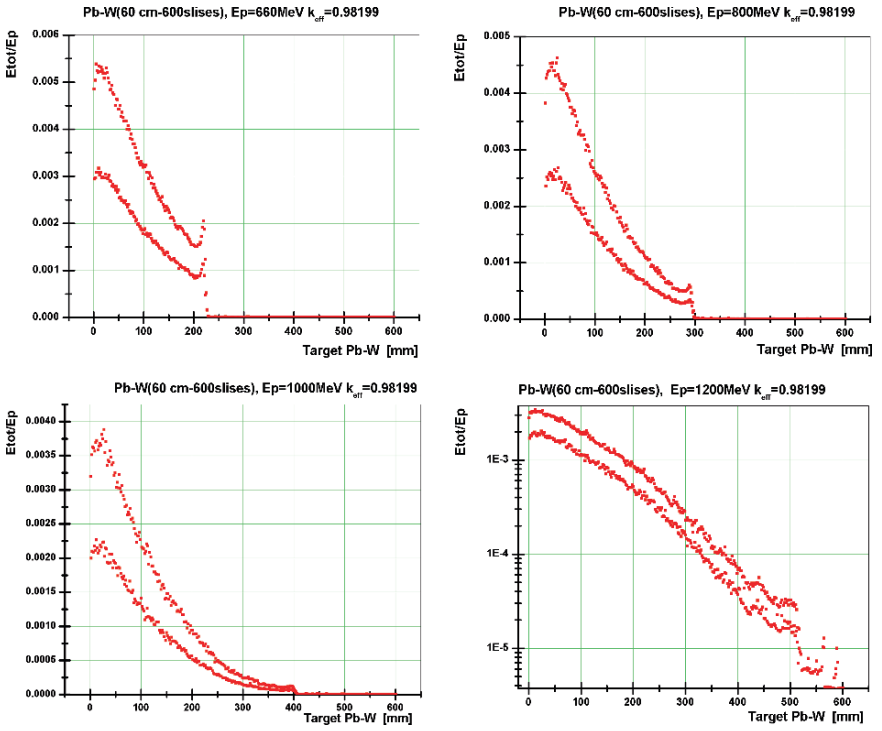

Fig. 6 The total energy deposition of charged particles in all target cells per proton energy. The target was irradiated by protons with energies Ep = 660, 800, 1,000, 1,200 MeV. Line 1 – energy deposition in tungsten slice, Line 2 – energy deposition in lead slice

end of the led target). It is results from the changing proton energy spectrum. At the end of the lead target the proton energy decreased where proton absorption cross section rose.

As we can see from Fig. 6 energy deposition (and activity) of tungsten is bigger than energy deposition for lead. It is connected with different density of materials. The macroscopic cross sections for absorption protons and neutrons are bigger for tungsten then for lead.

5 Neutron and proton fluxes and energy spectra

Secondly, we simulated irradiation of Pb or W targets by proton beams with energies 660, 800, 1,000, 1,200 and 1,500 MeV. The aim of these calculations was to optimize the positions of nuclear fuel in the sub-critical reactor or of nuclear waste transmutation samples by analyzing values such as the total neutron and the total proton flux in the targets, as well as the neutron and proton spectra in all parts of the targets. The simulations were organized in the following way: The targets were divided virtually into cylinders of equal size by parallel surfaces perpendicular to the target axis (Fig. 4). After that every cylinder was divided into concentric cylinders with the same length of 5 cm and wall thickness of 1 mm, but with different diameters ranging from 2 mm to 50 mm. Fig. 7a shows the total neutron flux and Fig. 7b shows the total proton flux over surfaces which were perpendicular to the proton beam. The tungsten target is long with L = 20 cm, D = 5 cm and irradiated by a proton beam with energy 660 MeV. The calculation is done by MCNPX 26.c (INCL-ABLA).

We analyzed the results obtained for the total neutron and proton fluxes for two targets – Pb and W – for all the proton beam energies mentioned above. The graphs of the total neutron flux as a function of the target depth and various energies of the proton beam demonstrate a shift of the spectra maximum. For the proton beams with energies 660, 800, 1,000, 1,200, 1,500 MeV the spectrum maximum is 34, 35, 39, 41 and 43 mm respectively for a Pb target, and 28, 29, 31, 33 and 35 mm respectively for a W target. The results for a proton flux maximum for the same energies of the

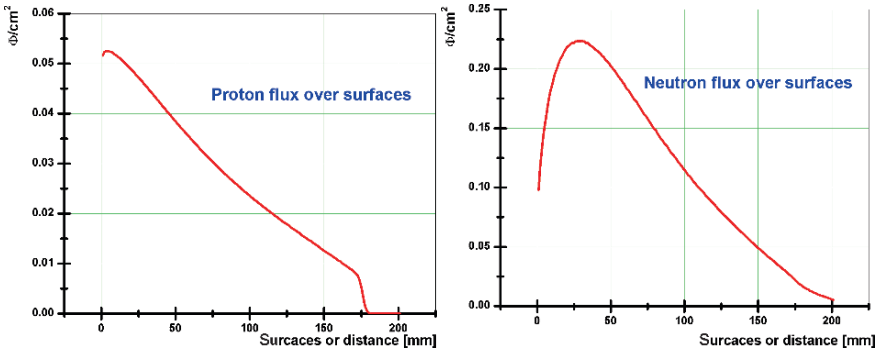

Fig. 7 (a) The total neutron flux over surfaces which are perpendicular to the proton beam. (b) The total proton flux over surfaces which are perpendicular to the proton beam

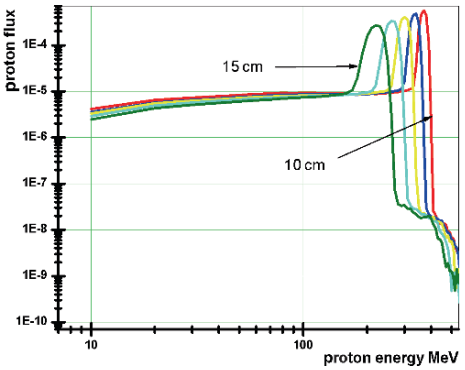

Fig. 8 The proton spectra in five cells from the 10th to the 15th over surfaces which are perpendicular to the proton beam

proton beam are present below: 7, 8, 10, 11 and 13 respectively for a Pb target, and 4, 6, 7, 8 and 10 mm respectively for a W target.

Figure 8 shows the proton spectra in five cells from the 10th to the 15th over surfaces which are perpendicular to the proton beam. The tungsten target is long with L = 20 cm, D = 5 cm and irradiated by a proton beam with energy 660 MeV. The calculation is done by MCNPX 26.c (INCL-ABLA).

The results for the proton and neutron spectra for each millimeter along the length of the target are obtained in the same way. These and some other results are still to be analyzed and the conclusions will provide us with a better picture of the neutron field inside and outside of the target. It is necessary in order to have a more exact spatial distribution of the nuclear fuel or the transmutation samples. What is important for the results and conclusions is to optimize the simulations. This includes duration of each simulation, results precision, physics parameters and calculation models (The Bertini, the INCL with ABLA, and the CEM).

Figure 9 presented the neutron spectra in two different points out of the Pb target in experimental channel (see Fig. 1) irradiated by E = 660 MeV a proton beam.

The energy spectrum of the detected neutrons out the lead target is typical for a high-energy proton beam. The shape of these spectra is generally characterized by an evaporation and fission shoulder around a few MeV and a high-energy spallation peak, which is indeed the case. The high-energy peak with a maximum at 30 MeV and about 150 MeV arises mainly from the neutrons that were emitted in the intranuclear cascade reactions in the spallation target. The major part of these high-energy neutrons, formed in direct head-on collisions between the incident source protons and the individual target nucleons, were emitted in the forward direction and have been transported through the target. The low energy neutrons comes from the spallation neutron induced fission reactions on the fissionable elements in the MOX fuel. The peak of evaporation-fission neutrons is located at about 2 MeV. The results of calculations of neutron spectra for low energy are different for different models. It is connected with different models of evaporation used for calculations.

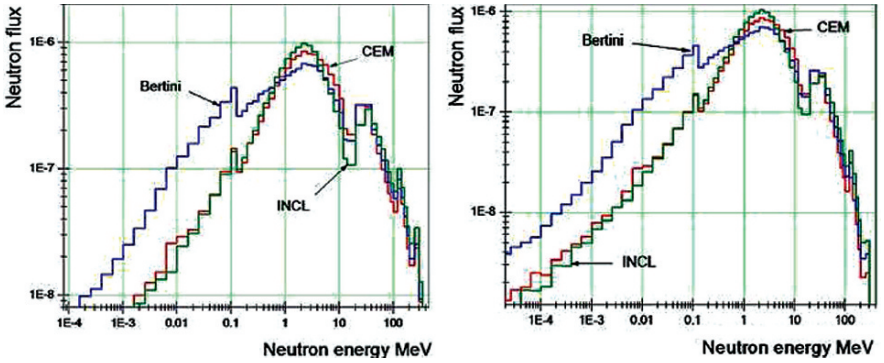

Fig. 9 The neutron spectra calculated in two different points out of the Pb target in experimental channel

6 Conclusions

The main objective of the present paper was to determine the energy deposition and neutron and proton flux in target and in subcritical core. The total energy deposition in target has two peaks – the spot where the total flux is maximum and the spot where the total proton absorption takes place (at the end of the led target). It results from the changing proton energy spectrum. At the end of the lead target the proton energy decreased where cross section for proton absorption rose. The high-energy neutrons created in the spallation process are deeply penetrating in subcritical core. The neutrons leaking out the target reached a peak at energy 2 MeV and energy 30 MeV. Neutrons with energy less then 2 MeV can be useful for reactions with fissile elements as the Uranium and Plutonium and high energy neutrons needs for fission of fissionable isotopes with threshold energy (e.g. 237Np, 241Am, 243Am and 244 Cm).

References

1. A. Polański. Monte Carlo Modeling of Electronuclear Processes in Experimental Accelerator Driven Systems. Acta Phys. Polonica, B **11**, No.1, 95 (2000).
2. A. Polański, S. Petrochenkov, V. Shvetsov, W. Gudowski, P. Seltborg. Power upgrade of the subcritical assembly in Dubna (SAD) to 100 kW. *Nucl. Instr. Meth. A Vol. 562, No 2, PP. 879–882 (2006)*.
3. W. Gudowski, V. Shvecov, A. Polański. The Subcritical Assembly in Dubna (SAD). Part II: Research program for ADS-demo experiment. *Nucl. Instr. Meth. A, Vol. 562, 887 (2006)*.
4. W. Gudowski, A. Polański, I.V. Puzynin and V. Shvetsov, "Monte Carlo modeling of a sub-critical assembly driven with the existing 660 MeV JINR Proton Accel-erator", Int. Meeting AccApp'01, November 11–15, 2001, Reno, Nevada, USA (2001).
5. L.S. Waters, "MCNPX^{TM}User's Manual – Version 2.1.5," Los Alamos National Laboratory, November 14, (1999).

6. H.W. Bertini, Phys. Rev. **131** 1801 (1963).
7. H.W. Bertini, Phys. Rev. **188** 1711 (1969).
8. S. Leray et al., "Spallation Neutron Production by 0.8, 1.2, and 1.6 GeV Protons on various Targets," Phys. Rev. C **65** (2002).

Spallation Neutron Energy Spectrum Determination with Yttrium as a Threshold Detector on U/Pb-assembly "Energy plus Transmutation"

S. Kilim, M. Bielewicz, E. Strugalska-Gola, M. Szuta, A. Wojciechowski, M.I. Krivopustov, A.D. Kovalenko, I. Adam, A. Krasa, M. Majerle, and V. Wagner

Abstract Results of two experiments with Yttrium-89 samples on U/Pb-assembly "Energy plus Transmutation" [1] are presented. The assembly is a lead cylindrical target (8.4 cm diameter, 45.6 cm length) with natural uranium blanket (206.4 kg). The lead target was irradiated with JINR Dubna NUCLOTRON with 1.60 and 2.52 GeV deuteron beam. The final purpose of the experiments was to measure neutron field inside the assembly. Yttrium-89 activation detectors were located throughout the entire U/Pb-assembly. Irradiated sample gamma activity was measured with HPGe spectrometer. The gamma spectra were analyzed and the net peak areas were calculated using the DEIMOS program [2]. After short presentation of the activation results neutron spectrum determination method is proposed and its results presented. Assuming reaction model through compound nucleus and using some mathematical tricks Yttrium isotope "*k*" production rate discrete formula

$$I_k = N \int_{E_{thr,k}}^{\infty} \varphi(E)\, \sigma_k(E, E_{thr})\, dE$$

was transformed into Volterra's integral equation of the first kind and then solved. The method and its applicability still to be discussed. The results as the preliminary ones are for illustrative purpose only.

Keywords: Spallation, neutron energy spectrum, Energy plus Transmutation

S. Kilim, M. Bielewicz, E. Strugalska-Gola, M. Szuta, A. Wojciechowski
Institute of Atomic Energy, 05-400 Otwock-Swierk, Poland,
e-mail: s.kilim@cyf.gov.pl

M.I. Krivopustov, A.D. Kovalenko, I. Adam
Joint Institute of Nuclear Research, 141980 Dubna, Russia

I. Adam, A. Krasa, M. Majerle, V. Wagner
Nuclear Physics Institute of CAS, 25068 Rez, Czech Republic

V. Begun et al. (eds.), *Progress in High-Energy Physics and Nuclear Safety*,

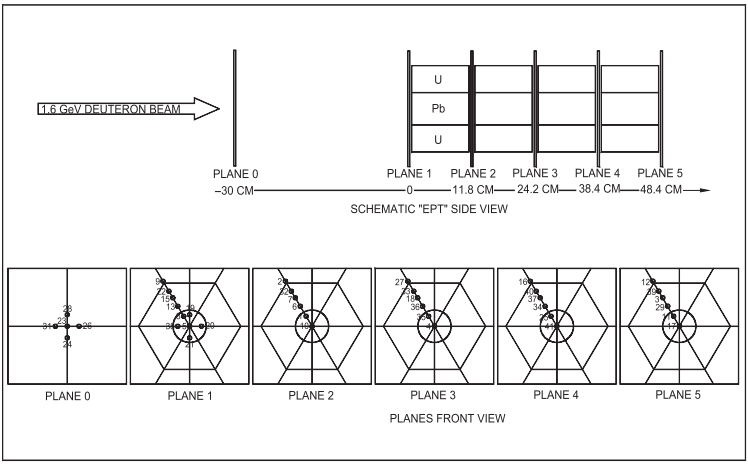

Fig. 1 "Energy plus Transmutation" setup schematic view and Y89 sample location

1 Introduction

Experiment description "Energy plus Transmutation" (EpT) is an international research project realized in JINR Dubna. Its purpose is to investigate spallation neutron source consisting of U/Pb-assembly "Energy plus Transmutation" driven by accelerator NUCLOTRON. The assembly is a lead cylindrical target (8.4 cm diameter, 45.6 cm length) with natural uranium blanket (206.4 kg) [1]. High energy particles impinged on lead nuclei spalling them and producing neutrons among many other spallation products. The neutrons were multiplied in the uranium blanket. The project is leaded by Dr. M.I. Krivopustov. The research team constitute researchers from 12 countries. Each research group applied its preferred methods of measurement. Various neutron detectors are used, mainly activation ones but also SSNTDs and ^{3}He neutron counter. Polish group used Yttrium-89 samples – see Fig. 1. for sample location. This work is based on two experiments with deuteron beam – 1.6 GeV and 2.52 GeV ones. The 1.6 GeV experiment was carried out on December 18, 2006. The time of irradiation in deuteron beam was 24,480 s to collect about 2.08×10^{13} deuterons. The 2.52 GeV was carried out on November 30, 2005 with irradiation time 21,600 s and collected deuterons 6.45×10^{12}.

2 Yttrium-89 as an activation detector

Yttrium-89 is the only stable isotope of Yttrium. It makes it very attractive for neutron measurements because of simplicity to trace the reaction. There are no overlapping reactions, reaction products. We used reactions Y89(n,2n)Y88, Y89(n,3n)Y87

Table 1 Yttrium-89 basic activation data

Reaction	Produced isotope	$T_{1/2}$	Reaction threshold [MeV]	Basic γ-lines energy [keV]	γ-line intensity [%]
Y89(n,2n)	Y88	106.65d	11.5	898.042	93.7
				1836.063	99.2
Y89(n,3n)	Y87	79.8h	20.8	388.53	82.0
				484.805	89.7
Y89(n,4n)	Y86	14.74h	32.7	1076.64	82.0

and Y89(n,4n)Y86 for our measurements – see Table 1 for details. Unfortunately the reaction cross section data in ENDFs cover only 0-20 MeV neutron energy range. Some assumptions had to be done to extend the cross sections to higher energies.

After some corrections for time, irradiation time, sample weight and more we got isotope k production rate in [nuclei/g/deuteron].

3 Results of measurements

The drawings below show the spatial distributions of Yttrium isotope production for the two experiments.

Yttrium isotope production distribution summary:

- Both experiment results are very similar. For the 1.6 GeV experiment there is axial distribution maximum on the second measurement plane – Plane 2, while for 2.52 GeV the maximum is between Plane 2 and Plane 3 (see Figs. 2, 3).
- Both experiment radial distribution has maximum in beam axis.

4 Spallation neutron spectrum unfolding

As the (n,xn) reactions are the threshold ones the yttrium isotope k production (I_k) depends on neutron spectrum in the way:

$$I_k = N \int_{E_{thr,k}}^{\infty} \varphi(E)\, \sigma_k\left(E, E_{thr,k}\right) dE, \quad k = 1,2,...,K \tag{1}$$

where: $N = 6.77 \times 10^{21}$ [nuclei/g]; $E_{thr,k}$ – reaction k threshold energy [MeV]; $\varphi(E)$ – neutron energy spectrum [n/cm^2/d/MeV]; $\sigma_k(E, E_{thr,k})$ – reaction k cross section [cm^2]; K – number of the threshold reactions.

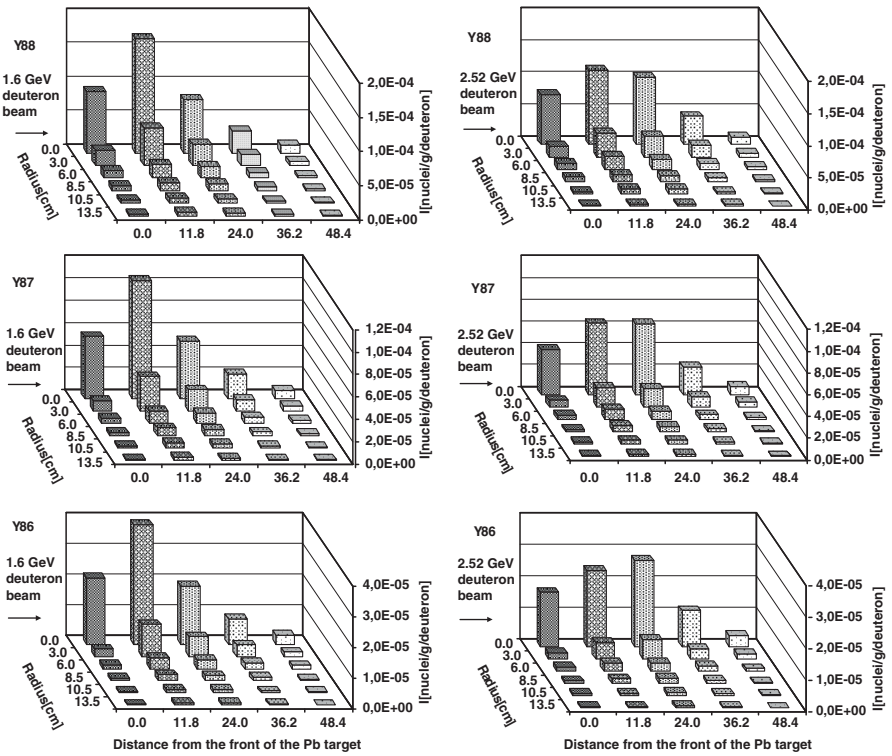

Fig. 2 Spatial distribution of ^{88}Y, ^{87}Y and ^{86}Y production comparison between the 1.6 GeV and 2.52 GeV experiment

To disclose the information about neutron energy spectrum in the EpT setup two spectral indexes $SI_{87/88}$ and $SI_{86/88}$ were defined:

$$SI_{87/88} = \frac{I_{87}}{I_{88}} = \frac{\int_{E_{87}}^{\infty} \varphi(E)\,\sigma_{87}(E,E_{87})\,dE}{\int_{E_{88}}^{\infty} \varphi(E)\,\sigma_{88}(E,E_{88})\,dE} \tag{2}$$

$SI_{86/88}$ index was defined in an analogical manner.

The drawings below show the spectral index spatial distributions.

Spatial distribution of the spectral indexes summary:

- Beam area out of consideration because of overlapping interactions with deuterons
- No dependence of the distribution on radius
- The distribution almost flat with slight growth while axial position growing
- Index values for Plane 1 (front of the target) are lesser than for the next planes

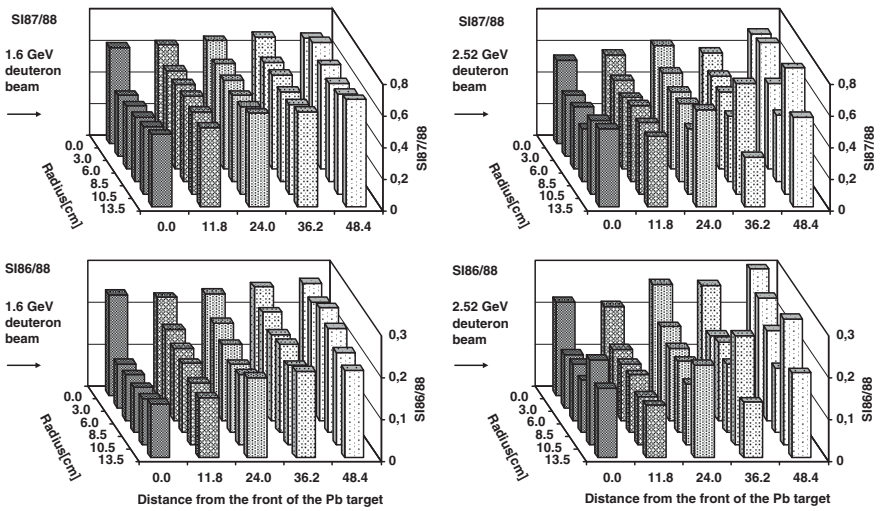

Fig. 3 Spatial distribution of spectral indexes $SI_{87/88}$ and $SI_{86/88}$ representing fast neutron spectrum above threshold energies 11.5, 20.8, and 32.7 MeV in "Energy plus Transmutation" setup

- $SI_{86/88}$ for 2.52 GeV experiment axial distribution differs from the 1.6 GeV one on Plane 2 (11.8 cm axial position) Plane 2 index for 2.52 GeV experiment has values lesser than for 1.6 GeV one, comparable with Plane 1 results. This suggests 2.52 GeV deuterons to penetrate dipper than 1.6 GeV ones.
- Plane 5 (rear of the target) index values are larger than on previous Planes. This seems to be the result of spallation neutron scattering while it flies along the axis.

Index spatial distributions suggest spallation neutron energy spectrum not to change much throughout the entire setup, slightly getting harder along the beam axis.

Nevertheless the two indexes are not enough to say what the neutron spectrum is like.

Purpose of this work is to present another method of neutron spectrum unfolding from yttrium sample irradiation results.

Equation (1) is in fact a set of equations. In our case it is the set of three equations:

$$\begin{aligned} I_{88} &= N \int_{E_{88}}^{\infty} \varphi(E)\, \sigma_{88}(E, E_{88})\, dE \\ I_{87} &= N \int_{E_{87}}^{\infty} \varphi(E)\, \sigma_{87}(E, E_{87})\, dE \\ I_{86} &= N \int_{E_{86}}^{\infty} \varphi(E)\, \sigma_{86}(E, E_{86})\, dE \end{aligned} \tag{3}$$

All the three values I_{88}, I_{87}, I_{86} are known from experiment. All three represent various yttrium isotope production rate in one point of the "Energy plus Transmutation" setup. Each of them differs from each other with reaction threshold energy. The idea is that all three points/values (I_{88}, I_{87}, I_{86}) define a continuous function $I(E_{thr})$ – see Fig. 4.

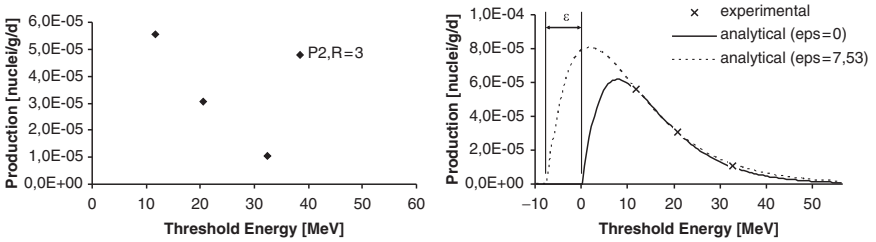

Fig. 4 Yttrium isotope production versus reaction threshold energy (left) and class of functions $I(E_{thr}, \varepsilon)$ defined by the isotope production points (right)

In fact they define a class of functions $I(E_{thr}, \varepsilon)$ with ε as the parameter of the class, expressed in units of energy. The function has no physical meaning but is very useful. Its analytical form is:

$$I\left(E'_{thr}\right) = \kappa E'_{thr} e^{-\eta E'_{thr}} = \kappa\left(E_{thr} + \varepsilon\right) e^{-\eta\left(E_{thr}+\varepsilon\right)} \tag{4}$$

Next assumption based on [6] is that reaction Y89(n,2n)Y88 cross section can be approximated by equation

$$\sigma_{88} = \alpha\left(E - E_{88}\right) e^{-\beta\left(E-E_{88}\right)} \tag{5}$$

throughout energy range E_{88} to infinity. It means that it is assumed reaction model through compound nucleus.[1]

The last assumption is based on fact that in compound nucleus nucleon excitation energy is so high, that energy levels are very dense, practically no nucleus structure is seen. The nuclei interact only when they collide, like particles of the ideal gas. It is assumed that the only difference between Y89(n,2n), (n,3n) and (n,4n) is threshold energy. What more the shape of the reaction cross section is the same, but shifted along the threshold energy axis – see Fig. 5.

For any threshold energy E_{thr} it can be expressed as:

$$\sigma\left(E, E_{thr}\right) = \alpha\left(E - E_{thr}\right) e^{-\beta\left(E-E_{thr}\right)} \tag{6}$$

Again, this is a class of functions with E_{thr} as the parameter of the class.

All the three assumptions transform the equation set (1) or (3) into one integral equation,

$$\alpha N \int_{\infty}^{E_{thr}} \left(E - E_{thr}\right) e^{-\beta E} \varphi\left(E\right) dE + I\left(E_{thr}, \varepsilon\right) e^{-\beta E_{thr}} = 0 \tag{7}$$

[1] Reaction model through compound nucleus – According to this model the reaction has two stages. In the first one the compound nucleus is created by absorption of the neutron. It has too much energy to be fully bound together. In the second stage, on a time scale of about 10^{-19} s, particles, usually neutrons, are "boiled" off. That is, it remains together until enough energy happens to be concentrated in one neutron to escape the mutual attraction.

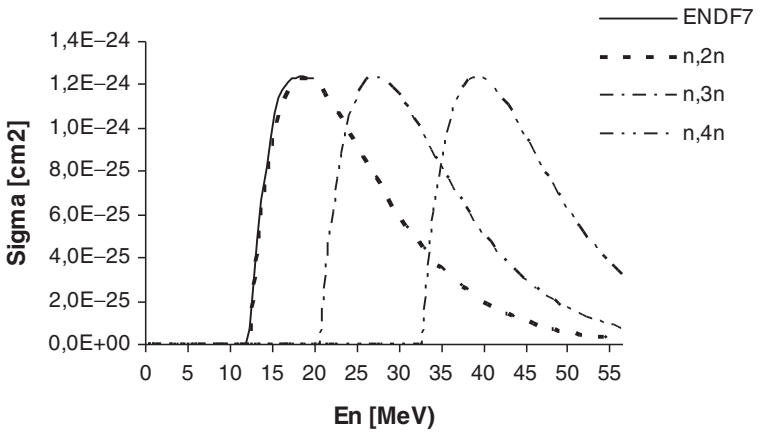

Fig. 5 Assumed Y89(n,xn) reaction cross section for various number of emitted neutrons. ENDF7 means data from ENDF/B-VII data file

example of Volterra's integral equation of the first kind with the nucleus $K(E,E_{thr}) = (E-E_{thr})E^{-\beta E}$. Its solution (spallation neutron spectrum) has a form:

$$\varphi(E_{thr}) = \frac{\kappa(\eta+\beta)^2}{\alpha N}\left[E_{thr}+\varepsilon-\frac{2}{(\eta+\beta)}\right]e^{-\eta(E_{thr}+\varepsilon)} \tag{8}$$

Requesting $\varphi(E\leq 0)=0$ and $\varphi(E\to\infty)\to 0$ one gets:

$$\varepsilon = \frac{2}{\eta+\beta} \tag{9}$$

and solution

$$\varphi(E) = \frac{\kappa(\eta+\beta)^2}{\alpha N}Ee^{-\eta\left(E+\frac{2}{\eta+\beta}\right)} \tag{10}$$

where the coefficients are determined experimentally as:

$$\begin{aligned}
\kappa &= \left(\frac{I_{88}}{E'_{88}}\right)^{\frac{E'_{87}}{E_{87}-E_{88}}}\left(\frac{E'_{87}}{I_{87}}\right)^{\frac{E'_{88}}{E_{87}-E_{88}}}\\
\eta &= \frac{1}{E_{87}-E_{88}}\ln\left(\frac{I_{88}E'_{87}}{E_{88}I_{87}}\right)\\
\alpha &= 5.2\times 10^{-25}\\
\beta &= 0.155
\end{aligned} \tag{11}$$

The coefficients are dimensioned: $[\kappa]$, $[\eta]$ and $[\beta]$ in $[\mathrm{MeV}^{-1}]$ and $[\alpha]$ in $[\mathrm{cm}^2/\mathrm{MeV}]$.

Table 2 Neutron spectrum function $\varphi(E)$ parameters

Param.	PLANE Ed	P1	P2	P3	P4	P5
η[MeV^{-1}]	1.6	0,15	0,11	0,10	0,10	0,08
	2.52	0,15	0,13	0,11	0,12	0,08
$E_{\varphi\max}$[MeV]	1.6	6,61	9,03	9,78	9,99	12,95
	2.52	6,61	7,97	8,80	8,41	12,87

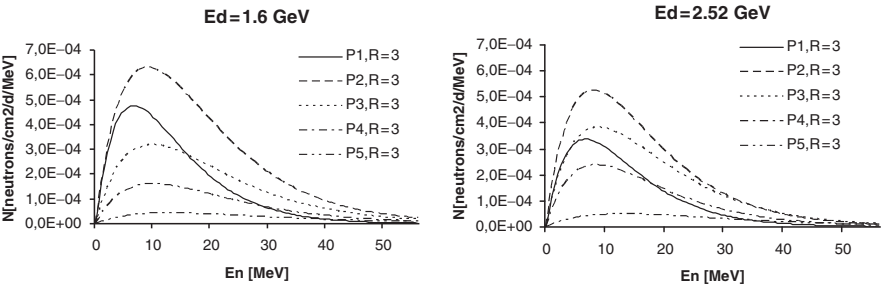

Fig. 6 Comparison of the spallation neutron spectra in several axial positions on $R = 3$ axis for 1.6 GeV and 2.52 GeV deuteron experiment

The formula (10) spectrum has maximum in:

$$\varphi_{\max} = \varphi\left(E = \frac{1}{\eta}\right) \tag{12}$$

The parameters η and $E_{\varphi\max}$ for various axial positions along axis $R = 3$ cm are shown in Table 2.

Below (see Figs. 6–9) there are various graphical comparisons of the results of the two experiments – 1.6 GeV and 2.52 GeV deuterons.

5 Conclusions

- "Energy plus Transmutation" project brings interesting results.
- The presented here method of pallation neutron spectrum unfolding makes possible to get a lot of information from a very limited number of the experimental data.
- The method needs more work. First of all it is to be explained why is the maximum of the spectrum shifted to high neutron energies.

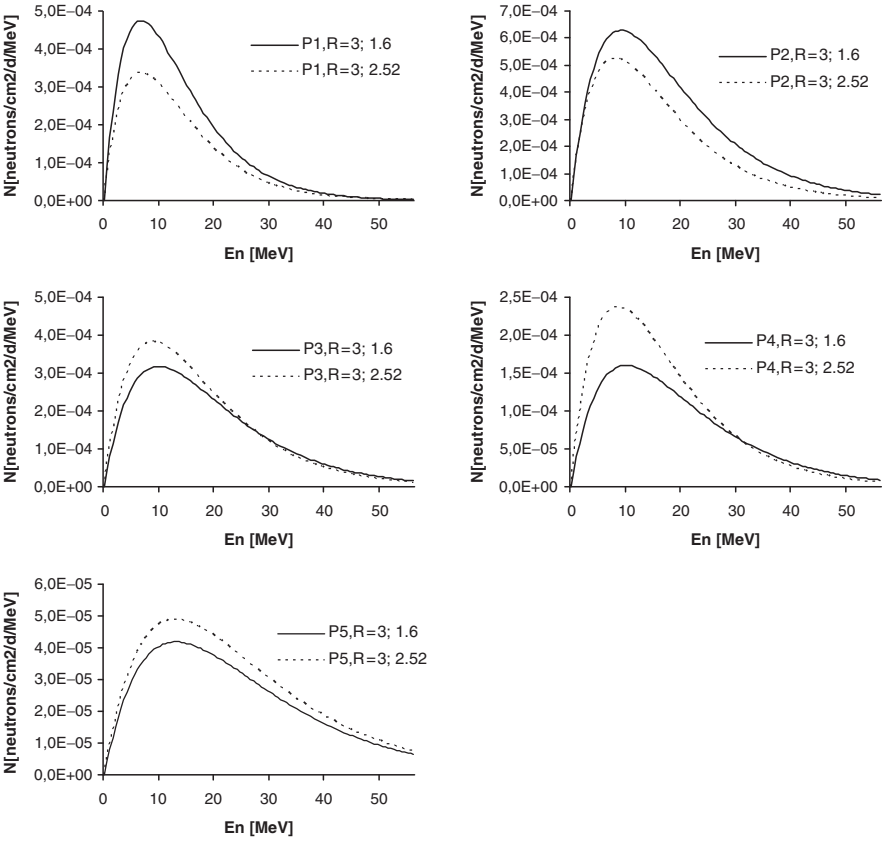

Fig. 7 Comparison "one by one" of the spallation neutron spectra in several axial positions on $R = 3$ axis for 1.6 GeV and 2.52 GeV deuteron experiment

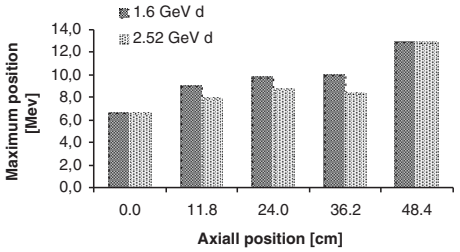

Fig. 8 Comparison of neutron spectrum maximum position (energy) versus axial position for 1.6 GeV and 2.52 GeV deuteron experiment

- It worth to check if the other activation detectors (Au) give the similar results.
- It worth to compare deuteron beam experiment results with the proton ones.
- Error analysis to be done yet.

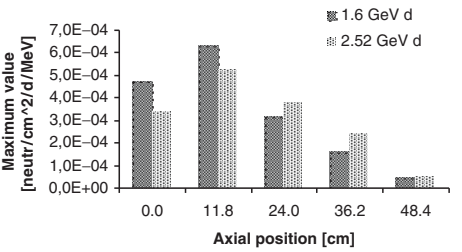

Fig. 9 Comparison of neutron spectrum maximum value versus axial position for 1.6 GeV and 2.52 GeV deuteron experiment

References

1. Krivopustov, M.I., et al.: On a First Experiment on the Calorimetry of an Uranium Blanket Using the Model of the U/Pb Electro-Nuclear Assembly "Energy Plus Transmutation" on a 1.5 GeV Proton Beam from the Dubna Synchrophasotron, Russ. JINR Preprint, P1-2000-168
2. Frana, J.: Program DEIMOS32 for Gamma Ray Spectra Evaluation. Radioanal. and Nucl. Chem. **257** (2003) 583
3. Bielevich, M., Szuta, M., Strugalska-Gola, E., et al.: On the Experiment of Neutron Spectrum Investigation on U/Pb-Assembly Using 0.7 GeV Proton Beam from the Nuclotron (Dubna). In Proceeding XVII International Baldin Seminar on High Energy Physics Problems. Relativistic Nuclear Physics and Quantum Chromodinamics (27 September–2 October, 2004, Dubna, Russia). Dubna (2005), V. II, pp. 125–132
4. Krivopustov, M.I., et al.: About the First Experiment on Investigation of ^{129}I, ^{237}Np, ^{238}Pu and ^{239}Pu Transmutation at the Nuclotron 2.52 GeV Deuteron Beam in Neutron Field Generated in U/Pb-Assembly "Energy Plus Transmutation". JINR Preprint E1-2007-7. Dubna (2007)
5. Martsynkevich, B.A., et al.: "Unfolding of Fast Neutron Spectra in the Wide Energy Range (up to 200 MeV) in Heterogeneous Subcritical Assembly of an Electronuclear System "Energy plus Transmutation". in Russ. JINR preprint P1-2002-65
6. Smith, A.B., Smith, D.L., Rousset, P., Lawson, R.D., and Howerton, R.J. "Evaluated Neutronic Data File for Yttrium", ANL/NDM-94, January 1986

Remarks on Muon Radiography

M. Szeptycka and P. Szymański

Abstract Non-proliferation is one of the key aspects of the safe use of nuclear energy. The legal framework on transport of nuclear material and other dual use technologies requires ways of control of its proper application. Verification of the cargo contents is one of such ways. Different methods can be applied. In this paper we discuss feasibility of the use cosmic muons for identification of materials transported in the sealed containers. The state-of-the-art in muon radiography is discussed. We present Monte Carlo based results on cargo material dependence of some observables. Influence of the detector system performance and layout on the detection capabilities is discussed.

Keywords: Non-proliferation, cosmic rays, illicit trafficking, nuclear material, homeland security, nuclear security, nuclear safety, cargo, inspection, boarder control

1 Introduction

The non-proliferation is one of the key aspects of the safe use of nuclear energy. Verification of the contents of cargo containers is one of the ways to prevent illicit trafficking of nuclear materials. It must be fast, reliable and safe for people working in the proximity of the test facility. Cargo examination method must not harm people hidden inside the container. Due to the large quantity of cargo transported in the world non-invasive control methods are necessary. Most of them use ionizing radiation to penetrate sealed containers and identify chemical composition

M. Szeptycka
The Andrzej Soltan Institute for Nuclear Studies, Hoza 69, 00-681 Warsaw, Poland,
e-mail: Maria-H.Szeptycka@fuw.edu.pl

P. Szymański
The Andrzej Soltan Institute for Nuclear Studies, 05-400 Otwock-Swierk, Poland,
e-mail: Piotr.Szymanski@ipj.gov.pl

V. Begun et al. (eds.), *Progress in High-Energy Physics and Nuclear Safety*,

and shapes of transported material. Balancing of the effectiveness and safety hazard represents one of the challenges in the design of the cargo inspection system. System exploiting the cosmic muons is free from the radiation safety restrictions. It could be deployed practically everywhere, especially at truck parking lots. Lack of the radiation source should make them relatively cheap. This justify the interest in use of the cosmic ray muons for the cargo inspection in a search for nuclear material.

2 Muons and their properties

Muons are produced by particles of cosmic radiation interacting with the Earth atmosphere. Charge of muons equals ± 1, mass 105.65 MeV/c^2. They decay predominantly into electron, neutrino and anti-neutrino. The lifetime of approximately 2.2 μs allows relativistic muons to travel up to 660 m in vacuum. The flux of muons at the sea level equals on average 100 muons/m^2/sr/s. Muons do not interact strongly. Relatively large lifetime and small interaction cross-section allow muons to travel large distances.

For relativistic muons energy loss is approximately independent from muon momentum and amounts to ≈ 2 MeV/g/cm^2 which corresponds to 1.4 GeV per meter of steel.

$$E_{tot}^{loss} \sim L\,[\mathrm{cm}] \cdot \rho\ [\mathrm{g/cm^3}] \tag{1}$$

E_{tot}^{loss} is the muon total energy loss in the layer of thickness L of the material of density ρ.

Muons passing through matter undergo multiple Coulomb scattering. For muon with momentum p [MeV/c] traversing material of thickness L average scattering angle $\Theta_0[rad]$ is approximated by the equation 2 where L_0 denotes material radiation length and β is muon reduced velocity.

$$\Theta_0 = \frac{13.6}{\beta cp}\sqrt{\frac{L}{L_0}}\left[1 + 0.038 \cdot \ln\left(\frac{L}{L_0}\right)\right] \tag{2}$$

Values of Θ_0 for 4GeV/c muons passing through 5 cm of various materials are shown in Table 1. The scattering angle Θ_0 can be MEASURed only if it is larger than the detector resolution.

Table 1 Mean scattering angle Θ_0 for 4 GeV/c muons passing through 5 cm of various materials

Material	Θ_0 [mrad]
Air	0.04
Plastic	1.5
Aluminum	3.5
Steel	8.4
Lead	15.6
Uranium	21.0

3 Comparison of cargo screening technologies

Comparison of various cargo screening technologies has been presented in [1], the source of Table 2. The methods using neutrons, X and γ rays are compared to cosmic ray muons.

The flux attenuation for muons as a function of lead layer thickness is presented in Fig. 1 taken from [2]. The 4 cm thick layer of lead stops approximately 90% of 500 keV X-rays.

One may conclude that cosmic muons are the most versatile radiation for the cargo inspection. It is naturally occurring radiation, with no danger of exposing persons hidden in cargo to dangerous doses of radiation. There are no radiation safety regulations to implement. Muons show detectable interactions with heavy elements, allowing for nuclear material detection. They can also penetrate heavy shielding. However intensity of the cosmic rays is relatively low, which may lead to long inspection times. Small scattering angles may require elaborate complicated systems, leading to operational problems and high cost. The detector system must be sensitive enough to measure quite small changes of muon characteristics caused by passing through matter.

Table 2 Comparison of the cargo screening technologies [1]

Feature	μ detector	Fast neutrons	X rays	γ rays
Identify nuclear weapons, materials and dirty bomb	Yes	Yes	0.1–5MeV; no	No
			Passive detection only	
Locate hidden voids	Yes	No	No	No
See through all materials	Yes	No not hydrocarbons, plastics	No	No
			not heavy metals	
Immunity to false alarms	Potentially high	High	Depends on operator skill	
Artificial radiation free operation	Yes	No	No	No
		special licensing required		

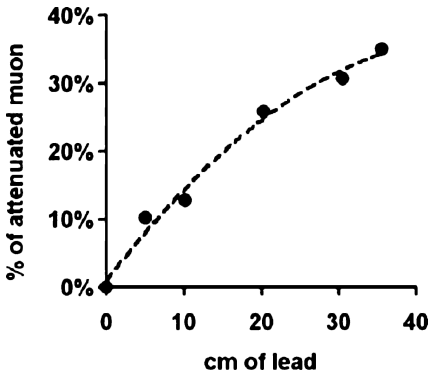

Fig. 1 Muon attenuation in lead [2]

4 The idea of the muon cargo screening technology

The idea of the cargo screening with muons relies on the measurement of the muon parameters before and after passing through the cargo container. The analysis of the muon trajectory and distribution of coordinates of scattering points allows to identify the change of the density of cargo material.

The Fig. 2 [2] shows the vehicle transporting nuclear explosive device and the muon detection system. Muon detectors installed above the inspected vehicle record the directions of muons before entering the inspected vehicle. Detectors under the road surface register directions of muons after passing through the cargo. The vehicle must remind stationary for the time necessary for the effective inspection. The detectors used for muon detection must be able to operate in variable conditions of temperature/humidity. For the detector design it is necessary to determine the precision necessary for material identification.

Some properties of muon detectors will be presented in the next section.

5 Muon detectors

Two types of muon detectors: scintillator counters and gas multiwire detectors. Both types require readout electronics, trigger system, data acquisition and analysis software. Typical sizes of the cargo containers will require large detector surfaces. This may rule out scintillator detectors due to their cost.

Multiwire chamber consists of thin, parallel and equally spaced anode wires symmetrically sandwiched between two cathode planes. Cathode can consist either of a plane of thin equally spaced wires or a conductor plane. Cathodes are connected to negative voltage. Anode wires are grounded. This creates homogeneous electric

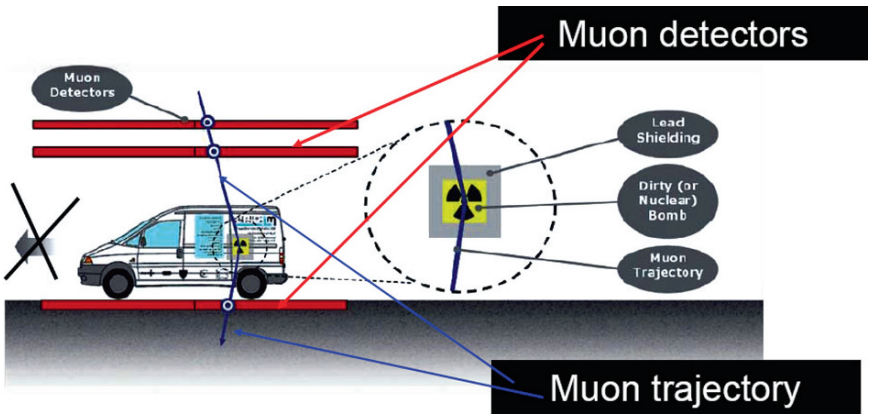

Fig. 2 Muon screening principle [2]

field in most regions of the chamber. Electric field increases rapidly around anode wires. A charged particle passing through the detector ionizes gas, liberated electrons follow electric field lines towards anode wires. Strong field very close to wire acts as a multiplication region: energy of electrons increases, they ionize gas and such created avalanche of electrons reaches the anode wire. Electrical pulses are read out from the anode wires. Pulse height depends on the composition of the gas, its temperature and pressure, applied voltage, geometry of the chamber.

Multiple plane wire chambers with different wire inclination angles allow reconstruction of particle trajectories in space.

Space resolution of detector is mostly defined by the distance between wires ("pitch"), lever arm of track measurement, alignment of the chambers.

Muon chambers of the HERMES experiment [3] may be used as an example of the muon detection system. Active area of the modules are between 263×996 mm^2 and 347×1424 mm^2. Sense and cathode wires are spaced by 2 mm and 0.5 mm respectively. Anode wires are made of 25 μm gold plated tungsten while cathode wires are of 90 μm gold plated bronze. Nonflammable gas mixture of Ar(65%), CO_2(30%) and CF_4(5%) at atmospheric pressure is used.

6 State of the art of muon radiography in cargo monitoring

We are not aware of any commercial cargo inspection equipment based on the muon radiography (see Fig. 3). Here we will present some pioneering work in this filed.

6.1 Images of tungsten cylinder

The work of K.N. Borozdin et al. [4] presents the results (4 on the reconstruction of the shape of tungsten cylinder (radius 5.5 cm, length 5.7 cm). It was supported by a plastic plate laying on two steel support rails. The wire chambers (60×60 cm^2) with two coordinates readout were placed at the distance of 27 cm, two chambers above and two chambers below the cylinder. It is clearly visible. It is not clear to us how long the measurement lasted to obtain this image.

6.2 Proposal to use LHC CMS muon chambers

M. Benettoni et al. [5] proposed to use for muon radiography muon chambers designed for the CMS experiment at CERN LHC accelerator. Detectors with active area of 7 m^2 have angular resolution of the order of 1mrad in one direction and 10 mrad in the other. Sandwich of chambers and iron layers is used for muon momentum estimation. Experiment in Padova is under way.

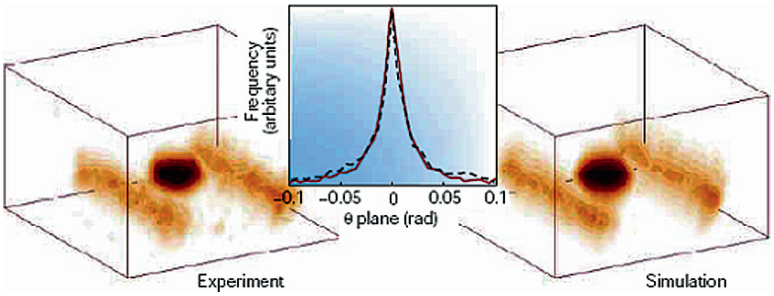

Fig. 3 Muon radiography experiment and Monte Carlo simulation of [4]

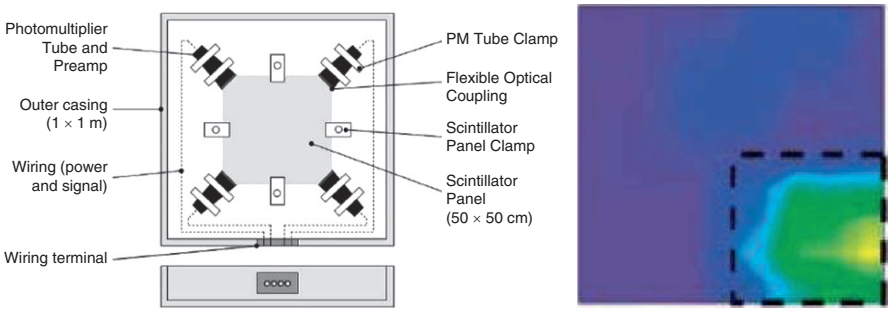

Fig. 4 (a) Muon detector of [2] (b) image of 15 cm thick lead brick seen with it

6.3 Two dimensional muon based density mapping

S.J.Stanley et al. [2] constructed detector (Fig. 4a) with plastic scintillator readout with four photomultipliers. Muon position is reconstructed through the center of gravity of photomultipliers' signals. Photomultipliers are calibrated with light emitting diodes. After 6 h of data taking and some image processing piece of lead 15 cm thick is clearly seen in Fig. 4b.

7 Present work – feasibility of the full scale muon cargo screening detector

We aim at the estimation of the measurement time and the detector parameters necessary for obtaining an information about the presence of a suspicious load in the cargo. For this purpose a GEANT4 [6] based Monte Carlo simulation is used. The geometry(shown in Fig. 5a) consists of two sets of chambers placed above and below the cargo. Each chamber measures two coordinates in the horizontal plane. Only events with one hit in each of the chambers are analyzed.

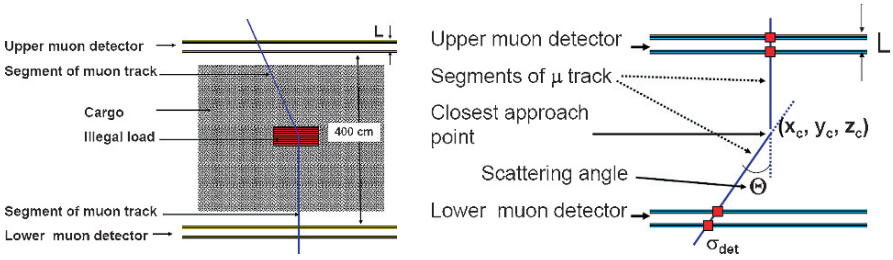

(a) Geometry (b) Observables related to the muon trajectory

Fig. 5 Simulation used in the current work

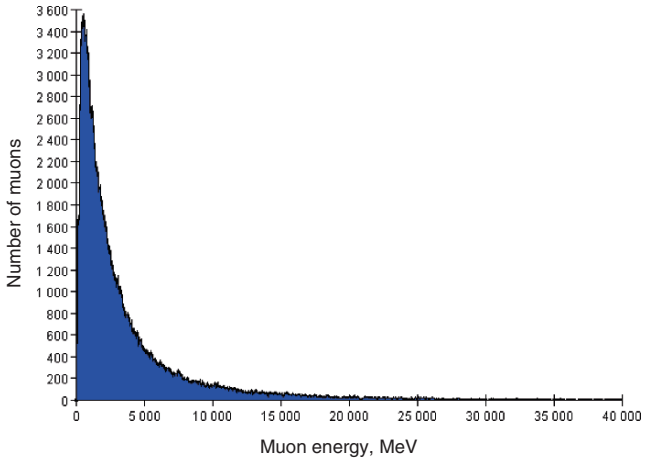

Fig. 6 Muon energy distribution used in the realistic version of the muon generator

We use observables related to the change of the muon direction due to the multiple scattering (Fig. 5b). From the measurements of the two points on the muon trajectory above and below the cargo we determine:

- The scattering angle Θ
- The distance of closest approach of the upper and lower track segments δ
- The coordinates of the region of the closest approach of the upper and lower track segments

Two effects are studied: dependence of the observables on cargo material and on the detector parameters. Two versions of muon generators are used. In the simplified version vertical muons with fixed momentum are generated. In the realistic version zenithal angle (θ) distribution proportional to $\cos^2\theta$ and energy distribution according to [7] (shown in Fig. 6) are used.

Table 3 Mean scattering angle Θ for various materials - Monte Carlo results

Material	Mean scattering angle Θ
400 cm air	0.04
395 cm air + 5 cm Al	0.4
395 cm air + 5 cm Pb	2

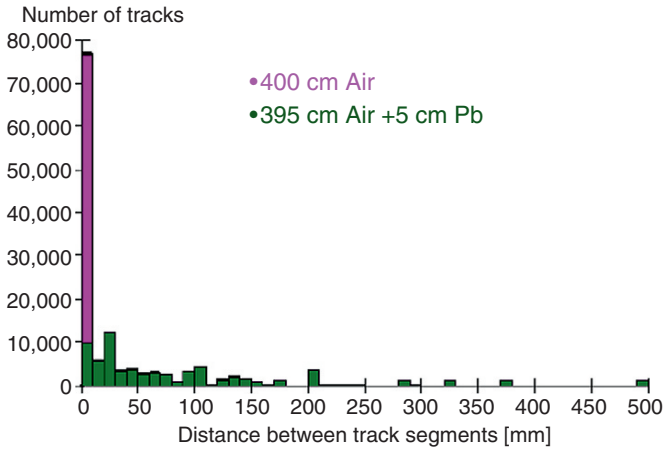

Fig. 7 Distributions of distance between track segments for muons traversing 400 cm of air, as well as 5 cm of lead and 395 cm of air

7.1 Dependence of observables on the cargo material

For various materials we present in Table 3 the mean scattering angle Θ for 30 GeV muons and the ideal detectors. The distributions of δ for 400 cm of air (395 cm of air and 5 cm of lead) are presented in Fig. 7.

Change of the muon generator from simplified to realistic results in change of the mean scattering angle from 0.04 mrad to 3.4 mrad for 400 cm air.

7.2 Dependence of the observables on the detector parameters

The spacial resolution σ_{det} is assumed to be the same for all the chambers in both horizontal directions. The vertical coordinate is measured perfectly well. Dependence of the scattering angle Θ on σ_{det} is presented in Table 4. The effect of the finite position resolution may be compensated by increasing the distance L between the chambers within upper (lower) detector. Summary of results is presented in Fig. 8.

Table 4 Dependence of the mean muon scattering angle Θ as a function of the detector spacial resolution σ_{det}. Simplified muon generator and 400 cm air

σ_{det} [mm]	Θ [mrad]
0.	0.04
0.3	3.4
3.0	34.

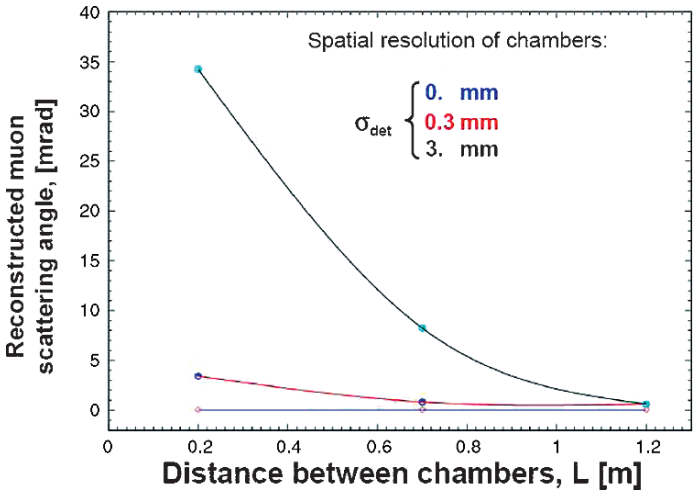

Fig. 8 Mean reconstructed muon scattering angle Θ as a function of the distance between the chambers L and chambers' spacial resolution σ_{det}

8 Conclusions

When designing the muon radiography system for cargo inspection one should keep in mind that detector performance may "shadow" the difference between various materials. The necessary irradiation time should be estimated and is one of the key performance figures of the system. The MC simulation with realistic momentum and angular distributions of muons is essential. The work is in progress.

Acknowledgements It is a great pleasure to thank the Organizers of the Conference for the very pleasant, interesting and stimulating meeting.

References

1. T. Kochanski, "A Novel Method of Detecting Shielded Nuclear Weapons and Voids in Cargo" (Revised Feb 28, 2008)
2. S.J. Stanley et al. in: Proceedings of an International Conference on Illicit Nuclear Trafficking: Collective Experience and the Way Forward. (Edinburgh, 2007), p. 571

3. K. Ackerstaff et al., Nucl. Instr. and Meth. A**417** (1998) 230
4. K.N. Borozdin et al., Rev. Sci. Instr. **74** (2003) 4294
5. M.Benettoni et al. in IEEE NSS Conference Record vol. 2 (2007) 1021
6. S. Agostinelli et al., Nucl. Instr. and Meth. A**506** (2003) 250, J.Allison et al., IEEE Trans. Nucl. Sci. **53** No. 1 (2006) 270
7. J. Kremer et al., Phys. Rev. Lett. **83** (1999) 4241

Author's Index

Subject Index